ECS The Electrochemical Society Series

Electrochemical Impedance Spectroscopy

Mark E. Orazem & Bernard Tribollet

WILEY

ELECTROCHEMICAL IMPEDANCE SPECTROSCOPY

THE ELECTROCHEMICAL SOCIETY SERIES

ECS-The Electrochemical Society
65 South Main Street
Pennington, NJ 08534-2839
http://www.electrochem.org

A complete list of the titles in this series appears at the end of this volume.

ELECTROCHEMICAL IMPEDANCE SPECTROSCOPY

MARK E. ORAZEM
University of Florida

BERNARD TRIBOLLET
Université Pierre et Marie Curie

WILEY

A JOHN WILEY & SONS, INC., PUBLICATION

Copyright © 2008 by John Wiley & Sons, Inc. All rights reserved.

Published by John Wiley & Sons, Inc., Hoboken, New Jersey.
Published simultaneously in Canada.

No part of this publication may be reproduced, stored in a retrieval system, or transmitted in any form or by any means, electronic, mechanical, photocopying, recording, scanning, or otherwise, except as permitted under Section 107 or 108 of the 1976 United States Copyright Act, without either the prior written permission of the Publisher, or authorization through payment of the appropriate per-copy fee to the Copyright Clearance Center, Inc., 222 Rosewood Drive, Danvers, MA 01923, (978) 750-8400, fax (978) 750-4470, or on the web at www.copyright.com. Requests to the Publisher for permission should be addressed to the Permissions Department, John Wiley & Sons, Inc., 111 River Street, Hoboken, NJ 07030, (201) 748-6011, fax (201) 748-6008, or online at http://www.wiley.com/go/permission.

Limit of Liability/Disclaimer of Warranty: While the publisher and author have used their best efforts in preparing this book, they make no representations or warranties with respect to the accuracy or completeness of the contents of this book and specifically disclaim any implied warranties of merchantability or fitness for a particular purpose. No warranty may be created or extended by sales representatives or written sales materials. The advice and strategies contained herein may not be suitable for your situation. You should consult with a professional where appropriate. Neither the publisher nor author shall be liable for any loss of profit or any other commercial damages, including but not limited to special, incidental, consequential, or other damages.

For general information on our other products and services or for technical support, please contact our Customer Care Department within the United States at (800) 762-2974, outside the United States at (317) 572-3993 or fax (317) 572-4002.

Wiley also publishes its books in a variety of electronic formats. Some content that appears in print may not be available in electronic format. For information about Wiley products, visit our web site at www.wiley.com.

Library of Congress Cataloging-in-Publication Data is available.

ISBN 978-0-470-04140-6

Printed in the United States of America.

10 9 8 7 6 5 4 3 2 1

Contents

Contents v

Preface xv

Acknowledgments xix

The Blind Men and the Elephant xxi

History of Impedance Spectroscopy xxv

I Background 1

1 Complex Variables 3

- 1.1 Why Imaginary Numbers? 3
- 1.2 Terminology 4
  - 1.2.1 The Imaginary Number 4
  - 1.2.2 Complex Variables 4
  - 1.2.3 Conventions for Notation in Impedance Spectroscopy . . 5
- 1.3 Operations Involving Complex Variables 5
  - 1.3.1 Multiplication and Division of Complex Numbers 6
  - 1.3.2 Complex Variables in Polar Coordinates 9
  - 1.3.3 Properties of Complex Variables 13
- 1.4 Elementary Functions of Complex Variables 13
  - 1.4.1 Exponential 15
  - 1.4.2 Logarithmic 16
  - 1.4.3 Polynomial 19
- Problems 20

2 **Differential Equations** . . . 23

2.1 Linear First-Order Differential Equations . . . 23
2.2 Homogeneous Linear Second-Order Differential Equations . . . 26
2.3 Nonhomogeneous Linear Second-Order Differential Equations . . 28
2.4 Partial Differential Equations by Similarity Transformations . . . 29
2.5 Differential Equations with Complex Variables . . . 32
Problems . . . 34

3 **Statistics** . . . 35

3.1 Definitions . . . 35
3.1.1 Expectation and Mean . . . 35
3.1.2 Variance, Standard Deviation, and Covariance . . . 35
3.1.3 Normal Distribution . . . 36
3.1.4 Probability . . . 38
3.1.5 Central-Limit Theorem . . . 39
3.2 Error Propagation . . . 43
3.2.1 Linear Systems . . . 43
3.2.2 Nonlinear Systems . . . 44
3.3 Hypothesis Tests . . . 47
3.3.1 Terminology . . . 48
3.3.2 Student's t-Test for Equality of Mean . . . 49
3.3.3 F-test for Equality of Variance . . . 50
3.3.4 Chi-Squared Test for Equality of Variance . . . 56
Problems . . . 58

4 **Electrical Circuits** . . . 61

4.1 Passive Electrical Circuits . . . 61
4.1.1 Circuit Elements . . . 61
4.1.2 Parallel and Series Combinations . . . 64
4.2 Fundamental Relationships . . . 66
4.3 Nested Circuits . . . 68
4.4 Mathematical Equivalence of Circuits . . . 69
4.5 Graphical Representation of Circuit Response . . . 70
Problems . . . 72

5 **Electrochemistry** . . . 73

5.1 Resistors and Electrochemical Cells . . . 73
5.2 Equilibrium in Electrochemical Systems . . . 74
5.3 Polarization Behavior for Electrochemical Systems . . . 76
5.3.1 Zero Current . . . 76
5.3.2 Kinetic Control . . . 78
5.3.3 Mass-Transfer Control . . . 79

5.4 Definitions of Potential . . . 80
5.5 Rate Expressions . . . 81
5.5.1 Law of Mass Action . . . 81
5.5.2 Generalized Electrode Kinetics . . . 83
5.6 Transport Processes . . . 85
5.6.1 Primary Current and Potential Distributions . . . 87
5.6.2 Application to Blocking Electrodes . . . 88
5.6.3 Secondary Current and Potential Distributions . . . 89
5.6.4 Tertiary Current and Potential Distributions . . . 90
5.6.5 Mass-Transfer-Controlled Current Distributions . . . 90
5.7 Potential Contributions . . . 90
5.7.1 Ohmic Potential Drop . . . 90
5.7.2 Surface Overpotential . . . 90
5.7.3 Concentration Overpotential . . . 91
5.8 Capacitance Contributions . . . 91
5.8.1 Double-Layer Capacitance . . . 91
5.8.2 Dielectric Capacitance . . . 95
Problems . . . 96

6 Electrochemical Instrumentation . . . 97

6.1 The Ideal Operational Amplifier . . . 97
6.2 Elements of Electrochemical Instrumentation . . . 99
6.3 Electrochemical Interface . . . 101
6.3.1 Potentiostat . . . 101
6.3.2 Galvanostat . . . 102
6.3.3 Potentiostat for EIS Measurement . . . 103
Problems . . . 105

II Experimental Considerations **107**

7 Experimental Methods . . . 109

7.1 Steady-State Polarization Curves . . . 109
7.2 Transient Response to a Potential Step . . . 109
7.3 Analysis in Frequency Domain . . . 110
7.3.1 Lissajous Analysis . . . 111
7.3.2 Phase-Sensitive Detection (Lock-in Amplifier) . . . 117
7.3.3 Single-Frequency Fourier Analysis . . . 119
7.3.4 Multiple-Frequency Fourier Analysis . . . 121
7.4 Comparison of Measurement Techniques . . . 122
7.4.1 Lissajous Analysis . . . 122
7.4.2 Phase-Sensitive Detection (Lock-in Amplifier) . . . 122
7.4.3 Single-Frequency Fourier Analysis . . . 123
7.4.4 Multiple-Frequency Fourier Analysis . . . 123

7.5 Specialized Techniques 123
7.5.1 Transfer Function Analysis 123
7.5.2 Local Electrochemical Impedance Spectroscopy 124
Problems 128

8 Experimental Design 129

8.1 Cell Design 129
8.1.1 Reference Electrodes 129
8.1.2 Flow Configurations 131
8.1.3 Current Distribution 132
8.2 Experimental Considerations 133
8.2.1 Frequency Range 133
8.2.2 Linearity 134
8.2.3 Modulation Technique 146
8.2.4 Oscilloscope 147
8.3 Instrumentation Parameters 147
8.3.1 Improve Signal-to-Noise Ratio 147
8.3.2 Reduce Bias Errors 149
8.3.3 Improve Information Content 151
Problems 152

III Process Models **153**

9 Equivalent Circuit Analogs 155

9.1 General Approach 155
9.2 Current Addition 156
9.2.1 Impedance at the Corrosion Potential 156
9.2.2 Partially Blocked Electrode 157
9.3 Potential Addition 158
9.3.1 Electrode Coated with an Inert Porous Layer 158
9.3.2 Electrode Coated with Two Inert Porous Layers 159
Problems 162

10 Kinetic Models 163

10.1 Electrochemical Reactions 163
10.2 Reaction Dependent on Potential Only 164
10.3 Reaction Dependent on Potential and Mass Transfer 169
10.4 Coupled Reactions Dependent on Potential and Surface Coverage 173
10.5 Reactions Dependent on Potential, Surface Coverage, and Transport 176
Problems 180

11 Diffusion Impedance 183

11.1 Uniformly Accessible Electrode 184
11.2 General Mathematical Framework 185
11.3 Stagnant Diffusion Layer 189
11.4 Diffusion through a Solid Film 191
    11.4.1 Region of Film Diffusion Control 191
    11.4.2 Film Impedance Response 194
11.5 Coupled Diffusion Impedance 198
11.6 Rotating Disk 198
    11.6.1 Fluid Flow 199
    11.6.2 Mass Transfer 200
    11.6.3 Classification of Models for Convective Diffusion 201
11.7 Submerged Impinging Jet 205
    11.7.1 Fluid Flow 206
    11.7.2 Mass Transfer 206
11.8 Rotating Cylinders 207
    Problems 210

12 Semiconducting Systems 211

12.1 Semiconductor Physics 211
    12.1.1 Electrons and Holes as Species 212
    12.1.2 Doping 214
    12.1.3 Deep-Level States 216
    12.1.4 Shockley-Read-Hall Processes 217
    12.1.5 Interfaces 218
12.2 Steady-State Models 219
    12.2.1 Mass Transfer 219
    12.2.2 Space-Charge Region 220
    12.2.3 Application to Electrolyte–Semiconductor Junctions 221
12.3 Impedance Models 223
    12.3.1 Equivalent Electrical Circuits 223
    12.3.2 Mott-Schottky Analysis 225
    Problems 230

13 Time-Constant Dispersion 233

13.1 Constant-Phase Elements 233
    13.1.1 2-D and 3-D Distributions 234
    13.1.2 Determination of Capacitance 236
    13.1.3 Limitations to the Use of the CPE 236
13.2 Convective Diffusion Impedance at Small Electrodes 237
    13.2.1 Analysis 238
    13.2.2 Local Diffusion Convective Impedance 239
    13.2.3 Global Convective Diffusion Impedance 242

13.3 Geometry-Induced Current and Potential Distributions 243
  13.3.1 Mathematical Development 244
  13.3.2 Global and Local Impedances 246
13.4 Porous Electrodes 252
13.5 Oxide Layers 260
  Problems 263

14 Generalized Transfer Functions 265

14.1 Multi-Input/Multi-Output Systems 265
  14.1.1 Current or Potential Are the Output Quantity 269
  14.1.2 Current or Potential Are the Input Quantity 270
  14.1.3 Experimental Quantities 272
14.2 Transfer Functions Involving Exclusively Electrical Quantities . . 273
  14.2.1 Ring-Disk Impedance Measurements 273
  14.2.2 Multifrequency Measurements for Double-Layer Studies . 275
14.3 Transfer Functions Involving Nonelectrical Quantities 278
  14.3.1 Thermoelectrochemical (TEC) Transfer Function 278
  14.3.2 Photoelectrochemical Impedance Measurements 282
  14.3.3 Electrogravimetry Impedance Measurements 283
  Problems 284

15 Electrohydrodynamic Impedance 285

15.1 Hydrodynamic Transfer Function 287
15.2 Mass-Transport Transfer Function 290
  15.2.1 Asymptotic Solution for Large Schmidt Numbers 293
  15.2.2 Asymptotic Solution for High Frequencies 294
15.3 Kinetic Transfer Function for Simple Electrochemical Reactions . 295
15.4 Interface with a 2-D or 3-D Insulating Phase 296
  15.4.1 Partially Blocked Electrode 296
  15.4.2 Rotating Disk Electrode Coated by a Porous Film 299
  Problems 306

IV Interpretation Strategies 307

16 Methods for Representing Impedance 309

16.1 Impedance Format 311
  16.1.1 Complex-Impedance-Plane Representation 312
  16.1.2 Bode Representation 314
  16.1.3 Electrolyte-Resistance-Corrected Bode Representation . . 316
  16.1.4 Impedance Representation 317
16.2 Admittance Format 319
  16.2.1 Admittance-Plane Representation 320
  16.2.2 Admittance Representation 321

16.2.3 Electrolyte-Resistance-Corrected Representation 324
16.3 Complex-Capacitance Format 324
16.3.1 Complex-Capacitance-Plane Representation 325
16.3.2 Complex-Capacitance Representation 326
16.4 Effective Capacitance 328
Problems 331

17 Preliminary Graphical Methods 333

17.1 Application to a Randles Circuit 334
17.1.1 Traditional Representation of Data 334
17.1.2 Phase Angle and Modulus Corrected for Ohmic Resistance 337
17.1.3 Real and Imaginary Components 338
17.1.4 Effective High-Frequency Capacity or CPE Coefficient . . 340
17.2 Application to Blocking Electrodes 342
17.2.1 Nyquist and Bode Representations 342
17.2.2 Imaginary Component 344
17.2.3 Effective CPE Coefficient 345
17.3 Overview 348
Problems 351

18 Model-Based Graphical Methods 353

18.1 Mass Transfer 353
18.1.1 Scaled Plots of Impedance 353
18.1.2 Asymptotic Behavior at Low-Frequency 355
18.2 Reaction Kinetics: Arrhenius Relations 357
18.3 Mott-Schottky Plots 360
Problems 362

19 Complex Nonlinear Regression 363

19.1 Concept 363
19.2 Objective Functions 365
19.3 Formalism of Regression Strategies 367
19.3.1 Linear Regression 367
19.3.2 Nonlinear Regression 368
19.4 Regression Strategies for Nonlinear Problems 370
19.4.1 Gauss-Newton Method 370
19.4.2 Method of Steepest Descent 371
19.4.3 Levenberg-Marquardt Method 371
19.4.4 Downhill Simplex Strategies 372
19.5 Influence of Data Quality on Regression 373
19.5.1 Presence of Stochastic Errors in Data 373
19.5.2 Ill-Conditioned Regression Caused by Stochastic Noise . . 375
19.5.3 Ill-Conditioned Regression Caused by Insufficient Range . 375

19.6 Initial Estimates for Regression 380
19.7 Regression Statistics 380
  19.7.1 Confidence Intervals for Parameter Estimates 381
  19.7.2 Statistical Measure of the Regression Quality 382
  Problems 382

20 Assessing Regression Quality 385

20.1 Methods to Assess Regression Quality 385
  20.1.1 Quantitative Methods 385
  20.1.2 Qualitative Methods 386
20.2 Application of Regression Concepts 386
  20.2.1 Finite-Diffusion-Length Model 388
  20.2.2 Measurement Model 393
  20.2.3 Convective-Diffusion-Length Model 395
  Problems 402

V Statistical Analysis **405**

21 Error Structure of Impedance Measurements 407

21.1 Error Contributions 407
21.2 Stochastic Errors in Impedance Measurements 408
  21.2.1 Stochastic Errors in Time-Domain Signals 409
  21.2.2 Transformation from Time Domain to Frequency Domain 411
  21.2.3 Stochastic Errors in Frequency Domain 413
21.3 Bias Errors 414
  21.3.1 Instrument Artifacts 415
  21.3.2 Ancillary Parts of the System under Study 415
  21.3.3 Nonstationary Behavior 415
  21.3.4 Time Scales in Impedance Spectroscopy Measurements . . 416
21.4 Incorporation of Error Structure 418
21.5 Measurement Models for Error Identification 420
  21.5.1 Stochastic Errors 422
  21.5.2 Bias Errors 423
  Problems 425

22 The Kramers-Kronig Relations 427

22.1 Mathematical Origin 427
  22.1.1 Background 428
  22.1.2 Application of Cauchy's Theorem 432
  22.1.3 Transformation from Real to Imaginary 432
  22.1.4 Transformation from Imaginary to Real 435
  22.1.5 Application of the Kramers-Kronig Relations 436
22.2 The Kramers-Kronig in an Expectation Sense 439

22.2.1 Transformation from Real to Imaginary 439
22.2.2 Transformation from Imaginary to Real 440
22.3 Methods for Application 442
22.3.1 Direct Integration of the Kramers-Kronig Relations 442
22.3.2 Experimental Assessment of Consistency 443
22.3.3 Regression of Process Models 443
22.3.4 Regression of Measurement Models 444
Problems 445

VI Overview 447

23 An Integrated Approach to Impedance Spectroscopy 449

23.1 Flowcharts for Regression Analysis 449
23.2 Integration of Measurements, Error Analysis, and Model 450
23.2.1 Impedance Measurements Integrated with Error Analysis 451
23.2.2 Process Models Developed Using Other Observations . . . 452
23.2.3 Regression Analysis in Context of Error Structure 453
23.3 Application 453
Problems 459

VII Reference Material 461

A Complex Integrals 463

A.1 Definition of Terms 463
A.2 Cauchy-Riemann Conditions 465
A.3 Complex Integration 467
A.3.1 Cauchy's Theorem 467
A.3.2 Improper Integrals of Rational Functions 471
Problems 473

B Tables of Reference Material 475

C List of Examples 477

List of Symbols 481

References 495

Index 518

Preface

This book is intended for use both as a professional reference and as a textbook suitable for training new scientists and engineers. As a textbook, this work is suitable for graduate students in a variety of disciplines including electrochemistry, materials science, physics, electrical engineering, and chemical engineering. As these audiences have very different backgrounds, a portion of the book reviews material that may be known to some students but not to others. There are many short courses offered on impedance spectroscopy, but formal courses on the topic are rarely offered in university settings. Accordingly, this textbook is designed to accommodate both directed and independent learning.

Organization

The textbook has been prepared in seven parts:

Part I Background

This part provides material that may be covered selectively depending on the background of the students. The subjects covered include complex variables, differential equations, statistics, electrical circuits, electrochemistry, and instrumentation. The coverage of these topics is limited to what is needed to understand the core of the textbook, which is covered in the subsequent parts.

Part II Experimental Considerations

This part introduces methods used to measure impedance and other transfer functions. The chapters in this section are intended to provide an understanding of frequency-domain techniques and the approaches used by impedance instrumentation. This understanding provides a basis for evaluating and improving experimental design. The material covered in this section is integrated with the discussion of experimental errors and noise. The extension of impedance spectroscopy to other transfer-function techniques is developed in Part III.

Part III Process Models

This part demonstrates how deterministic models of impedance response can be developed from physical and kinetic descriptions. When possible, correspondence is drawn between hypothesized models and electrical circuit analogues. The treatment includes electrode kinetics, mass transfer, solid-state systems, time-constant dispersion, models accounting for two- and three-dimensional interfaces, generalized transfer functions, and a more specific example of a transfer-function technique.in which the rotation speed of a disk electrode is modulated.

Part IV Interpretation Strategies

This part describes methods for interpretation of impedance data, ranging from graphical methods to complex nonlinear regression. The material covered in this section is integrated with the discussion of experimental errors and noise. Bias errors are shown to limit the frequency range useful for regression analysis, and the variance of stochastic errors is used to guide the weighting strategy used for regression.

Part V Statistical Analysis

This part provides a conceptual understanding of stochastic, bias, and fitting errors in frequency-domain measurements. A major advantage of frequency-domain measurements is that real and imaginary parts of the response must be internally consistent. The expression of this consistency takes different forms that are known collectively as the Kramers-Kronig relations. The Kramers-Kronig relations and their application to spectroscopy measurements are described. Measurement models, used to assess the error structure, are described and compared with process models used to extract physical properties.

Part VI Overview

The final chapter in this book provides a philosophy for electrochemical impedance spectroscopy that integrates experimental observation, model development, and error analysis. This approach is differentiated from the usual sequential model development for given impedance spectra by its emphasis on obtaining supporting observations to guide model selection, use of error analysis to guide regression strategies and experimental design, and use of models to guide selection of new experiments. These concepts are illustrated with examples taken from the literature. This chapter is intended to illustrate that selection of models, even those based on physical principles, requires both error analysis and additional experimental verification.

Part VII Reference Material

The reference material includes an appendix on complex integration needed to follow the derivation of the Kramers-Kronig relations, a list of tables, a list of examples, a list of symbols, and a list of references.

Pedagogical Approach

The material is presented in a manner that facilitates sequential development of understanding and expertise either in a course or in self-study. Illustrative examples are interspersed throughout the text to show how the principles described are applied to common impedance problems. These examples are in the form of questions, followed by the solution to the question posed. The student can attempt to solve the problem before reading how the problem is solved. Homework problems, suitable either for self-study or for study under direction of an instructor, are developed for each chapter. Important equations and relations are collected in tables, which can be easily accessed. Important concepts are identified and set aside at the bottom of pages as they appear in the text. Readily identifiable icons are used to distinguish examples and important concepts.

As can be found in any field, the notation used in the impedance spectroscopy literature is inconsistent. In treatments of diffusion impedance, for example, the symbol θ is used to denote the dimensionless oscillating concentration variable; whereas, the symbol θ used in kinetic studies denotes the fractional surface coverage by a reaction intermediate. Compromises were necessary to create a consistent notation for this book. For example, the dimensionless oscillating concentration variable was given the symbol θ, and γ was used to denote the the fractional surface coverage by a reaction intermediate. As discussed in Section 1.2.3, the book deviates from the IUPAC convention for the notation used to denote the imaginary number and the real and imaginary parts of impedance.

This book is intended to provide a background and training suitable for application of impedance spectroscopy to a broad range of applications, such as corrosion, biomedical devices, semiconductors and solid-state devices, sensors, batteries, fuel cells, electrochemical capacitors, dielectric measurements, coatings, electrochromic materials, analytical chemistry, and imaging. The emphasis is on generally applicable fundamentals rather than on detailed treatment of applications. The reader is referred to other sources for discussion of specific applications of impedance.[1–4]

Remember! 0.1 *The elephant at left is used to identify important concepts for each chapter. It is intended to remind the student of the parable of the blind men and the elephant.*

The active participation in related short courses demonstrates a rising interest in impedance spectroscopy. As discussed in the preliminary section on the history of the technique, the number of papers published that mention use of electrochemical impedance spectroscopy has increased dramatically over the past 10 years. Nevertheless, the question may be raised: *Why teach a full semester-long course on impedance spectroscopy? It is, after all, just an experimental technique.* In our view, impedance spectroscopy represents the confluence of a significant number of disciplines, and successful training in the use and interpretation of impedance requires a coherent education in the application of each of these disciplines to the subject. In addition to learning about impedance spectroscopy, the student will gain a better understanding of a general philosophy of scientific inquiry.

Mark E. Orazem Gainesville, Florida	Bernard Tribollet Paris, France

July, 2008

Acknowledgments

The authors met for the first time in 1981 in the research group of John Newman at the University of California, Berkeley. **Mark Orazem** was a graduate student, and **Bernard Tribollet** was a visiting scientist on sabbatical leave from the *Centre National de la Recherche Scientifique* (CNRS) in Paris. We have maintained a fruitful collaboration ever since and our careers, as well as the content of this book, build on the foundation we received from John. We owe an additional debt of gratitude to many persons, including:

- Our families, who have embraced our collaboration over the years
- *The Electrochemical Society* (ECS), who encouraged Mark Orazem to teach the ECS short course on impedance spectroscopy on an annual or more frequent basis, thus allowing us to test the pedagogical approach developed in this book
- The CNRS, who provided financial support for a sabbatical year spent by Mark Orazem in Paris in 2001/2002
- Graduate students Bryan Hirschorn, Vicky Huang, J. Patrick McKinney, Sunil Roy, and Shao-Ling Wu who read the book many times, helping with examples, solving homework problems, and identifying errors in the text
- Hubert Cachet, Sandro Cattarin, Isabelle Frateur, and Nadine Pébère who read different chapters and provided comments, corrections, and suggestions
- Michel Keddam who suggested the presentation of the historical perspective in terms of the categories presented in Table 1
- Max Yaffe of Gamry Instruments who provided assistance with the chapter on the Kramers-Kronig relations
- Christopher Brett, who graciously provided a last technical review of the text before publication
- Mary Yess of the ECS for her steady support of this project
- Dinia Agarwala of the ECS for designing the cover

- Our many colleagues and friends who assured us that there would be a demand for this book

While we have received help and support from many people, the remaining errors and omissions in this text are ours. We will gratefully receive corrections and suggestions from our readers to be implemented in future editions of this book.

The Blind Men and the Elephant

Impedance spectroscopy is a complicated area of research that has been subject to significant controversy. As we begin a study of this subject it is well to remember the Buddhist parable of the blind men and the elephant. American poet John Godfrey Saxe (1816–1887) based the following poem on the fable.[5]

The Blind Men and the Elephant

John Godfrey Saxe

It was six men of Indostan
To learning much inclined,
Who went to see the Elephant
(Though all of them were blind),
That each by observation
Might satisfy his mind.

The First approached the Elephant,
And happening to fall
Against his broad and sturdy side,
At once began to bawl:
God bless me! but the Elephant
Is very like a wall!

The Second, feeling of the tusk,
Cried, Ho! what have we here
So very round and smooth and sharp?
To me 'tis mighty clear
This wonder of an Elephant
Is very like a spear!

The Third approached the animal,
And happening to take
The squirming trunk within his hands,
Thus boldly up and spake:
I see, quoth he, the Elephant

Is very like a snake!

The Fourth reached out an eager hand,
And felt about the knee.
What most this wondrous beast is like
Is mighty plain, quoth he;
'Tis clear enough the Elephant
Is very like a tree!

The Fifth, who chanced to touch the ear,
Said: Een the blindest man
Can tell what this resembles most;
Deny the fact who can,
This marvel of an Elephant
Is very like a fan!?

The Sixth no sooner had begun
About the beast to grope,
Than, seizing on the swinging tail
That fell within his scope,
I see, quoth he, the Elephant
Is very like a rope!

And so these men of Indostan
Disputed loud and long,
Each in his own opinion
Exceeding stiff and strong,
Though each was partly in the right,
And all were in the wrong!

Moral:
So oft in theologic wars,
The disputants, I ween,
Rail on in utter ignorance
Of what each other mean,
And prate about an Elephant
Not one of them has seen!

The logo for the 2004 International Symposium on Impedance Spectroscopy, shown in Figure 1, was intended to evoke the lessons of the blind men and the elephant. The multiple loops resemble the Nyquist plots obtained in some cases for the impedance of corroding systems influenced by formation of surface films. The low-frequency inductive loop was deformed to evoke the image of the elephant's trunk, and the capacitive loops resemble the head and body of the elephant.

Impedance spectroscopy is, of course, not a religion, but an application of a frequency-domain measurement to a complex system that cannot be easily visu-

Figure 1: The logo for the 2004 International Symposium on Impedance Spectroscopy, held in Cocoa Beach, Florida.

alized. The quantities measured, e.g., current and potential for electrochemical or electronic systems and stress and strain for mechanical systems, are macroscopic values that represent the spatial average of individual events. These quantities are influenced by the desired physical properties, such as diffusivity, rate constants, and viscosity, but do not provide a direct measure of them.

Application of impedance spectroscopy is very much like feeling an elephant that we cannot see. Measurement of current and potential under a steady state yields some information concerning a given system. By adding frequency dependence to the macroscopic measurements, impedance spectroscopy expands the information that can be extracted from the measurements. Impedance measurements, however, are not sufficient. Additional observations are needed to gain confidence in the model identification.

History of Impedance Spectroscopy

Impedance spectroscopy is an electrochemical technique with broad applications that is growing in importance. As seen in Figure 2, the number of papers published in this area has doubled roughly every four or five years. In 2006, over 1,200 journal articles were published that mention the use of electrochemical impedance spectroscopy.

Timeline

By his application of Laplace transforms to the transient response of electrical circuits, Oliver Heaviside created the foundation for impedance spectroscopy. Heaviside coined the words *inductance, capacitance,* and *impedance* and introduced these concepts to the treatment of electrical circuits. His papers on the subject, published in *The Electrician* beginning in 1872, were compiled by Heaviside in book form in 1894.[6,7] From the perspective of the application to physical systems, however, the history of impedance spectroscopy begins in 1894 with the work of Nernst.[8]

Nernst applied the electrical bridge invented by Wheatstone[9,10] to the measurement of the dielectric constants for aqueous electrolytes and different organic fluids. Nernst's approach was soon employed by others for measurement of dielectric properties[11,12] and the resistance of galvanic cells.[13] Finkelstein[14] applied the technique to the analysis of the dielectric response of oxides. Warburg[15,16] developed expressions for the impedance response associated with the laws of diffusion, developed almost 50 years earlier by Fick,[17] and introduced the electrical circuit analogue for electrolytic systems in which the capacitance and resistance were functions of frequency. The concept of diffusion impedance was applied by Krüger to the capacitive response of mercury electrodes.[18]

In the 1920s, impedance was applied to biological systems, including the resistance and capacitance of cells of vegetables[19] and the dielectric response of blood suspensions.[20–22] Impedance was also applied to muscle fibers, skin tissues, and other biological membranes.[23,24] The capacitance of the cell membranes was found to be a function of frequency,[25] and Fricke observed a relationship between the frequency exponent of the impedance and the observed constant phase angle.[26] In 1941, brothers Cole and Cole showed that the frequency-dependent complex

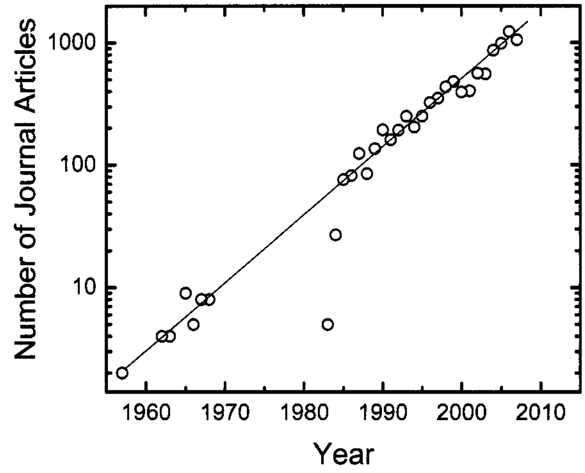

Figure 2: Number of journal articles on electrochemical impedance spectroscopy identified on October 3, 2007 using the Engineering Village search engine. The key words used were "(((impedance or admittance) and (Electrochemical)), Journal article only).

dielectric constant can be represented as a depressed semicircle in a complex admittance plane plot and suggested a formula, consistent with Fricke's law,[26] now known as a *constant-phase element*.[27]

In 1940, Frumkin[28] explored the relationships among the double-layer structure on mercury electrodes, the capacitance measured by use of a Wheatstone bridge, and the surface tension, following the theoretical underpinnings of the Lippmann equation. Grahame[29,30] expanded this treatment of the mercury electrode, providing a fundamental understanding of the structure of the electrical double layer. Dolin and Ershler applied the concept of an equivalent circuit to electrochemical kinetics for which the circuit elements were independent of frequency.[31] Randles developed an equivalent circuit for an ideally polarized mercury electrode that accounted for the kinetics of adsorption reactions.[32]

In the early 1950s, impedance began to be applied to more complicated reaction systems.[33–35] In subsequent years, Epelboin and Loric addressed the role of reaction intermediates in causing low-frequency inductive loops,[36] de Levie developed transmission line models for the impedance response of porous and rough electrodes,[37] and Newman showed that the nonuniform current and potential distribution of disk electrodes can result in high-frequency time-constant dispersion.[38] Levart and Schuhmann[39] developed a model for the diffusion impedance of a rotating disk that accounted for the influence of homogeneous chemical reactions. Kinetic models accounting for reaction intermediates were addressed in greater detail in publications by Armstrong et al.[40] and Epelboin et al.[41]

Nonlinear complex regression techniques, developed in the early 1970s,[42,43] were applied to impedance data by Macdonald et al.[44,45] and Boukamp.[46] The regression approaches were based on use of equivalent electrical circuits, which became the predominant method for interpretation of impedance data. The experimental investigations turned increasingly toward those associated with technical applications, such as electrodeposition and corrosion.[47–49] Gabrielli et al. introduced the concept of a generalized transfer function for impedance spectroscopy.[50–52] During this time, the Kramers-Kronig relations, developed in the late 1920s,[53,54] were applied for the validation of electrochemical impedance data.[55] Agarwal et al.[56] described an approach that eliminated problems associated with direct integration of the Kramers-Kronig integral equations and accounted explicitly for stochastic errors in the impedance measurement.

Several authors have described methods for generalized deconvolution of impedance data.[57,58] Stoynov and co-workers developed a robust method in which calculation of the local derivatives of the impedance with respect to frequency allows visualization of the distribution of time constants for a given spectrum without *a-priori* assumption of a distribution function.[59,60] Stoynov and Savova-Stoynov described a graphical method of estimating instantaneous impedance projections from consecutive series of impedance diagrams obtained during the time of system evolution.[61]

A conference dedicated to the development of electrochemical impedance spectroscopy techniques was initiated in 1989 in Bombannes, France. The subsequent meetings, held every three years, took place in California (1992), Belgium (1995), Brazil (1998), Italy (2001), Florida (2004), and France (2007). The special issues associated with these conferences provide unique triennial snapshots of the state of impedance research.[62–67] One driving concern reflected in these volumes is the heterogeneity of electrode surfaces and the correspondence to the use and misuse of constant phase elements. Local impedance spectroscopy, developed by Lillard et al.,[68] may prove to be a useful method for understanding this relationship.

Areas of Investigation

A historical perspective on impedance spectroscopy is presented in Table 1. A brief listing of advances in this field cannot be comprehensive, and many important contributions are not mentioned. The reader may wish to explore other historical perspectives, such as that provided by Macdonald.[69] Chapters written by Sluyters-Rehbach and Sluyters[70] and by Lasia[71] provide excellent overviews of the field. Nevertheless, Table 1 provides a useful guide to the trends in areas related to electrochemical impedance spectroscopy. These areas include the types of systems investigated, the instrumentation used to make the measurements, including changes in the accessible frequency range, the methods used to represent the resulting data, and the methods used to interpret the data in terms of quantitative properties of the system.

Experimental Systems

The early applications of what we now know as impedance spectroscopy were to the dielectric properties of fluids and metal oxides. Impedance measurements performed on mercury electrodes emphasized development of a fundamental understanding of the interface between the electrode and the electrolyte. The mercury drop electrodes were ideal for this purpose because they provided a uniform and easily refreshed interface that could be considered to be ideally polarizable over a broad range of potential. The impedance technique was used to identify an interfacial capacitance that could be compared to the theories for diffuse electrical double layers. In the 1920s, considerable effort was placed on biological systems, including the dielectric properties of blood and the impedance response of cell membranes. In the 1950s, impedance began to be used for studies of anodic dissolution. One may identify a trend from ideal surfaces suitable for fundamental studies to ones associated with technical materials. Impedance became useful for studying processes such as corrosion, deposition of films, and other electrochemical reactions. It became clear that the solid electrode surfaces were not uniform, and this complicated interpretation of impedance spectra in terms of meaningful physical properties. Recently, local impedance spectroscopy has emerged as a means of studying heterogeneous electrode surfaces.

Measurement Techniques

Early experimental techniques relied on use of Wheatstone bridges. The bridge is based on a nulling technique that requires manipulation of an adjustable resistor and capacitor at each frequency to obtain an effective frequency-dependent resistance and capacitance of the cell, from which can be derived an impedance. In time, the mechanical signal generator was replaced by an electronic signal generator, but the frequency range remained limited to acoustic frequencies (kHz to Hz). The ability to record time-domain signals on an oscilloscope enabled measurement to subacoustic frequencies (on the order of mHz). Subsequent development of digital signal analysis allowed automated recording of impedance spectra. These techniques are described in Chapter 7. Development of microelectrodes enabled local measurement of current density and local impedance spectra. These techniques are also described in Chapter 7.

A parallel development has taken place for related transfer-function methods. For electrochemical systems, impedance spectroscopy, which relies on measurement of current and potential, provides the general system response. As described in Chapters 14 and 15, transfer-function methods allow the experimentalist to isolate the portion of the response associated with specific inputs or outputs.

Impedance Representation

The methods used to plot impedance data began with plots of effective resistance and capacitance, reflecting the use of bridges for measurement. These plots gave way to Nyquist and Bode plots, which remain the traditional means of representing impedance data. More recently, authors have promoted the use of Bode plots corrected for Ohmic resistance and the use of logarithmic plots of the imaginary impedance as a function of frequency. As described in Chapter 17, such plots provide limited yet quantitative interpretation of impedance spectra.

Mathematical Analysis

The impedance response associated with diffusion in an infinite domain and in a solid film was developed in the very early twentieth century. Similarly quantitative models were developed in the 1940s for the capacitive behavior of the double layer. In the middle of the twentieth century, models were being developed that accounted for heterogeneous reactions and adsorbed intermediates. In the 1960s and 1970s, such models were being generalized to account for homogeneous reactions and reactions on porous electrodes. The development of quantitative models is presented in Part III.

These models provided a quantitative relationship between physicochemical parameters and impedance response, but the application of interpretation strategies did not keep pace with the model development. Interpretation was based on graphical examination of plotted data. In simple cases, plots could be used directly as described in Chapter 18. For more complicated cases, simulations could be compared graphically to data to reveal qualitative agreement.

Nonlinear regression analysis, described in Chapters 19 and 20, was developed for impedance spectroscopy in the early 1970s. The models were cast in the form of electrical circuits with mathematical formulas added to account for the diffusion impedance associated with simplified geometries.

There were significant difficulties associated with fitting models to impedance data. The electrochemical systems frequently did not conform to the assumptions made in the models, especially those associated with electrode uniformity. Constant-phase elements (CPEs), described in Chapter 13, were introduced as a convenient general circuit element that was said to account for distributions of time constants. The meaning of the CPE for specific systems was often disputed.

In addition, the variance of impedance measurements depends strongly on frequency, and this variation needs to be addressed by the regression strategies employed. An assumed dependence of the variance of the impedance measurement on impedance values was employed in early stages of regression analysis, and this gave rise to some controversy over what assumed error structure was most appropriate. An experimental approach using measurement models, described in Chapter 21, was later developed, which eliminated the need for assumed error structures.

The long time required to make impedance measurements in the acoustic to subacoustic frequency range caused the resulting impedance to be influenced by changes in the system properties during the course of the measurement. The Kramers-Kronig relations, described in Chapter 22, were employed to determine whether impedance spectra were corrupted by nonstationary behavior. This approach, too, was controversial due to the need to evaluate the Kramers-Kronig integrals over a frequency range extending from 0 to infinity, requiring extrapolation of the measured data. The use of a measurement model allowed assessment of the degree of consistency with the Kramers-Kronig relations without use of integration procedures.

Access to powerful computers and to commercial partial-differential-equation (PDE) solvers has facilitated modeling of the impedance response of electrodes exhibiting distributions of reactivity. Use of these tools, coupled with development of localized impedance measurements, has introduced a renewed emphasis on the study of heterogenous surfaces. This coupling provides a nice example for the integration of experiment, modeling, and error analysis described in Chapter 23.

Table 1: A time-line for the historical development of impedance spectroscopy. Contributions listed for any given range of time add to preceding contributions.

	1894–1920	1920–1952	1952–1960	1960–1972	1972–1990	1990–2007
Experimental system	Dielectric properties	Mercury drop, double layers, biological systems	Anodic dissolution	Electro-crystallization, corrosion, 3-D electrodes	Generators, mixed conductors, redox materials	Heterogeneous surfaces
Measurement techniques	Bridge: mechanical generator	Bridge: electronic generator	Impulse method, oscillograph, Laplace transform	Analogue impedance measurement, potentiostat (AC + DC)	Digital impedance measurement, connection with computer	Local electrochemical impedance spectroscopy (LEIS)
Frequency range	Acoustic, >100Hz	Acoustic, >100Hz	Acoustic and subacoustic, >1mHz	Acoustic and subacoustic, >1mHz	Acoustic and subacoustic, >1mHz	Acoustic and subacoustic, >1mHz
Representation	$R-C$	Electrical equivalent circuits	Nyquist plots	Bode plots		R_e-corrected Bode plots, $\log(\lvert Z_j\rvert)$ vs $\log(f)$
Mathematical analysis	Heaviside theory	Capacitance vs. frequency	$\sqrt{f}$	Fitting	Kramers-Kronig analysis, assumed error structure	Measurement model, measured error structure
Simulation				Mainframe computer	Personal computer	Commercial PDE solvers
Process models	Nernst: dielectrics (1894); Warburg: diffusion (1901); Finkelstein: Solid film (1902)	Randles: double layer and diffusion impedance (1947)	Gerischer: two heterogeneous steps with adsorbed intermediate (1955)	De Levie: porous electrodes (1967)	Schuhmann: homogeneous reactions and diffusion (1964); Gabrielli: generalized impedance (1977)	Isaacs: LEIS (1992)

Electrochemical Impedance Spectroscopy
by Mark E. Orazem and Bernard Tribollet

THE ELECTROCHEMICAL SOCIETY SERIES

Corrosion Handbook
Edited by Herbert H. Uhlig

Modern Electroplating, Third Edition
Edited by Frederick A. Lowenheim

Modern Electroplating, Fourth Edition
Edited by Mordechay Schlesinger and Milan Paunovic

The Electron Microprobe
Edited by T. D. McKinley, K. F. J. Heinrich, and D. B. Wittry

Chemical Physics of Ionic Solutions
Edited by B. E. Conway and R. G. Barradas

High-Temperature Materials and Technology
Edited by Ivor E. Campbell and Edwin M. Sherwood

Alkaline Storage Batteries
S. Uno Falk and Alvin J. Salkind

The Primary Battery (in Two Volumes)
Volume I *Edited by* George W. Heise and N. Corey Cahoon
Volume II *Edited by* N. Corey Cahoon and George W. Heise

Zinc-Silver Oxide Batteries
Edited by Arthur Fleischer and J. J. Lander

Lead-Acid Batteries
Hans Bode
Translated by R. J. Brodd and Karl V. Kordesch

Thin Films-Interdiffusion and Reactions
Edited by J. M. Poate, M. N. Tu, and J. W. Mayer

Lithium Battery Technology
Edited by H. V. Venkatasetty

Quality and Reliability Methods for Primary Batteries
P. Bro and S. C. Levy

Techniques for Characterization of Electrodes and Electrochemical Processes
Edited by Ravi Varma and J. R. Selman

Electrochemical Oxygen Technology
Kim Kinoshita

Synthetic Diamond: Emerging CVD Science and Technology
Edited by Karl E. Spear and John P. Dismukes

Corrosion of Stainless Steels
A. John Sedriks

Semiconductor Wafer Bonding: Science and Technology
Q.-Y. Tong and U. Göscle

Uhlig's Corrosion Handbook, Second Edition
Edited by R. Winston Revie

Atmospheric Corrosion
Christofer Leygraf and Thomas Graedel

Electrochemical Systems, Third Edition
John Newman and Karen E. Thomas-Alyea

Fundamentals of Electrochemistry, Second Edition
V. S. Bagotsky

Fundamentals of Electrochemical Deposition, Second Edition
Milan Paunovic and Mordechay Schlesinger

Electrochemical Impedance Spectroscopy
Mark E. Orazem and Bernard Tribollet

Electrochemical Impedance Spectroscopy
by Mark E. Orazem and Bernard Tribollet

Part I

Background

Electrochemical Impedance Spectroscopy
by Mark E. Orazem and Bernard Tribollet

Chapter 1

Complex Variables

A working understanding of complex variables is essential for the analysis of experiments conducted in the frequency domain, such as impedance spectroscopy. The objective of this chapter is to introduce the subject of complex variables at a level sufficient to understand the development of interpretation models in the frequency domain. Complex variables represent an exciting and important field in applied mathematics, and textbooks dedicated to complex variables can extend the introduction provided here.[72,73] The overview presented in this chapter is strongly influenced by the compact treatment presented by Fong et al.[74]

1.1 Why Imaginary Numbers?

The terminology used in the study of complex variables, in particular the term *imaginary number*, is particularly unfortunate because it provides an unnecessary conceptual barrier to the beginning student of the subject. Complex variables are ordered pairs of numbers, where the imaginary part represents the solution to a particular type of equation. As suggested by Cain in his introduction to complex variables,[73] complex numbers can be compared to other ordered pairs of numbers.

Rational numbers, for example, are defined to be ordered pairs of integers. For example, $(3,8)$ is a rational number. The ordered pair (n,m) can be written as $(\frac{n}{m})$. Thus the rational number $(3,8)$ can be represented as well by 0.375.

Two rational numbers (n,m) and (p,q) are defined to be equal whenever $nq = pm$. The sum of (n,m) and (p,q) is given by

$$(n,m) + (p,q) = (nq + pm, mq) \tag{1.1}$$

and the product by

$$(n,m)(p,q) = (np, mq) \tag{1.2}$$

Subtraction and division are defined to be the inverses of the addition and multiplication operations, respectively.

Irrational numbers were introduced because the set of rational numbers could not provide solutions to such equations as $z = \sqrt{2}$. As seen in the subsequent section, the set of real numbers, which encompasses rational and irrational numbers, is not adequate to provide solutions to yet other classes of equations. Thus, complex numbers were introduced, which can be seen in the following sections to be defined as ordered pairs (x, y) of real and imaginary numbers.[73]

1.2 Terminology

The concept of complex variables is used widely in mathematical and engineering analysis. Some definitions and concepts commonly encountered in the field of impedance spectroscopy are presented in this section.

1.2.1 The Imaginary Number

The imaginary number $j = \sqrt{-1}$ is the solution to the algebraic equation

$$z^2 = -1 \tag{1.3}$$

which yields $z = \pm j$. The imaginary number arises as well in the solution to differential equations such as

$$\frac{d^2y}{dx^2} + by = 0 \tag{1.4}$$

which, as shown in Chapter 2, has the characteristic equation

$$m^2 = -b \tag{1.5}$$

with solution

$$m = \pm\sqrt{-b} = \pm j\sqrt{b} \tag{1.6}$$

The homogeneous solution to equation (1.4) is given by

$$y = C_1 \exp\left(j\sqrt{b}x\right) + C_2 \exp\left(-j\sqrt{b}x\right) \tag{1.7}$$

Some useful identities for the complex number j are presented in Table 1.1.

1.2.2 Complex Variables

The solution to the quadratic equation

$$az^2 + bz + c = 0 \tag{1.13}$$

given as

$$z = \frac{-b \pm \sqrt{b^2 - 4ac}}{2a} \tag{1.14}$$

is a complex number if the argument $b^2 - 4ac < 0$. The complex variables can be written as

$$z = z_r + jz_j \tag{1.15}$$

where z_r and z_j are real numbers that represent the real and imaginary parts of z, respectively. Often the notations $\text{Re}\{z\}$ and $\text{Im}\{z\}$ are used to designate real and imaginary components of the complex number z, respectively.

1.2.3 Conventions for Notation in Impedance Spectroscopy

The IUPAC convention, as described in the overview by Sluyters-Rehbach,[75] is that $\sqrt{-1}$ should be denoted by the symbol i. To avoid confusion with current density, given the symbol i, we have chosen here to follow the electrical engineering convention in which $\sqrt{-1}$ is given the symbol j.

We also depart from the IUPAC convention in the notation used to denote real and imaginary parts of the impedance. The IUPAC convention is that the real part of the impedance is given by Z' and the imaginary part is given by Z''. We consider that the IUPAC notation can be confused with the use of primes and double primes to denote first and second derivatives, respectively. Thus, we choose to identify the real part of the impedance by Z_r and the imaginary part of the impedance by Z_j.

1.3 Operations Involving Complex Variables

As z is a single value with real and imaginary components, z can be represented as a point on a complex plane, as shown in Figure 1.1. The complex conjugate of a complex number $z = z_r + jz_j$ is defined to be $\overline{z} = z_r - jz_j$. Thus, in Figure 1.1, $\overline{z}$ is seen to be the reflection of z about the real axis.

As is evident in the graphical representation of a complex number in Figure 1.1, two complex numbers are equal if and only if both the real and the imaginary parts are equal. Thus, an equation involving complex variables requires that two equations are satisfied, one involving the real terms, and one involving the imaginary terms. Commutative, associative, and distributive laws hold for complex

Table 1.1: Identities for the complex number j.

$$j = \sqrt{-1} \tag{1.8}$$
$$j^2 = -1 \tag{1.9}$$
$$j^3 = -j \tag{1.10}$$
$$j^4 = 1 \tag{1.11}$$
$$1/j = -j \tag{1.12}$$

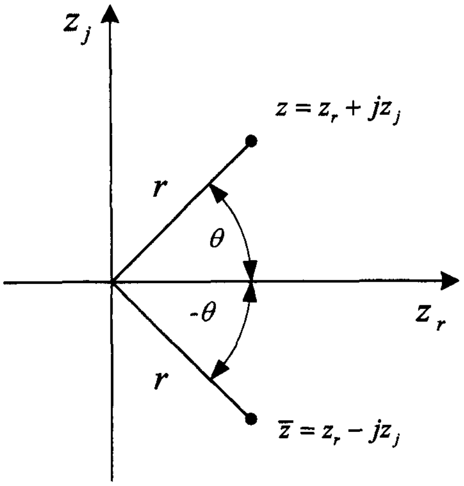

Figure 1.1: Argand diagram showing the position of a complex number and its complex conjugate on a complex plane.

numbers. Some useful relationships for complex variables are presented in Table 1.2, which demonstrate the commutative, associative, and distributive properties.

The commutative property states that, in addition and multiplication, terms may be arbitrarily interchanged. Thus, equation (1.16) applies for addition and equation (1.17) applies for multiplication of complex numbers z and w. The distributive property is demonstrated by equation (1.18), and the associative property is demonstrated by equation (1.19).

1.3.1 Multiplication and Division of Complex Numbers

Equations (1.20)–(1.24) illustrate the manner in which mathematical operations are carried out in terms of real and imaginary components. These results provide a foundation for the followings series of examples.

Example 1.1 Multiplication of Complex Numbers: *Does the imaginary part of the product of two complex numbers equal the product of the imaginary parts?*

Solution: *Consider two numbers* $z = z_r + jz_j$ *and* $w = w_r + jw_j$. *The multiplication of*

Remember! 1.1 *Complex numbers are ordered pairs* (x, y) *of real and imaginary numbers that represent the solution to a class of problems that cannot be solved using rational and irrational numbers.*

Table 1.2: Relationships for complex variables $z = z_r + jz_j$ and $w = w_r + jw_j$.

$$z + w = w + z \tag{1.16}$$

$$zw = wz \tag{1.17}$$

$$a(z + w) = az + aw \tag{1.18}$$

$$a(zw) = (az)w \tag{1.19}$$

$$z + w = (z_r + w_r) + j(z_j + w_j) \tag{1.20}$$

$$z - w = (z_r - w_r) + j(z_j - w_j) \tag{1.21}$$

$$zw = (z_r w_r - z_j w_j) + j(z_r w_j + z_j w_r) \tag{1.22}$$

$$w\overline{w} = w_r^2 + w_j^2 \tag{1.23}$$

$$\begin{aligned} \frac{z}{w} &= \frac{z\overline{w}}{w\overline{w}} \\ &= \frac{(z_r w_r + z_j w_j) + j(z_j w_r - z_r w_j)}{w_r^2 + w_j^2} \end{aligned} \tag{1.24}$$

---

z and w follows equation (1.22), i.e.,

$$\begin{aligned} zw &= (z_r + jz_j)(w_r + jw_j) \\ &= \left(z_r w_r + j^2 z_j w_j\right) + j\left(z_r w_j + w_r z_j\right) \\ &= \left(z_r w_r - z_j w_j\right) + j\left(z_r w_j + w_r z_j\right) \end{aligned} \tag{1.25}$$

The imaginary part of zw is $\left(z_r w_j + w_r z_j\right)$, *which is not equal to the product of the imaginary parts, i.e.,*

$$\left(z_r w_j + w_r z_j\right) \neq z_j w_j \tag{1.26}$$

Thus, the imaginary part of the product of two complex numbers does not equal the product of the imaginary parts.

Example 1.2 Division of Complex Numbers: *In a new experimental technique developed by Antaño-Lopez et al.,*[76] *an approximate formula for capacitance was used; i.e.,*

$$C = \frac{Y_j(\omega)}{\omega} \tag{1.27}$$

Remember! 1.2 *The notation used in this text provides that* $j = \sqrt{-1}$ *and that real and imaginary parts of complex numbers are denoted by subscripts r and j, respectively.*

---

where Y is the complex admittance $Y = Z^{-1}$, and ω is angular frequency. At frequencies sufficiently high to eliminate the contribution of Faradaic resistance, the capacitance is shown in Section 16.4 to be obtained correctly from

$$C = -\frac{1}{\omega Z_j(\omega)} \tag{1.28}$$

where Z_j is the imaginary part of the complex impedance Z. For capacitive systems, $Z_j < 0$. Under what conditions will equation (1.27) be accurate?

Solution: *Equation (1.27) would agree with equation (1.28) if*

$$Y_j = \mathrm{Im}\{Z^{-1}\} \overset{?}{=} -Z_j^{-1} \tag{1.29}$$

To test the validity of equation (1.29), consider the inverse of the complex number $Z = Z_r + jZ_j$.

$$\frac{1}{Z} = \frac{1}{Z_r + jZ_j} \tag{1.30}$$

Division is possible only after the denominator is converted into a real, rather than complex, number. Both the numerator and the denominator are multiplied by the complex conjugate (see equations (1.23)) and (1.24)).

$$\begin{aligned} \frac{1}{Z} &= \left\{\frac{1}{Z_r + jZ_j}\right\}\left\{\frac{Z_r - jZ_j}{Z_r - jZ_j}\right\} \\ &= \frac{Z_r - jZ_j}{Z_r^2 + Z_j^2} \\ &= \frac{Z_r}{Z_r^2 + Z_j^2} - j\frac{Z_j}{Z_r^2 + Z_j^2} \end{aligned} \tag{1.31}$$

Thus,

$$Y_j = \mathrm{Im}\{Z^{-1}\} = -\frac{Z_j}{Z_r^2 + Z_j^2} \neq -\frac{1}{Z_j} \tag{1.32}$$

Equation (1.29) is satisfied only if $Z_r = 0$. As discussed in Chapter 10, the real part of the impedance Z_r approaches the electrolyte resistance at high frequencies. The capacitance obtained by Antaño-Lopez et al.[76] is correct at high frequencies only if the electrolyte resistance can be neglected, i.e., $Z_r^2 \ll Z_j^2$.

Remember! 1.3 *The impedance is a complex number defined to be the ratio of complex potential and complex current.*

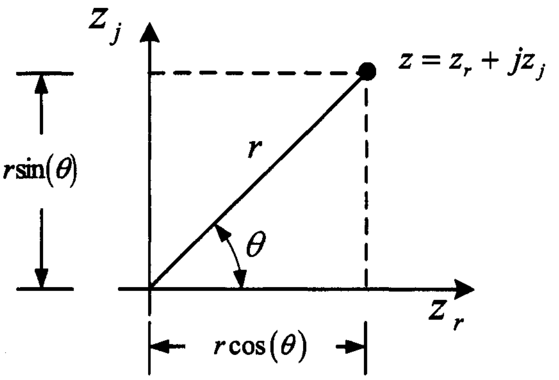

Figure 1.2: Argand diagram showing relationships among complex impedance, magnitude, and phase angle.

Example 1.3 Rectangular Coordinates: *The impedance of a parallel combination of a resistor and a capacitor can be expressed as*

$$Z = \frac{R}{1 + j\omega\tau} \tag{1.33}$$

where τ is the time constant $\tau = RC$. Express equation (1.33) in rectangular coordinates, i.e., find the real and imaginary components of Z.

Solution: *To express equation (1.33) in rectangular coordinates, the denominator must be converted into a real, rather than complex, number. Both the numerator and the denominator are multiplied by the complex conjugate (see equations (1.23) and (1.24)).*

$$\begin{aligned} Z &= \left\{\frac{R}{1 + j\omega\tau}\right\}\left\{\frac{1 - j\omega\tau}{1 - j\omega\tau}\right\} \\ &= \frac{R - j\omega R\tau}{1 + \omega^2\tau^2} \\ &= \frac{R}{1 + \omega^2\tau^2} - j\frac{\omega R\tau}{1 + \omega^2\tau^2} \end{aligned} \tag{1.34}$$

Thus,

$$\mathrm{Re}\{Z\} = \frac{R}{1 + \omega^2\tau^2}; \quad \mathrm{Im}\{Z\} = -\frac{\omega R\tau}{1 + \omega^2\tau^2} \tag{1.35}$$

1.3.2 Complex Variables in Polar Coordinates

The transformation from rectangular to polar coordinates is shown schematically in Figure 1.2. The variable r is the modulus or absolute value $|z|$, which always has a positive value. The phase angle is written as $\theta = \arg(z)$. The angle $\arg(z)$ has an infinite number of possible values because any multiple of 2π radians can be

---

Table 1.3: Relationships between polar and rectangular coordinates for the complex variable $z = z_r + jz_j$.

$$\begin{aligned}
z_r &= r\cos(\theta) && (1.36)\\
z_j &= r\sin(\theta) && (1.37)\\
r &= |z| \\
&= \sqrt{z_r^2 + z_j^2} && (1.38)\\
\theta &= \tan^{-1}\left(\frac{z_j}{z_r}\right) && (1.39)\\
|z| &= \sqrt{z\bar{z}} && (1.40)\\
z &= r\left(\cos(\theta) + j\sin(\theta)\right) && (1.41)\\
z^n &= r^n\left(\cos(n\theta) + j\sin(n\theta)\right) && (1.42)\\
z^{1/n} &= r^{1/n}\left[\cos\left(\frac{\theta}{n} + \frac{2\pi k}{n}\right) + j\sin\left(\frac{\theta}{n} + \frac{2\pi k}{n}\right)\right];\ k = 0, 1, \ldots, n-1 && (1.43)
\end{aligned}$$

---

added to it without changing the value of z. The value of θ that lies between $-\pi$ and π is called the *principal value* of $\arg(z)$.

Some useful relationships between polar and rectangular coordinates for complex variables are summarized in Table 1.3. Equation (1.42) is known as *De Moivre's theorem*. It is valid for all rational values of n.

Example 1.4 Polar Coordinates: *The impedance of a parallel combination of a resistor and a capacitor can be expressed as*

$$Z = \frac{R}{1 + j\omega\tau} \tag{1.44}$$

where τ is the time constant $\tau = RC$. Express equation (1.44) in polar coordinates; i.e., find the modulus and phase angle for Z.

Solution: *As shown in Example 1.3, equation (1.44) can be expressed in rectangular coordinates by*

$$\mathrm{Re}\{Z\} = \frac{R}{1 + \omega^2\tau^2}; \quad \mathrm{Im}\{Z\} = -\frac{\omega R\tau}{1 + \omega^2\tau^2} \tag{1.45}$$

Equations (1.38) and (1.39) can be used to convert equation (1.45) into polar coordinates. Thus,

$$r = \sqrt{\left(\frac{R}{1 + \omega^2\tau^2}\right)^2 + \left(\frac{\omega R\tau}{1 + \omega^2\tau^2}\right)^2} \tag{1.46}$$

or

$$r = \sqrt{\frac{R^2}{1+\omega^2\tau^2}} \tag{1.47}$$

$$\begin{aligned}\theta &= \tan^{-1}\left[-\frac{\omega R\tau}{1+\omega^2\tau^2}\frac{1+\omega^2\tau^2}{R}\right] \\ &= \tan^{-1}(-\omega\tau) \end{aligned} \tag{1.48}$$

The phase angle θ is a function only of frequency ω and the time constant τ. The modulus r depends on the value of R as well as on the frequency ω and the time constant τ.

The solution can be obtained more rapidly by casting the impedance in terms of admittance (see Section 16.2). The admittance can be expressed as

$$Y = \frac{1}{Z} = \frac{1+j\omega\tau}{R} \tag{1.49}$$

The modulus of the admittance is given by

$$|Y| = \sqrt{\frac{1+\omega^2\tau^2}{R^2}} \tag{1.50}$$

and the argument is given by

$$\theta_Y = \tan^{-1}(\omega\tau) \tag{1.51}$$

The modulus of the impedance and the corresponding argument can be deduced immediately as

$$|Z| = \frac{1}{|Y|} \tag{1.52}$$

and

$$\theta = -\theta_Y \tag{1.53}$$

respectively.

Example 1.5 De Moivre's Theorem: *Calculate* $(1+j)^{100}$.

Solution: *Following equations (1.38), (1.39), and (1.41), the polar form of* $(1+j)$ *is expressed as*

$$1+j = \sqrt{2}\left(\cos\left(\frac{\pi}{4}\right) + j\sin\left(\frac{\pi}{4}\right)\right) \tag{1.54}$$

From equation (1.42)

$$(1+j)^{100} = 2^{100/2}\left(\cos\left(\frac{100\pi}{4}\right) + j\sin\left(\frac{100\pi}{4}\right)\right) \tag{1.55}$$

As $\sin(25\pi) = 0$ *and* $\cos(25\pi) = -1$, $(1+j)^{100} = -2^{50}$.

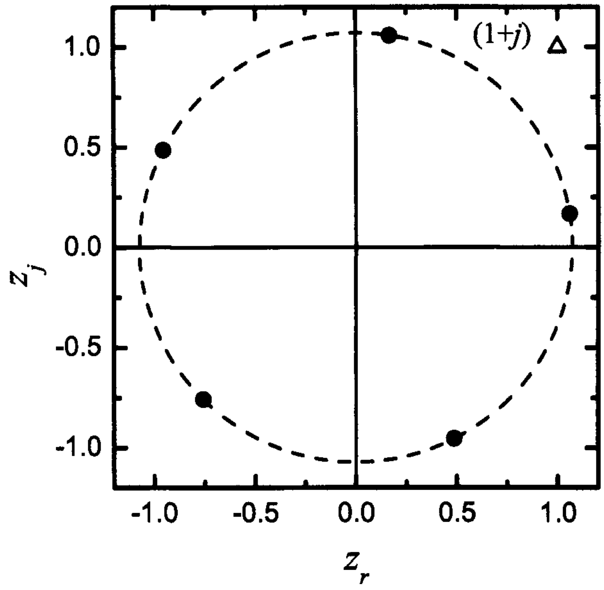

Figure 1.3: Argand diagram showing $1+j$ (△) and the five roots of $(1+j)^{1/5}$ (●) as calculated in Example 1.6.

Example 1.6 n

Example 1.6 n^{th} Roots of Complex Variables: *Calculate* $(1+j)^{1/5}$.

Solution: *The polar form of* $z = 1 + j$ *is expressed as*

$$z = \sqrt{2}\left(\cos\left(\frac{\pi}{4}\right) + j\sin\left(\frac{\pi}{4}\right)\right) \tag{1.56}$$

From equation (1.43)

$$z^{1/5} = 2^{1/10}\left(\cos\left(\frac{\pi}{20} + \frac{2k\pi}{5}\right) + j\sin\left(\frac{\pi}{20} + \frac{2k\pi}{5}\right)\right); \quad ; k = 0,\ldots,4 \tag{1.57}$$

As shown in Figure 1.3, the n roots lie on a circle of radius $\left(\sqrt{2}\right)^{1/n}$*, i.e.,* $r = 2^{1/10} = 1.07177$.

Example 1.7 Square Roots of Complex Variables: *The Warburg impedance associated with diffusion in an infinite medium takes the form* $Z = 1/\sqrt{j\omega\tau}$. *Find the roots of* Z.

Solution: *The polar form of* $z = 1/j\omega\tau = -j/\omega\tau$ *is expressed as*

$$z = \frac{1}{\omega\tau}\left(\cos\left(\frac{3\pi}{2}\right) + j\sin\left(\frac{3\pi}{2}\right)\right) \tag{1.58}$$

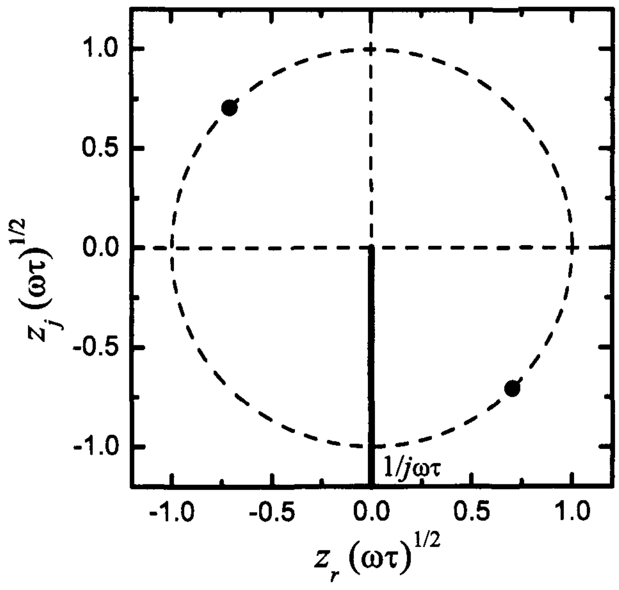

Figure 1.4: Argand diagram showing the angle associated with $1/j\omega\tau$ and the two roots $1/\sqrt{j\omega\tau}$ as calculated in Example 1.7.

From equation (1.43)

$$z^{1/2} = \sqrt{\frac{1}{\omega\tau}}\left(\cos\left(\frac{3\pi}{4}+k\pi\right)+j\sin\left(\frac{3\pi}{4}+k\pi\right)\right); \quad k=0,1 \tag{1.59}$$

The roots of $1/\sqrt{j\omega\tau}$ *are shown in Figure 1.4. The root with* $k = 0$ *can be rejected using the physical reasoning that the resistance associated with diffusion cannot have a negative sign. Thus, the Warburg impedance can be expressed in rectangular coordinates as*

$$Z = \sqrt{\frac{1}{2\omega\tau}} - j\sqrt{\frac{1}{2\omega\tau}} \tag{1.60}$$

The real and the negative imaginary components have the same magnitude and increase according to $\sqrt{1/\omega}$ *as frequency tends toward zero.*

1.3.3 Properties of Complex Variables

Some useful properties of the complex conjugates of $z = z_r + jz_j$ and $w = w_r + jw_j$ are presented in Table 1.4, and some relationships for the absolute value of $z = z_r + jz_j$ and $w = w_r + jw_j$ are presented in Table 1.5.

1.4 Elementary Functions of Complex Variables

The definition of many elementary functions can be extended to complex variables. Polynomial, exponential, and logarithmic functions are discussed here.

Table 1.4: Properties for the complex conjugates of $z = z_r + jz_j$ and $w = w_r + jw_j$.

$$\overline{z+w} = \overline{z} + \overline{w} \tag{1.61}$$

$$\overline{zw} = \overline{z}\,\overline{w} \tag{1.62}$$

$$\overline{\left[\frac{1}{z}\right]} = \frac{1}{\overline{z}} \tag{1.63}$$

$$\overline{\overline{z}} = z \tag{1.64}$$

Table 1.5: Properties for the absolute value of $z = z_r + jz_j$ and $w = w_r + jw_j$.

$$|z| = |\overline{z}| \tag{1.65}$$

$$z\overline{z} = |z|^2 \tag{1.66}$$

$$z_r \le |z| \tag{1.67}$$

$$z_j \le |z| \tag{1.68}$$

$$|zw| = |z||w| \tag{1.69}$$

$$\left|\frac{1}{z}\right| = \frac{1}{|z|}; \quad z \neq 0 \tag{1.70}$$

$$|z+w| \le |z| + |w| \tag{1.71}$$

1.4.1 Exponential

The exponential function e^z is of fundamental importance in impedance spectroscopy. The exponential function is defined such that it retains the properties of the real function e^x that

1. e^z, with argument $z = x + jy$, is single-valued and analytic (see Appendix A.1),
2. $de^z/dz = e^z$, and
3. $e^z \rightarrow e^x$, when $y \rightarrow 0$.

As a consequence of the above requirements, the exponential function with argument $z = x + jy$ can be shown to conform to

$$\begin{aligned} e^z &= e^{x+jy} \\ &= e^x\left[\cos(y) + j\sin(y)\right] \end{aligned} \tag{1.72}$$

Equation (1.72) can be considered to be the definition of e^z, which can be readily shown to meet the requirements expressed above.

Equation (1.72) is written in the standard polar form, equation (1.41), in which the modulus of e^z is

$$r = |e^z| = e^x \tag{1.73}$$

and the argument, or phase angle, is given by

$$\theta = \arg\left(e^z\right) = y \tag{1.74}$$

It is evident, then, that the exponential function is periodic, i.e.,

$$e^z = e^{z+j2k\pi} \tag{1.75}$$

for integer values of k.

Any complex number can be written in exponential form. For example, if $x = 0$ and $y = \theta$, application of equation (1.72) yields

$$\cos(\theta) + j\sin(\theta) = e^{j\theta} \tag{1.76}$$

In addition,

$$\begin{aligned} e^{-j\theta} &= \cos(-\theta) + j\sin(-\theta) \\ &= \cos(\theta) - j\sin(\theta) \end{aligned} \tag{1.77}$$

Equations (1.76) and (1.77) yield the Euler formulas

$$\cos(\theta) = \frac{e^{j\theta} + e^{-j\theta}}{2} \tag{1.78}$$

and

$$\sin(\theta) = \frac{e^{j\theta} - e^{-j\theta}}{2j} \tag{1.79}$$

These can be extended for $x \neq 0$ as

$$\cos(z) = \frac{e^{jz} + e^{-jz}}{2} \tag{1.80}$$

and

$$\sin(z) = \frac{e^{jz} - e^{-jz}}{2j} \tag{1.81}$$

Equations (1.80) and (1.81) provide relationships between complex variables and trigonometric functions. These can be manipulated to find relationships with hyperbolic function. Some important definitions and identities are presented in Table 1.6.

1.4.2 Logarithmic

Given

$$z = e^{w} \tag{1.99}$$

where z and $w = u + jv$ are complex numbers, the natural logarithm can be defined as

$$w = \ln(z) \tag{1.100}$$

As $w = u + jv$, equation (1.99) can be expressed as

$$z = e^{u}\left[\cos(v) + j\sin(v)\right] \tag{1.101}$$

The modulus of equation (1.101) is given as

$$|z| = e^{u} \tag{1.102}$$

and the phase angle is given by

$$\arg(z) = v \tag{1.103}$$

The complex number z can therefore be expressed as

$$z = |z|e^{j\arg(z)} = |z|e^{jv} \tag{1.104}$$

or

$$\ln(z) = \ln(|z|) + j\arg(z) = \ln(e^{u}) + jv \tag{1.105}$$

Remember! 1.4 *The exponential representation of a complex number plays an important role in impedance analysis. Remember that* $e^{\pm j\theta} = \cos(\theta) \pm j\sin(\theta)$.

Table 1.6: Trigonometric and hyperbolic relationships for the complex variable $z = z_r + jz_j$.

$$\sin(z) = \left(e^{jz} - e^{-jz}\right)/2j \tag{1.82}$$

$$\cos(z) = \left(e^{jz} + e^{-jz}\right)/2 \tag{1.83}$$

$$\frac{d\sin(z)}{dz} = \cos(z) \tag{1.84}$$

$$\frac{d\cos(z)}{dz} = -\sin(z) \tag{1.85}$$

$$\tan(z) = \frac{\sin(z)}{\cos(z)} \tag{1.86}$$

$$\cot(z) = \frac{\cos(z)}{\sin(z)} \tag{1.87}$$

$$\cos^2 z + \sin^2 z = 1 \tag{1.88}$$

$$\cos(z_1 \pm z_2) = \cos(z_1)\cos(z_2) \mp \sin(z_1)\sin(z_2) \tag{1.89}$$

$$\sin(z_1 \pm z_2) = \sin(z_1)\cos(z_2) \pm \cos(z_1)\sin(z_2) \tag{1.90}$$

$$\sinh(z) = \left(e^{z} - e^{-z}\right)/2 \tag{1.91}$$

$$\cosh(z) = \left(e^{z} + e^{-z}\right)/2 \tag{1.92}$$

$$\tanh(z) = \frac{\sinh(z)}{\cosh(z)} \tag{1.93}$$

$$\coth(z) = \frac{\cosh(z)}{\sinh(z)} \tag{1.94}$$

$$\cos(z) = \cos(x)\cosh(y) - j\sin(x)\sinh(y) \tag{1.95}$$

$$\sin(z) = \sin(x)\cosh(y) + j\cos(x)\sinh(y) \tag{1.96}$$

$$\cosh(z) = \cosh(x)\cos(y) + j\sinh(x)\sin(y) \tag{1.97}$$

$$\sinh(z) = \sinh(x)\cos(y) + j\cosh(x)\sin(y) \tag{1.98}$$

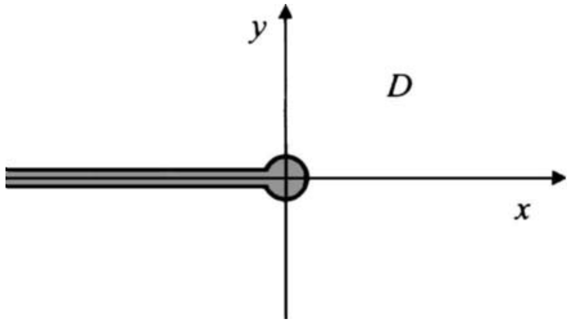

Figure 1.5: Representation of the domain D in which $\text{Ln}(z)$ is analytic.

There are an infinite number of values of $\ln(z)$ because $\arg(z)$ can differ by multiples of 2π. The *principal value* of $\ln(z)$ is defined for the *principal value* of $\arg(z)$, both designated by initial capital letters. Thus,

$$\text{Ln}(z) = \ln(|z|) + j\text{Arg}(z) \tag{1.106}$$

where

$$-\pi < \text{Arg}(z) \leq \pi \tag{1.107}$$

The function $\text{Ln}(z)$ is not defined at $z = 0$ and is not continuous anywhere on the negative real axis $z = x + 0j$, where $x < 0$. The negative real axis is a line of discontinuity because, on that line, the imaginary part of $\text{Ln}(z)$ has a jump discontinuity of 2π. If a cut is made, as shown in Figure 1.5, to remove the origin and the negative real axis, $\text{Ln}(z)$ is analytic in the resulting domain, and the derivative of $\text{Ln}(z)$ is given by

$$\frac{d\text{Ln}(z)}{dz} = \frac{1}{z} \tag{1.108}$$

The derivative of $\ln(z)$ is also given by equation (1.108) because $\text{Ln}(z)$ and $\ln(z)$ differ by a constant, $2\pi kj$.

Some functional relationships commonly used in impedance spectroscopy are presented in Table 1.7.

Example 1.8 Exponential Form: *Show that a time-dependent variable $i(t)$, expressed in terms of the steady-state value $\bar{i}$ and a sinusoidal time-dependent contribution as*

$$i(t) = \bar{i} + |i| \cos(\omega t + \varphi) \tag{1.115}$$

can be expressed as

$$i(t) = \bar{i} + \text{Re}\left\{\Delta i \exp(j\omega t)\right\} \tag{1.116}$$

where

$$\Delta i = |i| \exp(j\varphi) \tag{1.117}$$

Table 1.7: Functional relationships of complex variables commonly encountered in impedance spectroscopy, where x and y are real numbers, and $z = x + jy$.

$$\exp(jx) = \cos(x) + j\sin(x) \tag{1.109}$$

$$\exp(j(x+y)) = \exp(jx)\cdot\exp(jy) \tag{1.110}$$

$$\cos(\omega t + \varphi) = \mathrm{Re}\left\{\exp(j(\omega t + \varphi))\right\} \tag{1.111}$$

$$= \mathrm{Re}\left\{\exp(j\varphi)\cdot\exp(j\omega t)\right\} \tag{1.112}$$

$$\mathrm{Re}\{\ln(z)\} = \ln|z| \tag{1.113}$$

$$\mathrm{Im}\{\ln(z)\} = \arg(z) \tag{1.114}$$

is a complex number for $\varphi \neq 0$. Equation (1.116) is commonly used in the development of mathematical models for the transfer function, or impedance, response of electrochemical systems.

Solution: *From equation (1.109), the oscillating component of equation (1.116) can be expressed in terms of an exponential as*

$$|i|\cos(\omega t + \varphi) = |i|\exp(j(\omega t + \varphi)) - j|i|\sin(\omega t + \varphi) \tag{1.118}$$

or

$$|i|\cos(\omega t + \varphi) = \Delta i\exp(j\omega t) - j|i|\sin(\omega t + \varphi) \tag{1.119}$$

where Δi, given by equation (1.117), is a complex number for $\varphi \neq 0$. The quantity on the left-hand side of equation (1.117) must be a real number. Equation (1.119) is formally equivalent to

$$|i|\cos(\omega t + \varphi) = \mathrm{Re}\left\{|i|\cos(\omega t + \varphi)\right\} = \mathrm{Re}\left\{\Delta i\exp(j\omega t) - j\sin(\omega t + \varphi)\right\} \tag{1.120}$$

The imaginary term $j\sin(\omega t + \varphi)$ does not contribute to the real part of the complex number inside the brackets; thus,

$$|i|\cos(\omega t + \varphi) = \mathrm{Re}\left\{\Delta i\exp(j\omega t)\right\} \tag{1.121}$$

The above development could be considered to be a verification of equation (1.112) and justifies the treatment of the current and potential response of electrical circuits expressed as equation (4.8).

1.4.3 Polynomial

A polynomial function of degree n is defined to be

$$P_n(z) = a_n z^n + a_{n-1}z^{n-1} + \ldots + a_1 z + a_0 \tag{1.122}$$

where $a_n \neq 0, a_{n-1}, \ldots, a_0$ are all complex constants. The rational algebraic function

$$w(z) = \frac{P(z)}{Q(z)} \tag{1.123}$$

is defined where $P(z)$ and $Q(z)$ are polynomials.

A continued overview of complex variables is presented in Appendix A in the context of the complex integration used to establish the Kramers-Kronig relations.

Problems

1.1 For $z = 1 + j$ and $w = 5 - 2j$, perform the following operations:

- **(a)** $w + z$
- **(b)** $w - z$
- **(c)** wz
- **(d)** w/z

1.2 Calculate the phase angle and modulus for the following:

- **(a)** $z = 1/(j\omega C)$
- **(b)** $z = R$

1.3 The impedance associated with a single electrochemical reaction on a uniform surface can be expressed as

$$Z(\omega) = R_e + \frac{R_t}{1 + j\omega R_t C_{dl}} \tag{1.124}$$

where R_e is the electrolyte resistance, R_t is the charge-transfer resistance, and C_{dl} is the capacity of the double layer.

- **(a)** Find expressions for the real and imaginary parts of the impedance as a function of frequency.
- **(b)** Find expressions for the magnitude and phase angle of the impedance.
- **(c)** Find expressions for the real and imaginary parts of the admittance as a function of frequency.

1.4 The impedance associated with an ideally polarized (blocking) electrode can be expressed as

$$Z(\omega) = R_e + \frac{1}{j\omega C_{dl}} \tag{1.125}$$

where R_e is the electrolyte resistance and C_{dl} is the capacity of the double layer.

- **(a)** Find expressions for the real and imaginary parts of the impedance as a function of frequency.
- **(b)** Find expressions for the magnitude and phase angle of the impedance.
- **(c)** Find expressions for the real and imaginary parts of the admittance as a function of frequency.

1.5 The impedance associated with a constant phase element can be expressed as

$$Z(\omega) = R_e + \frac{1}{(j\omega)^\alpha Q} \tag{1.126}$$

where α and Q are parameters associated with a constant-phase element (CPE). When $\alpha = 1$, Q has units of a capacitance, i.e., μFcm^{-2}, and represents the capacity of the interface. When $\alpha \neq 1$, the system shows behavior that has been attributed to surface heterogeneity, oxide films, or to continuously distributed time constants for charge-transfer reactions.

- **(a)** Find expressions for the real and imaginary parts of the impedance as a function of frequency.
- **(b)** Find expressions for the magnitude and phase angle of the impedance.
- **(c)** Find expressions for the real and imaginary parts of the admittance as a function of frequency.

1.6 Consider a situation where the impedance of one layer is given by

$$Z_1(\omega) = \frac{R_1}{1 + j\omega R_1 C_1} \tag{1.127}$$

and the impedance of a second layer is given by

$$Z_2(\omega) = \frac{R_2}{1 + j\omega R_2 C_2} \tag{1.128}$$

Add the two impedances to find the overall impedance of the two layers.

Electrochemical Impedance Spectroscopy
by Mark E. Orazem and Bernard Tribollet

Chapter 2

Differential Equations

Development of models for impedance requires solution of differential equations. The method of solution requires two steps. In the first, a steady-state solution is obtained, which generally requires solution of ordinary differential equations.

In the second, a solution is obtained for the sinusoidal steady state. Generally, through transformations of the type discussed in Example 1.8, this too requires solutions of ordinary differential equations. While in some cases numerical solution is required, analytic solutions are possible for a large number of problems. Analytic solutions to some typical equations are reviewed in this chapter. For more details, see standard textbooks on engineering math.[74,77]

2.1 Linear First-Order Differential Equations

The general form of a linear first-order differential equation can be expressed as

$$\frac{dy}{dx} + P(x)y = Q(x) \tag{2.1}$$

The homogeneous equation corresponding to equation (2.1), for which $Q(x) = 0$, is given by

$$\frac{dy}{dx} + P(x)y = 0 \tag{2.2}$$

which has the solution

$$\Phi(x) = \exp\left(-\int P(x)dx\right) \tag{2.3}$$

$\Phi(x)$ is sometimes referred to as being an integrating factor, used to convert equation (2.1) to an exact differential equation.[78]

The solution of the heterogeneous equation (2.1) can be written in the form

$$y = \Phi(x)\lambda(x) \tag{2.4}$$

After simplification, equation (2.1) becomes

$$\Phi(x)\frac{d\lambda}{dx} = Q(x) \tag{2.5}$$

with solution

$$\lambda(x) = \int \left[Q(x) \exp\left[\int P(x)dx\right]\right] dx + C \tag{2.6}$$

The solution to equation (2.1) can be given as

$$y = \frac{\int Q(x)\exp\left[\int P(x)dx\right]dx}{\exp\left[\int Pdx\right]} + \frac{C}{\exp\left[\int Pdx\right]} \tag{2.7}$$

The right-hand side is a function of only x and can be integrated, and C is the constant of integration determined from the boundary condition.

The method for solving linear first-order differential equations involves the following steps:

1. Derive the solution to the homogeneous equation $\Phi(x)$.
2. Derive a new unknown function $\lambda(x)$ such that $y = \Phi(x)\lambda(x)$, using numerical integration if a formal analytic solution is not possible.
3. Develop the expression for y.

The method is illustrated in the following examples.

Example 2.1 Linear First-Order Differential Equation: *In the development of boundary-layer mass transfer to a planar electrode, a similarity transformation variable (see Section 2.4) can be identified through solution of*

$$\beta(x)g^2g' + \frac{1}{2}\beta'(x)g^3 = \ell \tag{2.8}$$

where ℓ *is a constant and* $g(0) = 0$. *Find an expression for* $g(x)$.

Solution: *Equation (2.8) can be placed in the form of equation (2.1) by introducing a new variable* $f(x) = g(x)^3$ *such that*

$$\frac{df}{dx} + \frac{3\beta'(x)}{2\beta(x)}f = \frac{3\ell}{\beta(x)} \tag{2.9}$$

where $P(x) = 3\beta'(x)/2\beta(x)$ *and* $Q(x) = 3\ell/\beta(x)$. *The solution to the homogeneous equation can be expressed, following equation (2.3), as*

$$\Phi(x) = \exp\left(-\int_0^x \frac{3\beta'(x)}{2\beta(x)}\right) = \exp\left(-\frac{3}{2}\ln\beta\right) = \beta^{-3/2} \tag{2.10}$$

Remember! 2.1 *The general solution to nonhomogeneous linear first-order differential equations can be obtained as the product of function to be determined and the solution to the homogeneous equation.*

Following equation (2.5), the governing equation for $\lambda(x)$*, defined by* $f = \Phi(x)\lambda(x)$*, is given by*

$$\frac{1}{\beta^{3/2}}\frac{d\lambda}{dx} = \frac{3\ell}{\beta(x)} \tag{2.11}$$

or

$$\frac{d\lambda}{dx} = 3\ell\beta(x)^{1/2} \tag{2.12}$$

with solution

$$\lambda(x) = \int_0^x 3\ell\beta^{1/2}dx + C \tag{2.13}$$

As $f(x) = g(x)^3 = \Phi(x)\lambda(x)$*,*

$$f(x) = \frac{1}{\beta^{3/2}}\int_0^x 3\ell\beta^{1/2}dx + \frac{C}{\beta^{3/2}} \tag{2.14}$$

The constant of integration C is evaluated from the requirement that $g(0) = 0$*, and thus,* $f(0) = 0$*. The constant of integration has a value* $C = 0$*. Thus,*

$$g(x) = \frac{1}{\sqrt{\beta}}\left[\int_0^x 3\ell\beta^{1/2}dx\right]^{1/3} \tag{2.15}$$

This example demonstrates the use of a simple variable transformation to convert a differential equation into a form suitable for application of the methods discussed in this section.

Example 2.2 Convective Diffusion Equation: *The material balance equation near a rotating disk electrode in an electrolyte solution where the migration can be neglected can be written as*

$$D\frac{d^2c}{dz^2} - v_z\frac{dc}{dz} = 0 \tag{2.16}$$

where $v_z = -a\frac{\Omega^{3/2}}{\sqrt{\nu}}z^2 = -\alpha z^2$*. Thus,*

$$D\frac{d^2c}{dz^2} + \alpha z^2\frac{dc}{dz} = 0 \tag{2.17}$$

Find an expression for the concentration c.

Solution: *Equation (2.17) is homogeneous. By introducing the new function* λ *defined as* $\lambda = \frac{dc}{dz}$*, the second-order differential equation becomes an equation of first order written as*

$$D\frac{d\lambda}{dz} + \alpha z^2\lambda = 0 \tag{2.18}$$

The solution is $\lambda = A\exp\left(-\frac{\alpha z^3}{3D}\right)$ *where A is a constant. The solution for concentration c is*

$$c(z) = \int_0^z A\exp\left(-\frac{\alpha z^3}{3D}\right)dz + c(0) \tag{2.19}$$

This expression for concentration is the starting point for the development of the Levich equation for the mass-transfer-limited current to a disk electrode.

2.2 Homogeneous Linear Second-Order Differential Equations

The general homogeneous linear second-order differential equation with constant coefficients can be written as

$$y'' + P(x)y' + Q(x)y = 0 \tag{2.20}$$

Consider here the special case of linear second-order differential equations with constant coefficients, written in general form as

$$ay'' + by' + cy = 0 \tag{2.21}$$

This equation can be written using operator notation as

$$\left(aD^2 + bD + c\right) y = 0 \tag{2.22}$$

where

$$Dy = \frac{dy}{dx} \tag{2.23}$$

A trial solution for equation (2.21) can be written as

$$y = \mathrm{e}^{mx} \tag{2.24}$$

where m is a constant to be determined. Substitution into equation (2.21) yields

$$\left(am^2 + bm + c\right) \mathrm{e}^{mx} = 0 \tag{2.25}$$

Equation (2.25) can be satisfied if and only if

$$\left(am^2 + bm + c\right) = 0 \tag{2.26}$$

Equation (2.26) is known as the characteristic or auxiliary equation of equation (2.21). As equation (2.26) takes the same form as equation (2.22), the usual practice is to write the differential operator form of the equation and solve for coefficients letting the symbol D play the role of m. The solution to the quadratic equation (2.26)

$$m = \frac{-b \pm \sqrt{b^2 - 4ac}}{2a} \tag{2.27}$$

provides values for m_1 and m_2. The solution to equation (2.21) is therefore

$$y = C_1\mathrm{e}^{m_1x} + C_2\mathrm{e}^{m_2x} \tag{2.28}$$

where C_1 and C_2 are constants to be determined from boundary conditions. If $m_1 = m_2$, equation (2.28) cannot provide a complete solution to equation (2.21). In this case, the solution can be shown to take the form

$$y = C_1\mathrm{e}^{m_1x} + C_2x\mathrm{e}^{m_1x} \tag{2.29}$$

In some cases, the roots can be complex. When the roots of the characteristic equation are complex, the general solution takes the form

$$y = C_1 e^{(p+jq)x} + C_2 e^{(p-jq)x} \tag{2.30}$$

where $m_1 = p + jq$ and $m_2 = p - jq$. It is usually convenient to use the Euler relations (1.78) and (1.79) to express the solution as

$$y = e^{px} \left(C_1 \cos(qx) + C_2 \sin(qx) \right) \tag{2.31}$$

where C_1 and C_2 are real constants to be determined from boundary conditions.

Example 2.3 Complex Roots for an ODE: *Find the roots for the differential equation*

$$\frac{d^2y}{dx^2} + by = 0 \tag{2.32}$$

discussed in Section 1.2.1.

Solution: *Equation (2.32) has the characteristic equation*

$$m^2 = -b \tag{2.33}$$

with solution

$$m = \pm\sqrt{-b} = \pm j\sqrt{b} \tag{2.34}$$

The homogeneous solution to equation (2.32) is given by

$$y = C_1 \exp\left(j\sqrt{b}x\right) + C_2 \exp\left(-j\sqrt{b}x\right) \tag{2.35}$$

Example 2.4 Diffusion in a Finite Domain: *The steady-state conservation equation for diffusion of species i in an finite medium can be expressed as*

$$D_i \frac{d^2 c_i}{dz^2} = 0 \tag{2.36}$$

with boundary conditions

$$\begin{aligned} c_i &\rightarrow c_{i,\infty} \quad \text{for} \quad z = \delta \\ c_i &= c_i(0) \quad \text{at} \quad z = 0 \end{aligned} \tag{2.37}$$

We seek an expression for the concentration profile.

Solution: *The solution to equation (2.36) can be obtained by direct integration to be*

$$c_i = Az + B \tag{2.38}$$

where A and B are constants of integration. Application of the boundary conditions (2.37) yields

$$\begin{aligned} c_i &= c_i(0) + \frac{z}{\delta}\left(c_{i,\infty} - c_i(0)\right) \quad \text{for} \quad z < \delta \\ c_i &= c_{i,\infty} \quad \text{for} \quad z \geq \delta \end{aligned} \tag{2.39}$$

The development of the impedance response is presented in Section 11.4.2.

2.3 Nonhomogeneous Linear Second-Order Differential Equations

The nonhomogeneous linear second-order differential equations with constant coefficients can be written in general form as

$$ay'' + by' + cy = f(x) \tag{2.40}$$

If $f(x) = 0$, the equation is called *homogeneous*. If $f(x) \neq 0$, the equation is called *nonhomogeneous*. The general solution to equation (2.40) is given as the product

$$y = \Phi(x)\lambda(x) \tag{2.41}$$

where $\Phi(x)$ is the solution to the homogeneous equation.

The homogeneous solution $\Phi(x)$ can be obtained using the methods described in Section 2.2. The unknown function $\lambda(x)$ is defined such that

$$y = \Phi(x)\lambda(x) \tag{2.42}$$

$$y' = \Phi(x)'\lambda(x) + \Phi(x)\lambda(x)' \tag{2.43}$$

$$y'' = \Phi(x)''\lambda(x) + 2\Phi(x)'\lambda(x)' + \Phi(x)\lambda(x)'' \tag{2.44}$$

Equation (2.40) becomes

$$a\left(\Phi''\lambda + 2\Phi'\lambda' + \Phi\lambda''\right) + b\left(\Phi'\lambda + \Phi\lambda'\right) + c\left(\Phi\lambda\right) = f \tag{2.45}$$

As Φ is the solution to the homogeneous equation, equation (2.46) is reduced to

$$a\left(2\Phi'\lambda' + \Phi\lambda''\right) + b\left(\Phi\lambda'\right) = f \tag{2.46}$$

Equation (2.46) can be solved by a reduction of order technique, i.e., by letting $\mu = \lambda'$, such that

$$\mu' a\Phi + \mu\left(2a\Phi' + b\Phi\right) = f \tag{2.47}$$

Remember! 2.2 *The general solution to nonhomogeneous linear second-order differential equations with constant coefficients can be obtained as the product of function to be determined and the solution to the homogeneous equation (see equation (2.41)).*

The resulting first-order equation may be solved numerically if analytic solutions are not available.

The method described here is general and can be applied to higher-order differential equations. The method provides an attractive alternative to the use of particular solutions obtained using trial solutions based on the form of the function $f(x)$ and, in some cases, on the form of the homogeneous solution.[74]

2.4 Partial Differential Equations by Similarity Transformations

Partial differential equations are generally solved by finding a transformation that allows the partial differential equation to be converted into two ordinary differential equations. A number of techniques are available, including separation of variables, Laplace transforms, and the method of characteristics.

A similarity transformation may be used when the solution to a parabolic partial differential equation, written in terms of two independent variables, can be expressed in terms of a new independent variable that is a combination of the original independent variables. The success of this transformation requires that:

- the governing partial differential equation can be expressed as an ordinary differential equation in terms of the similarity variable,
- the three boundary conditions for the original partial differential equation collapse to form two boundary conditions in terms of the similarity variable, and
- the original independent variables appear in neither the transformed ordinary differential equation nor the transformed and collapsed boundary conditions.

Similarity transformations are often used when the same condition applies when one independent variable is equal to zero and the other independent variable tends toward infinity.

The classic problem of diffusion in an infinite medium can be solved by use of a similarity transformation. The associated impedance response is discussed in Section 11.3. A general method for finding the time-dependent concentration profile is presented here in the form of an example.

Remember! 2.3 *Similarity transformations may be used for parabolic partial differential equations when the same condition applies when one independent variable is equal to zero and the other independent variable tends toward infinity.*

Example 2.5 Diffusion in an Infinite Domain: *The conservation equation for diffusion of species i in an infinite medium can be expressed as*

$$\frac{\partial c_i}{\partial t} - D_i \frac{\partial^2 c_i}{\partial z^2} = 0 \tag{2.48}$$

with boundary conditions

$$\begin{aligned} c_i &\rightarrow c_{i,\infty} \quad \text{for} \quad z \rightarrow \infty \\ c_i &= c_i(0) \quad \text{at} \quad z = 0 \\ c_i &= c_{i,\infty} \quad \text{at} \quad t = 0 \end{aligned} \tag{2.49}$$

We seek an expression for the time-dependent concentration profile.

Solution: *The method for solving partial differential equations generally involves finding a method to express them as coupled ordinary differential equations. A similarity transformation is possible if c_i can be expressed as a function of only a new variable. This requirement implies that equation (2.48) can be expressed as a function of only the new variable, and that the three conditions (2.49) in time and position can collapse into two conditions in the new variable.*

The observation that the same condition for c_i applies at $t = 0$ and $z \rightarrow \infty$ suggests that, through a transformation variable of the form $\eta = f(z)/g(t)$, the two boundary conditions at $z = 0$ and $z \rightarrow \infty$ and the initial condition at $t = 0$ could collapse into boundary conditions at $\eta = 0$ (corresponding to $z = 0$) and $\eta \rightarrow \infty$ (corresponding to both $t = 0$ and $z \rightarrow \infty$).

As a trial transformation, let η be given by

$$\eta = \frac{z}{g(t)} \tag{2.50}$$

Application of the chain rule yields

$$\frac{\partial c_i}{\partial t} = \frac{dc_i}{d\eta}\frac{\partial \eta}{\partial t} = \frac{dc_i}{d\eta}\left(-\frac{z}{g^2}\frac{dg}{dt}\right) \tag{2.51}$$

$$\frac{\partial c_i}{\partial z} = \frac{dc_i}{d\eta}\frac{\partial \eta}{\partial z} = \frac{dc_i}{d\eta}\left(\frac{1}{g}\right) \tag{2.52}$$

and

$$\frac{\partial^2 c_i}{\partial z^2} = \frac{d}{d\eta}\left(\frac{dc_i}{d\eta}\right)\frac{1}{g}\frac{\partial \eta}{\partial z} = \frac{d^2 c_i}{d\eta^2}\left(\frac{1}{g^2}\right) \tag{2.53}$$

Introduction of equations (2.50) and (2.53) into equation (2.48) yields

$$\frac{d^2 c_i}{d\eta^2} + \frac{gg'}{D_i}\eta\frac{dc_i}{d\eta} = 0 \tag{2.54}$$

Equation (2.54) will be a function of only η if g satisfies

$$\frac{g}{D_i}\frac{dg}{dt} = \lambda \tag{2.55}$$

where λ is a constant to be determined.

The problem now consists of finding the solution to two ordinary differential equations.

$$\frac{d^2c_i}{d\eta^2} + \lambda\eta\frac{dc_i}{d\eta} = 0 \tag{2.56}$$

and equation (2.55). The boundary condition for equation (2.55) is that $g = 0$ for $t = 0$. This will allow the conditions at $z \to \infty$ and $t = 0$ to apply for $\eta = \infty$. The boundary conditions for equation (2.56) are

$$\begin{aligned} c_i &\to c_{i,\infty} \quad \text{for} \quad \eta \to \infty \\ c_i &= c_i(0) \quad \text{at} \quad \eta = 0 \end{aligned} \tag{2.57}$$

Equation (2.55) is a linear first-order differential equation. It can be solved by use of a variable transformation $h = g^2$ such that

$$\frac{dh}{dt} = \frac{dg^2}{dt} = 2g\frac{dg}{dt} \tag{2.58}$$

Thus

$$\frac{dh}{dt} = 2D_i\lambda \tag{2.59}$$

which can be integrated directly to obtain

$$h = g^2 = 2D_i\lambda t + C \tag{2.60}$$

The requirement that $g = 0$ for $t = 0$ yields $C = 0$; thus,

$$g = \sqrt{2D_i\lambda t} \tag{2.61}$$

and

$$\eta = \frac{z}{\sqrt{2D_i\lambda t}} \tag{2.62}$$

In this case, equation (2.58) could be solved by a straightforward direct integration. Some other cases will require use of the integrating factor discussed in Section 2.1.

Equation (2.56) is a linear second-order differential equation. It can be solved by reduction of order. Let

$$P = \frac{dc_i}{d\eta} \tag{2.63}$$

such that

$$\frac{dP}{d\eta} + \lambda\eta P = 0 \tag{2.64}$$

Integration yields

$$P = Ae^{-\lambda\eta^2/2} \tag{2.65}$$

where A is a constant of integration. A second integration performed after substitution of equation (2.63) into equation (2.65) yields

$$c_i = A\int_0^{\eta} e^{-\lambda\eta^2/2} d\eta + B \tag{2.66}$$

where B is a constant of integration. The integrals can be placed in standard form by allowing the arbitrary constant to have a value $\lambda = 2$. *Evaluation of conditions (2.57) yields*

$$\frac{(c_i - c_i(0))}{(c_{i,\infty} - c_i(0))} = \frac{\int_0^{\eta} e^{-\eta^2} d\eta}{\int_0^{\infty} e^{-\eta^2} d\eta} \tag{2.67}$$

or

$$\frac{(c_i - c_i(0))}{(c_{i,\infty} - c_i(0))} = \frac{2}{\sqrt{\pi}}\int_0^{\eta} e^{-\eta^2} d\eta \tag{2.68}$$

The ratio of integrals appearing here is tabulated and is known as the error function, erf.

$$\frac{(c_i - c_i(0))}{(c_{i,\infty} - c_i(0))} = 1 - \operatorname{erf}\left(\frac{2}{\sqrt{4D_i t}}\right) \tag{2.69}$$

This is the solution presented in Section 11.3.

2.5 Differential Equations with Complex Variables

In the course of developing models for the impedance response of physical systems, differential equations are commonly encountered that have complex variables. For equations with constant coefficients, solutions may be obtained using the methods described in the previous sections. For equations with variable coefficients, a numerical solution may be required. The method for numerical solution is to separate the equations into real and imaginary parts and to solve them simultaneously.

An example is provided to illustrate the method.

Example 2.6 Foundation for Warburg Impedance: *The following differential equation appears in the treatment of impedance associated with diffusion:*

$$\frac{d^2\theta_i}{d\xi^2} - jK_i\theta_i = 0 \tag{2.70}$$

Remember! 2.4 *The method for numerical solution of differential equations with complex variables is to separate the equations into real and imaginary parts and to solve them simultaneously.*

---

where θ_i is a dimensionless complex number representing the oscillating contribution to concentration, ξ is a dimensionless position, and K_i is a frequency made dimensionless using the diffusion coefficient for species i. The complete development for this equation can be found in Chapter 11.

Solution: *Equation (2.70) is a linear second-order homogeneous differential equation with constant coefficients. It can be solved using the characteristic equation*

$$m^2 - jK_i = 0 \tag{2.71}$$

with solution

$$m = \pm\sqrt{jK_i} \tag{2.72}$$

The corresponding solution takes the form

$$\theta_i = A_i e^{\xi\sqrt{jK_i}} + B_i e^{-\xi\sqrt{jK_i}} \tag{2.73}$$

where constants A_i and B_i are to be determined so as to satisfy the boundary conditions. For diffusion in an infinite medium, the boundary conditions are

$$\theta_i = 0 \quad \text{at} \quad \xi \to \infty \tag{2.74}$$

and

$$\theta_i = 1 \quad \text{at} \quad \xi = 0 \tag{2.75}$$

Condition (2.74) requires that $A_i = 0$, and condition (2.75) provides that $B_i = 1$. Thus,

$$\theta_i = e^{-\xi\sqrt{jK_i}} \tag{2.76}$$

For diffusion in a finite domain, condition (2.74) is replaced by

$$\theta_i = 0 \quad \text{at} \quad \xi = 1 \tag{2.77}$$

In this case, application of conditions (2.75) and (2.77) provides that

$$0 = A_i e^{\sqrt{jK_i}} + B_i e^{-\sqrt{jK_i}} \tag{2.78}$$

and

$$1 = A_i + B_i \tag{2.79}$$

The resulting solution is

$$\begin{aligned} \theta_i = \frac{\sinh\left((\xi - 1)\sqrt{jK_i}\right)}{\sinh\left(-\sqrt{jK_i}\right)} \quad & \text{for} \quad \xi < 1 \\ \theta_i = 0 \quad & \text{for} \quad \xi \geq 1 \end{aligned} \tag{2.80}$$

As an exercise, the reader can verify that equation (2.73) satisfies both real and imaginary parts of equation (2.70). This development represents the starting point for both the Warburg impedance associated with diffusion in a stationary medium of infinite depth and the diffusion impedance associated with a stationary medium of finite depth.

Problems

2.1 Find the general solution for c as a function of y for:

- **(a)** $\frac{dc}{dy} + kc = 0$
- **(b)** $\frac{d^2c}{dy^2} + kc = 0$
- **(c)** $\frac{d^2c}{dy^2} + a\frac{dc}{dy} + kc = 0$
- **(d)** $\frac{d^2c}{dy^2} + a\frac{dc}{dy} + kc = b$

2.2 Show that equation (2.73) satisfies both real and imaginary parts of equation (2.70).

2.3 Verify that equation (2.80) represents the solution for equation (2.70) for diffusion in a finite domain.

2.4 Verify that equation (2.76) represents the solution for equation (2.70) for diffusion in an infinite domain.

Electrochemical Impedance Spectroscopy
by Mark E. Orazem and Bernard Tribollet

Chapter 3

Statistics

A working understanding of statistics is essential for the analysis of experiments conducted in the frequency domain, such as impedance spectroscopy. The objective of this chapter is to provide an overview of concepts and definitions used in statistics at a level sufficient to understand the interpretation of frequency domain data.

3.1 Definitions

Some basic statistical concepts are defined in this section. For a more comprehensive treatment, the reader is directed to standard statistical texts.[79]

3.1.1 Expectation and Mean

The *expectation* or *mean* of a quantity x_k, sampled $k = 1 \ldots n_x$ times, is given as

$$\mathrm{E}\{x\} = \mu_x = \frac{1}{n_x} \sum_{k=1}^{n_x} x_k \tag{3.1}$$

The quantity x is called a *variate* and has values x_k that are randomly distributed. Some useful properties of the expectations of constants and variates are given in Table 3.1.

3.1.2 Variance, Standard Deviation, and Covariance

The *variance* of a quantity x_k, sampled $k = 1 \ldots n_x$ times, is given as

$$\sigma_x^2 = \frac{1}{n_x - 1} \sum_{k=1}^{n_x} (x_k - \mu_x)^2 \tag{3.7}$$

In terms of expectations, the *variance* is given as

$$\sigma_x^2 = \frac{n_x}{n_x - 1} \mathrm{E}\left\{(x - \mathrm{E}\{x\})^2\right\} \tag{3.8}$$

Table 3.1: Properties of the *expectation* where c is a constant and x and y are random variates.

$$\mathrm{E}\{c\} = c \tag{3.2}$$

$$\mathrm{E}\{x+c\} = \mathrm{E}\{x\} + c \tag{3.3}$$

$$\mathrm{E}\{cx\} = c\mathrm{E}\{x\} \tag{3.4}$$

$$\mathrm{E}\{x+y\} = \mathrm{E}\{x\} + \mathrm{E}\{y\} \tag{3.5}$$

$$\mathrm{E}\{(x+y)^2\} = \mathrm{E}\{x\}^2 + \mathrm{E}\{y\}^2 + 2\mathrm{E}\{x\}\mathrm{E}\{y\} \tag{3.6}$$

Table 3.2: Properties of the *variance* where c is a constant and x and y are random variates.

$$\sigma^2(c) = 0 \tag{3.12}$$

$$\sigma^2(x+c) = \sigma_x^2 \tag{3.13}$$

$$\sigma^2(cx) = c^2\sigma_x^2 \tag{3.14}$$

$$\sigma^2(x+y) = \sigma_x^2 + \sigma_y^2 + \sigma_{x,y} \tag{3.15}$$

(3.16)

As $n_x \to \infty$, $n_x/(n_x - 1) \to 1$ in equation (3.8).

The *standard deviation* is given by the square root of the variance, i.e.,

$$\sigma_x = \sqrt{\sigma_x^2} \tag{3.9}$$

Both the standard deviation and variance are positive definite. The *standard error*

$$s_x = \frac{\sigma_x}{\sqrt{n_x}} \tag{3.10}$$

is the standard deviation scaled by the square root of the sample size n_x.

The *cross-covariance* can be defined to be

$$\sigma_{x_1x_2} = \frac{n_x}{n_x - 1}\mathrm{E}\left\{\left(x_{1,k} - \mathrm{E}\left\{x_1\right\}\right)\left(x_{2,k} - \mathrm{E}\left\{x_2\right\}\right)\right\} \tag{3.11}$$

Unlike the variance, the cross-covariance may have positive or negative values. If x_1 and x_2 are not correlated, $\sigma_{x_1x_2} = 0$. The techniques discussed in Section 3.2 can be used to demonstrate the properties of the variance given in Table 3.2.

3.1.3 Normal Distribution

The *normal distribution* is a function of the mean μ_x, given by equation (3.1), and the standard deviation σ_x, given by equation (3.9), i.e.,

$$y(x) = \frac{1}{\sigma_x\sqrt{2\pi}}\exp\left(-\frac{(x-\mu_x)^2}{2\sigma_x^2}\right) \tag{3.17}$$

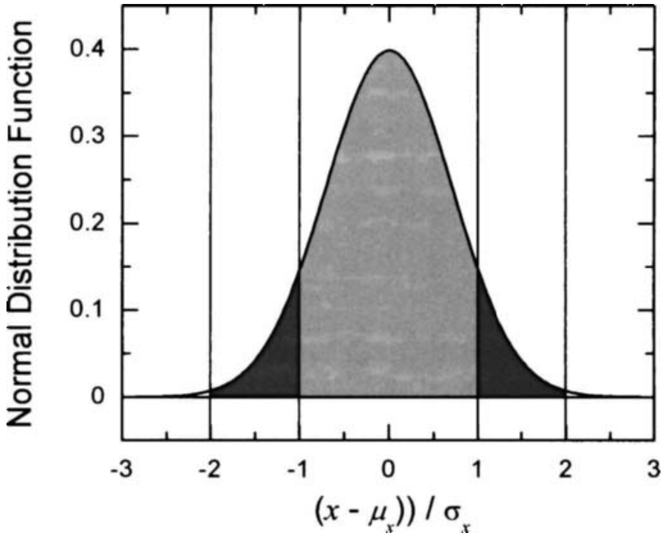

Figure 3.1: The *standard normal distribution* function, equation (3.17) with mean equal to zero and standard deviation equal to one: 68.26 percent of the distribution lies within $\pm\sigma$ (shown as the light gray region); 95.44 percent of the distribution lies within $\pm 2\sigma$ (shown as the sum of the light and dark gray regions); and 99.73 percent of the distribution lies within $\pm 3\sigma$.

The normal distribution function can be written as $\mathrm{N}(\mu_x, \sigma_x^2)$. If x has a normal distribution with parameters μ_x and σ_x^2, the variable transformation

$$x_{\text{norm}} = \frac{x - \mu_x}{\sigma_x} \tag{3.18}$$

will follow the *standard normal distribution*[80]

$$y_{\text{norm}}(x_{\text{norm}}) = \frac{1}{\sqrt{2\pi}} \exp\left(-\frac{x_{\text{norm}}^2}{2}\right) \tag{3.19}$$

With respect to equation (3.17), the standard normal distribution function has a mean value $\mu_x = 0$ and a standard deviation $\sigma_x = 1$. The area under a standard normal distribution is equal to unity. The standard normal distribution function can be written as $\mathrm{N}(0, 1)$.

The *standard normal distribution* function, with standard deviation equal to 1 and mean equal to zero, is presented in Figure 3.1. The confidence interval defined for an experimental set of data $x_1, \ldots, x_N$ by $\mu_x \pm \sigma_x$ means that there is a 68.26 percent probability (see Section 3.1.4) that the correct value lies within the interval. There is a 95.44 percent probability that the correct value lies within the interval confidence interval $\mu_x \pm 2\sigma_x$. The *Central-Limit Theorem* described in Section 3.1.5 is often invoked to justify using the normal distribution as a basis for interpreting experimental data.

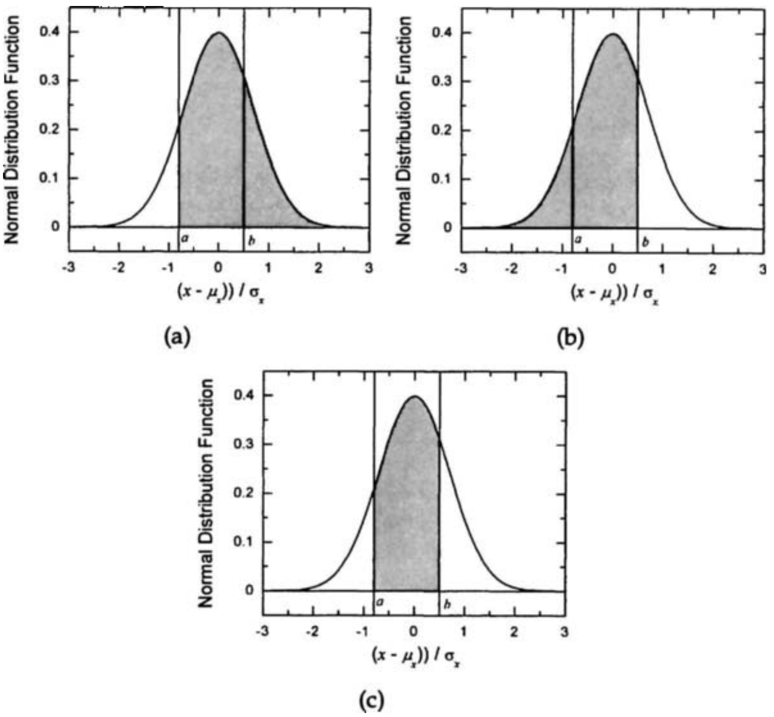

(a) (b) (c)

Figure 3.2: Probability distributions: a) $x > a$, equation (3.20); b) $x < b$, equation (3.21); and c) $a < x < b$, equation (3.22).

3.1.4 Probability

The *probability* is obtained by integrating the distribution function over the appropriate limits. For example, for x being a normal random variable with mean μ_x and standard deviation σ_x, the probability that $x > a$ can be expressed as

$$P(x > a) = \frac{1}{\sigma_x \sqrt{2\pi}} \int_a^\infty \exp\left(-\frac{(x-\mu_x)^2}{2\sigma_x^2}\right) dx \tag{3.20}$$

The probability $P(x > a)$ is shown as the shaded area in Figure 3.2(a). The probability that $x < b$ can be expressed as

$$P(x < b) = \frac{1}{\sigma_x \sqrt{2\pi}} \int_{-\infty}^b \exp\left(-\frac{(x-\mu_x)^2}{2\sigma_x^2}\right) dx \tag{3.21}$$

as shown in Figure 3.2(b), and the *probability* that $a < x < b$ can be expressed as

$$P(a < x < b) = \frac{1}{\sigma_x \sqrt{2\pi}} \int_a^b \exp\left(-\frac{(x-\mu_x)^2}{2\sigma_x^2}\right) dx \tag{3.22}$$

as shown in Figure 3.2(c). Tables of *cumulative standard normal distributions*

$$\Phi(x) = \frac{1}{\sqrt{2\pi}} \int_0^x \exp\left(-\frac{x_{\text{norm}}^2}{2}\right) dx_{\text{norm}} \tag{3.23}$$

are available in reference books and statistics textbooks.[81,82]

3.1.5 Central-Limit Theorem

The *Central-Limit Theorem* states that the sampling distribution of the mean, for any set of independent and identically distributed random variables, will tend toward the normal distribution, equation (3.17), as the sample size becomes large.[80]

Theorem 3.1 (Central-Limit Theorem) *Let S represent a sequence of independent discrete random variables. Let $X_1, X_2, \ldots, X_i, \ldots, X_n$ represent n subsets of S, such that each set X_i contains n_x values, has a mean value μ_{X_i}, and has a variance $\sigma_{X_i}^2$. The mean value for the global set S is μ_S and the variance is σ_S^2.*

$$\lim_{n\to\infty} \mathrm{P}\left(a < \frac{\mu_{X_i} - \mu_S}{\sigma_{X_i}} < b\right) = \frac{1}{\sqrt{2\pi}} \int_a^b \exp\left(-\frac{x^2}{2}\right) dx \tag{3.24}$$

and μ_{X_i} is distributed according to

$$\lim_{n\to\infty} \mu_{X_i} = \mathrm{N}(\mu_S, \frac{\sigma_S^2}{n_x}) \tag{3.25}$$

or

$$\lim_{n\to\infty} \frac{\mu_{X_i} - \mu_S}{\sigma_S/\sqrt{n_x}} = \mathrm{N}(0,1) \tag{3.26}$$

The Central-Limit Theorem gives rise to the following important observations:

- The mean of the sampling distribution of means is equal to the mean of the population from which the samples were drawn.
- The variance of the sampling distribution of means is equal to the variance of the population from which the samples were drawn divided by the size of the samples.
- If the original population is distributed normally (i.e., it is bell shaped), the sampling distribution of means will also be normal. Even if the original population is not normally distributed, the sampling distribution of means will increasingly approximate a normal distribution as sample size increases.

As an illustration of the Central-Limit Theorem, consider the distribution of 5,000 random numbers presented in Figure 3.3. The distribution shown in Figure 3.3 represents a global set S that is centered about zero and clearly does not follow

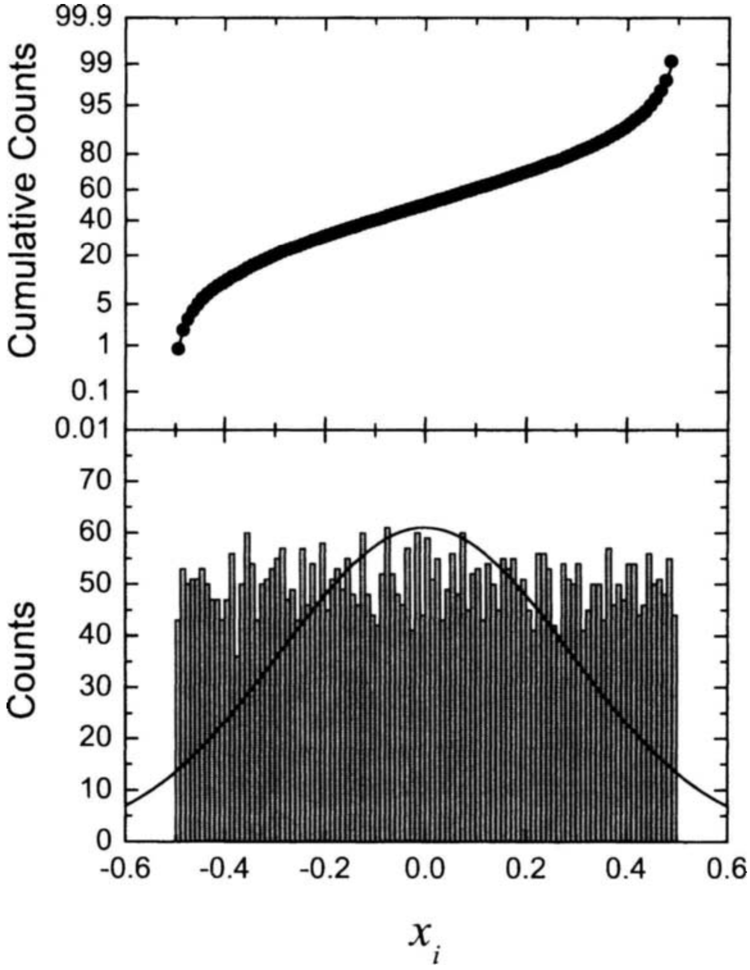

Figure 3.3: The histogram and a cumulative normal distribution plot for 5,000 uniformly distributed random numbers with mean $\mu_S = -8.06 \times 10^{-4}$ and standard deviation $\sigma_S = 0.28736$.

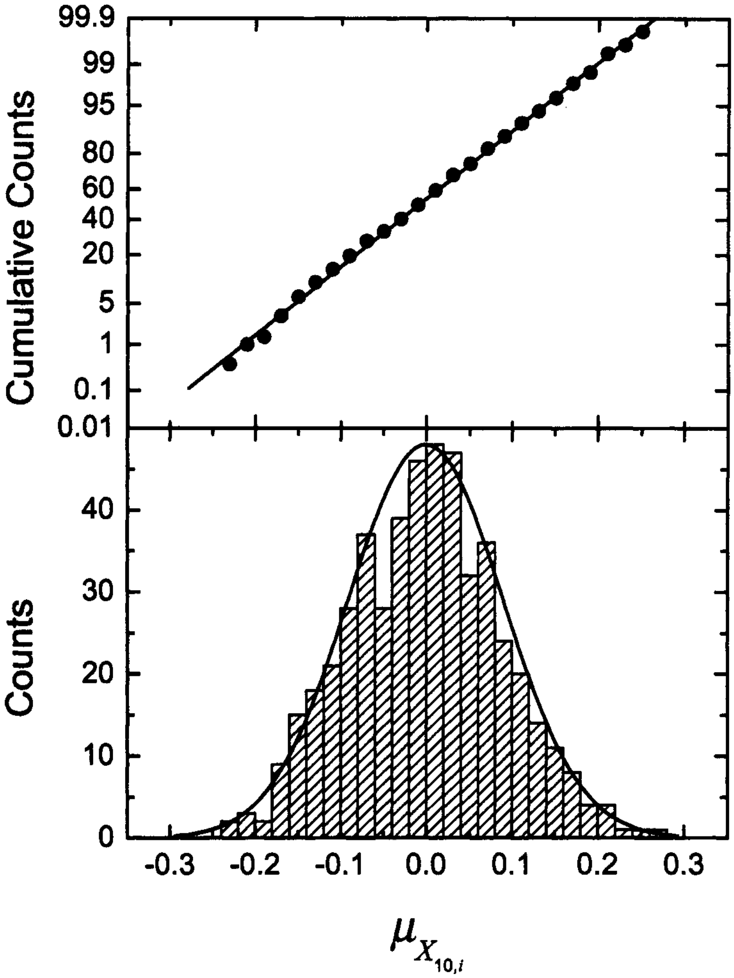

Figure 3.4: The histogram and a cumulative normal distribution plot for the means of subsets of the data shown in Figure 3.3. Each subset contained 10 points. The mean of the subset means is equal to $\mu_X = -8.06 \times 10^{-4}$ and standard deviation $\sigma_X = 0.09015$.

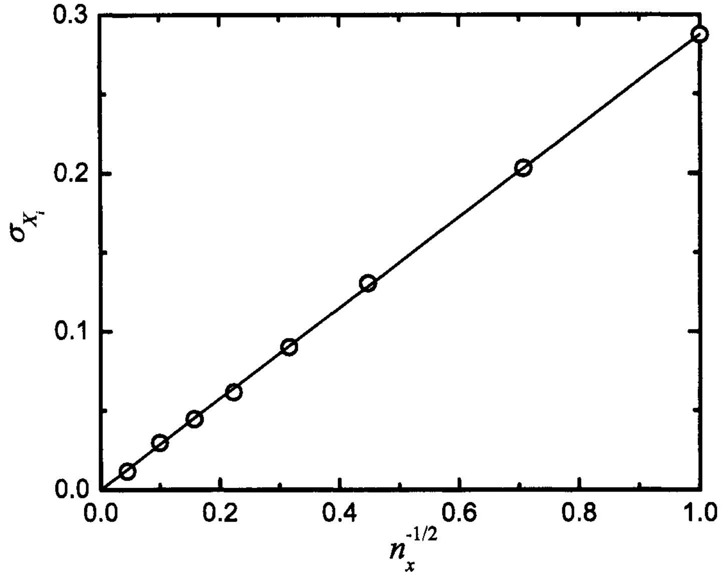

Figure 3.5: Standard deviations σ_X for the means of subsets of the data shown in Figure 3.3 as a function of $1/\sqrt{n_x}$, where n_x is the number of samples in each subset X_i.

a normal distribution. The mean value is $\mu_S = -8.06 \times 10^{-4}$ and the standard deviation is $\sigma_S = 0.28736$. The global set S can be subdivided into 500 subsets $X_{10,i}$, each containing 10 values. The distribution of the means μ_{X_i}, shown in Figure 3.4, appears to be normally distributed. The distribution, shown on normal cumulative probability scales, follows a straight line, thus confirming that the distribution of the sample means is normal. The mean of the subset means is equal to the mean of the original global set S, i.e., $\mu_X = \mu_S = -8.06 \times 10^{-4}$. The standard deviation of the subsets is equal to $\sigma_X = 0.09015$.

The standard deviation of the sample means is smaller than that of the global set S and is a function of the number of data n_x in each subset according to $\sigma_X = \sigma_S / \sqrt{n_x}$. A plot of standard deviation as a function of $1/\sqrt{n_x}$ yields a straight line, shown in Figure 3.5.

Thus, the sampling distribution of the mean becomes approximately normal regardless of the distribution of the original variable, and the sampling distribution of the mean is centered at the population mean of the original variable. In addition, the standard deviation of the sampling distribution of the mean approaches $\sigma_S / \sqrt{n}$.

Remember! 3.1 *The* Central-Limit Theorem *is often invoked to justify using the normal distribution as a basis for interpreting experimental data.*

3.2 Error Propagation

Analytic expressions are available for assessing the propagation of errors through linear systems. Such approaches can be used as well when the variances are sufficiently small that the system can be linearized about its expectation value. Numerical techniques are generally needed to assess the propagation of errors through nonlinear systems.

3.2.1 Linear Systems

Under the assumption that the system is linear, i.e., that derivatives of second and higher order can be neglected, a Taylor series expansion about the expectation value yields the kth observation of a function $f = f(x_1, x_2, \dots)$ as

$$f_k = \mathrm{E}\{f\} + \mathrm{E}\left\{\frac{\partial f}{\partial x_1}\right\}(x_{1,k} - \mathrm{E}\{x_1\}) + \mathrm{E}\left\{\frac{\partial f}{\partial x_2}\right\}(x_{2,k} - \mathrm{E}\{x_2\}) + \dots \tag{3.27}$$

In the limit that $N \to \infty$,

$$\sigma_f^2 = \mathrm{E}\left\{(f_k - \mathrm{E}\{f\})^2\right\} \tag{3.28}$$

and the variance of $f = f(x_1, x_2, \dots)$ can be expressed as

$$\sigma_f^2 = \left[\mathrm{E}\left\{\frac{\partial f}{\partial x_1}\right\}\mathrm{E}\{x_{1,k} - \mathrm{E}\{x_1\}\} + \mathrm{E}\left\{\frac{\partial f}{\partial x_2}\right\}\mathrm{E}\{x_{2,k} - \mathrm{E}\{x_2\}\} + \dots\right]^2 \tag{3.29}$$

Equation (3.29) can be expanded in terms of the variances of respective components as

$$\sigma_f^2 = \mathrm{E}\left\{\frac{\partial f}{\partial x_1}\right\}^2 \sigma_{x_1}^2 + \mathrm{E}\left\{\frac{\partial f}{\partial x_2}\right\}^2 \sigma_{x_2}^2 + 2\mathrm{E}\left\{\frac{\partial f}{\partial x_1}\right\}\mathrm{E}\left\{\frac{\partial f}{\partial x_2}\right\}\sigma_{x_1 x_2} + \dots \tag{3.30}$$

Thus, the variance of a general function f can be expressed in terms of the variance of its components as

$$\sigma_f^2 \cong \sigma_{x_1}^2\left(\frac{\partial f}{\partial x_1}\right)^2 + \sigma_{x_2}^2\left(\frac{\partial f}{\partial x_2}\right)^2 + \dots + \sigma_{x_1,x_2}\left(\frac{\partial f}{\partial x_1}\right)\left(\frac{\partial f}{\partial x_2}\right) + \dots \tag{3.31}$$

If the errors are not correlated, i.e., if the cross-covariance terms are equal to zero, the variance of f can be expressed as

$$\sigma_f^2 \cong \sigma_{x_1}^2\left(\frac{\partial f}{\partial x_1}\right)^2 + \sigma_{x_2}^2\left(\frac{\partial f}{\partial x_2}\right)^2 + \dots \tag{3.32}$$

Example 3.1 Error Propagation: *As discussed in Chapter 15, regression to electrohydrodynamic impedance data can be used to obtain values for the Schmidt number. If* *the Schmidt number for reduction of oxygen in 0.5 M NaCl was found to be equal to* 510 ± 25, *and the kinematic viscosity is equal to* $0.89 \times 10^{-2} \pm 0.05 \times 10^{-2}$ *cm*^{2}*s*$^{-1}$*, calculate the diffusivity and the standard deviation.*[83]

Solution: *The Schmidt number is expressed as* $Sc_{O_2} = \nu / D_{O_2}$*; thus* $D_{O_2} = \nu / Sc_{O_2}$*. Equation (3.32) yields*

$$\sigma^2_{D_{O_2}} \cong \sigma^2_{\nu} \left(\frac{1}{Sc_{O_2}}\right)^2 + \sigma^2_{Sc_{O_2}} \left(\frac{\nu}{Sc^2_{O_2}}\right)^2 \tag{3.33}$$

Upon inserting the numerical values,

$$\begin{aligned}\sigma^2_{D_{O_2}} &\cong (0.05 \times 10^{-2})^2 \left(\frac{1}{510}\right)^2 + (25)^2 \left(\frac{0.89 \times 10^{-2}}{(510)^2}\right)^2 \\ &= 1.7 \times 10^{-12}\end{aligned} \tag{3.34}$$

The result is $D_{O_2} = 1.75 \pm 0.13 \times 10^{-5}$ *cm*^{2}*s*$^{-1}$.

The estimate provided in Example 3.1 for the standard deviation may be approximate because the function is not linear with respect to Sc. The influence of nonlinearity is explored in the subsequent section.

3.2.2 Nonlinear Systems

Propagation of errors through nonlinear systems poses three issues. The first is that higher-order derivatives in the Taylor series expansion may make significant contribution to the error analysis. A second issue, demonstrated in Figure 3.6, is that the nonlinear relationships can distort the distributions such that the resulting variable is not normally distributed. The meaning of the variance calculated under these conditions can be questioned. The third is that correlation among parameters may lead to a reduction in the error propagated as compared to that calculated under the assumption that sources of error are not correlated.

Analytic means do not exist to solve the problem of propagation of errors through nonlinear systems. Monte Carlo simulations can be used to assess the magnitude and distribution of propagated errors.

Example 3.2 Continuation of Example 3.1: *Estimate the error in the assessment of the standard deviation for oxygen diffusivity obtained in Example 3.1.*

Remember! 3.2 *For linear systems with uncorrelated errors, the variance of a function of independent variables can be estimated by summing the variances of the independent variables weighted by the square of the derivative of the function with respect to the independent variable; see equation (3.32).*

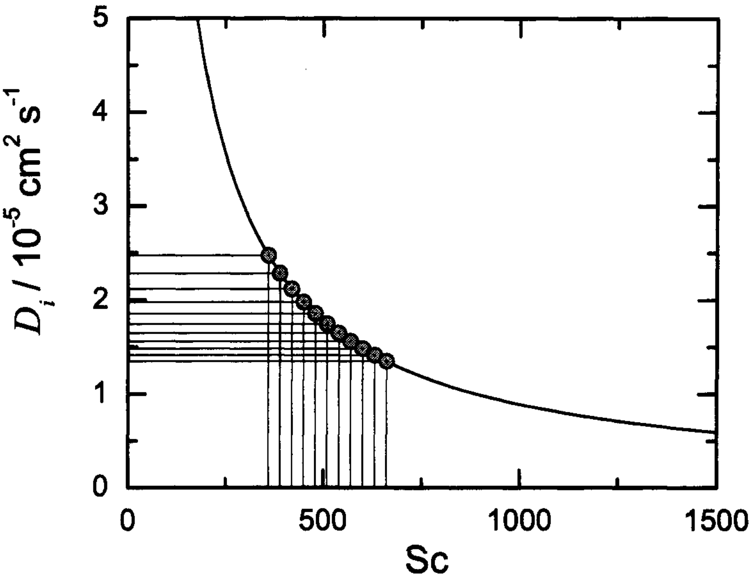

Figure 3.6: Diffusion coefficient as a function of Schmidt number for Example 3.1. The uneven spacing of diffusivity obtained for an even spacing of Schmidt number shows that a normal distribution of Schmidt number values would result in a distorted distribution of diffusivities.

Solution: *Monte Carlo simulations were performed using two independent sets of 1,000 normally distributed random numbers, one for each of the independent parameters. The values used to introduce noise for the Schmidt number had a standard deviation of 25, and the values used to introduce noise for the kinematic viscosity had a standard deviation of* 0.05×10^{-2} *cm*^{2}*s*$^{-1}$. *A scatter plot for the resulting calculations is shown in Figure 3.7. The resulting histogram for the diffusivity, shown in Figure 3.8, shows that the resulting distribution is normal. The mean value for the diffusivity obtained by use of Monte Carlo simulations to assess propagation of errors was* 1.751×10^{-5} *cm*^{2}*s*$^{-1}$, *and the standard deviation was* 1.3×10^{-6} *cm*^{2}*s*$^{-1}$. *These results are in excellent agreement with those obtained in Example 3.1.*

Example 3.3 Continuation of Example 3.2: *Estimate the error in the assessment of the standard deviation for oxygen diffusivity obtained in Example 3.1 with the exception that the estimated standard deviation for Schmidt number is increased by a factor of 10 such that* $\mathrm{Sc}_{O_2} = 510 \pm 250$.

Solution: *Note that the 95.4 percent* (2σ) *confidence interval for the Schmidt number does not quite include zero, so one may imagine that this value is statistically significant. In practice, the experimentalist should not be satisfied with this level of uncertainty and would want to devise a better experiment or a better model.*

Monte Carlo simulations were performed using two independent sets of 1,000 normally distributed random numbers, one for each of the independent parameters. The values used

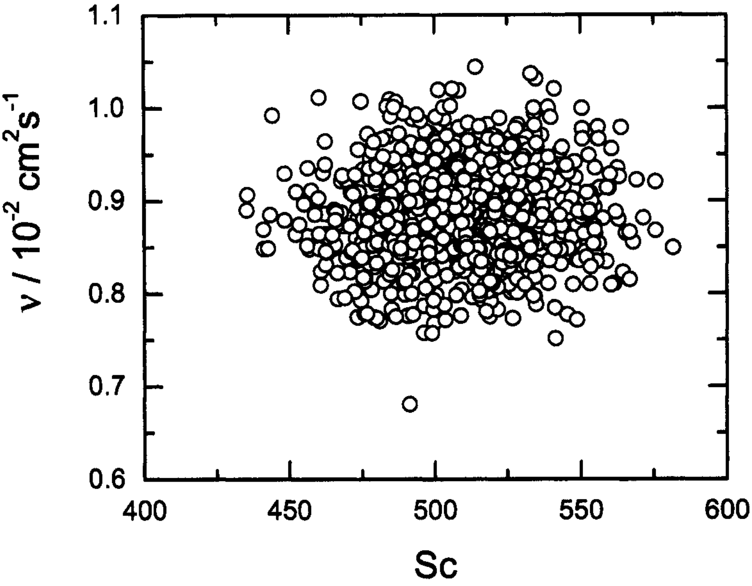

Figure 3.7: Scatter plot showing the use of Monte Carlo simulations for calculation of the diffusion coefficient. Kinematic viscosity is presented as a function of Schmidt number for Example 3.2.

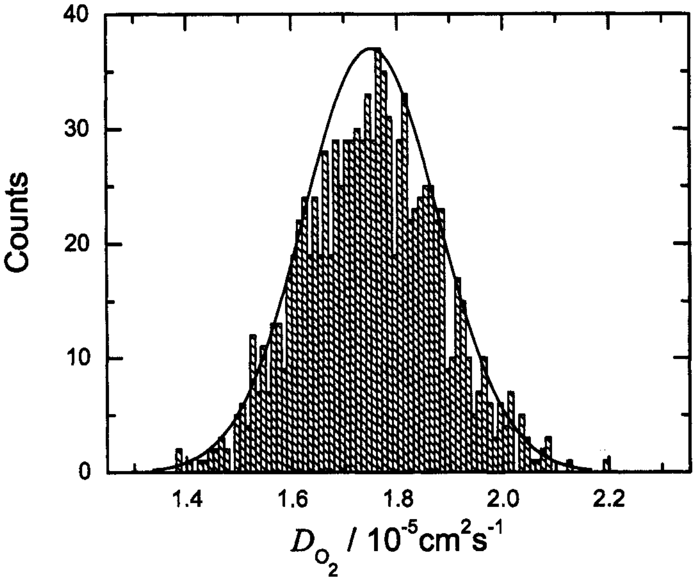

Figure 3.8: Distribution for the oxygen diffusion coefficient obtained by use of Monte Carlo simulations to assess propagation of errors for Example 3.2. The mean value for the diffusivity was 1.751×10^{-5} cm^{2}s^{-1}, and the standard deviation was 1.3×10^{-6} cm^{2}s^{-1}.

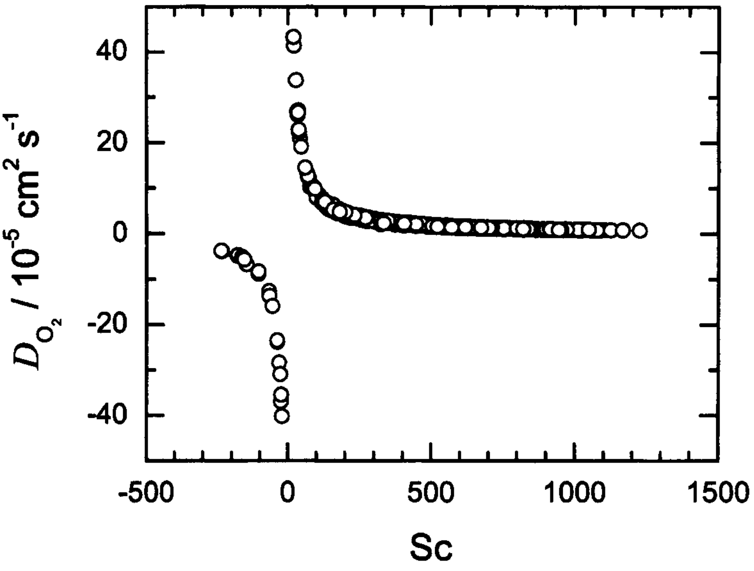

Figure 3.9: Scatter plot showing the use of Monte Carlo simulations for calculation of the diffusion coefficient. Diffusivity is presented as a function of Schmidt number for Example 3.3.

to introduce noise for the Schmidt number had a standard deviation of 250, and the values used to introduce noise for the kinematic viscosity had a standard deviation of 0.05×10^{-2} *cm*^{2}*s*$^{-1}$*. A scatter plot for the resulting calculations is shown in Figure 3.9. The calculations clearly trace the nonlinear portion of the curve given in Figure 3.6, and the occasional negative values for Schmidt number yield negative values for the diffusivity.*

The resulting histogram for the diffusivity, shown in Figure 3.10, shows that the resulting distribution is not normal. The mean value for the calculated diffusivity is $D_{O_2} = -1.03 \times 10^{-5} \pm 1.1 \times 10^{-3}$ *cm*^{2}*s*$^{-1}$*, but neither the mean nor the standard deviation estimated for this distribution has statistical meaning.*

3.3 Hypothesis Tests

A hypothesis test is a procedure for determining whether an assertion about a characteristic of a population is reasonable. The statistical tests described in this section cannot be used to prove a hypothesis, but rather, within a specified level of confidence, to disprove the hypothesis.

Often, the question at hand is whether two distributions have the same mean or the same variance. The question can be posed as: *Are the observed differences in mean or variance statistically significant?* The *Student's t-test* and the *F-test* can be used respectively to resolve these questions.

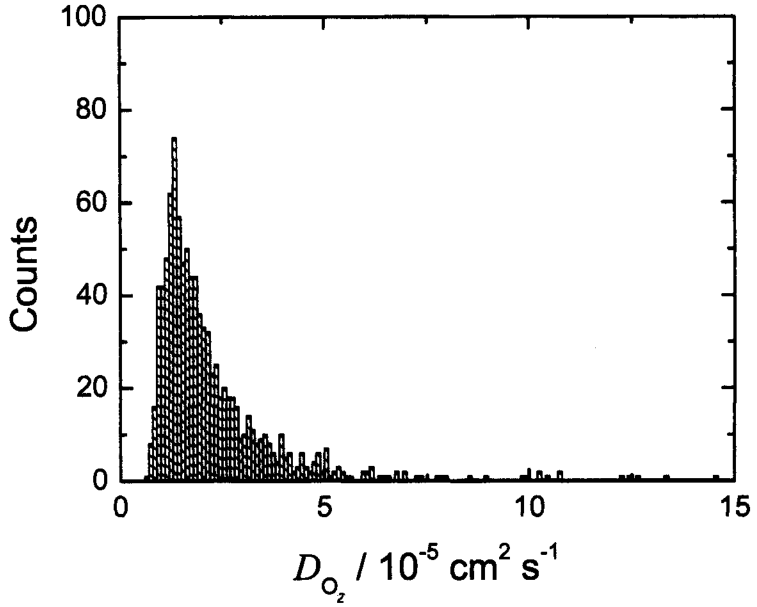

Figure 3.10: Distribution for the oxygen diffusion coefficient obtained by use of Monte Carlo simulations to assess propagation of errors for Example 3.1. The distribution is not normal, and the standard deviation estimated for such a distribution has no statistical meaning as a confidence interval.

3.3.1 Terminology

There is a specific terminology used for hypothesis tests. One might ask, for example, whether the rate of corrosion obtained for an aged steel coupon immersed in seawater is equal to that found in city drinking water.

- The *null hypothesis* is the original assertion. In this case, the null hypothesis is that the rate of corrosion obtained for an aged steel coupon immersed in seawater is equal to that found in city drinking water. The notation used is H_0: $\mu_1 = \mu_2$.

- There are three possibilities for the *alternative hypothesis* H_1: $\mu_1 > \mu_2$, $\mu_1 < \mu_2$, and $\mu_1 \neq \mu_2$.

- The *significance level* α is a number between 0 and 1 that represents the probability of incorrectly rejecting the null hypothesis when it is actually true. For a typical significance level of 5 percent, the notation is $\alpha = 0.05$. For this significance level, the probability of incorrectly rejecting the null hypothesis when it is actually true is 5 percent. A smaller value of α provides more protection from this error.

- The p-*value* is the probability of observing the given sample result under the assumption that the null hypothesis is true. In other words, p is the value of α that will yield the observed statistical test value. Example 3.4 provides an illustration of the relationship among the t-test parameter, α and p. If the p-value is less than α, the null hypothesis can be rejected. The converse is not true. If the p-value is greater than α, the null hypothesis cannot be accepted.

3.3.2 Student's t-Test for Equality of Mean

The *Student's* t-distribution was developed by William Sealy Gosset, 1876–1937, an English statistician, who published his distribution in 1908 under the pseudonym *Student.*[84] *Student's t-test* deals with the problems associated with inference based on small samples. The question is to determine the extent to which the calculated mean and standard deviation based on a small sample may, by chance, differ from the mean and standard deviation that would be obtained from a large distribution. Gosset developed these statistical methods during his employment in the Guinness brewery in Dublin. The experimental verification of his theories, however, was derived from published measurements of the heights and left-middle-finger lengths of 3,000 criminals.[84]

The Student's probability distribution function is given by

$$A(t|\nu) = 1 - \alpha = \frac{\Gamma\left(\frac{\nu+1}{2}\right)}{\sqrt{\nu}\Gamma\left(\frac{\nu}{2}\right)\Gamma\left(\frac{1}{2}\right)} \int_{-t}^{t} \left(1 + \frac{x^2}{\nu}\right)^{-(\nu+1)/2} dx \qquad (3.35)$$

where ν, the number of degrees of freedom, must be a positive integer. As $\nu \rightarrow \infty$, Student's probability distribution function approaches the normal distribution. The limiting values for equation (3.35) are $A(0|\nu) = 0$ and $A(\infty|\nu) = 1$.

The value of t obtained from equation (3.35) can be compared with the value obtained from the experimental observations, i.e.,

$$\mathrm{t} = \frac{\mu_x - \mu_{test}}{\sigma_x / \sqrt{n_x}} \qquad (3.36)$$

with $\nu = n_x - 1$ degrees of freedom, where n_x is the number of experimental data points, and $\sigma_x / \sqrt{n_x}$ represents the standard error for the data set. The corresponding expression for comparison of unpaired variates is given as

$$\mathrm{t} = \frac{\mu_{x_1} - \mu_{x_2}}{\sqrt{\frac{(n_{x_1}-1)\sigma_{x_1}^2 + (n_{x_2}-1)\sigma_{x_2}^2}{n_{x_1}+n_{x_2}-2}\left(\frac{1}{n_{x_1}} + \frac{1}{n_{x_2}}\right)}} \qquad (3.37)$$

with $\nu = n_{x_1} + n_{x_2} - 2$ degrees of freedom.

Remember! 3.3 *Statistical tests cannot be used to prove a given hypothesis. These tests can be used to identify conditions where the data do not support the hypothesis.*

Table 3.3: Student's t-test values.

ν/p	0.5	0.4	0.3	0.2	0.1	0.05	0.01
3	0.7649	0.9785	1.2498	1.6377	2.3534	3.1824	5.8409
4	0.7407	0.9410	1.1896	1.5332	2.1318	2.7764	4.6041
5	0.7267	0.9195	1.1558	1.4759	2.0150	2.5706	4.0321
10	0.6998	0.8791	1.0931	1.3722	1.8125	2.2281	3.1693
15	0.6912	0.8662	1.0735	1.3406	1.7531	2.1314	2.9467
20	0.6870	0.8600	1.0640	1.3253	1.7247	2.0860	2.8453
25	0.6844	0.8562	1.0584	1.3163	1.7081	2.0595	2.7874
30	0.6828	0.8538	1.0547	1.3104	1.6973	2.0423	2.7500
35	0.6816	0.8520	1.0520	1.3062	1.6896	2.0301	2.7238
40	0.6807	0.8507	1.0500	1.3031	1.6839	2.0211	2.7045
45	0.6800	0.8497	1.0485	1.3006	1.6794	2.0141	2.6896
50	0.6794	0.8489	1.0473	1.2987	1.6759	2.0086	2.6778
55	0.6790	0.8482	1.0463	1.2971	1.6730	2.0040	2.6682
60	0.6786	0.8477	1.0455	1.2958	1.6706	2.0003	2.6603
65	0.6783	0.8472	1.0448	1.2947	1.6686	1.9971	2.6536
70	0.6780	0.8468	1.0442	1.2938	1.6669	1.9944	2.6479
75	0.6778	0.8464	1.0436	1.2929	1.6654	1.9921	2.6430
80	0.6776	0.8461	1.0432	1.2922	1.6641	1.9901	2.6387
85	0.6774	0.8459	1.0428	1.2916	1.6630	1.9883	2.6349
90	0.6772	0.8456	1.0424	1.2910	1.6620	1.9867	2.6316
95	0.6771	0.8454	1.0421	1.2905	1.6611	1.9853	2.6286
100	0.6770	0.8452	1.0418	1.2901	1.6602	1.9840	2.6259
200	0.6757	0.8434	1.0391	1.2858	1.6525	1.9719	2.6006
500	0.6750	0.8423	1.0375	1.2832	1.6479	1.9647	2.5857

A comparison of means of paired samples is used when an external factor influences the data sets in a way that is point-by-point identical:

$$t = \frac{\mu_{x_1} - \mu_{x_2}}{\sqrt{\frac{\sum_{k=1}^{n}\left(x_{1,k} - x_{2,k} - \left(\mu_{x_1} - \mu_{x_2}\right)\right)^2}{n_x(n_x - 1)}}} \tag{3.38}$$

where $n_{x_1} = n_{x_2} = n_x$ and with $\nu = n_x - 1$ degrees of freedom. Such a test may be used, for example, for a comparison of two variables obtained as a function of frequency in the same experiment, where frequency may be expected to have the same influence on the two variables. Table 3.3 is useful for assessing the Student's t-test for equality of mean.

3.3.3 F-test for Equality of Variance

The F-test is used to test the null hypothesis that the two population variances corresponding to the two samples are equal.[79] Within each sample, the values are assumed to be independent and to have the identical normal distribution (i.e., the same mean and variance). In addition, the two samples are assumed to be independent of each other.

The value for F is obtained from the experimentally determined variances as

$$F = \frac{\sigma_1^2}{\sigma_2^2} \tag{3.39}$$

such that $F > 1$, i.e., $\sigma_1^2 > \sigma_2^2$. The null hypothesis is that the two variances are from the same population, i.e., they are not statistically different.

The significance level at which the hypothesis that the variances are not equal can be rejected is given by

$$Q(F|\nu_1, \nu_2) = \frac{\Gamma\left((\nu_1 + \nu_2)/2\right)}{\Gamma(\nu_1/2)\,\Gamma(\nu_2/2)} \int_0^{\nu_2/(\nu_2+\nu_1 F)} t^{\nu_2/2-1}(1-t)^{\nu_1/2-1} dt \tag{3.40}$$

with $\nu_1 = n_{x_1} - 1$ and $\nu_2 = n_{x_2} - 1$ degrees of freedom, respectively. Tables are provided for the value of F corresponding to a given number of degrees of freedom and for a given confidence level. If the calculated F is greater than the table value, then the null hypothesis must be rejected. Numerical values useful for assessing the F-test for equality of variance with samples of identical degree of freedom are presented in Table 3.4.

Example 3.4 Evaluation of Impedance Data: *The question of whether the real and imaginary parts of impedance measurements have the same variance or standard deviation has generated significant controversy in the impedance literature. Consider the standard deviations reported by Orazem et al.*[85] *for their impedance data obtained for the reduction of ferricyanide on a Pt rotating disk electrode. The methods of Agarwal et al.*[56,86] *were used to filter minor lack of replicacy from 26 repeated impedance experiments. Numerical values are presented in Table 3.5. The results, presented graphically in Figure 3.11, suggest that the standard deviations of the imaginary and real impedance values are equal. The question here is whether this apparent equality has statistical significance.*

Solution: *The standard deviations are clearly strong functions of frequency. Thus, the appropriate Student's* t*-test is that for paired variates, equation (3.38). The calculated* t*-value is* $t_{\mathrm{exp}} = 1.710$. *An interpolated table of* t*-test values is presented as Table 3.6. The significance level at a degree of freedom* $\nu = n - 1 = 73$ *corresponding to* $t_{\mathrm{exp}} = 1.710$ *is* $p = 0.0915$. *The value of* t *corresponding to the* $\alpha = 0.05$ *level is* $t_{0.05} = 1.993$. *As* $t_{\mathrm{exp}} < t_{0.05}$, *at the 0.05 significance level, the two means are not significantly different.*

A second approach is to consider the F*-test for comparison of variance at each frequency. As there were 26 repeated measurements, the degree of freedom for the two calculations of variance is* $\nu = 26 - 1 = 25$. *At the* $\alpha = 0.05$ *level, a value of 1.955 is obtained from Table 3.4, and a value of 2.604 is obtained at the* $\alpha = 0.01$ *level. These critical values can be*

Table 3.4: F-Test values for comparison of variance of samples with equal degrees of freedom, i.e., $\nu_1 = \nu_2 = \nu$.

ν/p	0.4	0.3	0.2	0.1	0.05	0.01	0.005
4	1.310	1.753	2.483	4.107	6.388	15.977	23.155
5	1.269	1.641	2.228	3.453	5.050	10.967	14.940
10	1.179	1.406	1.732	2.323	2.978	4.849	5.847
15	1.142	1.318	1.558	1.972	2.403	3.522	4.070
20	1.122	1.268	1.466	1.794	2.124	2.938	3.318
25	1.108	1.236	1.406	1.683	1.955	2.604	2.898
30	1.098	1.213	1.364	1.606	1.841	2.386	2.628
35	1.090	1.196	1.332	1.550	1.757	2.231	2.438
40	1.084	1.182	1.308	1.506	1.693	2.114	2.296
45	1.079	1.170	1.287	1.470	1.642	2.023	2.185
50	1.075	1.161	1.271	1.441	1.599	1.949	2.097
55	1.071	1.153	1.256	1.416	1.564	1.888	2.024
60	1.068	1.146	1.244	1.395	1.534	1.836	1.962
65	1.065	1.140	1.233	1.377	1.508	1.792	1.910
70	1.063	1.134	1.224	1.361	1.486	1.754	1.864
75	1.060	1.129	1.216	1.346	1.466	1.720	1.824
80	1.058	1.125	1.208	1.334	1.448	1.690	1.789
85	1.057	1.121	1.201	1.322	1.432	1.663	1.758
90	1.055	1.117	1.195	1.312	1.417	1.639	1.730
95	1.054	1.114	1.189	1.302	1.404	1.618	1.704
100	1.052	1.111	1.184	1.293	1.392	1.598	1.681
150	1.042	1.090	1.148	1.233	1.309	1.465	1.526
200	1.037	1.077	1.127	1.199	1.263	1.391	1.442
1000	1.016	1.034	1.055	1.084	1.110	1.159	1.177

Table 3.5: Standard deviations reported by Orazem et al.[85] for their impedance data obtained for the reduction of ferricyanide on a Pt rotating disk electrode. The methods of Agarwal et al.[56,86] were used to filter minor lack of replicacy from 26 repeated impedance experiments.

#	f/Hz	σ_{Z_r}/Ω	σ_{Z_j}/Ω	$\sigma^2_{Z_r}/\sigma^2_{Z_j}$	#	f/Hz	σ_{Z_r}/Ω	σ_{Z_j}/Ω	$\sigma^2_{Z_r}/\sigma^2_{Z_j}$
1	0.02154	0.35649	0.32284	1.21933	38	25.924	0.02548	0.05162	0.24363
2	0.02592	0.37169	0.28941	1.64949	39	31.408	0.02631	0.04885	0.29019
3	0.03141	0.39259	0.35798	1.20271	40	38.051	0.04043	0.02609	2.40076
4	0.03805	0.2963	0.26128	1.28603	41	55.851	0.03552	0.04002	0.78771
5	0.04610	0.32867	0.31740	1.07226	42	67.67	0.01624	0.04298	0.14275
6	0.05585	0.27794	0.29545	0.88497	43	81.98	0.02826	0.03509	0.64860
7	0.06767	0.25963	0.25954	1.00068	44	120.32	0.03647	0.02799	1.69838
8	0.08198	0.23957	0.20889	1.31536	45	145.78	0.02404	0.03468	0.48056
9	0.09932	0.22973	0.19401	1.40209	46	176.62	0.01793	0.03444	0.27096
10	0.12033	0.16701	0.20924	0.63707	47	213.98	0.02879	0.02481	1.34668
11	0.14578	0.17592	0.18912	0.86524	48	259.24	0.03131	0.01092	8.21824
12	0.17662	0.17040	0.15621	1.18989	49	314.08	0.02308	0.02322	0.98868
13	0.21398	0.13790	0.19223	0.51463	50	380.51	0.00862	0.03234	0.07106
14	0.25924	0.15611	0.09356	2.78387	51	461	0.01852	0.02867	0.41707
15	0.31408	0.15208	0.10010	2.30823	52	558.51	0.02876	0.01917	2.25168
16	0.38051	0.12977	0.07933	2.67563	53	676.7	0.02394	0.02158	1.23128
17	0.461	0.09682	0.10667	0.82375	54	819.8	0.01462	0.02766	0.27936
18	0.55851	0.07737	0.08260	0.87747	55	993.2	0.01562	0.02486	0.39474
19	0.6767	0.06474	0.05871	1.21583	56	1,203.3	0.02378	0.0132	3.24432
20	0.81979	0.08196	0.06187	1.75491	57	1,457.8	0.02292	0.01167	3.85855
21	0.9932	0.05799	0.05996	0.93517	58	1,766.2	0.01015	0.02118	0.22967
22	1.2033	0.06719	0.07872	0.72848	59	2,139.8	0.00779	0.01814	0.18415
23	1.4578	0.10232	0.06678	2.34811	60	2,592.4	0.01460	0.01261	1.33987
24	1.7662	0.11819	0.05019	5.54426	61	3,140.8	0.01076	0.01371	0.61607
25	2.1398	0.06228	0.06882	0.81897	62	3,805.1	0.00618	0.01626	0.14425
26	2.5924	0.06154	0.07755	0.62978	63	4,610	0.00974	0.01076	0.8183
27	3.1408	0.06852	0.05589	1.50346	64	5,585.1	0.01138	0.00427	7.09199
28	3.8051	0.06907	0.04163	2.75322	65	6,766.5	0.00700	0.00569	1.50972
29	4.61	0.03973	0.04051	0.96178	66	8,198	0.00222	0.00743	0.08963
30	5.5851	0.04068	0.04832	0.70865	67	9,932	0.00551	0.00396	1.92994
31	6.767	0.04501	0.04721	0.9089	68	12,033	0.00613	0.00475	1.66243
32	8.198	0.05002	0.0194	6.64847	69	14,578	0.00405	0.00796	0.25897
33	9.932	0.04242	0.02741	2.39524	70	17,662	0.00133	0.0091	0.02151
34	12.033	0.03215	0.04111	0.61162	71	21,397	0.00455	0.00646	0.49491
35	14.578	0.02422	0.03938	0.37827	72	25,924	0.00456	0.00226	4.08208
36	17.662	0.03756	0.02455	2.33978	73	31,407	0.00129	0.0035	0.13629
37	21.398	0.03679	0.02424	2.30361	74	38,051	0.01032	0.00567	3.31491

Table 3.6: Student's t-test values for the hypothesis that the standard deviations for real and imaginary parts of the impedance, shown in Table 3.5, are equal. See Example 3.4.

ν/α	0.1	**0.0915**	**0.05**
70	1.667	⇑	⇓
73	⇒	**1.710**	**1.993**
75	1.665	1.709	1.992

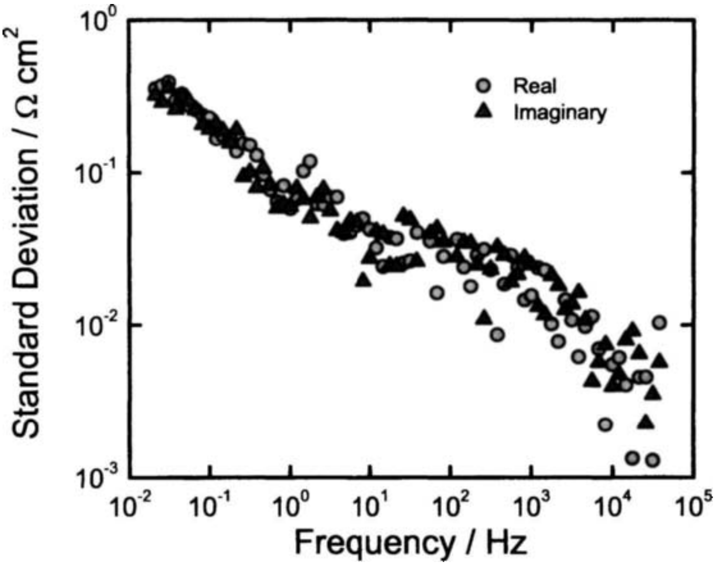

Figure 3.11: Standard deviations reported by Orazem et al.[85] for their impedance data obtained for the reduction of ferricyanide on a Pt rotating disk electrode.

compared with the ratio presented in Table 3.5. Ordinarily, the F*-test parameter is arranged such that the larger variance is divided by the smaller. As is evident in Figure 3.11, the variance of the real part of the impedance is sometimes larger and sometimes smaller than the variance of the imaginary part. One approach is to plot the ratio of variances on a logarithmic scale, as shown in Figure 3.12. While the ratio is scattered about unity, a frequency-by-frequency comparison of the calculated* F*-test values to the criteria obtained from Table 3.4 suggests that the hypothesis that the variances are equal can be rejected at the 0.05 significance level on an intermittent basis, but with the variance of the real part occasionally larger than that of the imaginary part, and the variance of the imaginary part occasionally larger than that of the real part.*

As the uncertainty in the assessment of the variance appears to be large, the Student's t*-test may represent the best assessment of the statistics of the error analysis described in Figure 3.11. A Student's* t*-test can be used to confirm that the ratio shown in Figure 3.12 has a mean value of unity. A comparison of the mean of* $\log_{10}\left(\sigma_r^2/\sigma_j^2\right)$ *to the expected value of zero (equation (3.36)) yields* $\mathrm{t}_{\mathrm{exp}} = -0.628$*. The correspondence of this value to critical values of* $\mathrm{t}_{0.05}$ *is seen in Table 3.7. The significance level corresponding to* $\mathrm{t}_{\mathrm{exp}} = 0.628$ *at a degree of freedom* $\nu = n - 1 = 73$ *is* $p = 0.532$*. The value of* t *corresponding to the* $\alpha = 0.05$ *level is* $\mathrm{t}_{0.05} = 1.993$*. At the 0.05 significance level, the mean is not significantly different from a value of zero.*

The statistical tests described here cannot prove that the variances for real and imaginary parts of the impedance are equal. They show only that, for the given data, the hypothesis that the variances for real and imaginary parts of the impedance are equal cannot be rejected.

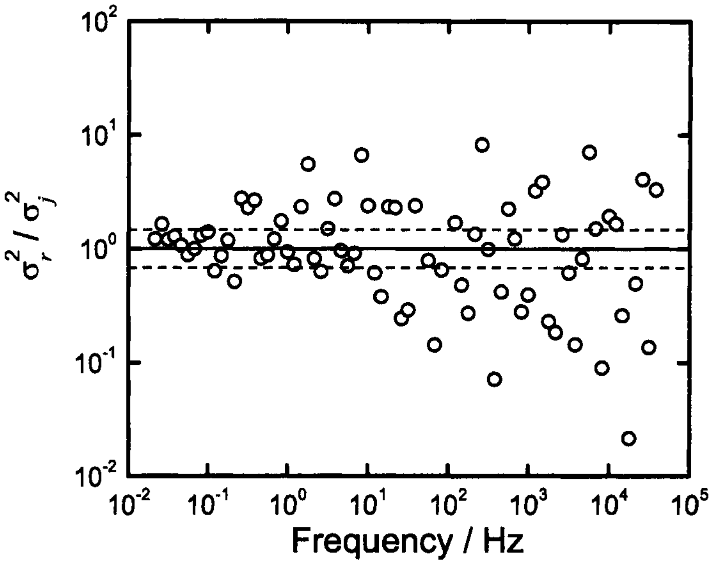

Figure 3.12: Ratio of the variance of the real part of the impedance to the variance of the imaginary part of the impedance for the data for the reduction of ferricyanide on a Pt rotating disk electrode.[85] Dashed lines represent the F-value corresponding to 0.05 significance level and its inverse.

Table 3.7: Student's t-test values for Example 3.4 for a test of $\log_{10}\left(\sigma_r^2/\sigma_j^2\right) = 0$.

ν/α	0.6	**0.532**	**0.05**
70	0.527	$\Uparrow$	$\Downarrow$
73	$\Rightarrow$	**0.628**	**1.993**
75	0.527	0.628	1.992

3.3.4 Chi-Squared Test for Equality of Variance

The χ^2 test is used to evaluate the probability that ν random normally distributed variables of unit variance would have a sum of squares greater than χ^2.

$$Q(\chi^2|\nu) = \frac{1}{\Gamma(\frac{\nu}{2})} \int_{\frac{\chi^2}{2}}^{\infty} e^{-t} t^{\nu/2-1} dt \tag{3.41}$$

If the χ^2 statistic originates from comparison of a model to experiment, the degree of freedom is given by

$$\nu = N_{\text{dat}} - N_p - 1 \tag{3.42}$$

where N_{dat} represents the number of observations and N_p is the number of adjusted parameters. Tables are provided for the value of χ^2 corresponding to a given number of degrees of freedom and for a given confidence level. If the calculated F is greater than the table value, then the null hypothesis must be rejected. Numerical values useful for assessing the χ^2-test for equality of mean are presented in Table 3.8.

Example 3.5 Evaluation of Chi-Squared Statistics: *Consider that, for a given measurement, regression of a model to real and imaginary parts of impedance data yielded* $\chi^2 = 130$. *Measurements were conducted at 70 frequencies. The regressed parameters needed to model the data included the solution resistance and 9 Voigt elements, resulting in use of 19 parameters. Under assumption that the variances used in the evaluation of* χ^2 *were obtained independently, evaluate the hypothesis that the* χ^2 *value cannot be reduced by refinement of the model.*

Solution: *As the fit was to both real and imaginary parts of the data, the degree of freedom for this problem is* $\nu = n - p = 140 - 19 - 1 = 120$. *The* χ^2 *value corresponding to a 0.05 significance level can be obtained from Table 3.8 to be equal to 146.6, and the probability corresponding to the measured* χ^2 *value is 0.25. Thus there is a 25 percent probability that the* χ^2 *statistic could exceed the observed value by chance, even for a correct model.*

Remember! 3.4 *The numerical value of the* χ^2 *statistic for a weighted regression depends on the estimated variance of the data. The numerical value has no meaning if the variance of the data is unknown.*

Table 3.8: χ^2-test values for degree of freedom ν and confidence level p.

ν/p	0.5	0.4	0.3	0.2	0.1	0.05	0.01
5	4.35	5.13	6.06	7.29	9.24	11.07	15.09
10	9.34	10.47	11.78	13.44	15.99	18.31	23.21
15	14.34	15.73	17.32	19.31	22.31	25.00	30.58
20	19.34	20.95	22.77	25.04	28.41	31.41	37.57
25	24.34	26.14	28.17	30.68	34.38	37.65	44.31
30	29.34	31.32	33.53	36.25	40.26	43.77	50.89
35	34.34	36.47	38.86	41.78	46.06	49.80	57.34
40	39.34	41.62	44.16	47.27	51.81	55.76	63.69
45	44.34	46.76	49.45	52.73	57.51	61.66	69.96
50	49.33	51.89	54.72	58.16	63.17	67.50	76.15
55	54.33	57.02	59.98	63.58	68.80	73.31	82.29
60	59.33	62.13	65.23	68.97	74.40	79.08	88.38
65	64.33	67.25	70.46	74.35	79.97	84.82	94.42
70	69.33	72.36	75.69	79.71	85.53	90.53	100.43
75	74.33	77.46	80.91	85.07	91.06	96.22	106.39
80	79.33	82.57	86.12	90.41	96.58	101.88	112.33
85	84.33	87.67	91.32	95.73	102.08	107.52	118.24
90	89.33	92.76	96.52	101.05	107.57	113.15	124.12
95	94.33	97.85	101.72	106.36	113.04	118.75	129.97
100	99.33	102.95	106.91	111.67	118.50	124.34	135.81
120	119.33	123.29	127.62	132.81	140.23	146.57	158.95
150	149.33	153.75	158.58	164.35	172.58	179.58	193.21

Table 3.9: Replicated impedance collected at a frequency of 1 Hz on the same Polymer Electrolyte Membrane (PEM) fuel cell using two different sets of instrumentation, the 850C provided by Scribner Associates and the FC350 provided by Gamry Instruments.

	850C		FC350	
Replicate	$Z_r\ \Omega$	$Z_j\ \Omega$	$Z_r\ \Omega$	$Z_j\ \Omega$
1	0.17117	−0.041791	0.167993	−0.038176
2	0.18236	−0.043494	0.173985	−0.040603
3	0.18606	−0.044666	0.176629	−0.041786
4	0.18941	−0.045946	0.1827	−0.044806

Problems

3.1 The steady-state mass-transfer-limited current density for a rotating disk (see Section 11.6) can be expressed as

$$i_{\text{lim}} = 0.62nFc_i(\infty)D_i^{2/3}\nu^{-1/6}\Omega^{1/2} \tag{3.43}$$

where $c_i(\infty)$ is the concentration of the limiting reacting species i far from the disk, D_i is the diffusivity of the reacting species i, ν is the kinematic viscosity, and Ω is the rotation speed for the disk. Consider that $i_{\text{lim}} = 60 \pm 0.5$ mA/cm^2, $c_i(\infty) = 0.1 \pm 0.005$ M, $\nu = 10^{-2} \pm 10^{-4}$ cm^2/s, and $\Omega = 1{,}000 \pm 1$ rpm. Find the value and standard deviation for the diffusivity of species i in units of cm^2/s.

3.2 The Schmidt number is expressed as $\text{Sc}_i = \nu / D_i$; Find the value and standard deviation for the Schmidt number if the kinematic viscosity is $\nu = 10^{-2} \pm 10^{-4}$ cm^2/s and the diffusivity of species i is $D_i = 10^{-5} \pm 10^{-7}$ cm^2/s.

3.3 Estimate the 95.4 percent confidence interval for the equivalent circuit model given in Figure 4.2(b) over the frequency range of 10 mHz to 10 kHz if the regressed parameter values are expressed as $R_e = 10 \pm 1\ \Omega\text{cm}^2$, $R_t = 100 \pm 15\ \Omega\text{cm}^2$, and $\tau = R_tC_{\text{dl}} = 0.01 \pm 0.001$ s.

3.4 Consider the replicated impedance measurements presented in Table 3.9 for a 5 cm^2 Polymer Electrolyte Membrane (PEM) fuel cell operating at a current of 1 A. The measurements were collected at a frequency of 1 Hz on the same cell using two different sets of instrumentation, the 850C provided by Scribner Associates and the FC350 provided by Gamry Instruments.

- **(a)** Test the hypothesis that the impedance values obtained by the two instruments are not distinguishable.
- **(b)** Test the hypothesis that the variances obtained by the two instruments are not distinguishable.

3.5 Consider the replicated impedance measurements presented in Table 3.10 for a 5 cm^2 PEM fuel cell operating at a current of 1 A. The measurements were collected at a frequency of 10 Hz on the same cell using a serpentine channel

Table 3.10: Replicated impedance collected at a frequency of 10 Hz on the same PEM fuel cell but using two flow channels.

	Serpentine		**Interdigitated**	
Replicate	Z_r Ω	Z_j Ω	Z_r Ω	Z_j Ω
1	0.055822	−0.048797	0.073113	−0.039505
2	0.0583180	−0.053851	0.074073	−0.04012
3	0.05861	−0.05494	0.074244	−0.040369
4	0.058842	−0.055843	0.074362	−0.040548

and an interdigitated channel that is believed to be more efficient but also more susceptible to flooding.

(a) Test the hypothesis that the impedance values obtained by the two instruments are not distinguishable.

(b) Test the hypothesis that the variances obtained by the two instruments are not distinguishable.

Electrochemical Impedance Spectroscopy
by Mark E. Orazem and Bernard Tribollet

Chapter 4

Electrical Circuits

Transfer function approaches are general and can be applied to a large variety of electrical, mechanical, and optical systems. For this reason, it is not surprising that the behavior of one system will resemble that of another. Electrochemists take advantage of this similarity by comparing the behavior of electrochemical systems to that of known electrical circuits.

A review of Chapter 1 may be useful. Summaries of relationships among complex impedance, real and imaginary parts of the impedance, and the phase angle and magnitude are found in Tables 1.1, 1.2, and 1.3. A more complete discussion of the use of graphical methods is presented in Chapters 16, 17, and 18.

4.1 Passive Electrical Circuits

Passive circuit elements are components that do not generate current or potential. A passive electrical circuit is composed only of passive elements. Only an element with two contacts is considered here, which is analyzed by considering the current flowing through and the potential difference between the contacts, shown as open circles in Figure 4.1.

4.1.1 Circuit Elements

Electrical circuits can be constructed from the passive elements shown in Figure 4.1. The fundamental relationship between current and potential for the resistor


(a) Resistor (b) Inductor (c) Capacitor

Figure 4.1: Passive elements that serve as components of an electrical circuit.

(Figure 4.1(a)) is

$$V(t) = RI(t) \tag{4.1}$$

where the value of the resistance R represents the fundamental property of the resistor and I is the current. In the notation of this text, I represents the current in units of A and i represents the current density in units of A/cm^2. At each point in time, the potential difference between the resistor clamps is proportional to the current flowing through the resistor. The steady-state current flowing through a resistor is finite and can be obtained from equation (4.1).

The relationship between current and potential difference for the inductor (Figure 4.1(b)) is

$$V(t) = L\frac{dI(t)}{dt} \tag{4.2}$$

which is the defining equation for the inductor. Under steady-state conditions, $dI(t)/dt = 0$, and, according to equation (4.2), $V(t) = 0$. Thus, the inductor is equivalent to a short circuit under steady-state conditions.

A capacitor (Figure 4.1(c)) is defined by

$$C = \frac{dq(t)}{dV(t)} \tag{4.3}$$

where $q(t)$ is the electric charge. The current flowing through the capacitor is obtained from the derivative of charge with respect to time, i.e.,

$$I(t) = \frac{dq(t)}{dt} \tag{4.4}$$

Then, from equations (4.3) and (4.4):

$$I(t) = C\frac{dV(t)}{dt} \tag{4.5}$$

which provides the relationship between current and potential for the capacitor. Under steady-state condition $dV/dt = 0$, and, according to equation (4.5), $I(t) = 0$. The capacitor is equivalent to an open circuit under steady-state conditions.

The impedance response of electrochemical systems is often normalized to the effective area of the electrode. Such a normalization applies only if the effective area can be well defined, and is not used in this chapter on the impedance response of electrical circuits. The capacitance used in this chapter, therefore, has units of F rather than F/cm^2, the resistance has units of Ω rather than Ω cm^2, and the inductance has units of H rather than H cm^2.

Response to a Sinusoidal Signal

The response in current of the passive elements to a pure sinusoidal potential modulation

$$V(t) = |\Delta V|\cos(\omega t) \tag{4.6}$$

can now be considered. The current response is given by

$$I(t) = |\Delta I| \cos(\omega t + \varphi) \tag{4.7}$$

According to the complex number properties described in Table 1.7, e.g., equations (1.109)–(1.112), equation (4.7) can be written as

$$\begin{aligned} I(t) &= \mathrm{Re}\left\{|\Delta I| \exp(j\varphi) \exp(j\omega t)\right\} \\ &= \mathrm{Re}\left\{\Delta I \exp(j\omega t)\right\} \end{aligned} \tag{4.8}$$

where $\Delta I = |\Delta I| \exp(j\varphi)$. Due to the fact that

$$\frac{d}{dt}\mathrm{Re}\left\{f(t)\right\} = \mathrm{Re}\left\{\frac{df(t)}{dt}\right\} \tag{4.9}$$

where f is a continuous function of t, then

$$\frac{dI(t)}{dt} = \mathrm{Re}\left\{j\omega \Delta I \exp(j\omega t)\right\} \tag{4.10}$$

In the same way,

$$\frac{dV(t)}{dt} = \mathrm{Re}\left\{j\omega \Delta V \exp(j\omega t)\right\} \tag{4.11}$$

According to expression (4.2), the response of an inductive element is given by

$$\mathrm{Re}\left\{\Delta V \exp(j\omega t)\right\} = L\mathrm{Re}\left\{j\omega \Delta I \exp(j\omega t)\right\} \tag{4.12}$$

As $j = \exp\left(j\pi/2\right)$ (see equation (1.72)),

$$\mathrm{Re}\left\{\Delta V \exp(j\omega t)\right\} = L\mathrm{Re}\left\{\omega \Delta I \exp\left(j(\omega t + \pi/2)\right)\right\} \tag{4.13}$$

Equation (4.13) shows that the potential difference is out of phase with the current. From expression (4.12),

$$\Delta V = j\omega L \Delta I \tag{4.14}$$

which provides the potential response of an inductor to a sinusoidal signal.

Following equation (4.5), the response of a capacitor is given by

$$\mathrm{Re}\left\{\Delta I \exp(j\omega t)\right\} = C\mathrm{Re}\left\{j\omega \Delta V \exp(j\omega t)\right\} \tag{4.15}$$

or

$$\mathrm{Re}\left\{\Delta I \exp(j\omega t)\right\} = C\mathrm{Re}\left\{\omega \Delta V \exp\left(j(\omega t + \pi/2)\right)\right\} \tag{4.16}$$

Remember! 4.1 *Under steady-state conditions, the inductor is equivalent to a* short circuit, *the capacitor is equivalent to an* open circuit, *and the resistor allows current in proportion to a potential driving force.*

The current is out of phase with the potential difference. From expression (4.15), the frequency domain current response to a sinusoidal potential input for a capacitor is given by

$$\Delta I = jC\omega\Delta V \tag{4.17}$$

The corresponding expression for a resistor, according to equation (4.1), can be written as

$$\Delta V = R\Delta I \tag{4.18}$$

The current and potential relationships obtained here are used in the subsequent section to establish the impedance response for each type of circuit element.

Impedance Response of Passive Circuit Elements

The impedance of a circuit element is defined to be

$$Z = \frac{\Delta V}{\Delta I} \tag{4.19}$$

For a pure resistor, equation (4.19) yields

$$Z_{\text{resistor}} = R \tag{4.20}$$

For a capacitor

$$Z_{\text{capacitor}} = \frac{1}{j\omega C} \tag{4.21}$$

and for an inductor

$$Z_{\text{inductor}} = j\omega L \tag{4.22}$$

The impedance responses for resistors, capacitors, and inductors are used to construct the impedance response of circuits.

4.1.2 Parallel and Series Combinations

For two passive elements in series, the same current must flow through the two elements, and the overall potential difference is the sum of the potential difference for each element. Thus, according to the definition of impedance given as equation (4.19), the impedance for the series arrangement shown in Figure 4.2(a) is given by

$$Z = Z_1 + Z_2 \tag{4.23}$$

For two passive elements in parallel, the overall current is the sum of the current flowing in each element, and the potential difference is the same for each dipole.

Remember! 4.2 *All physical time-dependant quantities, such as $I(t)$, $V(t)$, $dI(t)/dt$, and $dV(t)/dt$, are real quantities.*

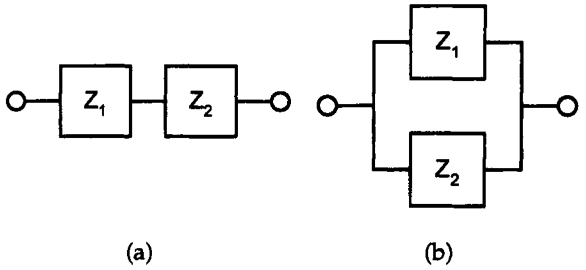

Figure 4.2: Combinations of passive elements: a) in series; and b) in parallel.

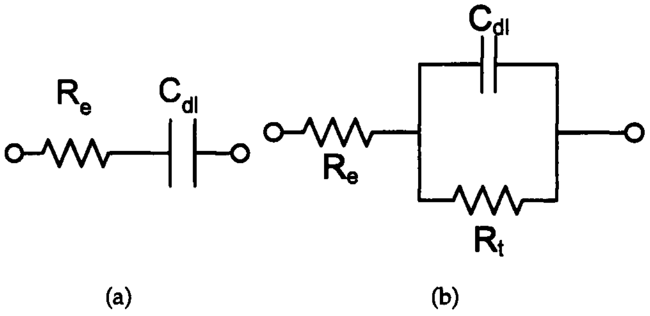

Figure 4.3: Electrical circuit consisting of a) a solution resistance in series with a capacitor; and b) a solution resistance in series with a Voigt element.

Then, according to the impedance definition, the impedance for the parallel arrangement shown in Figure 4.2(b) is given by

$$Z = \left[\frac{1}{Z_1} + \frac{1}{Z_2}\right]^{-1} \tag{4.24}$$

Impedance contributions are additive for elements in series, whereas the inverse of the impedance, or the admittance, is additive for elements in parallel.

Example 4.1 Impedance in Series: *Derive an expression for the impedance of the electrical circuit shown in Figure 4.3(a).*

Solution: *The contribution of the resistance term to the impedance is R_e, and the impedance of the capacitor is given by equation (4.21). Following equation (4.23), the impedance*

Remember! 4.3 *Impedance contributions are additive for elements in series; whereas, the admittance is additive for elements in parallel.*

of the circuit is therefore given by

$$Z = R_e + \frac{1}{j\omega C_{\mathrm{dl}}} \tag{4.25}$$

which can be rearranged to the form

$$Z = R_e - j\frac{1}{\omega C_{\mathrm{dl}}} \tag{4.26}$$

The real part of the impedance is equal to R_e and is independent of frequency. The imaginary part tends toward $-\infty$ as frequency tends toward zero. The dc *(zero-frequency) current is equal to zero at any applied potential, and the current at infinite frequency is equal to V/R_e.*

Example 4.2 Impedance in Parallel: *Derive an expression for the impedance of the electrical circuit shown in Figure 4.3(b).*

Solution: *The contribution of the resistance terms to the impedance are R_e and R_t, respectively. The impedance of the capacitor is given by equation (4.21). Following equations (4.23) and (4.24), the impedance of the circuit is therefore given by*

$$Z = R_e + \frac{1}{\frac{1}{R_t} + j\omega C_{\mathrm{dl}}} \tag{4.27}$$

which can be rearranged to the form

$$Z = R_e + \frac{R_t}{1 + j\omega R_t C_{\mathrm{dl}}} \tag{4.28}$$

Note that ω is in units of s^{-1}, and that $R_t C_{\mathrm{dl}}$ represents the characteristic time constant for the system. The dc *(zero-frequency) current is equal to $V/(R_e + R_t)$ at potential V, and the current at infinite frequency is equal to V/R_e.*

Examples 4.1 and 4.2 illustrate the manner in which the impedance response of complex arrangements of circuit elements can be derived. In addition to providing an intuitive understanding of the response to a sinusoidal input, these simple circuits often form the basis for a preliminary interpretation of impedance results for electrochemical systems.

4.2 Fundamental Relationships

The impedance response can be described as having real and imaginary components, i.e.,

$$Z = Z_r + jZ_j \tag{4.29}$$

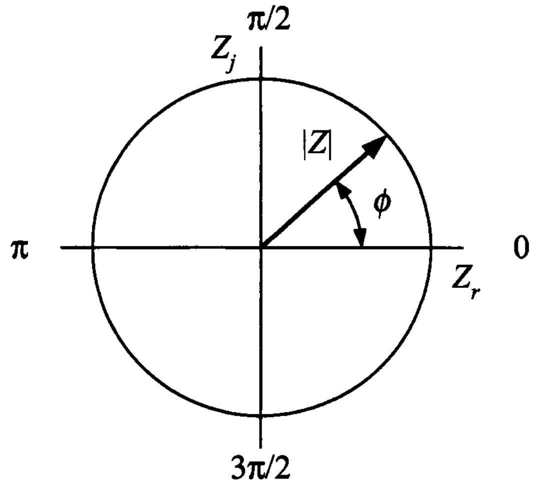

Figure 4.4: Phasor diagram showing relationships among complex impedance, magnitude, and phase angle.

When the input and output are in phase, as shown in equation (4.20), the imaginary part of the impedance has a value of zero, and the impedance has only a real contribution, Z_r. When the input and output are out of phase, as shown in equations (4.21) and (4.22), the real part of the impedance has a value of zero, and the impedance has only imaginary contribution, Z_j.

The relationship between the complex impedance and the phase angle is shown more clearly in the use of phasor diagrams and relationships. The impedance can be expressed as

$$Z = |Z| \exp{(j\phi)} \tag{4.30}$$

where $|Z|$ represents the magnitude of the impedance vector and ϕ represents the phase angle. The relationships among complex impedance, magnitude, and phase angle are shown in Figure 4.4. The magnitude of the impedance can be expressed in terms of real and imaginary components as

$$|Z(\omega)| = \sqrt{Z_r(\omega)^2 + Z_j(\omega)^2} \tag{4.31}$$

The phase angle can be obtained from

$$\phi(\omega) = \tan^{-1}\left(\frac{Z_j(\omega)}{Z_r(\omega)}\right) \tag{4.32}$$

or through geometric relationships that are evident in Figure 4.4, i.e.,

$$Z_r(\omega) = |Z(\omega)| \cos{(\phi(\omega))} \tag{4.33}$$

and

$$Z_j(\omega) = |Z(\omega)| \sin{(\phi(\omega))} \tag{4.34}$$

The representation of impedance in terms of magnitude and phase angle as functions of frequency on a logarithmic scale are called *Bode plots.*[87]

Example 4.3 Bode Representation of Elemental Circuits: *Derive an expression for the magnitude and phase angle for the circuit elements shown in Figure 4.1.*

Solution: Resistor. *The impedance for a resistor is given by* $Z = R + 0j$*; therefore, the magnitude is given by* $|Z| = R$ *and the phase angle is given by* $\phi = \tan^{-1}(0) = 0$.

Solution: Capacitor. *The impedance for a capacitor is given by* $Z = 0 - j\frac{1}{\omega C}$*; therefore, the magnitude is given by* $|Z| = \frac{1}{\omega C}$ *and the phase angle is given by* $\phi = \tan^{-1}(-\infty) = -\pi/2$. *The phase angle for a capacitor is* -90 *degrees.*

Solution: Inductor. *The impedance for an inductor is given by* $Z = 0 + j\omega L$*; therefore, the magnitude is given by* $|Z| = \omega L$ *and the phase angle is given by* $\phi = \tan^{-1}(\infty) = \pi/2$. *The phase angle for a capacitor is* $+90$ *degrees.*

The term *constant-phase element* (CPE) is applied to a general circuit element that shows a constant phase angle. Thus, the resistor, capacitor, and inductor can all be considered to be constant-phase elements.

4.3 Nested Circuits

The impedance response of more complicated circuits can be readily calculated using combinations of equations (4.23) and (4.24).

Example 4.4 Impedance Expression for a Nested Circuit: *Derive an expression for the impedance response of the circuit shown in Figure 4.5(a), and give expressions for the dc current and the current at infinite frequency for an applied potential* V.

Solution: *The circuit can be visualized, in a manner following Figure 4.2, to be a nested series of boxes, as seen in Figure 4.5(b). The parallel arrangement of* Z_3 *and* Z_4 *can be combined in terms of* $Z_{3,4}$ *(Figure 4.5(c)). Thus, the impedance of the circuit shown in Figure 4.5(c) can be expressed as*

$$Z = Z_0 + \left[\frac{1}{Z_1} + \frac{1}{Z_2 + Z_{3,4}}\right]^{-1} \tag{4.35}$$

where, following Figure 4.5(b),

$$Z_{3,4} = \left[\frac{1}{Z_3} + \frac{1}{Z_4}\right]^{-1} \tag{4.36}$$

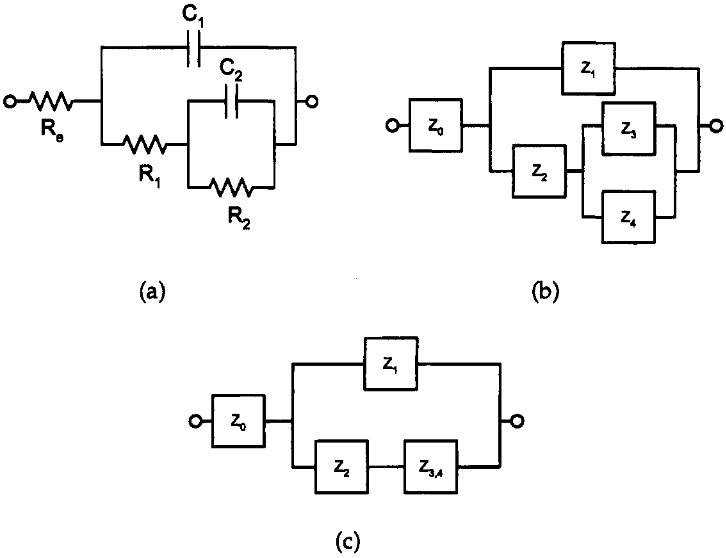

(a) (b)

(c)

Figure 4.5: Circuits demonstrating the calculation of the impedance of nested circuit elements: a) circuit with resistor and capacitor elements; b) reconstruction of the circuit in terms of the generic impedance Z_k; and c) secondary reconstruction to facilitate calculation.

The next step is to introduce the impedance for each individual unit, i.e., $Z_0 = R_e$, $Z_1 = 1/(j\omega C_1)$, $Z_2 = R_1$, $Z_3 = 1/(j\omega C_2)$, *and* $Z_4 = R_2$.

$$Z_{3,4} = \left[j\omega C_2 + \frac{1}{R_2} \right]^{-1} \tag{4.37}$$

or

$$Z_{3,4} = \frac{R_2}{1 + j\omega R_2 C_2} \tag{4.38}$$

In terms of circuit parameters,

$$Z = R_e + \left[j\omega C_1 + \frac{1}{R_1 + \frac{R_2}{1+j\omega R_2 C_2}} \right]^{-1} \tag{4.39}$$

At zero frequency the impedance is equal to $(R_e + R_1 + R_2)$, *and at infinite frequency the impedance is equal to* R_e.

4.4 Mathematical Equivalence of Circuits

Different electrical circuits possessing the same number of time constants can yield a mathematically equivalent frequency response. For example, the three circuits presented in Figure 4.6 arise from very different physical models and yet can have the same frequency response. Circuit 4.6(a) can describe two resistive layers and has been used as a measurement model, as described in Chapter 21. Circuit 4.6(b)

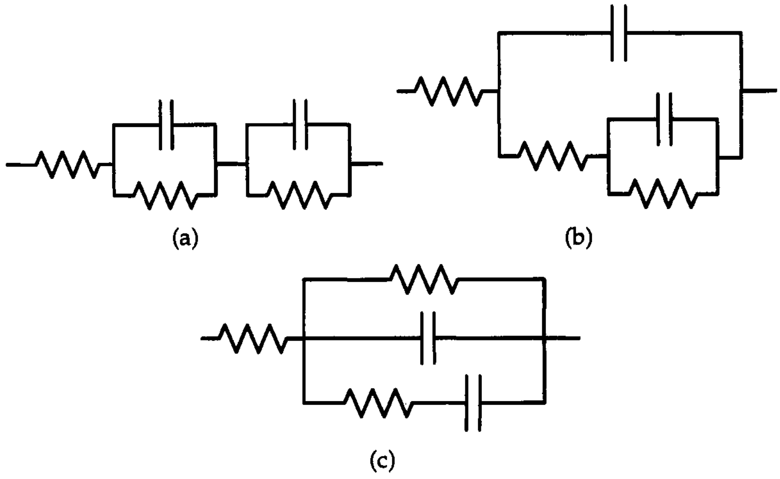

Figure 4.6: Three mathematically equivalent electrical circuits.

can describe a reaction mechanism comprising two electrochemical steps or a system consisting of a coated electrode. Development of such models is discussed in Chapter 10. As discussed in Chapter 12, circuit 4.6(c) has been used to describe a solid-state Schottky diode with a leakage current and deep-level electronic states.

The lack of uniqueness of circuit models creates ambiguity when interpreting impedance response using regression analysis. A good fit does not, in itself, validate the model used. As discussed in Chapter 23, impedance spectroscopy is not a standalone technique. Additional observations are needed to validate a model.

4.5 Graphical Representation of Circuit Response

The impedance response of a resistor in parallel to a capacitor is shown in Figure 4.7 as a function of frequency f in units of Hz. When plotted as a function of frequency ω in units of s^{-1} (the upper axis), the minimum in the imaginary part of the impedance appears clearly at a characteristic frequency of $\omega_c = 1/\tau_c$. The dashed line corresponds to the characteristic frequency of 1 s^{-1}. When plotted against frequency in units of Hertz, the characteristic frequency is shifted by a factor of 2π, i.e., $f_c = 1/2\pi\tau_c$.

The corresponding Bode representation of the impedance response is shown in Figure 4.8 as a function of frequency f in units of Hz and frequency ω in units of s^{-1}. When plotted as a function of frequency ω in units of s^{-1}, the phase angle reaches an inflection point (−45 degrees) at a characteristic frequency $\omega_c = 1/\tau_c$.

Remember! 4.4 *Electrical circuits are not unique. A good fit to experimental data is not sufficient to validate a model.*

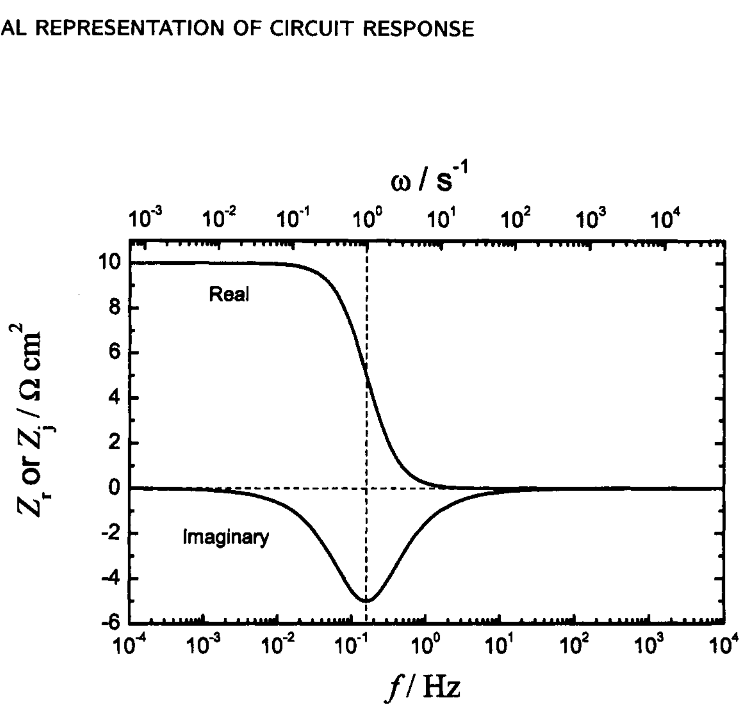

Figure 4.7: Real and imaginary parts of the impedance response for a 10 Ω resistor in parallel with a 0.1 F capacitor. The characteristic time constant for the element is 1 s.

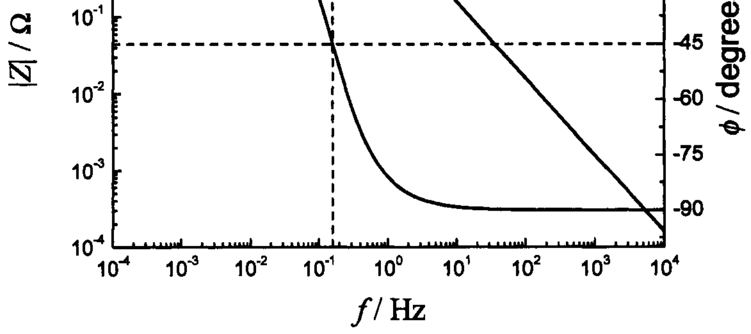

Figure 4.8: Bode representation of the impedance response for a 10 Ω resistor in parallel with a 0.1 F capacitor. The characteristic time constant for the element is 1 s.

Again, when plotted against frequency in units of Hz, the characteristic frequency is shifted by a factor of 2π.

Problems

4.1 Show that equation (4.12) for an inductor can lead to equation (4.13). Show that this result demonstrates that current and potential signals are out-of-phase for an inductor.

4.2 Follow the development leading to equation (4.16), and verify that equation (4.16) demonstrates that current and potential signals are out-of-phase for a capacitor.

4.3 Develop an expression for the impedance response of the circuit presented as Figure 4.6(a).

4.4 Develop an expression for the impedance response of the circuit presented as Figure 4.6(b).

4.5 Develop an expression for the impedance response of the circuit presented as Figure 4.6(c).

4.6 The use of inductors to model low-frequency inductive loops in an impedance response is somewhat controversial. Demonstrate that the circuit presented as Figure 4.6(b) with negative R and C in the nested element can be mathematically equivalent to a circuit containing an inductor.

4.7 Use a spreadsheet program to plot the impedance response of the circuit presented as Figure 4.3(a) using $R_e = 10\ \Omega$ and $C_{dl} = 20\ \mu\text{F/cm}^2$.

- **(a)** Plot the real and imaginary parts of the impedance as a function of frequency.
- **(b)** Plot the results in Bode format (magnitude and phase angle as a function of frequency).

4.8 Use a spreadsheet program to plot the impedance response of the circuit presented as Figure 4.3(b) using $R_e = 10\ \Omega$, $C_{dl} = 20\ \mu\text{F/cm}^2$, and $R_t = 100\ \Omega$.

- **(a)** Plot the real and imaginary parts of the impedance as a function of frequency.
- **(b)** Plot the results in Bode format (magnitude and phase angle as a function of frequency).

Electrochemical Impedance Spectroscopy
by Mark E. Orazem and Bernard Tribollet

Chapter 5

Electrochemistry

A number of excellent texts are available that provide a thorough discussion of electrochemical principles. Newman[88,89] provides a comprehensive and mathematically detailed treatment of electrochemical engineering. Prentice[90] provides slightly greater emphasis on applications. Bard and Faulkner[91] emphasize analytical methods, and Bockris and Reddy[92,93] provide a very approachable introduction to electrochemical processes. Gileadi[94] provides an excellent treatment of electrode kinetics, and Brett and Brett[95] provide a treatment that includes fundamentals as well as applications, including impedance spectroscopy.

5.1 Resistors and Electrochemical Cells

As Gileadi observes, the distinguishing feature of electrochemical reactions is that an electrical current is observed as a nonlinear function of electrode potential.[94] Consider, for example, the 1 Ω resistor represented in Figure 5.1(a). If a potential difference of 1 V is applied across the resistor, the resulting current would have a value of 1 A. The relationship between current and potential is linear, such that

$$I = V/R \tag{5.1}$$

as seen in Figure 5.2.

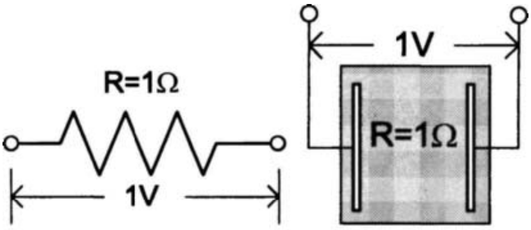

(a) (b)

Figure 5.1: Systems through which current is passed: a) 1 Ω resistor; and b) an electrochemical cell with an effective electrolyte resistance of 1 Ω.

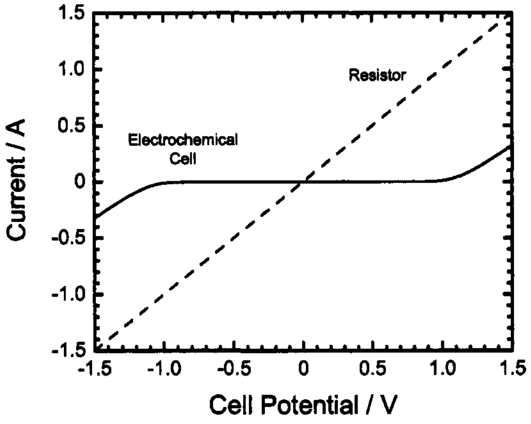

Figure 5.2: Polarization curves for a 1 Ω resistor and for a symmetric electrochemical cell with 1 Ω solution resistance and inert electrodes such as gold or platinum.

The behavior of the electrochemical cell is strikingly different. Consider, for example, the electrochemical cell shown schematically in Figure 5.1(b). Imagine that the electrodes are made of an inert material such as gold or platinum, and that the electrolyte consists of Na_2SO_4 in distilled water. The current flowing through the cell is influenced, not only by the Ohmic resistance of the cell, but also by the potential required to drive charge-transfer reactions. If electrochemical reactions cannot occur, current will not flow. In the cell envisioned here, the only electrochemical reactions that can take place involve decomposition of the water into hydrogen and oxygen. To conserve charge, the hydrogen evolution reaction

$$H_2O + e^- \leftrightarrows \frac{1}{2}H_2 + OH^- \tag{5.2}$$

must be balanced by oxygen evolution

$$H_2O \leftrightarrows \frac{1}{2}O_2 + 2H^+ + 2e^- \tag{5.3}$$

The experimental observation, as shown in Figure 5.2, is that a critical cell potential must be exceeded before current can flow. This critical potential is called a *standard cell potential* and has a value, for the reactions (5.2) and (5.3), of 1.229 V. No current, therefore, should flow over a broad range of potential. The result indicates that the polarization curve for the electrochemical cell is distinctly nonlinear.

If the inert electrodes were replaced by copper or if electroactive species were placed in the electrolyte, the current would flow more readily in the cell, but the resulting polarization curve would still be nonlinear.

5.2 Equilibrium in Electrochemical Systems

The electrochemical system shown in Figure 5.1(b) can be described as consisting of several phases, including the metal phase of the wire attached to the left elec-

LW	LE	E	RE	RW
Wire	Left electrode	Electrolyte	Right electrode	Wire

Figure 5.3: Representation of phases associated with the electrochemical system shown in Figure 5.1(b).

trode, the metal phase of the left electrode, the electrolyte, the metal phase of the right electrode, and the metal phase of the wire attached to the right electrode. These phases are represented schematically in Figure 5.3. Equality of thermodynamic properties between these phases can be used to describe the equilibrium condition of this system. Thermal equilibrium requires that temperatures of adjoining phases are equal, e.g.,

$$T^{\mathrm{LW}} = T^{\mathrm{LE}} = T^{\mathrm{E}} = T^{\mathrm{RE}} = T^{\mathrm{RW}} \tag{5.4}$$

Mechanical equilibrium requires that the pressures of adjoining phases are equal, e.g.,

$$p^{\mathrm{LW}} = p^{\mathrm{LE}} = p^{\mathrm{E}} = p^{\mathrm{RE}} = p^{\mathrm{RW}} \tag{5.5}$$

Chemical equilibrium requires that, if species exist in adjoining phases, their electrochemical potentials must be equal, e.g., for electrons

$$\mu_{\mathrm{e^-}}^{\mathrm{LW}} = \mu_{\mathrm{e^-}}^{\mathrm{LE}} \tag{5.6}$$

and

$$\mu_{\mathrm{e^-}}^{\mathrm{RE}} = \mu_{\mathrm{e^-}}^{\mathrm{RW}} \tag{5.7}$$

The electrochemical potential can be considered to be a generalization of the chemical potential that applies to charged species. For an isothermal system, a gradient of electrochemical potential, for example, within the electrolyte, will drive the motion of chemical species.

Relationships such as those expressed in equation (5.6) cannot be employed for species that are in chemical equilibrium but do not exist in the adjoining phases. Electrons, for example, are present in the metal of the electrode (phase LE) and in chemical equilibrium with ionic species in the electrolyte (phase E), but are not present in the electrolyte. An equilibrium relationship between the electrons and ionic species can be expressed, however, in terms of electrochemical reactions, and

---

Remember! 5.1 *Electrochemical reactions, which transfer charge between electrons and soluble species, are required for current to flow in an electrochemical cell.*

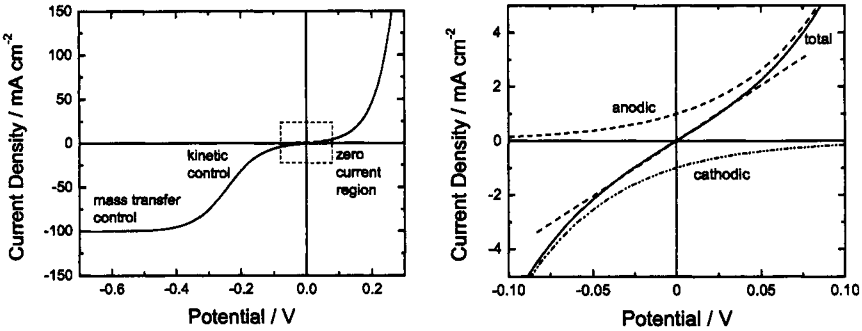

(a) (b)

Figure 5.4: Polarization curves for a system with mass-transfer control at cathodic potentials: a) broad range of potential with regions of behavior identified; and b) expanded representation of the zero-current region with cathodic and anodic current contributions identified.

the equilibrium condition for an electrochemical reaction can be expressed in terms of the equality of electrochemical potentials. For reaction (5.2), the condition of equilibrium is expressed as

$$\mu_{H_2O} + \mu_{e^-} = \frac{1}{2}\mu_{H_2} + \mu_{OH^-} \tag{5.8}$$

Similar equilibrium relationships can be developed for homogeneous reactions involving species that exist in a given phase.

For isothermal systems, expressions of phase and chemical equilibrium, such as are given in equations (5.6) and (5.8), provide the foundation for the derivation of equilibrium cell potentials in terms of electrolyte and electrode compositions. The reader is referred to other textbooks, e.g., Newman,[88,89] for methods used to derive equilibrium cell potentials.

5.3 Polarization Behavior for Electrochemical Systems

The nonlinear current–voltage behavior associated with an electrochemical system is illustrated in Figure 5.4(a). In the case shown here, the anodic (positive) current has an exponential dependence on potential; whereas, the cathodic (negative) current displays an influence of mass-transfer limitations. Regions are identified for which the current has a value equal to zero, the current is controlled by reaction kinetics, and the current is controlled by mass transfer.

5.3.1 Zero Current

An expanded representation of the zero-current region of Figure 5.4(a) is presented as Figure 5.4(b). The positive current contributed by the anodic reaction is balanced by the negative current contributed by the cathodic reaction. If the anodic and cathodic reactions represent forward and backward rates of the same reaction, a zero current can be obtained under the condition of reaction equilibrium. If the anodic and cathodic reactions represent forward and backward rates of different reactions, a true equilibrium is not reached as neither reaction is equilibrated. Thus, the net current may have a value equal to zero under either equilibrium or nonequilibrium conditions.

Equilibrium

If the current corresponds to a single electrochemical reaction, a zero current is observed if the forward and backward rates for the reaction are equal. For example, if the forward (or anodic) reaction is given by

$$\mathrm{Cu} \longrightarrow \mathrm{Cu}^{2+} + 2\mathrm{e}^{-} \tag{5.9}$$

the backward (or cathodic) reaction is given by

$$\mathrm{Cu}^{2+} + 2\mathrm{e}^{-} \longrightarrow \mathrm{Cu} \tag{5.10}$$

If a current i_a is assigned to reaction (5.9), and a current i_c is assigned to reaction (5.10), the net current will be given by

$$i = i_a + i_c \tag{5.11}$$

where $i_a > 0$ and $i_c < 0$. At equilibrium, $i_a = -i_c$, and $i = 0$. The potential at which the current for a single electrochemical reaction is equal to zero is termed the *equilibrium potential*. The value for the equilibrium potential can be calculated using thermodynamic arguments.[88,89]

Nonequilibrium

If the zero current condition arises through a balancing of different reactions, equilibrium is not achieved because the net rate for each reaction is not equal to zero. For example, if the corrosion of iron

$$\mathrm{Fe} \longrightarrow \mathrm{Fe}^{2+} + 2\mathrm{e}^{-} \tag{5.12}$$

is balanced by reduction of oxygen

$$\mathrm{O}_2 + 2\mathrm{H}_2\mathrm{O} + 4\mathrm{e}^{-} \longrightarrow 4\mathrm{OH}^{-} \tag{5.13}$$

the net current can be equal to zero while dissolution of iron continues and oxygen is consumed. This is clearly not an equilibrium condition.

The potential at which the current for multiple electrochemical reactions is equal to zero is termed the *mixed potential* or, in the case of metal dissolution, the *corrosion potential*. Concepts of thermodynamics, kinetics, and transport must be applied to calculate values for the mixed or corrosion potential.

5.3.2 Kinetic Control

The region of kinetic control of electrochemical reactions is characterized by current densities that are exponential functions of potential. For a single reversible reaction, the Butler-Volmer equation

$$i = i_0 \left\{ \exp\left(\frac{(1-\alpha)nF}{RT}\eta_s \right) - \exp\left(-\frac{\alpha nF}{RT}\eta_s \right) \right\} \tag{5.14}$$

is commonly used to describe the influence of potential on the current density. Here, i_0 is the exchange current density, so defined because at $\eta_s = 0$, $i_a = -i_c = i_0$. The surface overpotential η_s represents the departure from an equilibrium potential such that, at $\eta_s = 0$, the total current $i = i_a + i_c$ is equal to zero. The symmetry factor α is the fraction of the surface overpotential potential that promotes the cathodic reaction. Usually, α is assumed to have the value close to 0.5 and must have a value between 0 and 1.

As shown in Chapter 10, electrochemical kinetics plays a major role in the interpretation of impedance spectra. To streamline the discussion of electrochemical kinetics, a more compact notation will be used in which

$$b_a = \frac{(1-\alpha)nF}{RT} \tag{5.15}$$

for anodic reactions and

$$b_c = \frac{\alpha nF}{RT} \tag{5.16}$$

for cathodic reactions where b_a and b_c have units of inverse potential. Thus, equation (5.14) can be written

$$i = i_0 \left\{ \exp\left(b_a\eta_s \right) - \exp\left(-b_c\eta_s \right) \right\} \tag{5.17}$$

The parameters b_a and b_c are closely related to the Tafel slope, e.g.,

$$\beta_c = \frac{2.303RT}{\alpha nF} = 2.303/b_c \tag{5.18}$$

which has units of V/decade.

The current density presented in Figure 5.4(b) can be described as being a linear function of potential over a narrow range of potential near the zero-current potential. Taylor series expansions of the exponential terms in equation (5.14) yield

$$i = \frac{ni_0F}{RT}\eta_s \tag{5.19}$$

In the compact notation introduced in equations (5.15) and (5.16),

$$i = i_0\left(b_a + b_c \right)\eta_s \tag{5.20}$$

A similar linear regime can be identified when the zero-current condition arises from the balancing of different anodic and cathodic reactions.

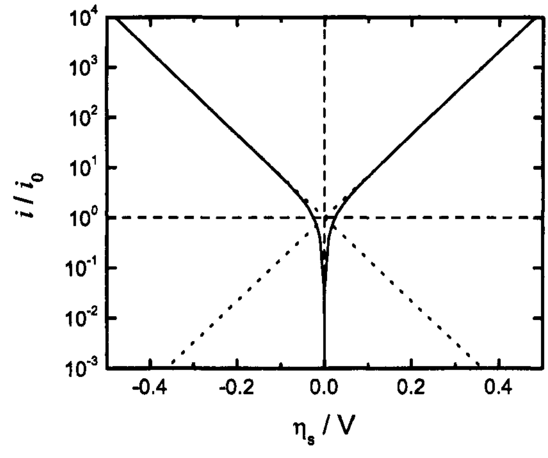

Figure 5.5: Polarization curves on a logarithmic scale reveal straight lines with slope of $1/beta$.

At very positive potentials, the cathodic term is negligible, and the current density can be expressed by

$$i = i_0 \exp\left(b_a \eta_s\right) \tag{5.21}$$

At very negative potentials, the anodic term can be neglected, and

$$i = -i_0 \exp\left(-b_c \eta_s\right) \tag{5.22}$$

Equations (5.21) and (5.22) are examples of Tafel equations in which the current is an exponential function of potential. The Tafel behavior is illustrated in Figure 5.5. The intersection of the extrapolated lines for anodic and cathodic currents yields the equilibrium potential and the exchange current density.

5.3.3 Mass-Transfer Control

The rate of the electrochemical reactions may be limited by the finite rate at which reacting species may be carried to the electrode surface. Such a case is illustrated in Figure 5.4(a) at negative values of potential. In this case, the exchange current density is proportional to the concentration at the interface of the reacting species i with a power $|s_i|$, where s_i is the stoichiometric coefficient. With $s_i = 1$, the cathodic current density can be written as

$$i = -k_c n F c_i(0) \exp\left(-b_c \eta_s\right) \tag{5.23}$$

The current density corresponds to the flux density of the reacting species, i.e.,

$$i = -nFD_i \left.\frac{dc_i}{dy}\right|_{y=0} \tag{5.24}$$

By assuming a linear concentration gradient in the diffusion layer of thickness δ_i, equation (5.24) becomes

$$i = -nFD_i \frac{c_i(\infty) - c_i(0)}{\delta_i} \tag{5.25}$$

Where $c_i(\infty)$ is the concentration of species i in the bulk solution.

A formal treatment for determination of the value of δ_i requires solution of the convective-diffusion equations, as described in Chapter 11. By eliminating $c_i(0)$ from equations (5.23) and (5.25), the value of the current density is obtained as

$$i^{-1} = i_{\text{lim}}^{-1} + i_k^{-1} \tag{5.26}$$

where $i_{\text{lim}} = -nFD_ic_i(\infty)/\delta_i$ is the mass-transfer-limited current density and $i_k = -k_cnFc_i(\infty)\exp(-b_c\eta_s)$ is the kinetic current based on the bulk concentration. The numerical value for the mass-transfer-limited current density is influenced by the bulk concentration and diffusivity of the limiting reactant, by the extent of convection, and by the cell geometry. The student is referred to Problems 5.3 and 5.4.

5.4 Definitions of Potential

The potential of the electrode U is defined to be the difference between the potential of the working electrode Φ_m and the potential of a reference electrode Φ_{ref} located in the bulk of the electrolyte solution, i.e.,

$$U = \Phi_m - \Phi_{\text{ref}} \tag{5.27}$$

The cell potential can be expressed in terms of the potential in the electrolyte adjacent to the electrode Φ_0 as

$$U = (\Phi_m - \Phi_0) + (\Phi_0 - \Phi_{\text{ref}}) \tag{5.28}$$

The position at which Φ_0 is evaluated is generally taken to be the inner limit of the electrically neutral diffusion layer, shown in Figure 5.6(b). In this way, the interface is assumed to incorporate the detailed structure of the double layer, including the diffuse region of charge and the inner Helmholtz plane associated with specifically adsorbed charged species.

Equation (5.28) can be written as

$$U = V + iR_e \tag{5.29}$$

where the interfacial potential V is defined by:

$$V = (\Phi_m - \Phi_0) \tag{5.30}$$

and the Ohmic potential drop in the electrolyte is given as

$$iR_e = (\Phi_0 - \Phi_{\text{ref}}) \tag{5.31}$$

The surface overpotential η_s for a given reaction k is given by

$$\eta_s = V - V_{0,k} \tag{5.32}$$

where $V_{0,k}$ is the equilibrium potential difference that depends on the electrode reaction under consideration. The definitions of potentials used in electrochemical systems are summarized in Table 5.1.

Table 5.1: Definitions and notation for potentials used in electrochemical systems.

V	Interfacial potential for the working electrode, $V = \Phi_m - \Phi_0$.
$V_{0,k}$	Interfacial potential at equilibrium for a given reaction k, $V_{0,k} = (\Phi_m - \Phi_0)_{0,k}$.
U	Electrode potential with respect to a reference electrode, $U = \Phi_m - \Phi_{ref}$.
η_s	Surface overpotential for a given reaction k, $\eta_s = V - V_{0,k}$.
η_c	Concentration overpotential defined by equation (5.75).
Φ_m	Electrode potential with respect to an unspecified but common reference potential.
Φ_0	Potential of the electrolyte adjacent to the working electrode with respect to an unspecified but common reference potential.
Φ_{ref}	Potential of a reference electrode with respect to an unspecified but common reference potential.
iR_e	Ohmic potential drop between the solution adjacent to the working electrode and the location of a reference electrode, i.e., $iR_e = \Phi_0 - \Phi_{ref}$.

5.5 Rate Expressions

The rates of electrochemical reactions can be expressed in terms of concentration and potential.

5.5.1 Law of Mass Action

The electrochemical oxidation of ferrocyanide to form ferricyanide

$$\mathrm{Fe(CN)_6^{4-}} \rightleftarrows \mathrm{Fe(CN)_6^{3-}} + \mathrm{e^-} \tag{5.33}$$

is represented schematically in Figure 5.6(a). The rate of the reaction can be expressed in terms of current density as

$$r = \frac{i}{nF} \tag{5.34}$$

where i is the current density and n is the number of electrons transferred. In the case of reaction (5.33), $n = 1$. The rate of the reaction depends on the nature and preparation of the interface, the composition of the electrolyte adjacent to the electrode, the electrode potential, and temperature.

A kinetic expression for reaction (5.33) can be developed, following the laws of mass action generally applied for chemical or non-electrochemical systems. Thus,

$$r = k_a^* c_{\mathrm{Fe(CN)_6^{4-}}}(0) - k_c^* c_{\mathrm{Fe(CN)_6^{3-}}}(0) \tag{5.35}$$

where k_a^* and k_c^* are rate constants for the anodic and cathodic reactions, respectively. The concentrations $c_{\mathrm{Fe(CN)_6^{4-}}}(0)$ and $c_{\mathrm{Fe(CN)_6^{3-}}}(0)$ are generally taken to be at the inner limit of the diffusion layer as shown in Figure 5.6(b).

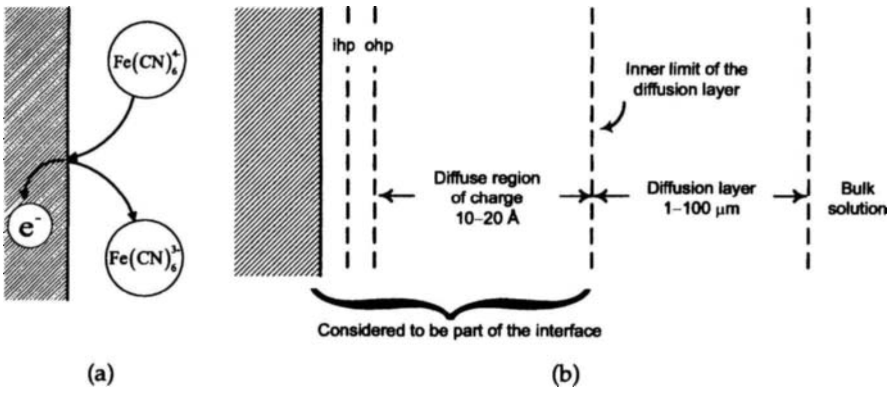

Figure 5.6: Schematic representation of an electrochemical reaction: a) oxidation of ferrocyanide to form ferricyanide; and b) proposed double-layer structure revealing the components included as part of the interface where *ihp* refers to the inner Helmholtz plane and *ohp* refers to the outer Helmholtz plane.

The rate constants k_a^* and k_c^* are expressed in terms of activation free energies as

$$k_a^* = k_{a,0} \exp\left(-\frac{\Delta G_a^\ddagger}{RT}\right) \tag{5.36}$$

and

$$k_c^* = k_{c,0} \exp\left(-\frac{\Delta G_c^\ddagger}{RT}\right) \tag{5.37}$$

respectively. The activation energies are shown in the reaction coordinate diagram presented as Figure 5.7. All electrochemical reactions, such as reactions (5.2) and (5.3), have an electron as a reactant. One consequence is that, unlike most chemical reactions, the reaction must take place at an interface with an electrode that is a conductor of electrons. A second consequence is that the energy of the electrons participating in the reaction can be influenced by changing the electrical potential. The activation energy $\Delta G_a^\ddagger$, for example, can be separated into chemical and electrical contributions such that

$$\Delta G_a^\ddagger = \Delta G_{a,\text{chem}}^\ddagger + \Delta G_{a,\text{elec}}^\ddagger \tag{5.38}$$

The terms $\Delta G_{a,\text{elec}}^\ddagger$ and $\Delta G_{c,\text{elec}}^\ddagger$ can be expressed in terms of potential as

$$\Delta G_{a,\text{elec}}^\ddagger = -(1-\alpha)\, nF(V - V^\ddagger) \tag{5.39}$$

and

$$\Delta G_{c,\text{elec}}^\ddagger = \alpha nF(V - V^\ddagger) \tag{5.40}$$

respectively, where $V^\ddagger$ is a reference potential at which the chemical contribution is evaluated, and α represents a symmetry factor which has meaning as the fractional probability that a molecule at the activated complex energy will proceed in the

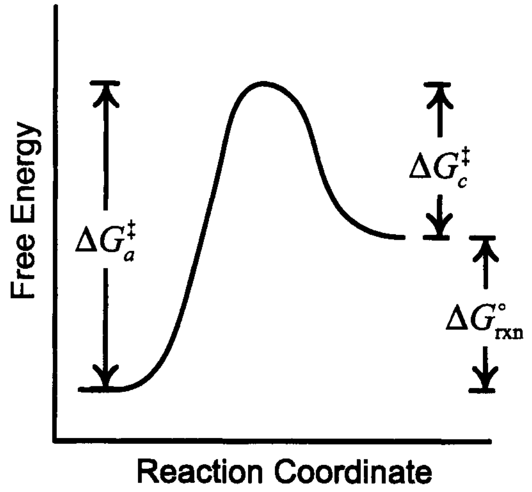

Figure 5.7: Free energy as a function of reaction coordinate for an elementary single-step reaction.

forward direction. Thus, an electrochemical reaction can be expected to have an exponential dependence on potential, as seen in Section 5.3.

5.5.2 Generalized Electrode Kinetics

A generalized expression for reaction k can be expressed as

$$\sum_i s_{i,k}\mathrm{M}_i \rightarrow n\mathrm{e}^- \tag{5.41}$$

where $s_{i,k}$ is the stoichiometric coefficient for species i and M_i represents the species i. The rate of reaction k can be expressed as

$$r_k = k_a \exp\left(\frac{(1-\alpha)nF}{RT}V\right)\prod_i c_i^{p_{i,k}}(0) - k_c \exp\left(-\frac{\alpha nF}{RT}V\right)\prod_i c_i^{q_{i,k}}(0) \tag{5.42}$$

where for $s_{i,k} = 0$, the species i is not a reactant and $p_{i,k} = 0$ and $q_{i,k} = 0$; for $s_{i,k} > 0$, species i is a reactant for reaction k and $p_{i,k} = s_{i,k}$ and $q_{i,k} = 0$; and for $s_{i,k} < 0$, species i is a product of reaction k and $p_{i,k} = 0$ and $q_{i,k} = -s_{i,k}$.

The rate expression given as equation (5.42) raises questions concerning the location at which concentrations and potentials are measured. The concentration of reacting species, for example, should be that measured at the inner limit of the

Remember! 5.2 *Kinetic expressions of the law of mass action provide the foundation for modeling the charge-transfer resistance commonly encountered in electrochemical impedance spectroscopy.*

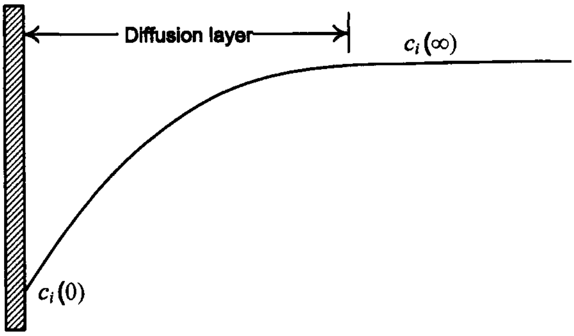

Figure 5.8: Concentration profile near an electrode surface showing the presence of a concentration diffusion layer.

diffusion layer, as shown in Figure 5.8. Similarly, the potential V given in equation (5.42) represents the potential difference between the electrode and the solution adjacent to the electrode.

The equilibrium potential can be expressed as

$$V_{0,k} = \frac{RT}{nF}\left[\ln\left(\frac{k_c}{k_a}\right) + \sum_i (q_{i,k} - p_{i,k}) \ln c_i(\infty)\right] \tag{5.43}$$

where the interfacial concentration $c_i(0)$ is equal to the bulk concentration $c_i(\infty)$. The surface overpotential can be expressed as a departure of V from its equilibrium value, e.g.,

$$\eta_s = V - V_{0,k} \tag{5.44}$$

Equation (5.42) can be expressed in terms of the Butler-Volmer equation (5.14) as

$$i = i_0\left\{\exp\left(\frac{(1-\alpha)nF}{RT}\eta_s\right) - \exp\left(-\frac{\alpha nF}{RT}\eta_s\right)\right\} \tag{5.45}$$

where

$$i_0 = nFk_c^{1-\alpha}k_a^{\alpha}\prod_i c_i^{(q_{i,k}+\alpha s_{i,k})}(0) \tag{5.46}$$

Here, α, the symmetry factor, is generally assigned a value of 0.5. As concentrations $c_i(0)$ are measured at the electrode surface, the exchange current density is a function of applied potential.

Example 5.1 Rate Expression for Copper Dissolution: *Develop expressions corresponding to equations (5.41–5.46) for the reaction*

$$\mathrm{Cu} \rightleftarrows \mathrm{Cu}^{2+} + 2\mathrm{e}^- \tag{5.47}$$

where copper is assumed to dissolve directly to form the cupric ion.

Solution: *For the reaction (5.47), the stoichiometric coefficients are* $s_{Cu} = +1$, $s_{Cu^{2+}} = -1$, *and* $n = 2$. *Thus, equation (5.41) is expressed*

$$\mathrm{Cu} \rightarrow \mathrm{Cu}^{2+} + 2\mathrm{e}^- \tag{5.48}$$

The corresponding expression for the reaction rate (5.42) is given as

$$r_{Cu} = \frac{i_{Cu}}{2F} = k_a \exp\left(\frac{F}{RT}V\right) - k_c \exp\left(-\frac{F}{RT}V\right) c_{Cu^{2+}}(0) \tag{5.49}$$

with the value of n as given above. The equilibrium potential can be expressed as

$$V_{0,Cu} = \frac{RT}{2F}\left[\ln\left(\frac{k_c}{k_a}\right) + \ln c_{Cu^{2+}}(\infty)\right] \tag{5.50}$$

and the exchange current density can be written as

$$i_0 = 2Fk_c^{1/2}k_a^{1/2}c_{Cu^{2+}}(0) \tag{5.51}$$

A different expression is obtained if the reaction to form cupric ion is considered to consist of two elementary reactions in which copper react to form cuprous ions and the cuprous ions subsequently reacts to form cupric ions.

5.6 Transport Processes

In the bulk of a well-stirred electrolytic solution, potential is governed by Laplace's equation, i.e.,

$$\nabla^2\Phi = 0 \tag{5.52}$$

where Φ is the potential and ∇ is the vector differential operator. Equation (5.52) applies to all coordinate systems, and is written in rectangular coordinates as

$$\frac{\partial^2\Phi}{\partial x^2} + \frac{\partial^2\Phi}{\partial y^2} + \frac{\partial^2\Phi}{\partial z^2} = 0 \tag{5.53}$$

The current density i is given by Ohm's Law

$$i = -\kappa\nabla\Phi \tag{5.54}$$

where κ is the electrolyte conductivity. Equation (5.54) applies to all coordinate systems, and is written in rectangular coordinates as

$$i = -\kappa\left(\frac{\partial\Phi}{\partial x} + \frac{\partial\Phi}{\partial y} + \frac{\partial\Phi}{\partial z}\right) \tag{5.55}$$

For dilute solutions, the electrolyte conductivity can be expressed as a sum of contributions from each of the ionic species as

$$\kappa = F^2\sum_i z_i^2 u_i c_i = \frac{F^2}{RT}\sum_i z_i^2 D_i c_i \tag{5.56}$$

Table 5.2: Typical values of diffusion coefficients for ions at infinite dilution in water at 25 °C.

Cation	z_i	$D_i/\mathrm{cm^2s^{-1}}$	Anion	z_i	$D_i/\mathrm{cm^2s^{-1}}$
H^+	+1	9.312×10^{-5}	OH^-	−1	5.260×10^{-5}
Na^+	+1	1.334×10^{-5}	Cl^-	−1	2.032×10^{-5}
K^+	+1	1.957×10^{-5}	NO_3^-	−1	1.902×10^{-5}
Ag^+	+1	1.648×10^{-5}	SO_4^{2-}	−2	1.065×10^{-5}
Mg^{2+}	+2	0.7063×10^{-5}	$Fe(CN)_6^{3-}$	−3	0.896×10^{-5}
Cu^{2+}	+2	0.72×10^{-5}	$Fe(CN)_6^{4-}$	−4	0.739×10^{-5}

where D_i is the diffusion coefficient for species i, z_i is the charge on species i, u_i is the mobility, and F is Faraday's constant. The mobility can be related to the diffusion coefficient by the Nernst-Einstein equation

$$D_i = RTu_i \tag{5.57}$$

Typical values of diffusion coefficients for ions at infinite dilution in water at 25 °C are presented in Table 5.2.

The current density satisfies conservation of charge; therefore,

$$\nabla \cdot i = 0 \tag{5.58}$$

Equation (5.52) applies when the conductivity is uniform and there are no concentration gradients for ionic species.

The assumption that there are no concentration gradients is not valid near electrode surfaces. For example, oxygen reduction at an electrode surface causes the pH at the surface of the electrode to reach 10 or 11, even when the pH in the bulk electrolyte is equal to 7.

A more general description of transport is based on conservation of species, as given by[88]

$$\frac{\partial c_i}{\partial t} = -\left(\nabla \cdot N_i\right) + R_i \tag{5.59}$$

where c_i is the concentration of species i, N_i is the net flux vector for species i, and R_i is the rate of generation of species i. In a dilute solution, the flux for any species can be written in terms of contributions from convection, diffusion, and migration, i.e.,

$$N_i = vc_i - D_i\nabla c_i - z_iu_iFc_i\nabla\Phi \tag{5.60}$$

Remember! 5.3 *The electrolyte resistance commonly encountered in electrochemical impedance spectroscopy arises from transport processes in the bulk electrolyte.*

Table 5.3: Hierarchy of current distribution model assumptions.

Solution	Ohmic Resistance	Kinetic Resistance	Mass-Transfer Resistance
Primary	✓	×	×
Secondary	✓	✓	×
Tertiary	✓	✓	✓
Mass-transfer-limited	×	×	✓

where v is the fluid velocity. The current density i is given by the sum of contributions from the flux of each ionic species, i.e.,

$$i = F\sum_i z_i N_i \tag{5.61}$$

Conservation of charge, equation (5.58), and electroneutrality,

$$\sum_i z_i c_i = 0 \tag{5.62}$$

requires that

$$\nabla \cdot (\kappa \nabla \Phi) + F\sum_i z_i \nabla \cdot (D_i \nabla c_i) = 0 \tag{5.63}$$

Laplace's equation (5.52) does not apply in the presence of concentration gradients because the conductivity κ is not a constant and because the right-hand term in equation (5.63) is not equal to zero. In the absence of concentration gradients and with a uniform value of κ, equation (5.63) reduces to equation (5.52). Thus, a series of approximate solutions may be obtained, as summarized in Table 5.3 and discussed in the subsequent sections.

5.6.1 Primary Current and Potential Distributions

The impedance response can be strongly influenced by the distribution of current and potential at the electrode under study. Some general guidelines can be established to help determine conditions under which a nonuniform distribution can arise.

Under the assumption that the concentrations are uniform within the electrolyte, potential is governed by Laplace's equation (5.52). Under these conditions, the passage of current through the system is controlled by the Ohmic resistance to passage of current through the electrolyte and by the resistance associated with reaction kinetics. The primary distribution applies in the limit that the Ohmic resistance dominates and kinetic limitations can be neglected. The solution adjacent to the electrode can then be considered to be an equipotential surface with value Φ_0. The boundary condition for insulating surfaces is that the current density is equal to zero.

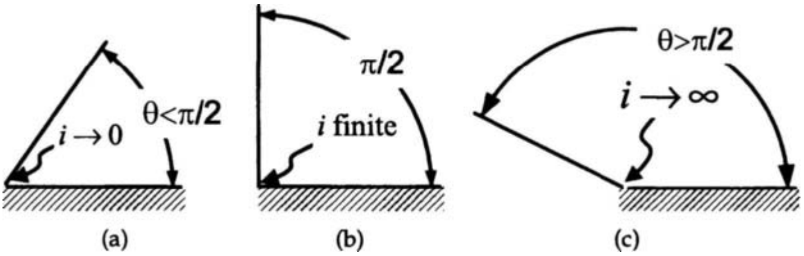

Figure 5.9: Behavior of the primary current distribution following equation (5.64) near the edge of an electrode: a) $i \longrightarrow 0$ for $\theta < \pi/2$; b) i is finite for $\theta = \pi/2$; and c) $i \longrightarrow \infty$ for $\theta > \pi/2$.

The primary current distribution generally represents a worse-case scenario for electrode design. At boundaries between an electrode and an insulator, the current density can be shown to approach

$$i \propto r^{(\pi-2\theta)/\pi} \tag{5.64}$$

where r is the radial distance from the point of intersection and θ is the angle between the electrode and insulator measured in radians. As shown in Figure 5.9, equation (5.64) shows that the current tends toward zero for angles $\theta < \pi/2$, toward infinity for angles $\theta > \pi/2$, and is uniform only if $\theta = \pi/2$.

For a disk of radius r_0, embedded in an insulating plane and with a counter-electrode infinitely far away, the primary current density is given by

$$\frac{i}{\langle i \rangle} = \frac{1}{2\sqrt{1-\left(\frac{r}{r_0}\right)^2}} \tag{5.65}$$

where $\langle i \rangle$ represents the area-averaged current density. The normalized primary current distribution depends only on the electrode geometry. The current density tends toward infinity at the periphery of the disk. The corresponding primary resistance is given by

$$R_e = \frac{1}{4\kappa r_0} \tag{5.66}$$

The dimensionless primary resistance can be written as $R_e \kappa r_0 = 1/4$.

5.6.2 Application to Blocking Electrodes

Some electrochemical systems can be described as blocking electrodes for which no Faradaic reaction can occur. At steady state, the current density for such a system must be equal to zero. The transient response of a blocking electrode is due to the charging of the double layer. At short times or high frequency, the interfacial impedance tends toward zero, and the solution adjacent to the electrode can then be considered to be an equipotential surface. The short-time or high-frequency current distribution, therefore, follows the primary distribution described in the

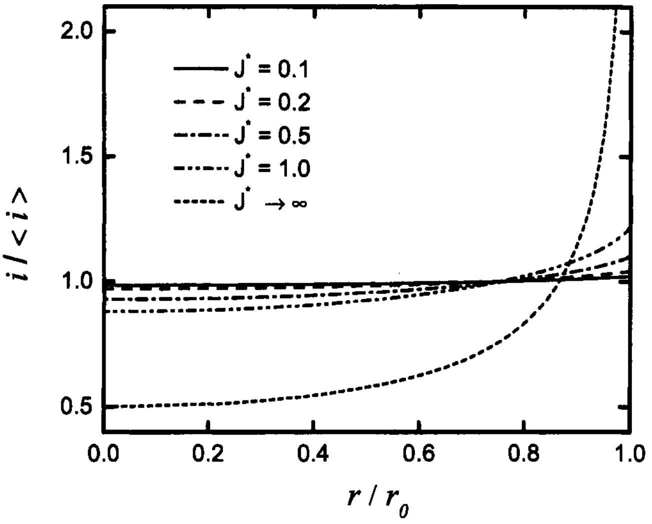

Figure 5.10: Secondary current distribution for linear polarization at a disk electrode. (Taken from Huang et al.[97])

previous section. At intermediate frequencies, the solution potential adjacent to the electrode is not uniform, and the resulting current distribution deviates from the primary distribution.

5.6.3 Secondary Current and Potential Distributions

The secondary distribution applies when kinetic limitations cannot be neglected. The solution adjacent to the electrode can no longer be considered to be an equipotential surface. The condition at the electrode can be replaced by

$$i = -\kappa \left. \frac{\partial \Phi}{\partial y} \right|_{y=0} = f(\eta_s) \tag{5.67}$$

where y is the coordinate normal to the electrode surface and $f(\eta_s)$ is a general function that could be given by the Butler-Volmer equation (5.14). At sufficiently small overpotentials, equation (5.14) can be linearized such that

$$\left. \frac{\partial \Phi}{\partial y} \right|_{y=0} = -J\eta_s \tag{5.68}$$

where $J = ni_0F/\kappa RT$ (see Problem 5.5). The parameter J is a dimensionless exchange current density that is the inverse of the Wagner number.[96] The resulting current distributions, obtained by numerical solution of Laplace's equation, are presented in Figure 5.10. The parameter J represents a ratio of Ohmic resistance to kinetic resistance. When $J \rightarrow \infty$, the Ohmic resistance dominates, and the current density follows that of the primary distribution given as equation (5.65).

5.6.4 Tertiary Current and Potential Distributions

Tertiary distributions apply when Laplace's equation is replaced by a series of n equations of the form (5.59) coupled with electroneutrality (5.62) where n represents the number of ionic species in the system. Thus, tertiary distributions relax the assumption that concentrations are uniform. Ohmic, kinetic, and mass-transfer resistances all play a role.

5.6.5 Mass-Transfer-Controlled Current Distributions

Mass-transfer-controlled distributions apply under the assumptions that Ohmic and kinetic resistances can be neglected.

5.7 Potential Contributions

The cell potential can be decomposed into contributions corresponding to different loss terms within the cell. For example, the difference in potential between two electrodes can be expressed as

$$(V_a - V_c) = (V_a - \Phi_{0,a}) + (\Phi_{0,a} - \Phi_{0,c}) + (\Phi_{0,c} - V_c) \tag{5.69}$$

where $\Phi_{0,a}$ represents the potential at the inner limit of the diffusion layer at the anode and $\Phi_{0,c}$ represents the potential at the inner limit of the diffusion layer at the cathode. The terms collected in the right-hand side of equation (5.69) are developed in terms of Ohmic and kinetic contributions in sections 5.7.1 and 5.7.2, respectively. This book employs a formalism that does not require use of the concentration overpotential. To place this approach into perspective with a commonly used approach, the concentration overpotential is discussed briefly in Section 5.7.3.

5.7.1 Ohmic Potential Drop

The term $(\Phi_{0,a} - \Phi_{0,c})$ represents the potential drop through the electrolyte. As defined here, the numerical evaluation of the potential drop requires accounting for the variation in electrolyte conductivity within the diffusion layer. An alternative approach is to define the Ohmic potential drop as being that calculated using Laplace's equation with a uniform solution conductivity. In this case, an additional term is required to account for the influence of the conductivity variation within the diffusion layer on the measured potential. This is incorporated into a concentration overpotential, discussed in Section 5.7.3.

5.7.2 Surface Overpotential

The term $(V_a - \Phi_{0,a})$ can be expressed in terms of the surface overpotential, noting that

$$\eta_{s,a} = (V_a - \Phi_{0,a}) - (V_a - \Phi_{0,a})_0 \tag{5.70}$$

where $(V_a - \Phi_{0,a})_0$ is the equilibrium difference between the electrode potential and the potential of the electrolyte adjacent to the electrode, generally taken to be at the inner limit of the diffusion layer. If the equilibrium potential is measured at the composition existing at the inner limit of the diffusion layer, $c_i(0)$, then

$$(V_a - V_c) = \eta_{s,a} + (V_a - \Phi_{0,a})_0 + (\Phi_{0,a} - \Phi_{0,c}) - \eta_{s,c} - (V_c - \Phi_{0,c})_0 \tag{5.71}$$

If, instead, the equilibrium potential is measured at the composition $c_i(\infty)$ of the bulk electrolyte, then an additional term is needed to account for influence of the diffusion layer on the measured potential. This is incorporated into a concentration overpotential, discussed in Section 5.7.3.

5.7.3 Concentration Overpotential

A concentration overpotential is often invoked to account for the influence of concentration distribution on potential. Consider for example, that the concentration at the inner limit of the diffusion layer is $c_{i,0}$. Consistent with equation (5.23), the current for a single anodic reaction can be expressed as

$$i = k_a nFc_i(0) \exp(b_a \eta_s) \tag{5.72}$$

Equation (5.72) can be written in terms of the bulk concentration as

$$i = k_a nFc_i(\infty) \frac{c_i(0)}{c_i(\infty)} \exp(b_a \eta_s) \tag{5.73}$$

or

$$i = k_a nFc_i(\infty) \exp(b_a(\eta_s + \eta_c)) \tag{5.74}$$

where

$$\eta_c = \frac{1}{b_a} \ln\left(\frac{c_i(0)}{c_i(\infty)}\right) \tag{5.75}$$

The concentration overpotential is not needed if the concentrations used in the kinetic expressions are those evaluated at the electrode surface.

5.8 Capacitance Contributions

In electrochemical systems, the capacitance may arise due to charge redistribution at interfaces or to dielectric phenomena. The charge redistribution takes place at an electrolytic double layer.

5.8.1 Double-Layer Capacitance

Away from solid surfaces, the electrolyte can be said to be electrically neutral, and, in the absence of concentration gradients, equation (5.62) is satisfied exactly. If

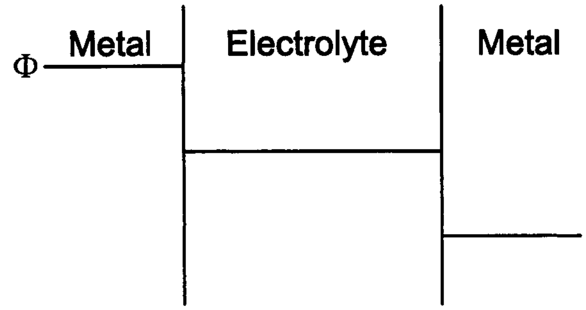

Figure 5.11: Potential distribution for a cell at open circuit consisting of ideally polarized electrodes.

concentration gradients exist for species of differing diffusion coefficients, equation (5.62) is satisfied approximately, but the charge is so small that equation (5.62) can be used. This can be seen from a rearrangement of Poisson's equation as

$$\sum_i z_i c_i = -\frac{\varepsilon\varepsilon_0}{F}\nabla^2\Phi \tag{5.76}$$

where ε is the dielectric constant of the medium and ε_0 is the permittivity of a vacuum ($\varepsilon_0 = 8.8542 \times 10^{-14}$ F/cm or 8.8542×10^{-14} C/V cm). The constant $\varepsilon\varepsilon_0/F$ is very small and typically has a value on the order of 10^{-16} equiv/V cm. Thus, for moderate values of $\nabla^2\Phi$, $\sum_i z_i c_i \approx 0$.

The situation is fundamentally different near an interface due to a significant redistribution of charge. Consider, for example, the potential distribution in an electrochemical cell at open circuit. Consider that a potential can be applied between the two metal electrodes such that no current flows. A situation like this is described in Section 5.1. The electrodes can be considered to be ideally polarized since a potential can be applied without passage of current.

The corresponding potential distribution is given in Figure 5.11. As no current flows in the cell, the potential must be uniform in the electrolytic solution. The only place where the potential can change in the cell is at the electrode–electrolyte interface. In this region, the second derivative of potential with respect to position $d^2\Phi/dy^2$ must be very large. Equation (5.76) suggests that a substantial redistribution of charge is required to accommodate the abrupt change in potential.

A redistribution of charge is possible because the electrons that accumulate near the metal surface have associated with them a charge. In addition, some ionic species may have a tendency to accumulate preferentially at the electrode–

Remember! 5.4 *The capacitance commonly encountered in electrochemical impedance spectroscopy may arise from charge redistribution at interfaces or from dielectric phenomena.*

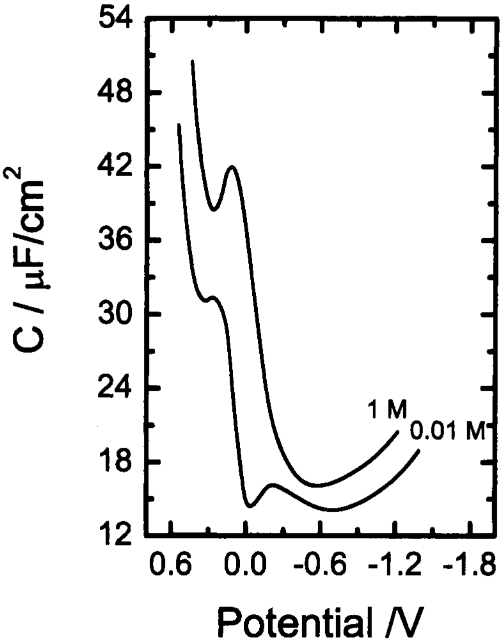

Figure 5.12: Double-layer capacitance obtained by Grahame[29] for a mercury electrode in contact with a NaCl electrolyte at a temperature of 25°C. Potentials are referenced to the electrocapillary maximum or potential of zero charge.

electrolyte interface. Finally, as the interface taken as a whole must be electrically neutral, a diffuse region of charge may be present in the electrolyte adjacent to the electrode.

Experimental measurements on mercury electrodes have contributed significantly to the understanding of the nature of the electrical double layer. The double-layer capacitance obtained by Grahame[29] for a mercury electrode in contact with a NaCl electrolyte at a temperature of 25°C is presented in Figure 5.12 where potentials are referenced to the electrocapillary maximum or potential of zero charge. The capacitance values range between 14 and 50 μF/cm^2 and are seen to be strong functions of potential. This range of values and dependence of potential is typical of the results reported by Grahame for mercury electrodes immersed in other electrolytes.[29]

Numerous models of the electrode–electrolyte interface have been developed. The simplest of these is the Helmholtz double-layer model, which posits that the charge associated with a discrete layer of ions balances the charge associated with electrons at the metal surface. The Helmholtz double-layer model predicts incorrectly that the interfacial capacitance is independent of potential. Nevertheless, current models of the charge redistribution at electrode–electrolyte interfaces owe their terminology to the original Helmholtz model.

A schematic representation of an electrical double layer is presented as Figure

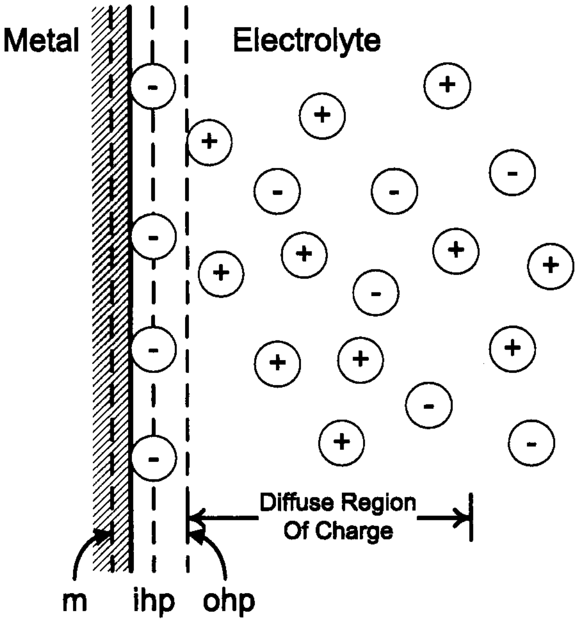

Figure 5.13: The structure of the electrical double layer.

5.13. A plane (m) is associated with an excess concentration of electrons near the physical surface of the electrode, represented by a solid line. The *inner Helmholtz plane* (ihp) is associated with ions that are specifically adsorbed onto the metal surface. The *outer Helmholtz plane* (ohp) is the plane of closest approach for solvated ions that are free to move within the electrolyte. The ions within the electrolyte near the electrode surface contribute to a *diffuse region of charge*. The diffuse region of charge has a characteristic Debye length,

$$\lambda = \sqrt{\frac{\varepsilon\varepsilon_0 RT}{F^2 \sum\limits_i z_i^2 c_i(\infty)}} \tag{5.77}$$

which is typically on the order of 10 Å for electrolytic solutions.

The charge held in each of the layers must cancel such that

$$q_{\mathrm{m}} + q_{\mathrm{ihp}} + q_{\mathrm{d}} = 0 \tag{5.78}$$

where q_m is the charge of electrons at the electrode surface, q_{ihp} is the charge associated with adsorbed ions, and q_d is the charge held in the diffuse region. There is no plane of charge associated with the outer Helmholtz plane as this represents only an inner limit to the diffuse region of charge.

The potential of the metal referenced to an electrode located outside the diffuse region of charge can be expressed as

$$U - \Phi_{\mathrm{ref}} = \left(U - \Phi_{\mathrm{ihp}}\right) + \left(\Phi_{\mathrm{ihp}} - \Phi_{\mathrm{ref}}\right) \tag{5.79}$$

Table 5.4: Typical ranges of values for capacitance.

System	ε	$\delta/\text{Å}$	$C/\mu\text{Fcm}^{-2}$
Double layer on bare metal	—	—	10–50
Al_2O_3 oxide[98]	6.7	120	0.5
Fe_2O_3 oxide[99]	7	30	2
Ni_2O_5 oxide	42	30	2
Asphalt coatings	2.6	5×10^{7}	5×10^{-7}
Epoxy cast resin	3.6	5×10^{6}	6×10^{-6}

The capacitance of the interface is defined to be the derivative of charge density with respect to electrode potential at fixed electrochemical potential μ_i and temperature T, i.e.,

$$C=\left(\frac{\partial q}{\partial U}\right)_{\mu_i,T} \tag{5.80}$$

Thus, following equation (5.79), the capacitance of the interface can be expressed in terms of respective contributions as

$$\frac{1}{C}=\frac{1}{C_{\text{m-ihp}}}+\frac{1}{C_{\text{d}}} \tag{5.81}$$

As seen in equation (5.81), the capacitance of an interface is dominated by the part with the smaller capacitance. For this reason, the capacitance of semiconductor electrodes can be expressed as consisting only of the capacitance of the space-charge region.

5.8.2 Dielectric Capacitance

The capacitance associated with oxide layers and polymeric coatings can be expressed as

$$C=\frac{\varepsilon\varepsilon_0}{\delta} \tag{5.82}$$

where δ is the film thickness, ε is the dielectric constant of the material, and ε_0 is the permittivity of vacuum $\varepsilon_0 = 8.8542\times10^{-14}$ F/cm. The capacitance of such oxide and polymeric layers is typically sufficiently small that the contribution of an electrolytic double layer in series can be generally neglected. Some typical values for capacitance are presented in Table 5.4.

Problems

5.1 Estimate the electrolyte resistance for a 0.25 cm radius disk electrode in 0.1 M NaCl solution at 25°C.

5.2 Use a Taylor's series expansion in terms of potential to obtain a relationship for the charge-transfer resistance in the Tafel regime.

5.3 Show that the concentration of a reactant at the surface of an electrode can be expressed as a function of current density as

$$\frac{c_i(0)}{c_i(\infty)} = 1 - \frac{i}{i_{\text{lim}}} \tag{5.83}$$

5.4 Following equation (5.83), use a spreadsheet program to plot the current density as a function of surface overpotential for $b_c = 20\ \text{V}^{-1}$ and i_{lim} equal to 0.1, 1.0, and 10 mA/cm^2.

5.5 Use a Taylor's series expansion about the equilibrium potential to obtain a relationship for the charge-transfer resistance in terms of the parameter $J = ni_0F/\kappa RT$.

5.6 Estimate the capacitance for an oxide layer on a steel surface that is 50 Å thick.

5.7 Estimate the surface area for an electrode in a 0.1 M NaCl solution if the capacitance is measured to be 120 μF. What might be a reasonable confidence interval for this estimate?

Electrochemical Impedance Spectroscopy
by Mark E. Orazem and Bernard Tribollet

Chapter 6

Electrochemical Instrumentation

Operational amplifiers provide the foundation for electrochemical instrumentation. The aim of this chapter is to describe the main properties of an operational amplifier so as to understand the principles of potentiostats and galvanostats and to understand how they can be used for impedance measurements.

6.1 The Ideal Operational Amplifier

For the purpose of this text, an operational amplifier consists of a series of solid-state components designed to have certain functional characteristics. A schematic representation of an operational amplifier, given in Figure 6.1(a), shows 5 leads attached to the operational amplifier. The vertical leads, marked V_{S+} and V_{S-}, provide power to the amplifier and are connected to a direct-current power supply. The two leads on the left, termed the noninverting (+) and the inverting (−) input, have potentials V_+ and V_-, respectively. The output potential is V_0.

The amplifier is designed to sense the difference between the voltage signals applied at its two input terminals, to multiply this by a number A_{op}, and to cause the output voltage to be

$$V_0 = A_{\text{op}}\left(V_+ - V_-\right) \tag{6.1}$$

A typical response for an operational amplifier is given in Figure 6.1(b). The output potential V_0 must have a value between V_{S+} and V_{S-}. For an ideal operational amplifier, the *open-loop gain* A_{op} is very large (ideally infinite), such that

$$V_+ - V_- = \frac{V_0}{A_{\text{op}}} \approx 0 \tag{6.2}$$

Remember! 6.1 *Operational amplifiers provide the foundation for electrochemical instrumentation.*

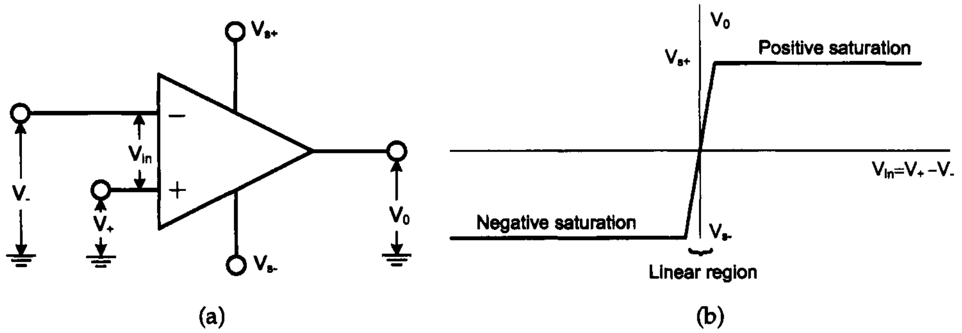

Figure 6.1: The ideal operational amplifier: a) the circuit symbol for an operational amplifier showing the five principal terminals and b) output potential as a function of input potential. The linear range for the output potential is very small.

The open-loop gain A_{op} for typical operational amplifiers is on the order of 10^4 to 10^6; thus, for supply voltages V_S of 10 to 15 V, the input voltage difference in the linear regime can be on the order of 1 mV and can be as small as a few μV.

The requirement for operation within the linear regime is that

$$|V_+ - V_-| < \left|\frac{V_S}{A_{\text{op}}}\right| \tag{6.3}$$

As A_{op} is very large, the linear region of operation is correspondingly very small.

The characteristics of an ideal operational amplifier are that:

- The constant A_{op} is very large such that the voltage difference $V_+ - V_- \approx 0$.
- The input impedances are very large such that the currents at the noninverting (+) and the inverting (-) inputs are equal to zero.
- The output potential at saturation is V_{S+} or V_{S-}.
- The output potential in the linear regime is given by equation (6.1).

The equations that govern the ideal operational amplifier are expressions of current balances. For the operational amplifier shown in Figure 6.1(a), the current balance is given as

$$i_+ + i_- + i_0 + i_{S+} + i_{S-} = 0 \tag{6.4}$$

As the input impedance is large, $i_+ = i_- = 0$, and

$$i_0 + i_{S+} + i_{S-} = 0 \tag{6.5}$$

To reduce clutter in circuit diagrams, it is common to omit the power terminals, for example, as shown in Figure 6.2. The presence of power terminals is nevertheless assumed.

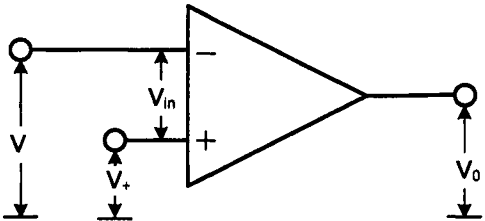

Figure 6.2: The circuit symbol for an operational amplifier showing input and output terminals, but omitting the power terminals. The presence of power terminals is nevertheless assumed.

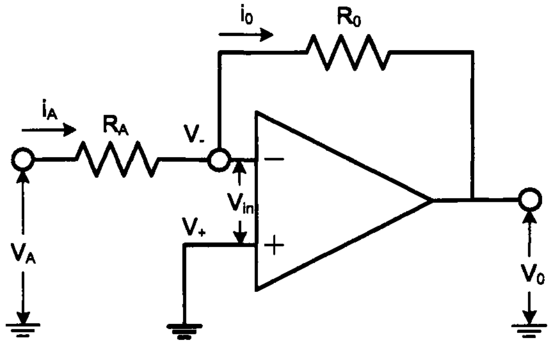

Figure 6.3: Negative feedback: inverting voltage amplifier.

6.2 Elements of Electrochemical Instrumentation

As shown in Figure 6.1(b), the output of the operational amplifier under open-loop conditions tends to be in the saturation region. Operation within the linear region is made possible by inclusion of feedback loops, leading to operational characteristics important for electrochemical instrumentation. This is termed *operation under closed-loop conditions*.

Example 6.1 Negative Feedback: *Find the electrical characteristics of an ideal operational amplifier with negative feedback, shown schematically in Figure 6.3.*

Solution: *Due to the fact that the input current is equal to zero, the currents flowing through R_A and R_0 are equal; $i = i_A = i_0$ and*

$$i = \frac{V_- - V_A}{R_A} = \frac{V_0 - V_-}{R_0} \tag{6.6}$$

V_- is equal to zero, due to the fact that the potential of the input + is at the ground. Thus,

$$V_0 = -\frac{R_0}{R_A} V_A \tag{6.7}$$

The output voltage has an opposite sign with respect to the input voltage V_A.

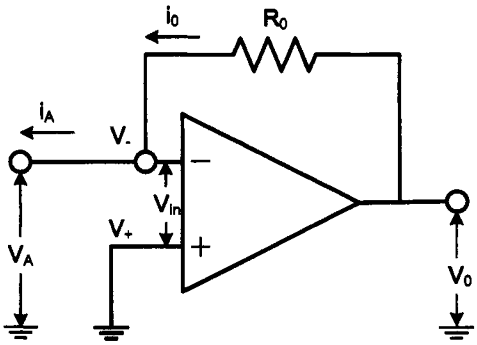

Figure 6.4: The current follower.

The quantity R_0/R_A is called the *closed-loop gain*. The requirement for operation within the linear regime for the inverting amplifier is that

$$|V_+ - V_-| < \left|\frac{V_S}{R_0/R_A}\right| \tag{6.8}$$

The effect of the feedback is to reduce the overall gain, to permit correspondingly larger input voltages without saturation, and to replace the open-loop gain with a gain that depends only on passive resistors. The open-loop gain of an operational amplifier depends strongly on temperature and varies from unit to unit. Thus, use of a feedback circuit improves control over the gain of an amplifier. The requirements are that the open-loop gain must be large as compared to the closed loop gain and equation (6.8) should be satisfied, i.e., the system must not be driven to saturation.

The output potential V_0 has the opposite sign as the input potential V_A. A noninverting amplifier is presented in Problem 6.3.

Example 6.2 Current Follower: *Find the operational characteristics of an ideal current follower, shown schematically in Figure 6.4.*

Solution: *This circuit is very similar to an inverting voltage amplifier without resistance R_A in the input line. The input point A is at a virtual ground potential, and V_o is proportional to the current; i.e., $V_o = R_o i$.*

Example 6.3 Voltage Adder: *Find the operational characteristics of an ideal voltage adder, shown schematically in Figure 6.5.*

Solution: *The example is given with the sum of two voltages, but obviously a larger number of potentials can be added following the same principle. The currents i_1 and i_2 are equal respectively to V_1/R_1 and V_2/R_2. Thus, the output voltage is given by*

$$V_o = -R_0(V_1/R_1 + V_2/R_2) \tag{6.9}$$

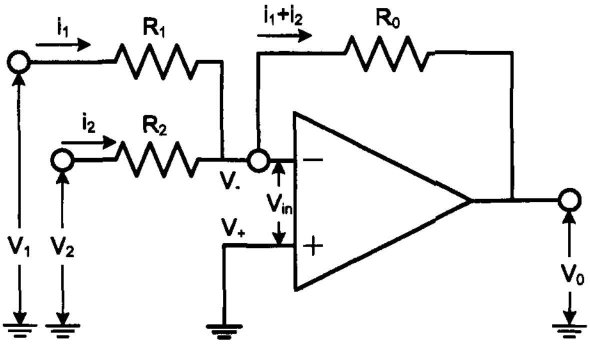

Figure 6.5: The voltage adder.

Different applications can be developed following the relative values of R_0, R_1, *and* R_2. *In particular, for* $R_0 = R_1 = R_2$, *the output takes the form*

$$V_o = -(V_1 + V_2) \tag{6.10}$$

6.3 Electrochemical Interface

Electrochemical interfaces consist of potentiostats and galvanostats. These devices can be described in terms of combinations of operational amplifiers and resistors.

6.3.1 Potentiostat

The aim of a potentiostat is to maintain a constant potential difference between the working electrode WE and a reference electrode REF. In the simplest scheme the reference electrode is connecting to the inverting input of the operational amplifier as shown in Figure 6.6(a). The potential of the working electrode is at ground potential, and the potential of the reference electrode is held at a potential V_{set}, also referenced to the ground potential. Thus, the potentiostat shown in Figure 6.6(a) controls the potential difference between the working and reference electrodes.

The potentiostat requires as well a means of measuring the current. One approach is to measure the potential difference across a resistance as shown in Figure 6.6(b). The current is given by $I = V_m/R_m$. In the second approach, the current is measured in the working electrode circuit by means of a current follower (Figure 6.6(c)). In this last case, the working electrode is not directly at the ground but at a virtual ground potential.

Remember! 6.2 *A basic potentiostat can consist of two operational amplifiers: one to control potential and one to follow current.*

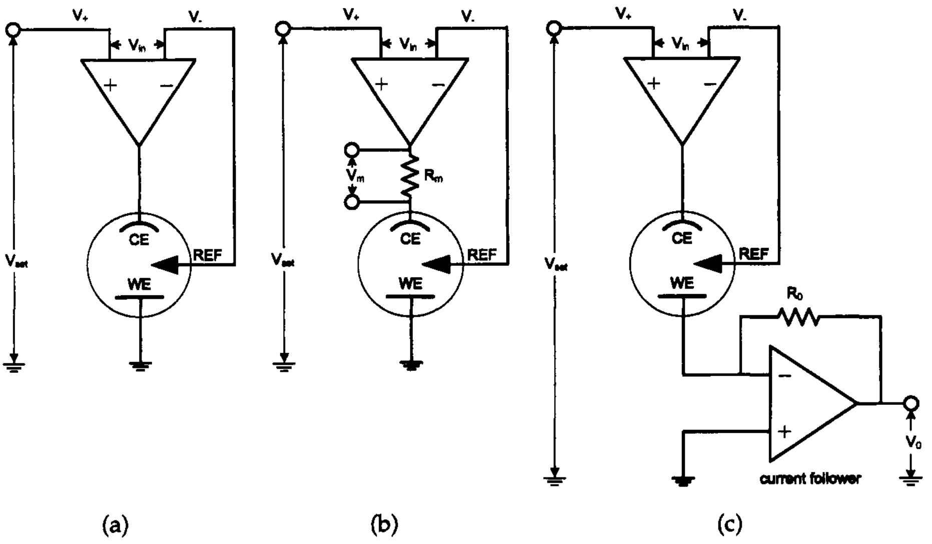

Figure 6.6: The potentiostat: a) simple scheme for controlling the potential of a working electrode with respect to a reference electrode, b) potentiostat with current measurement by potential drop across a measuring resistor, and c) potentiostat with current measurement by use of a current follower.

In each of the different configurations of Figure 6.6, the potential of the working electrode is controlled with respect to the reference electrode. The WE is at the ground, and the potential V between the + entry of the operational amplifier and the ground is the difference of potential between the reference electrode and the WE. There is no potential difference between the entry + and the entry −. The operational amplifier delivers the current through the counterelectrode to have the corresponding difference of potential between the reference electrode and the WE.

6.3.2 Galvanostat

A scheme of a galvanostat is given in Figure 6.7. The point A and then the working electrode is at a virtual ground potential. The current I is given by the relation $I = V/R$. The current value could be adjusted by varying either R or V. The potential can be easily measured between the reference electrode and the working electrode.

Remember! 6.3 *A basic potentiostat for impedance measurements requires a voltage adder to superimpose the sinusoidal signal onto an imposed potential.*

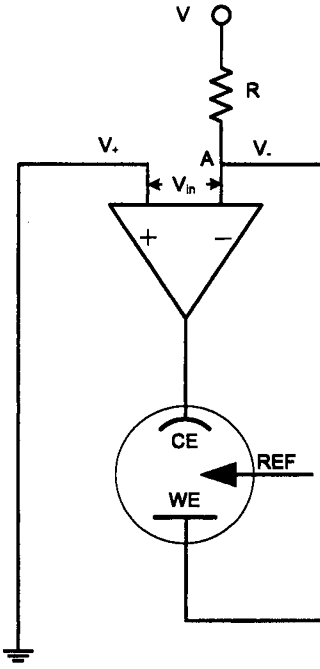

Figure 6.7: A simple scheme for controlling the current through a working electrode.

6.3.3 Potentiostat for EIS Measurement

Impedance measurements may be made under potentiostatic regulation by making the small modifications to the potentiostat shown as Figure 6.6(c). In the example given as Figure 6.8, a voltage adder is introduced to sum the dc potential corresponding to the polarization point and the ac potential delivered by the generator of the frequency function analyzer. With a judicious choice of R_0, R_1 , and R_2 in equation (6.9), it could be easy to have an ac input with a potential divided by 100 (e.g., $R_0 = R_1 = 100R_2$).

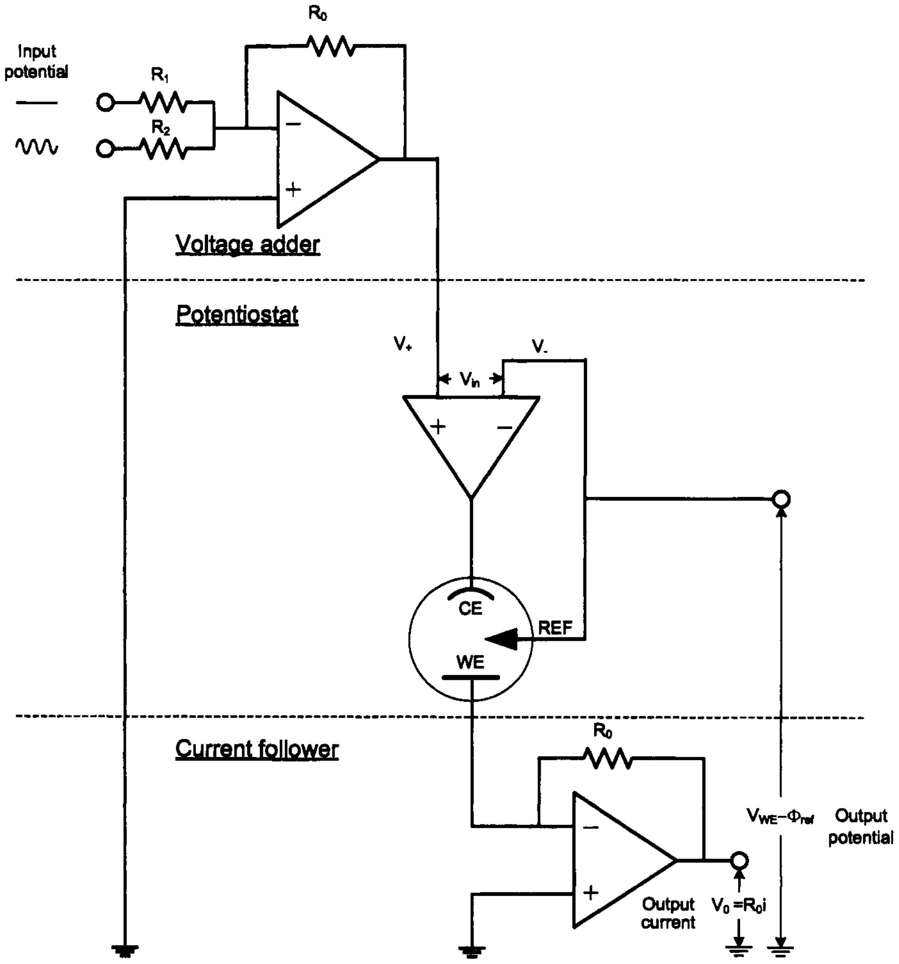

Figure 6.8: Potentiostat for EIS measurement.

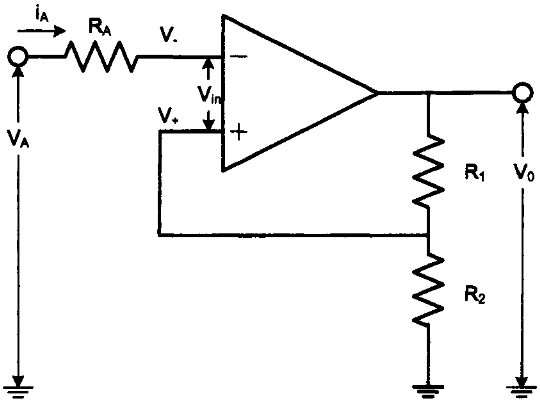

Figure 6.9: Schematic representation of a noninverting amplifier.

Problems

6.1 Devise a circuit for adding a steady baseline potential, a ramped potential, and a sinusoidal perturbation.

6.2 Estimate the maximum error in the term $V - \Phi_{\text{ref}}$ if the operational amplifiers used in Figure 6.8 had an open-loop gain of 10^5 and power source of ±10 V.

6.3 Show that the output potential for the noninverting amplifier shown in Figure 6.9 can be expressed as

$$V_0 = V_A \left(\frac{R_2}{R_1 + R_2} \right) \tag{6.11}$$

6.4 Devise a system similar to that shown in Figure 6.8 in which impedance measurements are performed under galvanostatic regulation.

Electrochemical Impedance Spectroscopy
by Mark E. Orazem and Bernard Tribollet

Part II

Experimental Considerations

Electrochemical Impedance Spectroscopy
by Mark E. Orazem and Bernard Tribollet

Chapter 7

Experimental Methods

Impedance experiments involve the conversion of time-domain input and output signals into a complex quantity that is a function of frequency. As seen in Figure 6.8, a signal generator is used to drive a potentiostat to induce a perturbed signal. The input signal and the resulting output signal is processed by instrumentation to yield a frequency-dependent transfer function. If the transfer function takes the form of a ratio of potential over current, the transfer function is called an *impedance*. The nature of the instrumentation used to generate the transfer function is described in the following section.

7.1 Steady-State Polarization Curves

Steady-state polarization curves, such as that presented in Figure 5.4(a), provide a means of identifying such important electrochemical parameters as exchange current densities, Tafel slopes, and diffusion coefficients. The influence of exchange current density and Tafel slopes on the steady-state current density can be seen in equations (5.17) and (5.18), and the influence of mass transfer and diffusivities on the current density is described in Section 5.3.3. Steady-state measurements, however, cannot provide information on the RC time constants of the electrochemical process. Such properties must be identified by using transient measurements.

7.2 Transient Response to a Potential Step

A calculated transient current response to a 10 mV step in potential, introduced at time t_0, is presented in Figure 7.1 for the electrical circuit inserted in the figure. The time constants for the circuit under the conditions of the simulation were $\tau_1 = 0.0021$ s (76 Hz) and $\tau_2 = 0.02$ s (8 Hz). The potential dependence of parameter R_1 is consistent with the behavior of the charge-transfer resistance described in Chapter 10.

The calculated current increases instantaneously and then decreases rapidly. On the linear scale presented in Figure 7.1, it is evident that precise current mea-

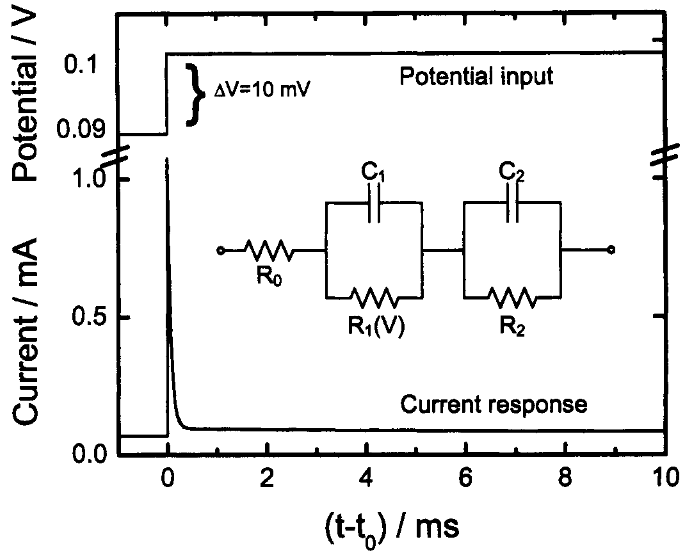

Figure 7.1: The current response of an electrochemical system to a 10 mV step change in applied potential from 0.09 V to 0.1 V for the inserted electrical circuit with parameters $R_0 = 1\ \Omega$, $R_1 = 10^{4-V/0.060}\ \Omega$, $C_1 = 10\ \mu\mathrm{F}$, $R_2 = 10^3\ \Omega$, and $C_2 = 20\ \mu\mathrm{F}$. The potential dependence of parameter R_1 is consistent with the behavior of the charge-transfer resistance described in Chapter 10.

surement is needed to observe the features associated with the *RC* elements in Figure 7.1. Presentation in a logarithmic format, as shown in Figure 7.2, allows a clearer representation of the distinct features of the circuit presented in Figure 7.1. The dashed lines show the deconvolution of the current response into the components presented in Figure 7.1. The results presented in Figures 7.1 and 7.2 demonstrate that use of step-transient experiments for identification of the phenomena that govern an electrochemical system requires accurate measurements of current in a very short period of time.

Frequency-domain measurements provide an attractive alternative to transient techniques involving steps in potential or current because their capability to make repeated measurements at a single frequency improves the signal-to-noise ratio and extends the range of characteristic frequencies sampled. These measurements are a type of transient measurement in which the input signal is cyclic.

7.3 Analysis in Frequency Domain

Fourier analysis and *phase-sensitive detection* are commonly used to convert time-domain signals into the frequency domain. For contextual purposes, the mathematical transformations used by Fourier analysis and phase-sensitive detection instruments are reviewed in the following subsections. Such systems have replaced the Lissajous analysis described in Section 7.3.1. The Lissajous analysis is useful,

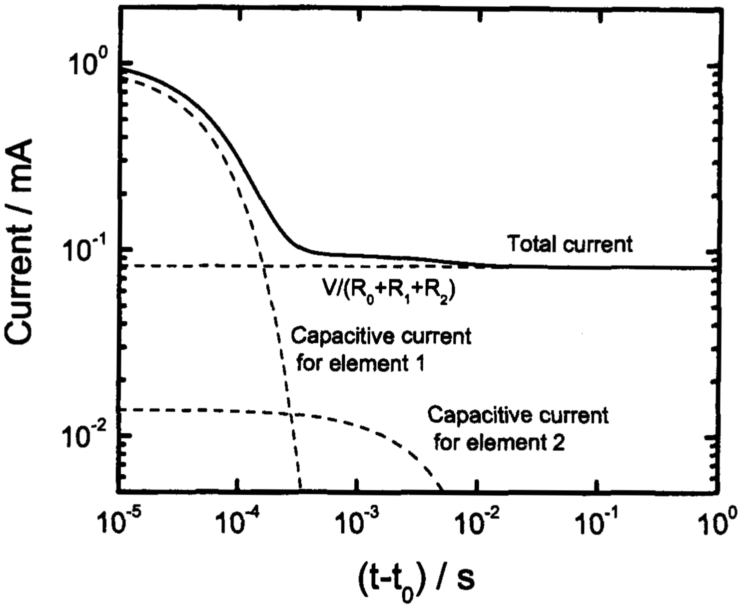

Figure 7.2: The current response in a logarithmic scale of an electrochemical system to a 10 mV step change in applied potential from 0.09 V to 0.1 V applied to the circuit presented in Figure 7.1. The dashed lines show the deconvolution of the current response into components associated with the different circuit elements.

however, for providing real-time assessment of the quality of impedance measurements and for developing an appreciation for impedance measurements.

7.3.1 Lissajous Analysis

The electronics associated with measurement of the impedance response of a system is presented schematically in Figure 6.8. The input signal can be represented by

$$V = \overline{V} + \Delta V \cos(2\pi f t) \tag{7.1}$$

where $\overline{V}$ is an applied bias potential and ΔV is the amplitude of the sinusoidal perturbation. The current response is dependent on the characteristics of the system under study. For example, following the discussion in Section 5.3.2, the Faradaic current density can be expressed as

$$i_f = nFk_a \exp(b_a V) - nFk_c \exp(-b_c V) \tag{7.2}$$

The current density associated with the capacitive charging of the electrode can be expressed as

$$i_C = -C_{\mathrm{dl}} \frac{dV}{dt} = 2\pi f \Delta V C_{\mathrm{dl}} \sin(2\pi f t) \tag{7.3}$$

where the sign accounts for the difference in the direction of the potential difference between that used for the Faradaic and charging currents. As suggested in

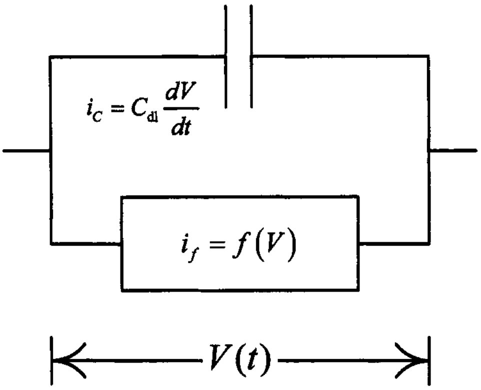

Figure 7.3: Schematic representation of an electrode interface demonstrating the contribution of charging and Faradaic current densities.

Figure 7.3, the total current density is the sum of the Faradaic and charging contributions.

The simulation results presented in this section were obtained by solution of equations (7.1)–(7.3) with parameters $C_{dl} = 31\ \mu\text{F/cm}^2$, $nFk_a = 0.5\ \text{mA/cm}^2$, $nFk_c = 0.5\ \text{mA/cm}^2$, $b_a = 19.5\ \text{V}^{-1}$, $b_c = 19.5\ \text{V}^{-1}$, $\overline{V} = 0$ V, and $\Delta V = 1$ mV. The value of the charge-transfer resistance, given by

$$R_t = \frac{1}{\left(b_a nFk_a \exp(b_a\overline{V}) + b_c nFk_c \exp(-b_c\overline{V})\right)} \tag{7.4}$$

had a value of 51.28 Ωcm^2, yielding a characteristic frequency $f_c = (2\pi R_t C_{dl})^{-1} =$ 100 Hz. The current response to the input potential is presented for different applied frequencies in Figure 7.4 as functions of time where the solid line represents the potential input and the dashed line represents the resulting current density. The signals presented in Figure 7.4 were scaled by the amplitude of the perturbation.

At frequencies much below the characteristic frequency, i.e., 1 mHz, the current density is in phase with the potential perturbation, as shown in Figure 7.4(a). At the characteristic frequency, Figure 7.4(b), the current signal lags the potential input by 45°. At the characteristic frequency, the amplitude of the out-of-phase charging current is equal to the amplitude of the in-phase Faradaic current for a linear system. As shown in Figure 7.4(c), the current response lags the potential input by 90° at frequencies much higher than the characteristic frequency.

The phase behavior of the input and output signals is seen more clearly in a Lissajous plot in which the output signal is plotted as a function of the input signal. A Lissajous representation of the signals presented in Figure 7.4 is given in Figure 7.5 with frequency as a parameter. The signals were normalized by the perturbation amplitude such that the values for current and potential ranged between ±1. At low frequencies, e.g., 1 mHz, the current density is in phase with the potential perturbation, yielding a straight line in Figure 7.5. At large frequencies, e.g., 10 kHz,

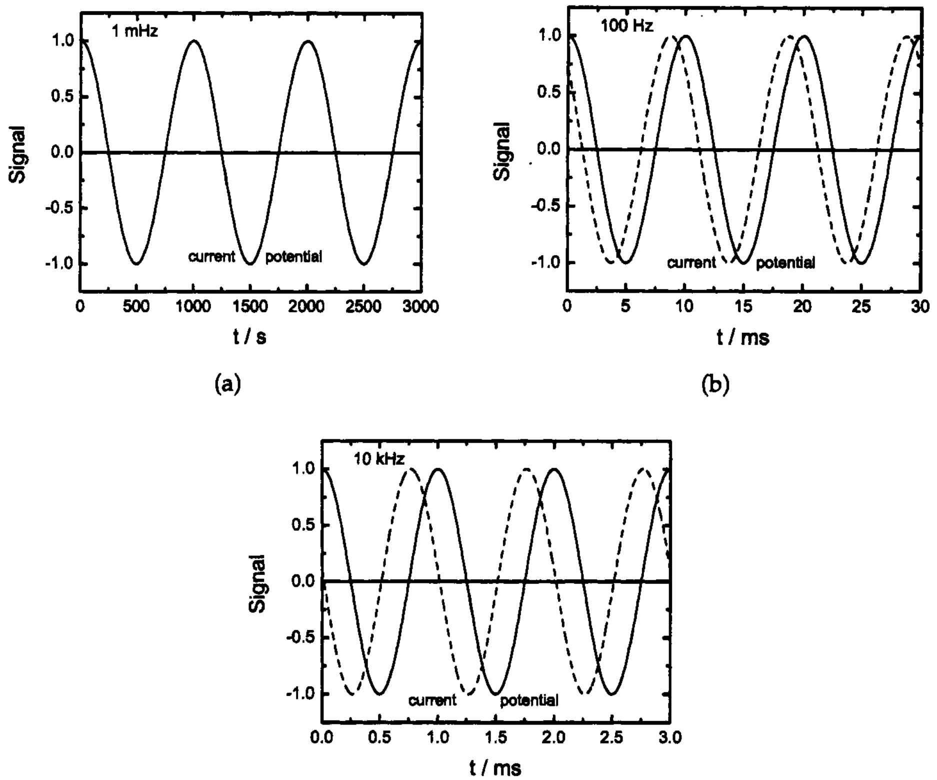

(a) (b)

(c)

Figure 7.4: The current density response to a sinusoidal potential input for a system with parameters $C_{dl} = 31\ \mu F/cm^2$, $nFk_a = nFk_c = 0.5\ mA/cm^2$, $b_a = 19.5\ V^{-1}$, $b_c = 19.5\ V^{-1}$, $\overline{V} = 0$ V, and $\Delta V = 1$ mV: a) 1 mHz; b) 100 Hz; and c) 10 kHz. The solid line represents the potential input and the dashed line represents the resulting current density.

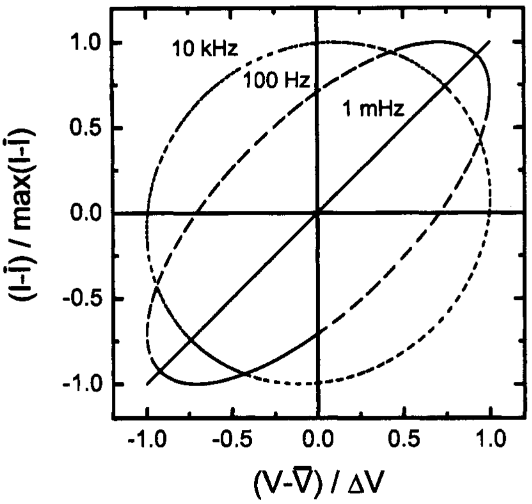

Figure 7.5: Lissajous representation of the signals presented in Figure 7.4 with frequency as a parameter. The signals were normalized by the perturbation amplitude such that the values for current and potential ranged between ±1.

the current is dominated by the charging current, which is out of phase with the potential. The resulting Lissajous trace appears as a circle in Figure 7.5 where both the potential and current values were normalized. At the characteristic frequency (100 Hz), the Lissajous plot takes the shape of an ellipse.

The magnitude of the time-domain signals and the shape of the ellipse provide information concerning the magnitude of the transfer function and the corresponding phase angle between input and output signals. The method for extracting the impedance response from the Lissajous plot is illustrated using the labeled positions given in Figure 7.6. The frequency is given by the time required to complete a cycle, t_{cycle}, i.e.,

$$\frac{1}{t_{\text{cycle}}} = f \tag{7.5}$$

where f has units of Hz. In frequency domain, the ratio of the potential over the current takes the form of an impedance. The magnitude of the impedance transfer function is therefore obtained by

$$|Z| = \frac{\Delta V}{\Delta I} = \frac{OA}{OB} = \frac{\Delta Y}{\Delta X} \tag{7.6}$$

The phase angle is obtained from

$$\sin(\phi) = -\frac{OD}{OA} \tag{7.7}$$

or

$$\phi = \sin^{-1}\left(-\frac{OD}{OA}\right) \tag{7.8}$$

where the lengths OD, OA, and OB are defined in Figure 7.6.

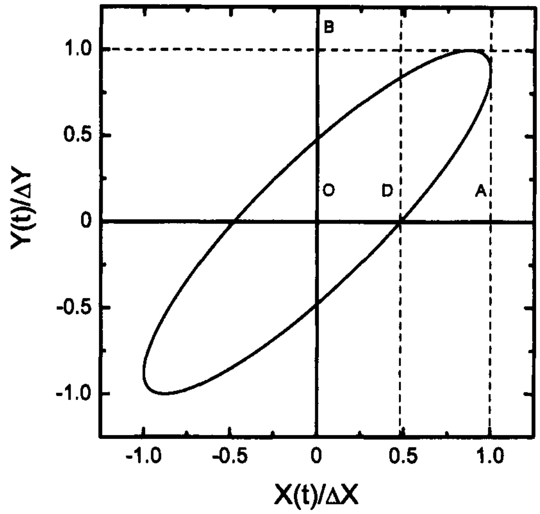

Figure 7.6: The interpretation of a Lissajous plot of time-domain signals in terms of impedance.

Example 7.1 Lissajous Analysis: *Use a Lissajous plot to find the impedance at a frequency of 100 Hz for a linear system with capacity* $C_{\mathrm{dl}} = 31\ \mu F/cm^2$*, charge-transfer resistance* $R_t = 51.34\ \Omega cm^2$*, and a potential perturbation* $\Delta V = 0.01$ *V.*

Solution: *The time required for a single cycle is* $T = 1/100$ *Hz = 0.01 s. The potential over this period of time is given by*

$$V = \Delta V \cos(2\pi f t) \tag{7.9}$$

The Faradaic current density for a linear system can be expressed as

$$i_f = \frac{V}{R_t} \tag{7.10}$$

and the current density associated with the capacitive charging of the electrode can be expressed by equation (7.3). The results are presented in Figure 7.7. The magnitude of the impedance can be found as

$$|Z| = \frac{10\ \mathrm{mV}}{0.275\ \mathrm{mAcm}^2} = 36.4\ \Omega\mathrm{cm}^2 \tag{7.11}$$

and the phase angle is given by

$$\phi = \sin^{-1}\left(-\frac{7.07}{10}\right) = -45° \tag{7.12}$$

The results presented in Figure 7.7 correspond to the characteristic frequency for the given values of capacitance and charge-transfer resistance of 100 Hz. At this frequency, the phase angle is equal to 45°.

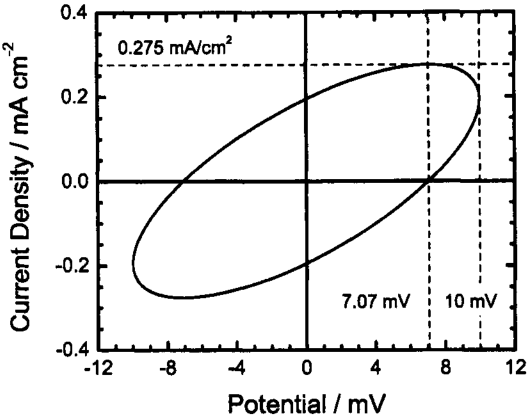

Figure 7.7: The interpretation of a Lissajous plot of time-domain signals in terms of impedance for Example 7.1.

As illustrated in Section 21.2.2, Lissajous plots can be used to explain the mechanism whereby the frequency-domain analysis yields transfer functions with extremely large signal-to-noise ratios, even when the time-domain signals contain a significant level of noise. By measuring the signals over many cycles, the resolution of the ellipse improves by an averaging process, thereby yielding a small stochastic error in the calculated transfer function.

The Lissajous plots presented in Figure 7.5 correspond to the interfacial impedance of a system and do not account for Ohmic resistance. This is the reason that the current-potential trace appears as a circle at high frequencies. In fact, the current corresponding to charging the interfacial capacitance is proportional to frequency, as expressed by equation (7.3). The influence of the Ohmic resistance is to limit the magnitude of the charging current at high frequencies. The resulting Lissajous plots are given in Figure 7.8 for a system with an Ohmic resistance $R_e = 10\ \Omega\text{cm}^2$, effective charge-transfer resistance $R_t = 26\ \Omega\text{cm}^2$, and capacitance $C_{\text{dl}} = 20\ \mu\text{F/cm}^2$. The input potential perturbation ΔV was 10 mV, yielding a value of $b_a \Delta V = 0.19$ and conforming to a linear response following the criteria developed in Example 8.1. The characteristic frequency for this system was 302 Hz. The Lissajous plot reveals a straight line at low frequency where the current and potential signals are in phase and a straight line again at high frequencies where the current and potential signals are again in phase. The slopes of these lines differ at high and low frequencies because, at low frequencies, the effective resistance is given by $R_e + R_t$, whereas at high frequencies the effective resistance is given by R_e. Comparison of Figures 7.5 and 7.8 illustrates the manner in which the Ohmic resistance obscures the behavior of the interfacial processes at high frequencies. This concept motivates the use of the Ohmic-resistance-corrected Bode plots discussed in Section 17.1.2.

It is useful to include in the experimental setup an oscilloscope capable of dis-

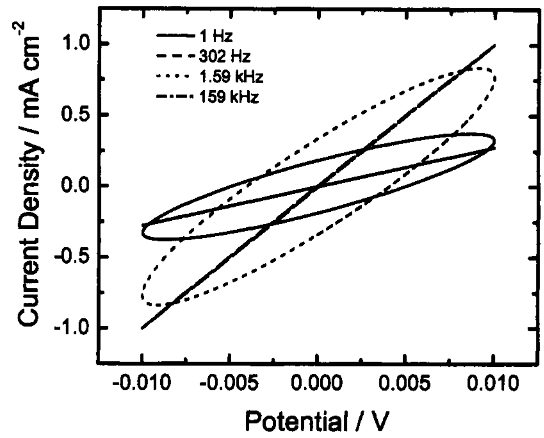

Figure 7.8: Lissajous representation for time-domain signals corresponding to a system with an Ohmic resistance $R_e = 10\ \Omega\text{cm}^2$, exchange current density $nFk_a = nFk_c = 1$ mA/cm^2, $b_a = 19\ \text{V}^{-1}$, $b_c = 19\ \text{V}^{-1}$, $\overline{V} = 0$ V, $\Delta V = 10$ mV, and capacitance $C_{\text{dl}} = 20\ \mu\text{F/cm}^2$. The effective charge-transfer resistance was equal to $R_t = 26\ \Omega\text{cm}^2$, and the characteristic frequency for this system was 302 Hz.

playing a Lissajous plot. As discussed in Chapter 8, distortions of the elliptical shape can be used to signal nonlinear behavior associated with an input perturbation that is too large. Scatter in the results reveals that the time-domain data may be excessively noisy, reflecting perhaps the need to adjust the instrumental parameters.

7.3.2 Phase-Sensitive Detection (Lock-in Amplifier)

A lock-in amplifier uses phase-sensitive detection, in conjunction with a potentiostat, to measure the complex impedance. The algorithm is fundamentally different from that of the Fourier-based analyzers. These analyzers perform an assessment of the Fourier coefficients of the input and output signals, whereas the lock-in amplifier measures the amplitudes of the two signals and the phase angle of each signal with respect to some reference signal. Thus, the impedance is measured in polar, rather than Cartesian, coordinates.

A reference square wave of unity amplitude is generated at the same frequency as the sinusoidal signal

$$X = \Delta X \sin(\omega t + \phi_X) \tag{7.13}$$

Remember! 7.1 *While use of Lissajous plots for numerical evaluation of impedance can be considered obsolete, it is useful to include an oscilloscope capable of displaying a Lissajous plot in the experimental setup.*

---

to be analyzed. The square wave can be represented by the Fourier series

$$S = \frac{4}{\pi}\sum_{n=0}^{\infty}\frac{1}{2n+1}\sin\left[(2n+1)\,\omega t + \phi_S\right] \tag{7.14}$$

where ϕ_S is the phase angle of the reference signal. The measured and reference signals are multiplied, resulting in

$$XS = \frac{4\Delta X}{\pi}\sum_{n=0}^{\infty}\frac{1}{2n+1}\sin\left(\omega t + \phi_X\right)\sin\left[(2n+1)\,\omega t + \phi_S\right] \tag{7.15}$$

Equation (7.15) can be rewritten, using trigonometric identities, as

$$\begin{aligned} XS \; = \; & \sum_{n=0}^{\infty}\frac{2\Delta X}{(2n+1)\,\pi}\left\{\cos\left[-2n\omega + \phi_X - (2n+1)\,\phi_S\right]\right. \\ & \left. - \cos\left[(2n+2)\,\omega t + \phi_X + (2n+1)\,\phi_S\right]\right\} \end{aligned} \tag{7.16}$$

The product of the signals can be expanded using the trigonometric identity for the cosine of the sum of two angles and integrated over each cycle. Only the leading term of the series has a nonzero value, thus,

$$\frac{\omega}{2\pi}\int_0^{2\pi/\omega} XSdt = \frac{2\Delta X}{\pi}\cos\left(\phi_X - \phi_S\right) \tag{7.17}$$

The integral in equation (7.17) has a maximum value when the phase angle of the square wave is equal to the phase angle of the measured signal. In practice, the phase angle of the generated square wave is adjusted such that the integral is maximized. The phase angle of the square wave at the maximum value of the integral yields the phase angle of the measured signal. In addition, the maximum value of the integral can be used to determine the amplitude of the measured signal.

The same procedure is used to analyze the second signal

$$Y = \Delta Y \sin(\omega t + \phi_Y) \tag{7.18}$$

yielding

$$\frac{\omega}{2\pi}\int_0^{2\pi/\omega} YSdt = \frac{2\Delta Y}{\pi}\cos\left(\phi_Y - \phi_S\right) \tag{7.19}$$

The phase angle of the generated square wave is adjusted such that the integral is maximized. The phase angle of the square wave at the maximum value of the integral yields the phase angle of the measured signal, and the maximum value of the integral is used to determine the amplitude of the measured signal.

The magnitude of the impedance can be obtained from the ratio of the amplitudes, i.e.,

$$|Z| = \frac{\Delta Y}{\Delta X} \tag{7.20}$$

and the corresponding phase angle can be obtained as the difference between the phase angles of the output and input signals, i.e.,

$$\phi = (\phi_Y - \phi_S) - (\phi_X - \phi_S) \tag{7.21}$$

Carson et al.[100] showed that phase-sensitive detection measurements with a single reference signal biases the error structure of the impedance data due to errors introduced when the square-wave reference signal is in phase with the measured signal. Modern phase-sensitive detection instruments employ more than one reference signal and may thereby avoid this undesired correlation.

7.3.3 Single-Frequency Fourier Analysis

Single-frequency Fourier analyzers make use of the orthogonality of sines and cosines to determine the complex impedance representing the ratio of the response to a single-frequency input signal. A brief outline of the approach is presented in this section.

Consider that a periodic function of time can be expressed as a Fourier series, e.g.,[74,101]

$$f(t) = a_0 + \sum_{n=1}^{\infty} \left(a_n \cos(n\omega t) + b_n \sin(n\omega t)\right) \tag{7.22}$$

The trigonometric functions can be expressed in terms of exponentials following equations (1.82) and (1.83) to yield

$$f(t) = \tilde{c}_0 + \sum_{n=1}^{\infty} \left(\tilde{c}_n \exp(jn\omega t) + \tilde{c}_{-n} \exp(-jn\omega t)\right) \tag{7.23}$$

where the coefficients $\tilde{c}_n$ are complex numbers, related to the coefficients a_n and b_n of equation (7.22) by

$$\tilde{c}_n = \frac{a_n - jb_n}{2} \tag{7.24}$$

or

$$\tilde{c}_n = \frac{a_n - jb_n}{2} \tag{7.25}$$

$$\tilde{c}_{-n} = \frac{a_n + jb_n}{2} \tag{7.26}$$

and

$$\tilde{c}_0 = a_0 \tag{7.27}$$

Equation (7.23) can be written in more compact form as

$$f(t) = \sum_{n=-\infty}^{\infty} \tilde{c}_n \exp(jn\omega t) \tag{7.28}$$

where n may take values ranging from $-\infty$ to $+\infty$, and the coefficients $\widetilde{c}_n$ can be evaluated from

$$\widetilde{c}_n = \frac{1}{T}\int_0^T f(t)\exp\left(-jn\omega t\right)dt \tag{7.29}$$

where T represents the period of an integer number of cycles at frequency ω. Using equation (1.109), Equation (7.29) can be expressed in terms of trigonometric functions as

$$\widetilde{c}_n = \frac{1}{T}\int_0^T f(t)\left(\cos\left(n\omega t\right) - j\sin\left(n\omega t\right)\right)dt \tag{7.30}$$

Equation (7.30) provides the basis for single-frequency Fourier analysis for impedance measurement.

Linear sinusoidal input and output signals can be expressed in terms of equation (7.22) with $n = 1$. For example, for an input potential

$$V(t) = \Delta V\cos\left(\omega t\right) \tag{7.31}$$

the output current can be expressed by

$$I(t) = \Delta I\cos\left(\omega t + \phi_I\right) \tag{7.32}$$

or

$$I(t) = a_1\cos\left(\omega t\right) + b_1\sin\left(\omega t\right) \tag{7.33}$$

The constant coefficients ΔI and ΔV represent the amplitudes of the respective signals and the parameter ϕ_I represents the phase lag of the current signal with reference to the input potential signal.

The mapping of the time-domain signals (7.32) and (7.31) to the frequency domain is done via a Fourier complex representation.[2–4] For signals expressed in terms of a cosine, the in-phase or real part of the current signal can be expressed as

$$I_r\left(\omega\right) = \frac{1}{T}\int_0^T I(t)\cos(\omega t)dt \tag{7.34}$$

and the imaginary part of the current signal is

$$I_j\left(\omega\right) = -\frac{1}{T}\int_0^T I(t)\sin(\omega t)dt \tag{7.35}$$

The real part of the voltage signal is

$$V_r\left(\omega\right) = \frac{1}{T}\int_0^T V(t)\cos(\omega t)dt \tag{7.36}$$

and the imaginary part of the voltage signal is

$$V_j(\omega) = -\frac{1}{T}\int_0^T V(t)\sin(\omega t)dt \tag{7.37}$$

The integration converts the time-domain quantities into the respective frequency-domain quantities. Integration is carried out over a period T comprising an integer number of cycles. This serves to filter errors in the measurement. The complex current $I_r + jI_j$ and potential $V_r + jV_j$ are the coefficients $\widetilde{c}_1$ of the Fourier series expressed as equation (7.30).

The impedance is calculated as the complex ratio of the complex representations of the output signal to the input signal. Thus,

$$Z_r(\omega) = \mathrm{Re}\left\{\frac{V_r + jV_j}{I_r + jI_j}\right\} \tag{7.38}$$

and

$$Z_j(\omega) = \mathrm{Im}\left\{\frac{V_r + jV_j}{I_r + jI_j}\right\} \tag{7.39}$$

The real and imaginary parts of the impedance are thereby extracted from the same ratio of complex numbers.

Example 7.2 Fourier Analysis: *Apply the Fourier analysis to the calculations presented in Section 7.3.1.*

Solution: *For the calculations presented in Section 7.3.1 where potential is the input signal with a phase lag $\phi_V = 0$, equation (7.36) yields $V_r = \Delta V/2$ and equation (7.37) yields $V_j = 0$. The impedance response obtained by Fourier analysis is given in Figure 7.9. Because the perturbation magnitude was sufficiently small, the results are in good agreement with the expected value for the given kinetic parameters. The zero-frequency asymptotic value for the real impedance is in excellent agreement with the value of 51.28 Ωcm^2 obtained from equation (7.4).*

7.3.4 Multiple-Frequency Fourier Analysis

Impedance transfer functions may be determined through use of an input signal containing more than a single frequency. Such signals may be a tailored multi-sine

---

Remember! 7.2 *The input and output signals used to generate impedance spectra are functions of time, not frequency. The frequency dependence of the impedance results from the processing of time-domain signals.*

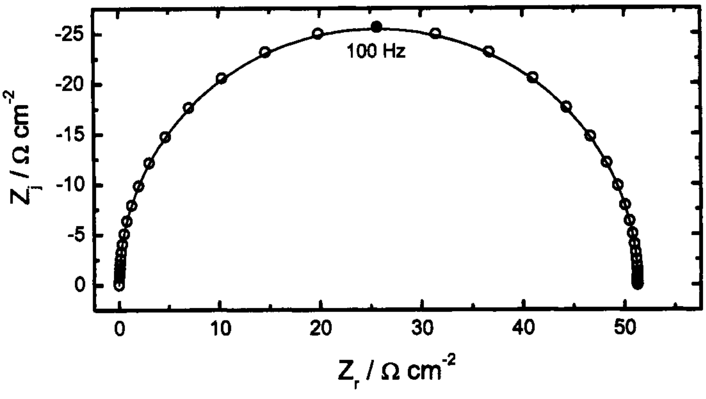

Figure 7.9: The impedance response obtained by Fourier analysis for the calculations presented in Section 7.3.1 (symbols) as compared to the theoretical value (solid line).

signal or a signal containing white noise. If the signal amplitude is sufficiently small that the response is linear, the system output response will also be a signal containing the same frequencies as found in the input signal. A fast Fourier transform algorithm may be used to extract the frequency-dependent transfer function. Because all frequencies are measured at the same time, the multifrequency approach allows completion of a spectrum in a shorter time than is required for a stepped single-frequency approach.

7.4 Comparison of Measurement Techniques

Each of the frequency-response analysis methods described in the previous section has its place in the experimental arsenal. Their relative merits are summarized in the following sections.

7.4.1 Lissajous Analysis

Lissajous analysis, as an experimental approach for impedance measurement, is obsolete and has been replaced by methods using automated instrumentation. Lissajous plots, however, have great pedagogical value as a means of learning impedance spectroscopy. In addition, as discussed in Section 8.2, use of oscilloscopes is recommended for monitoring the progress of impedance measurements, and oscilloscopes capable of displaying Lissajous plots are particularly useful.

7.4.2 Phase-Sensitive Detection (Lock-in Amplifier)

Phase-sensitive detection is accurate and can be relatively inexpensive. Modern instrumentation uses more than one reference signal and can mitigate the bias in the error structure.

7.4.3 Single-Frequency Fourier Analysis

Sequential measurement of impedance by Fourier analysis provides good accuracy for stationary systems. The sequence of frequencies can be arbitrarily selected, and therefore frequency intervals of $\Delta f/f$, considered to be the most economical use of frequencies, can be employed. Because the measurements at each frequency are independent of each other, frequencies found to be inconsistent with the Kramers-Kronig relations can be deleted.

7.4.4 Multiple-Frequency Fourier Analysis

Multifrequency fast Fourier analysis yields good accuracy for stationary systems and has the advantage that it can be performed more rapidly than an equivalent single-sine measurement. Frequency intervals of Δf and dense sampling at high frequency are required to get good resolution at low frequency. The spectra obtained are always consistent with the Kramers-Kronig relations, so the Kramers-Kronig relations cannot be used to determine whether the measurement was corrupted by instrument artifacts or nonstationary behavior. A correlation coefficient can be calculated and used to determine whether the spectrum is inconsistent with the Kramers-Kronig relations.

7.5 Specialized Techniques

The methods described in this chapter and this book apply to electrochemical impedance spectroscopy. Impedance spectroscopy should be viewed as being a specialized case of a transfer-function analysis. The principles apply to a wide variety of frequency-domain measurements, including non-electrochemical measurements. The application to generalized transfer-function methods is described briefly with an introduction to other sections of the text where these methods are described in greater detail. Local impedance spectroscopy, a relatively new and powerful electrochemical approach, is described in detail.

7.5.1 Transfer Function Analysis

While the emphasis of this book is on electrochemical impedance spectroscopy, the methods described in Section 7.3 for converting time-domain signals to frequency-domain transfer functions clearly are general and can be applied to any type of input and output. Some generalized transfer-function approaches are described in Chapters 14 and 15.

Remember! 7.3 *The techniques described here for measuring impedance spectra are, in fact, very general and can be used to measure any transfer function.*

Table 7.1: Generalized transfer functions for a rotating disk electrode at fixed temperature.

Fixed Variable	Input	Output	Transfer Function
Rotation speed	Current	Potential	Impedance
Rotation speed	Potential	Current	Admittance
Current	Rotation speed	Potential	Electrohydrodynamic impedance
Potential	Rotation speed	Current	Electrohydrodynamic impedance

Four state variables may be defined, for example, for the rotating disk described in Chapter 11. These may include the rotation speed, the temperature, the current, and the potential. At a fixed temperature, three variables remain from which a transfer function may be calculated. As shown in Table 7.1, the generalized transfer functions include impedance, admittance (see Chapter 16), and two types of electrohydrodynamic impedance (see Chapter 15).

7.5.2 Local Electrochemical Impedance Spectroscopy

Local impedance measurements represent another form of generalized transfer-function analysis. In these experiments, a small probe is placed near the electrode surface. The probe uses either two small electrodes or a vibrating wire to allow measurement of potential at two positions. Under the assumption that the electrolyte conductivity between the two points of potential measurement is uniform, the current density at the probe can be estimated from the measured potential difference ΔV_{probe} by

$$i_{\text{probe}} = \Delta V_{\text{probe}} \frac{\kappa}{d} \tag{7.40}$$

where d is the distance between the potential sensing probes and κ is the conductivity of the electrolyte.

A schematic representation of the electrode–electrolyte interface is given as Figure 7.10, where the block used to represent the local Ohmic impedance reflects the complex character of the Ohmic contribution to the local impedance response. The impedance definitions presented in Table 7.2 were proposed by Huang et al.[102] for local impedance variables. These differ in the potential and current used to calculate the impedance. To avoid confusion with local impedance values, the symbol y is used to designate the axial position in cylindrical coordinates.

Remember! 7.4 *Local Electrochemical Impedance Spectroscopy (LEIS) is a relatively new and underutilized technique that is useful for exploring the influence of surface heterogeneities on the impedance response.*

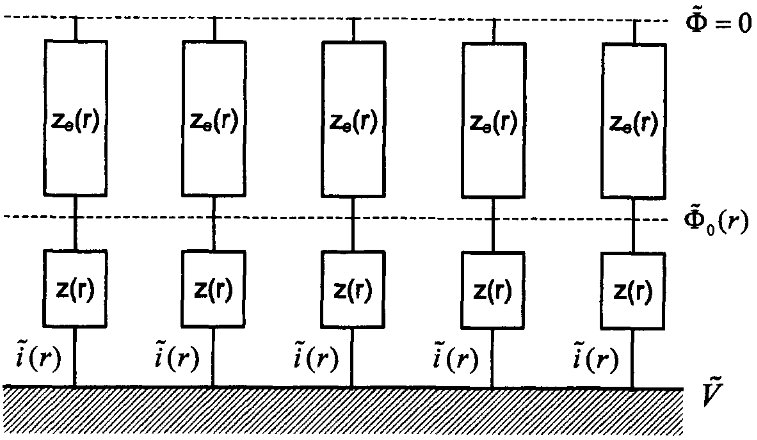

Figure 7.10: The location of current and potential terms that make up definitions of global and local impedance.

Table 7.2: Definitions and notation for local impedance variables.

Symbol	Meaning	Units
Z	Global impedance (equation (7.41))	Ω or Ωcm^2
Z_r	Real part of global impedance	Ω or Ωcm^2
Z_j	Imaginary part of global impedance	Ω or Ωcm^2
Z_0	Global interfacial impedance (equation (7.48))	Ω or Ωcm^2
$Z_{0,r}$	Real part of global interfacial impedance	Ω or Ωcm^2
$Z_{0,j}$	Imaginary part of global interfacial impedance	Ω or Ωcm^2
Z_e	Global Ohmic impedance (equation (7.50))	Ω or Ωcm^2
$Z_{e,r}$	Real part of global Ohmic impedance	Ω or Ωcm^2
$Z_{e,j}$	Imaginary part of global Ohmic impedance	Ω or Ωcm^2
z	Local impedance (equation (7.43))	Ωcm^2
z_r	Real part of local impedance	Ωcm^2
z_j	Imaginary part of local impedance	Ωcm^2
z_0	Local interfacial impedance (equation (7.45))	Ωcm^2
$z_{0,r}$	Real part of local interfacial impedance	Ωcm^2
$z_{0,j}$	Imaginary part of local interfacial impedance	Ωcm^2
z_e	Local Ohmic impedance (equation (7.46))	Ωcm^2
$z_{e,r}$	Real part of local Ohmic impedance	Ωcm^2
$z_{e,j}$	Imaginary part of local Ohmic impedance	Ωcm^2
$\langle\Phi\rangle$	Spatial average of potential	V
$\overline{\Phi}$	Time average or steady-state value of potential	V
$\langle i\rangle$	Spatial average of current density	A/cm^2
$\bar{i}$	Time average or steady-state value of current density	A/cm^2
y	Axial position variable	cm

Global Impedance

The *global impedance* is defined to be

$$Z = \frac{\widetilde{V}}{\widetilde{I}} \tag{7.41}$$

where the complex current contribution for a disk electrode is given by

$$\widetilde{I} = \int_0^{r_0} \widetilde{i}(r) 2\pi r dr \tag{7.42}$$

The use of an uppercase letter signifies that Z is a global value. The global impedance may have real and imaginary values designated as Z_r and Z_j, respectively. The total current could also be represented by $\widetilde{I} = \pi r_0^2 < \widetilde{i}(r) >$ where the brackets signify the area-average of the current density.

Local Impedance

The term *local impedance* traditionally involves the potential of the electrode measured relative to a reference electrode far from the electrode surface.[68,103] Thus, the local impedance is given by

$$z = \frac{\widetilde{V}}{\widetilde{i}(r)} \tag{7.43}$$

The use of a lowercase letter signifies that z is a local value. The local impedance may have real and imaginary values designated as z_r and z_j, respectively.

The global impedance can be expressed in terms of the local impedance as

$$Z = \left\langle \frac{1}{z} \right\rangle^{-1} \tag{7.44}$$

Equation (7.44) is consistent with the treatment of Brug et al.[104] in which the admittance of the disk electrode was obtained by integration of a local admittance over the area of the disk.

Local Interfacial Impedance

The *local interfacial impedance* involves the potential of the electrode measured relative to a reference electrode $\Phi_0(r)$ located at the outer limit of the diffuse double layer. Thus, the local interfacial impedance is given by

$$z_0 = \frac{\widetilde{V} - \widetilde{\Phi}_0(r)}{\widetilde{i}(r)} \tag{7.45}$$

The use of a lowercase letter again signifies that z_0 is a local value, and the subscript 0 signifies that z_0 represents a value associated only with the surface. The local interfacial impedance may have real and imaginary values designated as $z_{0,r}$ and $z_{0,j}$, respectively.

Local Ohmic Impedance

The *local Ohmic impedance* involves the potential of a reference electrode $\Phi_0(r)$ located at the outer limit of the diffuse double layer and the potential of a reference electrode located far from the electrode $\widetilde{\Phi}(\infty) = 0$; see Figure 7.10. Thus, the local Ohmic impedance is given by

$$z_e = \frac{\widetilde{\Phi}_0(r)}{\widetilde{i}(r)} \tag{7.46}$$

The use of a lowercase letter again signifies that z_e is a local value, and the subscript e signifies that z_e represents a value associated only with the Ohmic character of the electrolyte. The local Ohmic impedance may have real and imaginary values designated as $z_{e,r}$ and $z_{e,j}$, respectively. The local impedance

$$z = z_0 + z_e \tag{7.47}$$

can be represented by the sum of local interfacial and local Ohmic impedances.

The representation of an Ohmic impedance as a complex number represents a departure from standard practice. As will be shown in subsequent sections, the local impedance has inductive features that are not seen in the local interfacial impedance. As the calculations assumed an ideally polarized blocking electrode, the result is not influenced by Faradaic reactions and can be attributed only to the Ohmic contribution of the electrolyte.

Global Interfacial Impedance

The *global interfacial impedance* is defined to be

$$Z_0 = 2\pi \left(\int_0^{r_0} \frac{1}{z_0(r)} r dr \right)^{-1} \tag{7.48}$$

or

$$Z_0 = \left\langle \frac{1}{z_0(r)} \right\rangle^{-1} \tag{7.49}$$

The use of an uppercase letter signifies that Z_0 is a global value. The global interfacial impedance may have real and imaginary values designated as $Z_{0,r}$ and $Z_{0,j}$, respectively.

Global Ohmic Impedance

The *global Ohmic impedance* is defined to be

$$Z_e = Z - Z_0 \tag{7.50}$$

The use of an uppercase letter signifies that Z is a global value. As will be shown in subsequent sections, the global Ohmic impedance has a complex behavior in a midfrequency range near $K = 1$ (see equation (13.47)). The global Ohmic impedance may have real and imaginary values designated as $Z_{e,r}$ and $Z_{e,j}$, respectively.

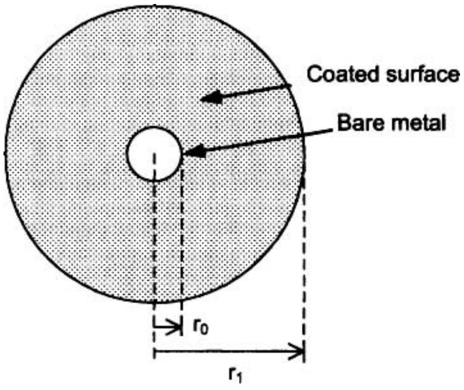

Figure 7.11: Schematic representation of a disk electrode corresponding to Problem 7.5 with bare metal exposed from the origin to a radius r_0 and coated metal surface from radius r_0 to r_1.

Problems

The following problems require use of a spreadsheet program such as Microsoft Excel® or a computational programming environment such as Matlab®.

7.1 Reproduce the results presented in Figures 7.4 and 7.5.

7.2 Use a Lissajous plot to calculate the phase angle and magnitude of the impedance for the system described in Example 7.1 at frequencies of 1 Hz and 10 kHz. This approach requires calculating the potential perturbation, the charging current, and the Faradaic current as functions of time.

7.3 Calculate the ratio of the amplitude of the charging current to the amplitude of the Faradaic current for the system described in Example 7.1 at frequencies of 1 Hz, 100 Hz, and 10 kHz.

7.4 Use a Fourier analysis to calculate the impedance as a function of frequency for the system described in Example 7.1. Compare your results to the theoretical value obtained using the methods described in Chapter 4.

7.5 Consider the disk electrode shown in Figure 7.11 with bare metal exposed from the origin to a radius r_0 and coated metal surface from radius r_0 to r_1. Estimate the global interfacial impedance response of this electrode for the following geometries if the coating consists of an organic material of 100 μm thickness and the charge-transfer resistance on the bare metal is 100 Ωcm^2. Hint: Guidelines for estimation of capacitance are given in Table 5.4.

(a) $r_0 = 0.25$ cm and $r_1 = 1.0$ cm.
(b) $r_0 = 0.5$ cm and $r_1 = 1.0$ cm.
(c) $r_0 = 0.75$ cm and $r_1 = 1.0$ cm.

7.6 Develop an expression for the error in the global interfacial impedance response of the bare metal referenced in Problem 7.5 as a function of the relative area of the coated metal r_1^2/r_0^2 and the coating property ε/δ.

Electrochemical Impedance Spectroscopy
by Mark E. Orazem and Bernard Tribollet

Chapter 8

Experimental Design

Impedance measurements are often used to identify physical phenomena that control an electrochemical reaction and to determine the corresponding physical properties. This chapter provides guidelines for the design of experimental cells, for selection of appropriate impedance parameters, and for selection of appropriate instrument controls.

8.1 Cell Design

Proper cell design is essential to reduce the uncertainty of the interpretation. Reference electrodes can be used to isolate the impedance of cell components, well-defined convective systems can be employed to quantify the role of mass transfer, and electrode configurations can be selected to minimize the role of current and potential distributions across the surface of the electrodes.

8.1.1 Reference Electrodes

As discussed in Section 5.7, the potential drop across an electrochemical cell can be expressed as the sum of contributions

$$V_{\mathrm{WE}} - V_{\mathrm{CE}} = (V_{\mathrm{WE}} - \Phi_{0,\mathrm{WE}}) + (\Phi_{0,\mathrm{WE}} - \Phi_{0,\mathrm{CE}}) - (V_{\mathrm{CE}} - \Phi_{0,\mathrm{CE}}) \tag{8.1}$$

Reference electrodes are used to isolate influence of electrodes and membranes. Some typical cell configurations are shown schematically in Figure 8.1. In the two-electrode configuration represented in Figure 8.1(a), the impedance

$$Z_{\mathrm{cell}} = \frac{\widetilde{V}_{\mathrm{WE}} - \widetilde{V}_{\mathrm{CE}}}{\widetilde{I}} \tag{8.2}$$

Remember! 8.1 *Reference electrodes can be used to isolate the impedance of cell components.*

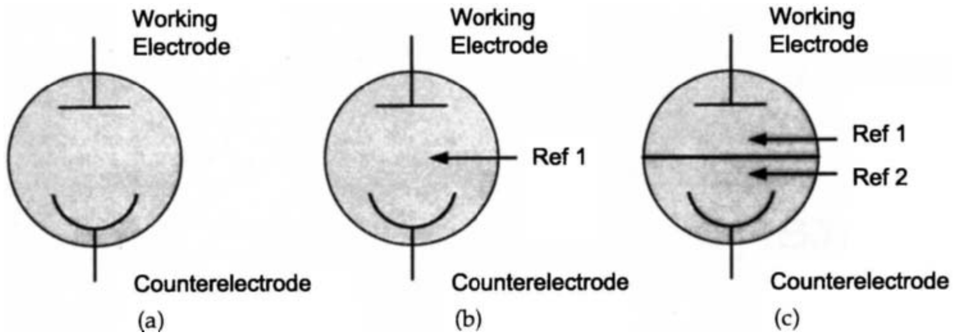

Figure 8.1: Schematic illustration of cell configurations employing reference electrodes to isolate the impedance response of working electrodes and membranes. a) 2-electrode; b) 3-electrode; and c) 4-electrode cell design.

includes the impedance response associated with the working electrode interface, the counterelectrode interface, and the electrolyte between the working and the counterelectrodes. The three-electrode configuration shown in Figure 8.1(b) allows measurement of three impedances; i.e., equation (8.2),

$$Z_{\mathrm{WE}} = \frac{\widetilde{V}_{\mathrm{WE}} - \widetilde{\Phi}_{ref}}{\widetilde{I}} \tag{8.3}$$

at the working electrode interface and

$$Z_{\mathrm{CE}} = \frac{\widetilde{V}_{\mathrm{CE}} - \widetilde{\Phi}_{ref}}{\widetilde{I}} \tag{8.4}$$

at the counterelectrode interface. The impedance measurements are related by

$$Z_{\mathrm{cell}} = Z_{\mathrm{WE}} + Z_{\mathrm{CE}} \tag{8.5}$$

Thus, only two of the impedance measurements are independent. For systems containing a membrane separating the working and counterelectrodes, it is useful to use a four-electrode configuration as shown in Figure 8.1(c). The impedance of the membrane can be obtained as

$$Z_{1,2} = \frac{\widetilde{\Phi}_{\mathrm{ref},2} - \widetilde{\Phi}_{ref,1}}{\widetilde{I}} \tag{8.6}$$

The impedance measurements are related by

$$Z_{\mathrm{cell}} = Z_{\mathrm{WE},1} + Z_{\mathrm{CE},2} + Z_{1,2} \tag{8.7}$$

where $Z_{\mathrm{WE},1}$ is the impedance of the working electrode measured with reference Ref1 and $Z_{\mathrm{CE},2}$ is the impedance of the counterelectrode measured with reference Ref2. Only three of the impedance measurements are independent.

8.1.2 Flow Configurations

Use of well-defined convective systems allows the influence of mass transfer to be treated explicitly and quantitatively; thus the interpretation of impedance data in terms of interfacial processes can be emphasized. Several experimental systems are commonly employed.

Rotating Disk

The rotating disk electrode, described in Section 11.6, has the advantage that the fluid flow is well defined and that the system is compact and simple to use. The rotation of the disk imposes a centrifugal flow that in turn causes a radially uniform flow toward the disk. If the reaction on the disk is mass-transfer controlled, the associated current density is uniform, which greatly simplifies the mathematical description. As discussed in sections 5.6.1 and 8.1.3, the current distribution below the mass-transfer-limited current is not uniform. The distribution of current and potential associated with the disk geometry has been demonstrated to cause a frequency dispersion in impedance results. The rotating disk is therefore ideally suited for experiments in which the disk rotation speed is modulated while under the mass-transfer limited condition. Such experiments yield another type of impedance known as the *electrohydrodynamic impedance*, discussed in Chapter 15.

Disk under Submerged Impinging Jet

The disk subjected to a submerged impinging jet, described in Section 11.7, has, under certain geometric constraints, the same attributes as the rotating disk with the exceptions that the electrode is stationary and the experimental system requires a pump and a flow loop. For electrodes that are within the stagnation region of the impinging flow, the flow is well-defined and has been modeled. The flow to the electrode surface is radially uniform; thus, at the mass-transfer-limited condition, the current density is uniform. The geometry induces a current and potential distribution that is similar to that observed for the rotating disk.

Rotating Cylinders

Rotating cylinders, described in Section 11.8, are popular experimental systems because the system setup is relatively simple to use and, at moderate rotation speeds, the flow is turbulent and yields a uniform mass-transfer-controlled current density. Empirical correlations are available that relate the cylinder rotation speed to the mass-transfer coefficient.[105]

Rotating Hemispherical Electrode

The rotating hemispherical electrode, introduced by Chin,[106] has a uniform primary current distribution and would therefore be a suitable configuration for experiments conducted under conditions such that the current distribution is not influenced by the nonuniform accessibility to mass transfer. Nisancioglu and Newman[107] showed that the current distribution in the rotating hemispherical electrode is uniform so long as the average current density has a value smaller than 68 percent of the average mass-transfer-limited value. A refined mathematical model for the convective-diffusion impedance of a rotating hemispherical electrode, developed by Barcia et al.,[108] provided an excellent match to experimental impedance measurements conducted under these conditions.

While a disk electrode under a submerged impinging jet has flow characteristics that resemble those of a rotating disk electrode, the flow experienced by a hemispherical electrode under jet impingement differs greatly from that of a rotating hemisphere. Shukla and Orazem showed through calculations and experiments that boundary-layer separation is observed at an colatitude angle of 54.8 degrees.[109,110] A subsequent analysis of the current distribution below the mass-transfer-limited current indicated that the current distribution on the stationary hemispherical electrode under submerged jet impingement should be uniform so long as the average current density was less than 25 percent of the mass-transfer-limited value.[111] The appearance of boundary-layer separation suggests that the hemispherical electrode under jet impingement is not an appropriate system for electrochemical studies.

8.1.3 Current Distribution

The distribution of impedance along the surface of an electrode greatly complicates the interpretation of the resulting spectra. Such an impedance distribution may result from a variation of surface properties caused, for example, by differences of grain orientation in a polycrystalline material, residual stresses associated with fabrication, or nonuniform distributions of surface films. A distribution of impedance may also be attributed to the current and potential distributions associated with the electrode geometry.

The uncertainty associated with the interpretation of the impedance response can be reduced by using an electrode for which the current and potential distribution is uniform. There are two types of distributions that can be used to guide electrode design. As described in Section 5.6.1, the primary distribution accounts for the influence of Ohmic resistance and mass-transfer-limited distributions account for the role of convective diffusion. The secondary distributions account for the role of kinetic resistance which tends to reduce the nonuniformity seen for a primary distribution. Thus, if the primary distribution is uniform, the secondary

---

Remember! 8.2 *Impedance measurements are sensitive to nonuniform surface reactivity, which may be caused by surface heterogeneities, nonuniform mass transfer, or geometry-induced current and potential distributions.*

Table 8.1: Current distribution characteristics for different electrode designs.

System	Primary Distribution	Mass-Transfer-Controlled Distribution
Rotating disk	Not uniform	Uniform
Disk under submerged impinging jet	Not uniform	Uniform
Partial rotating cylinder	Not uniform	Uniform
Complete rotating cylinder	Uniform	Uniform
Rotating hemisphere	Uniform	Not uniform
Hemisphere under Submerged Jet	Uniform	Not uniform

current distributions will also be uniform. The guidelines illustrated in equation (5.64) and Figure 5.9 can be used to assess the uniformity of current on different electrode geometries. The results are given in Table 8.1. As discussed in Section 13.3, the frequency dispersion associated with a nonuniform primary or secondary current distribution for elementary reactions is not evident at frequencies below a critical value. Thus, the influence of geometry-induced nonuniform current and potential distributions can be avoided by designing experiments for frequencies below the critical value. Figure 13.7 provides a convenient guide for selecting a disk electrode size that will avoid the frequency dispersion effects associated with the geometry-induced current and potential distributions.

8.2 Experimental Considerations

The experimental design parameters described in this section are influenced by the system under investigation, the objective of the investigation, and the capabilities of the instrumentation. The objective is to maximize the information content of the measurement while minimizing bias and stochastic errors.

8.2.1 Frequency Range

The objective of impedance measurements is typically to capture the frequency response of the system under study. To that end, the measured frequency range should include frequencies sufficiently large and frequencies sufficiently small to reach asymptotic limits in which the imaginary impedance tends toward zero. In some cases, for example, blocking electrodes, the low-frequency asymptotic behavior does not exist. In other cases, a true dc limit is not achievable due to nonstation-

---

Remember! 8.3 *Impedance measurements entail a compromise balance between minimizing bias errors, minimizing stochastic errors, and maximizing the information content of the resulting spectrum. The optimal instrument settings and experimental parameters are not universal and must be selected for each system under study.*

---

ary behavior of the system. Instrument artifacts may limit the performance at high frequency. While experimentalists often routinely base the frequency range on the limits of the instrument, it is important to choose a frequency range that meets the dynamic response of the system under study. The considerations described in Section 13.3 may also constrain the frequency range.

8.2.2 Linearity

As discussed in Section 5.3.2, linearity in electrochemical systems is controlled by potential. The use of a low-amplitude perturbation allows application of a linear model for interpretation of spectra. The correct amplitude represents a compromise between the desire to minimize nonlinear response (by using a small amplitude) and the desire to minimize noise in the impedance response (by using a large amplitude). The amplitude depends on the system under investigation. For systems exhibiting a linear current–voltage curve, a very large amplitude can be used. For systems exhibiting very nonlinear current–voltage curves, a much smaller amplitude is needed.[112–114]

Example 8.1 Guideline for Linearity: *We wish to establish a guideline for the perturbation amplitude needed to maintain linearity under potentiostatic regulation. An electrochemical system that follows a Tafel law is polarized at a potential $\overline{V}$. If a large potential sinusoidal modulation is superimposed, write the current response in the form of a Taylor series and calculate the complete expression of the dc current. By considering only the first three terms of the Taylor series, write the expression of the current under the form of the first three harmonics.*

Solution: *For a system that follows Tafel behavior, the current density response to a potential perturbation*

$$V(t) = \overline{V} + \Delta V \cos(\omega t) \tag{8.8}$$

is given by

$$i(t) = K \exp(bV(t)) \tag{8.9}$$

Thus,

$$i(t) = K \exp\left(b(\overline{V} + \Delta V \cos \omega t)\right) \tag{8.10}$$

or

$$i(t) = i_0 \exp(b \Delta V \cos \omega t) \tag{8.11}$$

Remember! 8.4 *The optimal perturbation amplitude depends on the polarization curve for the system under study.*

---

where

$$i_0 = K\exp(b\overline{V}) \tag{8.12}$$

A Taylor series expansion yields

$$\begin{aligned} i(t) &= i_0\Bigg(1 + b\Delta V\cos\omega t + \frac{b^2\Delta V^2\cos^2\omega t}{2!} + \frac{b^3\Delta V^3\cos^3\omega t}{3!} + \\ &\quad \ldots + \frac{b^n\Delta V^n\cos^n\omega t}{n!} + \ldots\Bigg) \end{aligned} \tag{8.13}$$

The mean value of the current $i(t)$ is, for T equal to an integer number of cycles,

$$\bar{i}(t) = \frac{1}{T}\int_0^T i(t)dt \tag{8.14}$$

By taking into account the formula

$$\int \cos^n x dx = \frac{1}{n}\cos^{n-1}x\sin x + \frac{n-1}{n}\int \cos^{n-2}x dx \tag{8.15}$$

and observing that $\sin T = 0$,

$$\int_0^T \cos^n x dx = \frac{n-1}{n}\int_0^T \cos^{n-2}x dx \tag{8.16}$$

If n is an even number,

$$\int_0^T \cos^n x dx = \frac{n-1}{n}\frac{n-3}{n-2}\cdots\frac{1}{2}T \tag{8.17}$$

and if n is an odd number, the value of the integral is equal to zero. Thus, the mean value of $i(t)$ is

$$\bar{i}(t) = i_0\left(1 + \sum_{n=1}^{\infty}\frac{b^{2n}\Delta V^{2n}}{(2^n n!)^2}\right) \tag{8.18}$$

To have a variation of the dc current lower than 1 percent, ΔV must be lower than $0.2/b$.

Evaluation of the harmonics of the nonlinear current response can be achieved by introduction of the trigonometric expressions

$$\cos 2x = 2\cos^2 x - 1 \tag{8.19}$$

and

$$\cos 3x = 4\cos^3 x - 3\cos x \tag{8.20}$$

By considering only the first three terms of the Taylor series, $i(t)$ becomes

$$\begin{aligned} i(t) = i_0\Bigg(&\left(1 + \frac{b^2\Delta V^2}{4}\right) + \left(b\Delta V + \frac{3b^3\Delta V^3}{24}\right)\cos(\omega t) \\ &+ \frac{b^2\Delta V^2}{4}\cos(2\omega t) + \frac{b^3\Delta V^3}{24}\cos(3\omega t)\Bigg) \end{aligned} \tag{8.21}$$

The limitation to the first three terms of the Taylor series gives for the mean value only the first term of the series (see equation (8.18)).

Equation (8.21) shows that the dc current is given by

$$i_0\left(1+\frac{b^2\Delta V^2}{4}\right) \tag{8.22}$$

and the first harmonic or fundamental is given by

$$i_0\left(b\Delta V+\frac{3b^3\Delta V^3}{24}\right) \tag{8.23}$$

For ΔV smaller than $0.2/b$, the variation of the dc current is smaller than 1 percent and the variation of the fundamental is smaller than 0.22 percent.

Example 8.1 demonstrates that application of a large-amplitude potential perturbation to a nonlinear system results in harmonics that appear at frequencies corresponding to multiples of the fundamental or applied frequency. A second result of Example 8.1 is the observation that application of a large-amplitude potential perturbation to a nonlinear system changes both the steady-state current density and the fundamental current response. The implication of this result is that the impedance response will also be distorted by application of a large-amplitude potential perturbation.

The influence of large potential perturbations on the impedance response can be illustrated by an extension of the analysis presented in Section 7.3 for large-amplitude perturbations. The current density response to a 40 mV-amplitude ($b_a\Delta V = 0.78$) sinusoidal potential input is presented in Figure 8.2 for the system presented in Section 7.3 with parameters $C_{\text{dl}} = 31\ \mu\text{F/cm}^2$, $nFk_a = nFk_c = 0.14\ \text{mA/cm}^2$, $b_a = 19.5\ \text{V}^{-1}$, $b_c = 19.5\ \text{V}^{-1}$, and $\overline{V} = 0.1$ V. Following equation (7.4), these parameters yield a value of charge-transfer resistance $R_t = 51.28\ \Omega\text{cm}^2$ and a characteristic frequency of 100 Hz. The potential and current signals were scaled by the maximum value of the signal.

The current response associated with a 1 mHz 40 mV potential perturbation is given in Figure 8.2(a). The indication that the response is nonlinear is given by the observation that the current density is not symmetric about zero, whereas the current response to a 1 mHz 1 mV potential perturbation, given in Figure 7.4(a), is symmetric about zero. A similar indication is evident at 10 Hz (Figure 8.2(b)). At the characteristic frequency of 100 Hz, a shift in the phase lag is apparent, as seen in Figure 8.2(c). The shape of the current signal is clearly distorted as compared to the results presented in Figure 7.4(b) for a 100 Hz 1 mV potential perturbation. At frequencies much higher than the characteristic frequency, however, the linear charging current dominates over the nonlinear Faradaic current, and the resulting current response shows a linear behavior as seen in Figure 8.2(d) for a 10 kHz 40 mV potential perturbation. These results resemble closely the results presented in Figure 7.4(c) for a 10 kHz 1 mV potential perturbation.

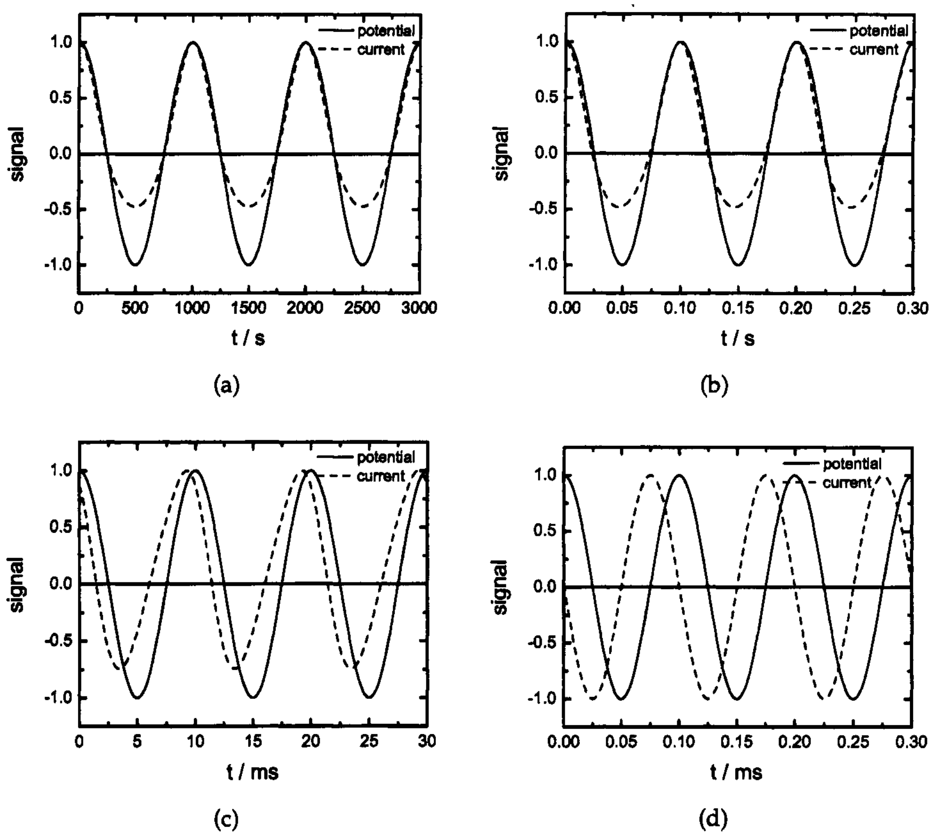

Figure 8.2: The current density response to a sinusoidal potential input with $\Delta V = 40$ mV for the system presented in Section 7.3 with parameters $C_{\mathrm{dl}} = 31\ \mu\mathrm{F/cm^2}$, $nFk_a = nFk_c = 0.14\ \mathrm{mA/cm^2}$, $b_a = 19.5\ \mathrm{V^{-1}}$, $b_c = 19.5\ \mathrm{V^{-1}}$, and $\overline{V} = 0.1$ V: a) 1 mHz; b) 10 Hz; c) 100 Hz; and d) 10 kHz. The solid line represents the potential input and the dashed line represents the resulting current density.

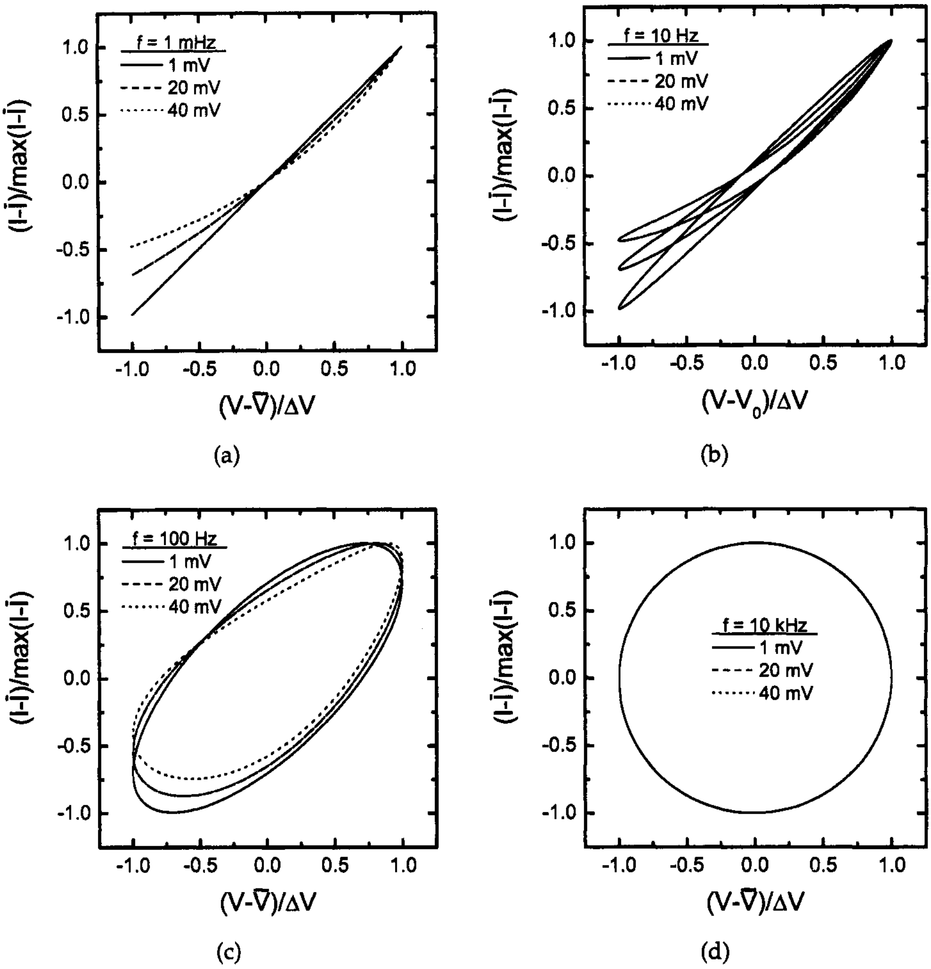

Figure 8.3: Lissajous plots for the system presented in Figure 8.2 with potential perturbation amplitude ΔV as a parameter: a) 1 mHz; b) 10 Hz; c) 100 Hz; and d) 10 kHz. $b_a\Delta V = 0.0195$ for $\Delta V = 1$ mV, $b_a\Delta V = 0.39$ for $\Delta V = 20$ mV, and $b_a\Delta V = 0.78$ for $\Delta V = 40$ mV.

The resulting Lissajous plots are presented in Figure 8.3. The value of $b_a \Delta V$ was 0.0195 for $\Delta V = 1$ mV, 0.39 for $\Delta V = 20$ mV, and 0.78 for $\Delta V = 40$ mV. A perturbation amplitude of 10 mV yields $b_a \Delta V = 0.195$, which is consistent with the guideline developed in Example 8.1. The influence of a large-amplitude potential perturbation is most evident at low frequencies, e.g., Figures 8.3(a) and (b), where the Faradaic current is much larger than the charging current. At the characteristic frequency for this system of 100 Hz, the Faradaic and charging currents are of the same magnitude. Careful examination of Figure 8.3(c) shows that the shapes of the loops are distorted from being elliptical, but the effect is not as evident as it is in Figures 8.3(a) and (b). At frequencies higher than the characteristic frequency, as shown in Figure 8.3(d), all curves are superposed. The nonlinear behavior arises from the nonlinear behavior of the Faradaic current. The charging current, in contrast, is linear. The system behaves as a linear system at high frequencies where the charging current dominates.

The impedance can be calculated from the potential and current time-domain signals using the Fourier analysis presented in Section 7.3.3. The resulting impedance spectra are presented in Nyquist format in Figure 8.4(a). The use of an excessive potential perturbation amplitude causes an error in the impedance response. The error arises from the nonlinear behavior of the Faradiac current, which is in phase with the applied potential. This effect is seen most clearly in the real part of the impedance shown in Figure 8.4(b). Nevertheless, as seen in Figure 8.4(c), an error is also seen in the imaginary part of the impedance due to the corresponding shift in the characteristic frequency to larger values.

The percent error in the low-frequency impedance asymptote associated with use of a large-amplitude potential perturbation is given in Figure 8.5 with $b_a \Delta V$ as a parameter. At a value of $b_a \Delta V = 0.2$, the error in the low-frequency impedance asymptote is 0.5 percent. This value can also be calculated using equation (8.21) of Example 8.1.

Example 8.2 Influence of Ohmic Resistance on Linearity: *As an extension of Example 8.1, establish a guideline for the perturbation amplitude needed to maintain linearity under potentiostatic regulation for a system with a nonnegligible Ohmic resistance.*

Solution: *The presence of an Ohmic resistance will reduce the portion of the potential perturbation experienced by the inferfacial reactions and double-layer charging. This can be seen in the expression for the impedance of the circuit given in Figure 8.6, i.e.,*

$$Z = R_e + \frac{1}{\frac{1}{Z_f} + j\omega C_{\mathrm{dl}}} \tag{8.24}$$

The potential drop across the resistor is given by iR_e *and the potential drop across the interface* η_s *is given by* $i/\left(\frac{1}{Z_f} + j\omega C_{\mathrm{dl}}\right)$. *At large frequencies, the interfacial impedance tends toward zero and the linear Ohmic resistance dominates. At low frequency, the capacitive charging has negligible effect and the interfacial impedance is dominated by the*

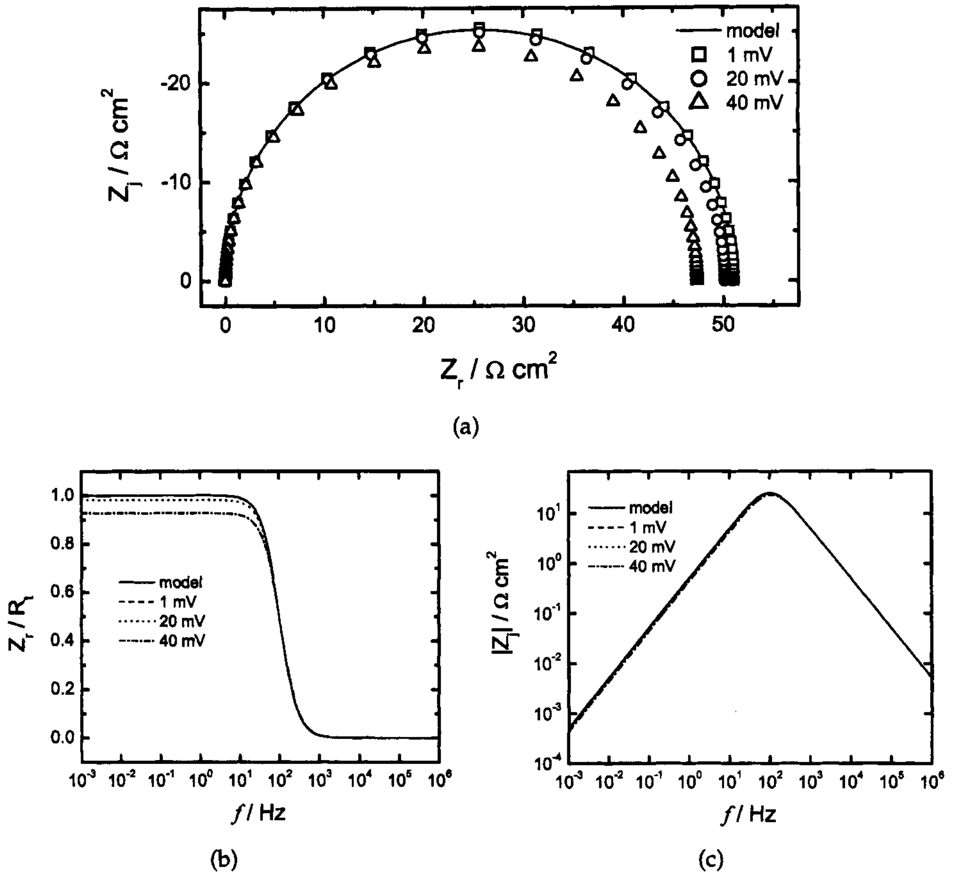

Figure 8.4: Impedance results obtained for the time-domain results presented in Figure 8.3 by use of the Fourier analysis presented in Section 7.3.3 with potential perturbation amplitude ΔV as a parameter: a) Nyquist representation; b) real part of the impedance as a function of frequency; and c) imaginary part of the impedance as a function of frequency.

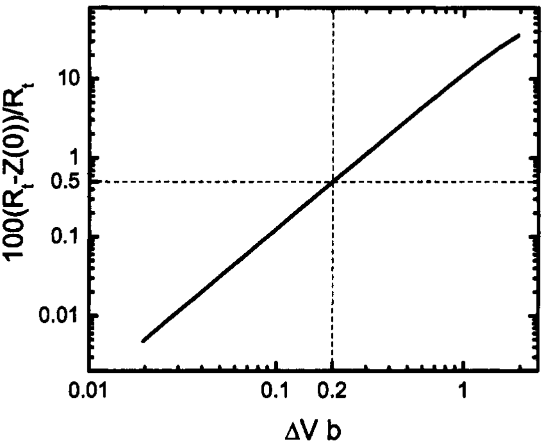

Figure 8.5: The error in the low-frequency impedance asymptote associated with use of a large-amplitude potential perturbation.

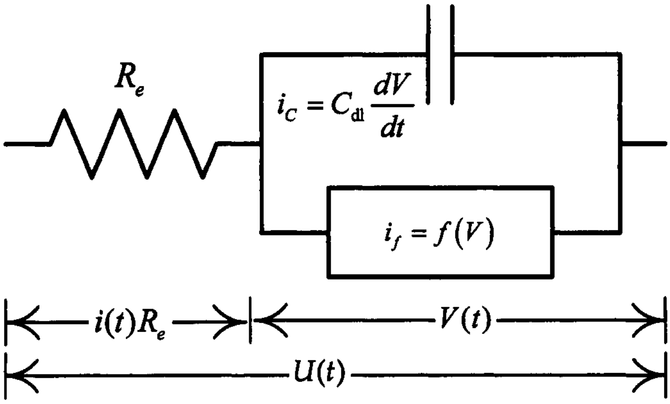

Figure 8.6: Electrical circuit showing the distribution of potential across the Ohmic resistance and the interface.

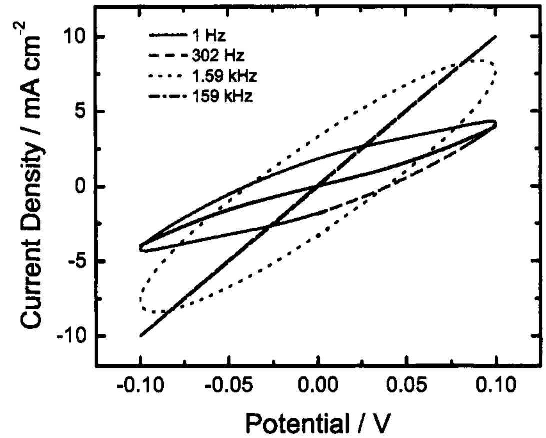

Figure 8.7: Lissajous representation for current and applied potential time-domain signals corresponding to a system presented in Figure 7.8 but with a potential perturbation amplitude $\Delta V = 100$ mV.

Faradaic contribution Z_f. This result supports the observation presented in Figure 8.3, which indicates that the nonlinear effects are most significant at low frequency.

The guidelines for the potential perturbation can therefore be determined by the behavior at low frequency. If the goal is to achieve $b_a \Delta V \leq 0.2$, this can be achieved by

$$b_a \Delta U \frac{R_t}{R_e + R_t} \leq 0.2 \tag{8.25}$$

Thus, the influence of Ohmic resistance is to increase the allowable magnitude for the potential perturbation.

The Lissajous plot corresponding to the influence of a large (100 mV) potential perturbation is given in Figure 8.7 for the system presented in Figure 7.8. The influence of the nonlinear response is clearly evident as a distortion in the straight lines at low frequency. The response at high frequencies, which are dominated by the Ohmic resistance, is linear.

The reason for the linear response at high frequency can be seen in the Lissajous plot of surface overpotential as a function of applied potential, given in Figure 8.8. At low frequencies, the surface overpotential is large and is scaled by $R_t/(R_t + R_e)$, whereas at high frequencies the surface overpotential tends toward zero. It is interesting to note that, at low frequencies, the surface overpotential is influenced by the nonlinearity associated with the faradaic reaction.

The frequency dependence of the surface overpotential is shown more clearly in Figure 8.9, where the magnitude of the surface overpotential is presented as a function of frequency with the magnitude of the applied potential perturbation as a parameter. The approach to unity at low frequencies for small perturbations shows that the surface overpotential is properly scaled by $R_t/(R_t + R_e)$. For larger perturbation amplitudes, the nonlinear response reduces the effective charge-transfer

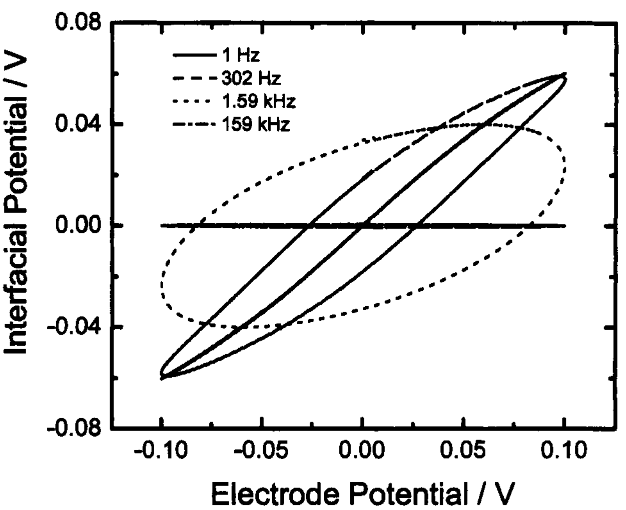

Figure 8.8: Lissajous representation for surface overpotential and applied potential time-domain signals corresponding to a system presented in Figure 8.7.

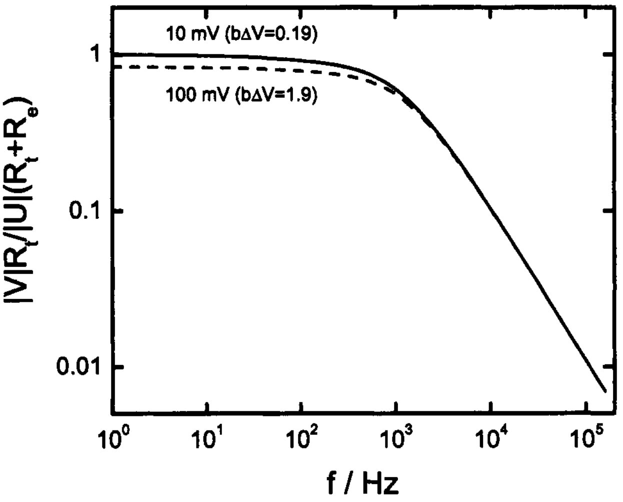

Figure 8.9: The magnitude of the surface overpotential as a function of frequency with the magnitude of the applied potential perturbation as a parameter for the system presented in Figure 8.7.

resistance, leading to an asymptotic low-frequency value that is less than unity. At higher frequencies, the 10 mV and 100 mV lines converge, indicating that the high-frequency response is linear for both perturbation amplitudes. The system is controlled by two characteristic frequencies. The characteristic frequency associated with the Faradaic reaction, $1/(2\pi R_t C_{\mathrm{dl}})$, indicates the frequency at which the charging and Faradaic currents are equal, and the characteristic frequency associated with the Ohmic resistance, $1/(2\pi R_e C_{\mathrm{dl}})$, indicates the frequency at which the capacitive current becomes limited by the Ohmic resistance.

Example 8.3 Influence of Capacitance on Linearity: *While the capacitance for a coated surface may be independent of applied potential, as shown in Figure 5.12, the capacitance for a bare electrode may be a function of potential. Explore the influence of a potential dependent capacitance on the linearity of the impedance response.*

Solution: *The potential dependence of capacitance will play the largest role at high frequencies where the current is due to the charging of the interface. The role of a potential-dependent capacitance will therefore be most visible in the absence of an Ohmic resistance. To consider the influence of potential-dependent capacitance, allow the capacitance to follow*

$$C = C_0(1 + aV) \tag{8.26}$$

where $a = 1.61\ V^{-1}$. *This allows a linear change in capacitance of 32 percent for a* ±100 *mV perturbation, which is consistent with the experimental results reported in Figure 5.12. All other parameters are the same as developed for Figure 8.2. The resulting Lissajous plots are similar to those presented in Figure 8.2 with the exception that, as seen in Figure 8.10, a distortion is evident at high frequencies. As shown in Figures 8.11(a) and (b), the effect on the impedance response, however, is minimal. As shown in Figure 8.11(a), the real part of the impedance response at low frequencies shows a dependence on potential perturbation amplitude that is consistent with that observed in Figure 8.4(b) for a constant capacitance. The imaginary part of the impedance, shown in Figure 8.11(b), is similar to that shown in Figure 8.4(c) for a constant capacitance. As shown in Figure 8.12, the estimation of the capacitance following equation (16.41) yields the correct value for the potential* $\overline{V}$ *about which the impedance measurement is made.*

The optimal perturbation amplitude may be best determined experimentally. Distortions in Lissajous plots at low frequency (see Figure 8.3) may be attributed to a nonlinear response. If the shape is distorted from an ellipse, one should reduce the amplitude. A second approach is to compare the impedance response for several amplitudes as demonstrated in Figure 8.4. If the magnitude of the impedance at low frequencies depends on amplitude of perturbation, the perturbation amplitude is too large.

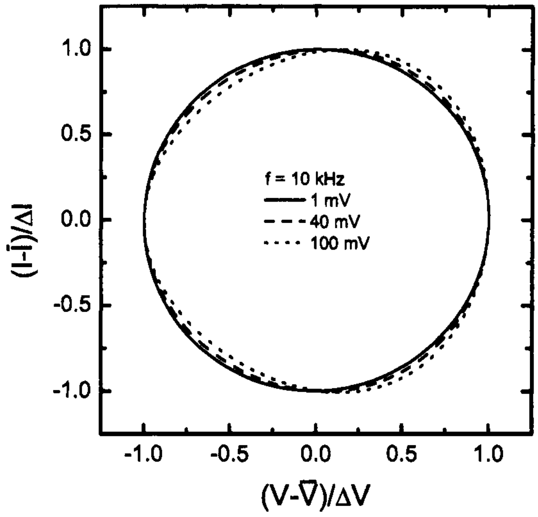

Figure 8.10: Lissajous plot for a capacitance dependent on potential following equation (8.26) at a frequency of 10 kHz.

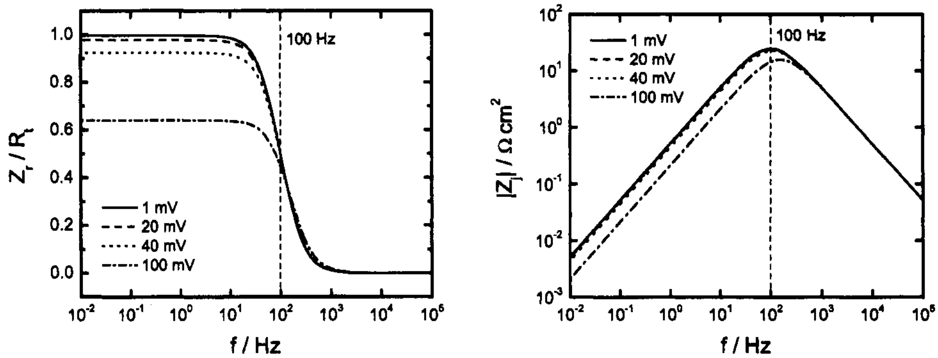

(a) (b)

Figure 8.11: Impedance results obtained for the electrochemical system used to generate Figure 8.3 but with an interfacial capacitance that follows equation (8.26) with potential perturbation amplitude ΔV as a parameter: a) normalized real part of the impedance as a function of frequency; and b) imaginary part of the impedance as a function of frequency.

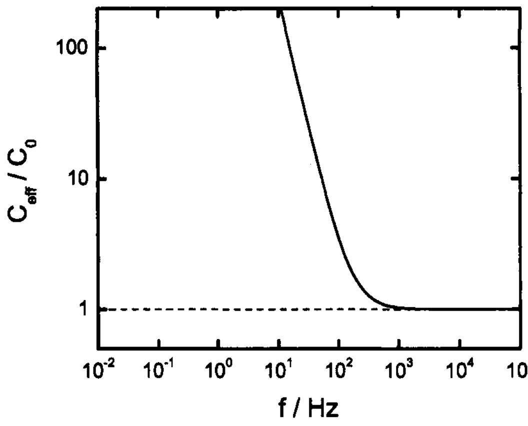

Figure 8.12: The effective capacitance calculated using equation (16.41) and the imaginary impedance given in Figure 8.11(b).

8.2.3 Modulation Technique

Electrochemical impedance measurements are often performed under potentiostatic regulation. In these measurements the potential is a fixed value with a superimposed (often sinusoidal) perturbation of fixed amplitude. This approach is attractive because, as discussed in Section 8.2.2, linearity in electrochemical systems is controlled by potential.

Galvanostatic regulation is required, however, when the system is to be studied under constant current density. For example, the evaluation of the resistance of skin to iontophoresis is typically done under constant current because the delivery of therapeutic drugs is more directly governed by current density than by potential. Galvanostatic control is also preferred for the use of impedance spectroscopy as a noninvasive tool for periodically observing the condition of a metal coupon held at the corrosion potential for a long period of time. As illustrated by the arrows in Figure 8.13, a drift in the open-circuit potential during the course of the measurement of a impedance spectrum will, in the case of potentiostatic regulation, result in application of a potential that is anodic (or, depending on the direction of the drift, cathodic) to the true open-circuit potential, thus perturbing the long-term measurement at the zero-current condition. Under galvanostatic control, the desired zero-current condition is maintained throughout the impedance measurement.

The difficulty with galvanostatic measurements with a fixed amplitude for the current perturbation is that such measurements can result in severe swings in potential, especially at low frequencies where the impedance is large. The amplitude of the potential variation associated with a perturbation of current is given by

$$\Delta \tilde{V} = \Delta \tilde{I} \left| Z(\omega) \right| \tag{8.27}$$

A current perturbation as small as 10 μA can result in potential swings of 1 V for

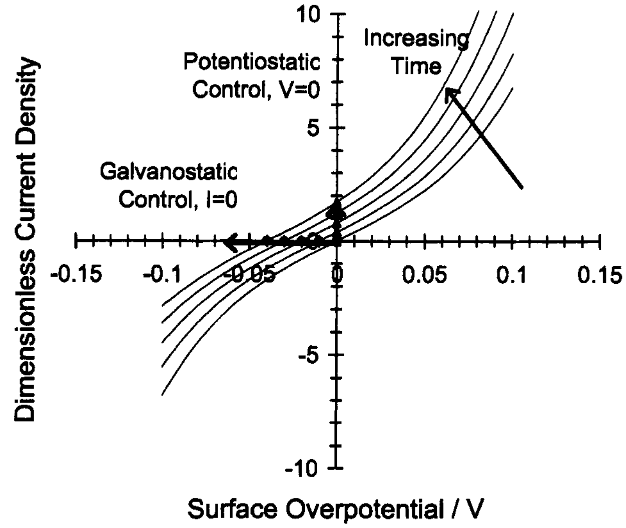

Figure 8.13: The error in the low-frequency impedance asymptote associated with use of a large-amplitude potential perturbation.

systems with a polarization resistance of $10^5\Omega$, a value typical of many membranes and some slowly corroding systems. Nonlinear behavior of skin has, for example, been reported for impedance measurements conducted under galvanostatic regulation. An algorithm for a variable amplitude galvanostatic modulation has been described by Wocjik et al.[115,116]

8.2.4 Oscilloscope

It is strongly advised to use an oscilloscope while making impedance measurements. It is useful to monitor the time-domain signals that are processed in the impedance instrumentation. It is particulary useful to monitor the signals in the form of a Lissajous plot as discussed in Section 7.3.1.

8.3 Instrumentation Parameters

The contributions to the error structure of impedance measurements are described in Section 21.1. Impedance measurements entail a compromise between minimizing bias errors, minimizing stochastic errors, and maximizing the information content of the resulting spectrum. The parameter settings described in this section may not apply to all impedance instrumentation.

8.3.1 Improve Signal-to-Noise Ratio

The following steps may be taken to reduce the role of stochastic errors (see Section 21.2) in impedance measurements.

- *Use the optimal current measuring range:* Current is converted to a potential signal through circuitry in the potentiostat. Potentiostats may employ a version of a current follower, for example, as described in Example 6.2. A mismatch between the measured current and the range set in the potentiostat can cause either excessive stochastic noise (if the set range is too high) or bias errors caused by current overloads (if the set range is too low). Some instrumentation vendors require that the user guess the correct current measuring range. Estimating the current range is not difficult for experiments conducted under a dc current. Under open-circuit conditions, the desired current range will vary considerably with frequency. Automatic selection of current measuring range is discouraged if the approach imposes a current on the system that may induce a change in system properties. An algorithm for a noninvasive approach for estimating the current at a given frequency has been described by Wocjik et al.[115,116]

- *Increase the integration time/cycles:* As described in Section 7.3, impedance measurements involve the conversion of time-domain signals to a complex value for each frequency. Stochastic errors in this measurement can be reduced by increasing the time allowed for integration at each frequency. As shown in Figure 21.6(a), the number of cycles required to achieve a set error level at each frequency depends on the frequency of the measurement. Many cycles are required at high frequencies, but only three or four cycles are needed at low frequency. Some instruments allow setting autointegration modes in which the system determines the number of cycles needed to converge to a given criterion. The noise levels can be reduced by selecting the tighter convergence criterion. This choice is termed *long/short integration* on some instrumentation.

- *Increase the amplitude of modulated signal:* As described in Section 8.2.2, the polarization curve for a given system dictates the size of the modulation amplitude that may be used while retaining a linear system response. Many high-impedance systems are characterized by a relatively large linear range of potential. In such cases, the stochastic errors can be reduced significantly by using a large modulation amplitude.

- *Introduce a delay time:* Impedance measurements are taken at the sinusoidal steady state, meaning that the sinusoidal response to the sinusoidal input is unchanging with respect to time. A transient is observed as the system responds to a change from one frequency to another, and this transient is incorporated into the integrated value of the impedance. Pollard and Compte have shown that this transient can introduce as much as a 4 percent error in the impedance response measured by integration over the first cycle.[117] To avoid this undesired error caused by the transient, it is better to introduce a delay of one or two cycles between the change of frequency and impedance measurement.

- *Ignore the first frequency measured:* The impedance measured at the first frequency of measurement is often corrupted by a startup transient. The best option is to ignore the first measured frequency when regressing models to the data.

- *Avoid the line frequency and harmonics:* Modern impedance instruments provide very effective filters for stochastic noise, but these filters are generally inadequate for measurements conducted at the line frequency. The resulting measurements generally appear as outliers in an impedance spectrum, and such outliers have a profound impact on nonlinear regression used to extract parameters from the data. Measurement of impedance should be avoided at line frequency and its first harmonic, i.e., 60 ± 5 Hz and 120 ± 5 Hz in the United States and 50 ± 5 Hz and 100 ± 5 Hz in Europe.

- *Avoid external electric fields:* External devices such as electric motors, pumps, and fluorescent lighting emanate electric fields that can contribute significantly to the apparent noise in a system. This influence, seen most easily in high-impedance systems, can be mitigated by use of a Faraday cage, described in the following section.

8.3.2 Reduce Bias Errors

The steps described in this section may be taken to reduce the role of systematic bias errors (see Section 21.3) in impedance measurements. Bias errors associated with nonstationary effects have greatest impact at low frequencies where each measurement requires a significant amount of time.

Nonstationary Effects

A systematic change in system properties will have a significant influence on measurements made at low frequencies. The time required for measurements at each frequency is discussed in Figures 21.6 and 21.7.

- *Reduce time for measurement:* The total time required to measure an impedance spectrum can be reduced by reducing the time allowed for integration at each frequency, thereby increasing the magnitude of stochastic errors in the measurement. In effect, this approach requires accepting more stochastic noise to achieve a smaller bias error. A second approach is to reduce the number of measured frequencies by reducing the frequency range or the number of frequencies measured per decade. As the greater number of measured frequencies yields better parameter estimates, this approach requires accepting a lesser ability for model discrimination to achieve a smaller bias error.

- *Introduce a delay time:* As discussed above, the transient seen as the system adjusts to a changed modulation frequency yields a bias error in the measured impedance. This undesired error can be avoided by introducing a delay of one or two cycles between the change of frequency and impedance measurement.

- *Avoid the line frequency and harmonics:* As discussed above, measurements made at the line frequency or its first harmonic typically have a significant error that will appear as an outlier when compared to the rest of the spectrum. Measurement within ±5 Hz of the line-frequency and its first harmonic should be avoided.

- *Select an appropriate modulation technique:* Proper selection of modulation technique, discussed in Section 8.2.3, can have a significant impact on presence of bias errors. Use of potentiostatic modulation for a system in which the potential changes with time can increase measurement time on autointegration. The user should consider what should be held constant (e.g., current or potential).

Instrument Bias

Instrument bias errors are often seen at high frequencies, especially for systems exhibiting a small impedance.

- *Use a faster potentiostat:* The influence of high-frequency bias errors can be mitigated by proper selection of potentiostat. The capability of potentiostats to perform measurements at high frequency differs from brand to brand.

- *Use short shielded leads:* High-frequency bias errors can be seen when the cell impedance is of the same order as the internal impedance of the instrumentation. Under these circumstances, it is essential to minimize the impact of ancillary pieces such as wires. Use of short shielded cables is highly recommended.

- *Use a Faraday cage:* A Faraday cage consists of a metallic conductor that surrounds the cell under study and is intended to shield the cell from the influence of external electric fields. The conductor may be in the form of a fine wire mesh or metal sheets. Typically the cage is grounded. It is important to avoid placing electrical components such as motors inside the Faraday cage because such devices can induce the electric fields that the cage is intended to shield. Faraday cages are essential for high-impedance systems that are characterized by a small electrical current. The wires act as an antenna, collecting stray electric fields, which induce a supplementary current. This current may be a significant portion of the signal if the cell current is small.

- *Check the results:* The presence of instrument bias errors can be difficult to discern. The Kramers-Kronig relations may provide a suitable guide, but as discussed in Chapter 22, some instrument-imposed bias errors are Kramers-Kronig transformable. If possible, high-frequency asymptotic values should be compared to independently obtained parameters. A third and highly recommended approach is to measure the impedance response of an electrical circuit exhibiting the same impedance magnitude and characteristic frequencies as seen in the measured impedance response. Systematic instrument errors should be evident in the measured response.

8.3.3 Improve Information Content

The information content of the impedance spectrum can be enhanced by increasing the frequency range, increasing the number of measured frequencies, reducing the magnitude of the bias and stochastic errors, and optimizing the measured frequencies.

- *Broaden the frequency range:* As described in Section 19.5.3, an insufficient frequency range will reduce the ability to identify system characteristics by regression. Typically, an increase in frequency range is constrained at high frequencies by instrument limitations and at low frequencies by nonstationary behavior.

- *Include more frequencies per decade:* The quality of a regression is generally enhanced by increasing the number of measured frequencies, thereby increasing the degree of freedom for the regression. An increased number of measured frequencies requires an increase in the time required for the impedance measurement, thus increasing the potential for nonstationary behavior.

- *Reduce bias and stochastic errors:* The efforts described in Sections 8.3.1 and 8.3.2 to reduce bias and stochastic errors will also improve the information content of the data.

- *Optimize measured frequencies:* The information content of a regression can be enhanced by ensuring the measurements are made at frequencies at which the measurements are sensitive to model parameters. For example, model discrimination will be poor if almost all the impedance data are collected at high frequencies where the impedance approaches an asymptotic value and few measurements are made at lower frequencies that are sensitive to kinetic and transport parameters. There is general agreement that a logarithmic spacing of frequencies maximizes the ability to discriminate between models and to extract model parameters.

Problems

8.1 Following the discussion presented in Example 8.2, estimate the effect an Ohmic resistance has on the maximum potential perturbation amplitude that can be applied to an electrochemical system while satisfying the guidelines presented in Example 8.1.

8.2 Estimate the maximum amplitude one should use for a potential perturbation for a system under Tafel kinetics with:

- **(a)** A Tafel slope of 60 mV/decade and negligible Ohmic resistance. Keep in mind the relationsip between Tafel slope β and Tafel constant b given in equation (5.18).
- **(b)** A Tafel slope of 120 mV/decade and negligible Ohmic resistance.
- **(c)** A Tafel slope of 60 mV/decade, an exchange current density equal to 1 mA/cm^2, an applied potential of 100 mV, and an Ohmic resistance of 10 Ωcm^2.
- **(d)** A Tafel slope of 60 mV/decade, an exchange current density equal to 1 mA/cm^2, an applied potential of 200 mV, and an Ohmic resistance of 10 Ωcm^2.

8.3 Use the methods described in Section 3.2 to estimate the error in the real part of the impedance associated with a 0.22 percent error in the fundamental current response.

8.4 Should the same potential perturbation amplitude be applied for all parts of the polarization curve? Give examples to demonstrate your answer.

8.5 Will a spatial distribution of capacitance lead to a nonlinear current response to a sinusoidal potential input?

8.6 Reproduce the results presented in Figures 8.3 and 8.4. This problem requires use of a spreadsheet program such as Microsoft Excel® or a computational programming environment such as Matlab®.

8.7 Researchers have reported that, for impedance measurements on human skin under fixed-amplitude galvanostatic modulation, significant changes in skin properties were observed that could be attributed to the impedance measurement. The magnitude of the skin impedance varied from about 10 Ωcm^2 at high frequency to 100 $k\Omega$cm^2 at low frequency. The perturbation amplitude was 0.1 mA on an exposed skin sample of 1 cm^2 area. Explain the reasons for their observation and suggest an improved experimental protocol.

Electrochemical Impedance Spectroscopy
by Mark E. Orazem and Bernard Tribollet

Part III

Process Models

Electrochemical Impedance Spectroscopy
By Mark E. Orazem & Bernard Tribollet

Chapter 9

Equivalent Circuit Analogs

As described in the subsequent chapters in Part III, models for the impedance response can be developed from proposed hypotheses involving reaction sequences (e.g., Chapters 10 and 12), mass transfer (e.g., Chapters 11 and 15), and physical phenomena (e.g., Chapters 13 and 14). These models can often be expressed in the mathematical formalism of electrical circuits. Electrical circuits can also be used to construct a framework for accounting for the phenomena that influence the impedance response of electrochemical systems. A method for using electrical circuits is presented in this chapter.

9.1 General Approach

The first step in developing an equivalent electrical circuit for an electrochemical system is to analyze the nature of the overall current and potential. For example, in the simple case of the uniformly accessible electrode shown in Figure 9.1(a), the overall potential is the sum of the interfacial potential V plus the Ohmic drop $R_e i$. Accordingly, the overall impedance is the sum of the interfacial impedance Z_0 plus the electrolyte resistance R_e. At the interface itself, shown in Figure 9.1(b), the overall current is the sum of the Faradaic current i_f plus the charging current i_C through the double layer capacitor C_{dl}. Thus, the interfacial impedance results from the double-layer capacity in parallel with the Faradaic impedance Z_f.

Boxes are used in Figure 9.1 to designate impedances that cannot be generally described in terms of passive elements such as resistors and capacitors. In the case of a single reaction on a uniform electrode, the Faradaic impedance Z_f shown in Figure 9.1(b) can be represented as a charge-transfer resistance. The representation is, however, more complicated for the interfacial response of coupled reactions, reactions involving mass transfer, reactions involving adsorbed species, and reactions on nonuniform surfaces.

Nevertheless, Figure 9.1 illustrates the procedure to be used in more complicated situations. When the current flowing through circuit elements is the same, but the potential drop is different, the respective impedances must be added in se-

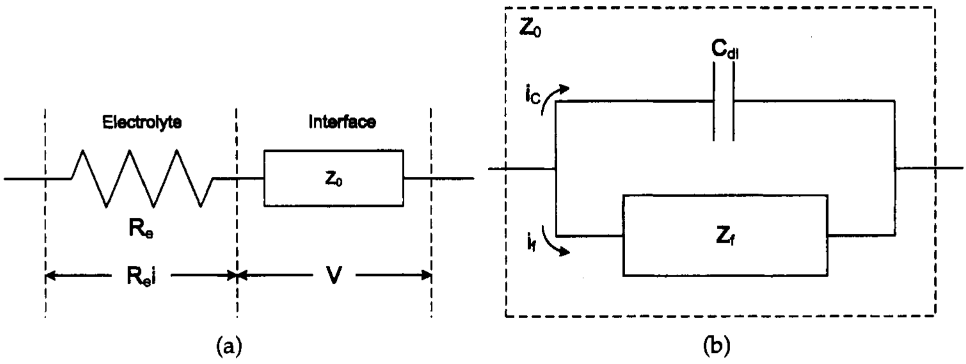

Figure 9.1: Electrical circuit corresponding to a single reaction on a uniformly accessible electrode: a) series combination of the electrolyte resistance and the interfacial impedance; and b) parallel combination of the Faradaic impedance and the double-layer capacitance, which comprise the interfacial impedance.

ries. This case is illustrated in Figure 9.1(a). When the current flowing through circuit elements is different, but the potential drop is the same, the respective impedances must be added in parallel. This case is illustrated in Figure 9.1(b). See Section 4.1.2 for a review of methods for parallel and series addition of circuit components.

The physical understanding of the current paths and potential drops in the system serves to guide the structure of the corresponding electrical circuit. The mathematical expression for the interfacial impedance can be obtained following the development presented in the subsequent chapters. Several examples are given in the following sections to illustrate the procedure.

9.2 Current Addition

Figure 9.1(b) provides an example of the case where the circuit development is based on the addition of current contributions. The examples provided in this section illustrate the application of the principle to more complex situations.

9.2.1 Impedance at the Corrosion Potential

The electrical circuit corresponding to a freely corroding electrode can be developed in two steps. As shown in Figure 9.1(a), the electrolyte resistance will be in series with an interfacial impedance. The interfacial impedance can be developed considering the diagram shown in Figure 9.2. As is the case described in Figure

---

Remember! 9.1 *In an equivalent electrical circuit, boxes should be used to designate impedances that cannot be generally described in terms of passive elements.*

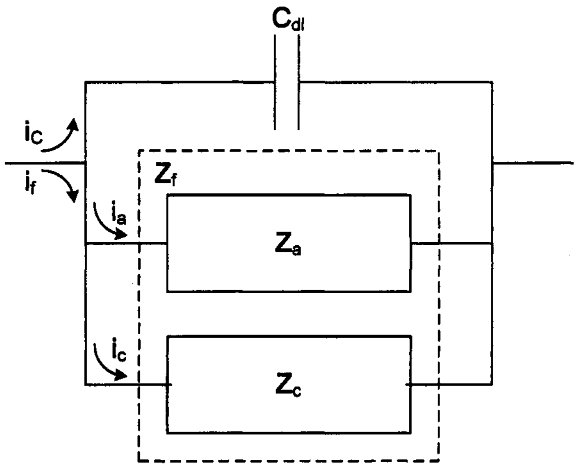

Figure 9.2: Equivalent electrical circuit of the interfacial impedance at the corrosion potential, where i_C represents the charging current and i_c represents the cathodic current.

9.1(b), the total current consists of the sum of charging and Faradaic currents. At the corrosion potential, the sum of the anodic and cathodic Faradaic currents is equal to zero, i.e., $i_a + i_c = 0$. The Faradaic impedance must, therefore, be a parallel combination of Z_a and Z_c. The contribution of the double-layer capacitance is added in parallel. Expressions for the impedances Z_a and Z_c must be developed separately according to proposed reaction mechanisms (see Chapter 10).

9.2.2 Partially Blocked Electrode

Partial coverage of an electrode by a surface film, e.g., an oxide layer, may block passage of Faradaic current. In some cases, the fractional coverage of the surface is influenced by the modulation of potential and must be treated by the methods presented in sections 10.4 and 10.5.

The case considered here is one where the blocked surface is independent of the potential. As shown in Figure 9.3, the blocked site is assumed to be a perfect insulator with fractional coverage γ, and the fractional area of active surface is $(1-\gamma)$. If the system is not mass-transport limited, the effect of the partial coverage is simply to reduce the active area. The Faradaic impedance is inversely proportional to the active area; thus, if the capacity of the covered surface can be neglected with respect to the double-layer capacity of the active surface, all impedance values are inversely proportional to $(1-\gamma)$. The normalized impedance $Z_f(\omega)/Z_f(0)$ is

Remember! 9.2 *Electrical circuit components must be added in parallel when the total current is the sum of individual current contributions. Electrical circuit components must be added in series when the total potential drop is the sum of individual contributions.*

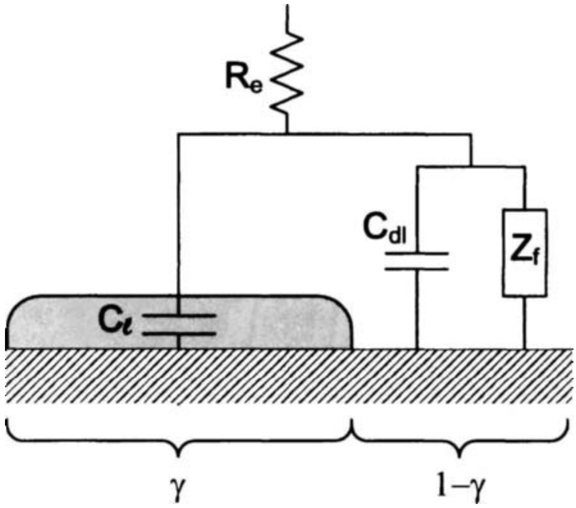

Figure 9.3: Equivalent electrical circuit for a partially blocked surface.

therefore independent of surface coverage γ.

If the capacity of the covered surface cannot be neglected, the overall capacity will be the area-weighted sum of capacitances for coated and uncoated areas, i.e.,

$$C = \gamma C_{\ell} + (1-\gamma)C_{\mathrm{dl}} \tag{9.1}$$

This impedance technique was used to follow the surface coverage of an electrode by a scale deposit during a short immersion time.[118] If the system is limited by mass-transport, the effect of the partial coverage is more complex and no analytic solution exists for the general case. Electrohydrodynamic (EHD) impedance, discussed in Chapter 15, provides an appropriate technique to analyze this problem.

9.3 Potential Addition

Figure 9.1(a) provides an example of the case where the circuit development is based on the addition of potential contributions. The examples provided in this section illustrate the application of the principle to more complex situations.

9.3.1 Electrode Coated with an Inert Porous Layer

Surface films commonly form in electrochemical studies, and these films can influence the impedance response. The electrode coated with an inert porous layer may be considered to be an extension of the case described in Section 9.2.2 in which the film is thicker and the fractional surface coverage approaches unity.

The layer shown in Figure 9.4 is considered to be porous with electrochemical reactions occurring only on the exposed electrode surface at the end of the pore. The Faradaic impedance is the same as discussed in Section 9.2.2. However, in the

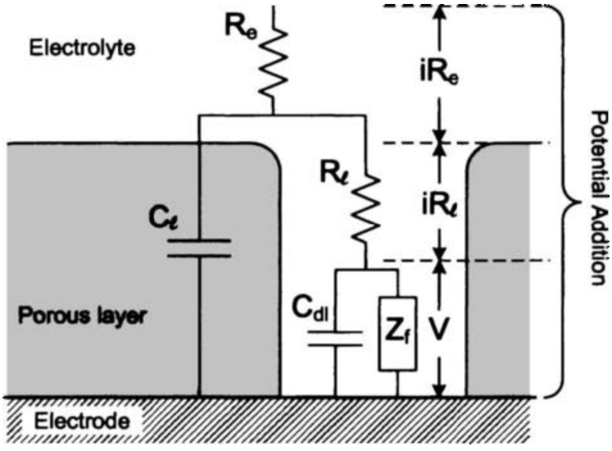

Figure 9.4: Equivalent electrical circuit of the impedance for a electrode coated by a porous layer.

kinetic model, it could be necessary to take into account the fact that in the pore, the concentration of the different species involved in the reaction could differ from the bulk concentration.

The equivalent circuit corresponding to the scheme of the coated electrode is presented in Figure 9.4.[119] At the interface localized at the end of the pore, the corresponding impedance is the parallel combination of Z_f and C_{dl}. Within the pore length, the electrolyte resistance is R_ℓ, and the insulating part of the coating can be considered to be a capacitor C_ℓ, which is in parallel with the impedance in the pore. The capacitance can be related to the permittivity and thickness of the coating according to equation (5.82) with typical values presented in Table 5.4.

The electrolyte resistance R_e is added in series with the previous impedance. If the electrochemical reaction is mass-transport limited, the previous equivalent circuit is still valid, but the Faradaic impedance includes a diffusion impedance Z_d as described in Chapter 11.

9.3.2 Electrode Coated with Two Inert Porous Layers

In corrosion systems, a salt film may cover an electrode that is itself covered by a porous oxide layer. If two different layers are superimposed, the geometrical analysis shows that the equivalent circuit corresponds to that described in Section 9.3.1 with an additional series $R_{\ell 2}C_{\ell 2}$ circuit to take into account the effect of the second porous layer. The circuit shown in Figure 9.5 is approximate because it assumes that the boundary between the inner and outer layers can be considered to be an equipotential plane. This plane will, however, be influenced by the presence of pores. The circuit shown in Figure 9.5 will provide a good representation for systems with an outer layer that is much thicker than the inner layer and with an inner layer that has relatively few pores.

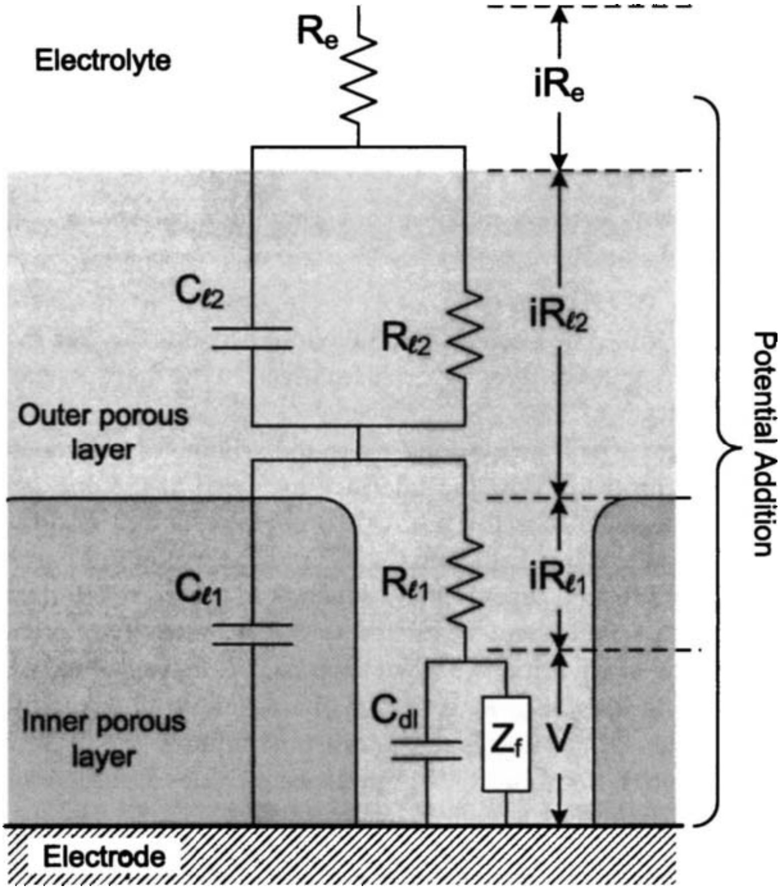

Figure 9.5: Equivalent electrical circuit of the impedance for a electrode coated by two superimposed porous layers.

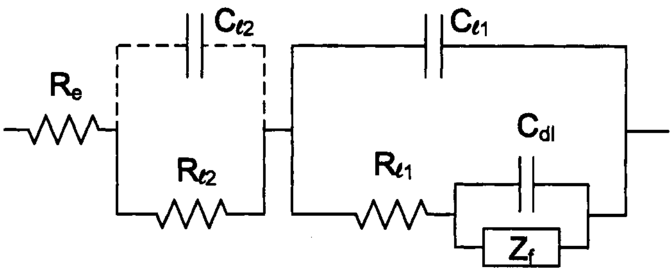

Figure 9.6: Equivalent electrical circuit for a electrode coated by two superimposed porous layers with the capacitance $C_{\ell 2}$ indicated by dashed lines to denote its experimental inaccessibility.

Example 9.1 Time-Dependent Ohmic Resistance: *It is sometimes observed that the impedance of the outer layer in a system similar to that shown in Figure 9.5 is negligible, but that the Ohmic resistance increased with time. Explain this phenomenon.*

Solution: *The characteristic frequency of the outer porous layer shown in Figure 9.5 is*

$$f_{\ell 2} = \frac{2\pi}{R_{\ell 2}C_{\ell 2}} \tag{9.2}$$

The capacitance can be estimated using equation (5.82). With a dielectric constant $\epsilon_{\ell 2} = 10$ *and coating thickness* $\delta_{\ell 2} = 100\ \mu m$, *the capacitance takes the value of* $C_{\ell 2} = 9 \times 10^{-11}\ F/cm^2$. *The resistance can be estimated from*

$$R_{\ell 2} = \delta_{\ell 2}/\kappa_{\ell 2} \tag{9.3}$$

where $\kappa_{\ell 2}$ *is the effective coating conductivity. For a salt film, the value will be on the order of* $\kappa_{\ell} = 10^{-4}\ \Omega^{-1}cm^{-1}$.

The corresponding time constant will be $\tau_{\ell 2} = 9 \times 10^{-9}$ *s, and the corresponding characteristic frequency will be* $f_{\ell 2} = 7 \times 10^{8}$ *Hz or 700 MHz. This frequency is well above the capabilities of electrochemical impedance instrumentation. Thus, the capacitive loop corresponding to the outer layer will not be observed experimentally. The resistance of the layer influences measurements at all frequencies; thus, the presence of a growing layer thickness will be manifested as an apparent increase of the Ohmic resistance. For the situation described in this example, the circuit shown in Figure 9.5 should be amended as shown in Figure 9.6.*[120] *The ability to measure the capacitive loop associated with the outer porous layer does not depend on layer thickness, but it is sensitive to the effective conductivity of the layer. The effective conductivity of paints and polymer films is much*

Remember! 9.3 *While all resistance contributions to an electrical circuit can be observed at low frequencies, the inability to measure at sufficiently high frequencies may make it impossible to obtain all capacitance values.*

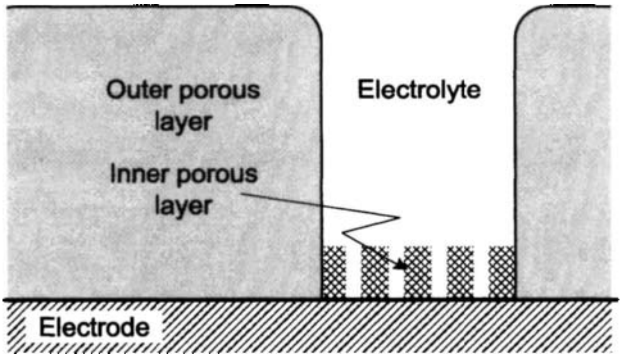

Figure 9.7: Schematic representation for the electrode coated by two superimposed porous layers discussed in Problem 9.1.

lower, resulting in a smaller characteristic frequency that is closer to the experimentally accessible range of frequencies.

Problems

9.1 Consider the schematic representation of a coated electrode presented in Figure 9.7. Develop the corresponding equivalent electrical circuit.

9.2 Is the circuit developed for Problem 9.1 mathematically equivalent to that developed for Section 9.3.2?

9.3 Show that the characteristic frequency for the impedance of the outer porous layer of the system shown in Figure 9.5 is independent of film thickness. Show the influence of layer thickness on the resistance of the layer.

9.4 Estimate the characteristic frequency for the impedance response of the outer porous layer of the system shown in Figure 9.5 for the following materials:

(a) Salt film with effective conductivity $\kappa = 10^{-4}\ \Omega^{-1}\text{cm}^{-1}$

(b) Polymer coating with effective conductivity $\kappa = 10^{-8}\ \Omega^{-1}\text{cm}^{-1}$

(c) Epoxy coating with effective conductivity $\kappa = 10^{-9}\ \Omega^{-1}\text{cm}^{-1}$

Electrochemical Impedance Spectroscopy
by Mark E. Orazem and Bernard Tribollet

Chapter 10

Kinetic Models

The electrical circuits developed in Chapter 9 made use of boxes and undefined transfer functions Z_f to account for the impedance associated with interfacial reactions. In some cases, the interfacial impedance may be described in terms of such circuit elements as resistors and capacitors, but the nature of the impedance response depends on the proposed reaction mechanism. The objective of this chapter is to explore the relationship between proposed reaction mechanisms and the interfacial impedance response.

10.1 Electrochemical Reactions

The current density corresponding to a Faradaic reaction can be expressed as a function of an interfacial potential V, as presented in equation (5.30), the surface concentration of bulk species $c_{i,0}$, and the surface coverage of adsorbed species γ_k as

$$i_f = f\left(V, c_{i,0}, \gamma_k\right) \tag{10.1}$$

where the interfacial potential can be considered to be the difference between the potential of the electrode Φ_{m} and the potential in the electrolyte adjacent to the electrode Φ_0, measured with respect to the same reference electrode as used to measure the cell potential U (see equation (10.18)). The current density can be expressed in terms of a steady, time-independent value and an oscillating value (see equation (1.121)) as

$$i_f = \bar{i}_f + \mathrm{Re}\left\{\tilde{i}_f e^{j\omega t}\right\} \tag{10.2}$$

where $\tilde{i}_f$ is a complex number that is a function only of position. A Taylor series expansion about the steady value can be written as

$$\tilde{i}_f = \left(\frac{\partial f}{\partial V}\right)_{c_{i,0},\gamma_k} \tilde{V} + \sum_i \left(\frac{\partial f}{\partial c_{i,0}}\right)_{V,c_{\ell,\ell\neq i}} \tilde{c}_{i,0} + \sum_k \left(\frac{\partial f}{\partial \gamma_k}\right)_{V,c_{i,0},\gamma_{\ell,\ell\neq k}} \tilde{\gamma}_k \tag{10.3}$$

where $\tilde{V}$, $\tilde{c}_{i,0}$, and $\tilde{\gamma}_k$ are assumed to have a small magnitude such that the higher-order terms can be neglected. Equation (10.3) represents a general result that can

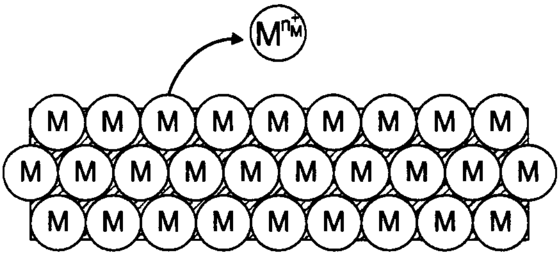

Figure 10.1: Schematic representation of a metal dissolution reaction.

be applied to any electrochemical reaction.

The general expression (10.3) guides development of impedance models from proposed reaction sequences. The reaction mechanisms considered here include reactions dependent only on potential, reactions dependent on both potential and mass transfer, coupled reactions dependent on both potential and surface coverage, and coupled reactions dependent on potential, surface coverage, and mass transfer. The proposed reaction sequence has a major influence on the frequency dependence of the interfacial Faradaic impedance described in Chapter 9.

10.2 Reaction Dependent on Potential Only

Consider the dissolution of metal in an aqueous medium

$$\mathrm{M} \rightarrow \mathrm{M}^{n_\mathrm{M}+} + n_\mathrm{M}\mathrm{e}^- \tag{10.4}$$

represented schematically in Figure 10.1. The steady Faradaic current associated with this reaction can be expressed in terms of Tafel kinetics as (5.21)

$$i_\mathrm{M} = K_\mathrm{M}^* \exp\left(b_M\left(V - V_{0,M}\right)\right) \tag{10.5}$$

where K_M^* is equal to $n_\mathrm{M}Fk_\mathrm{M}$ with units of current density, and b_M is $\alpha_\mathrm{M}n_\mathrm{M}F/RT$ where n_M is the number of electrons transferred per mole of reacting species in reaction (10.4), F is Faraday's constant (96,487 Coulombs/equivalent), k_M is the rate constant for the reaction, α_M is the symmetry factor, R is the universal gas constant (8.3147 J/mol K), T is temperature in absolute units, V is the interfacial potential, and $V_{0,M}$ represents the interfacial equilibrium potential as discussed in Section 5.4.

For systems involving single reactions, it is convenient to incorporate the interfacial equilibrium potential $V_{0,M}$ into the effective rate constant as

$$i_\mathrm{M} = K_\mathrm{M}^* \exp\left(-b_M V_{0,M}\right) \exp\left(b_M V\right) \tag{10.6}$$

or

$$i_\mathrm{M} = K_M \exp\left(b_M V\right) \tag{10.7}$$

where $K_M = K_M^* \exp\left(-b_M V_{0,M}\right)$. Under the assumption that the reaction is not influenced by the presence of adsorbed intermediates or layers of corrosion products, the concentration of the reactant can be considered to be a constant embedded within the effective rate constant k_{M} for the reaction. The current density given in equation (10.5) is a function only of potential. The steady current density increases exponentially as the potential V becomes more positive.

The Faradaic current response to a potential perturbation can be expressed as:

$$\tilde{i}_{\mathrm{M}} = K_M \exp\left(b_M \overline{V}\right) b_M \tilde{V} \tag{10.8}$$

where $\tilde{V}$ represents the perturbation of potential. A charge-transfer resistance for this reaction can be identified such that

$$\tilde{i}_{\mathrm{M}} = \frac{\tilde{V}}{R_{t,\mathrm{M}}} \tag{10.9}$$

Equation (10.9) corresponds to equation (10.3) with only the first term of the expression.

The charge-transfer resistance is defined in terms of kinetic parameters as

$$R_{t,\mathrm{M}} = \left[K_M \exp\left(b_M \overline{V}\right) b_M\right]^{-1} \tag{10.10}$$

The charge-transfer resistance is a function of the steady-state potential $\overline{V}$. Equation (10.5) can be expressed in terms of the Tafel slope

$$\beta_{\mathrm{M}} = 2.303 / b_M \tag{10.11}$$

as

$$\bar{i}_{\mathrm{M}} = K_M \exp\left(2.303\overline{V} / \beta_{\mathrm{M}}\right) \tag{10.12}$$

The potential dependence of the charge-transfer resistance can be expressed in terms of the Tafel slope as

$$R_{t,\mathrm{M}} = \frac{\beta_{\mathrm{M}}}{2.303\bar{i}_{\mathrm{M}}} \tag{10.13}$$

or

$$\bar{i}_{\mathrm{M}} = \frac{\beta_{\mathrm{M}}}{2.303 R_{t,\mathrm{M}}} \tag{10.14}$$

Equations (10.13) and (10.14) represent a very important result because the charge-transfer resistance obtained from impedance measurements is related to two well-defined steady-state variables: the steady-state current density and the Tafel slope.

In order to obtain the impedance response for this reaction, an expression for the total current density is needed in terms of the Faradaic and charging current density, i.e.,

$$i = i_{\mathrm{M}} + C_{\mathrm{dl}} \frac{dV}{dt} \tag{10.15}$$

Table 10.1: Some useful relationships for the development of the impedance response associated with Faradaic reactions.

$$\tilde{i} = \tilde{i}_f + j\omega C_{\mathrm{dl}}\tilde{V} \tag{10.22}$$

$$\tilde{U} = \tilde{i}R_e + \tilde{V} \tag{10.23}$$

$$Z(\omega) = \frac{\tilde{U}}{\tilde{i}} \tag{10.24}$$

where C_{dl} represents the double-layer capacitance. The addition of charging and Faradaic currents is illustrated in Figure 9.1(b). Under the convention that

$$V = \overline{V} + \mathrm{Re}\left\{\tilde{V}e^{j\omega t}\right\} \tag{10.16}$$

$$\tilde{i} = \tilde{i}_{\mathrm{M}} + j\omega C_{\mathrm{dl}}\tilde{V} \tag{10.17}$$

The relationship between the potential evaluated at the electrode surface and the potential measured with respect to a reference electrode some distance away from the electrode is given by

$$U = iR_e + V \tag{10.18}$$

which leads to

$$\tilde{U} = \tilde{i}R_e + \tilde{V} \tag{10.19}$$

Insertion of equation (10.9) into equation (10.17) yields

$$\tilde{i} = \tilde{V}\left(\frac{1}{R_{t,\mathrm{M}}} + j\omega C_{\mathrm{dl}}\right) \tag{10.20}$$

The cell impedance, corresponding to reaction (10.4), is given by

$$Z_{\mathrm{M}}(\omega) = \frac{\tilde{U}}{\tilde{i}} = R_e + \frac{\tilde{V}}{\tilde{i}} \tag{10.21}$$

Equations (10.17), (10.19), and (10.21) are extremely useful relationships for the development of the impedance response associated with Faradaic reactions. As they are used repeatedly in this chapter, generalized forms of these equations are summarized in Table 10.1.

Introduction of equation (10.20) yields

$$Z_{\mathrm{M}}(\omega) = R_e + \frac{R_{t,\mathrm{M}}}{1 + j\omega R_{t,\mathrm{M}}C_{\mathrm{dl}}} \tag{10.25}$$

An electrical circuit that yields the impedance response equivalent to equation (10.25) for a single Faradaic reaction is presented in Figure 10.2. Such a circuit may provide a building block for development of circuit models as shown in Chapter 9 for the impedance response of a more complicated system involving, for example, coupled reactions or more complicated 2- or 3-dimensional geometries.

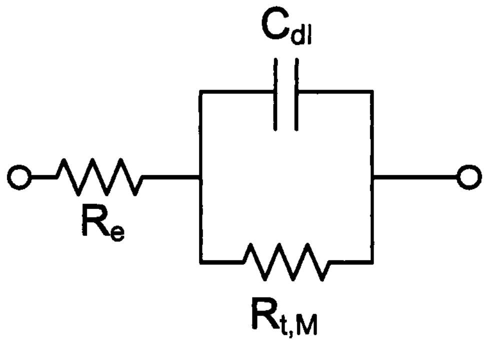

Figure 10.2: Electrical circuit providing the equivalent to the impedance response for a single electrochemical reaction.

Example 10.1 Iron in Anaerobic Solutions: *Consider the anodic reaction corresponding to the corrosion of iron at the corrosion potential in an anaerobic aqueous medium:*

$$Fe \rightarrow Fe^{2+} + 2e^- \qquad (10.26)$$

and consider as cathodic reaction the water electrolysis:

$$H_2O + e^- \rightarrow \frac{1}{2}H_2 + OH^- \qquad (10.27)$$

Find an expression for the Faradaic impedance response.

Solution: *According to equation (10.5) or equation (5.21) and equation (5.22), the steady-state anodic current density and the steady-state cathodic current are given by*

$$\bar{i}_{Fe} = K_{Fe} \exp\left(b_{Fe}\bar{V}\right) \qquad (10.28)$$

and

$$\bar{i}_{H_2} = -K_{H_2} \exp\left(-b_{H_2}\bar{V}\right) \qquad (10.29)$$

respectively, where the effective rate constants K_{Fe} and K_{H_2} include the respective equilibrium potentials for the corrosion and hydrogen evolution reactions.

At the corrosion potential, $\bar{i}_{Fe} + \bar{i}_{H_2} = 0$, and the overall oscillating component of the current density is given by $\tilde{i} = \tilde{i}_{Fe} + \tilde{i}_{H_2}$. The steady potential and the oscillating potential are the same for both reactions; thus,

$$\frac{\tilde{i}}{\tilde{V}} = \frac{\tilde{i}_{Fe}}{\tilde{V}} + \frac{\tilde{i}_{H_2}}{\tilde{V}} \qquad (10.30)$$

Remember! 10.1 *While some Faradaic impedances can be expressed in terms of passive elements, the development of such models from proposed reaction sequences provides insight and physical meaning to the circuit parameters.*

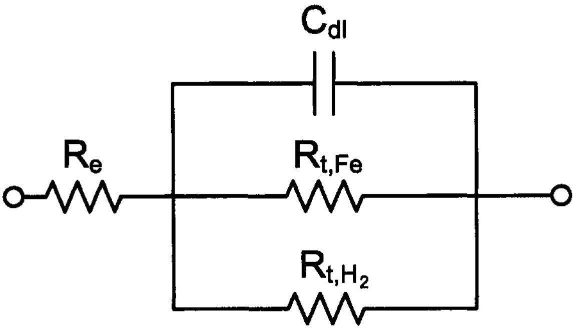

Figure 10.3: Electrical circuit providing the equivalent to the impedance response for a single electrochemical reaction.

or, with the impedance notation,

$$Z^{-1} = Z_{H_2}^{-1} + Z_{Fe}^{-1} \tag{10.31}$$

The oscillating form of the anodic and cathodic current density can be expressed as

$$\tilde{i}_{Fe} = K_{Fe} \exp\left(b_{Fe}\overline{V}\right) b_{Fe}\tilde{V} \tag{10.32}$$

and

$$\tilde{i}_{H_2} = K_{H_2} \exp\left(-b_{H_2}\overline{V}\right) b_{H_2}\tilde{V} \tag{10.33}$$

respectively. Then,

$$Z_{Fe} = R_{t,Fe} = \left[K_{Fe}b_{Fe} \exp\left(b_{Fe}\overline{V}\right)\right]^{-1} \tag{10.34}$$

and

$$Z_{H_2} = R_{t,H_2} = \left[K_{H_2}b_{H_2} \exp\left(-b_{H_2}\overline{V}\right)\right]^{-1} \tag{10.35}$$

The relationships presented in Table 10.1 (equations (10.22)–(10.24)) can be introduced to obtain the overall impedance:

$$Z_T(\omega) = R_e + \frac{Z}{1 + j\omega Z C_{dl}} \tag{10.36}$$

where Z is given by equation (10.31). In the present example, Z is a pure resistance. An equivalent circuit providing the impedance response at corrosion potential is given in Figure 10.3. This circuit shows the two parallel impedances corresponding to the anodic process and to the cathodic process, but, on an experimental point of view, only the overall charge-transfer resistance R_t can be obtained.

Each charge-transfer resistance can be written by using the Tafel slope (see equation (10.13)) as

$$R_{t,Fe} = \frac{\beta_{Fe}}{2.303\bar{i}_{Fe}} \tag{10.37}$$

and

$$R_{t,H_2} = \frac{\beta_{H_2}}{2.303\bar{i}_{H_2}} \tag{10.38}$$

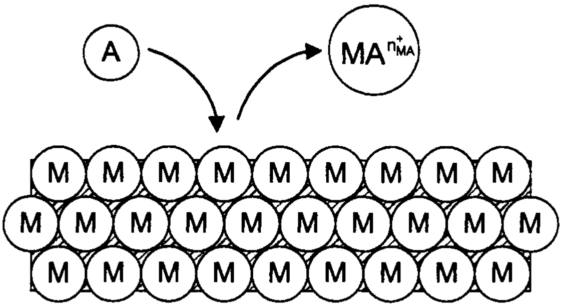

Figure 10.4: Schematic representation of metal dissolution by reaction with an electrolytic species.

where both β_{H_2} *and* $\bar{i}_{H_2}$ *are negative. At the corrosion potential,* $\bar{i}_{corr} = \bar{i}_{Fe} = -\bar{i}_{H_2}$. *The overall charge-transfer resistance is given by:*

$$R_t = \frac{-\beta_{H_2}\beta_{Fe}}{2.303\bar{i}_{corr}(\beta_{Fe} - \beta_{H_2})} \tag{10.39}$$

From this last equation, $\bar{i}_{corr}$ *can be obtained if the Tafel slopes and the overall charge-transfer resistance are measured. This relation was first developed by Stern and Geary*[121] *and is applied by some industrial instrumentation to determine the corrosion rate.*

10.3 Reaction Dependent on Potential and Mass Transfer

Many electrochemical reactions are influenced by the rate of transport of reactants to the electrode surface. Formal treatment of the impedance response for such a system requires both the kinetic analysis presented in this chapter and consideration of mass transfer as presented in Chapter 11.

Consider, as an example, the corrosion of a metal in an aqueous medium where the metal reacts with a species A as shown in Figure 10.4. The reaction mechanism is given as

$$\mathrm{M} + \mathrm{A} \rightarrow \mathrm{MA}^{n_{MA}+} + n_{MA}\mathrm{e}^- \tag{10.40}$$

The steady-state current density is given by

$$\bar{i}_{MA} = K_{MA}\bar{c}_{A,0}\exp\left(b_{MA}\bar{V}\right) \tag{10.41}$$

where K_{MA} is equal to $n_{MA}Fk_{MA}\exp\left(-b_{MA}V_{0,MA}\right)$ and $K_{MA}\bar{c}_{A,0}$ has the units of a current density. The current density is a function of both concentration of species A at the electrode surface and the potential difference between the electrode and the solution adjacent to the electrode. Oxidation of a species A on an inert electrode such as platinum or gold gives the same equation for the current.

The oscillating component of the current density is given by

$$\tilde{i}_{MA} = K_{MA}b_{MA}\bar{c}_{A,0}\exp\left(b_{MA}\bar{V}\right)\tilde{V} + K_{MA}\exp\left(b_{MA}\bar{V}\right)\tilde{c}_{A,0} \tag{10.42}$$

where $\tilde{c}_{\mathrm{A},0}$ represents the oscillating component of the concentration of species A evaluated at the electrode surface. Equation (10.42) takes the form of equation (10.3) with $\tilde{\gamma}_k = 0$.

A second equation is needed in order to evaluate the oscillating component of the current density with respect to the oscillating component of the interfacial potential, i.e.,

$$\bar{i}_{\mathrm{MA}} = -n_{\mathrm{MA}}FD_{\mathrm{A}} \left.\frac{d\bar{c}_{\mathrm{A}}}{dy}\right|_{y=0} \tag{10.43}$$

which can be expressed in terms of the oscillating contributions as

$$\tilde{i}_{\mathrm{MA}} = -n_{\mathrm{MA}}FD_{\mathrm{A}} \left.\frac{d\tilde{c}_{\mathrm{A}}}{dy}\right|_{y=0} \tag{10.44}$$

The approximation of a linear concentration gradient used in equation (5.25) can apply only for the steady-state condition, and cannot be employed for equation (10.44). It can be convenient to write equation (10.44) in terms of dimensionless position $\xi = y/\delta_A$ and dimensionless concentration $\theta_{\mathrm{A}} = \tilde{c}_{\mathrm{A}}/\tilde{c}_{\mathrm{A},0}$ as

$$\tilde{i}_{\mathrm{MA}} = -n_{\mathrm{MA}}FD_{\mathrm{A}}\frac{\tilde{c}_{\mathrm{A},0}}{\delta_{\mathrm{A}}}\tilde{\theta}'_{\mathrm{A}}(0) \tag{10.45}$$

where $\tilde{\theta}'_{\mathrm{A}}(0)$ is the derivative of $\tilde{\theta}_{\mathrm{A}}$ at the electrode with respect to the dimensionless position ξ.

The surface concentration $\tilde{c}_{\mathrm{A},0}$ can be eliminated in equations (10.42) and (10.45) to obtain

$$\tilde{i}_{\mathrm{MA}} = \frac{\tilde{V}}{R_{t,\mathrm{MA}} + Z_{\mathrm{D,MA}}} \tag{10.46}$$

where

$$Z_{\mathrm{D,MA}} = \frac{\delta_{\mathrm{A}}}{n_{\mathrm{MA}}FD_{\mathrm{A}}\bar{c}_{\mathrm{A},0}}\frac{1}{b_{MA}}\left(-\frac{1}{\tilde{\theta}'_A(0)}\right) \tag{10.47}$$

is the convective-diffusion impedance, and the charge-transfer resistance for reaction (10.40) is defined in terms of kinetic parameters to be

$$R_{t,\mathrm{MA}} = \left[K_{\mathrm{MA}}b_{\mathrm{MA}}\bar{c}_{\mathrm{A},0}\exp\left(b_{\mathrm{MA}}\overline{V}\right)\right]^{-1} \tag{10.48}$$

Remember! 10.2 *Transfer functions such as impedance provide the relationship between two oscillating variables, e.g.,* $\tilde{i}$ *and* $\tilde{V}$. *When the expression for* $\tilde{i}$ *is given in terms of two or more oscillating variables, additional relationships must be found to relate the additional variables to* $\tilde{i}$ *or to* $\tilde{V}$.

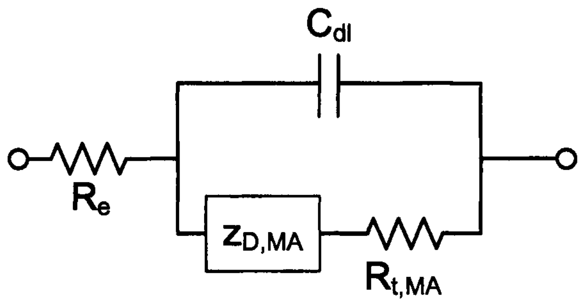

Figure 10.5: Electrical circuit providing the equivalent to the impedance response for a single electrochemical reaction coupled with a mass transfer impedance.

The relationships presented in Table 10.1 (equations (10.22)–(10.24)) can be introduced to obtain a relationship for impedance in terms of capacitance and electrolyte resistance as

$$Z_{\mathrm{MA}}(\omega) = R_e + \frac{R_{t,\mathrm{MA}} + Z_{\mathrm{D,MA}}(\omega)}{1 + j\omega\left(R_{t,\mathrm{MA}} + Z_{\mathrm{D,MA}}(\omega)\right)C_{\mathrm{dl}}} \tag{10.49}$$

The electrical circuit presented in Figure 10.5 yields the impedance response equivalent to equation (10.49) for a single Faradaic reaction coupled with a mass transfer. This circuit is known as the *Randles circuit*.[32] Such a circuit may provide a building block for development of circuit models as shown in Chapter 9 for the impedance response of a more complicated system involving, for example, coupled reactions or more complicated 2- or 3-dimensional geometries.

Example 10.2 Iron in Aerobic Solutions: *Consider a system at open circuit in an aerobic aqueous medium in which the anodic reaction corresponds to the corrosion of iron, i.e.,*

$$\mathrm{Fe} \rightarrow \mathrm{Fe}^{2+} + 2\mathrm{e}^- \tag{10.50}$$

and the cathodic reaction is the reduction of oxygen

$$\mathrm{O_2} + 2\mathrm{H_2O} + 4\mathrm{e}^- \rightarrow 4\mathrm{OH}^- \tag{10.51}$$

Find an expression for the impedance response.

Solution: *The steady-state anodic current density is given by equation (10.28). According to equation (10.41), the steady-state cathodic current is given by*

$$\bar{i}_{\mathrm{O_2}} = -K_{\mathrm{O_2}}\bar{c}_{\mathrm{O_2},0}\exp\left(-b_{\mathrm{O_2}}\bar{V}\right) \tag{10.52}$$

At the corrosion potential, $\bar{i}_{\mathrm{Fe}} + \bar{i}_{\mathrm{O_2}} = 0$, *and the overall oscillating component of the current density is* $\tilde{i} = \tilde{i}_{\mathrm{Fe}} + \tilde{i}_{\mathrm{O_2}}$. *The steady potential and the oscillating potential are the same for both reactions; thus,*

$$\frac{\tilde{i}}{\tilde{V}} = \frac{\tilde{i}_{\mathrm{Fe}}}{\tilde{V}} + \frac{\tilde{i}_{\mathrm{O_2}}}{\tilde{V}} \tag{10.53}$$

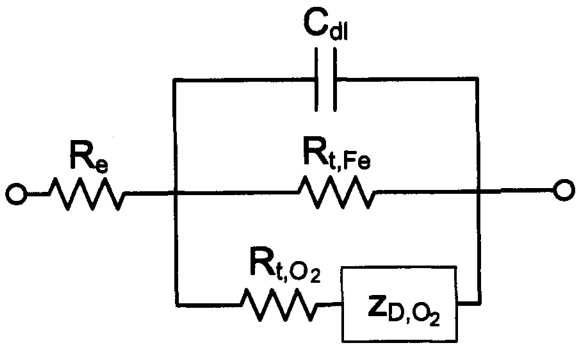

Figure 10.6: Electrical circuit providing the equivalent to the impedance response for iron dissolution and oxygen reduction.

or with the impedance notation

$$Z^{-1} = Z_{O_2}^{-1} + Z_{Fe}^{-1} \tag{10.54}$$

The oscillating form of the anodic current density is given by equation (10.32), and the oscillating form of the cathodic current density is given by

$$\begin{aligned} \tilde{i}_{O_2} = {} & K_{O_2}\bar{c}_{O_2,0}b_{O_2}\exp\left(-b_{O_2}\overline{V}\right)\tilde{V} \\ & - K_{O_2}\exp\left(-b_{O_2}\overline{V}\right)\tilde{c}_{O_2,0} \end{aligned} \tag{10.55}$$

Then, the impedance for the iron dissolution is given by equation (10.34), and

$$Z_{O_2} = R_{t,O_2} + Z_{D,O_2} \tag{10.56}$$

with

$$R_{t,O_2} = \left[K_{O_2}\bar{c}_{O_2,0}b_{O_2}\exp\left(-b_{O_2}\overline{V}\right)\right]^{-1} \tag{10.57}$$

and

$$Z_{D,O_2} = \frac{\delta_{O_2}}{4FD_{O_2}\bar{c}_{O_2,0}}\frac{1}{b_{O_2}}\left(-\frac{1}{\tilde{\theta}'_{O_2}(0)}\right) \tag{10.58}$$

The relationships presented in Table 10.1 (equations (10.22)–(10.24)) can be introduced to obtain the overall impedance as

$$Z_T(\omega) = R_e + \frac{Z(\omega)}{1 + j\omega Z(\omega)C_{dl}} \tag{10.59}$$

where Z is given by equation (10.54). An equivalent circuit providing the impedance response at corrosion potential is given in Figure 10.6. This circuit shows the two parallel impedances corresponding to the anodic and the cathodic processes.

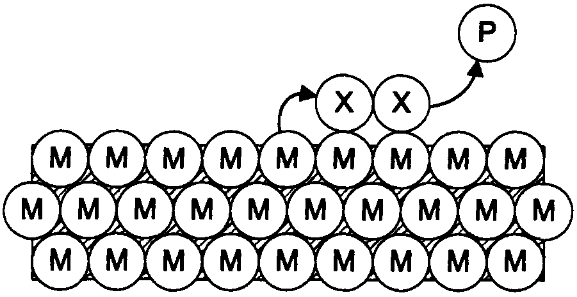

Figure 10.7: Schematic representation of metal dissolution through an adsorbed intermediate.

10.4 Coupled Reactions Dependent on Potential and Surface Coverage

Consider a hypothetical reaction sequence shown in Figure 10.7 in which a metal M dissolves through an adsorbed intermediate X following

$$\mathrm{M} \rightarrow \mathrm{X} + \mathrm{e}^- \tag{10.60}$$

which reacts in a second electrochemical step

$$\mathrm{X} \rightarrow \mathrm{P} + \mathrm{e}^- \tag{10.61}$$

to form the final product P. Adsorption of reaction intermediate X obeys a Langmuir isotherm and is characterized by a surface coverage γ_X. The steady-state current density associated with reaction (10.60) is given by

$$\bar{i}_M = K_M (1 - \bar{\gamma}_X) \exp\left(b_M \bar{V}\right) \tag{10.62}$$

where γ_X represents the fractional surface coverage by the intermediate X. The steady-state current density associated with reaction (10.61) is given by

$$\bar{i}_X = K_X \bar{\gamma}_X \exp\left(b_X \bar{V}\right) \tag{10.63}$$

where the rate constant K_X includes the maximum surface concentration of the intermediate X, defined in equation (10.64) as Γ.

The variation of the surface coverage by the intermediate X is given by the expression

$$\Gamma \frac{d\gamma_X}{dt} = \frac{i_M}{F} - \frac{i_X}{F} \tag{10.64}$$

Under a steady-state condition, $d\gamma_X/dt = 0$ and $\bar{i}_M = \bar{i}_X$. By using the corresponding equations (10.62) and (10.63), an expression for the steady-state surface coverage $\bar{\gamma}_X$ is obtained as

$$\bar{\gamma}_X = \frac{K_M \exp\left(b_M \bar{V}\right)}{K_M \exp\left(b_M \bar{V}\right) + K_X \exp\left(b_X \bar{V}\right)} \tag{10.65}$$

Examination of equation (10.65) reveals that, if $K_{\mathrm{M}}\exp\left(b_{\mathrm{M}}\overline{V}\right) \gg K_{\mathrm{X}}\exp\left(b_{\mathrm{X}}\overline{V}\right)$, then $\overline{\gamma}_{\mathrm{X}} \rightarrow 1$. If $K_{\mathrm{M}}\exp\left(b_{\mathrm{M}}\overline{V}\right) \ll K_{\mathrm{X}}\exp\left(b_{\mathrm{X}}\overline{V}\right)$, then $\overline{\gamma}_{\mathrm{X}} \rightarrow 0$. An expression for the total steady-state current density is then given by

$$\bar{i}_t = \bar{i}_{\mathrm{M}} + \bar{i}_{\mathrm{X}} = \frac{2K_{\mathrm{M}}\exp(b_{\mathrm{M}}\bar{V})K_{\mathrm{X}}\exp(b_{\mathrm{X}}\bar{V})}{K_{\mathrm{M}}\exp(b_{\mathrm{M}}\bar{V}), +K_{\mathrm{X}}\exp(b_{\mathrm{X}}\bar{V})} \tag{10.66}$$

The oscillating component of the current density for each reaction is given respectively by

$$\widetilde{i}_{\mathrm{M}} = R_{t,\mathrm{M}}{}^{-1}\widetilde{V} - K_{\mathrm{M}}\exp\left(b_{\mathrm{M}}\overline{V}\right)\widetilde{\gamma}_{\mathrm{X}} \tag{10.67}$$

and

$$\widetilde{i}_{\mathrm{X}} = R_{t,\mathrm{X}}{}^{-1}\widetilde{V} + K_{\mathrm{X}}\exp\left(b_{\mathrm{X}}\overline{V}\right)\widetilde{\gamma}_{\mathrm{X}} \tag{10.68}$$

where the charge-transfer resistances are defined by

$$R_{t,\mathrm{M}} = \left[K_{\mathrm{M}}\left(1-\overline{\gamma}_{\mathrm{X}}\right)b_{\mathrm{M}}\exp\left(b_{\mathrm{M}}\overline{V}\right)\right]^{-1} \tag{10.69}$$

and

$$R_{t,\mathrm{X}} = \left[K_{\mathrm{X}}\overline{\gamma}_{\mathrm{X}}b_{\mathrm{X}}\exp\left(b_{\mathrm{X}}\overline{V}\right)\right]^{-1} \tag{10.70}$$

According to equation (10.64), the oscillating component of the surface coverage can be expressed as

$$\Gamma Fj\omega\widetilde{\gamma}_{\mathrm{X}} = \left(R_{t,\mathrm{M}}{}^{-1} - R_{t,\mathrm{X}}{}^{-1}\right)\widetilde{V} - \left(K_{\mathrm{X}}\exp\left(b_{\mathrm{X}}\overline{V}\right) + K_{\mathrm{M}}\exp\left(b_{\mathrm{M}}\overline{V}\right)\right)\widetilde{\gamma}_{\mathrm{X}} \tag{10.71}$$

yielding

$$\widetilde{\gamma}_{\mathrm{X}} = \left[\frac{\left(R_{t,\mathrm{M}}{}^{-1} - R_{t,\mathrm{X}}{}^{-1}\right)}{\Gamma Fj\omega + \left(K_{\mathrm{X}}\exp\left(b_{\mathrm{X}}\overline{V}\right) + K_{\mathrm{M}}\exp\left(b_{\mathrm{M}}\overline{V}\right)\right)}\right]\widetilde{V} \tag{10.72}$$

The net Faradaic current density, given by the sum of contributions from reactions (10.60) and (10.61), is a function of γ_{X} and V, i.e.,

$$i_f = f\left(\gamma_{\mathrm{X}}, V\right) \tag{10.73}$$

Thus, the oscillating current density is given by

$$\widetilde{i}_f = \left.\frac{\partial f}{\partial \gamma_{\mathrm{X}}}\right|_V \widetilde{\gamma}_{\mathrm{X}} + \left.\frac{\partial f}{\partial V}\right|_{\gamma_{\mathrm{X}}} \widetilde{V} \tag{10.74}$$

In the present case, this oscillating current can be expressed as:

$$\begin{aligned}\widetilde{i}_f &= \widetilde{i}_{\mathrm{X}} + \widetilde{i}_{\mathrm{X}} & (10.75)\\ &= \left(R_{t,\mathrm{M}}{}^{-1} + R_{t,\mathrm{X}}{}^{-1}\right)\widetilde{V} + \left(K_{\mathrm{X}}\exp\left(b_{\mathrm{X}}\overline{V}\right) - K_{\mathrm{M}}\exp\left(b_{\mathrm{M}}\overline{V}\right)\right)\widetilde{\gamma}_{\mathrm{X}}\end{aligned}$$

The expression of the impedance is

$$Z^{-1} = \frac{\widetilde{i}_f}{\widetilde{V}} \tag{10.76}$$

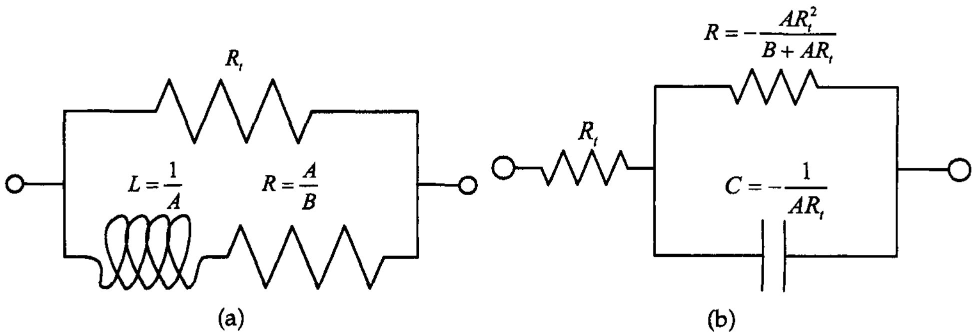

(a) (b)

Figure 10.8: Electrical circuit providing the equivalent to the impedance response for two coupled reactions with surface coverage: a) case of an inductive impedance where $A > 0$; and b) case of a capacitive impedance where $A < 0$.

or

$$Z^{-1} = R_t{}^{-1} + \frac{\left(K_X \exp\left(b_X \overline{V}\right) - K_M \exp\left(b_M \overline{V}\right)\right)\left(R_{t,M}{}^{-1} - R_{t,X}{}^{-1}\right)}{\Gamma F j\omega + \left(K_X \exp\left(b_X \overline{V}\right) + K_M \exp\left(b_M \overline{V}\right)\right)} \tag{10.77}$$

where

$$R_t{}^{-1} = R_{t,M}{}^{-1} + R_{t,X}{}^{-1} \tag{10.78}$$

The impedance given in equation (10.77) can be expressed in the form

$$Z^{-1} = R_t{}^{-1} + \frac{A}{j\omega + B} \tag{10.79}$$

where A can have a positive or negative sign according to the constant parameter values and the potential. If A is positive, the electrical circuit providing the impedance response equivalent to equation (10.79) is a charge-transfer resistance R_t in parallel with an inductance in series with a resistance (Figure 10.8(a)). This inductance has a value of $1/A$ and the resistance has a value of A/B. If A is negative, the impedance can be written under the following expression:

$$Z = R_t + \frac{\frac{-AR_t}{B+AR_t}}{\frac{j\omega}{B+AR_t} + 1} \tag{10.80}$$

The electrical circuit providing the impedance response equivalent to the same equation (10.79) is a charge-transfer resistance in series with a Voigt element composed of a capacitance in parallel with a resistance (Figure 10.8(b)). The capacitance has a value of $-1/AR_t$ and the resistance has a value of $-AR_t{}^2/(B + AR_t)$.

It is easy to show that $(B + AR_t)$ always has a positive value. The easiest way to determine whether the low-frequency loop is inductive or capacitive is to calculate $(Z^{-1} - R_t^{-1})$ at zero frequency. If the value is positive, an inductive loop is present; if the value is negative, a capacitive loop appears. Thus the same impedance expression (10.77) can yield two completely different equivalent circuits according to the potential and the constant parameter values.

To illustrate the previous calculation, some typical simulation results are provided in Figure 10.9. Points A, B, and C labeled on the current-potential curve given in Figure 10.9(a) correspond to potentials at which impedance simulations were performed. Two capacitive loops are observed in Figure 10.9(b) for a potential $V = -0.5$ V. At a slightly higher potential, the two capacitive loops merge into a single loop as shown in Figure 10.9(c). A high-frequency capacitive loop coupled with a low-frequency inductive loop is evident at still higher potentials (Figure 10.9(d)).

Kinetic models such as that presented in this section are superior to the use of electrical circuit analogues because the same model can account for the broad range of behavior shown in Figure 10.9. A second advantage is that the examination of the variables such as the surface coverage shown in Figure 10.10 can give insight into the reaction mechanism. In this case, the low-frequency loops are evident when the surface coverage is small.

10.5 Reactions Dependent on Potential, Surface Coverage, and Transport

The approach developed in the previous sections can be applied to situations such as that shown in Figure 10.11 in which an ionic product species diffuses from the surface and reacts through a backward reaction with the intermediate adsorbed species. This situation resembles the one presented in Section 10.4 with the exception that the mass transfer of product species affects the current.

Example 10.3 Corrosion of Magnesium: *Consider that the corrosion of magnesium proceeds according to the two-step reaction sequence in which*

$$\mathrm{Mg} \xrightarrow{k_1} \mathrm{Mg}^{+}_{\mathrm{ads}} + \mathrm{e}^- \tag{10.81}$$

involves production of an adsorbed reaction intermediate ($\mathrm{Mg}^{+}_{\mathrm{ads}}$)*, which reacts further to form the divalent* Mg^{2+} *ion, i.e.,*

$$\mathrm{Mg}^{+}_{\mathrm{ads}} \underset{k_{22}}{\overset{k_2}{\rightleftarrows}} \mathrm{Mg}^{2+} + \mathrm{e}^- \tag{10.82}$$

The product Mg^{2+} *diffuses through a porous layer of* $\mathrm{Mg(OH)_2}$ *that has a thickness of* δ*. Find the impedance response for this reaction sequence.*

Remember! 10.3 *The easiest way to determine whether the low-frequency loop is inductive or capacitive is to calculate* $(Z^{-1} - R_t^{-1})$ *at zero frequency. If the value is positive an inductive loop is present, and, if the value is negative, a capacitive loop appears.*

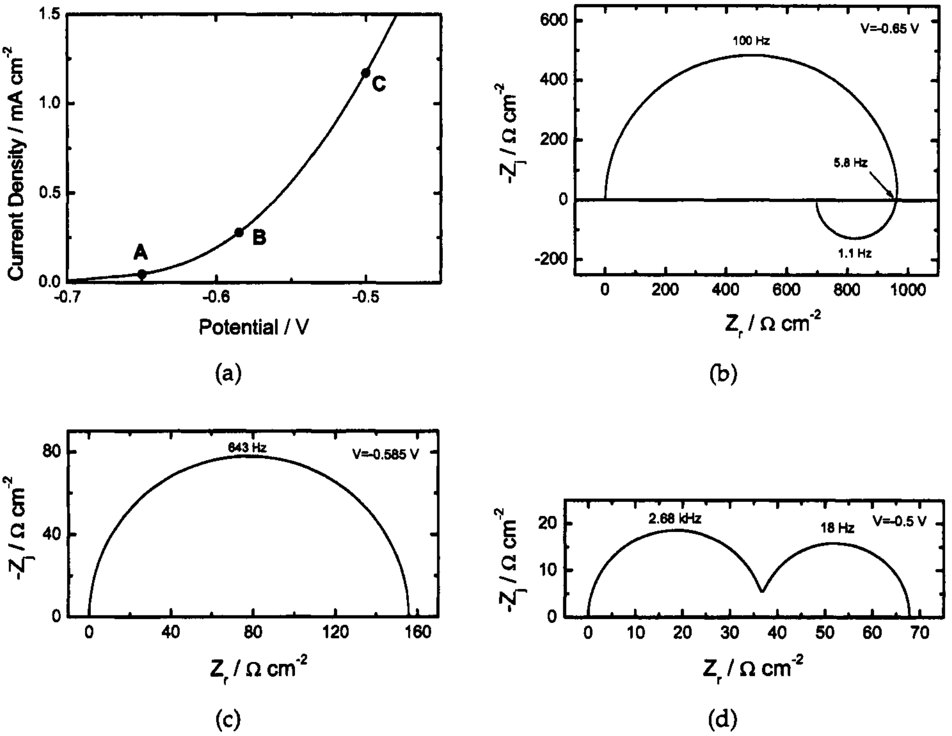

Figure 10.9: Calculated steady-state and impedance response for coupled reactions dependent on potential and surface coverage. a) Simulated current-potential curve following equation (10.66) with the kinetic parameters $K_M = 4F$ A/cm^2, $b_M = 36$ V^{-1}, $K_X = 10^{-6}F$ A/cm^2, $b_x = 10$ V^{-1}, $\Gamma = 2 \times 10^{-9}$ mol/cm^2, and $C_{dl} = 20\mu$F/cm^2. The points A, B and C correspond to the simulated impedance. b) impedance diagram simulated at the point A ($V = -0.65$ V); c) impedance diagram simulated at the point B ($V = -0.585$ V); and d) impedance diagram simulated at the point C ($V = -0.50$ V).

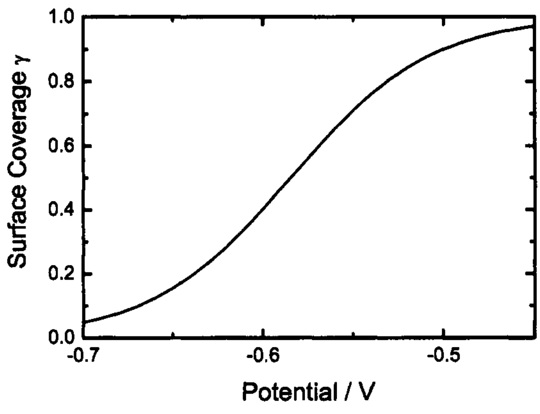

Figure 10.10: Calculated surface coverage γ corresponding to Figure 10.9.

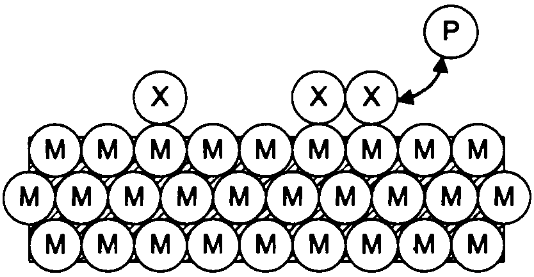

Figure 10.11: Schematic representation of mass-transfer controlled reaction by an ionic species formed through an adsorbed intermediate.

Solution: *On the basis of the reaction model (equations (10.81) and (10.82)), the impedance can be derived under the assumption that the adsorbate* $\mathrm{Mg}^{+}_{\mathrm{ads}}$ *obeys a Langmuir isotherm and that the rate constants of electrochemical reactions are exponentially dependent on potential (e.g., following Tafel's law). Each reaction with index i has a normalized rate constant* K_i *corresponding to its rate constant* k_i *by*

$$K_i = k_i F \exp\left(-b_i V\right) \tag{10.83}$$

Under the assumption that the maximum number of sites per surface unit that can be occupied by the adsorbate $\mathrm{Mg}^{+}_{\mathrm{ads}}$ *is* Γ*, the mass and charge balances are expressed in function of the fraction of the surface coverage by the adsorbed species* γ *as*

$$\begin{aligned}\Gamma\frac{d\gamma}{dt} &= K_1(1-\gamma)\exp\left(b_1 V\right) - K_2\gamma\exp\left(b_2 V\right) \\ &\quad + K_{22}c_{\mathrm{Mg}^{2+}}(0)(1-\gamma)\exp\left(-b_{22}V\right)\end{aligned} \tag{10.84}$$

where the normalized rate constants K_1*,* K_2*, and* K_{22} *include the maximum coverage* Γ*. A material balance on* Mg^{2+} *under the steady-state condition yields*

$$\frac{D_{\mathrm{Mg}^{2+}}c_{\mathrm{Mg}^{2+}}(0)}{\delta} = K_2\gamma\exp\left(b_2 V\right) - K_{22}c_{\mathrm{Mg}^{2+}}(0)\exp\left(-b_{22}V\right) \tag{10.85}$$

The total Faradaic current I_f *can be expressed as*

$$I_f = A\left[K_1(1-\gamma) + K_2\gamma - K_{22}c_{\mathrm{Mg}^{2+}}(0)\right] \tag{10.86}$$

where A *is the electrode surface area,* δ *is the thickness of the Nernst diffusion layer,* I_f *is the Faradic current, and* $c_{\mathrm{Mg}^{2+}}(0)$ *is the concentration of the* Mg^{2+} *ion at the electrode*

Remember! 10.4 *Low-frequency inductive loops in the impedance response can be attributed to Faradaic reactions that involve adsorbed intermediate species. Such systems can be described in terms of electrical circuits that involve inductances.*

interface. At the steady state, γ *and* $c_{\mathrm{Mg}^{2+}}(0)$ *are thus given by*

$$\gamma = \frac{K_1\left(D_{\mathrm{Mg}^{2+}}/\delta + K_{22}\right)}{K_1\left(D_{\mathrm{Mg}^{2+}}/\delta + K_{22}\right) + K_2 D_{\mathrm{Mg}^{2+}}/\delta} \tag{10.87}$$

and

$$c_{\mathrm{Mg}^{2+}}(0) = \frac{\gamma K_2}{D_{\mathrm{Mg}^{2+}}/\delta + K_{22}} \tag{10.88}$$

respectively. The faradic impedance Z_f*, is thus calculated by linearizing the mathematical expressions (10.85), (10.85), and (10.86) for small sine wave perturbations to obtain*

$$\begin{aligned}(F\Gamma j\omega + K_1 + K_2)\,\widetilde{\gamma} = {} & \\ & \left[(1-\gamma)K_1 b_1 - \gamma K_2 b_2 - c_{\mathrm{Mg}^{2+}}(0) K_{22} b_{22}\right]\widetilde{V} + K_{22}\widetilde{c}_{\mathrm{Mg}^{2+}}(0)\end{aligned} \tag{10.89}$$

and

$$\begin{aligned}\frac{\widetilde{I}}{A} = {} & (K_2 - K_1)\,\widetilde{\gamma} \\ & + \left[(1-\gamma)K_1 b_1 + \gamma K_2 b_2 + c_{\mathrm{Mg}^{2+}}(0) K_{22} b_{22}\right]\widetilde{V} - K_{22}\widetilde{c}_{\mathrm{Mg}^{2+}}(0)\end{aligned} \tag{10.90}$$

Equation (10.91) has the form of the general expression (10.3).

Since the specie Mg^{2+} *diffuses toward the electrode surface, the resulting concentration perturbation* $\widetilde{c}_{\mathrm{Mg}^{2+}}(0)$ *is obtained from the finite-length diffusion impedance, represented by* $-1/\theta'_{\mathrm{Mg}^{2+}}(0)$ *and given in equation (11.70). The resulting impedance response is given by*

$$Z_f = \frac{\widetilde{V}}{\widetilde{I}} = \frac{1 + K_{22}\left(-1/\theta'_{\mathrm{Mg}^{2+}}(0)\right)\left(1 - \frac{K_2 - K_1}{F\Gamma j\omega + K_1 + K_2}\right)}{A\left(\frac{(r_1 - r_2)(K_2 - K_1)}{F\Gamma j\omega + K_1 + K_2} + (r_1 + r_2)\right)} \tag{10.91}$$

with $r_1 = (1-\gamma)K_1 b_1$ *and* $r_2 = K_2 b_2 \gamma + K_{22} b_{22} c_{\mathrm{Mg}^{2+}}(0)$*. An example of a simulated diagram is given in Figure 10.12. The impedance response is characterized by three loops: a charge-transfer resistance loop at high frequency, a diffusion impedance loop proportional to* $-1/\theta'_{\mathrm{Mg}^{2+}}$*, and an inductive loop at low frequency.*

The reaction sequence described in Example 10.3 represents a simplification of a model developed by Baril et al.[122] who included an additional reaction

$$2\mathrm{Mg}^{+} + 2\mathrm{H_2O} \rightarrow 2\mathrm{Mg}^{2+} + 2\mathrm{OH}^{-} + \mathrm{H_2} \tag{10.92}$$

Reaction (10.92) is a chemical reaction that results in hydrogen evolution at potentials associated with Mg dissolution. Due to the anomalous production of hydrogen at anodic rather than cathodic potentials, this reaction was termed the *Negative difference effect* (NDE). The result presented in Example 10.3 can be obtained from that presented by Baril et al.[122] by setting their k_3 from reaction (10.92) equal to zero.

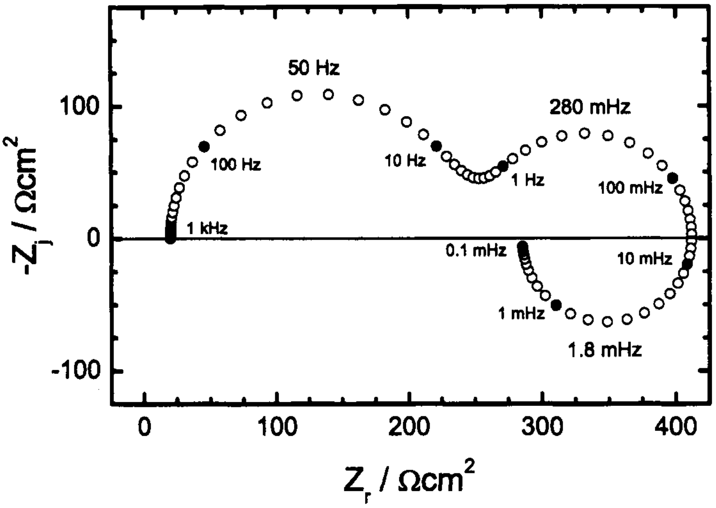

Figure 10.12: Simulated impedance diagram following the expression given in equation (10.91) for the Faradaic impedance. This Faradaic impedance is simulated in parallel with a high-frequency capacitance. (Taken from Baril et al.[122] and reproduced with permission of The Electrochemical Society.)

Problems

10.1 Develop an expression for the Faradaic impedance for the reaction

$$Ag \rightarrow Ag^+ + e^- \tag{10.93}$$

10.2 Develop an expression for the Faradaic impedance for the reaction

$$Ag^+ + e^- \rightarrow Ag \tag{10.94}$$

in which the concentration of Ag^+ is influenced by mass transfer. Use a spreadsheet program to plot the current density as a function of potential. Use the same estimated parameters to plot the impedance response at a potential corresponding to 1/4, 1/2, and 3/4 of the mass-transfer-limited current density.

10.3 Consider the reaction sequence

$$M + A \rightarrow MA^+_{ads} + e^- \tag{10.95}$$

where MA^+_{ads} is an adsorbed intermediate that reacts according to

$$MA^+_{ads} + A \rightarrow MA_2^{2+} + e^- \tag{10.96}$$

Derive the Faradaic impedance taking into account the mass-transfer limitation to the species A.

10.4 Derive the Faradaic impedance for the anodic dissolution of copper at low overpotential in a chloride medium where the reactions proceed according to

$$\mathrm{Cu} + \mathrm{Cl}^- \rightleftarrows \mathrm{CuCl_{ads}} + \mathrm{e}^- \tag{10.97}$$

where $\mathrm{CuCl_{ads}}$ is an adsorbed intermediate that reacts with chloride ions to form $\mathrm{CuCl_2^-}$, i.e.,

$$\mathrm{CuCl_{ads}} + \mathrm{Cl}^- \rightleftarrows \mathrm{CuCl_2^-} \tag{10.98}$$

The mass-transfer limitation is due only to $\mathrm{CuCl_2^-}$.

10.5 Re-derive the Faradaic impedance developed in Example 10.3 taking into account the NDE reaction (10.92).

10.6 Perform the calculations needed to generate Figure 10.9.

10.7 Explain why K_M^*, defined in equation (10.5), has a value that is independent of the reference electrode.

10.8 If $V_{\mathrm{ref1}} - V_{\mathrm{ref2}} = 0.4$ V, give the expression of $K_{M,\mathrm{ref2}}$ with respect to $K_{M,\mathrm{ref1}}$ where $K_{M,\mathrm{ref}i}$ is the value corresponding to an experiment performed with reference electrode ref$i$. Show that the value of the charge-transfer resistance R_t is independent of the reference electrode used.

Electrochemical Impedance Spectroscopy
by Mark E. Orazem and Bernard Tribollet

Chapter 11

Diffusion Impedance

The development of kinetic models presented in Sections 10.3 and 10.5 required expressions for the concentrations of reacting species at the electrode surface. The development was expressed in terms of an inverse dimensionless concentration gradient given as $-1/\widetilde{\theta}'(0)$. The objective of this chapter is to explore conditions and systems for which expressions for $-1/\widetilde{\theta}'(0)$ can be developed.

Experimental systems used for electrochemical measurements should be selected to take maximum advantage of well-understood phenomena such as mass transfer so as to focus attention on the less-understood phenomena such as electrode kinetics. For example, the study of electrochemical reactions in stagnant environments should be avoided because concentration and temperature gradients give rise to natural convection, which has an effect on mass transfer that is difficult to characterize. It is better to engage in such experimental investigations in systems for which mass transfer is well defined. To simplify interpretation of the impedance data, the electrode should be uniformly accessible to mass transfer.

Some issues pertaining to mass transfer to electrodes are described in Section 5.6, and the associated issues for cell design are considered further in Section 8.1.2. In many cases, a uniformly accessible electrode cannot be used. The time-constant dispersion that can arise as a result of nonuniform mass transfer is discussed in Section 13.2.

Remember! 11.1 *Experimental systems used for electrochemical measurements should be selected to take maximum advantage of well-understood phenomena such as mass transfer so as to focus attention on the less-understood phenomena such as electrode kinetics.*

11.1 Uniformly Accessible Electrode

A uniformly accessible electrode is an electrode where, at the interface, the flux and the concentration of a species produced or consumed on the electrode are independent of the coordinates that define the electrode surface. The mass flux at the interface is obtained by solving the material balance equation. If migration can be neglected, the material balance equation for dilute electrolytic solutions is reduced to the convective-diffusion equation. For an axisymmetric electrode, the concentration derivatives with respect to the angular coordinate θ are equal to zero, and the convective-diffusion equation can be expressed in cylindrical coordinates as

$$\frac{\partial c_i}{\partial t} + v_r \frac{\partial c_i}{\partial r} + v_y \frac{\partial c_i}{\partial y} = D_i \left\{ \frac{1}{r} \frac{\partial}{\partial r} \left(r \frac{\partial c_i}{\partial r} \right) + \frac{\partial^2 c_i}{\partial y^2} \right\} \tag{11.1}$$

with the boundary conditions:

$$\begin{aligned} c_i &\rightarrow c_{i,\infty} \quad \text{for} \quad y \rightarrow \infty \\ f\left[c_i(0), \left.\frac{\partial c_i}{\partial y}\right|_{y=0} \right] &= 0 \quad \text{for} \quad y = 0 \end{aligned} \tag{11.2}$$

where c_i is the concentration of the species i and D_i is the corresponding diffusion coefficient. The condition that $f\left[c_i(0), \left.\frac{\partial c_i}{\partial y}\right|_{y=0}\right] = 0$ is imposed, not only by the electrochemical reaction taking place at the electrode surface, but also by the type of regulation imposed, e.g., galvanostatic or potentiostatic. This condition corresponds generally to a fixed concentration or a fixed concentration gradient at the electrode surface.

If a flow exists with axial velocity v_y independent of the radial coordinate and if the boundary condition at $y = 0$ is also independent of the radial coordinate, then the concentration is only a function of y and the convective-diffusion equation is reduced to

$$\frac{\partial c_i}{\partial t} + v_y \frac{\partial c_i}{\partial y} - D_i \frac{\partial^2 c_i}{\partial y^2} = 0 \tag{11.3}$$

Equation (11.3) represents a uniformly accessible electrode because the concentration is a function only of time t and the axial position variable y.

The simplest uniformly accessible electrode is a planar electrode under conditions where the convection can be neglected. When the convection cannot be neglected, it is necessary to impose a flow that yields, with respect to the electrode surface, a uniform normal velocity component. Since the work of Levich,[123] the rotating disk system has been well known to provide a uniformly accessible electrode. Electrodes placed in some other flow geometries, such as within the stagnation region of a submerged impinging jet cell or as a rotating cylinder, can also be uniformly accessible. Electrodes placed in the above flow geometries can have more complex electrode/solution interfaces and yet can still be considered to be uniformly accessible. Examples include an electrode coated by a porous layer or an electrode in the presence of a viscosity gradient. For a uniformly accessible electrode the problem is reduced to one dimension: the distance to the interface.

11.2 General Mathematical Framework

A generalized heterogeneous reaction mechanism can be expressed in symbolic form as

$$\sum_i s_i M_i^{z_i} \leftrightarrows ne^- \tag{11.4}$$

where the stoichiometric coefficient s_i has a positive value for a reactant, has a negative value for a product, and is equal to zero for a species that does not participate in the reaction. Thus, the boundary condition at the electrode is

$$D_i \left.\frac{\partial c_i}{\partial y}\right|_{y=0} = \frac{s_i i_f}{nF} \quad \text{at} \quad y = 0 \tag{11.5}$$

The Faradaic current density is expressed as a function of interfacial concentration as

$$i_f = f(V, c_i(0)) \tag{11.6}$$

Thus, the concentration at the surface is dependent on applied potential through a reaction mechanism leading to equation (11.6).

All oscillating quantities, such as concentration, current, or potential, can be written in the form

$$X = \overline{X} + \operatorname{Re}\left\{\widetilde{X}e^{j\omega t}\right\} \tag{11.7}$$

where the overbar represents the steady value, j is the imaginary number $\sqrt{-1}$, ω is the frequency, and the tilde denotes a complex variable that is a function of frequency.

If the magnitude of the oscillating terms is sufficiently small to allow linearization of the governing equation, then

$$\widetilde{i}_f = \left(\frac{\partial f}{\partial V}\right)_{c_i,0} \widetilde{V} + \sum_i \left(\frac{\partial f}{\partial c_i(0)}\right)_{V,c_{j,j\neq i}} \widetilde{c}_i(0) \tag{11.8}$$

Equation (11.8) represents a special case of the more general equation (10.3). Following the approach presented in Chapter 10, the charge-transfer resistance is defined to be

$$R_t = \left[\left.\frac{\partial f}{\partial V}\right|_{c_i(0)}\right]^{-1} \tag{11.9}$$

Thus,

$$\widetilde{i}_f = \frac{1}{R_t}\widetilde{V} + \sum_i \left(\frac{\partial f}{\partial c_i(0)}\right)_{V,c_{j,j\neq i}} \widetilde{c}_i(0) \tag{11.10}$$

Equation (11.10) can be expressed in terms of interfacial potential as

$$\tilde{V} = R_t\tilde{i}_f - R_t\sum_i \left(\frac{\partial f}{\partial c_i(0)}\right)_{V,c_{j,j\neq i}} \tilde{c}_i(0) \tag{11.11}$$

The oscillating concentration gradient at the electrode can be expressed in function of the oscillating part of the Faradaic current from equation (11.5)

$$\left.\frac{d\tilde{c}_i}{dy}\right|_{y=0} = \frac{s_i\tilde{i}_f}{nFD_i} \tag{11.12}$$

Equation (11.11) becomes

$$\tilde{V} = R_t\tilde{i}_f + R_t\sum_i \left(\frac{\partial f}{\partial c_i(0)}\right)_{V,c_{j,j\neq i}} \frac{s_i}{nFD_i}\frac{-\tilde{c}_i(0)}{\left.\frac{d\tilde{c}_i(0)}{dy}\right|_{y=0}}\tilde{i}_f \tag{11.13}$$

or

$$\tilde{V} = \tilde{i}_f\left(R_t + Z_D\right) \tag{11.14}$$

where

$$Z_D = R_t\sum_i \left(\frac{\partial f}{\partial c_i(0)}\right)_{V,c_{j,j\neq i}} \frac{s_i}{nFD_i}\frac{-\tilde{c}_i(0)}{\left.\frac{d\tilde{c}_i(0)}{dy}\right|_{y=0}} \tag{11.15}$$

Equation (11.15) is the convection diffusion impedance. The electrode potential measured with respect to the potential of a reference electrode, following equation (10.18), is given by

$$U = R_e i + V \tag{11.16}$$

Equation (11.16) can be written in terms of oscillating variables as

$$\tilde{U} = R_e\tilde{i} + \tilde{V} \tag{11.17}$$

If the current density consists of contributions from Faradaic reactions and charging of the double layer as

$$i = i_f + C_{\mathrm{dl}}\frac{dV}{dt} \tag{11.18}$$

then equation (11.18) can be written in terms of oscillating variables as

$$\tilde{i} = \tilde{i}_f + j\omega C_{\mathrm{dl}}\tilde{V} \tag{11.19}$$

Equations (11.14), (11.17), and (11.19) result in

$$Z(\omega) = \frac{\tilde{U}}{\tilde{i}} = R_e + \frac{R_t + Z_D(\omega)}{1 + j\omega C_{\mathrm{dl}}\left(R_t + Z_D(\omega)\right)} \tag{11.20}$$

Equation (11.20) represents a generalized form of the impedance response of a uniformly accessible electrode. Note that, in the limit that $R_t >> Z_D$, equation (11.20) yields the impedance response of a single electrochemical reaction as discussed in Chapter 10.

Example 11.1 Diffusion with First-Order Reaction: *Develop an expression for the impedance response for the reduction of ferricyanide at potentials sufficiently cathodic to allow the anodic reaction to be ignored, yet sufficiently anodic to avoid reduction of oxygen (as a side reaction). Under these conditions, the reaction*

$$\mathrm{Fe(CN)_6^{3-}} + e^- \rightarrow \mathrm{Fe(CN)_6^{4-}} \tag{11.21}$$

provides an example of a first-order reaction involving only one mass-transfer-limited species.

Solution: *For a simple first-order reaction where only one species is involved, the Faradaic current can be written as*

$$i_{\mathrm{Fe(CN)_6^{3-}}} = K_{\mathrm{Fe(CN)_6^{3-}}} \frac{c_{\mathrm{Fe(CN)_6^{3-}}}(0)}{c_{\mathrm{Fe(CN)_6^{3-}},\infty}} \exp\left(b_{\mathrm{Fe(CN)_6^{3-}}} V\right) \tag{11.22}$$

where, as described in equation (5.18), $b_{\mathrm{Fe(CN)_6^{3-}}}$ is related to the Tafel slope. Following equation (11.9), the charge-transfer resistance is given by

$$R_{t,\mathrm{Fe(CN)_6^{3-}}} = \frac{1}{\bar{i}_{\mathrm{Fe(CN)_6^{3-}}} b_{\mathrm{Fe(CN)_6^{3-}}}} \tag{11.23}$$

and with equation (11.15) the expression of the convective-diffusion impedance is reduced to

$$Z_D(\omega) = Z_D(0) \frac{-\tilde{c}_{\mathrm{Fe(CN)_6^{3-}}}(0)}{\left.\dfrac{d\tilde{c}_{\mathrm{Fe(CN)_6^{3-}}}}{dy}\right|_{y=0}} \tag{11.24}$$

where

$$Z_D(0) = \frac{K_{\mathrm{Fe(CN)_6^{3-}}}}{c_{\mathrm{Fe(CN)_6^{3-}},\infty}} \exp\left(b_{\mathrm{Fe(CN)_6^{3-}}} \mathrm{V}\right) \tag{11.25}$$

The impedance is given by equation (11.20), i.e.,

$$Z(\omega) = R_e + \frac{R_{t,\mathrm{Fe(CN)_6^{3-}}} + Z_D(\omega)}{1 + j\omega C_{\mathrm{dl}}\left(R_{t,\mathrm{Fe(CN)_6^{3-}}} + Z_D(\omega)\right)} \tag{11.26}$$

Equation (11.26) contains explicit parameters $Z_D(0)$, C_{dl}, $R_{t,\mathrm{Fe(CN)_6^{3-}}}$, and R_e in addition to parameters that influence the value of

$$\frac{Z_D(\omega)}{Z_D(0)} = \frac{-\tilde{c}_{\mathrm{Fe(CN)_6^{3-}}}(0)}{\left.\dfrac{d\tilde{c}_{\mathrm{Fe(CN)_6^{3-}}}}{dy}\right|_{y=0}} \tag{11.27}$$

The term $Z_D(0)$ is often treated as an adjustable parameter, but, as shown in equation (11.25), it has explicit meaning in terms of kinetic parameters.

Example 11.2 Diffusion of Two Species: *At sufficiently high overpotentials, the deposition of zinc from zincate solutions can be assumed to follow a simplified reaction scheme as a chemical step*

$$\mathrm{Zn(OH)_4^{2-}} \rightleftarrows \mathrm{Zn(OH)_3^-} + \mathrm{OH^-} \tag{11.28}$$

followed by an electrochemical step

$$\mathrm{Zn(OH)_3^-} + 2\mathrm{e^-} \rightarrow \mathrm{Zn} + 3\mathrm{OH^-} \tag{11.29}$$

Under the assumption that reaction (11.28) is fast, an empirical relation has been established for zinc deposition from basic media at the equlibrium potential as[124]

$$i_{\mathrm{Zn}} = K_{\mathrm{Zn}} \frac{c_{\mathrm{Zn(OH)_3^-}}}{c_{\mathrm{OH^-}}} \tag{11.30}$$

Develop an expression for the impedance response, taking into account diffusion of the reactant $\mathrm{Zn(OH)_3^-}$ *toward the electrode and of the product* $\mathrm{OH^-}$ *away from the electrode.*

Solution: *The formal dependence of equation (11.30) on potential can be obtained under the assumption of a Tafel behavior, e.g.,*

$$i_{\mathrm{Zn}} = K_{\mathrm{Zn}} \frac{c_{\mathrm{Zn(OH)_3^-}}}{c_{\mathrm{OH^-}}} \exp\left(b_{\mathrm{Zn}} V\right) \tag{11.31}$$

Following equation (10.3),

$$\begin{aligned}\tilde{i}_{\mathrm{Zn}} = {} & \frac{1}{R_{t,\mathrm{Zn}}}\tilde{V} + \frac{K_{\mathrm{Zn}}}{\bar{c}_{\mathrm{OH^-}}} \exp\left(b_{\mathrm{Zn}}\overline{V}\right) \tilde{c}_{\mathrm{Zn(OH)_3^-}} \\ & - K_{\mathrm{Zn}} \frac{\bar{c}_{\mathrm{Zn(OH)_3^-}}}{\left(\bar{c}_{\mathrm{OH^-}}\right)^2} \exp\left(b_{\mathrm{Zn}}\overline{V}\right) \tilde{c}_{\mathrm{OH^-}}\end{aligned} \tag{11.32}$$

The charge-transfer resistance can be obtained, following equation (11.9), as

$$R_{t,\mathrm{Zn}} = \frac{1}{K_{\mathrm{Zn}} \frac{\bar{c}_{\mathrm{Zn(OH)_3^-}}(0)}{\bar{c}_{\mathrm{OH^-}}(0)} \exp\left(b_{\mathrm{Zn}}\overline{V}\right) b_{\mathrm{Zn}}} \tag{11.33}$$

or

$$R_{t,\mathrm{Zn}} = \frac{1}{\bar{i}_{\mathrm{Zn}} b_{\mathrm{Zn}}} \tag{11.34}$$

By taking into account the expressions for diffusion of $\mathrm{Zn(OH)_3^-}$

$$\tilde{i}_{\mathrm{Zn}} = -2FD_{\mathrm{Zn(OH)_3^-}} \left.\frac{d\tilde{c}_{\mathrm{Zn(OH)_3^-}}}{dy}\right|_{y=0} \tag{11.35}$$

Similarly for OH^-,

$$\tilde{i}_{\mathrm{Zn}} = +\frac{2}{3} F D_{\mathrm{OH}^-} \left. \frac{d\tilde{c}_{\mathrm{OH}^-}}{dy} \right|_{y=0} \tag{11.36}$$

Following equation (11.15), the expression of the convective-diffusion impedance can be found to be

$$Z_D = Z_{D,\mathrm{Zn(OH)}_3^-} + Z_{D,(\mathrm{OH})^-} \tag{11.37}$$

where

$$Z_{D,\mathrm{Zn(OH)}_3^-} = R_{t,\mathrm{Zn}} \frac{K_{\mathrm{Zn}} \exp\left(b_{\mathrm{Zn}} \overline{V}\right)}{2F\bar{c}_{\mathrm{OH}^-}(0) D_{\mathrm{Zn(OH)}_3^-}} \frac{-\tilde{c}_{\mathrm{Zn(OH)}_3^-}(0)}{\left. \frac{d\tilde{c}_{\mathrm{Zn(OH)}_3^-}}{dy} \right|_{y=0}} \tag{11.38}$$

and

$$Z_{D,\mathrm{OH}^-} = R_{t,\mathrm{Zn}} \frac{K_{\mathrm{Zn}} \exp\left(b_{\mathrm{Zn}} \overline{V}\right) \bar{c}_{\mathrm{Zn(OH)}_3^-}(0)}{2F \left(\bar{c}_{\mathrm{OH}^-}(0)\right)^2 D_{\mathrm{OH}^-}} \frac{-3\tilde{c}_{\mathrm{OH}^-}(0)}{\left. \frac{d\tilde{c}_{\mathrm{OH}^-}}{dy} \right|_{y=0}} \tag{11.39}$$

Thus, the impedance response is given by

$$Z = R_e + \frac{R_t + Z_{D,\mathrm{Zn(OH)}_3^-} + Z_{D,(\mathrm{OH})^-}}{1 + j\omega C_{\mathrm{dl}} \left(R_t + Z_{D,\mathrm{Zn(OH)}_3^-} + Z_{D,(\mathrm{OH})^-}\right)} \tag{11.40}$$

11.3 Stagnant Diffusion Layer

In stagnant environments, if natural convection can be ignored, the convective-diffusion equation is reduced to

$$\frac{\partial c_i}{\partial t} - D_i \frac{\partial^2 c_i}{\partial y^2} = 0 \tag{11.41}$$

which is known as Fick's second law. The boundary conditions may be given as

$$\begin{array}{rcl} c_i \rightarrow c_{i,\infty} & \text{for} & y \rightarrow \infty \\ c_i = c_i(0) & \text{at} & y = 0 \\ c_i = c_{i,\infty} & \text{at} & t = 0 \end{array} \tag{11.42}$$

No steady-state solution is possible. As shown in Example 2.5, the concentration is given in terms of a similarity variable as[125]

$$\Theta_i = \frac{c_i(y) - c_i(0)}{c_{i,\infty} - c_i(0)} = 1 - \operatorname{erf}\left(\frac{y}{\sqrt{4D_i t}}\right) \tag{11.43}$$

In principle, impedance measurements are possible only for stationary systems, i.e., those systems for which a steady solution is possible. However, after a sufficient time, the concentration profile near the electrode can be considered to be stationary with respect to the time required for the impedance measurement.

Following equation (11.7), the concentration is given by

$$c_i = \overline{c}_i + \operatorname{Re}\left\{\widetilde{c}_i e^{j\omega t}\right\} \tag{11.44}$$

Substitution of the definition for concentration (equation (11.44) into the expression for conservation of species i (equation (11.41)) yields

$$j\omega\widetilde{c}_i e^{j\omega t} - D_i \frac{d^2\overline{c}_i}{dy^2} - D_i \frac{d^2\widetilde{c}_i}{dy^2} e^{j\omega t} = 0 \tag{11.45}$$

Upon cancellation of the steady-state terms and division by the term $e^{j\omega t}$,

$$j\omega\widetilde{c}_i - D_i \frac{d^2\widetilde{c}_i}{dy^2} = 0 \tag{11.46}$$

In terms of the dimensionless concentration $\theta_i(y) = \widetilde{c}_i/\widetilde{c}_i(0)$, equation (11.46) becomes

$$j\frac{\omega}{D_i}\theta_i - \frac{d^2\theta_i}{dy^2} = 0 \tag{11.47}$$

The general solution to equation (11.47) is given by:

$$\theta_i = Ae^{y\sqrt{j\frac{\omega}{D_i}}} - Be^{-y\sqrt{j\frac{\omega}{D_i}}} \tag{11.48}$$

and the boundary conditions are:

$$\begin{aligned} \theta_i &\rightarrow 0 \quad \text{as} \quad y \rightarrow \infty \\ \theta_i &= 1 \quad \text{at} \quad y = 0 \end{aligned} \tag{11.49}$$

Thus, $A = 0$ and

$$\theta_i = e^{-y\sqrt{j\frac{\omega}{D_i}}} \tag{11.50}$$

The inverse of the derivative with respect to position y is given by:

$$\frac{-1}{\theta_i'(0)} = \frac{1}{\sqrt{j\frac{\omega}{D_i}}} \tag{11.51}$$

and, following equation (11.27) and the definition of θ_i,

$$\frac{Z_D(\omega)}{Z_D(0)} = \frac{-\widetilde{c}_i(0)}{\left.\frac{d\widetilde{c}_i}{dy}\right|_{y=0}} = \frac{1}{\sqrt{j\frac{\omega}{D_i}}} \tag{11.52}$$

Equation (11.52) is known as the *Warburg impedance*.[15] The expression of the cell impedance is obtained by inserting equation (11.52) into equation (11.20).

11.4 Diffusion through a Solid Film

Diffusion through a stagnant layer of finite thickness can also yield a uniformly accessible electrode. The diffusion impedance response of a coated (or film-covered) electrode, under the condition that the resistance of the coating to diffusion is much larger than that of the bulk electrolyte, is approximated by the diffusion impedance of the coating. This problem is also analyzed in Section 15.4.2.

11.4.1 Region of Film Diffusion Control

On a film-covered rotating disk electrode, for example, the concentration of a mass-transfer-limited species is given by[126]

$$c_i = \frac{c_\infty}{\left(1+\frac{D_f\delta_N}{D\delta_f}\right)}\frac{y}{\delta_f} \tag{11.53}$$

in the coating ($0 < y < \delta_f$), and

$$c_i = c_\infty \left\{ \left[1 - \frac{1}{\left(1+\frac{D_f\delta_N}{D\delta_f}\right)}\right] \operatorname{erf}\left(\frac{y\Gamma(4/3)}{\delta_N}\right) + \frac{1}{\left(1+\frac{D_f\delta_N}{D\delta_f}\right)} \right\} \tag{11.54}$$

in the bulk region ($\delta_f < y < \infty$). The concentration distribution through the stationary film and the bulk region is controlled by two parameters, i.e.,

$$\psi = \frac{D_f\delta_N}{D\delta_f} \tag{11.55}$$

and the ratio of diffusion lengths, δ_N/δ_f. Under the assumption that the diffusivity within the film of porosity ϵ is related to the bulk diffusivity by[88,127]

$$D_f = D\epsilon^{1.5} \tag{11.56}$$

equation (11.55) can be expressed as

$$\psi = \frac{\delta_N}{\delta_f}\epsilon^{1.5} \tag{11.57}$$

Thus, concentration profiles within the coating and the bulk region can be seen to be controlled by the coating porosity ϵ and by the ratio of diffusion lengths δ_N/δ_f.

Remember! 11.2 *The Warburg impedance, equation (11.52), applies for diffusion in an infinite stagnant domain. This expression applies as a high-frequency limit for diffusion in a finite domain.*

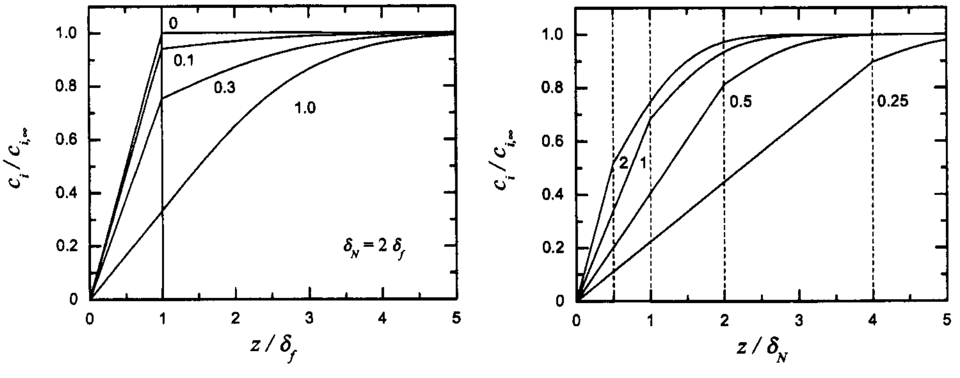

(a) (b)

Figure 11.1: Concentration distribution for a coated rotating disk electrode: a) results obtained for $\delta_N/\delta_f = 2$ with coating porosity as a parameter; b) results obtained for a porosity $\epsilon = 0.3$ and relative coating thickness δ_N/δ_f as a parameter.

The concentration distributions obtained for a film-covered rotating disk electrode are presented in Figure 11.1(a) for $\delta_N/\delta_f = 2$ and with coating porosity as a parameter. As the coating porosity tends toward zero, the resistance of the coating to diffusion dominates, and the concentration at the interface between the coating and the bulk solution is equal to the bulk concentration c_∞. In this case, the diffusion impedance for the electrochemical system is given by that developed in Section 11.4.2 for a stagnant layer of finite thickness. At larger values of coating porosity, both convective diffusion and diffusion through the film are important and should be treated. The manner of treating coupled diffusion impedances is discussed in Section 11.5.

The coating on the electrode can be deposited (e.g., a polymer coating) or it can be produced by the electrochemical reactions. For many electrochemical systems, the growth of a porous film causes it to become the dominant resistance to mass transfer, as is shown in Figure 11.1(b) for a porosity $\epsilon = 0.3$ and with relative film thickness δ_N/δ_f as a parameter. The position variable is scaled to δ_N to emphasize the changing dimension of the coating layer.

Example 11.3 Diffusion through a Film with Porosity = 1: *Does the lack of an abrupt change in slope for a coating porosity equal to* 1.0 *in Figure 11.1(a) mean that the role of a coating can be ignored when calculating the flux and diffusion impedance? Note that some coatings, for example, those formed by microbiological organisms, have a porosity approaching* 1.0.[128]

Solution: *While the concentration profile shown for* $\epsilon = 1.0$ *in Figure 11.1(a) resembles that for an uncoated rotating disk, the flux is affected by the fact that, within the coating, the velocity is equal to zero. The flux to the surface can be given in terms of the concentration*

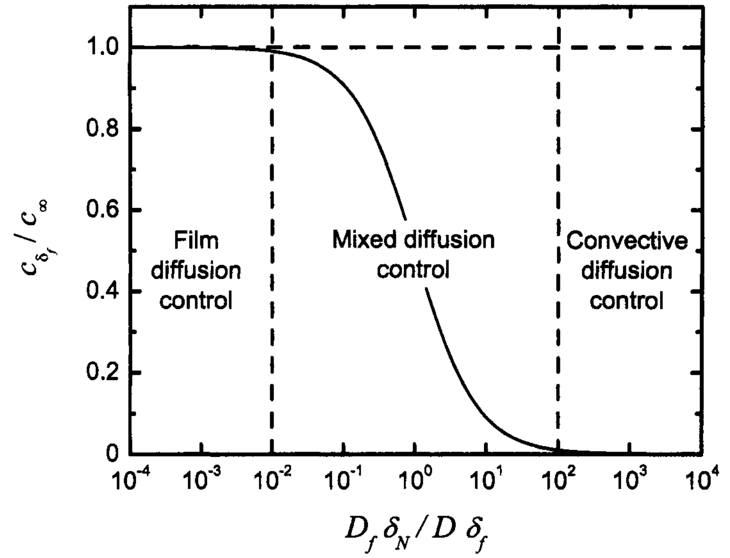

Figure 11.2: Concentration at the interface between the coating and the bulk solution as a function of $\psi = \frac{D_f\delta_N}{D\delta_f}$.

at the coating/bulk solution interface as

$$N_i = D\epsilon^{1.5}\frac{c_{i,\delta_f}}{\delta_f} \tag{11.58}$$

or, for $\epsilon = 1$

$$N_i = D\frac{c_{i,\delta_f}}{\delta_f} \tag{11.59}$$

For a given film thickness δ_f*, the important parameter is the concentration at the film surface. If this concentration tends toward zero, the film has a negligible influence on mass transfer. Otherwise, the influence of the film cannot be neglected.*

The concentration at the interface between the film and the bulk electrolyte indicates whether the diffusion impedance of the system can be assumed to be that of the stationary film. The interface concentration, given by

$$\frac{c_{i,\delta_f}}{c_{i,\infty}} = \frac{1}{1+\psi} \tag{11.60}$$

is a function only of $\psi = D_f\delta_N/D\delta_f$. Regions of mass-transfer control can be identified, as shown in Figure 11.2. When the dimensionless interface concentration approaches 1, the film diffusion impedance discussed in Section 11.4.2 dominates. When the dimensionless interface concentration approaches 0, the film diffusion impedance can be neglected, and the convective-diffusion response discussed in Section 11.6 dominates. In the intermediate region, both convective diffusion and diffusion through the film are important, as discussed in Section 11.5.

Example 11.4 Continuation of Example 11.3: *Can the diffusion impedance of a film with $\epsilon = 1.0$ be ignored?*

Solution: *As seen from equation (11.59), for a given film thickness δ_f, the important parameter is the concentration at the film surface. If this concentration tends toward zero, the film has a negligible influence on mass transfer. Otherwise, the influence of the film cannot be neglected. As*

$$\lim_{\epsilon \to 1} \frac{D_f \delta_N}{D \delta_f} = \frac{\delta_N}{\delta_f} \tag{11.61}$$

the role of a film of fixed thickness of $\epsilon = 1.0$ depends solely on the rotation speed of the disk. As the disk speed increases, δ_N decreases, and the film diffusion becomes more important.

11.4.2 Film Impedance Response

Equation (11.41) governs the diffusion response of a stationary film. The steady-state boundary conditions are applied at $y = \delta_f$ and $y = 0$ as

$$\begin{aligned} \overline{c_i} &= c_{i,\infty} \quad \text{at} \quad y = \delta_f \\ \overline{c_i} &= c_{i,0} \quad \text{at} \quad y = 0 \end{aligned} \tag{11.62}$$

and the steady-state solution is given as

$$\begin{aligned} \overline{c_i} = c_i(0) + \frac{y}{\delta_f}\left(c_{i,\infty} - c_i(0)\right) \quad &\text{for} \quad y < \delta_f \\ \overline{c_i} = c_{i,\infty} \quad &\text{for} \quad y \geq \delta_f \end{aligned} \tag{11.63}$$

Equation (11.63) represents an asymptotic limit for the solution presented as equations (11.53) and (11.54).

Equation (11.41) can be written in terms of the oscillating concentration and dimensionless position as

$$\frac{d^2\theta_i}{d\xi^2} - j\mathrm{K}_i\theta_i = 0 \tag{11.64}$$

where

$$\xi = \frac{y}{\delta_f} \tag{11.65}$$

and

$$\mathrm{K}_i = \frac{\omega \delta_f^2}{D_i} \tag{11.66}$$

represents a dimensionless frequency for species i.

The general solution to equation (11.64) is given by

$$\theta_i = A_i e^{\xi\sqrt{j\mathrm{K}_i}} - B_i e^{-\xi\sqrt{j\mathrm{K}_i}} \tag{11.67}$$

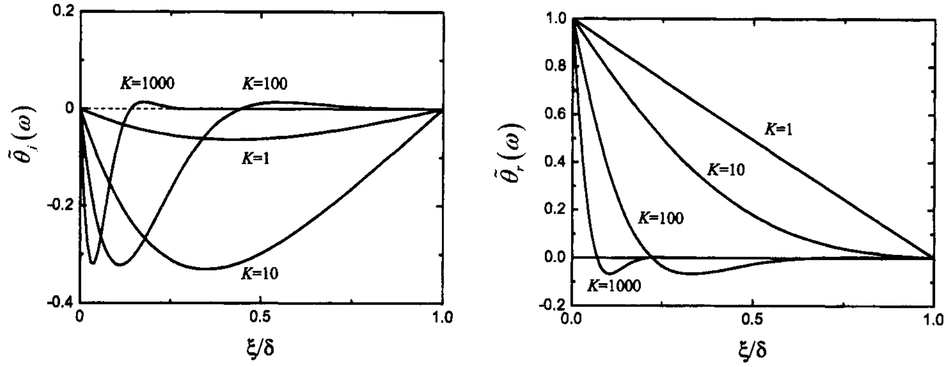

(a) (b)

Figure 11.3: Oscillating concentration profiles for a finite stagnant diffusion layer: a) imaginary part; b) real part.

The appropriate boundary conditions for a diffusion layer of finite thickness are that

$$\begin{aligned} \theta_i &= 0 \quad \text{at} \quad \zeta = 1 \\ \theta_i &= 1 \quad \text{at} \quad \zeta = 0 \end{aligned} \tag{11.68}$$

Thus,

$$\begin{aligned} \theta_i &= \frac{\sinh\left((\zeta - 1)\sqrt{j\mathrm{K}_i}\right)}{\sinh\left(-\sqrt{j\mathrm{K}_i}\right)} \quad \text{at} \quad \zeta < 1 \\ \theta_i &= 0 \quad \text{at} \quad \zeta \geq 1 \end{aligned} \tag{11.69}$$

The oscillating concentration variables are given in Figure 11.3 as a function of dimensionless position. The behavior of $\theta_i(\zeta)$ for high frequencies, e.g., $\mathrm{K}_i = 100$, resembles that obtained for a stagnant medium of infinite dimension, whereas the behavior at low frequencies, e.g., $\mathrm{K}_i < 10$, is influenced by the finite extent of the diffusion layer.

It is perhaps more instructive to explore the behavior of the concentration, given by equation (11.44). The oscillating contribution to the concentration, given by $\mathrm{Re}\left\{\tilde{c}_i e^{j\omega t}\right\}$, is presented in Figures 11.4(a) and (b) for dimensionless frequencies of 100 and 1, respectively, with dimensionless time as a parameter. At the higher frequency, the concentration perturbation does not extend to the limits of the diffusion layer. At the lower frequency, the perturbation extends to the limit of the diffusion layer, and an abrupt change is seen at $\zeta = 1$, the limit of the stagnant film.

The concentration profile expected for a system at one-half of the mass-transfer-limited current and for a concentration perturbation of 20 percent at the interface (see equation (11.44)) is presented in Figure 11.5 with dimensionless time as a parameter. At the higher frequency, the propagation of the disturbance away from

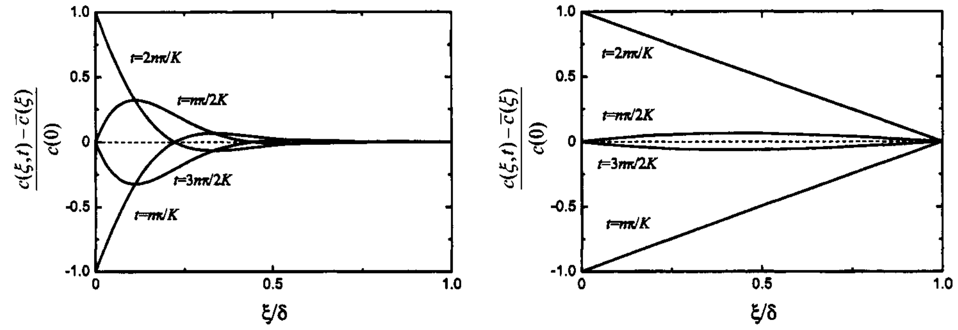

(a) (b)

Figure 11.4: Oscillating concentration as a function of position with time as a parameter for a finite stagnant diffusion layer: a) K=100; b) K=1.

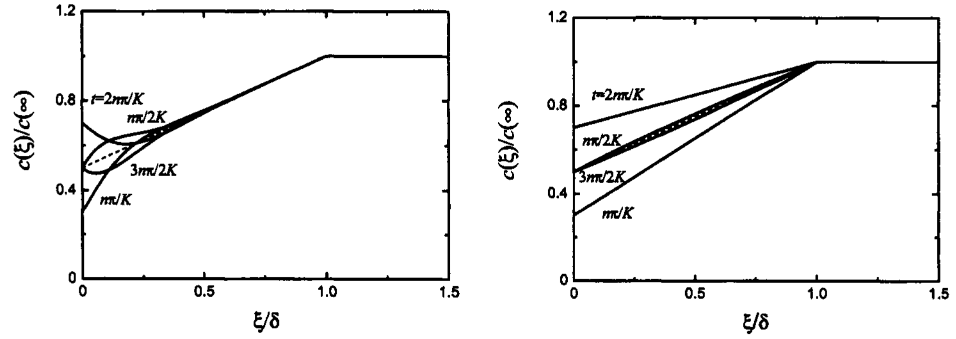

(a) (b)

Figure 11.5: Concentration as a function of position with time as a parameter for a finite stagnant diffusion layer: a) K=100; b) K=1.

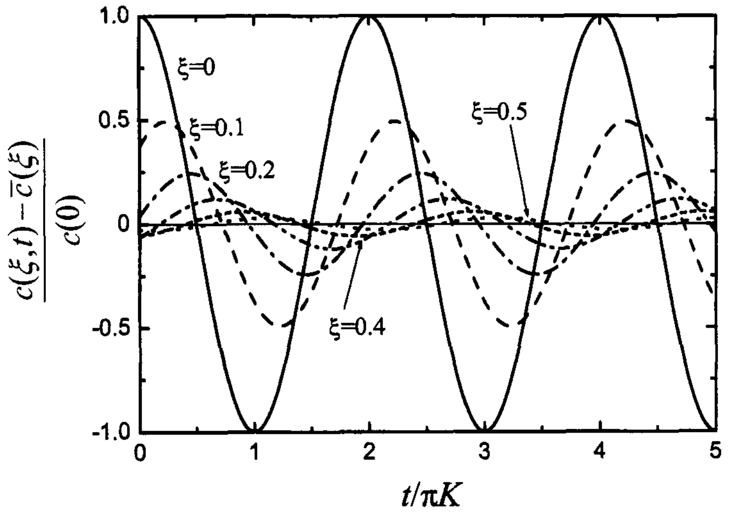

Figure 11.6: Oscillating concentration as a function of time with position as a parameter for a finite stagnant diffusion layer.

the electrode surface lags behind the perturbation at the surface. At lower frequencies, the concentration far from the surface responds with almost no phase lag. In the limit that $K_i \to 0$, the phase lag tends toward zero and, correspondingly, the imaginary part of the impedance tends toward zero.

The concentration perturbation for $K_i = 100$ is given in Figure 11.6 as a function of time with dimensionless position as a parameter. The extent to which the concentration at any position lags behind the concentration at the surface is a function of position. The variation of phase lag with position is consistent with the propagation of a wave through a dissipating medium.

The reciprocal of the derivative with respect to position ξ is given by

$$\frac{-1}{\theta_i'(0)} = \frac{\tanh\left(\sqrt{jK_i}\right)}{\sqrt{jK_i}} \tag{11.70}$$

Equation (11.70) can be considered to be a finite-length diffusion impedance. As $\tanh(\infty) = 1$, the impedance response asymptotically approaches the response for an infinite domain at high frequencies, i.e.,

$$\lim_{K_i \to \infty} \frac{-1}{\theta_i'(0)} = \frac{1}{\sqrt{jK_i}} \tag{11.71}$$

Equation (11.71) is the Warburg impedance. The impedance response for a stagnant layer is often imposed incorrectly for situations where convective diffusion takes place. The more correct approach is to account explicitly for the role of convection.

11.5 Coupled Diffusion Impedance

As shown in Figure 11.2, there exists a significant parameter space for film-covered electrodes in which the diffusion impedance must account for both convective diffusion associated with the external imposed flow and diffusion through a stagnant layer. Following Deslouis et al.,[126] the net diffusion impedance can be expressed as being composed of contributions from film and convective-diffusion terms

$$Z_{\mathrm{D,net}} = \frac{Z_{\mathrm{D}} + \frac{D}{D_f}\frac{\delta_f}{\delta_N} Z_{\mathrm{D},f}}{Z_{\mathrm{D},f} Z_{\mathrm{D}} \left(j\omega \frac{\delta_f^2}{D_f} \right) + \frac{D}{D_f}\frac{\delta_f}{\delta_N}} \tag{11.72}$$

where the inner term $Z_{\mathrm{D},f}$ is the finite-length diffusion impedance corresponding to a porous layer of thickness δ_f, and the outer term Z_{D} may correspond to either a stagnant or a convective region of finite thickness δ_N. In this case, the effective diffusion impedance $Z_{\mathrm{D,net}}$ is a function of the time constant $\tau_f = \delta_f^2/D_f$, the ratio $D\delta_f/D_f\delta_N$, and the Schmidt number Sc. The coupling of film and convective-diffusion impedances is also developed in Section 15.4.2 for electrohydrodynamic impedance measurements.

Example 11.5 Diffusion Impedances in Series: *If, as is shown in equation (4.23), the impedance corresponding to two resistors in series is equal to the sum of the resistances, why is it incorrect to treat diffusion through two layers by adding two diffusion impedances?*

Solution: *The issue is that the condition at the interface between the two diffusion layers is not treated correctly when diffusion impedances, such as presented in equation (11.70), are added. The solutions to the two sets of equations are coupled by the continuity of concentration at the interface, as seen in Figure 11.1.*

11.6 Rotating Disk

A schematic illustration of the flow field generated by a rotating disk is presented in Figure 11.7. The rotation of the disk causes a spiral movement of the fluid, seen in Figure 11.7(a), which results in a net velocity toward the disk and in the radial direction. A projection of the trajectories onto a plane at a fixed axial position,

Remember! 11.3 *The impedance associated with diffusion through a series of layers cannot be modeled by adding the diffusion impedances for each individual layer. Such a treatment does not account correctly for the conditions at the interface between the layers.*

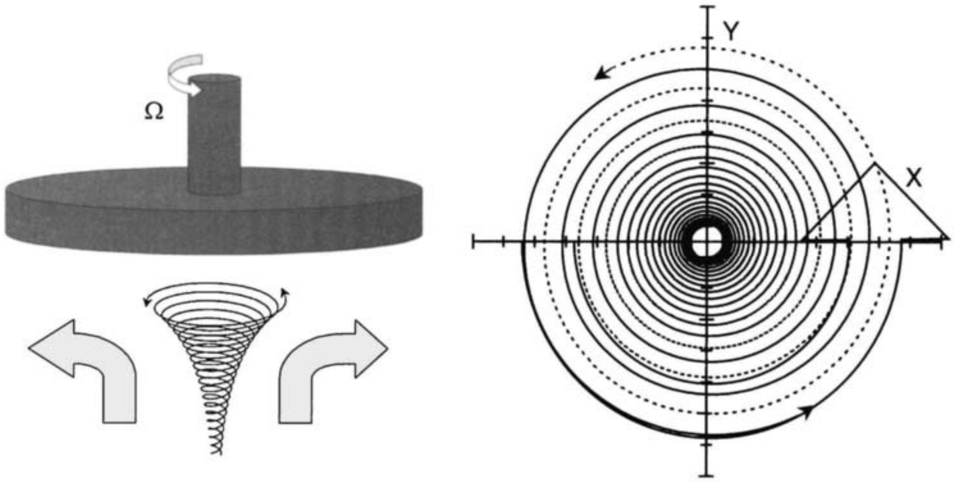

(a) (b)

Figure 11.7: Flow patterns associated with a rotating disk: a) a three-dimensional representation of flow trajectories that lead to a net flow toward the disk and in the radial direction. The axial scale was expanded greatly in order to allow visualization of the flow trajectories. b) a projection of the flow trajectories onto a plane at a fixed axial position.

shown in Figure 11.7(b), shows that the dominant velocity component is in the θ-direction. The corresponding radial and axial velocities are much smaller. The rotating disk, therefore, can be regarded to be an inefficient pump that draws fluid toward the disk surface and ejects it in the radial direction. The popularity of the rotating disk electrode in the use of frequency-domain techniques has motivated development of sophisticated models for interpretation of experimental data.

11.6.1 Fluid Flow

The steady flow created by an infinite disk rotating at a constant angular velocity in a fluid with constant physical properties was first studied by von Kármán.[129] The solution was sought by using a separation of variables using a dimensionless distance

$$\zeta = y\sqrt{\overline{\Omega}/\nu} \tag{11.73}$$

and dimensionless radial velocity

$$v_r = r\overline{\Omega}F(\zeta) \tag{11.74}$$

angular velocity

$$v_\theta = r\overline{\Omega}G(\zeta) \tag{11.75}$$

and axial velocity

$$v_y = \sqrt{\nu\overline{\Omega}}H(\zeta) \tag{11.76}$$

where ν is the kinematic viscosity and $\overline{\Omega}$ the rotation speed.

Upon introduction of equations (11.74), (11.75), and (11.76), the equation of continuity and the Navier-Stokes equations can be solved numerically.[88,129] As shown by Cochran,[130] the variables F, G, and H can be written as two sets of series expansions for small and large values of ζ, respectively. The series solutions for small values of ζ are especially relevant to the mass-transfer problem. In particular, the derivatives at $\zeta = 0$ are essential in order to determine the first coefficient of the series expansions. The other coefficients are deduced from the first one by using the equation of continuity and the Navier-Stokes equations,

$$H = -a\zeta^2 + \frac{\zeta^3}{3} + \frac{b}{6}\zeta^4 + \dots \tag{11.77}$$

$$F = a\zeta - \frac{\zeta^2}{2} - \frac{b}{3}\zeta^3 + \dots \tag{11.78}$$

$$G = 1 + b\zeta + \frac{1}{3}\zeta^3 + \dots \tag{11.79}$$

where $a = 0.51023$ and $b = -0.61592$. The contribution of the second and third terms in the velocity expansion becomes more significant farther from the disk electrode.

11.6.2 Mass Transfer

The mathematical models for the convective-diffusion impedance associated with convective diffusion to a disk electrode are developed here in the context of a generalized framework in which a normalized expression accounts for the influence of mass transfer.

Substitution of the definition for concentration (equation (11.44)) into the expression for conservation of species i (equation (11.3)) in one dimension yields

$$j\omega\widetilde{c}_i e^{j\omega t} + v_y \frac{d\overline{c}_i}{dy} + v_y \frac{d\widetilde{c}_i}{dy} e^{j\omega t} - D_i \frac{d^2\overline{c}_i}{dy^2} - D_i \frac{d^2\widetilde{c}_i}{dy^2} e^{j\omega t} = 0 \tag{11.80}$$

The solution to the steady-state equation

$$v_y \frac{d\overline{c}_i}{dy} - D_i \frac{d^2\overline{c}_i}{dy^2} = 0 \tag{11.81}$$

with boundary conditions given as equation (11.42), is given as

$$\Theta_i = \frac{c_i(y) - c_i(0)}{c_{i,\infty} - c_i(0)} = \frac{\int\limits_0^y \exp\left[\int\limits_0^y \frac{v_y}{D_i} dy\right] dy}{\int\limits_0^\infty \exp\left[\int\limits_0^y \frac{v_y}{D_i} dy\right] dy} \tag{11.82}$$

where the axial velocity can be expressed in terms of the expansion presented as equation (11.77).[88]

Upon cancellation of the steady-state terms and division by the term $e^{j\omega t}$, equation (11.80) can be expressed as

$$j\omega\tilde{c}_i + v_y\frac{d\tilde{c}_i}{dy} - D_i\frac{d^2\tilde{c}_i}{dy^2} = 0 \tag{11.83}$$

Following Tribollet and Newman,[131] the dimensionless form of the equation governing the contribution of mass transfer to the impedance response of the disk electrode is developed here in terms of dimensionless position

$$\xi = \frac{y}{\delta_i} \tag{11.84}$$

where

$$\delta_i = \left(\frac{3D_i}{a\nu}\right)^{1/3}\sqrt{\frac{\nu}{\Omega}} = \left(\frac{3}{a}\right)^{1/3}\frac{1}{\mathrm{Sc}^{1/3}}\sqrt{\frac{\nu}{\Omega}} \tag{11.85}$$

is a characteristic distance for mass transport of species i, and dimensionless frequency

$$\mathrm{K}_i = \frac{\omega}{\Omega}\left(\frac{9\nu}{a^2D_i}\right)^{1/3} = \frac{\omega}{\Omega}\left(\frac{9}{a^2}\right)^{1/3}\mathrm{Sc}^{1/3} = \frac{\omega\delta_i^2}{D_i} \tag{11.86}$$

By introducing the dimensionless concentration $\theta_i(\xi) = \tilde{c}_i/\tilde{c}_i(0)$, equation (11.83) becomes

$$\frac{d^2\theta_i}{d\xi^2} + \left(3\xi^2 - \left(\frac{3}{a^4}\right)^{1/3}\frac{\xi^3}{Sc^{1/3}} - \frac{b}{6}\left(\frac{3}{a}\right)^{5/3}\frac{\xi^4}{Sc^{2/3}}\right)\frac{d\theta_i}{d\xi} - j\mathrm{K}_i\theta_i = 0 \tag{11.87}$$

where three terms were included in the expansion for axial velocity given as equation (11.77).

A solution to equation (11.87) can be found that satisfies the boundary conditions

$$\begin{aligned} \theta_i &\rightarrow 0 \quad \text{as} \quad \xi \rightarrow \infty \\ \theta_i &= 1 \quad \text{at} \quad \xi = 0 \end{aligned} \tag{11.88}$$

The approaches made to obtain such a solution differ in the types of assumptions made concerning the velocity expansions.

11.6.3 Classification of Models for Convective Diffusion

A significant effort has been expended to identify analytic solutions for equation (11.87). These differ primarily in the manner in which the convective contribution is approximated. The different models and their influence on the impedance response are described in this section.

The classification of models for convective diffusion to a rotating disk electrode may be understood in the context of the solution to the steady-state equation (11.3).

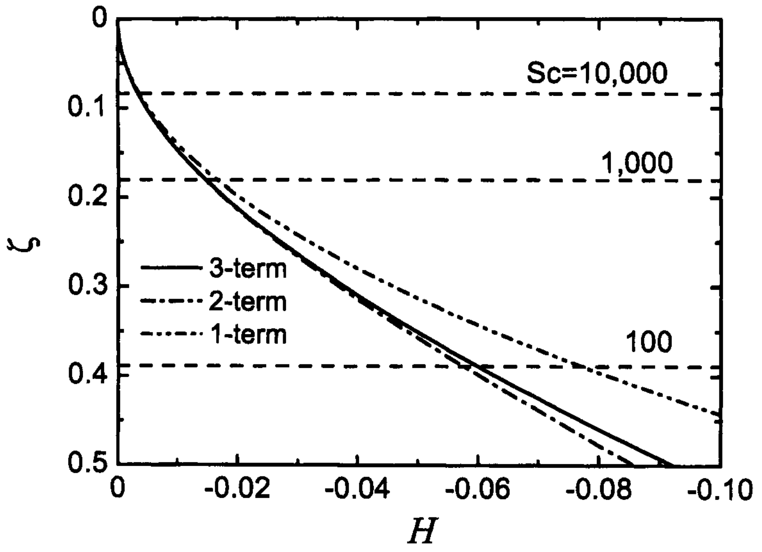

Figure 11.8: Distribution of axial velocity for a region near a rotating disk. The characteristic length for mass transfer is indicated by dashed lines for Schmidt numbers of 10,000, 1,000, and 100, respectively.

The current density can be expressed in terms of the gradient of dimensionless concentration at the electrode surface as[132]

$$\frac{1}{\mathrm{Sc}}\Theta'(0) = \frac{0.62045\mathrm{Sc}^{-2/3}}{1 + 0.2980\mathrm{Sc}^{-1/3} + 0.14514\mathrm{Sc}^{-2/3} + \mathrm{O}(\mathrm{Sc}^{-1})} \tag{11.89}$$

The corrections to the current density were obtained by accounting for additional terms in the velocity expansion given as equation (11.77).

The influence of the accuracy of the velocity expansion is illustrated in Figure 11.8. The characteristic length for mass transfer to a disk electrode is given by $\zeta/\xi = \left(\frac{a\mathrm{Sc}}{3}\right)^{-1/3}$. For Sc = 10,000, the characteristic length for mass transfer is 0.084 of that for the velocity boundary layer. The error associated with using only the first term in the velocity expansion (11.77) is −0.02 percent of the free-stream velocity 0.88447 (or −5 percent of the local value). For Sc = 1,000, the characteristic length for mass transfer is 0.18 of that for the velocity boundary layer. The error associated with using only the first term in the velocity expansion is −0.2 percent of the free-stream velocity (or −12 percent of the local value). For Sc = 100, the characteristic length for mass transfer is 0.39 of that for the velocity boundary layer. The error associated with using only the first term in the velocity expansion is −2 percent of the free-stream velocity (or −29 percent of the local value). Most electrolytic systems have a Schmidt number on the order of 1,000. The error in equation (11.89) caused by neglecting the second and higher terms in the velocity expansion is less than 3 percent. The errors have been shown to be significantly larger for frequency-domain calculations.

Nernst Hypothesis

Within the Nernst hypothesis, the diffusion impedance is assumed to be that for a stagnant film of effective thickness $\delta_{N,i}$ that is related to velocity by

$$\delta_{N,i} = \Gamma(4/3)\left(\frac{3}{a}\right)^{1/3}\frac{1}{\mathrm{Sc}_i^{1/3}}\sqrt{\frac{\nu}{\Omega}} \tag{11.90}$$

The impedance response is given by equation (11.70), where the film thickness is replaced by the effective thickness $\delta_{N,i}$. As shown in Figure 11.5, a nonphysical abrupt change in the concentration is seen at $\xi = 1$. Such an abrupt change may be expected for diffusion through a truly stagnant medium such as a solid, but should not be expected for a convective-diffusion problem. This lack of agreement with the physics of the system causes the Nernst hypothesis to yield incorrect results at low frequencies, although the asymptotic behavior at large frequencies is in agreement with that obtained by a correct solution for the convective-diffusion impedance.

Assumption of an Infinite Schmidt Number

Under the assumption that the Schmidt number is infinitely large, the axial velocity can be approximated by the first term of the expansion given as equation (11.77). Under steady-state conditions, neglect of higher-order terms in the expansion causes an error on the order of about 3 percent in the value of the mass-transfer-limited current density. As discussed later, the errors caused by neglecting higher-order terms in the expansion can be significantly larger in the frequency domain.

The convective-diffusion equation (11.87) is reduced to:

$$\frac{d^2\theta_i}{d\xi^2} + 3\xi^2\frac{d\theta_i}{d\xi} - j\mathrm{K}_i\theta_i = 0 \tag{11.91}$$

Many authors have given analytic solutions with differing degrees of accuracy. Deslouis et al.[133] developed a method that, after an approximation, reduces the problem to the canonical equation for Airy functions. Tribollet and Newman[134] gave a solution under the form of two series: one for $K < 10$ and one for $K > 10$. The two series overlapped well.

Treatment of a Finite Schmidt Number

For a Schmidt number of 1,000, use of an infinite Schmidt number approximation in the evaluation of the Schmidt number from impedance data resulted in 24.4

Remember! 11.4 *The formula for impedance obtained under the Nernst hypothesis, as given by equation (11.70), provides a poor model for convective-diffusion impedance.*

---

percent error in the estimation of Sc.[135] The consequence of neglecting higher-order terms in the velocity expansion is therefore much more significant than is seen for the steady-state case. The complete solution for the convective-diffusion impedance requires, in general, a numerical solution. The discussion here follows that presented by Tribollet and Newman.[131]

Several authors have addressed the influence of a finite value of the Schmidt number on expressions for the convective-diffusion impedance. Levart and Schuhmann[136] showed that the concentration term could be expressed as a series expansion in $\mathrm{Sc}^{1/3}$, i.e.,

$$\theta_i(\xi, \mathrm{Sc}, K) = \theta_{i,0}(\xi, K) + \frac{\theta_{i,1}(\xi, K)}{\mathrm{Sc}^{1/3}} + \frac{\theta_{i,2}(\xi, K)}{\mathrm{Sc}^{2/3}} + \ldots \tag{11.92}$$

where $\theta_{i,0}$, $\theta_{i,1}$, and $\theta_{i,2}$ are the solutions of the corresponding coupled differential equations

$$\frac{d^2\theta_{i,0}}{d\xi^2} + 3\xi^2 \frac{d\theta_{i,0}}{d\xi} - j\mathrm{K}_i\theta_{i,0} = 0 \tag{11.93}$$

$$\frac{d^2\theta_{i,1}}{d\xi^2} + 3\xi^2 \frac{d\theta_{i,1}}{d\xi} - j\mathrm{K}_i\theta_{i,1} = \left(\frac{3}{a^4}\right)^{1/3} \xi^3 \frac{d\theta_{i,0}}{d\xi} \tag{11.94}$$

and

$$\frac{d^2\theta_{i,2}}{d\xi^2} + 3\xi^2 \frac{d\theta_{i,2}}{d\xi} - j\mathrm{K}_i\theta_{i,2} = \frac{b}{6}\left(\frac{3}{a}\right)^{1/3} \xi^4 \frac{d\theta_{i,0}}{d\xi} + \left(\frac{3}{a^4}\right)^{1/3} \xi^3 \frac{d\theta_{i,1}}{d\xi} \tag{11.95}$$

subject to boundary conditions

$$\begin{aligned} &\theta_{i,0} \rightarrow 0; \quad \theta_{i,1} \rightarrow 0; \quad \text{and} \quad \theta_{i,2} \rightarrow 0 \quad \text{as} \quad \xi \rightarrow \infty \\ &\theta_i = 1; \quad \theta_{i,1} = 0; \quad \text{and} \quad \theta_{i,2} = 0 \quad \text{at} \quad \xi = 0 \end{aligned} \tag{11.96}$$

The convective-diffusion impedance can be tabulated directly as a function of the Schmidt number as

$$\frac{-1}{\theta_i'(0)} = Z_{(0)} + \frac{Z_{(1)}}{\mathrm{Sc}^{1/3}} + \frac{Z_{(2)}}{\mathrm{Sc}^{2/3}} + \ldots \tag{11.97}$$

Tabulated values of $Z_{(0)}$, $Z_{(1)}$, and $Z_{(2)}$ have been presented by Tribollet and Newman as a function of $p\mathrm{Sc}^{1/3}$ where p is the frequency made dimensionless by the steady rotation rate of the disk electrode, $p = \omega/\overline{\Omega}$.[131] In terms of p, $\mathrm{K}_i = 3.258p\mathrm{Sc}^{1/3}$. The relative contributions of the terms can be seen in Figure 11.9.

A similar development was provided by Tribollet and Newman[131] for electrohydrodynamic impedance. The use of look-up tables facilitates regression of models to experimental data that take full account of the influence of a finite Schmidt number on the convective-diffusion impedance. Use of only the first term in equation (11.97) yields a numerical solution for an infinite Schmidt number. Tribollet and Newman report use of the first two terms in equation (11.97).[131] The low level of stochastic noise in experimental data justifies use of the three-term expansion reported here.

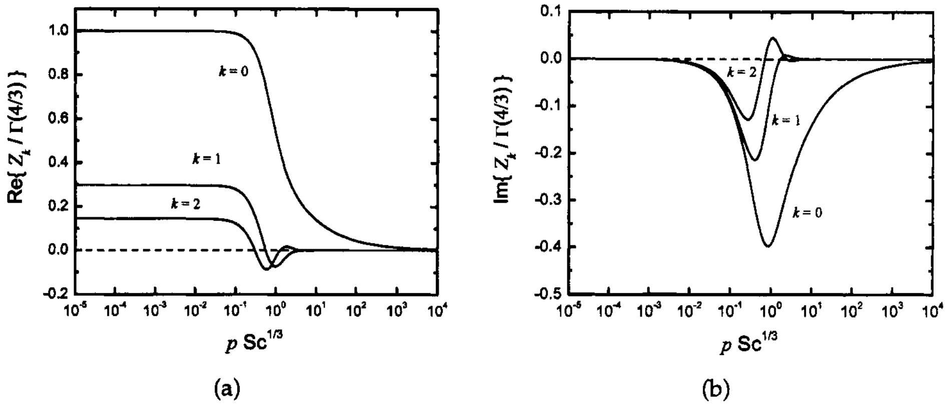

Figure 11.9: Values for dimensionless contributions $Z_{(0)}$, $Z_{(1)}$, and $Z_{(2)}$ to the diffusion impedance (see equation (11.97)) as a function of $p\mathrm{Sc}^{1/3}$: a) real part; and b) imaginary part.[131]

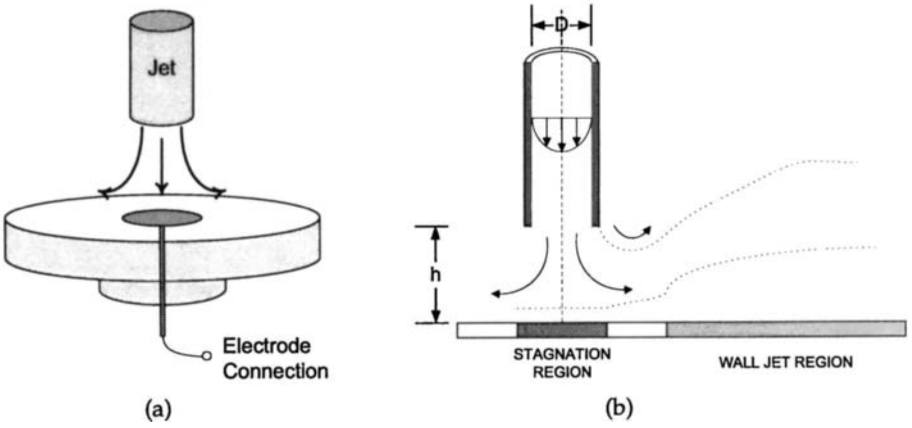

Figure 11.10: A disk electrode subjected to a submerged impinging jet: a) schematic illustration; b) identification of flow regimes.

11.7 Submerged Impinging Jet

The axisymmetric impinging jet, shown in Figure 11.10(a), is a very attractive, if somewhat underemployed, system for electrochemical investigations. Within the stagnation region, shown in Figure 11.10(b), the axial velocity is independent of radial position and convective diffusion to the disk is uniform, much as is seen for the rotating disk electrode.[137–139] Because the mass-transfer rate is uniform for an electrode that lies entirely within the stagnation region, differential mass-transfer cells are not established. Thus, the impinging jet has the attractive uniform accessibility to mass transfer seen for the rotating disk. In contrast to the rotating disk, the electrode is stationary and is therefore suitable for *in-situ* observation.[139–142]

11.7.1 Fluid Flow

The fluid flow within the region of the electrode in an impinging jet cell is well-defined.[143–147] The submerged impinging jet geometry can be made to give uniform mass-transfer rates across a disk electrode within the stagnation region. The stagnation region is defined to be the region surrounding the stagnation point in which the axial velocity, given by

$$v_y = -\sqrt{a_{\mathrm{IJ}}\nu}\,\phi(\eta) \tag{11.98}$$

is independent of radial position, and the radial velocity is given by

$$v_r = \frac{a_{\mathrm{IJ}} r}{2}\frac{d\phi(\eta)}{d\eta} \tag{11.99}$$

where a_{IJ} is the hydrodynamic constant that is a function only of geometry and fluid velocity, r and y are the radial and axial positions, respectively, ν is the kinematic viscosity, and ϕ is the stream function that is given in terms of dimensionless axial position $\eta = y\sqrt{a_{\mathrm{IJ}}/\nu}$ as[147]

$$\phi(\eta) = 1.352\eta^2 - \frac{1}{3}\eta^3 + 7.2888\times 10^{-3}\eta^6 + \ldots \tag{11.100}$$

Esteban et al. used ring electrodes to find that the stagnation region extends to a radial distance roughly equal to the inside radius of the nozzle.[138] A refined analysis by Baleras et al. showed that the stagnation region becomes smaller at large values of the ratio of nozzle height h to nozzle diameter d.[148]

Within the stagnation region, the surface shear stress τ_{ry} is given by

$$\tau_{ry} = -1.312 r(\mu\rho)^{\frac{1}{2}} a_{\mathrm{IJ}}^{\frac{3}{2}} \tag{11.101}$$

where μ and ρ are the viscosity and density of the fluid, respectively. The hydrodynamic constant a_{IJ} can be determined experimentally using ring or disk electrodes at the mass-transfer-limited condition and is proportional to the jet velocity.

11.7.2 Mass Transfer

The equation that governs steady-state mass transfer to the impinging jet electrode is equation (11.81), the same as that for the rotating disk. The boundary conditions are given as equation (11.42), and the solution is given as equation (11.82). The only difference between the solution presented for the rotating disk and here for the impinging jet is that the axial velocity for the disk is expressed as equation (11.77), whereas the expansion for the impinging jet system is given as equation (11.100).

Under the assumption that the electrode is uniformly accessible, the equation governing mass transfer in the frequency domain is given by

$$\frac{d^2\widetilde{\theta}_i}{d\xi^2} + \left(3\xi^2 - \left(\frac{3}{1.352^4}\right)^{1/3}\frac{\xi^3}{\mathrm{Sc}^{1/3}} + \ldots\right)\frac{d\widetilde{\theta}_i}{d\xi} - j\mathrm{K}_i\widetilde{\theta}_i = 0 \tag{11.102}$$

where

$$\mathrm{K}_i = \frac{\omega}{a_{\mathrm{IJ}}}\left(\frac{9}{(1.352)^2}\right)^{1/3}\mathrm{Sc}_i^{1/3} = 1.70123\frac{\omega \mathrm{Sc}_i^{1/3}}{a_{\mathrm{IJ}}} \tag{11.103}$$

represents a dimensionless frequency, and $\xi = y/\delta_i$ is a dimensionless position where

$$\delta_i = \left(\frac{3}{1.352}\right)^{1/3}\frac{1}{\mathrm{Sc}^{1/3}}\sqrt{\frac{\nu}{a_{\mathrm{IJ}}}} = 1.180\frac{1}{\mathrm{Sc}^{1/3}}\sqrt{\frac{\nu}{a_{\mathrm{IJ}}}} \tag{11.104}$$

is a characteristic length for transport of species i.

Following Tribollet and Newman,[131] the concentration term could be expressed as a series expansion in $\mathrm{Sc}^{-1/3}$ as

$$\widetilde{\theta}_i = \widetilde{\theta}_{i,0} + \frac{\widetilde{\theta}_{i,1}}{\mathrm{Sc}^{1/3}} + \frac{\widetilde{\theta}_{i,2}}{\mathrm{Sc}^{2/3}} + \ldots \tag{11.105}$$

where $\widetilde{\theta}_{i,k}$ represents the solution to

$$\frac{d^2\widetilde{\theta}_{i,0}}{d\xi^2} + 3\xi^2\frac{d\widetilde{\theta}_{i,0}}{d\xi} - j\mathrm{K}_i\widetilde{\theta}_{i,0} = 0 \tag{11.106}$$

$$\frac{d^2\widetilde{\theta}_{i,1}}{d\xi^2} + 3\xi^2\frac{d\widetilde{\theta}_{i,1}}{d\xi} - j\mathrm{K}_i\widetilde{\theta}_{i,1} = \left(\frac{3}{(1.352)^4}\right)^{1/3}\xi^3\frac{d\widetilde{\theta}_{i,0}}{d\xi} \tag{11.107}$$

and

$$\frac{d^2\widetilde{\theta}_{i,2}}{d\xi^2} + 3\xi^2\frac{d\widetilde{\theta}_{i,2}}{d\xi} - j\mathrm{K}_i\widetilde{\theta}_{i,2} = \left(\frac{3}{(1.352)^4}\right)^{1/3}\xi^3\frac{d\widetilde{\theta}_{i,1}}{d\xi} \tag{11.108}$$

The convective-diffusion impedance can be tabulated directly as a function of the Schmidt number as

$$\frac{1}{\widetilde{\theta}_i'(0)} = Z_{(0)} + \frac{Z_{(1)}}{\mathrm{Sc}^{1/3}} + \frac{Z_{(2)}}{\mathrm{Sc}^{2/3}} + \ldots \tag{11.109}$$

Tabulated values of $Z_{(0)}$, $Z_{(1)}$, and $Z_{(2)}$ were found as a function of $p\mathrm{Sc}^{1/3}$ where p is the frequency made dimensionless by the hydrodynamic constant, $p = \omega/a_{\mathrm{IJ}}$. The relative contributions of the terms can be seen in Figure 11.11.

11.8 Rotating Cylinders

The rotating cylinder is a popular tool for electrochemical research because it is convenient to use and both the primary and mass-transfer-limited current distributions are uniform.[149] A schematic representation of the rotating cylinder is presented in Figure 11.12. At very low rotation speeds, the fluid flows in concentric circles around the rotating cylinder, satisfying a no-slip condition at the rotating inner cylinder and at the stationary outer cylinder. Since there is no velocity component in the radial direction, there is no convective enhancement to mass transfer.

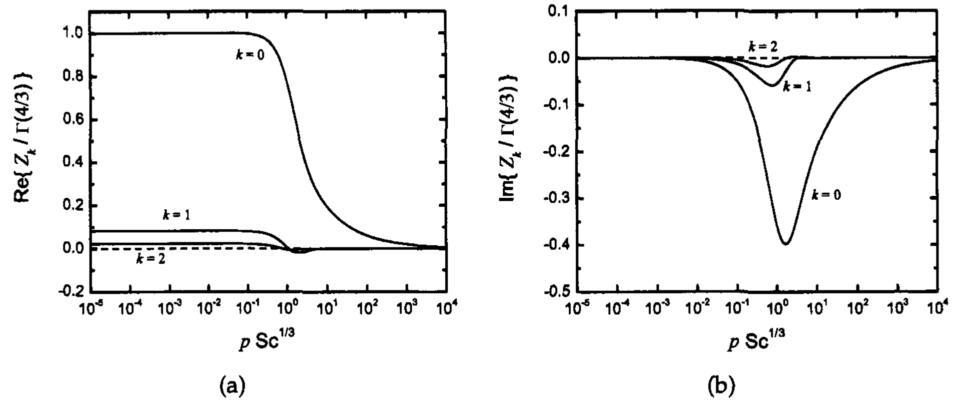

Figure 11.11: Values for dimensionless contributions $Z_{(0)}$, $Z_{(1)}$, and $Z_{(2)}$ to the diffusion impedance (see equation (11.109)) as functions of $p\mathrm{Sc}^{1/3}$; a) real part; and b) imaginary part.[131]

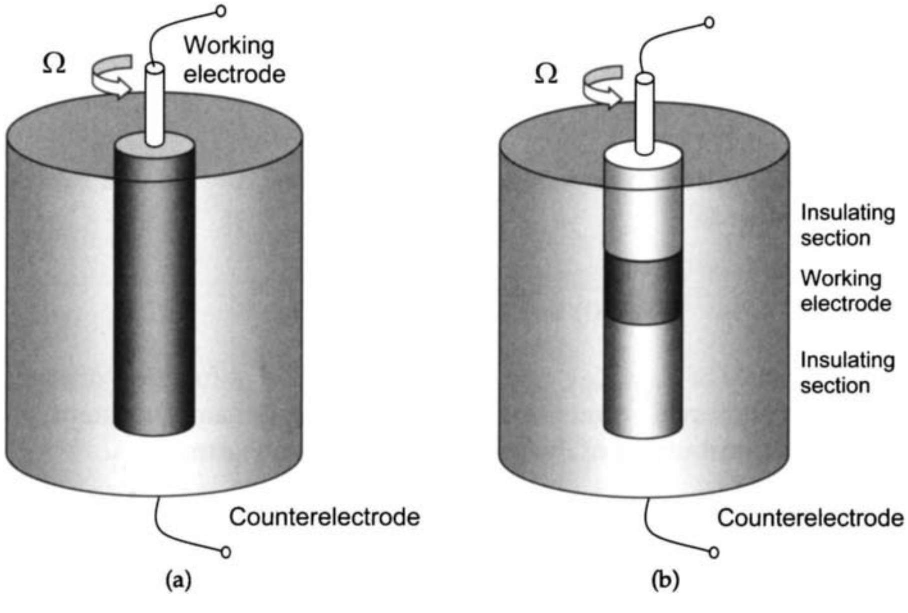

Figure 11.12: Schematic representation of a rotating cylinder electrode; a) entire cylinder used as working electrode. This geometry provides a uniform current and potential distribution at and below the mass-transfer-limited current. b) band-shape cylindrical coupon used as a working electrode. This geometry is useful for studies conducted at the open-circuit condition.

This simple flow pattern becomes unstable at higher rotation speeds, and a cellular flow pattern (termed *Taylor vortices*) is observed. Taylor vortices provide an irregular enhancement to mass transfer. At still higher rotation speeds, the flow becomes fully turbulent. Mass-transfer studies with rotating cylinders are conducted in the turbulent flow regime because the flow provides a uniform enhancement to mass transfer.

Two configurations have been described in the literature. When the electrode encompasses the entire length of the inner cylinder, as shown in Figure 11.12(a), the mass-transfer-controlled and primary current distributions are both uniform at any applied potential. Often, such a geometry is not practical, and a coupon electrode (see Figure 11.12(b)) is used that has insulating cylinders above and below the active surface. The mass-transfer-controlled current distribution for the geometry of Figure 11.12(b) is still uniform, but the primary distribution is not uniform. The nonuniform primary distribution poses no significant problem for corrosion experiments conducted at the open-circuit condition because the Ohmic potential drop is insignificant when the net current is equal to zero.

Analytic expressions cannot be derived for the turbulent flow regime, but empirical correlations are available that relate the cylinder rotation speed to the mass-transfer coefficient for a given geometry. The correlation of Eisenberg et al.[105] is given by

$$\mathrm{Sh} = 0.0791\left(\mathrm{Re}\frac{d_R}{d_L}\right)^{0.7}\mathrm{Sc}_i^{0.356} \tag{11.110}$$

where d_R is the diameter of the inner, rotating cylinder, d_L is the diameter of the cylinder at which the current is limited by mass transfer (usually the inner cylinder), Sh is the Sherwood number, related to the mass-transfer coefficient k_M by $\mathrm{Sh} = k_M d/D_i$, Re is the Reynolds number for the cylinder geometry given by $\mathrm{Re} = \Omega d_R^2/2\nu$, and Sc_i is the Schmidt number given by $\mathrm{Sc}_i = \nu/D_i$.

In principle, development of the convective-diffusion impedance for this system requires solution in the frequency domain to

$$\frac{\partial c_i}{\partial t} + \frac{1}{r}\left[\frac{\partial}{\partial r}\left(r\left(D_i + D_i^t(r)\right)\frac{\partial c_i}{\partial r}\right)\right] = 0 \tag{11.111}$$

where $D_i^t(r)$ represents the eddy diffusivity that arises from the enhancement to mass transfer caused by turbulent eddies. The dependence of $D_i^t(r)$ on position can be estimated from comparison to the universal velocity profile established for turbulent flow in pipes. As a result of the approximate character of the treatment of mass transfer, the rotating cylinder is used primarily for cases where qualitative comparisons are satisfactory, for example, in the ranking of corrosion in different environments.

Problems

11.1 Starting with the material balance equation, develop the expression for the impedance response for mass transfer through a stagnant film.

11.2 Plot, on an impedance plane format, the impedance obtained for a Nernst stagnant diffusion layer and the impedance obtained for a rotating disk electrode under assumption of an infinite Schmidt number. Show that, while the behaviors of the two models at high and low frequencies are in agreement, the two models do not agree at intermediate frequencies.[150] Explain.

Electrochemical Impedance Spectroscopy
by Mark E. Orazem and Bernard Tribollet

Chapter 12

Semiconducting Systems

Just as was presented in Chapters 10 and 11 respectively for kinetics and mass transfer in electrolytic systems, mathematical models for the impedance response of semiconductors require development of a steady-state model followed by development of a model treating the sinusoidal perturbation of voltage or current about the steady-state values. A key difference between the treatment of semiconducting systems and that of electrochemical systems is that the capacity associated with the diffuse region of charge is treated explicitly. In other respects, the analysis of semiconductors parallels that of electrochemical systems. The electrostatic potential and the concentrations of charged species, e.g., electrons, holes, and ionized defect states, become dependent variables for this system. Shallow-level doping species are usually assumed to be completely ionized at room temperatures and thus contribute to a fixed concentration of charge. The approach presented in this chapter is relevant to the impedance response of both solid-state systems and semiconductor electrodes.

12.1 Semiconductor Physics

Treatment of solid-state systems and semiconductor electrodes requires a basic understanding of solid-state physics. A brief simplified review of the physics of semiconductors is presented here. For a more complete treatment, the reader is referred to other textbooks.[151,152]

Remember! 12.1 *The development of impedance models for semiconductors is similar to that for electrolytic systems with the exception that the capacity associated with the diffuse region of charge is modeled explicitly.*

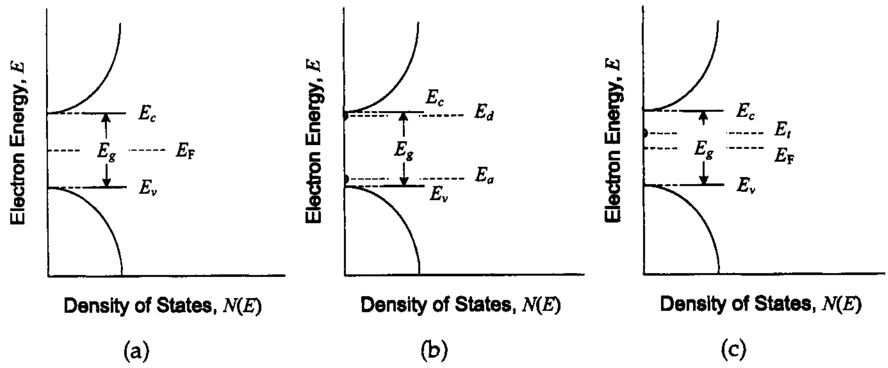

Figure 12.1: Schematic representation for the quantum mechanical energy band structure of a semiconductor: a) intrinsic semiconductor without dopants or deep-level states; b) semiconductor showing energy levels for electron donors E_d and electron acceptors E_a; and c) semiconductor with deep-level states of energy E_t as presented in Section 12.1.3.

12.1.1 Electrons and Holes as Species

Electrons have a spin of 1/2 and follow Fermi-Dirac statistics. The occupancy of a state of energy E is given by

$$f(E) = \frac{1}{1 + \exp\left(\frac{E-E_F}{kT}\right)} \tag{12.1}$$

where k is Boltzmann's constant in units of eV/K and E_F represents the *Fermi Energy*, in units of eV, at which the probability of occupancy of a state is 1/2. The probability of occupancy tends toward unity a few kT below E_F and tends toward zero a few kT above E_F. The energies used in equation (12.1) can also be expressed in units of J/mol, e.g.,

$$f(E) = \frac{1}{1 + \exp\left(\frac{E-E_F}{RT}\right)} \tag{12.2}$$

The change of units serves to emphasize the similarities between the analysis of semiconductors and electrolytic systems (see, e.g., Chapter 5). The Fermi energy E_F is closely related to the electrochemical potential of electrons introduced in Section 5.2. Statistical mechanical arguments have been used to show that, under equilibrium conditions, the Fermi energy is equal to the electrochemical potential of electrons.[153,154] At equilibrium, a single value of Fermi energy is sufficient to define the state of the system. Under nonequilibrium conditions, a separate Fermi energy can be defined for electrons and holes.

A schematic representation of the quantum mechanical energy band structure with energies near the band edges is presented in Figure 12.1(a) for an intrinsic semiconductor without dopants or deep-level states. The lower edge of the conduction band is at energy E_c, and the upper edge of the valence band is at energy E_v. The energy gap between the valence and conduction-band energies is

$$E_g = E_c - E_v \tag{12.3}$$

The number of electrons within the conduction band can be expressed as an integral over the occupied states, i.e.,

$$n = \int_{E_c}^{\infty} f(E)N(E)dE \tag{12.4}$$

where $N(E)$ is the number density of available states at energy E. The number of electrons within the valence band can be expressed as an integral over the occupied states, i.e.,

$$n_v = \int_{-\infty}^{E_v} f(E)N(E)dE \tag{12.5}$$

where $N(E)$ is the number density of available states at energy E. It is convenient to work in terms of the vacant states within the valence band, which are termed holes, i.e.,

$$p = \int_{-\infty}^{E_v} (1 - f(E))\, N(E)dE \tag{12.6}$$

The limit of ∞ in equation (12.4) could be replaced by the upper energy of the conduction band, and the limit of $-\infty$ in equation (12.6) could be replaced by the lower energy of the valence band.

At moderate temperatures, electrons in the conduction band have energies close to E_c, and holes in the valence band have energies close to E_v. Under the assumption that the Fermi energy is not close to the band edges, the Fermi-Dirac distribution, equation (12.1), can be approximated by Boltzmann distribution functions. The concentration of conduction-band electrons can be expressed as

$$n = N_c \exp\left(\frac{E_F - E_c}{kT}\right) \tag{12.7}$$

and the concentration of valence-band holes can be expressed by

$$p = N_v \exp\left(\frac{E_v - E_F}{kT}\right) \tag{12.8}$$

where N_c and N_v are the effective density of states for the conduction and valence band, respectively.

Under conditions such that equations (12.7) and (12.8) apply, the product of the electron and hole concentration is independent of Fermi energy, i.e.,

$$\begin{aligned} np &= N_v N_c \exp\left(\frac{-E_g}{kT}\right) \\ &= n_i^2 \end{aligned} \tag{12.9}$$

where n_i is the *intrinsic concentration*. Equation (12.9) is consistent with the laws of mass action.

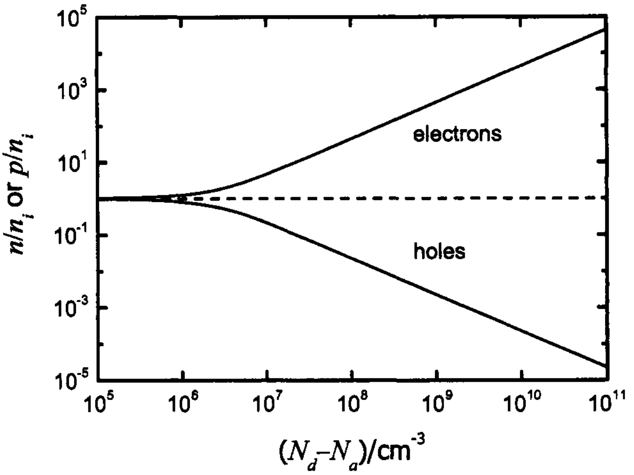

Figure 12.2: Electron and hole concentrations at the flat-band potential as a function of doping level for an n-type GaAs semiconductor. Physical properties of GaAs are presented in Table 12.1.

12.1.2 Doping

The properties of semiconductors can be modified by addition of dopants, which contribute electrons or holes to the semiconductor. The energies associated with electron acceptors and donors are shown schematically in Figure 12.1(b). The energy levels are such that the dopants can be completely ionized at room temperatures. Electron acceptors exist at energies just above the valence-band edge E_v. The resulting semiconductor will have an increased concentration of holes and is called a p-type semiconductor. Electron donors exist at energies just below the conduction-band edge E_c. The resulting semiconductor will have an increased concentration of electrons and is called an n-type semiconductor. The charge density of the semiconductor is given by

$$\rho_{sc} = F\left(p - n + (N_d - N_a)\right) \tag{12.10}$$

where N_d and N_a are the concentrations of ionized electron donors and acceptors, respectively.

The potential at which, under equilibrium conditions, the charge density is equal to zero is called the *flat-band potential*. An increase in electron donor concentration results in a decrease in the concentration of holes and an increase in the concentration of conduction-band electrons.

The scale of the variables used to describe semiconductors can be appreciated by examining the properties of the technologically important GaAs. The concentrations of electrons and holes at the flat-band condition are presented in Figure 12.2 for an n-type GaAs semiconductor. The concentrations of electrons and holes presented in Figure 12.2 were obtained by solving equations (12.9) and (12.10) with $\rho_{sc} = 0$. At low doping levels, the concentration of electrons and holes are equal.

Table 12.1: Physical properties for GaAs at 300 K extracted from Blakemore.[155]

Bandgap energy, E_g	1.423 eV 1.37×10^5 J/mol
Intrinsic carrier concentration, n_i	2.25×10^6 cm^{-3} 3.74×10^{-18} mol/cm^3
Effective conduction-band density of states, N_c	4.21×10^{17} cm^{-3} 6.99×10^{-7} mol/cm^3
Effective valence-band density of states, N_v	9.51×10^{18} cm^{-3} 1.58×10^{-5} mol/cm^3
Dielectric constant (static), ε	12.85
Mobility of electrons, μ_n	8000 cm^2/V s
Diffusion coefficient of electrons, D_n	207 cm^2/s
Mobility of holes, μ_p	320 cm^2/V s
Diffusion coefficient of holes, D_p	8.3 cm^2/s

At larger doping levels, the concentration of majority carriers (electrons, for *n*-type semiconductors) is equal to the doping level, and the concentration of minority carriers (holes, for *n*-type semiconductors) is established by equation (12.9).

Some relevant physical properties of GaAs are presented in Table 12.1. The properties are given both in the units generally used for semiconductor physics and in the units that are used for electrolytic systems. The bandgap energy, for example, has a value of 1.423 eV or 137 kJ/mol. The concentrations n, p, N_c, N_v, and n_i presented in equations (12.4) to (12.9) are generally expressed in units of cm^{-3}. Division by Avogadro's number $N_A = 6.0221367 \times 10^{23}$ mol^{-1} yields a concentration in units of mol/cm^3. The values presented for concentrations in Table 12.1 show that the concentrations of charged species in semiconductors are quite small as compared to that in even dilute electrolytic solutions.

The Fermi energy of the semiconductor under given doping levels can be obtained by solving equations (12.7) and (12.8), i.e.,

$$E_F = E_v - kT \ln\left(\frac{p}{N_v}\right) \tag{12.11}$$

or

$$E_F = E_c + kT \ln\left(\frac{n}{N_c}\right) \tag{12.12}$$

The Fermi energy obtained from the calculated concentrations of electrons and holes presented in Figure 12.2 is presented in Figure 12.3 as a function of doping level for an *n*-type GaAs semiconductor. The bandgap energy for GaAs is 1.424 eV. At low doping levels, the Fermi energy lies in the middle of the bandgap. As the doping level increases, the Fermi energy approaches the conduction-band energy.

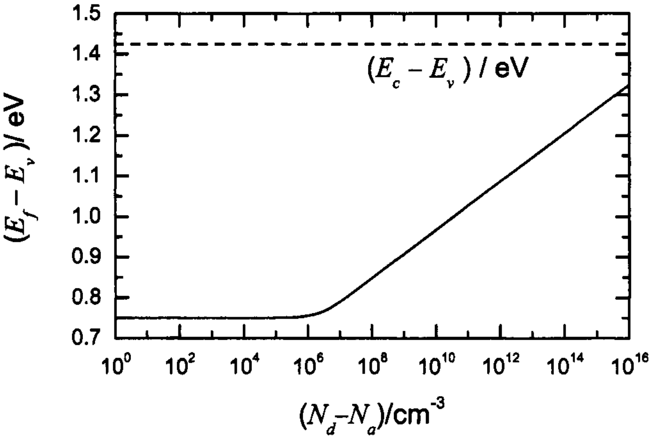

Figure 12.3: Fermi energy at the flat-band potential, referenced to the valence band energy, as a function of doping level for an *n*-type GaAs semiconductor. The corresponding concentrations of electrons and holes are presented in Figure 12.2.

12.1.3 Deep-Level States

Deep-level states play an important role in solid-state devices through their behavior as recombination centers.[156] For example, deep-level states are undesirable when they facilitate electronic transitions that reduce the efficiency of photovoltaic cells. In other cases, the added reaction pathways for electrons result in desired effects. Electroluminescent panels, for example, rely on electronic transitions that result in emission of photons. The energy level of the states caused by introduction of dopants determines the color of the emitted light. Interfacial states are believed to play a key role in electroluminescence, and commercial development of this technology will hinge on understanding the relationship between fabrication techniques and the formation of deep-level states. Deep-level states also influence the performance of solid-state varistors.

The position of a deep-level state with energy E_t with respect to the bandgap is illustrated in Figure 12.1(c). Under equilibrium conditions, the occupancy of the state is governed by the Fermi-Dirac distribution function, equation (12.1). In the absence of illumination, the deep-level state will influence the impedance response of the semiconductor only if the probability of occupancy of the state is close to 1/2, i.e., if the state energy is close to the Fermi energy. If, for example, the probability of occupancy is essentially zero, the unfavorable energetics of the transition prevent the electrical excitation from moving electrons into the state. On the other hand, if the probability of occupancy is essentially unity, the need to satisfy Pauli exclusion prohibits transfer of electrons into the state.

The impact of deep-level states can be significant, even in concentrations that are very low by normal chemical standards. Several states can be associated with a chemical species, and such states may also appear as a result of vacancies or other crystalline defects. Traditional chemical means of detection, therefore, do not pro-

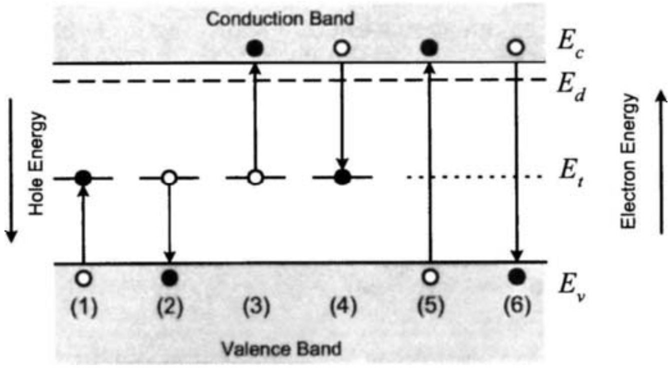

Figure 12.4: Schematic representation of electronic transitions, including Shockley-Read-Hall processes for a deep-level state.

vide complete identification of deep-level electronic states. The techniques commonly employed to detect deep-level states tend to be electrical in nature since it is through their electronic behavior that these states influence device performance.

12.1.4 Shockley-Read-Hall Processes

The influence of deep-level states or traps on the statistics of electron–hole recombination was first described by Shockley and Read[157] and Hall.[158] Deep-level states, as their name implies, lie close to the middle of the energy bandgap of the semiconductor. Due to the large energy separation from the valence-band and conduction-band edges, deep-level states are not fully ionized at room temperature. In contrast, shallow-level states are those considered to be fully ionized at room temperature due to thermal excitation.

The interaction between a deep-level state and electrons and holes can be described by processes 1 to 4 represented in Figure 12.4. Process 1 involves the emission of a valence-band electron to the deep-level state after receiving energy $(E_t - E_v)$. This can also be thought of as hole emission from the deep-level state to the valence band since an electron vacant deep-level state has been filled by a valence-band electron, thus leaving a hole in the valence band.

Process 2 is the capture of a deep-level-state electron by the valence band. Valence-band electrons are more tightly bound to the crystal atom than are the conduction-band electrons, which have a much larger radius of travel (of several lattice constants). This allows the analogy that conduction-band electrons can be considered to be negative charges floating in a sea of fixed positive nuclei (lattice sites) as in a metal. Valence-band electrons are held in a tight sphere about a nucleus and can move only if the neighboring nucleus has an electron-vacant site that it can jump into. Once the electron moves into this vacant site, it leaves a net positive charge behind. This positive charge will appear to be an entity, a hole, moving in a direction opposite that of the valence-band electron. Thus, it is feasible to consider process 2 as being the capture of a valence-band hole. For a deep-level-state electron to be captured by the valence band, it must lose an amount of energy equal to $(E_t - E_v)$, or likewise, for a valence-band hole to be captured by the trap, it must gain the same amount of energy.

Process 3 involves a trapped electron being emitted to the conduction band after receiving an amount of energy equal to $(E_c - E_t)$ from optical or thermal excitation. Process 4 involves a conduction-band electron that comes in the vicinity of a deep-level state and is "trapped" by it. In order for this electron to be trapped, it must lose an amount of energy equal to $(E_c - E_t)$ by radiative (photon) or nonradiative (phonon) processes.

Process 5 represents excitation of a valence-band electron to the conduction band, thus producing an electron and a hole. The reverse process 6 can be considered to be recombination of an electron and hole. Processes 5 and 6 do not require presence of deep-level states.

12.1.5 Interfaces

At an interface with a dissimilar material, a redistribution of charged species occurs which results in the formation of a space-charge region in the semiconductor, which is the solid-state analog to the diffuse region of charge described in connection with Figure 5.6(b) and associated with an electrolytic double layer. A space-charge region can be formed at an interface with a metal, another semiconductor, or an electrolyte. In polycrystalline materials, a space-charge region can also be formed at a grain boundary. Within the space-charge region, the electron energy for the valence band, the conduction band, and the deep-level state can be described as varying with reference to a fixed Fermi energy. Thus the probability of occupancy of the deep-level state is a function of position, and, since the degree of band bending is determined by the potential applied to the system, the degree of occupancy is a function of applied potential.

A schematic representation of the band bending at an interface is presented in Figure 12.5. The probability of occupancy of a state is equal to 1/2 at the Fermi energy. The band bending shown in Figure 12.5 causes the deep-level state to make the transition from being fully occupied far from the interface to being fully vacant at the interface.

The spatial dependence of the energy bands can be described in terms of a single potential variable. In terms of a potential referenced to the potential in the electrically neutral region of the semiconductor, the valence-band energy can be expressed as

$$E_v = E_v^* - F\Phi \tag{12.13}$$

where energies are given in units of J/mol and E_v^* represents the valence-band energy within the electrically neutral region where the potential is uniform. Similarly, the conduction-band energy can be expressed as

$$E_c = E_c^* - F\Phi = E_v^* + E_g - F\Phi \tag{12.14}$$

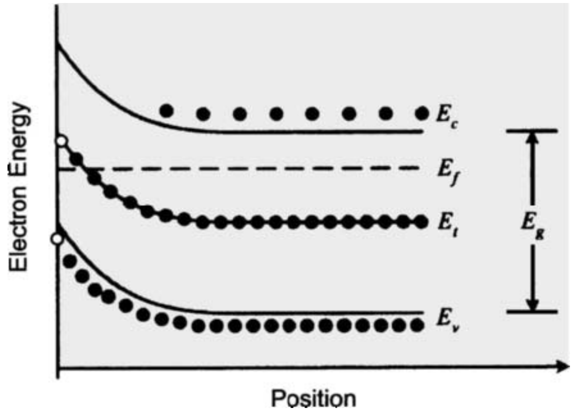

Figure 12.5: Schematic representation of band bending at an interface between a metal phase and an n-type semiconductor. Filled circles represent electron-occupied states and open circles represent vacant states.

As shown by equations (12.13) and (12.14), variations in conduction and valence-band energies are linked to the variation of the electrical potential.

12.2 Steady-State Models

Development of mathematical models for the impedance response of semiconducting systems generally takes place in two steps: development of a steady-state model followed by development of a model treating the sinusoidal perturbation of voltage or current about the steady-state values. Since the species of interest have a charge associated with them, both the electrical potential and species concentrations must be treated. Thus, the electrostatic potential and the concentrations of electrons, holes, and ionized defect states become dependent variables for this system. The shallow-level doping species are usually assumed to be completely ionized at room temperatures and thus contribute to a fixed concentration of charge.

12.2.1 Mass Transfer

The mathematical development presented here is intended to emphasize the similarities between the analysis of transport in semiconductors and that in electrolytic systems as presented in Chapter 5. In doing so, concentrations of electrons and holes, typically presented on an atomistic basis, e.g., in units of cm^{-3}, are given in a molar basis.

The electrochemical potential μ_i of a given species i, introduced in Section 5.2 for electrolytic systems, can be applied to electrons and holes in a semiconductor. The electrochemical potential can be arbitrarily separated into terms representing a secondary reference state μ_i°, a chemical contribution, and an electrical contribution, i.e.,

$$\mu_i = \mu_i^\circ + RT\ln(c_i f_i) + z_i F\Phi \tag{12.15}$$

where c_i is the volumetric concentration of species i, f_i is the activity coefficient, z_i is the charge number, and Φ is a potential that characterizes the electrical state of the system and can be defined in many ways. This treatment is identical to the definition of an electrochemical potential for ionic species and is entirely analogous to the definition of chemical potentials as used for electrically neutral systems. The usual chemical potential is recovered for the case where z_i is equal to zero.

The flux N_i of species i is governed by the gradient of the electrochemical potential, given in one dimension by

$$N_i = -u_i c_i \frac{d\mu_i}{dy} \tag{12.16}$$

where u_i is the mobility of species i. If the semiconductor is nondegenerate, the electron and hole activity coefficients f_i can be considered to be constant, and equation (12.15) can be substituted into equation (12.16) to give the dilute solution transport expression

$$N_i = -D_i \frac{dc_i}{dy} - u_i z_i F c_i \frac{d\Phi}{dy} \tag{12.17}$$

where the transport properties D_i and u_i are related through the Nernst-Einstein equation; i.e.,

$$D_i = RTu_i \tag{12.18}$$

According to equation (12.17), the fluxes of electrons and holes are driven by concentration and potential gradients. This distinction is a result of the separation of the chemical and electrical contributions given in equation (12.15). If desired, degenerate semiconductor conditions can be modeled by calculating the value of the activity coefficients f_i for electrons and holes as described by Hwang and Brews[159] and Bonham and Orazem.[160] The flux expression for species i is constrained by the equation of continuity, i.e.,

$$\frac{\partial c_i}{\partial t} = \frac{\partial N_{yi}}{\partial y} + G_i \tag{12.19}$$

Usually electrons in interband defect states are considered to be immobile; the rate of change of the concentration of ionized interband states is equal to their (position-dependent) rate of production, G_i.

12.2.2 Space-Charge Region

For most electrochemical systems, the separation of charge associated with interfacial regions can be treated simply as contributing to rate constants associated with

---

Remember! 12.2 *Expressions for transport of electrons and holes in a semiconductor can be treated in terms of gradients of the corresponding electrochemical potential.*

---

electrode kinetics. This is not appropriate for a semiconductor because this separation of charge is integral to the operation of electronic devices. Poisson's equation,

$$\frac{\partial^2 \Phi}{\partial y^2} = -\frac{F}{\varepsilon\varepsilon_0}\left[p - n + N_d - N_a\right] \tag{12.20}$$

can be used to relate the electrostatic potential Φ to the charge held within the semiconductor. The scaling length for this system, found by making the governing equations dimensionless, is given by the Debye length,

$$\lambda = \left[\frac{\varepsilon\varepsilon_0 RT}{F^2(N_d - N_a)}\right]^{1/2} \tag{12.21}$$

The term $(N_d - N_a)$ includes the charge associated with partially ionized midbandgap acceptors (which may be a function of applied potential) as well as the completely ionized dopant species (which may have an arbitrary distribution, but is usually assumed to be independent of operating conditions).

12.2.3 Application to Electrolyte–Semiconductor Junctions

Formation of an interface with an electrolyte perturbs the potential distribution in the semiconductor, and this perturbation creates the junction necessary for the photovoltaic effect in solar cells. Examination of the potential distribution provides insight into the forces driving the cell. Orazem and Newman calculated the potential distribution in an n-type GaAs semiconductor in contact with an electrolyte containing a selenium redox couple.[161] Interfacial reactions were assumed to be fast such that the potential and concentration distributions could be controlled by mass transport and generation of electrons and holes. The resulting potential distribution is presented in Figure 12.6. The potential is referenced to the potential at the Ohmic contact located far from the electrolyte–semiconductor interface. The potential was nearly uniform in the electrolyte but varies within the semiconductor in response to the distribution of charge associated with the electrolyte–semiconductor interface. This is consistent with the *band-bending* described in Figure 12.5. In the context of Figure 12.6, the *flat-band potential* is the applied potential required to achieve a uniform potential in the semiconductor.

In the absence of illumination and at open circuit (curve a in Figure 12.6) the interface is equilibrated. The potential difference between the interface and the Ohmic contact located far from the interface represents the available photovoltaic

---

Remember! 12.3 *The redistribution of charge at the semiconductor–electrolyte interface creates a space-charge region in the semiconductor that is generally much thicker than that found in the electrolyte.*

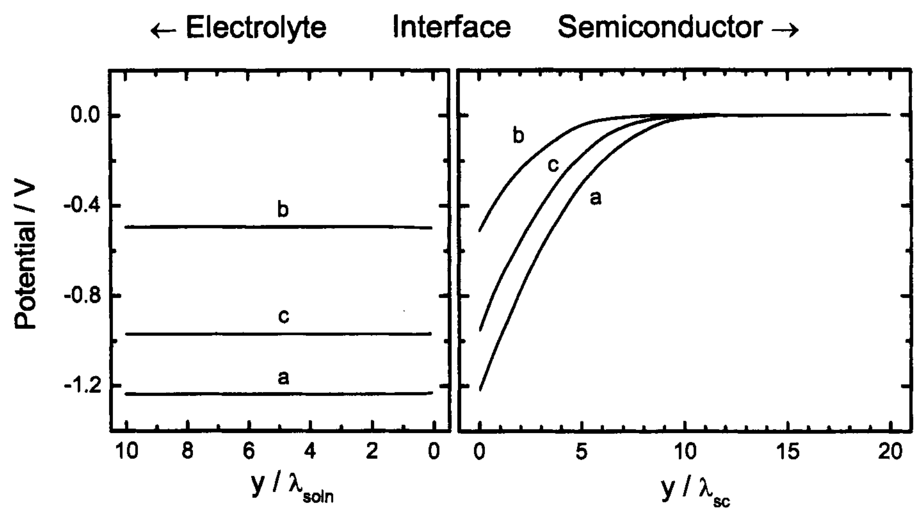

Figure 12.6: Potential distribution for an *n*-GaAs electrode in contact with a selenium redox couple with fast interfacial reactions: curve a in the absence of illumination; curve b at open circuit with 882 W/m^2 illumination; and curve c under illumination near the short-circuit condition (-23.1 mA/cm^2). The Debye length in the electrolyte was 0.2 nm, and the Debye length in the semiconductor was 70 nm. (Taken from Orazem and Newman.[161])

driving force. Under illumination at open-circuit (curve b in Figure 12.6), electron–hole pairs generated by the light are separated by the electric field, resulting in a *straightening of the bands*. The accumulation of electrons and holes creates an electric field that tends to oppose the field formed at equilibrium. The difference between the potential at equilibrium and under illumination at open-circuit represents the driving force for flow of electrical current. The potential distribution under illumination and near the short-circuit condition (curve c in Figure 12.6) tends to approach the equilibrium distribution. All the variation in potential takes place within the semiconductor. The potential drop across the electrolyte is comparatively insignificant.

The selection of a reference potential at the Ohmic contact is arbitrary and was chosen to emphasize the degree of band bending and straightening in the semiconductor. The development of Mott-Schottky theory in Section 12.3.2 employs a potential referenced to the Ohmic contact. A difference in sign will be seen if the potential is referenced instead to a reference electrode located in the electrolyte. The potential of the electrolyte has been found to be independent of current and illumination intensity when referenced to an external quantity such as the Fermi energy of an electron in vacuum.[162,163] This concept has proved useful for predicting the interaction between semiconductors and a variety of redox couples. The IUPAC standard for photoelectrochemical systems, in fact, is that the potential is referred to a reference electrode in the electrolyte.[164,165]

The potential distributions in Figure 12.6 can be interpreted in terms of the associated concentration distributions for electrons and holes presented in Figure 12.7.

The linear scale presented in Figure 12.7(a) emphasizes the depletion of electrons near the interface and the corresponding increase in hole concentrations. The logarithmic scale presented in Figure 12.7(b) emphasizes the change in electron and hole concentrations over many orders of magnitude.

Under equilibrium conditions (curve a in Figure 12.7), the hole concentration is very small far from the interface but increases near the negatively charged interface. Conduction-band electrons are depleted near the interface but reach a value close to the net dopant concentration ($N_d - N_a$) in the electrically neutral region far from the interface. As shown by curve a in Figure 12.7, the equilibrated semiconductor can be described as having an inversion region from the interface to $y/\lambda_{sc} = 3$, in which the minority carrier concentration exceeds that of the majority carrier, a depletion region from $y/\lambda_{sc} = 3$ to $y/\lambda_{sc} = 8$, in which the scaled majority carrier concentration is smaller than unity, and an electrically neutral region extending beyond $y/\lambda_{sc} = 8$. These positions can be compared to the potential distribution given by curve a in Figure 12.6.

As shown by curve b in Figure 12.7, illumination at the open-circuit condition produces electron–hole pairs that are separated by the potential gradient associated with the interface. The concentration of holes increases at all positions within the semiconductor, and the concentration of electrons increases in the space-charge region, thus straightening the equilibrium potential variation. As the system approaches the short-circuit condition under illumination (curve c in Figure 12.7), the concentrations of electrons and holes tends toward the equilibrium distributions.

12.3 Impedance Models

Numerical solutions have been presented for the impedance response of semiconducting systems that account for the coupled influence of transport and kinetic phenomena, see, e.g., Bonham and Orazem.[166,167] Simplified electrical-circuit analogues have been developed to account for deep-level electronic states, and a graphical method has been used to facilitate interpretation of high-frequency measurements of capacitance. The simplified approaches are described in the following sections.

12.3.1 Equivalent Electrical Circuits

Sah and coworkers have developed a quasi-analytic calculation that can be expressed as a detailed equivalent electrical circuit.[168–171] This development is summarized by Jansen et al.[172] and used to justify the application of the simplified equivalent circuit shown in Figure 12.8 to the analysis of the impedance response of semiconductors containing deep-level electronic states. This circuit was used to analyze the impedance data presented in Section 18.2 (see, e.g., Figure 18.4). In Figure 12.8, C_n is the space-charge capacitance, R_n is a resistance that accounts for a small but finite leakage current,[173–175] and the parameters $R_1 \ldots R_k$ and $C_1 \ldots C_k$ are attributed to the response of discrete deep-level energy states.

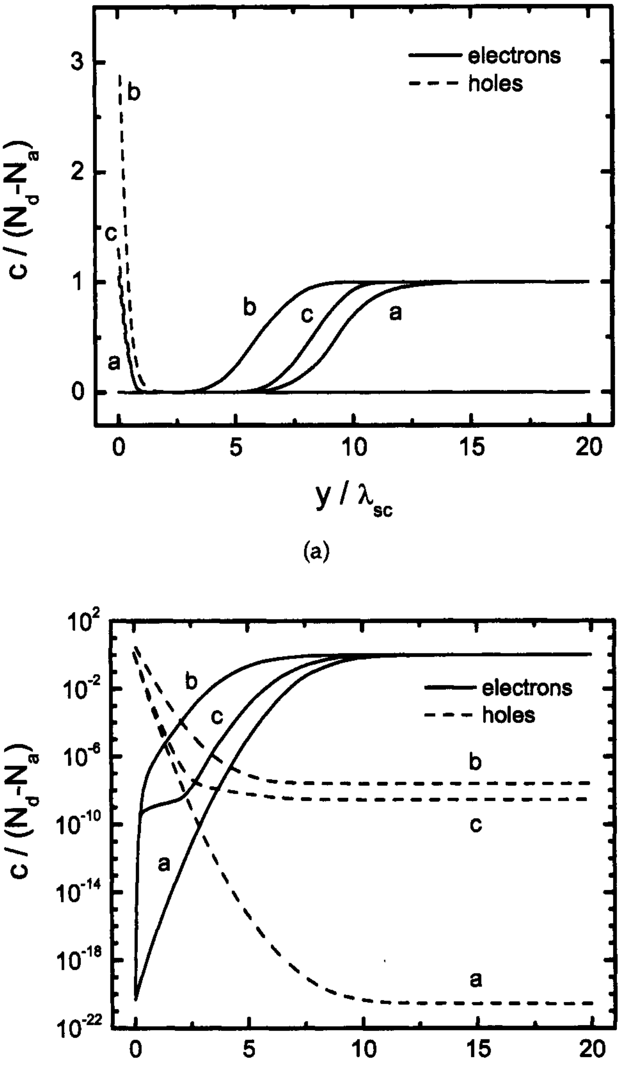

(a)

(b)

Figure 12.7: Concentration distributions for electrons (solid lines) and holes (dashed lines) for an n-GaAs electrode in contact with a selenium redox couple with fast interfacial reactions: curve a in the absence of illumination; curve b at open circuit with 882 W/m^2 illumination; and curve c under illumination near the short-circuit condition (-23.1 mA/cm^2). Concentrations were scaled to the net dopant concentration ($N_d - N_a$): a) concentrations given in a linear scale; and b) concentrations given in a logarithmic scale. (Taken from Orazem and Newman.[161])

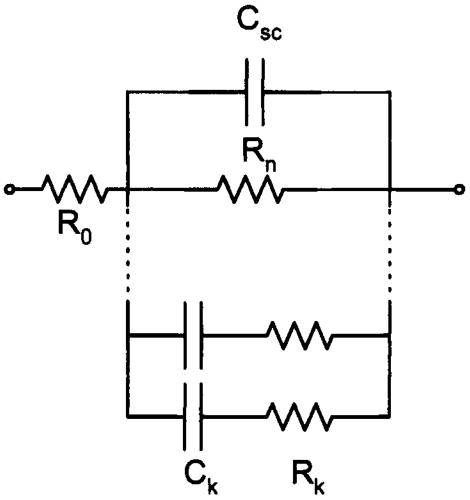

Figure 12.8: Electrical circuit corresponding to the model presented by Jansen et al.[172] in which C_n is the space-charge capacitance, R_n is a resistance that accounts for a small but finite leakage current, and the parameters $R_1 \ldots R_k$ and $C_1 \ldots C_k$ are attributed to the response of discrete deep-level energy states.

Similar circuits have been used to account for both homogeneous[176,177] and interfacial electronic states.[178,179] The circuit shown in Figure 12.8 cannot be used to distinguish between surface and bulk deep-level states. It is possible to distinguish the two types of states by means of the Mott-Schottky plots described in Sections 12.3.2 and 18.3.

12.3.2 Mott-Schottky Analysis

Graphical techniques can be applied for single-frequency measurements when the frequency selected excludes the contributions of confounding phenomena. For example, impedance measurements on a semiconductor diode at a sufficiently high frequency exclude the influence of leakage currents and of electronic transitions between deep-level and band-edge states. Thus, as discussed in Section 16.4, the capacitance can be extracted from the imaginary part of the impedance as

$$C = \frac{1}{\omega Z_j} \tag{12.22}$$

The problem is reduced to one of identifying the relationship between semiconductor properties and the capacitance as a function of applied potential.

The capacitance of the space-charge region C is determined through

$$C_{sc} = \left.\frac{\partial q_{sc}}{\partial \Phi}\right|_{y=0} \tag{12.23}$$

where the charge density of the space-charge region q_{sc} is related to potential through Poisson's equation (12.20). Solution of equation (12.20) is facilitated by expressing the concentration of electrons and holes in terms of potential through insertion of equations (12.14) and (12.13) into the Boltzmann distributions for electrons and holes, equations (12.7) and (12.8), respectively. Thus, Poisson's equation can be expressed as

$$\frac{d^2\Phi}{dy^2} = -\frac{F}{\varepsilon\varepsilon_0}\left[Pe^{-F\Phi/RT} - Ne^{F\Phi/RT} + (N_d - N_a)\right] \tag{12.24}$$

where Φ is the electrostatic potential, $(N_d - N_a)$ is the doping level, and P and N are the hole and electron concentrations, respectively, at the flat-band potential. Deep-level states were not included in the expression for charge density. The occupancy of deep-level states is a function of potential, and a similar development can be made to take such states into account.[180] The charge density used in equation (12.24)

$$\rho_{sc}(\Phi) = F\left[Pe^{-F\Phi/RT} - Ne^{F\Phi/RT} + (N_d - N_a)\right] \tag{12.25}$$

is now an explicit function of potential rather than position. Equation (12.25) can be compared to the definition provided as equation (12.10).

Integration of Poisson's equation is facilitated by posing equation (12.24) in terms of the electric field

$$E = -\frac{\partial\Phi}{\partial y} \tag{12.26}$$

The second derivation of potential with respect to position can be expressed in terms of a derivative with respect to potential as

$$\frac{d^2\Phi}{dy^2} = -\frac{dE}{dy} = -\frac{dE}{d\Phi}\frac{d\Phi}{dy} = E\frac{dE}{d\Phi} = \frac{1}{2}\frac{dE^2}{d\Phi} \tag{12.27}$$

Thus,

$$\frac{dE^2}{d\Phi} = -\frac{2}{\varepsilon\varepsilon_0}\rho_{sc}(\Phi) \tag{12.28}$$

Integration yields

$$E^2 = -\frac{2}{\varepsilon\varepsilon_0}\int_{\Phi_{fb}}^{\Phi}\rho_{sc}(\Phi)d\Phi \tag{12.29}$$

where the flat-band potential Φ_{fb} is the potential in the electrically neutral region far from the interface.

The charge held within the space-charge region is given by

$$q_{sc} = \int_0^{\infty}\rho_{sc}dy \tag{12.30}$$

Remember! 12.4 *Mott-Shottky theory provides a relationship between the experimentally measured capacitance, the doping level, and the flat-band potential.*

Under the assumption that there are no surface states or specific adsorption of charged species, the space charge q_{sc} in a semiconductor in contact with an electrolyte is balanced by the charge in the diffuse part of the double layer q_d; thus, $q_{sc} = q_d$. Gauss's law can therefore be used to provide a boundary condition for the electric field at the surface of the semiconductor as

$$E(\Phi(0)) = -\left.\frac{d\Phi}{dy}\right|_{y=0} = \frac{q_{sc}}{\varepsilon\varepsilon_0} \tag{12.31}$$

Thus

$$q_{sc} = \varepsilon\varepsilon_0 E(\Phi(0)) \tag{12.32}$$

The space-charge capacitance is given by

$$C_{sc} = -\frac{dq_{sc}}{d\Phi(0)} = \varepsilon\varepsilon_0 \frac{dE(\Phi(0))}{d\Phi(0)} \tag{12.33}$$

or

$$C_{sc} = -\frac{\rho_{sc}(\Phi(0))}{E(\Phi(0))} \tag{12.34}$$

Equation (12.34) provides a relationship between the capacitance of the space-charge region of the semiconductor, the electric field at the interface, and the charge density at the interface.

Under the convention that the potential is referenced to the flat-band potential Φ_{fb}, i.e., the potential is equal to zero far from the interface where the electric field is also equal to zero, integration of equation (12.29) yields

$$E^2 = \frac{2RT}{\varepsilon\varepsilon_0}\left[P(\mathrm{e}^{-F\Phi/RT} - 1) + N(\mathrm{e}^{F\Phi/RT} - 1) - \frac{F\Phi}{RT}(N_d - N_a)\right] \tag{12.35}$$

A general expression for capacity can be found to be

$$\frac{1}{C_{sc}^2} = \frac{2RT}{F^2\varepsilon\varepsilon_0}\frac{P(\mathrm{e}^{-F\Phi(0)/RT} - 1) + N(\mathrm{e}^{F\Phi(0)/RT} - 1) - \frac{F\Phi(0)}{RT}(N_d - N_a)}{\left[-P\mathrm{e}^{-F\Phi(0)/RT} + N\mathrm{e}^{F\Phi(0)/RT} - (N_d - N_a)\right]^2} \tag{12.36}$$

The values for N and P can be evaluated at the flat-band potential under the assumptions of equilibrium (i.e., $np = n_i^2$) and electroneutrality (i.e., $\rho_{sc} = 0$).

$$N = \frac{1}{2}\left[(N_d - N_a) + \sqrt{(N_d - N_a)^2 + 4n_i^2}\right] \tag{12.37}$$

and

$$P = \frac{1}{2}\left[-(N_d - N_a) + \sqrt{(N_d - N_a)^2 + 4n_i^2}\right] \tag{12.38}$$

Equations (12.37) and (12.38) can be inserted into equation (12.36) to provide an expression for capacitance as a function of potential, with doping level as a parameter.

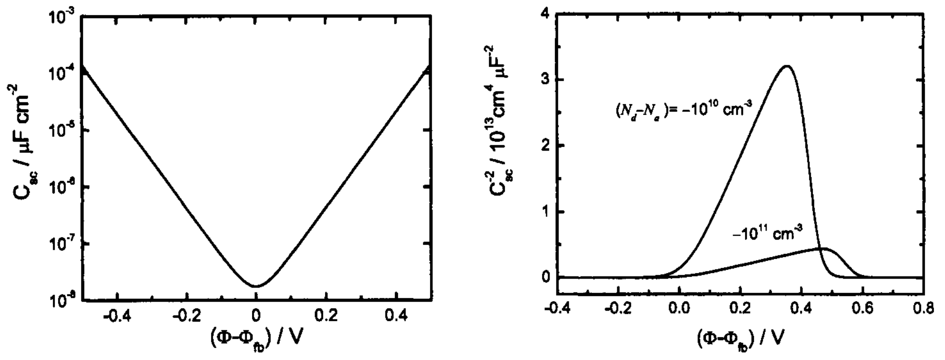

(a)

(b)

Figure 12.9: Calculated capacitance for a GaAs Schottky diode (see Table 12.1 for relevant parameters for GaAs semiconductors): a) capacitance as a function of potential referenced to the flat-band potential for an intrinsic semiconductor; and b) $1/C_{sc}^2$ as a function of potential referenced to the flat-band potential for a lightly doped *p*-type semiconductor.

The capacitance is presented in Figure 12.9(a) for an intrinsic GaAs semiconductor diode. Some relevant physical properties of GaAs are presented in Table 12.1. The capacitance is symmetric with respect to potential referenced to the flat-band potential. At modest doping levels, as shown in Figure 12.9(b) for *p*-type semiconductors, the plot of $1/C_{sc}^2$ has a significant linear portion with respect to potential. At more positive potentials, the plot deviates from a straight line due to the contribution of minority carriers.

Mott-Shottky plots of $1/C_{sc}^2$ as a function of potential are particularly useful at larger doping levels. Calculated values for $1/C_{sc}^2$ are presented in Figure 12.10(a) for a GaAs diode with potential referenced to the Ohmic contact, as was used in Figure 12.6. The corresponding values are presented in Figure 12.10(b) for potentials referenced to a reference electrode located in the electrolyte in accordance with the IUPAC convention for semiconductor electrodes.[164,165] The principal distinction between the two plots is that the positive slopes correspond to a *p*-type semiconductor in Figure 12.10(a) and to an *n*-type semiconductor in Figure 12.10(b). All concentration terms were included in the analysis.

As seen in Figure 12.10, $1/C_{sc}^2$ is linear over a broad range of potential. The linear portion for Figure 12.10(a) is given by

$$\frac{1}{C_{sc}^2} = -\frac{2(\Phi(0) - \Phi_{fb} + RT/F)}{\varepsilon\varepsilon_0 F(N_d - N_a)} \tag{12.39}$$

for an *n*-type semiconductor and by

$$\frac{1}{C_{sc}^2} = -\frac{2(\Phi(0) - \Phi_{fb} - RT/F)}{\varepsilon\varepsilon_0 F(N_d - N_a)} \tag{12.40}$$

for a *p*-type semiconductor.

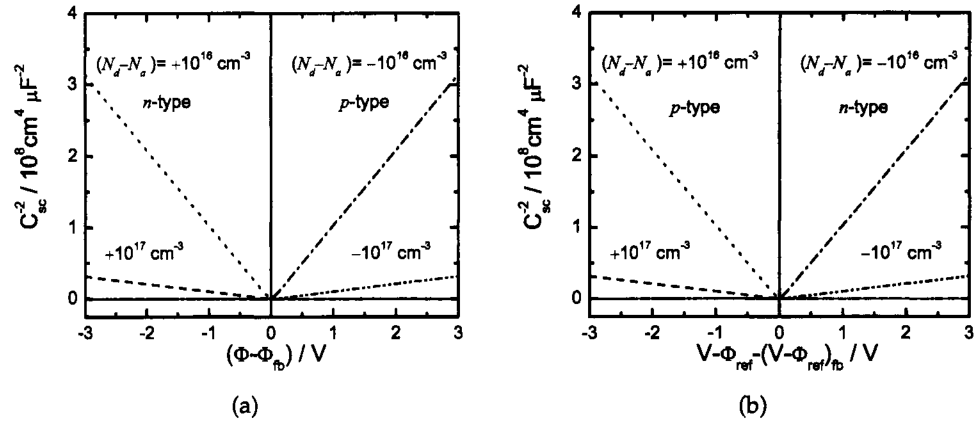

Figure 12.10: Mott-Schottky plot of $1/C_{sc}^2$ as a function of potential referenced to the flat-band potential for a GaAs Schottky diode: a) potential referenced to the Ohmic contact; and b) potential referenced to a reference electrode located in the electrolyte according to the IUPAC convention for semiconductor electrodes.[164,165]

Example 12.1 Mott-Schottky Plots: *Beginning with equation (12.36), derive equation (12.39) for an n-type semiconductor.*

Solution: *For an n-type semiconductor,* $(N_d - N_a)$ *is positive and much larger than the intrinsic concentration* n_i*; thus,* $N \rightarrow (N_d - N_a)$ *and* $P \rightarrow 0$*. In the denominator,* $P\exp(-F\Phi(0)/RT)$ *can be neglected. In the numerator,* $P(\exp(-F\Phi(0)/RT) - 1)$ *can also be neglected. The linear portion of the curve lies at negative potentials, referenced to the flat-band potential; thus,* $\exp(F\Phi(0)/RT) \rightarrow 0$ *and*

$$N(\exp(-F\Phi(0)/RT) - 1) \approx -(N_d - N_a) \tag{12.41}$$

Equation (12.36) can be expressed as

$$\frac{1}{C_{sc}^2} = \frac{2RT}{F^2\varepsilon\varepsilon_0}\frac{-(N_d - N_a)\left(\frac{F\Phi(0)}{RT} + 1\right)}{(N_d - N_a)^2} \tag{12.42}$$

or

$$\frac{1}{C_{sc}^2} = -\frac{2(\Phi(0) - \Phi_{fb} + RT/F)}{\varepsilon\varepsilon_0 F(N_d - N_a)} \tag{12.43}$$

A similar development at positive potentials will yield equation (12.40).

The assumptions implicit in the Mott-Schottky theory are:

- The potential is restricted to the range where both the majority (in this case, electrons) and the minority carriers (holes) are negligible as compared to the doping level. These constraints are violated at small and large magnitudes of potential (referenced to the flat-band potential), respectively. This potential range becomes increasingly restrictive as the doping level decreases, and the technique is unusable for semi-insulating materials.

- The semiconductor electrode must be ideally polarizable over the potential range of interest. This means that there is no leakage current or Faradaic reaction to allow charge transfer across the semiconductor–electrolyte interface. This restriction is not too important if measurements are taken at sufficiently high frequency that the effects of Faradaic reactions are suppressed.
- Electron and hole concentrations follow a Boltzmann distribution, i.e., activity coefficient corrections can be neglected.

Equations (12.39) and (12.40) form the basis of a method, described in Section 18.3, used to extract doping levels and flat-band potentials for semiconducting materials.

Problems

12.1 Develop the relationship needed to convert the mobility given in Table 12.1, e.g., μ_n, to diffusivity.

12.2 Calculate the Debye length in units of μm expected for an n-type GaAs semiconductor with a dopant concentration of 10^{16}. Compare the value you obtain to the Debye length obtained for an electrolytic system with a NaCl concentration of 0.1 M.

12.3 Plot the equilibrium concentration and potential distribution in the space-charge region of an n-type GaAs semiconductor (doped 10^{16} cm^{-3}) if the electron concentration at the surface is 20 orders of magnitude less than the bulk concentration. Use semilogarithmic plots for concentration and linear plots for potential.

12.4 The capacity of the space-charge region can be related to the dopant concentration (or fixed charge) in a semiconductor. The space-charge region is essentially equivalent to the diffuse double layer treated in electrolytes with the exception that ionized impurities are present that, at room temperatures, are immobile. For this case, Poisson's equation becomes

$$\nabla^2\Phi = -\frac{F}{\varepsilon\varepsilon_0}\left\{n - p - (N_d - N_a)\right\} \tag{12.44}$$

Show that the capacity can be related to doping level $(N_d - N_a)$ and potential by the Mott-Schottky relationship

$$\frac{1}{C^2} = -\frac{2}{F\varepsilon\varepsilon_0}\frac{(V + RT/F)}{(N_d - N_a)} \tag{12.45}$$

12.5 Deviations from straight lines in Mott-Schottky plots can be attributed to the influence of potential-dependent charging of surface or bulk states. This interpretation is supported by analytic calculations of the contribution of defects to the space charge as a function of applied potential. In principle, the effect of applied potential of the state of charge of defects can be used to determine the distribution of defects within the space-charge region. Apply the Fermi-Dirac distribution function to the defects to obtain a relationship for the space-charge capacitance for a semiconductor that is sufficiently n-type that the contribution of holes to the charge can be regarded to be negligible.

12.6 Changes in space-charge capacity can be used to observe the effect of charging and discharging of electronic states in a semiconductor subject to sub-bandgap illumination. Show that the change in observed capacity caused by illumination can be referenced to the unilluminated case by

$$\frac{\Delta C}{C} = \sqrt{\frac{\Delta c_d^+}{(N_d - N_a)}} \tag{12.46}$$

where Δc_d^+ is the change in the state of charge of the interband state caused by illumination. It is clear from this problem that identification of defects by this method requires excellent resolution for moderate doping levels and that the concentration measured in this way is the change in the state of charge of the defect, not the actual defect concentration.

12.7 The capacity of the electrolytic diffuse double layer is often ignored when Mott-Schottky plots are used to characterize semiconductor–electrolyte interfaces. Under what conditions is this assumption justified?

12.8 Mott-Schottky plots are often generated by using measurements at a single frequency, often 1 kHz. Explain the limitations of this approach.

12.9 A claim is made in Section 12.3.1 that Mott-Schottky plots may be used to distinguish between surface and bulk deep-level states. Explain how this may be accomplished.

Electrochemical Impedance Spectroscopy
by Mark E. Orazem and Bernard Tribollet

Chapter 13

Time-Constant Dispersion

The impedance models developed in Chapters 9, 10, 11, and 12 are based on the assumption that the electrode behaves as a uniformly active surface where each physical phenomenon or reaction has a single-valued time constant. The assumption of a uniformly active electrode is generally not valid. Time-constant dispersion can be observed due to variation along the electrode surface of reactivity or of current and potential. Such a variation is described in Section 13.1.1 as resulting in a 2-dimensional distribution. Time-constant dispersion can also be caused by a distribution of time constants that reflect a local property of the electrode, resulting in a 3-dimensional distribution.

The presence of time-constant (or frequency) distribution is frequently modeled by use of a constant-phase-element (CPE), discussed in Section 13.1. As discussed in Section 13.1.3, use of a CPE assumes a specific distribution of time constants that may apply only approximately to a given system. The objective of this chapter is to describe specific situations for which time-constant dispersion can be predicted based on fundamental phenomena such as are associated with distributions of mass-transfer rates and Ohmic currents.

13.1 Constant-Phase Elements

The impedance response of electrodes rarely show the ideal response expected for single electrochemical reactions. The impedance response typically reflects a distribution of reactivity that is commonly represented in equivalent electrical circuits as a constant phase element (CPE).[3,71,104] For a blocking electrode, the impedance can be expressed in terms of a CPE as

$$Z(\omega) = R_\mathrm{e} + \frac{1}{(j\omega)^\alpha Q} \tag{13.1}$$

The impedance associated with a simple Faradaic reaction without diffusion can be expressed in terms of a CPE as

$$Z(\omega) = R_\mathrm{e} + \frac{R_t}{1 + (j\omega)^\alpha Q R_t} \tag{13.2}$$

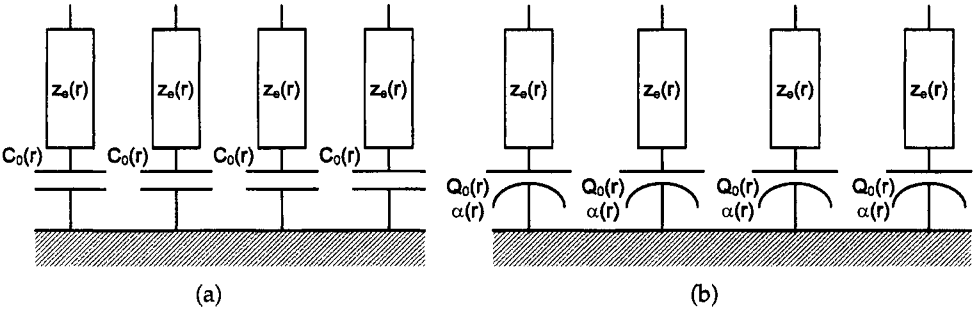

Figure 13.1: Schematic representation of an impedance distribution for a blocking disk electrode where $z_e(r)$ represents the local Ohmic impedance, $C_0(r)$ represents the interfacial capacitance, and $Q_0(r)$ and $\alpha(r)$ represent local CPE parameters: a) 2-dimensional distribution; and b) combined 2-dimensional and 3-dimensional distribution.

In both equations (13.1) and (13.2), the parameters α and Q are independent of frequency. When $\alpha = 1$, Q has units of a capacitance, i.e., F/cm^2, and represents the capacity of the interface. When $\alpha \neq 1$, Q has units of s$^\alpha$/Ωcm^2 and the system shows behavior that has been attributed to surface heterogeneity[181,182] or to continuously distributed time constants for charge-transfer reactions.[183–187] Independent of the cause of CPE behavior, the phase angle associated with a CPE is independent of frequency.

Different expressions for a CPE have been presented in the literature,[188] e.g.,

$$Z(\omega) = R_e + \frac{1}{(j\omega\tau_0)^\alpha} \tag{13.3}$$

where the parameter τ_0 is a characteristic time constant for the distribution. Brug et al.[104] used a formula in which Q was defined to be in the numerator of equation (13.1) rather than the denominator. The formulas presented in this chapter as equations (13.1) and (13.2) have the advantages that Q is proportional to the active area and the definition of Q for $\alpha = 1$ is simply the capacitance.

13.1.1 2-D and 3-D Distributions

Time-constant dispersion leading to CPE behavior can be attributed to distributions of time constants along either the area of the electrode (involving only a 2-dimensional surface) or along the axis normal to the electrode surface (involving a 3-dimensional aspect of the electrode). A 2-D distribution could arise from surface heterogeneities such as grain boundaries, crystal faces on a polycrystalline electrode, or other variations in surface properties. As shown in Section 13.3, the time-constant dispersion associated with geometry-induced nonuniform current and potential distributions results from a 2-D distribution.

A schematic representation of a 2-D distribution for an ideally polarized disk electrode is presented in Figure 13.1(a). For a 2-D distribution, the circuit parameters, e.g., capacitance and Ohmic resistance, could be a function of radial position along the electrode. The global admittance is obtained by integration of the admittance associated with these circuit elements over the electrode area, i.e.,

$$Y = Z^{-1} = \int_A z^{-1} dA \tag{13.4}$$

where A is the electrode area, Y is the global admittance, Z is the global impedance, and z is the local impedance. Depending on the nature of the local distribution, equation (13.4) may yield a global impedance with a CPE behavior. The local impedance, in the case of a 2-D distribution, would, however, show ideal RC behavior.

CPE behavior may also arise from a variation of properties in the direction that is normal to the electrode surface. Such variability may be attributed, for example, to changes in the conductivity of oxide layers[189–191] (see Section 13.5) or from porosity or surface roughness (see Section 13.4).[192,193] This CPE behavior is said to arise from a 3-dimensional distribution, with the third direction being the direction normal to the plane of the electrode.[194]

A 3-D distribution of blocking components in terms of resistors and constant-phase elements is presented in Figure 13.1(b). Such a system will yield a local impedance with a CPE behavior, even in the absence of a 2-D distribution of surface properties. If the 3-D system shown schematically in Figure 13.1(b) is influenced by a 2-D distribution, the local impedance should reveal a variation along the surface of the electrode. Thus, local impedance measurements can be used to distinguish whether the observed global CPE behavior arises from a 2-D distribution, from a 3-D distribution, or from a combined 2-D and 3-D distribution.

Equations (13.1) and (13.2) embody an implicit assumption that the RC time constant is not, in fact, a constant but, rather, a parameter that follows a specific distribution. Equation (13.1), for example, can be imagined as arising from a 2-D distribution of time constants $\tau_i = (R_e C_0)_i$, e.g.,

$$Z^{-1} = \frac{1}{R_e} \sum_{i=1}^{\infty} (1 - \frac{1}{1 + j\omega\tau_i}) \tag{13.5}$$

If τ is a continuous function, equation (13.5) can be written as[104]

$$Z^{-1} = \frac{1}{R_e} \left(1 - \int_0^{\infty} \frac{1}{1 + j\omega\tau} G(\tau) d\tau \right) \tag{13.6}$$

where $G(\tau)$ is the distribution function of τ, which represents a normal distribution of a function of $\ln(\tau/\tau_0)$, i.e.,

$$G(\tau) = \frac{1}{2\pi\tau} \frac{\sin(\alpha\pi)}{\cosh\left[(1-\alpha)\ln(\frac{\tau}{\tau_0})\right] - \cos(\alpha\pi)} \tag{13.7}$$

A similar development can be made for equation (13.2), also leading to equation (13.7).

13.1.2 Determination of Capacitance

It is incorrect to equate the CPE parameter Q to the interfacial capacitance. A number of researchers have explored the relationship between CPE parameters and the interfacial capacitance. Hsu and Mansfeld[195] proposed

$$C_{\text{eff}} = Q(\omega_{\text{max}})^{\alpha-1} = Q\left(\frac{\kappa K_{\mathbf{max}}}{C_0 r_0}\right)^{\alpha-1} \tag{13.8}$$

where ω_{max} (or K_{max}) is the characteristic frequency at which the imaginary part of the impedance reaches its maximum magnitude and C_{eff} is the estimated interfacial capacitance. Brug et al.[104] developed a relationship for a blocking electrode between the interfacial capacitance and the CPE coefficient Q as

$$C_{\text{eff}} = \left[QR_e^{(1-\alpha)}\right]^{1/\alpha} \tag{13.9}$$

A similar relationship between the interfacial capacitance and the CPE coefficient Q was developed for a Faradaic system as

$$C_{\text{eff}} = \left[Q\left(\frac{1}{R_e} + \frac{1}{R_t}\right)^{(\alpha-1)}\right]^{1/\alpha} = \left[Q\left(\frac{1}{R_e}\left(1+\frac{\pi J}{4}\right)\right)^{(\alpha-1)}\right]^{1/\alpha} \tag{13.10}$$

For CPE behavior caused by 2-D distributions of current and potential on a disk electrode, equations (13.9) and (13.10) provided the most reliable estimate for interfacial capacitance (see Section 13.3).[97] Similar formulas for 3-D distributions do not exist.

13.1.3 Limitations to the Use of the CPE

As compared to a parallel combination of a resistor and capacitor, the CPE is able to provide a much better fit to most impedance data. The CPE can achieve this fit using only three parameters, which is only one parameter more than a typical RC couple. Some investigators allow α to take values from -1 to 1, thus treating the CPE as an extremely flexible fitting element. For $\alpha = 1$, the CPE behaves as a capacitor; for $\alpha = 0$, the CPE behaves as a resistor; and for $\alpha = -1$ the CPE behaves as an inductor (see Section 4.1.1).

It must be emphasized that the mathematical simplicity of equations (13.1) and (13.2) is the consequence of a specific time-constant distribution. As shown in this chapter, time-constant distributions can result from nonuniform mass transfer, geometry-induced nonuniform current and potential distributions, electrode porosity, and distributed properties of oxides. At first glance, the associated impedance responses may appear to have a CPE behavior, but the frequency dependence of the phase angle shows that the time-constant distribution differs from that presented in equation (13.7).

There are, therefore, two primary concerns with the use of the CPE for modeling impedance data:

1. While assumption that the time constant is distributed can be better than assuming that the time constant has a single value, the physical system may not follow the specific distribution implied in equation (13.7). The examples presented in the subsequent sections illustrate systems for which a time-constant dispersion results that resembles that of a CPE, but with different distributions of time constants.
2. A satisfactory fit of a CPE to experimental data may not necessarily be correlated to the physical processes that govern the system. As shown in Section 4.4, models for impedance are not unique; thus, an excellent fit to the data does not in itself guarantee that the model describes correctly the physics of a given system.

The graphical methods described in Chapter 17 can be used to determine whether a system follows CPE behavior in a given frequency range.

13.2 Convective Diffusion Impedance at Small Electrodes

Small electrodes are currently used to study fast electrochemical kinetics or as flow measurement devices in chemical engineering systems. In the latter case, the first experimental and theoretical studies appeared in the early fifties. The goal of these studies was to achieve probes sensitive to the local wall velocity gradient

$$\beta_y = \frac{\partial v_x}{\partial y} \tag{13.11}$$

The well-known property of those probes is that the limiting diffusion current is proportional to $\beta_y^{1/3}$ under steady-state conditions.[196] For use in electrochemical engineering, an increasing interest is now focused on the nonsteady behavior of those small electrodes under conditions of fluctuating velocity gradient $\beta_y(t)$.

Theoretical developments show that it is possible to deduce hydrodynamic information from the limiting current measurement, either in quasi-steady state where $I(t) \propto \beta_y^{1/3}(t)$ or, at higher frequency, in terms of spectral analysis. In the latter case, it is possible to obtain the velocity spectra from the mass-transfer spectra, where the transfer function between the mass-transfer rate and the velocity perturbation is known. However, in most cases, charge transfer is not infinitely fast, and the analysis also requires knowledge of the convective-diffusion impedance, i.e., the transfer function between a concentration modulation at the interface and the resulting flux of mass under steady-state convection.

Remember! 13.1 *While use of a CPE may lead to improved regressions, the meaning can be ambiguous, and the physical system may not follow the specific distribution implied in the CPE model.*

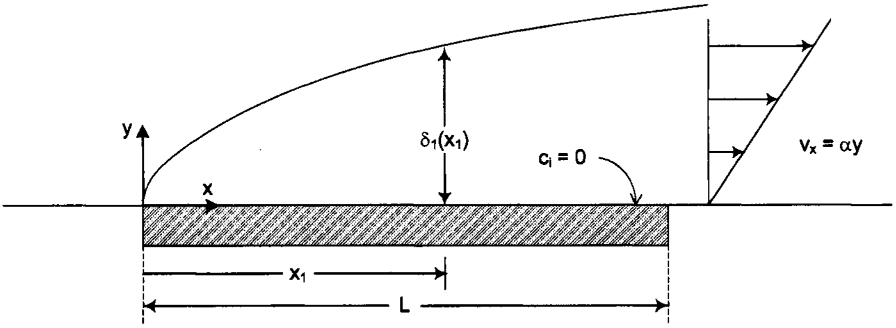

Figure 13.2: Schematic representation of flow past a small electrode where the coordinate y is in the direction perpendicular to the plane of the electrode (x, y).

13.2.1 Analysis

A schematic representation of a small electrode embedded in an insulating wall is given in Figure 13.2 on which a fast electrochemical reaction occurs under mass-transport limitation, i.e., $c_i(0) = 0$. The length of this electrode in the mean flow direction is small enough that the diffusion layer thickness δ_i is very small, thus minimizing the effect of the normal velocity component. The normal velocity is proportional to y^2, whereas the longitudinal velocity component is proportional to y, where y is the coordinate normal to the wall. Under these conditions, the boundary layer approximations apply. Using a local frame of reference (x, y) attached to the electrode, the mass conservation equation governing the concentration distribution c_i of a species transported by convective diffusion can be expressed as

$$\frac{\partial c_i}{\partial t} + \beta_y y \frac{\partial c_i}{\partial x} = D_i \frac{\partial^2 c_i}{\partial y^2} \tag{13.12}$$

where $v_x = \beta_y y$. For simplification, the electrode can be considered to be sufficiently small that the flow is uniform in the diffusion layer and β_y is independent of the space coordinates. The time-average solution for the concentration distribution has been given by Lévêque.[196] As shown in Example 2.2, the concentration in the diffusion layer can be expressed as

$$\bar{c}_i = \frac{c_i(\infty) - c_i(0)}{3^{2/3}\Gamma(4/3)} \int_0^{y/\delta_i} \exp\left(-\eta^3/9\right) d\eta + c_i(0) \tag{13.13}$$

where $3^{2/3}\Gamma(4/3)\delta_i$ represents the local value of the diffusion layer thickness with $\delta_i = \left(D_i x/\beta_y\right)^{1/3}$, $0 \le x \le L$, and $c_i(\infty)$ is the concentration in the bulk. On a small rectangular electrode of width W, the steady flux is

$$\overline{N}_i = W \int_0^L D_i \frac{\partial \bar{c}_i}{\partial y} dx = \frac{3^{1/3}\left(c_i(\infty) - c_i(0)\right) D_i^{2/3} \beta_y^{1/3} L^{2/3} W}{2\Gamma\left(4/3\right)} \tag{13.14}$$

or

$$\overline{N}_i = 0.80755 (c_i(\infty) - c_i(0)) D_i^{2/3} \beta_y^{1/3} L^{2/3} W \tag{13.15}$$

Equation (13.15) shows that the steady mass-transfer-controlled flux of a reacting species is proportional to the cube root of the velocity gradient, i.e., $\overline{N}_i \propto \beta_y^{1/3}$.

Example 13.1 Flux on a Small Circular Electrode: *Derive an expression for the steady flux on a circular small electrode of radius R.*

Solution: *Equation (13.13) can be used to calculate the flux on a circular small electrode by summing along z, the effect of elementary rectangular strips. In this case, x contained in the definition of δ_i must be replaced by $(x - x_1)$, which actually corresponds in the local Cartesian frame of reference to the distance from the leading edge of any elementary strip. The position of the leading edge $x_1(z)$ is a function of R and z as*

$$x_1(z) = R - \sqrt{R^2 - z^2} \tag{13.16}$$

Thus, the expression of the flux is

$$\overline{N}_{\text{circ}} = \int_{-R}^{R} dz \int_{R-\sqrt{R^2-z^2}}^{R+\sqrt{R^2-z^2}} D_i \frac{\partial \overline{c}_i}{\partial y} dx \tag{13.17}$$

or

$$\overline{N}_{\text{circ}} = 0.84 \frac{3^{1/3}\left(c_i(\infty) - c_i(0)\right) D_i^{2/3} \beta_y^{1/3} (2R)^{5/3}}{2\Gamma(4/3)} \tag{13.18}$$

Comparison with equation (13.14) reveals that the flux at a circular electrode is 84 percent smaller than that at a square electrode with L = W = 2R.

13.2.2 Local Diffusion Convective Impedance

The nonsteady part of the mass balance equation (13.12) may be written as:

$$j\omega\widetilde{c}_i - \frac{\partial^2 \widetilde{c}_i}{\partial y^2} + y\beta_y \frac{\partial \widetilde{c}_i}{\partial x} = 0 \tag{13.19}$$

The boundary conditions for the nonsteady equations are

$$\begin{aligned} \widetilde{c}_i &= \widetilde{c}_i(0) \quad \text{for} \quad y = 0 \quad \text{and} \quad x \geq x_1 \\ \frac{\partial \widetilde{c}_i}{\partial y} &= 0 \quad \text{for} \quad y = 0 \quad \text{and} \quad x \geq x_1 \\ \widetilde{c}_i &= 0 \quad \text{for} \quad y \rightarrow \infty \quad \text{and all} \quad x \end{aligned} \tag{13.20}$$

A dimensionless concentration θ_i can be defined such that

$$\theta_i = \frac{\widetilde{c}_i}{\widetilde{c}_i(0)} \tag{13.21}$$

The dimensionless normal distance to the wall can be defined to be

$$\eta = y/\delta_i = y\left(\frac{\beta_y}{D_i(x - x_1)}\right)^{1/3} \tag{13.22}$$

where x_1 is the coordinate of the leading edge of the electrode as shown in Figure 13.2. Equation (13.22) represents a similarity variable (see Section 2.4). Introduction of η into equation (13.19) results in definition of a dimensionless position-dependent frequency given by

$$\mathrm{K}_{x,i} = \omega \left(\frac{(x - x_1)^2}{\beta_y^2 D_i} \right)^{1/3} \tag{13.23}$$

In terms of equations (13.21) to (13.23), equation (13.19) becomes

$$j\mathrm{K}_{x,i}\theta_i + \frac{2}{3}\mathrm{K}_{x,i}\eta \frac{\partial \theta_i}{\partial \mathrm{K}_{x,i}} - \frac{\eta^2}{3}\frac{\partial \theta_i}{\partial \eta} - \frac{\partial^2 \theta_i}{\partial \eta^2} = 0 \tag{13.24}$$

The spatial dependence of the sinusoidal perturbation is evident in the definition of $\mathrm{K}_{x,i}$.

As $\mathrm{K}_{x,i}$ contains a dependence on the space coordinates, it is necessary to derive first the local solution. A solution in the form of a series can be obtained as

$$\theta_i = \sum_{m=0}^{\infty} (j\mathrm{K}_{x,i})^m \, \theta_{i,m}(\eta) \tag{13.25}$$

For this solution the number of terms that play a role in the series increases with the frequency. Generally the solution given by equation (13.25) is used for the low-frequency solution, and the high-frequency solution is derived by another method.

Low-Frequency Solution

The elementary functions $h_m(\eta)$ are real and obey

$$\frac{\partial^2 \theta_{i,0}}{\partial \eta^2} + \frac{\eta^2}{3}\frac{\partial \theta_{i,0}}{\partial \eta} = 0 \tag{13.26}$$

and

$$\frac{\partial^2 \theta_{i,m}}{\partial \eta^2} + \frac{\eta^2}{3}\frac{\partial \theta_{i,m}}{\partial \eta} - \frac{2m\eta}{3}\theta_{i,m} = \theta_{i,m-1} \tag{13.27}$$

The boundary conditions at $\eta = 0$ are $\theta_i(0) = 1$, $\theta_{i,0}(0) = 1$, and $\theta_{i,m}(0) = 0$ for all $m > 0$. The boundary condition at $\eta \to \infty$ is $h(\infty) = 0$. In fact, since the only observable quantity is the interfacial flux, only its expression is needed, i.e.,

$$\left.\frac{d\theta_i}{d\eta}\right|_0 = \sum_{m=0}^{\infty} (j\mathrm{K}_{x,i})^m \left.\frac{d\theta_{i,m}}{d\eta}\right|_0 \tag{13.28}$$

The terms $d\theta_{i,m}/d\eta|_0$ are tabulated by Deslouis et al.[197] for $0 \leq m \leq 79$.

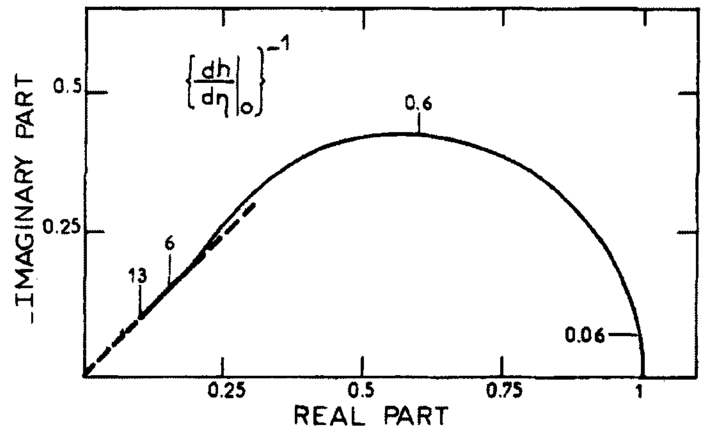

Figure 13.3: Local normalized diffusion impedance for the small electrode given in Figure 13.2. The solid line represents the low-frequency solution (equation (13.28)), and the dashed line represents the high-frequency solution (equation (13.31)). Overlap is obtained for $6 \leq K_{x,i} \leq 13$, with the dimensionless frequency $K_{x,i}$ given by equation (13.23). (Taken from Delouis et al.[197] and reproduced with permission of The Electrochemical Society.)

High-Frequency Solution

Since the concentration modulation is rapidly damped close to the wall at high frequencies, the convective term can be disregarded and equation (13.24) becomes

$$jK_{x,i}\theta_i - \frac{\partial^2\theta_i}{\partial\eta^2} = 0 \tag{13.29}$$

The solution to equation (13.29) can be found using the methods described in Section 2.2.

Due to the boundary conditions ($\theta_i = 0$ when $\eta \rightarrow \infty$ and $\theta_i = 1$ when $\eta = 0$), the analytic solution is, as given for equation (11.46),

$$\theta_i = \exp\left[-\left(jK_{x,i}\right)^{1/2}\eta\right] \tag{13.30}$$

The local dimensionless impedance is obtained as

$$\frac{z_D}{z_D(0)} = \left[\frac{d\theta_i}{d\eta}\Big|_0\right]^{-1} = -\left(jK_{x,i}\right)^{-1/2} \tag{13.31}$$

which is a normalized Warburg impedance as described in Section 11.3. As seen in Figure 13.3, the high-frequency solution (13.28) and the low-frequency solution (13.31) present a satisfactory overlap for $6 \leq K_{x,i} \leq 13$.

13.2.3 Global Convective Diffusion Impedance

The dimensionless impedance of a small electrode can be defined by summing the effects of the local convective-diffusion impedance, i.e.,

$$\frac{Z_D(0)}{Z_D} = \iint z_D^{-1} dxdz = -\iint \frac{1}{\tilde{c}(0)} \left.\frac{\partial \tilde{c}}{\partial y}\right|_0 dxdz = -\iint \left.\frac{dh}{d\eta}\right|_0 \frac{dxdz}{\delta_i(x)} \tag{13.32}$$

For a rectangular electrode of length L and of width W, the expression of the impedance is given by

$$\frac{Z_D(0)}{Z_D} = -W \int_0^L \left(\sum_{m=0}^{\infty} (j\mathrm{K}_{x,i})^m \left.\frac{d\theta_{i,m}}{d\eta}\right|_0 \right) \frac{dx}{\delta_i(x)} \tag{13.33}$$

By using the dimensionless frequency

$$\mathrm{K}_i = \omega \left(L^2 / D_i \beta_y^2 \right)^{1/3} \tag{13.34}$$

equation (13.33) can be expressed as

$$\frac{Z_D(0)}{Z_D} = \left(\frac{\beta_y L^2}{D_i} \right)^{1/3} W D_i H(\mathrm{K}_i) \tag{13.35}$$

with

$$H(\mathrm{K}_i) = \frac{3}{2\mathrm{K}_i} \int_0^{\mathrm{K}_i} \left.\frac{d\theta_i}{d\eta}\right|_0 d\mathrm{K}_{x,i} \tag{13.36}$$

In the low-frequency range, the expression of $H(\mathrm{K}_i)$ is obtained from the series expansion (13.28)

$$H(\mathrm{K}_i) = \frac{3}{2} \sum_{m=0}^{\infty} \frac{(j\mathrm{K}_i)^m}{m+1} \left.\frac{d\theta_{i,m}}{d\eta}\right|_0 \tag{13.37}$$

In the high-frequency range, the integration must be split in two parts since the leading edge of an electrode will be always under a low-frequency regime. Indeed, the local thickness of the diffusion layer, equal to $3^{2/3}\Gamma(4/3)\delta_i(x)$ and thus proportional to $x^{1/3}$, is very small at the leading edge, and $\mathrm{K}_{x,i}$ remains there always small even for high values of $\omega/2\pi$. Thus,

$$H(\mathrm{K}_i) = \frac{3}{2\mathrm{K}_i} \left(\int_0^{\sigma_1} \left.\frac{d\theta_i}{d\eta}\right|_0 d\mathrm{K}_{x,i} + \int_{\sigma_1}^{\mathrm{K}_i} \left.\frac{d\theta_i}{d\eta}\right|_0 d\mathrm{K}_{x,i} \right) \tag{13.38}$$

The first integral corresponds to the low-frequency regime and the second one to the high-frequency regime where equations (13.28) and (13.31) must be used, respectively. Equation (13.38) becomes

$$H(\mathrm{K}_i) = -\frac{B(\sigma_1)}{\mathrm{K}_i} + (j\mathrm{K}_i)^{1/2} \tag{13.39}$$

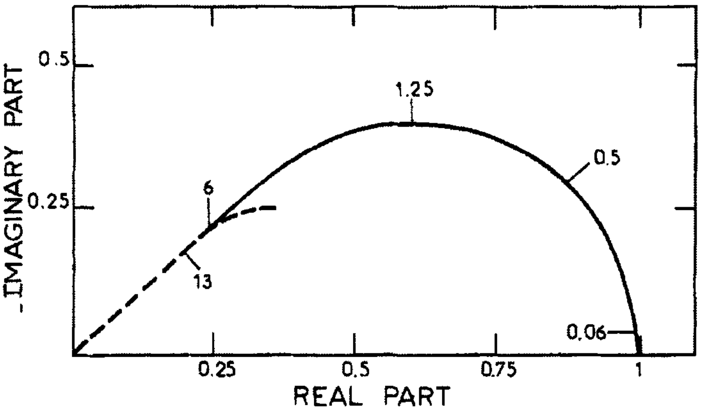

Figure 13.4: Normalized global convective-diffusion impedance for a small rectangular electrode. The solid line represents the low-frequency solution (equation (13.37)), and the dashed line represents the high-frequency solution (equation (13.40)). Overlap is obtained for $6 \leq K_i \leq 13$, with the dimensionless frequency K_i given by equation (13.34). (Taken from Delouis et al.[197] and reproduced with permission of The Electrochemical Society.)

The term $B(\sigma_1)$ has been calculated for $\sigma_1 \leq 13$, and $B(\sigma_1)$ was found to be constant and equal to $0.25j$ in the frequency range $6 \leq \sigma_1 \leq 13$. This result means that equation (13.39) is valid for $K_i \geq 6$ and therefore can be written as

$$H(K_i) = -\frac{0.25j}{K_i} + (jK_i)^{1/2} \tag{13.40}$$

As a consequence, a fair overlap between equation (13.37) and equation (13.40) is obtained for $6 \leq K_i \leq 13$ as shown in Figure 13.4.

13.3 Geometry-Induced Current and Potential Distributions

The geometry of an electrode frequently constrains the distribution of current density and potential in the electrolyte adjacent to the electrode in such a way that both cannot simultaneously be uniform. The primary and secondary current and potential distributions associated with a disk embedded in an insulating plane, originally developed by Newman,[198,199] are presented in Section 5.6. The potential distribution on the disk electrode is not uniform under conditions where the current density is uniform and, conversely, the current distribution is nonuniform under the primary condition where the solution potential is uniform.

The nonuniform current and potential distribution associated with the disk geometry influences the transient and the impedance response. Nisancioglu and

---

Remember! **13.2** *Not all time-constant distributions give rise to a CPE.*

Newman[200,201] modeled the transient response of a disk electrode to step changes in current. The solution to Laplace's equation was performed using a transformation to rotational elliptic coordinates and a series expansion in terms of Lengendre polynomials. Antohi and Scherson expanded the solution to the transient problem by expanding the number of terms used in the series expansion.[202]

The geometry-induced current and potential distributions cause a frequency or time-constant dispersion that distorts the impedance response of a disk electrode.[38,203,204] Huang et al.[97,102,205] have shown that current and potential distributions induce a high-frequency pseudo-CPE behavior in the global impedance response of a disk electrode with a local ideally capacitive behavior, a blocking disk electrode exhibiting a local CPE behavior, and a disk electrode exhibiting Faradaic behavior.

13.3.1 Mathematical Development

The mathematical development presented here follows that presented by Newman.[38] The development in terms of rotational elliptic coordinates, i.e.,

$$y = r_0\xi\eta \tag{13.41}$$

and

$$r = r_0\sqrt{(1+\xi^2)(1-\eta^2)} \tag{13.42}$$

was summarized by Huang et al. for blocking electrodes.[102,205]

The problem was solved for two kinetic regimes. Under linear kinetics, following Newman[38] and Nisancioglu,[203,204] the current density at the electrode surface could be expressed as

$$\begin{aligned} i &= C_0\frac{\partial(V-\Phi_0)}{\partial t} + \frac{(\alpha_a+\alpha_c)\,i_0F}{RT}(V-\Phi_0) \\ &= -\kappa\left.\frac{\partial\Phi}{\partial y}\right|_{y=0} = -\frac{\kappa}{r_0\eta}\left.\frac{\partial\Phi}{\partial\xi}\right|_{\xi=0} \end{aligned} \tag{13.43}$$

The assumption of linear kinetics applies for $\bar{i} << i_0$. Under assumption of Tafel kinetics, the current density at the electrode surface could be expressed as

$$\begin{aligned} i &= C_0\frac{\partial(V-\Phi_0)}{\partial t} - i_0\exp\left(-\frac{\alpha_cF}{RT}(V-\Phi_0)\right) \\ &= -\kappa\left.\frac{\partial\Phi}{\partial y}\right|_{y=0} = -\frac{\kappa}{r_0\eta}\left.\frac{\partial\Phi}{\partial\xi}\right|_{\xi=0} \end{aligned} \tag{13.44}$$

where the current in the Tafel regime was assumed to be cathodic. A similar expression can be developed under assumption of anodic currents. The results presented here are general because the impedance results do not depend on whether the current is anodic or cathodic.

The flux boundary conditions (13.43) or (13.44) apply at the electrode surface ($\xi = 0$). The boundary conditions (13.43) or (13.44) were written in the frequency-domain as

$$\mathrm{K}\widetilde{\Phi}_{0,j} + J\left(\widetilde{V}_r - \widetilde{\Phi}_{0,r}\right) = -\frac{1}{\eta}\left.\frac{\partial \widetilde{\Phi}_r}{\partial \xi}\right|_{\xi=0} \tag{13.45}$$

for linear kinetics and

$$\mathrm{K}\left(\widetilde{V}_r - \widetilde{\Phi}_{0,r}\right) + J\widetilde{\Phi}_{0,j} = -\frac{1}{\eta}\left.\frac{\partial \widetilde{\Phi}_j}{\partial \xi}\right|_{\xi=0} \tag{13.46}$$

for Tafel. Here $\widetilde{V}_r$ represents the imposed perturbation in the electrode potential referenced to an electrode at infinity, and K is the dimensionless frequency

$$\mathrm{K} = \frac{\omega C_0 r_0}{\kappa} \tag{13.47}$$

Under the assumption of linear kinetics, valid for $\bar{i} << i_0$, the parameter J was defined to be

$$J = \frac{(\alpha_a + \alpha_c) F i_0 r_0}{RT\kappa} \tag{13.48}$$

For Tafel kinetics, valid for $\bar{i} >> i_0$, the parameter J was defined to be a function of radial position on the electrode surface as

$$J(\eta) = \frac{\alpha_c F \left|\bar{i}(\eta)\right| r_0}{RT\kappa} \tag{13.49}$$

where $\bar{i}(\eta)$ was obtained from the steady-state solution as

$$\bar{i}(\eta) = -i_0 \exp\left(-\frac{\alpha_c F}{RT}\left(\bar{V} - \Phi_0(\eta)\right)\right) \tag{13.50}$$

The local charge-transfer resistance for linear kinetics can be expressed in terms of parameters used in equation (13.48) as

$$R_t = \frac{RT}{i_0 F(\alpha_a + \alpha_c)} \tag{13.51}$$

The local charge-transfer resistance for Tafel kinetics can be expressed in terms of parameters used in equation (13.49) as

$$R_t = \frac{RT}{\bar{i}(\eta)\alpha_c F} \tag{13.52}$$

For linear kinetics, R_t is independent of radial position, but, under Tafel kinetics, as shown in equation (13.52), R_t depends on radial position. From a mathematical perspective, the principal difference between the linear and Tafel cases is that J and R_t are held constant for linear polarization; whereas, for the Tafel kinetics,

J and R_t are functions of radial position determined by solution of the nonlinear steady-state problem.

The relationship between the parameter J and the charge-transfer and Ohmic resistances can be established using the high-frequency limit for the Ohmic resistance to a disk electrode obtained by Newman,[198] i.e.,

$$R_e = \frac{\pi r_0}{4\kappa} \tag{13.53}$$

where R_e has units of $\Omega\mathrm{cm}^2$. The parameter J can therefore be expressed in terms of the Ohmic resistance R_e and charge-transfer resistance R_t as

$$J = \frac{4}{\pi}\frac{R_e}{R_t} \tag{13.54}$$

Large values of J are seen when the Ohmic resistance is much larger than the charge-transfer resistance, and small values of J are seen when the charge-transfer resistance dominates.

13.3.2 Global and Local Impedances

Following Huang et al.,[102] a notation is presented in Section 7.5.2 that addresses the concepts of a global impedance, which involved quantities averaged over the electrode surface; a local interfacial impedance, which involved both a local current density and the local potential drop $\widetilde{V} - \widetilde{\Phi}_0(r)$ across the diffuse double layer; a local impedance, which involved a local current density and the potential of the electrode $\widetilde{V}$ referenced to a distant electrode; and a local Ohmic impedance, which involved a local current density and potential drop $\widetilde{\Phi}_0(r)$ from the outer region of the diffuse double layer to the distant electrode. The corresponding list of symbols is provided in Table 7.2.

The local impedance z can be represented by the sum of local interfacial impedance z_0 and local Ohmic impedance z_e as

$$z = z_0 + z_e \tag{13.55}$$

Huang et al.[102,205] demonstrated for blocking disk electrodes that, while the local interfacial impedance represents the behavior of the system unaffected by the current and potential distributions along the surface of the electrode, the local impedance shows significant time-constant dispersion. The local and global Ohmic impedances were shown to contain the influence of the current and potential distributions.

While the calculations presented here were performed in terms of solution of Laplace's equation for a disk geometry, the nature of the electrode–electrolyte interface can be understood in the context of the schematic representation given in Figure 13.5. Under linear kinetics, both C_0 and R_t can be considered to be independent of radial position, whereas, for Tafel kinetics, $1/R_t$ varies with radial position in accordance with the current distribution presented in Figure 5.10. The calculated results for global impedance, local impedance, local interfacial impedance, and both local and global Ohmic impedances are presented in this section.

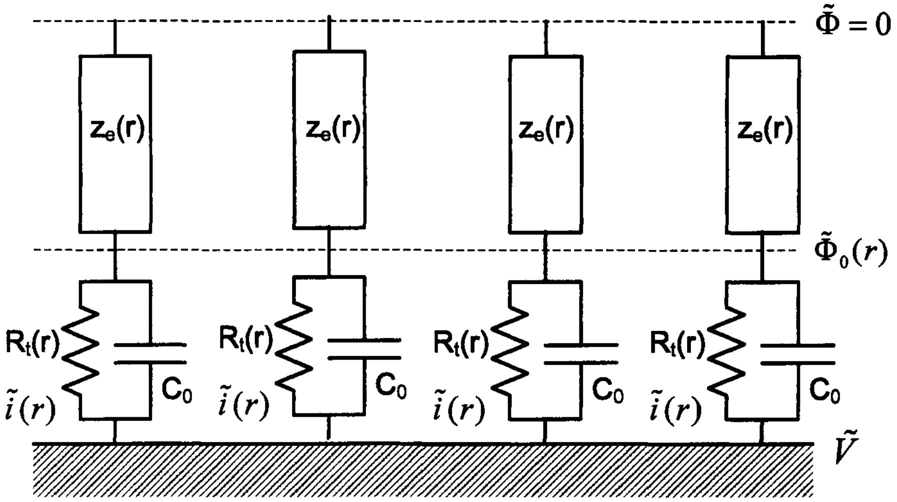

Figure 13.5: Schematic representation of an impedance distribution for a disk electrode where z_e represents the local Ohmic impedance, C_0 represents the interfacial capacitance, which in this case can be considered to be associated with the double-layer, and R_t represents the charge-transfer resistance. (Taken from Huang et al.[97] and reproduced with permission of The Electrochemical Society.)

Global Impedance

The calculated real and imaginary parts of the global impedance response are shown in Figures 13.6(a) and (b), respectively. At low frequencies, values for the real part of the impedance differ for impedance calculated under the assumptions of linear and Tafel kinetics, whereas, the values of the imaginary impedance calculated under the assumptions of linear and Tafel kinetics are superposed for all frequencies. The slopes of the lines presented in Figure 13.6(b) are equal to +1 at low frequencies but differ from −1 at high frequencies. As discussed in Section 17.1.3, the slope of these lines in the high-frequency range can be related to the exponent α used in models for CPE behavior.[206]

Following the definition of J given in equation (13.49), the curves for $J = 0$ in Figures 13.6(a) and (b) correspond to an ideally capacitive blocking electrode. The steady-state solution for the current distribution at a blocking electrode is that the current is equal to zero. The primary current distribution given as equation (5.65) therefore applies, not at the steady state, but at infinite frequency. For the special case of a Faradaic system with an Ohmic resistance that is much larger than the kinetic resistance, $J \rightarrow \infty$, and equation (5.65) provides the steady-state current distribution.

Two characteristic frequencies are evident in Figure 13.6. The characteristic frequency $K = 1$ is associated with the influence of current and potential distributions and can be expressed in terms of the capacitance C_0 and the Ohmic resistance to a

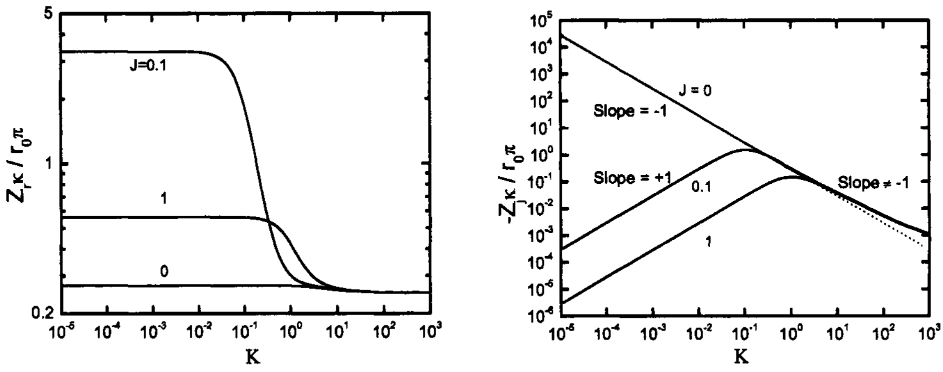

(a) (b)

Figure 13.6: Calculated representation of the impedance response for a disk electrode under assumption of Tafel kinetics with J as a parameter. The value $J = 0$ corresponds to an ideally capacitive blocking electrode: a) real part; and b) imaginary part.

disk electrode given in equation (13.53) as

$$K = \frac{4}{\pi}\omega R_e C_0 \tag{13.56}$$

The characteristic frequency $\mathrm{K}/J = 1$ is associated with the $R_t C_0$-time constant for the Faradaic reaction.

The frequency $\mathrm{K} = 1$ at which the current and potential distributions begin to influence the impedance response can be expressed as

$$f = \frac{\kappa}{2\pi C_0 r_0} \tag{13.57}$$

or, in terms of electrolyte resistance, as

$$f = \frac{1}{8 C_0 R_e} \tag{13.58}$$

The frequency $\mathrm{K} = 1$ at which the current distribution influences the impedance response is shown in Figure 13.7 with κ / C_0 as a parameter. As demonstrated in Example 13.2, the influence of high-frequency geometry-induced time-constant dispersion can be avoided for reactions that do not involve adsorbed intermediates by conducting experiments below the characteristic frequency given in equation (13.57). The characteristic frequency can be well within the range of experimental measurements. The value $\kappa / C_0 = 10^3$ cm/s, for example, can be obtained for a capacitance $C_0 = 10$ μF/cm^2 (corresponding to the value expected for the double layer on a metal electrode) and conductivity $\kappa = 0.01$ S/cm (corresponding roughly to a 0.1 M NaCl solution). Equation (13.57) suggests that time-constant dispersion should be expected above a frequency of 600 Hz on a disk with radius $r_0 = 0.25$ cm.

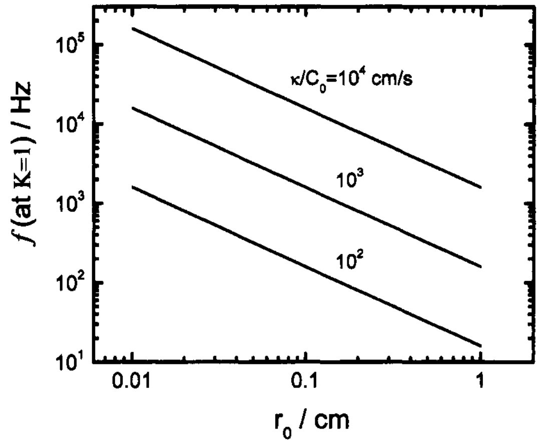

Figure 13.7: The frequency K = 1 at which the current distribution influences the impedance response with κ/C_0 as a parameter. (Taken from Huang et al.[102] and reproduced with permission of The Electrochemical Society.)

Example 13.2 Characteristic Frequency: *Consider an experimental system involving a Pt disk in 0.1 M NaCl solution at room temperature for which impedance measurements are desired to a maximum frequency of 10 kHz. Estimate the maximum radius for a disk electrode that will avoid the influence of high-frequency geometry-induced time-constant dispersion.*

Solution: *The characteristic frequency given in equation (13.57) depends on the ratio* κ/C_0. *The conductivity can be estimated using equation (5.56) and values of diffusivity taken from Table 5.2. The conductivity can be estimated to be* $\kappa = 0.013\ (\Omega cm)^{-1}$. *The double-layer capacitance for a bare electrode is of the order of* $C_0 = 10\ \mu F/cm^2$. *Thus,* $\kappa/C_0 = 1.3 \times 10^3$ *cm/s, and, following*

$$r_0 = \frac{\kappa}{2\pi f C_0} \tag{13.59}$$

the maximum disk radius is 0.02 cm. This result can also be obtained from Figure 13.7.

Local Interfacial Impedance

For the linear kinetics calculation, where J is independent of radial position, the scaled real part of the local interfacial impedance follows

$$\frac{z_{0,r}\kappa}{r_0\pi} = \frac{J}{\pi(J^2+K^2)} \tag{13.60}$$

and the imaginary part of the local interfacial impedance follows

$$\frac{z_{0,j}\kappa}{r_0\pi} = \frac{-K}{\pi(J^2+K^2)} \tag{13.61}$$

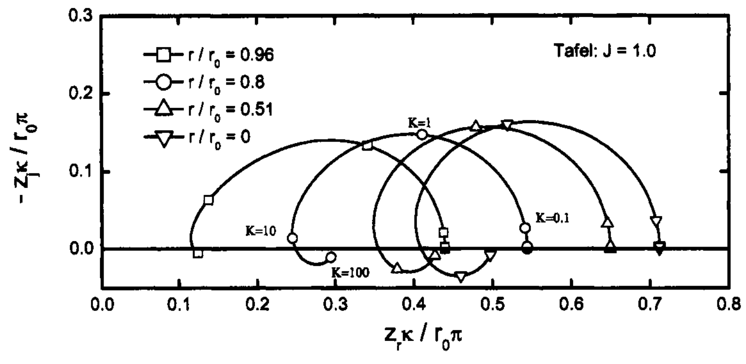

Figure 13.8: Calculated representation of the local impedance response for a disk electrode as a function of dimensionless frequency K under assumptions of Tafel kinetics with $J = 1$. (Taken from Huang et al.[97] and reproduced with permission of The Electrochemical Society.)

The local interfacial impedance is that associated with the boundary at the electrode surface. For a simple Faradaic system, the local interfacial impedance is that of an resistor in parallel connection to a capacitor and includes no Ohmic resistance. For an ideally capacitive electrode, the local interfacial impedance is that of a capacitor with no real component.

Local Impedance

The calculated local impedance is presented in Figure 13.8 for Tafel kinetics with $J = 1$ and with radial position as a parameter. The impedance is largest at the center of the disk and smallest at the periphery, reflecting the greater accessibility of the periphery of the disk electrode. Similar results were also obtained for $J = 0.1$, but the differences between radial positions were much less significant. Inductive loops are observed at high frequencies, and these are seen in both Tafel and linear calculations for $J = 0.1$ and $J = 1.0$.[97]

Local Ohmic Impedance

The local Ohmic impedance z_e accounts for the difference between the local interfacial and the local impedances. The calculated local Ohmic impedance for Tafel kinetics with $J = 1.0$ is presented in Figure 13.9 in Nyquist format with normalized radial position as a parameter. The results obtained here for the local Ohmic impedance are very similar to those reported for the ideally polarized electrode and for the blocking electrode with local CPE behavior.[102,205] At the periphery of the electrode, two time constants (inductive and capacitive loops) are seen, whereas at the electrode center only an inductive loop is evident. These loops are distributed around the asymptotic real value of 1/4.

The representation of an Ohmic impedance as a complex number represents a departure from standard practice. As shown in previous sections, the local impe-

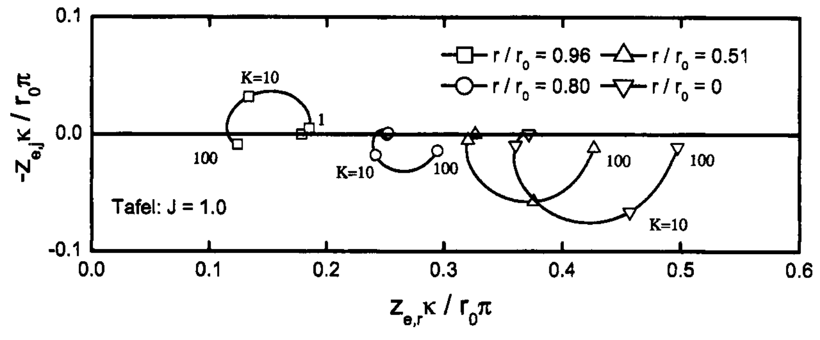

Figure 13.9: Calculated representation of the local Ohmic impedance response for a disk electrode as a function of dimensionless frequency K under assumptions of Tafel kinetics with $J = 1$. (Taken from Huang et al.[97] and reproduced with permission of The Electrochemical Society.)

dance has inductive features that are not seen in the local interfacial impedance. These inductive features are implicit in the local Ohmic impedance. As similar results were obtained for ideally polarized[102] and blocking electrodes with local CPE behavior,[205] the result cannot be attributed to Faradaic reactions and can be attributed only to the Ohmic contribution of the electrolyte.

Global Interfacial and Global Ohmic Impedance

The global interfacial impedance for linear kinetics is independent of radial position and is given by

$$Z_0 = \frac{R_t}{1 + j\omega C_0 R_t} \tag{13.62}$$

The global Ohmic impedance Z_e is obtained from the global impedance Z by the expression

$$Z_e = Z - Z_0 \tag{13.63}$$

The real part of Z_e, obtained for linear kinetics, is given in Figure 13.10(a), and the imaginary part of Z_e is given in Figure 13.10(b) as functions of dimensionless frequency K with J as a parameter. In the low-frequency range $Z_e\kappa/r_0\pi$ is a pure resistance with a numerical value that depends weakly on J. All curves converge in the high-frequency range such that $Z_e\kappa/r_0\pi$ tends toward $1/4$. The imaginary part of the global Ohmic impedance shows a non-zero value in the frequency range that is influenced by the current and potential distributions.

Remember! 13.3 *The Ohmic impedance is a complex quantity that is influenced by geometry-induced current and potential distributions.*

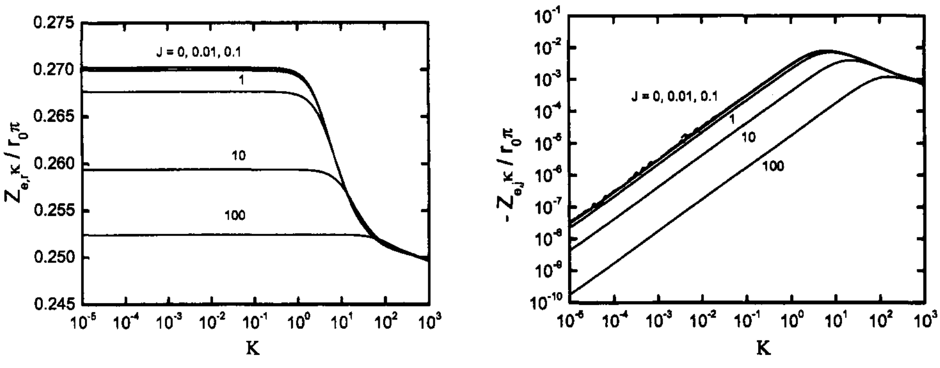

(a) (b)

Figure 13.10: Calculated global Ohmic impedance response for a disk electrode as a function of dimensionless frequency for linear kinetics with J as a parameter: a) real part; and b) imaginary part.

At high and low-frequency limits, the global Ohmic impedance defined in this section is consistent with the accepted understanding of the Ohmic resistance to current flow to a disk electrode. The global Ohmic impedance approaches, at high frequencies, the primary resistance for a disk electrode (equation (13.53)) described by Newman.[198] This result was obtained as well for ideally polarized[102] and blocking electrodes with local CPE behavior.[205] The global Ohmic impedance approaches, at low frequencies, the value for the Ohmic resistance calculated by Newman[38] for a disk electrode. Again, this result was seen as well for blocking electrodes.[102,205] The complex nature of the global and local Ohmic impedances is seen at intermediate frequencies. This complex value is the origin of the inductive features calculated for the local impedance and the quasi-CPE behavior found at high frequency for the global impedance.

13.4 Porous Electrodes

Porous electrodes are used in numerous industrial applications because they have the advantage of an increased effective active area. A porous electrode can be obtained by such different techniques as pressing metal powder or dissolution.[192] This type of porous electrode structure is also observed on some corroded electrodes.[207] It is important to recognize that a porous electrode is not the same as a porous layer. The structure may be the same, but, while the pore walls are electroactive for a porous electrode, the pore walls are inert for a porous layer.

The random structure of the porous electrode, illustrated in Figure 13.11(a), leads to a distribution of pore diameters and lengths. Nevertheless, the porous electrode is usually represented by the simplified single-pore model shown in Figure 13.11(b) in which pores are assumed to have a cylindrical shape with a length ℓ and a radius r. The impedance of the pore can be represented by the transmission

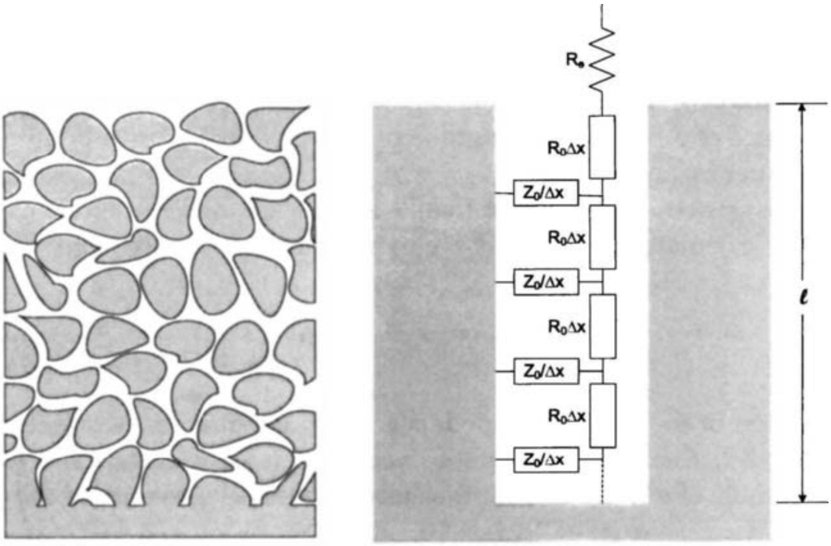

(a) (b)

Figure 13.11: Schematic representations of a porous electrode: a) porous electrode with irregular channels between particles of electrode material; and b) transmission line inside a cylindrical pore.

line presented in Figure 13.11(b) where R_0 is the electrolyte resistance for one-unit length pore, with units of Ωcm^{-1}, Z_0 is the interfacial impedance for a unit length pore, with units of Ωcm, r is the pore radius in cm, and ℓ is the pore length in cm. The specific impedances R_0 and Z_0 can be expressed in function of the pore radius as

$$R_0 = \frac{\rho}{\pi r^2} \tag{13.64}$$

and

$$Z_0 = \frac{Z_{eq}}{2\pi r} \tag{13.65}$$

respectively, where Z_{eq} is the interfacial impedance per surface unit, with units of Ωcm^2, and ρ is the electrolyte resistance, with units of Ωcm.

In the general case, Z_0 and R_0 are functions of the distance x. This dependence is due to the potential distribution or/and to the concentration distribution in the pore. The general solution can be obtained only by a numerical calculation of the corresponding transmission line. For example, the impedance of a porous elec-

---

Remember! 13.4 *A porous electrode is not the same as a porous layer. The structure may be the same, but, while the pore walls are electroactive for a porous electrode, the pore walls are inert for a porous layer.*

trode in the presence of a concentration gradient was numerically studied by Keddam et al.[208] but only a totally irreversible charge-transfer reaction was considered and the Ohmic drop in the pore was neglected. A complete numerical calculation in the presence of a concentration gradient and a potential drop in the pores was developed later by Lasia.[209]

With the restrictive assumption that Z_0 and R_0 are independent of the distance x, de Levie[37] calculated analytically the impedance of one pore to be

$$Z_{\text{deLevie}} = (R_0 Z_0)^{1/2}\coth(\ell\sqrt{\frac{R_0}{Z_0}}) \tag{13.66}$$

The derivation of the de Levie impedance, given in equation (13.66), is presented in Example 13.3. The impedance of the overall electrode is obtained by accounting for the ensemble of n pores and for the electrolyte resistance outside the pore, i.e.,

$$Z = R_e + \frac{Z_{\text{deLevie}}}{n} \tag{13.67}$$

The set of equations (13.64)–(13.67) yields an expression for the impedance of the porous electrode Z that is a function of three geometrical parameters ℓ, r, and n as

$$Z = R_e + \frac{(\rho Z_{eq})^{1/2}}{\sqrt{2}\pi n r^{3/2}}\coth\left(\ell\sqrt{\frac{2\rho}{rZ_{eq}}}\right) \tag{13.68}$$

The shape of the pores influences the value of the impedance,[210] but, in the high-frequency range, this geometrical influence disappears and the impedance is proportional to $(Z_{eq})^{1/2}$

Example 13.3 Derivation of the de Levie Formula: *Derive the de Levie formula given as equation (13.66).*

Solution: *The transmission line corresponding to transport within a pore is given in Figure 13.11(b). At a distance x from the pore edge, the potential is $u(x)$ and the current crossing a resistance R_0dx is $i(x)$. The difference of potential at the edges of the resistance is*

$$du(x) = R_0 i(x)dx \tag{13.69}$$

The current flowing through the impedance Z_0/dx is given by

$$di(x) = \frac{u(x)}{Z_0}dx \tag{13.70}$$

From equations (13.69) and (13.70), the differential equation

$$\frac{d^2u}{dx^2} = \frac{R_0}{Z_0}u \tag{13.71}$$

is obtained. The solution of equation (13.71) is

$$u(x) = A\exp\left[-x\sqrt{R_0/Z_0}\right] + B\exp\left[x\sqrt{R_0/Z_0}\right] \tag{13.72}$$

For $x = 0, i = 0$; *thus,* $A = B$. *The overall current is given by*

$$i(\ell) = \int_0^\ell \frac{u(x)}{Z_0}dx = \frac{A}{Z_0}\sqrt{\frac{Z_0}{R_0}}\left[\exp\left[-x\sqrt{R_0/Z_0}\right] + B\exp\left[x\sqrt{R_0/Z_0}\right]\right] \tag{13.73}$$

and the overall impedance is obtained as

$$Z = \frac{u(\ell)}{i(\ell)} = \sqrt{Z_0R_0}\coth\left(\ell\sqrt{\frac{R_0}{Z_0}}\right) \tag{13.74}$$

Equation (13.74) is the de Levie impedance given in equation (13.66).

Several limiting behaviors can be seen in equation (13.68). For example, recognizing that

$$\lim_{x\to\infty}\coth(x) = 1 \tag{13.75}$$

when the argument to the coth function, $\ell\sqrt{2\rho/rZ_{eq}}$ is sufficiently large,

$$\coth(\ell\sqrt{2\rho/rZ_{eq}}) \to 1 \tag{13.76}$$

and

$$(Z - R_e) \to (\rho Z_{eq})^{1/2}/\sqrt{2}\pi n r^{3/2} \tag{13.77}$$

In this particular case, the pores behave as though they are semi-infinitely deep. The parameters r and n cannot be determined separately by regression analysis. Only the product $(r^{3/2}n)$ can be obtained. Other limiting behaviors of equation (13.68) are explored in Problems 13.8 and 13.9.

Example 13.4 Corrosion of Cast Iron in Drinking Water: *The internal corrosion rate of drinking water pipes is very small and, in itself, corrosion is generally not a problem. But free chlorine (*FCl*) (the sum of hypochlorous acid* HOCl *and hypochlorite ions* ClO^-*) introduced in water at the treatment plant in order to maintain microbiological quality, gradually disappears throughout the distribution system, which necessitates rechlorination. In order to optimize rechlorination procedures, the different sources of chlorine consumption must be identified. The most often invoked and investigated causes of chlorine decay are the chemical bulk oxidation of organic compounds dissolved in water and the reactions with biofilms on the pipe surface. Furthermore, chlorine reacts with the pipe materials themselves in the corrosion process of cast iron pipes. The corrosion has been invoked as an important source of chlorine decay and thus the corrosion rate must be evaluated.*[207] *Derive a model for the impedance response of an iron electrode, taking into* *account the material presented in Chapters 9, 10, and 11 and treating the iron as a porous electrode with pores filled with corrosion product as shown in Section 9.3.2.*

Solution: *Free chlorine can be directly involved in the corrosion process and reduced at the metal–water interface, following the electrochemical reaction, given for acidic pH by*

$$\mathrm{HOCl} + \mathrm{H}^+ + 2\mathrm{e}^- \rightleftarrows \mathrm{Cl}^- + \mathrm{H_2O} \tag{13.78}$$

coupled with the anodic dissolution of ferrous material

$$\mathrm{Fe} \rightleftarrows \mathrm{Fe}^{2+} + 2\mathrm{e}^- \tag{13.79}$$

On the other hand, chlorine can be chemically reduced by ferrous ions produced by reaction (13.79), according to the homogeneous reaction (in acidic media)

$$2\mathrm{Fe}^{2+} + \mathrm{HOCl} + \mathrm{H}^+ \rightleftarrows 2\mathrm{Fe}^{3+} + \mathrm{Cl}^- + \mathrm{H_2O} \tag{13.80}$$

In aerated and chlorinated waters, the rate of reaction (13.78) can be considered to be negligibly small, and the single cathodic process coupled with the dissolution of iron is the reduction of dissolved oxygen, written in acidic media as

$$\frac{1}{2}\mathrm{O_2} + 2\mathrm{H}^+ + 2\mathrm{e}^- \rightleftarrows \mathrm{H_2O} \tag{13.81}$$

The analysis of the corrosion products suggests the scheme presented in Figure 13.12 for the cast iron–drinking water interface:

- *On top, the red rust layer explains the absence of hydrodynamic effects after two days of immersion. This layer, which is an electronic insulator but an ionic conductor, does not play any role on the kinetics.*
- *Below the reddish layer, an electronically conductive layer of black rust, pictured as an arrangement of macropores, covers the metal except at the end of the pores. The flattened aspect of the diagrams reflects the presence of this macroporous layer.*
- *The black rust is covered by a very compact microporous layer, made up of green rust and calcium carbonates. This film influences the high-frequency loop of the impedance diagrams.*

From this physical model, an electrical model of the interface can be given. Free corrosion is the association of an anodic process (iron dissolution) and a cathodic process (electrolyte reduction). Therefore, as discussed in Section 9.2.1, the total impedance of the system near the corrosion potential is equivalent to an anodic impedance Z_a in parallel with a cathodic impedance Z_c with a solution resistance R_e added in series as shown in Figure 13.13(a). The anodic impedance Z_a is simply depicted by a double-layer capacitance in parallel with a charge-transfer resistance (Figure 13.13(b)). The cathodic branch is described, following the method of de Levie,[37] by a distributed impedance in space as a transmission line in the conducting macropore (Figure 13.12). The interfacial impedance of the microporous

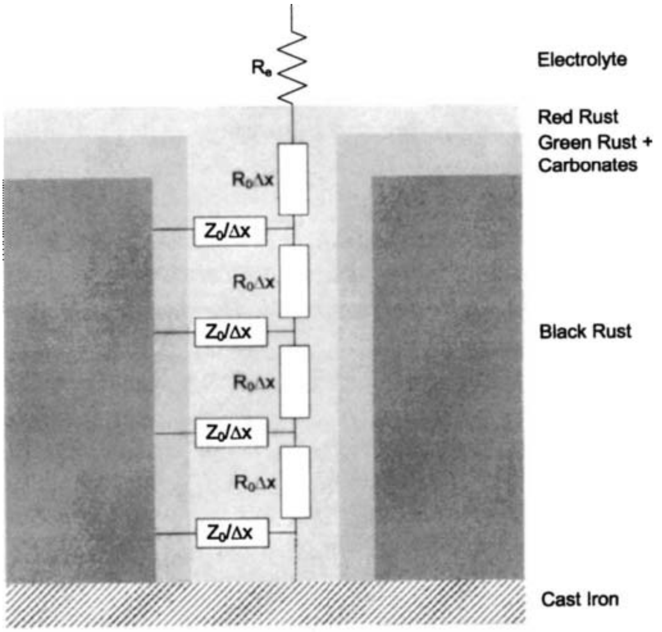

Figure 13.12: Schematic representation of the cast iron - water interface. (Taken from Frateur et al.[207])

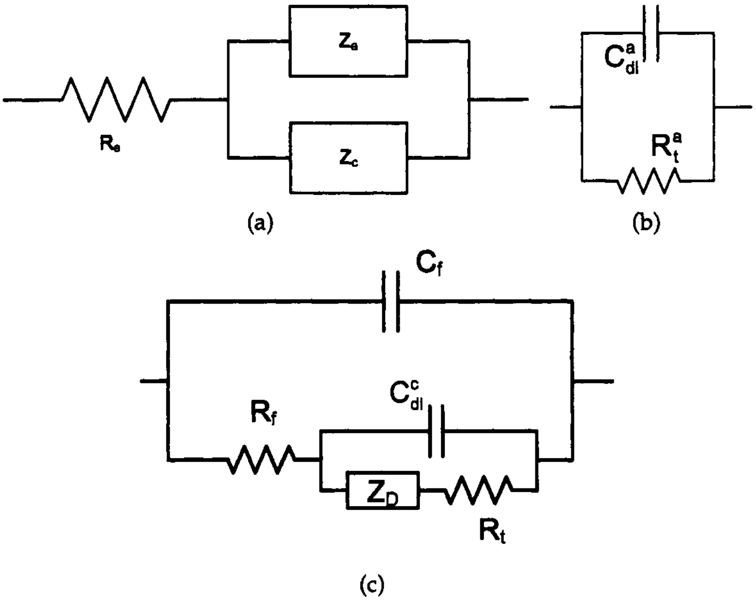

Figure 13.13: Equivalent circuit for: a) the total impedance of the cast iron–water interface; b) the anodic impedance; and c) the interfacial impedance of the microporous layer.

layer Z_0 *is given in Figure 13.13(c). The term* R_f *represents the Ohmic resistance of the electrolyte through the film, and the term* C_f *represents the film capacitance. The Ohmic resistance* R_f *is in series with the parallel arrangement of the cathodic double-layer capacitance* C_{dl}^{c} *and the Faradaic branch consisting of a cathodic charge-transfer resistance* R_t^c *in series with a diffusion impedance* Z_D *(see also Figure 9.4). The term* Z_D*, which describes the radial diffusion in the macropores, i.e., through the red rust, is given by equation (11.70).*

Thus, the anodic surface corresponds to the end of the macropores, whereas the cathodic reaction occurs at the end of the micropores, which are located at the walls of the macropores. It should be noted that this physical–electrical model describes the behavior of cast iron at any time of immersion.

The calculation gives, for the cathodic impedance, the general form

$$Z_c = \sqrt{R_0 Z_0} \coth\left(\frac{\ell}{\lambda}\right) \tag{13.82}$$

with

$$\lambda = \sqrt{\frac{Z_0}{R_0}} \tag{13.83}$$

and where ℓ *is the mean length of the macropores and* λ *is the penetration depth of the electrical signal. When* ℓ *is small with respect to* λ*, the macropores respond like a flat electrode and the cathodic impedance tends to* Z_0/ℓ*. In this case, the angle made by the diffusion impedance is equal to 45°. When* ℓ/λ *becomes large, the macropores behave as though they were semi-infinitely deep. Thus,* $\coth(\ell/\lambda)$ *tends to unity, and* Z_c *equals* $\sqrt{R_0 Z_0}$*, which gives an angle of about 22.5° in the so-called Warburg domain.*

With the model illustrated in Figures 13.12 and 13.13, the impedance diagrams were analyzed by using a nonlinear least-squares regression procedure to extract physically meaningful parameters. For each time of immersion, the electrolyte resistance was measured separately and fixed in order to decrease the number of unknown parameters. The error structures identified by means of the measurement model described in Chapter 21 were used to weight the data during regression of the physical model.

The results of the fitting for water containing 2 mg l^{-1} *of* FCl *after 3, 7, and 28 days of immersion are presented in Figures 13.14(a), (b), and (c), respectively. The model fits the experimental data very well, even under conditions where the diffusion loop is badly defined (i.e., at long times of immersion). Therefore, despite the large number of parameters imposed by the physical model, each parameter could be determined with a narrow confidence interval. The calculated diagrams show that the HF loop is, in fact, composed of two capacitive loops: one related to the microporous film and the other to the cathodic charge transfer. Due to the similar values of the time constants* $R_t^c C_{\text{dl}}^c$ *and* $R_f C_f$*, the two corresponding half-circles were nearly indistinguishable. The low-frequency loop characterizes the diffusion of the solute as well as the anodic charge transfer. After 28 days of immersion, the theoretical diagram makes an angle of 45° in the very-high-frequency range and the angle of the diffusion impedance is 22.5°, which means that the pores behave as though they are semi-infinitely deep at these frequencies.*

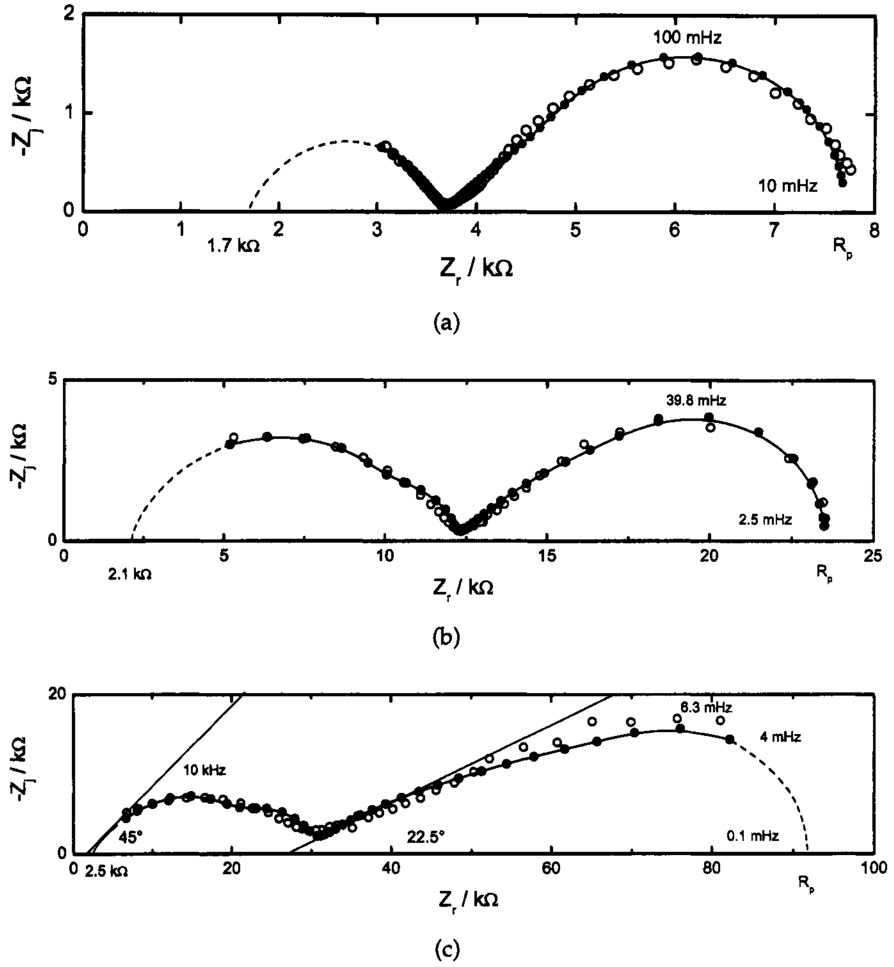

Figure 13.14: Regression results for the impedance diagrams of the cast iron rotating disk electrode after (a) 3, (b) 7, and (c) 28 days of immersion in Evian water with 2 mg l^{-1} of FCl. (•) Experimental data and (○) fitted values using the equivalent circuits given in Figure 13.13. (Taken from Frateur et al.[207])

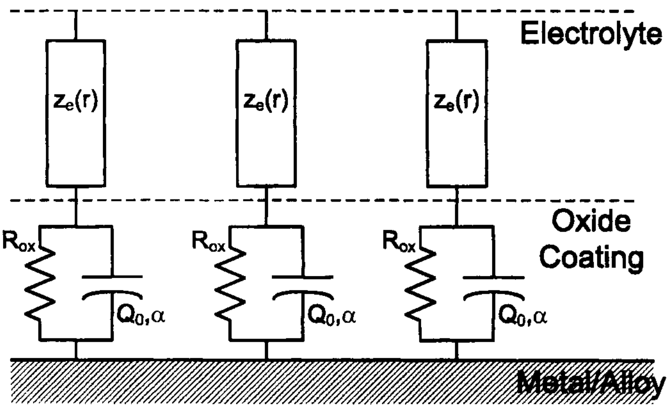

Figure 13.15: Equivalent circuit corresponding to an electrode covered by an oxide layer.

The anodic charge-transfer resistance could be extracted from the fitting procedure. Thus the method provided a reliable value of the corrosion current and rate. This corrosion rate is about 10 *micrometers per year, which is not negligible if the chlorine consumption is considered.*

13.5 Oxide Layers

The electrochemical impedance of an oxide layer reveals an apparent CPE behavior in the high-frequency range, and the origin of the CPE behavior is generally attributed to a distribution of time constants. The influence of a distribution of time constants along the electrode surface (i.e., a 2-D distribution) was discussed in Section 13.3. A time-constant dispersion can also be attributed to a distribution along the dimension normal to the electrode surface (i.e., a 3-D distribution). The LEIS technique described in Section 7.5.2 can be used to distinguish between a 2-D and a 3-D distribution.[194] With the LEIS technique, a 2-D distribution is characterized at high frequencies by pure capacitance behavior, and a 3-D distribution is characterized by an apparent CPE behavior. Of course, a local CPE behavior characteristic of a 3-D distribution can be also be involved in a 2-D current and potential distribution as discussed in Section 13.3.[205] For an oxide layer, the distribution in the direction normal to the electrode surface can be due to varying oxide composition.

In a first approximation, the equivalent circuit presented in Figure 13.15 can be used to represent the electrode in which the interfacial impedance between the oxide and the electrolyte was assumed to be negligible as compared to the coating impedance. The impedance of the oxide layer can be considered to correspond to a

---

Remember! **13.5** *Not all depressed semicircles correspond to a CPE behavior.*

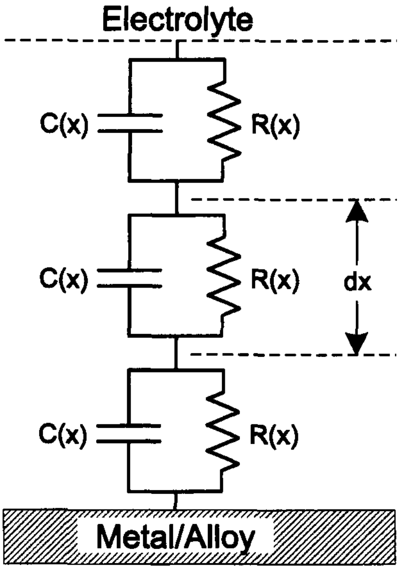

Figure 13.16: Equivalent circuit corresponding to an oxide layer with an axial distribution of dielectric and resistive properties.

large number of Voigt elements as represented in Figure 13.16. The capacity $C(x)$ is the capacity of a dielectric with a thickness dx, and the resistance $R(x)$ corresponds to a layer of same thickness dx with a conductivity $\kappa(x)$.

The local impedance is obtained by integration along the distance x from 0 to the coating thickness d, i.e.,

$$Z_Y = \int_0^d \frac{dx}{\kappa(x)\left(1 + j\omega\varepsilon_0\varepsilon/\kappa(x)\right)} \tag{13.84}$$

As shown in Table 5.4, the dielectric constant ε varies in a narrow range for a metal oxide. Thus, to a first approximation, ε can be considered to be independent of x, and the conductivity κ may be assumed to be a function of x.

For an oxide layer, Young[189] assumed that the nonstoichiometry of the oxide layer resulted in an exponential variation of the conductivity with the normal distance to the electrode as

$$\kappa(x) = \kappa(0)\exp\left(-x/d\right) \tag{13.85}$$

The Young impedance for the gradient presented in equation (13.85) can be expressed as

$$Z_Y = \frac{\delta}{j\omega d C_Y}\ln\left[\frac{1 + j\omega\tau\exp\left(\frac{d}{\delta}\right)}{1 + j\omega\tau}\right] \tag{13.86}$$

where $C_Y = \varepsilon_0\varepsilon S/d$ is the oxide film capacity, and $\tau = RC_Y = \varepsilon_0\varepsilon/\kappa(0)$ is the time constant.[191]

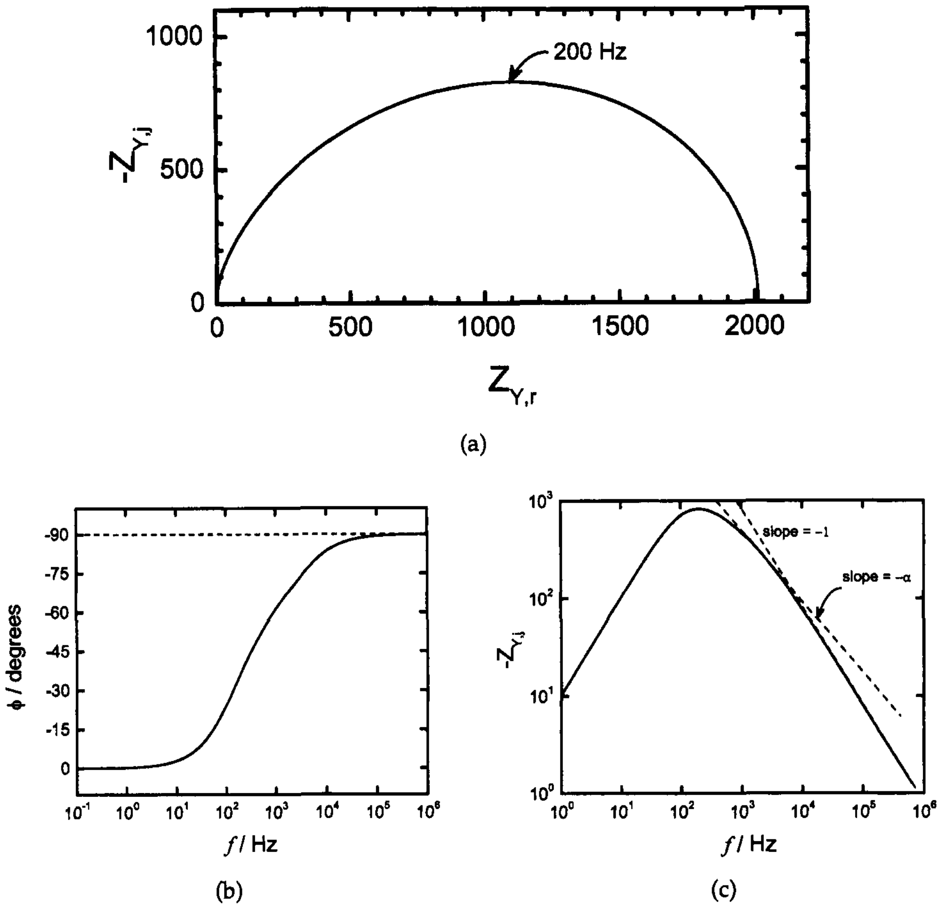

(a)

(b)

(c)

Figure 13.17: Young impedance given by equation (13.86) and obtained with C_Y = 1.25 μF/cm^2, δ/d = 0.26, and τ = 2.11 × 10^{-4} s.: a) Nyquist representation; b) phase angle as a function of frequency; and c) imaginary impedance as a function of frequency on a logarithmic scale.

An example of the Young impedance is plotted in Figure 13.17 in different coordinates. In Figure 13.17(a), the Young impedance appears as a depressed semicircle, similar to what is obtained for a resistance in parallel with a CPE (see Section 13.1). The phase angle is given in Figure 13.17(b) as a function of frequency. Clearly no constant phase angle is found, but, in spite of the depressed semicircle of Figure 13.17(a), the phase angle approaches −90 degrees at high frequencies. The slope of the lines in Figure 13.17(c) confirms that the CPE exponent α is not independent of frequency and approaches a value of unity at large frequencies. However, if only a limited frequency range is considered, the data can be described by a CPE with $\alpha < 1$.

In this case, a CPE could be used to describe the experimental data obtained in a limited frequency range, but, when a physical model is assumed, as for the

Young impedance, true CPE behavior is not found. It should be noted that the CPE model corresponds to a specific distribution of time constants that may or may not correspond to a given physical situation. Local impedance measurements can give information about the nature of this distribution, whether 2-D, 3-D, or both. This example shows that not all depressed semicircles correspond to a CPE behavior.

Problems

13.1 Provide an analytic solution to equations (13.26) and (13.27), and write explicitly the equation corresponding to $m = 1$.

13.2 Consider a 0.25 cm radius Pt disk in a 0.1 M NaCl solution at room temperature. Estimate the frequency above which geometry-induced time-constant dispersion will influence the impedance response.

13.3 Consider a 0.25 cm radius steel disk covered with a native oxide layer. The electrolyte is a 0.1 M NaCl solution at room temperature. Estimate the frequency above which geometry-induced time-constant dispersion will influence the impedance response.

13.4 Consider a 0.25 cm radius steel disk covered with a polymer coating that has a thickness of 100 μm. The electrolyte is a 0.1 M NaCl solution at room temperature. Estimate the frequency above which geometry-induced time-constant dispersion will influence the impedance response.

13.5 Time-constant distributions were described in Section 13.1.1 as having either a 2-D or a 3-D character. Under what conditions could a system show CPE behavior resulting from a distribution in only the axial direction?

13.6 Find the equations that are necessary to solve the response of a small electrode to a rotation speed modulation.

13.7 A thin layer cell is comprised of an isolated plane at a very short distance ε from a working electrode. By considering the system with a cylindrical symmetry, calculated the impedance of a disk electrode in this configuration.

13.8 Explore the limiting behavior of equation (13.68) when $\ell\sqrt{2\rho/rZ_{eq}}$ is very small. What independent parameters or combinations of parameters can be obtained by regression of this model to experimental data? To what geometry does this limit conform?

13.9 Explore the behavior of equation (13.68) when $\ell\sqrt{2\rho/rZ_{eq}}$ is neither very small nor very large. What independent parameters or combinations of parameters can be obtained by regression of this model to experimental data?

Electrochemical Impedance Spectroscopy
by Mark E. Orazem and Bernard Tribollet

Chapter 14

Generalized Transfer Functions

Electrochemical measurements are generally designed either to analyze an interfacial mechanism by kinetic characterization and chemical identification of the reaction intermediates or to estimate a parameter characteristic of some process (i.e., corrosion rate, deposition rate, and state of charge of a battery) from the measurement of a well-defined quantity.

Electrical techniques are extremely efficient for disentangling the coupling between mass-transport and chemical and electrochemical reactions or for performing a test, because they allow *in situ* study of the electrochemical system. The techniques placed at the electrochemist's disposal are founded on an application of signal processing to electrochemistry. By using a small-amplitude sine-wave perturbation, electrochemical systems can be considered to be linear, and they can be investigated on the basis of a frequency analysis of a transfer function involving at least one electrical quantity (current or potential). So far, most significant results have been obtained by measurements of the electrochemical impedance, which leads to kinetic characterization of the phenomena in terms of process rates (mass transport, electrochemical, or chemical reaction). More recently, use of nonelectrical quantities has been introduced in impedance spectroscopy, which complements those obtained by measuring the electrochemical impedance.

The object of this chapter is to provide a framework for the variety of electrical and nonelectrical impedance techniques that have emerged and to provide a consistent set of notations that can be used to describe the results of these measurements. The presentation follows the treatment of Gabrielli and Tribollet.[52]

14.1 Multi-Input/Multi-Output Systems

During the last 30 years, the measurement of the impedance of an electrode has become a technique widely used for investigating numerous interfacial processes. The interpretation of this quantity is based on models obtained from the equations governing the coupled transport and kinetic processes, which may include heterogeneous and/or homogeneous reaction steps. Although these models are able to

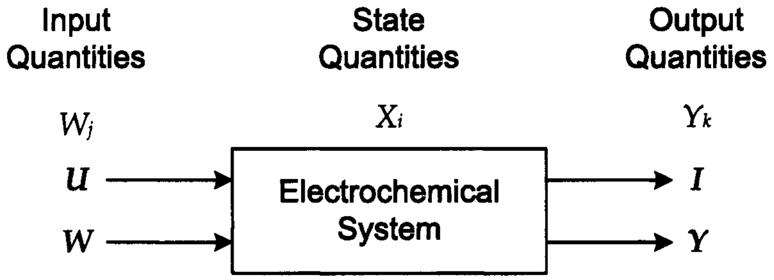

Figure 14.1: Schematic representation of an electrochemical system with input, output, and state variables. (Taken from Gabrielli and Tribollet.[52])

explain many complex behaviors, they can be questioned so long as they are not supported by additional experimental evidence.

Unfortunately, *in situ* analytical identification of reaction intermediates or of surface layers remains extremely difficult. Therefore, it is convenient to complement the impedance measurement, which relates only electrical quantities, with the measurement of complex transfer functions of different natures, which involve other types of quantities. In fact, the modeling of these new quantities is carried out on the same basis as those that govern the electrochemical impedance. As an example, the ac impedance measured on the diffusion plateau of the anodic dissolution of metal is often very difficult to analyze because of the close coupling between kinetics and mass transport. By perturbing the rotation speed of the electrode and measuring the current, the electrohydrodynamic (EHD) impedance is obtained (see Chapter 15). EHD impedance reveals directly the influence of mass transport on surface phenomena and thereby gives additional information on the process. The model that expresses the coupling between surface kinetics and mass transport can be tested against both the EHD impedance and the electrochemical impedance.

For any electrochemical system, the state of the electrochemical interface is defined by three classes of quantities that are shown in Figure 14.1:

1. The input quantities or constraints W_j impose the experimental conditions. These may include the electrode potential U (or overall current I), the temperature T, the pressure p, the rotation velocity of the electrode Ω, and the magnetic field B.

2. The values of state quantities X_i fix the state of the system. These may include the concentration of the reacting species c_i, the coverage of the electrode by the intermediate species γ_i, and the local interfacial potential $V(x,y,z)$.

Remember! 14.1 *Measurement of different transfer functions provides a convenient* in-situ *method to probe electrochemical systems.*

---

3. The output quantities Y_k allow observation of the state of the system. These may include the current I (or potential U), the reflective power of the electrode surface R, the mass added or removed from the electrode M, and the current flowing through a secondary electrode (often a concentric ring to a disk electrode) I_{ring}.

Each output quantity Y_k can be considered to be a function, which is often very complicated, of the constraints or input quantities.

$$Y_k = G(W_j) \qquad (\text{for } j \text{ and } k = 1, 2 \ldots) \tag{14.1}$$

Equation (14.1) may be called the *input–output relationship*. In order to write equation (14.1), different steps involving the evolution equation of the state quantities generally have to be considered, i.e.,

$$\frac{dX_i}{dt} = H_i(X_l, W_j) \qquad (\text{for } i,\ l, \text{ and } j = 1, 2 \ldots) \tag{14.2}$$

$$Y_k = F_k(X_i, W_j) \qquad (\text{for } k,\ i, \text{ and } j = 1, 2 \ldots) \tag{14.3}$$

The set of equations (14.2) governs the time change of the state quantities. The set of equations (14.3) allows the output quantities to be obtained. Equations (14.3) can be called the *observation equations.*

In general, the functions H_i and F_k are nonlinear. These nonlinearities are usually due to the exponential activation of the electrochemical rate constants by the potential (see Section 5.5). In addition, even for time-invariant electrochemical systems, equations (14.2) can comprise either differential equations, when only kinetic equations are considered to be involved at the interface, or partial differential equations, when distributed processes occur in the bulk of the solution (such as may result from transport of the reacting species or a temperature gradient in the solution).

A general time-dependent solution of the set of differential equations given by equations (14.2) and (14.3) is usually impossible or very difficult to obtain. This general solution corresponds, for example, to cyclic voltammetry or step responses. The steady-state solution of this set of equations obtained for $dX_i/dt = 0$ can be derived more easily, and then, if a small perturbation of the input quantities $dW_j(t)$ about the steady-state value $\overline{W}_j$ is imposed, a small change of the output quantities $dY_k(t)$ about the steady value $\overline{Y}_k$ is observed. A linearization of equations (14.2) and (14.3), for example, by neglecting the expansions above the first order, gives an approximate description of the real system in the time domain

$$\frac{dX}{dt} = \mathbf{A}dX + \mathbf{B}dW \tag{14.4}$$

$$dY = \mathbf{C}dX + \mathbf{D}dW \tag{14.5}$$

where **A**, **B**, **C**, and **D** are matrixes whose components are equal to

$$A_{ij} = \left.\frac{\partial H_i}{\partial X_j}\right|_{X_k, W_m, j \neq k} \tag{14.6}$$

$$B_{ij} = \left.\frac{\partial H_i}{\partial W_j}\right|_{X_k, W_m, j\neq m} \tag{14.7}$$

$$C_{kj} = \left.\frac{\partial F_k}{\partial X_j}\right|_{X_k, W_m, j\neq k} \tag{14.8}$$

$$D_{kj} = \left.\frac{\partial F_k}{\partial W_j}\right|_{X_k, W_m, j\neq m} \tag{14.9}$$

respectively, and dX, dY, and dW are column vectors whose components are dX_i, dY_k, and dW_m respectively.

When a small-amplitude sine wave perturbation is added to one input quantity, under linear conditions, each state quantity and each output quantity can be written formally for the quantity of interest χ as

$$\chi = \overline{\chi} + \mathrm{Re}\left\{\widetilde{\chi}(\omega)\exp(j\omega t)\right\} \tag{14.10}$$

where $\mathrm{Re}\{\chi\}$ represents the real part of χ, and $\widetilde{\chi}(\omega)$ is generally a complex quantity independent of the time but depending on the frequency, i.e.,

$$\widetilde{\chi}(\omega) = |\widetilde{\chi}(\omega)|\exp(j\varphi) \tag{14.11}$$

where φ is the phase shift. With the previous notation, the perturbation of the quantity χ in the time domain, $d\chi(t)$, is related to the perturbation of the same quantity in the frequency domain, $\widetilde{\chi}(\omega)$, by

$$d\chi(t) = \mathrm{Re}\{\widetilde{\chi}(\omega)\exp(j\omega t)\} \tag{14.12}$$

Equations (14.6), (14.7), (14.8), and (14.9), which describe the system in the time domain, become, in the frequency domain,

$$j\omega\widetilde{X} = \mathbf{A}\widetilde{X} + \mathbf{B}\widetilde{W} \tag{14.13}$$

and

$$\widetilde{Y} = \mathbf{C}\widetilde{X} + \mathbf{D}\widetilde{W} \tag{14.14}$$

where $\widetilde{X}$, $\widetilde{Y}$, and $\widetilde{W}$ are column vectors, with components $\widetilde{X}_i$, $\widetilde{Y}_k$, and $\widetilde{W}_m$.

By eliminating $\widetilde{X}$, the output quantity $\widetilde{Y}$ is obtained as a function of the input quantity $\widetilde{W}$

$$\widetilde{Y} = (\mathbf{C}(j\omega\mathbf{J} - \mathbf{A})^{-1}\mathbf{B} + \mathbf{D})\widetilde{W} \tag{14.15}$$

The matrix $(\mathbf{C}(j\omega\mathbf{J} - \mathbf{A})^{-1}\mathbf{B} + \mathbf{D})$ is the generalized transfer function of the electrochemical interface considered as a multi-input W_j/multi-output Y_k system. Each term of the matrix is an elementary transfer function and $\mathbf{J}$ is the identity matrix. The transfer function may be analyzed as a function of the static property space, which represents a linearized characterization of the system. The same information is obtained as would be obtained by analyzing the entire nonlinear electrochemical system, which is much more complex. As an example, for the electrical quantities the measurement of the impedance about each polarization point of the steady-state current–voltage curve leads to an exhaustive analysis of the electrochemical interface. No information is lost as compared to a large-amplitude perturbation technique such as cyclic voltammetry. It is equivalent to carrying out several impedance measurements all along the current–voltage curve or cyclic voltammetry at different sweep rates, but the mathematical analysis of the impedance measurements is much simpler due to the linearity of the equations.

If the k^{th} row of the matrix that gives the transfer function is developed,

$$\widetilde{Y}_k = \sum_i Z_{j,k} \widetilde{W}_j \tag{14.16}$$

where $Z_{j,k}$ is the elementary transfer function between Y_k and W_j. Each elementary transfer function is generally a complex quantity, but, when the frequency tends toward zero, $Z_{j,k}$ tends toward $\partial Y_k/\partial W_j|_{W_i}$, which is the partial derivative of the steady-state solution $\overline{Y}_k$ with respect to $\overline{W}_j$ (e.g., polarization resistance $\partial U/\partial I|_{W_i}$ for the electrical quantities).

The proliferation of different and conflicting sets of notation for different impedance techniques makes necessary a unified approach for describing the transfer function resulting from all impedance measurements. A unified notation is presented in the following section for cases where the electrical properties (current or potential) are the measured output quantity and where the input forcing function is nonelectrical. A subsequent section addresses cases for which the input forcing function is electrical.

14.1.1 Current or Potential Are the Output Quantity

As I and U play a particular role in an electrochemical system, and both can be considered to be either input or output quantities, according to the type of regulation of the polarization (potentiostat or galvanostat), $\tilde{I}$ and $\tilde{U}$ appear in either the input or the output vector columns. According to equation (14.16)

$$\tilde{I} = Z^{-1}\tilde{U} + \sum_m Z_{I,m}\widetilde{W}_m \tag{14.17}$$

$$\tilde{U} = Z\tilde{I} + \sum_m Z_{U,m}\widetilde{W}_m \tag{14.18}$$

Remember! 14.2 *The small-signal transfer function may be analyzed at different values of the static property space, which represents a linearized characterization of the system. The same information is obtained as would be obtained by analyzing the entire nonlinear electrochemical system using a large-amplitude perturbation technique such as cyclic voltammetry, but the analysis is simpler.*

where Z is the usual electrochemical impedance, $Z_{I,m}$ is the elementary transfer function between the current response to the perturbation of the m^{th} input quantity, and $Z_{U,m}$ is the elementary transfer function between the overvoltage response to the perturbation of the m^{th} input quantity.

Equations (14.17) and (14.18) are simultaneously satisfied; therefore, by replacing $\widetilde{U}$ in equation (14.17) by its value given by equation (14.18),

$$\widetilde{I} = Z^{-1}\left(Z\widetilde{I} + \sum_m Z_{U,m}\widetilde{W}_m\right) + \sum_m Z_{I,m}\widetilde{W}_m \tag{14.19}$$

i.e.,

$$\sum_m (Z_{U,m}Z^{-1} + Z_{I,m})\widetilde{W}_m = 0 \tag{14.20}$$

Thus, for any input quantity m

$$Z_{U,m}\, Z^{-1} + Z_{I,m} = 0 \tag{14.21}$$

Therefore, the elementary transfer functions that give the response of current and potential to the perturbation of the m^{th} input quantity are related by the electrochemical impedance. For a given experiment, only one input quantity is sinusoidally modulated around a mean value, and all others are maintained constant by different regulations.

The notation such as the ratio $\widetilde{Y}_k/\widetilde{W}_m$ means that all input quantities W_i (with $i \neq m$) are fixed. Then equation (14.21) can be written as

$$\left(\frac{\widetilde{U}}{\widetilde{W}_m}\right) = -\left(\frac{\widetilde{U}}{\widetilde{I}}\right)\left(\frac{\widetilde{I}}{\widetilde{W}_m}\right) \tag{14.22}$$

According to this notation, $(\widetilde{U}/\widetilde{W}_m)$ is obtained in galvanostatic regulation ($\widetilde{I} = 0$), $\widetilde{U}/\widetilde{I}$ is the usual electrochemical impedance Z obtained for $\widetilde{W}_m = 0$, and $(\widetilde{I}/\widetilde{W}_m)$ is obtained in potentiostatic regulation ($\widetilde{U} = 0$). Equation (14.22) has been given previously in the particular cases of the speed modulation of a rotating disk electrode,[211] of a magnetic field modulation,[124] and for a temperature modulation.[212]

The experimental arrangement devised for the transfer-function measurements involving electrical input and output quantities is illustrated in Figure 14.2. The transfer-function analyzer generates the perturbing signal $dE(t)$ and the control device of the electrical quantity delivers the responses $dI(t)$ or $dU(t)$ of the current or potential to channel 1 of the analyzer. As shown in Figure 14.2, a sensor adapted to the observed output quantity Y_2 allows measurement of the response $dY_2(t)$ of this output quantity. The analyzer measures the transfer function between Y_2 and U ($\widetilde{Y}_2/\widetilde{U}$) or between Y_2 and I, i.e., ($\widetilde{Y}_2/\widetilde{I}$).

14.1.2 Current or Potential Are the Input Quantity

For any output k, if a galvanostatic regulation is considered, equation (14.16) can be written as

$$\widetilde{Y}_k = Z_{k,i}\widetilde{I} + \sum_m Z_{k,m}\widetilde{W}_m \tag{14.23}$$

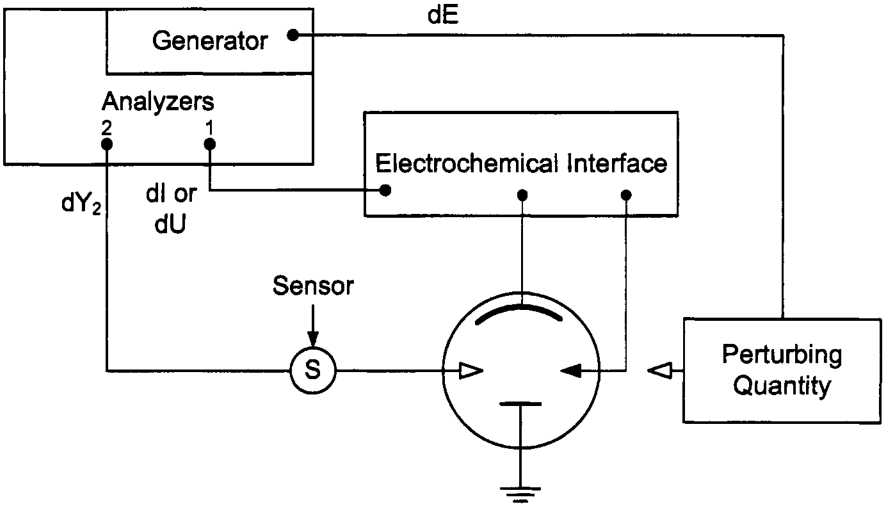

Figure 14.2: The experimental arrangement devised for the transfer function measurements involving nonelectrical input quantity and electrical output quantity.

where $Z_{k,i}$ is the elementary transfer function between the response of the k^{th} output quantity and the perturbation of the current and $Z_{k,m}$ is the elementary transfer function between the response of the k^{th} output and the perturbation of the m^{th} input quantity.

If only the input I is modulated, the output Y_k and U can be written

$$\tilde{Y}_k = Z_{k,I}\tilde{I} \tag{14.24}$$

$$\tilde{U} = Z\tilde{I} \tag{14.25}$$

Then

$$\frac{\tilde{Y}_k}{\tilde{U}} = \frac{Z_{k,I}}{Z} = \frac{\tilde{Y}_k}{\tilde{I}}\frac{\tilde{I}}{\tilde{U}} \tag{14.26}$$

where $\tilde{U}/\tilde{I}$ is the usual electrochemical impedance Z, $\tilde{Y}_k/\tilde{I}$ is the transfer function between Y_k and I, and $\tilde{Y}_k/\tilde{U}$ is the transfer function between Y_k and U. Note that the only difference between equation (14.22) and equation (14.26) is a minus sign coming from the implicit function derivation.

The experimental arrangement devised for the transfer-function measurements involving a nonelectrical output quantity, the current or the potential being the

---

Remember! 14.3 *Equation (14.22) provides the relationship between the usual electrochemical impedance response and the transfer function for cases where current or potential is the output. Equation (14.26) provides the corresponding relationship for cases where current or potential is the input. Equation (14.22) and equation (14.26) are distinguished by a minus sign resulting from the implicit function derivation.*

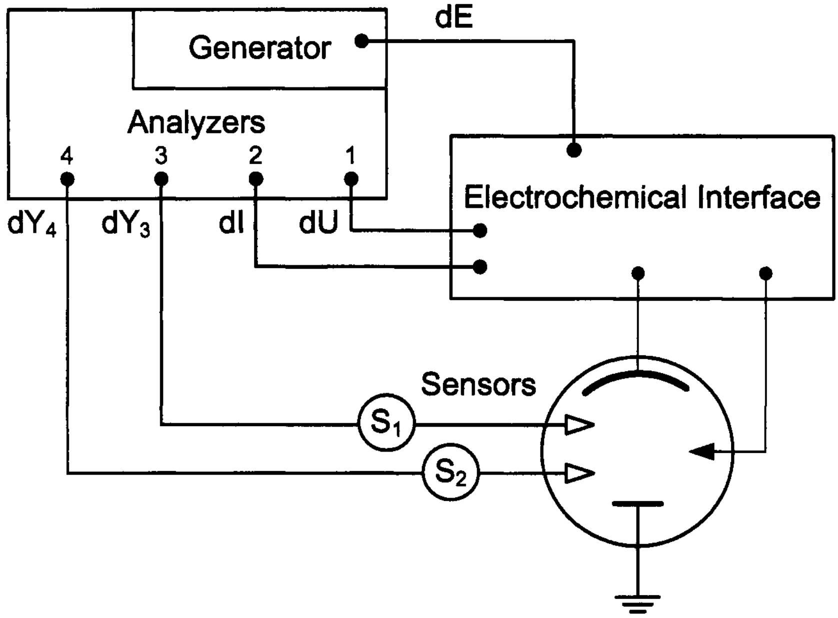

Figure 14.3: Principles of the experimental arrangement used for transfer-function measurements where current or potential is the input quantity.

input quantity is illustrated in Figure 14.3. The transfer-function analyzer generates the perturbing signal $dE(t)$ and the control device of the electrical quantity delivers the responses $dI(t)$ and $dU(t)$ of the current and potential to channels 1 and 2 of the transfer-function analyzer. A sensor adapted to the observed output quantity Y_3 allows the response $dY_3(t)$ of this output quantity (see Figure 14.3). The transfer-function analyzer simultaneously measures the electrochemical impedance $\tilde{U}/\tilde{I}$ and the transfer function between Y_3 and U $\tilde{Y}_3/\tilde{U}$ and between Y_3 and I $\tilde{Y}_3/\tilde{I}$. If required, a second sensor, also shown in Figure 14.3, can measure the response $dY_4(t)$ of a second output quantity. This last feature makes this multi-transfer-function technique very flexible. The simultaneous measurement of the electrochemical impedance $\tilde{U}/\tilde{I}$ and of the transfer function $\tilde{Y}_3/\tilde{I}$ requires the use of a four-channel transfer-function analyzer.

14.1.3 Experimental Quantities

It is necessary to notice that the interfacial potential V and the Faradaic current I_f are state quantities generally related to the observable experimental quantities U and I by

$$U = V + R_e I \tag{14.27}$$

and

$$I = I_f + C_{\text{dl}} \frac{dV}{dt} \tag{14.28}$$

where R_e is the electrolyte resistance and C_{dl} is the double-layer capacitance.

From a modeling point of view, the kinetic equations and the evolution equations generally involve I_f and V, so, in a first step, it is more convenient to write the different equations by considering I_f and V to be the observable quantities (input or output) and, at the end, to use equations (14.27) and (14.28) to write the final relation with I and U.

14.2 Transfer Functions Involving Exclusively Electrical Quantities

The examples of transfer functions presented here involve exclusively electrical quantities, but are distinct from the usual impedance measurements described in other parts of this book.

14.2.1 Ring-Disk Impedance Measurements

In the late sixties, Albery et al.[213] investigated extensively the *rotating ring-disk electrode* (rrde). The extension to the dynamic regime, in principle, can, by studying the species collected on the ring, yield information on changes with time and potential of the number of species trapped on the disk surface during the electrode process. This approach was extended to the study of the collection efficiency response to a sine wave perturbation to the disk potential.[214]

The principle of an rrde is the following:

1. The species A transforms electrochemically into B at the disk, e.g.,

$$\mathrm{A} \rightarrow \mathrm{B} + n_{\mathrm{disk}} e^{-} \tag{14.29}$$

   where the charges carried by A and B are such that reaction (14.29) is electrically balanced.

2. The species B leaves the disk and is transported by convective diffusion to the ring.

3. The species B reacts at the ring and is transformed into P, e.g.,

$$\mathrm{B} \rightarrow \mathrm{P} + n_{\mathrm{ring}} e^{-} \tag{14.30}$$

   The product P may be identical to A, the initial species, as in the case of a redox system, or may be different.

The number of electrons concerned in reaction (14.29) or (14.30), i.e., n_{disk} or n_{ring}, is positive for an anodic and negative for a cathodic process. It can be seen that the rrde operates in three distinct processes: electrochemical reaction at the disk, coupling between the disk and the ring through the convective diffusion, and collection at the ring.

At the steady state, the collection efficiency is defined to be

$$\overline{\mathcal{N}} = \frac{\bar{i}_{\mathrm{ring}}}{\bar{i}_{\mathrm{disk}}} \tag{14.31}$$

In a similar way, the collection efficiency under an ac signal at the angular frequency ω is defined by:

$$\mathcal{N}(\omega) = \frac{\widetilde{i}_{\mathrm{ring}}}{\widetilde{i}_{\mathrm{disk}}} \tag{14.32}$$

As the disk and the ring current are linked through three distinct steps, $\mathcal{N}(\omega)$ can hence be split as the product of three transfer functions, i.e.,

$$\mathcal{N}(\omega) = \frac{\widetilde{i}_{\mathrm{ring}}}{\widetilde{i}_{\mathrm{disk}}} = \frac{\widetilde{N}_{\mathrm{B,disk}}}{\widetilde{i}_{\mathrm{disk}}} \frac{\widetilde{N}_{\mathrm{B,ring}}}{\widetilde{N}_{\mathrm{B,disk}}} \frac{\widetilde{i}_{\mathrm{ring}}}{\widetilde{N}_{\mathrm{B,ring}}} = \mathcal{N}_{\mathrm{disk}}(\omega)\mathcal{N}_t(\omega)/\mathcal{N}_{\mathrm{ring}}(\omega) \tag{14.33}$$

where $N_{\mathrm{B,disk}}$ is the flux of species B at the disk interface and $N_{\mathrm{B,ring}}$ is the flux of species B at the ring interface. In equation (14.33), $\mathcal{N}_{\mathrm{ring}}(\omega) = \widetilde{N}_{\mathrm{B,ring}}/\widetilde{i}_{\mathrm{ring}}$ is the kinetic efficiency of the ring process. If this process is sufficiently fast that it is controlled entirely by convective diffusion, then $\mathcal{N}_{\mathrm{ring}}(\omega) = 1/n_{\mathrm{ring}}F$, where F is Faraday's constant. The applicability of the rrde is in fact closely dependent on the possibility of finding a suitable ring material and electrochemical system for which $\mathcal{N}_{\mathrm{ring}}(\omega)$ can be considered constant.

The term $\mathcal{N}_t(\omega) = \widetilde{N}_{\mathrm{B,ring}}/\widetilde{N}_{\mathrm{B,disk}}$ is determined completely by mass transport, and, therefore, $\mathcal{N}_t(\omega)$ can be reduced by the dimensionless frequency $pSc^{1/3}$ (see Chapter 11). No analytic expression is available, and a numerical solution must be derived for each geometry.

The term $\mathcal{N}_{\mathrm{disk}}(\omega) = \widetilde{N}_{\mathrm{B,disk}}/\widetilde{i}_{\mathrm{disk}}$ is the kinetic emission efficiency, which depends only on the kinetics at the disk electrode. At the steady state,

$$\lim_{\omega \to 0} \mathcal{N}_{\mathrm{disk}}(\omega) = \frac{1}{n_{\mathrm{disk}}F} \tag{14.34}$$

In the transient regime, a fraction of the disk current $\widetilde{i}_{\mathrm{disk}}$ may be stored at the disk surface as the charge $\widetilde{q}$, implied in the Faradaic process through the formation of adsorbed intermediate species (2-D) or of films (3-D). From the conservation of electrical charge,

$$\widetilde{i}_{\mathrm{disk}} = n_{\mathrm{disk}}F\widetilde{N}_{\mathrm{B,disk}} + j\omega\widetilde{q} \tag{14.35}$$

Equation (14.35) becomes

$$\frac{\widetilde{N}_{\mathrm{B,disk}}}{\widetilde{i}_{\mathrm{disk}}} = \frac{1}{n_{\mathrm{disk}}F} - \frac{j\omega}{n_{\mathrm{disk}}F}\frac{\widetilde{q}}{\widetilde{i}_{\mathrm{disk}}} \tag{14.36}$$

By introducing the Faradaic impedance of the disk electrode Z_{disk}, the transfer function can be written as

$$\mathcal{N}(\omega) = \mathcal{N}_0(\omega) - j\omega\frac{\widetilde{q}}{\widetilde{V}}Z_{\mathrm{disk}}\mathcal{N}_t(\omega)n_{\mathrm{ring}}F \tag{14.37}$$

where

$$\mathcal{N}_0(\omega) = \frac{n_{\mathrm{ring}}}{n_{\mathrm{disk}}}\mathcal{N}_t(\omega) \tag{14.38}$$

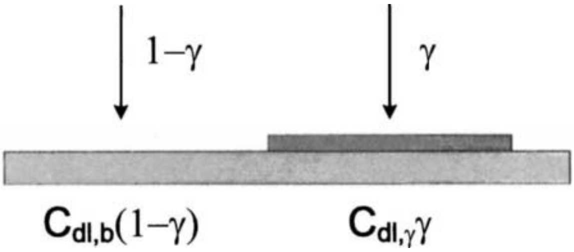

Figure 14.4: Schematic diagram showing the different values of the double-layer capacitance in the presence of a surface coverage.

The transfer function $\widetilde{q}/\widetilde{V}$ can be determined from the Faradaic impedance Z_{disk} and the transfer function $\mathcal{N}(\omega)$. It is an important kinetic parameter that allows evaluation of the frequency dependence of the amount of charge stored at the electrode surface.

14.2.2 Multifrequency Measurements for Double-Layer Studies

The Faradaic impedance is linked in parallel to the double-layer capacitance C_{dl} and then to the solution resistance R_e as illustrated in Figure 9.1. The double-layer capacitance is in general considered to be constant. It is frequently observed, however, that C_{dl} changes with the dc current at which the impedance measurements were carried out. The capacitance C_{dl} has been observed, for example, to increase with increasing current density.

The double-layer capacitance C_{dl} may be assumed to be linked to the surface coverage γ_i, where C_{dl} is a function of frequency due to the frequency dependence of γ_i. The kinetic description of electrochemical impedance involving the surface coverage of intermediates was especially promoted by Epelboin et al.[215] They considered that, for a reaction mechanism involving few reactions, some reaction intermediates adsorb following a Langmuir isotherm and are characterized by a surface coverage γ_i. In this framework, all the loops except the diffusion ones are semicircles centered on the real axis. These semicircles could be capacitive or inductive loops. To explore the role of surface coverage in the modulation of double-layer capacitance, a new technique was invented to measure this frequency dependence, and in this way to verify directly the theory developed a long time ago.[216]

As suggested by Figure 14.4, the double-layer capacitance at the bare surface and at a surface covered by the reaction intermediate can be given as $C_{\text{dl},b}$ and $C_{\text{dl},\gamma}$, respectively. Under the assumption that these double-layer capacitances are different, the effective capacitance can be given by

$$C_{\text{dl}} = C_{\text{dl},b}(1-\gamma) + C_{\text{dl},\gamma}\gamma \tag{14.39}$$

A capacitance transfer function based on the total double-layer capacitance can be shown to be a linear function of the surface coverage γ as

$$\frac{\widetilde{C}_{\mathrm{dl}}}{\widetilde{V}} = (C_{\mathrm{dl},\gamma} - C_{\mathrm{dl},b})\frac{\widetilde{\gamma}}{\widetilde{V}} \tag{14.40}$$

This conceptual approach can be illustrated for a simple system involving adsorbed intermediates such as is described in Section 10.4.

For a system without mass-transport dependence, $i_f = f(V, \gamma)$, and, according to equation (10.3), the admittance is

$$\widetilde{i}_f/\widetilde{V} = 1/Z_f = 1/R_t + \left(\frac{\partial f}{\partial \gamma}\right)_V \frac{\widetilde{\gamma}}{\widetilde{V}} \tag{14.41}$$

The overall impedance is given by

$$Z(\omega) = R_e + \frac{1}{j\omega C_{\mathrm{dl}} + 1/Z_f(\omega)} \tag{14.42}$$

where C_{dl} is a function of γ_i according to equation (14.39). At high enough frequencies ω_{HF}, the contribution of the Faradaic impedance to the overall impedance becomes negligible, and the current response $\widetilde{i}(\omega_{\mathrm{HF}})$ to a potential perturbing signal $\widetilde{U}(\omega_{\mathrm{HF}})$ is expressed as

$$\widetilde{i}(\omega_{\mathrm{HF}}) = \frac{\widetilde{U}(\omega_{\mathrm{HF}})}{R_e + 1/(j\omega_{\mathrm{HF}} C_{\mathrm{dl}})} \tag{14.43}$$

The transfer function $\widetilde{\gamma}_i/\widetilde{V}$ and the transfer function $\widetilde{C}_{\mathrm{dl}}/\widetilde{V}$ can be neglected at this frequency. Thus the capacitance C_{dl} may be considered to have its steady-state value. If R_e can be neglected with respect to $1/(j\omega_{\mathrm{HF}} C_{\mathrm{dl}})$, the capacitance is obtained from the expression

$$C_{\mathrm{dl}} = \frac{1}{j\omega_{\mathrm{HF}}} \frac{\widetilde{i}(\omega_{\mathrm{HF}})}{\widetilde{U}(\omega_{\mathrm{HF}})} \tag{14.44}$$

in which $\widetilde{U}(\omega_{\mathrm{HF}})$ is the perturbing quantity, and, therefore, $\widetilde{U}(\omega_{\mathrm{HF}})$ has a real value. As C_{dl} is also a real number, $\widetilde{i}(\omega_{\mathrm{HF}})$ must have an imaginary value. For a high frequency ω_{HF}, C_{dl} is directly proportional to $|\widetilde{i}(\omega_{\mathrm{HF}})|$. If two additive perturbing signals $\widetilde{U}(\omega_{\mathrm{HF}})$ and $\widetilde{U}(\omega)$ are superimposed, one gets the linear (first-order) response of current $\widetilde{i}$ as the sum of the elementary currents at frequencies ω_{HF} and ω

$$\widetilde{i} = \widetilde{i}(\omega_{\mathrm{HF}}) + \widetilde{i}(\omega) = \widetilde{U}(\omega_{\mathrm{HF}}) j\omega_{\mathrm{HF}} C_{\mathrm{dl}} + \frac{\widetilde{U}(\omega)}{Z(\omega)} \tag{14.45}$$

If the capacitance measured at high frequency ω_{HF} using equation (14.44) is modulated at a lower frequency ω, $\widetilde{i}(\omega_{\mathrm{HF}})$ will also be modulated at the frequency ω. This approach can yield simultaneous measurement of $Z(\omega)$ and $\widetilde{C}_{\mathrm{dl}}(\omega)/\widetilde{U}(\omega)$.

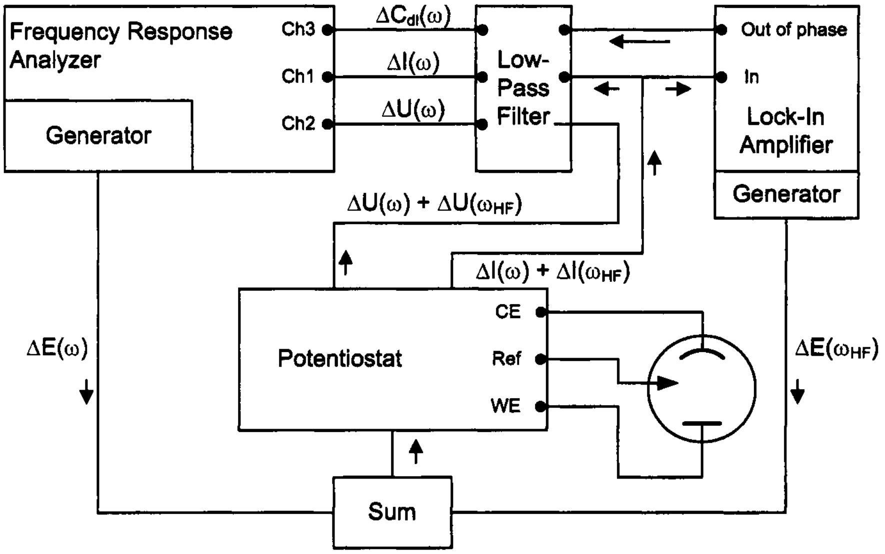

Figure 14.5: Experimental setup used to determine the variation of interface capacitance with a low frequency perturbing signal.

An original experimental setup was devised by Antaño-Lopez et al.[216] to determine simultaneously the transfer functions $Z(\omega)$ and $\widetilde{C}_{\mathrm{dl}}(\omega)/\widetilde{U}(\omega)$. The experimental setup simultaneously measured $\widetilde{U}(\omega)$, $\widetilde{i}(\omega)$, and $\widetilde{C}_{\mathrm{dl}}(\omega)$. A lock-in amplifier determined the latter signal with the reference frequency ω_{HF} as illustrated in Figure 14.5. The sine-wave generator of the lock-in amplifier delivered a perturbing signal $\Delta E(\omega_{\mathrm{HF}})$ to the voltage adder of the potentiostat. The generator of the frequency response analyzer delivered a perturbing signal $\Delta E(\omega)$ to the voltage adder of the potentiostat. Electronic summation of the two signals by the potentiostat synthesized the composite perturbation $(\Delta E(\omega) + \Delta E(\omega_{\mathrm{HF}}))$. The electrochemical cell was connected as usual to the potentiostat. The potentiostat outputs two ac signals, ΔU and ΔI, both containing a composite ac signal produced by superposition of the frequencies ω_{HF} and ω. A low-pass filter eliminated the high frequency signal at frequency ω_{HF} and both signals were sent back to the frequency response analyzer; $\Delta E(\omega_{\mathrm{HF}})$ to input channel ch2 and $\Delta I(\omega)$ to input ch1. The current output signal was also sent to the input of the lock-in amplifier. The out-of-phase component of the current response at frequency ω_{HF} was linked through the low-pass filter to input ch3 of the frequency response analyzer. By correlation at frequency ω, the frequency response analyzer calculated two transfer functions, $Z(\omega)$ from channels 1 and 2 and $\widetilde{C}_{\mathrm{dl}}(\omega)/\widetilde{U}(\omega)$ from channels 3 and 2. In fact, the transfer function $\widetilde{C}_{\mathrm{dl}}(\omega)/\widetilde{U}(\omega)$ must be corrected by the transfer function $F(\omega)$ corresponding to the instrumental frequency response of the built-in filters of the lock-in amplifier. This method was applied to the anodic dissolution of iron.[216] The authors verified experimentally the close correlation between the relaxations of the interface capacitance and that of Faradaic current.

14.3 Transfer Functions Involving Nonelectrical Quantities

The principle of the experimental arrangement devised for the transfer-function measurements involving a nonelectrical input quantity was given previously in Figures 14.2 and 14.3. In this section, a few examples are presented. The transfer function corresponding to the response of the electrochemical system to a perturbation of the rotation speed of a rotating disk electrode is given in Chapter 15.

14.3.1 Thermoelectrochemical (TEC) Transfer Function

The technique introduced by Citti et al.[217] and then by Rotenberg[218] used a vertical electrode heated by a laser beam or by an infrared diode. In this case, the same order of magnitude is obtained for the free convection and the thermal convection, and experiments can be performed with a sufficient accuracy. A fast redox reaction at a heated vertical electrode is considered. The motion of the solution is spontaneous and arises due to forces originating from heterogeneous reactions. Such forces result from density variation in the solution produced by both thermal and concentration gradients near the electrode.

A perturbation of the electrode temperature generates a perturbation of the velocity field and then a perturbation of the concentration field near the electrode. According to Fick's law

$$i_f = -nFD_i \left.\frac{dc_i}{dy}\right|_{y=0} \tag{14.46}$$

the TEC transfer function corresponding to the Faradaic current can be divided in two terms

$$\frac{\widetilde{i}_f}{\widetilde{T}} = \bar{i}_f \frac{1}{D_i} \frac{\widetilde{D}_i}{\widetilde{T}} - nFD_i \frac{\left.\frac{d\widetilde{c}_i}{dy}\right|_{y=0}}{\widetilde{T}} \tag{14.47}$$

in agreement with the theory developed by Aaboubi et al.[212] and by Rotenberg.[218] Taking into account the temperature dependence of the diffusion coefficient in which $D_i \propto \exp(-A_i/RT)$, the first term becomes $A_i i_f/RT^2$, where A_i is the activation energy for diffusion. The second term is frequency dependent and is limited by mass transport. Rotenberg introduced a term corresponding to the response of the charging current to a temperature perturbation: $\widetilde{i}_C = j\omega(\widetilde{q}/\widetilde{T})$. The transfer function corresponding to the overall current is the sum of three terms, i.e.,

$$\frac{\widetilde{i}}{\widetilde{T}} = \frac{\widetilde{i}_f}{\widetilde{T}} + \frac{\widetilde{i}_C}{\widetilde{T}} = \frac{A_i \bar{i}_f}{RT^2} - nFD_i \frac{\left.\frac{d\widetilde{c}_i}{dy}\right|_{y=0}}{\widetilde{T}} + j\omega \frac{\widetilde{q}}{\widetilde{T}} \tag{14.48}$$

Remember! 14.4 *Transfer functions serve to isolate the influence of specific independent variables that contribute to the electrochemical impedance response of a system.*

Motion of the solution in thermal laminar free convection is spontaneous and arises due to forces originating from heterogeneous reactions and from the release of heat from the electrode. Such forces follow the modification of the solution density caused by two phenomena. The concentration in the proximity of the reaction surface changes in the course of heterogeneous reaction and leads to changes in the density of solution. In addition, the release of heat induces variations of solution density from point to point as a result of nonuniform changes in the temperature of the solution. The density of the solution is a function of concentration and temperature and can be expressed by

$$\rho = \rho_0 + \left(\frac{\partial \rho}{\partial c}\right)(c - c_0) + \left(\frac{\partial \rho}{\partial T}\right)(T - T_0) \tag{14.49}$$

where c_0, T_0, and ρ_0 are the concentration of reacting species, the temperature, and the density, respectively, measured in the bulk solution.

The body force acting on a unit of fluid volume is equal to ρg and changes from point to point in the solution. It is natural to consider that most of the change in concentration occurs in a very thin layer and most of the change in temperature occurs in a larger, but still thin layer. The changes in temperature and in concentration are the causes of fluid motion. Therefore, one can safely assume that fluid motion also occurs in this layer. Thus, the theories for the hydrodynamic boundary layer can also be applied to fluid motion in thermal free convection. In this case, the hydrodynamic boundary layer coincides with the thermal diffusion layer.

The concentration distribution of the electroactive species is determined from the solution of the convective-diffusion equation

$$\frac{\partial c}{\partial t} = -\nabla\,(D(y)\,\nabla c + V c) \tag{14.50}$$

or

$$\frac{\partial c}{\partial t} + v_x \frac{\partial c}{\partial x} + v_y \frac{\partial c}{\partial y} = D(y)\frac{\partial^2 c}{\partial y^2} + \frac{\partial D}{\partial y}\frac{\partial c}{\partial y} \tag{14.51}$$

with the boundary conditions: for $y = 0$, $c = 0$; and for $y \to \infty$, $c = c_0$.

The diffusion coefficient D(y) is a function of temperature, and it varies with position near the electrode according to the local temperature variation. However, as the thermal layer thickness is about five times larger than the diffusion layer thickness, the diffusion coefficient has in fact a variation that can be assumed to be negligible within the mass-transfer diffusion layer corresponding to the integration domain of equation (14.51). Thus, in the following development, $D(y) = D$, and $\partial D/\partial y = 0$.

The tangential and normal velocity components are, respectively, v_x and v_y. According to Marchiano and Arvia,[219] the velocity components can be expressed as a function of dimensionless coordinate

$$v_x = 4\nu\left(\frac{g}{4\nu^2}\right)^{1/4} x^{1/2} f'(\mu) \tag{14.52}$$

and

$$v_y = \nu\left(\frac{g}{4\nu^2}\right)^{1/4} \frac{\mu f'(\mu) - 3f(\mu)}{x^{1/4}} \tag{14.53}$$

where $\mu = (g/4\nu^2)^{1/4}$, ν is the kinematic viscosity, g is the acceleration of gravity, and $f(\mu)$ can be written as a series development in μ, which can be limited near the electrode to the first term: $f(\mu) = \mathcal{A}(T)\mu^2$.

The expression of the steady-state local flux at a vertical electrode under simultaneous effects of concentration and thermal gradients is given by

$$N = -\left. D\frac{d\overline{c}}{dy}\right|_{y=0} = Dc_0\frac{(\mathcal{A}Sc)^{1/3}}{\Gamma(4/3)}\left(\frac{g}{4\nu^2}\right)^{1/4} x^{-1/4} \tag{14.54}$$

As the electrode temperature is larger than the bulk temperature, a modulation of the temperature of the electrochemical interface induces a modulation of the thermal gradient in the solution while the bulk temperature is kept constant. Then the temperature-dependent parameters, like buoyancy forces, are modulated inside the thermal diffusion layer adjacent to the surface and, consequently, a modulation of the velocity is induced near the electrode. Therefore, the transient material balance equation may be written as

$$j\omega\widetilde{c} + \overline{v}_x\frac{\partial\widetilde{c}}{\partial x} + \overline{v}_y\frac{\partial\widetilde{c}}{\partial y} - D\frac{\partial^2\widetilde{c}}{\partial y^2} = -\widetilde{v}_x\frac{d\overline{c}}{dx} - \widetilde{v}_y\frac{d\overline{c}}{dy} \tag{14.55}$$

with the boundary conditions that, for $y = 0$, $\widetilde{c}(0) = 0$; and, for $y \rightarrow \infty$, $\widetilde{c} = 0$.

Equation (14.55) is a partial differential equation in two-dimensions that can be solved by following the method described in Section 13.2.2. The first step is to use a set of dimensionless variables that can be defined as a dimensionless normal distance from the electrode $\xi = y/\delta(x)$ and an x-dependent dimensionless frequency $\mathrm{K}_x = \omega\delta^2(x)/D$. Equation (14.55) can be written as

$$j\mathrm{K}_x\tilde{c} + \frac{4\xi\mathrm{K}_x}{9}\frac{\partial\tilde{c}}{\partial\mathrm{K}_x} - \frac{\xi^2}{3}\frac{\partial\tilde{c}}{\partial\xi} - \frac{\partial^2\tilde{c}}{\partial\xi^2} = \frac{\xi^2}{3}\frac{d\bar{c}}{d\xi}\frac{\widetilde{\mathcal{A}}}{\overline{\mathcal{A}}} \tag{14.56}$$

The material balance equation is written as a partial differential equation of two variables: ξ and K_x. In the low-frequency range, a solution exists in the form of a series

$$\tilde{c} = \sum_{m=0}^{\infty}(j\mathrm{K}_x)^m h_m(\xi) \tag{14.57}$$

The solution for $h_m(\xi)$ is obtained by a method similar to that presented in Section 13.2.2.

In the high-frequency range, the temperature perturbation is rapidly damped close to the wall; thus, the convective term can be disregarded, and equation (14.55) reduces to

$$j\mathrm{K}_x\tilde{c} - \frac{\partial^2\tilde{c}}{\partial\xi^2} = \frac{\xi^2}{3}\frac{d\bar{c}}{d\xi}\frac{\widetilde{\mathcal{A}}}{\overline{\mathcal{A}}} \tag{14.58}$$

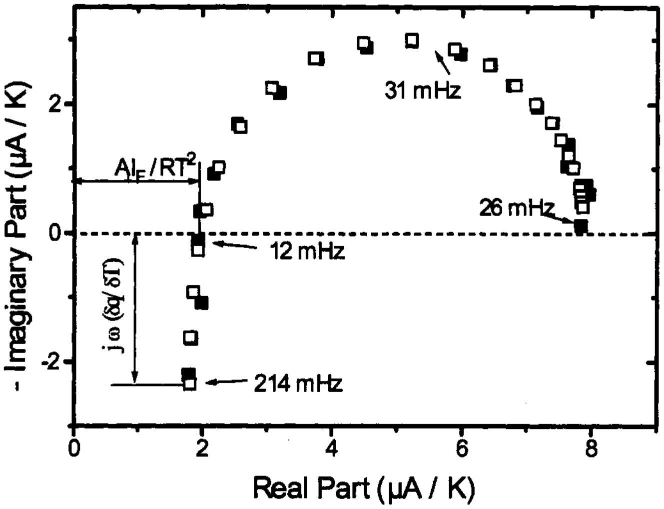

Figure 14.6: Experimental TEC transfer function compared with the model: □ represents the theoretical points and ■ the experimental points. (Taken from Aaboubi et al.[212])

Since the frequency is large, the distance over which a temperature perturbation prevails is small and some simplifications can be made to facilitate analytic solution of this last equation.

The series corresponding to the low-frequency solution needs a number of terms that increases with frequency; thus, the number of terms was chosen to provide a sufficient overlap between the low- and high-frequency solutions. In the present case, 80 terms were used to provide an overlap for $8 \leq K_x \leq 11$. These 80 terms are given by Aaboubi et al.[212]

The previous equations allow determination of the local flux. To obtain the response of the electrode itself, it is necessary to integrate the local flux over the electrode surface. For a rectangular electrode,

$$\tilde{i}_{\text{rect}} = L \int_0^{\ell} nFD \left. \frac{\partial \tilde{c}}{\partial y} \right|_0 dx \tag{14.59}$$

and, for a circular electrode,

$$\tilde{i}_{\text{circ}} = \int_{-R}^{+R} dz \int_{R-\sqrt{R^2-z^2}}^{R+\sqrt{R^2-z^2}} nFD \left. \frac{\partial \tilde{c}}{\partial y} \right|_0 dx \tag{14.60}$$

The experimental TEC transfer function is compared with the model in Figure 14.6. The three terms of equation (14.48) appear clearly in this figure.

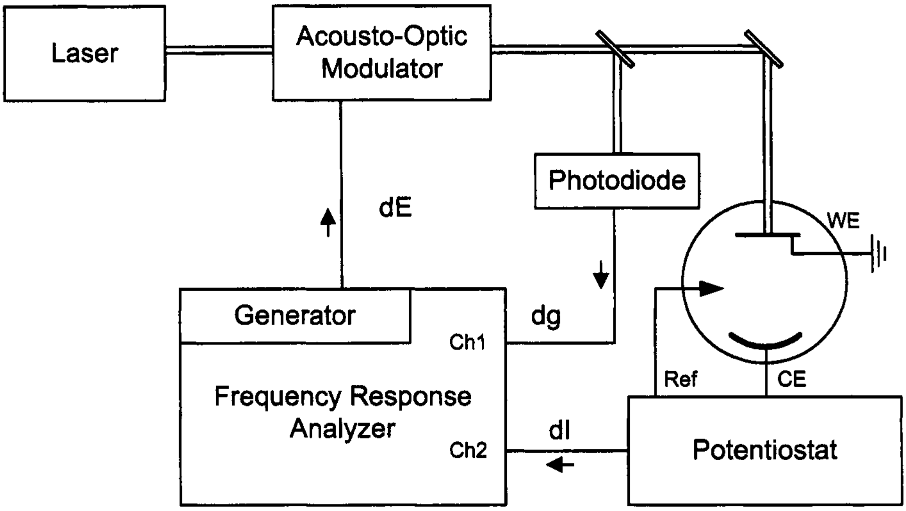

Figure 14.7: Experimental device for the measurement of impedance obtained by IMPS.

14.3.2 Photoelectrochemical Impedance Measurements

Modulation of light intensity provides an attractive method for probing the response of photoactive materials and systems. The required sinusoidal modulation of the intensity of the incident light is achieved by using the apparatus shown in Figure 14.7, and the technique is referred to as *intensity-modulated photocurrent spectroscopy* (IMPS).[220] The intensity of the incident laser beam is modulated by an acousto-optic modulator driven by the dc-biased output of a frequency response analyzer. Up to now, measurements have been made only under potentiostatic control. The complex ratio of the ac component of the photocurrent to the incident modulated light flux is obtained by deriving a reference signal from a fast photodiode that samples the laser beam. The time-dependent flux of minority carriers into the surface follows the excitation profile with a delay less than 1 ns, so the transfer function between the flux of minority carriers and the illumination can be considered to be a real number. The net photocurrent response, which is made up of the instantaneous minority carrier flux and the coupled majority carrier flux, can be derived. Finally, the output current response is determined by taking into account the cell transfer function, which is determined by the combination of the space-charge capacitance C_{sc} and the solution resistance R_e.

The general transfer function appears as the product of three transfer functions, i.e.,

$$\frac{\widetilde{I}}{h\widetilde{\nu}} = \frac{\widetilde{F}_{\text{minority}}}{h\widetilde{\nu}} \times \frac{\widetilde{F}_{\text{majority}}}{\widetilde{F}_{\text{minority}}} \times \frac{\widetilde{I}}{\widetilde{F}_{\text{majority}}} \tag{14.61}$$

where the first transfer function is a real number, $h\widetilde{\nu}$ is the input quantity, $\widetilde{F}_{\text{minority}}$ and $\widetilde{F}_{\text{majority}}$ are state quantities, and $\widetilde{I}$ is the output quantity.

This frequency-response analysis offers unique insights into complex photoelectrode processes. The analysis of surface recombination and photocurrent multiplication has shown that it is possible to deconvolute the contributions to the photocurrent of minority, majority, and injected carriers. The dependence of the rates of surface processes on potential, solution composition, and surface orientation and preparation can now be studied in detail. The systems investigated include the reduction of oxygen at p-Gas, the photooxidation of Si in NH_4F,[220] and the anodic dissolution of InP.[221]

14.3.3 Electrogravimetry Impedance Measurements

The use of a quartz microbalance to measure the mass loading on one face of a quartz crystal through the change of its resonance frequency (often of the order of 6 MHz) in electrolytic medium was introduced at the beginning of the 1980s. If the electrode is polarized in a potentiostatic circuit, the microbalance can be used to measure the change of the mass of the reacting species involved in a reaction occurring on the electrode. The sensitivity reached ($\approx 10^{-9}$ g cm^{-2}) is sufficient to allow determination of mass changes associated with adsorbed reaction intermediates or ion insertion in films coating the electrode.

Under steady-state or quasi-steady-state operation, the mass change as a function of time is followed by measuring directly the frequency f_w of the quartz oscillator by means of a frequency counter. The use of this microbalance in a sinusoidal regime is carried out by measuring the difference between the frequencies f_w of the working oscillator and f_o of a reference oscillator in air. This difference $df = f_w - f_o$, which is proportional to the mass change and sinusoidal in linear regime, is converted to a voltage by means of a converter. The resulting signal can be simultaneously analyzed by the transfer-function analyzer with the current response $\widetilde{I}$ to a potential perturbation ΔE generated by the analyzer. The electrochemical response between $\widetilde{U}$ and $\widetilde{I}$ is simultaneously measured, which allows measurement of the mass relaxation at the interface between the electrolyte and the electrode coating the quartz crystal.[214]

A schematic representation of the system is given in Figure 14.8. In this case, the output quantities are the current $Y_1 = I$ and the mass $Y_2 = M$. In addition to the charge and mass balances the equation governing the change of mass can be established

$$\frac{dM}{dt} = H(\theta_i, c_j, U) \tag{14.62}$$

The usual derivation based on the linearization procedure allows calculation of the electrochemical impedance and the $\widetilde{M}/\widetilde{U}$ transfer function. Two types of behavior occur, depending on whether the average mass of the electrode changes continuously with time.

1. When the mass increases or decreases (e.g., for deposition or dissolution of a metal) at a constant current, the low-frequency limit of $\widetilde{M}/\widetilde{U}$ tends to infinity.

2. When the mass does not change (e.g., a polymer film at zero current), the low-frequency limit of $\widetilde{M}/\widetilde{U}$ tends to a finite value.

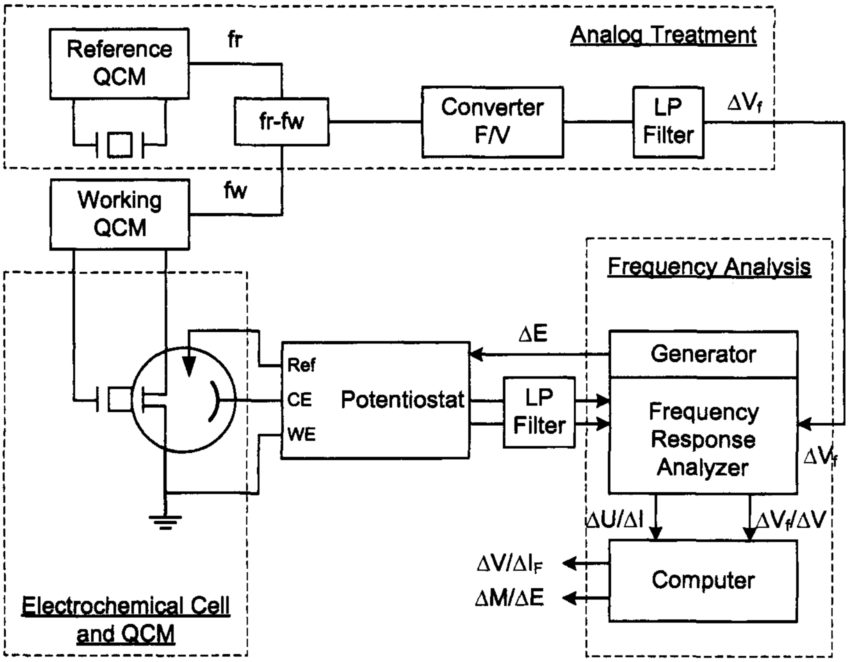

Figure 14.8: Experimental device for the measurement of the electrogravimetric transfer function.

The simultaneous measurement of the impedance and mass/potential transfer function leads to new information on the kinetics of the processes involved. It may lead to chemical identification of the species involved in the intermediate reaction steps by allowing the atomic masses of the adsorbed intermediates of the multistep reaction mechanisms to be estimated.

Problems

14.1 Derive the steady-state concentration gradient corresponding to equation (14.55).

14.2 Derive the high-frequency solution corresponding to equation (14.59) and, in particular, show that the phase shift is constant and equal to $-135°$.

Electrochemical Impedance Spectroscopy
by Mark E. Orazem and Bernard Tribollet

Chapter 15

Electrohydrodynamic Impedance

Electrohydrodynamic (EHD) impedance provides a practical example of a generalized transfer function involving nonelectrical quantities. In this chapter, a rotating disk electrode is considered. The current is a function of the rotation speed, which means that the current is totally or partially limited by mass transport. This measurement technique, based on the analysis of the current response to a rotation speed perturbation, was proposed at the beginning of the seventies by Bruckenstein et al.[222] Very early, these authors suggested application of sinusoidal hydrodynamic modulations. Bruckenstein et al.[222] derived the first theoretical analysis of the problem by considering the response of the mass-transfer rate to a modulation of the angular velocity of a rotating disk electrode such that[223]

$$\Omega^{1/2} = \overline{\Omega}^{1/2}\left(1 + \left(\frac{\Delta\Omega}{\overline{\Omega}}\right)^{1/2}\cos\omega t\right) \tag{15.1}$$

where ω is the modulation frequency.

The concept that the response to a modulation of rotation speed Ω should be seen as a modulation of the square root of Ω was naturally supported by the results of the Levich theory in steady-state conditions.[123] However, due to the fact that $i = f(\Omega) = k\Omega^{1/2}$,

$$\frac{\partial f}{\partial \Omega} = \left(\frac{1}{2}\Omega^{-1/2}\right)\frac{\partial f}{\partial \Omega^{1/2}} \tag{15.2}$$

Equation (15.2) shows that the transfer function corresponding to a modulation of the angular velocity is directly proportional to the transfer function corresponding to a modulation of the square root of the angular velocity, and the coefficient of proportionality is $\frac{1}{2}\Omega^{-1/2}$. Therefore, after the pioneer works of Bruckenstein et al.,[222,223] a direct modulation of the angular velocity was considered. With the increasing development of impedance techniques, aided by development of increasingly sophisticated instrumentation,[50] Deslouis and Tribollet promoted the use of impedance concept for this type of perturbation and introduced the *electrohydrodynamic* (EHD) impedance.[224]

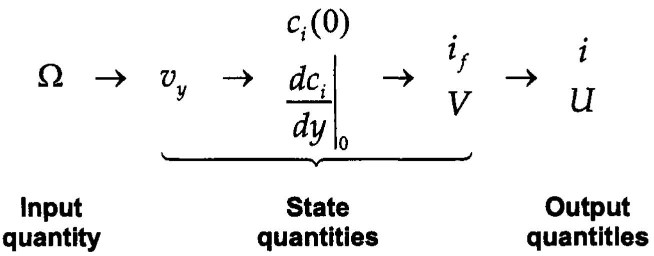

Figure 15.1: Schematic representation of the different transfer functions existing between the input quantity and the output quantities.

The EHD impedance is useful for analysis of electrochemical systems that are either partially or completely limited by mass transport. For a rotating disk electrode, the input quantities are, at least, one electrical quantity, e.g., overall current or electrode potential, and one nonelectrical quantity, i.e., the rotation speed of the rotating disk electrode Ω. For EHD impedance, the input quantity is the rotation speed. Under galvanostatic regulation, the output quantity is the electrode potential; under potentiostatic regulation, the output quantity is the overall current. To analyze this problem, the mass conservation equation must be considered with the normal velocity v_y near the electrode and the concentration of the involved species $c_i(0)$ as state quantities.

A perturbation of the rotation speed Ω induces a perturbation of the normal velocity v_y, which, in turn, induces a perturbation of the concentration field of the electroactive species and in particular of $c_i(0)$ and $\left.\frac{dc_i}{dy}\right|_0$. These last interfacial state quantities are linked to the surface-averaged Faradaic current density i_f and to the interfacial potential V by the kinetic equations. Finally, by taking into account the double-layer capacitance and the electrolyte resistance, these last electrical quantities are linked to the output quantities of the average current density i and the electrode potential U. The relationship among input, state, and output quantities is shown schematically in Figure 15.1. The transfer functions associated with several applications of electrohydrodynamic impedance are developed in the subsequent sections.

Remember! 15.1 EHD *provides a means to isolate the influence of mass transfer the electrochemical impedance response of a system.*

15.1 Hydrodynamic Transfer Function

Through the von Karman transformation, the steady-state Navier-Stokes equations for a rotating disk can be expressed in terms of three coupled, nonlinear, ordinary differential equations as[89]

$$2F + H' = 0 \tag{15.3}$$

$$F^2 - G^2 + HF' - F'' = 0 \tag{15.4}$$

and

$$2FG + HG' - G'' = 0 \tag{15.5}$$

where F, H, and G represent the dimensionless radial, angular, and axial velocity components, respectively. Equations (15.3), (15.4), and (15.5) are functions only of the axial dimensionless distance $\zeta = y\sqrt{\overline{\Omega}/\nu}$ and can be solved subject to boundary conditions

$$F(0) = H(0) = 0 \tag{15.6}$$

$$G(0) = 1 \tag{15.7}$$

and

$$F(\infty) = G(\infty) = 0 \tag{15.8}$$

The steady flow field created by an infinite disk rotating at a constant angular velocity in a fluid with constant physical properties was presented in Chapter 11.

For the unsteady situation, the instantaneous value of rotation speed Ω can be defined by

$$\Omega = \overline{\Omega} + \operatorname{Re}\{\widetilde{\Omega} \exp j\omega t\} \tag{15.9}$$

where $\omega/2\pi$ is the modulation frequency and $\widetilde{\Omega} = \Delta\Omega$ is a real number. Large-amplitude modulations induce a nonlinear flow response.[225,226] This nonlinear problem is outside the scope of an impedance study, which is defined here to be based on a linearized system response. A periodic flow generated by small oscillations of a body in a fluid at rest involves nonlinearities in the mass-transport problem or in the secondary flow and is therefore also outside the scope of this presentation. The electrohydrodynamic impedance concept is developed here following the work of Tribollet and Newman[227] for small-amplitude modulation such that $(\Delta\Omega \ll \overline{\Omega})$. Under these conditions, the system response is linear.

Following the development in Chapters 10 and 11 for a current or potential response to a perturbation, the radial, angular, and axial velocity components can be expressed as

$$v_r = r\overline{\Omega}[F(\zeta) + \frac{\Delta\Omega}{\overline{\Omega}} \operatorname{Re}\{\widetilde{f} \exp j\omega t\}] \tag{15.10}$$

$$v_\theta = r\overline{\Omega}[G(\zeta) + \frac{\Delta\Omega}{\overline{\Omega}} \operatorname{Re}\{\widetilde{g} \exp j\omega t\}] \tag{15.11}$$

and

$$v_y = r\overline{\Omega}[H(\zeta) + \frac{\Delta\Omega}{\overline{\Omega}} \operatorname{Re}\{\widetilde{h} \exp j\omega t\}] \tag{15.12}$$

where $\tilde{f}$, $\tilde{g}$, and $\tilde{h}$ are complex functions. The equation of continuity and the unsteady Navier-Stokes equations are linearized, i.e., the quadratic terms, proportional to $(\Delta\Omega/\overline{\Omega})^2$, are neglected.

The time-dependent forms of equations (15.3), (15.4), and (15.5) may be written as

$$2\tilde{f} + \tilde{h}' = 0 \tag{15.13}$$

$$j\tilde{f}p + 2F\tilde{f} - 2G\tilde{g} + H\tilde{f}' + F'\tilde{h} = f'' \tag{15.14}$$

and

$$j\tilde{g}p + 2G\tilde{f} + 2F\tilde{g} + \tilde{h}G' + H\tilde{g}' = g'' \tag{15.15}$$

where $p = \omega/\overline{\Omega}$ is the dimensionless modulation frequency. Equations (15.13), (15.14), and (15.15) may be solved subject to the boundary conditions

$$\tilde{f}(0) = \tilde{h}(0) = 0 \tag{15.16}$$

$$\tilde{g}(0) = 1 \tag{15.17}$$

and

$$\tilde{f}(\infty) = 0 \tag{15.18}$$

As discussed in Section 1.2.2, each complex function may be written as the sum of a real function and an imaginary function. The set of the three coupled equations (15.13), (15.14), and (15.15) then becomes a set of six coupled linear ordinary differential equations. By using Newman's method,[228] a numerical solution for the six equations can be obtained for each dimensionless frequency.

In a manner similar to that developed for the steady-state solution in Chapter 11, the complex functions $\tilde{f}$, $\tilde{g}$, and $\tilde{h}$ can be written in terms of series expansions for small values of ζ. Of particular importance is the derivative $\tilde{f}'(0)$ obtained from equations (15.13), (15.14), and (15.15) and given in Table 15.1 for different values of dimensionless frequency p. The real and imaginary parts of the derivative $\tilde{f}'(0)$ are also presented in Figure 15.2 as a function of $p = \omega/\Omega$. These derivatives are essential to determination of the first coefficients of the series expansions. The other coefficients are deduced from the first one by using the set of equations (15.13), (15.14), and (15.15). In particular,

$$\tilde{h} = -\tilde{f}'(p)\zeta^2 + \frac{2}{3}\zeta^3 \tag{15.19}$$

where $\tilde{h}$ represents the complex function associated with the axial velocity.

Remember! 15.2 *The methods described in this section allow the numerical calculation of generalized functions that can be used, via a look-up table, to model any* EHD *response.*

Table 15.1: Calculated values for real and imaginary parts of $\tilde{f}'(0)$ as a function of dimensionless frequency p. (Taken from Deslouis and Tribollet.[229])

$p = \omega/\Omega$	$\mathrm{Re}\{\tilde{f}'(0)\}$	$\mathrm{Im}\{\tilde{f}'(0)\}$
0.0631	0.7652	−0.0130
0.1000	0.7650	−0.0206
0.1585	0.7645	−0.0329
0.2512	0.7630	−0.0527
0.3981	0.7579	−0.0849
0.6310	0.7410	−0.1356
1.0000	0.6943	−0.2035
1.5849	0.6020	−0.2642
2.5119	0.4832	−0.2842
3.9811	0.3748	−0.2652
6.3095	0.2906	−0.2297
10.000	0.2272	−0.1922

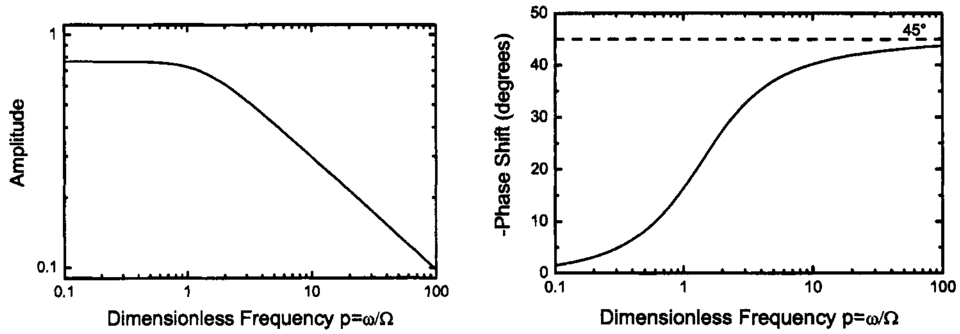

(a)

(b)

Figure 15.2: Dimensionless function $f'(0)$ in Bode representation: a) modulus versus the dimensionless frequency p; and b) phase shift versus the dimensionless frequency p.

By using the results of Sparrow and Gregg,[230] who solved the nonsteady flow problem, the low-frequency expression of $\tilde{f}'$ can be obtained following the present notation as

$$\tilde{f}' = (0.765345 - 0.023112p^2) - 0.204835pj \tag{15.20}$$

As the frequency modulation tends toward zero, $r\tilde{f}_1$ tends toward the derivative of $\overline{v}_r$ with respect to $\overline{\Omega}$ (see equation 15.10) and $\tilde{f}_2'$ tends toward zero. Therefore, $\tilde{f}'(0) = \frac{3}{2}\frac{dF}{d\zeta}\Big|_0 = 0.765345$. Sharma[231] obtained an asymptotic solution for $\tilde{f}'$ appropriate for high frequencies as

$$\tilde{f}' = \frac{1}{\sqrt{2p}} - j\left(\frac{1}{\sqrt{2p}} - \frac{0.313}{p}\right) \tag{15.21}$$

From this expression and as shown in Figure 15.2(b), the phase shift of f' tends toward −45° as p tends toward infinity. Equation (15.20) may be used with an accuracy better than 1 percent for $p < 0.1$. Equation (15.21) may be used with an accuracy better than 1 percent for $p > 7$. Between these two p values, Table 15.1 must be used.

The hydrodynamic transfer function is given by

$$\frac{\tilde{v}_y}{\Delta\Omega} = r\tilde{h}(\zeta) = r\left(\tilde{f}'(p)\,\zeta^2 + \frac{2}{3}\zeta^3\right) \tag{15.22}$$

Equation (15.22) is implicit in the subsequent development of transfer functions involving concentrations of reacting species.

15.2 Mass-Transport Transfer Function

The mass-transfer problem for a rotating disk electrode at a constant rotation speed is presented in Section 11.6.2. Under modulation of the rotation speed of the electrode, equation (11.80) becomes

$$j\omega\tilde{c}_i e^{j\omega t} + \overline{v}_y\frac{d\overline{c}_i}{dy} + \overline{v}_y\frac{d\tilde{c}_i}{dy}e^{j\omega t} + \tilde{v}_y\frac{d\overline{c}_i}{dy}e^{j\omega t} - D_i\frac{d^2\overline{c}_i}{dy^2} - D_i\frac{d^2\tilde{c}_i}{dy^2}e^{j\omega t} = 0 \tag{15.23}$$

where the second-order term $\tilde{v}_y\frac{d\tilde{c}_i}{dy}e^{2j\omega t}$ is neglected in agreement with the hypothesis of linearity. The solution of the steady-state equation (11.81) was given by equation (11.82). Upon cancelation of the steady-state terms and division by $e^{j\omega t}$, equation (15.23) becomes

$$j\omega\tilde{c}_i + \overline{v}_y\frac{d\tilde{c}_i}{dy} - D_i\frac{d^2\tilde{c}_i}{dy^2} = -\tilde{v}_y\frac{d\overline{c}_i}{dy} \tag{15.24}$$

Remember! 15.3 *The phase shift of the hydrodynamic transfer function f' tends toward −45° as the dimensionless frequency $p = \omega/\Omega$ tends toward infinity.*

By using the same dimensionless position ξ and the same dimensionless frequency K_i as was used to solve equation (11.83), equation (15.24) can be written in the form

$$\frac{d^2\tilde{c}_i}{d\xi^2}+\left(3\xi^2-\left(\frac{3}{a^4}\right)^{1/3}\frac{\xi^3}{Sc^{1/3}}\right)\frac{d\tilde{c}_i}{d\xi}-jK_i\tilde{c}_i= \tag{15.25}$$
$$-\frac{\Delta\Omega}{\overline{\Omega}}\left(\frac{3\tilde{f}'(p)\xi^2}{a}-2\left(\frac{3}{a^4}\right)^{1/3}\frac{\xi^3}{Sc^{1/3}}\right)\frac{d\bar{c}_i}{d\xi}$$

where only the two first terms of the velocity expansion were considered.

The solution of equation (15.25) can be obtained by the technique of reduction of order by setting $\tilde{c}_i = \lambda(\xi)\theta_i(\xi)$, where $\theta_i(\xi)$ is a solution of the homogeneous equation satisfying the boundary conditions (11.88) (see Section 11.6) and λ satisfies

$$\frac{d^2\lambda}{d\xi^2}+\left(3\xi^2-\left(\frac{3}{a^4}\right)^{1/3}\frac{\xi^3}{Sc^{1/3}}+\frac{2\theta_i'}{\theta_i}\right)\frac{d\lambda}{d\xi}= \tag{15.26}$$
$$-\frac{\Delta\Omega}{\overline{\Omega}}\left(\frac{3\tilde{f}'(p)\xi^2}{a}-2\left(\frac{3}{a^4}\right)^{1/3}\frac{\xi^3}{Sc^{1/3}}\right)\frac{1}{\theta_i}\frac{d\bar{c}_i}{d\xi}$$

Integration gives

$$\tilde{c}_i = K_2\theta_i + K_1\theta_i\int_0^{\xi}\frac{\exp\left(-\chi^3+\left(\frac{3}{a^4}\right)^{1/3}\frac{\chi^4}{4Sc^{1/3}}\right)}{\theta_i^2(\chi)}d\chi \tag{15.27}$$
$$-\frac{\Delta\Omega}{\overline{\Omega}}\left.\frac{d\bar{c}}{d\xi}\right|_0\int_0^{\xi}\frac{\exp\left(-\chi^3+\left(\frac{3}{a^4}\right)^{1/3}\frac{\chi^4}{4Sc^{1/3}}\right)}{\theta_i^2(\chi)}$$
$$\times\int_0^{\chi}\left(3\frac{\tilde{f}'(p)}{a}\chi_1^2-\left(\frac{3}{a^4}\right)^{1/3}\frac{2\chi_1^3}{Sc^{1/3}}\right)\theta_i(\chi_1)d\chi_1 d\chi$$

where K_1 and K_2 are integration constants. The boundary condition $\theta_i(0) = 1$ at $\xi = 0$ yields the value of $K_2 = \tilde{c}_i(0)$. The value of K_1 can be obtained from the boundary condition that $\tilde{c}_i$ approaches zero as ξ approaches infinity, with the results

$$K_1 = \frac{\Delta\Omega}{\overline{\Omega}}\left.\frac{d\bar{c}}{d\xi}\right|_0 W_i \tag{15.28}$$

where

$$W_i = \int_0^{\infty}\left(3\frac{\tilde{f}'(p)}{a}\xi^2-\left(\frac{3}{a^4}\right)^{1/3}\frac{2\xi_1^3}{Sc^{1/3}}\right)\theta_i d\xi \tag{15.29}$$

is a dimensionless quantity whose value is worth recording.

Table 15.2: Coefficients for the calculation of W_i with a Schmidt number correction.[229]

$p\mathrm{Sc}^{1/3}$	t_1	t_2	t_3	t_4	t_5	t_6
0	0.6533	0	0.7788	0	−0.5961	0
0.1000	0.6513	−0.0397	0.7729	−0.0830	−0.5939	0.0408
0.1585	0.6484	−0.0626	0.7639	−0.1307	−0.5907	0.0644
0.2512	0.6410	−0.0983	0.7418	−0.2037	−0.5828	0.1010
0.3981	0.6230	−0.1525	0.6888	−0.3098	−0.5634	0.1564
0.6310	0.5807	−0.2291	0.5696	−0.4437	−0.5181	0.2341
1.0000	0.4905	−0.3204	0.3404	−0.5541	−0.4218	0.3245
1.5849	0.3325	−0.3873	0.0251	−0.5181	−0.2556	0.3834
2.5119	0.1380	−0.3680	−0.1905	−0.2833	−0.0586	0.3442
3.9811	−0.0036	−0.2576	−0.1686	−0.0415	0.0664	0.2101
6.3095	−0.0483	−0.1352	−0.0562	0.0334	0.0787	0.0807
10.0000	−0.0385	−0.0600	−0.0054	0.0169	0.0435	0.0195
15.8488	−0.0218	−0.0263	0.0008	0.0035	0.0178	0.0035
25.1187	−0.0112	−0.0122	0.0003	0.0006	0.0068	0.0006
39.8104	−0.0056	−0.0059	0.0001	0.0001	0.0026	0.0001
63.0952	−0.0028	−0.0029	0	0	0.0010	0
100.000	−0.0014	−0.0014	0	0	0.0004	0

The expansion for θ_i is given by equation (11.92) in terms of powers of $pSc^{1/3}$. The expansion for W_i is more complicated because, while the expansion of θ_i depends on $pSc^{1/3}$, $\tilde{f}'(p)$ depends on p without $Sc^{1/3}$. The expansion for W_i takes the form

$$W_i = \tilde{f}'(p)\left(t_1 + jt_2\right) + \frac{1}{Sc^{1/3}}\left[\tilde{f}'(p)\left(t_3 + jt_4\right) + t_5 + jt_6\right] \tag{15.30}$$

where the functions t_k, given in Table 15.2 as function of $p\mathrm{Sc}^{1/3}$, are calculated from the following definitions:

$$t_1 = \frac{3}{a}\int_0^\infty \xi^2 \mathrm{Re}\left\{\theta_{i,0}\right\} d\xi \tag{15.31}$$

$$t_2 = \frac{3}{a}\int_0^\infty \xi^2 \mathrm{Im}\left\{\theta_{i,0}\right\} d\xi \tag{15.32}$$

$$t_3 = \frac{3}{a}\int_0^\infty \xi^2 \mathrm{Re}\left\{\theta_{i,1}\right\} d\xi \tag{15.33}$$

$$t_4 = \frac{3}{a}\int_0^\infty \xi^2 \mathrm{Im}\left\{\theta_{i,1}\right\} d\xi \tag{15.34}$$

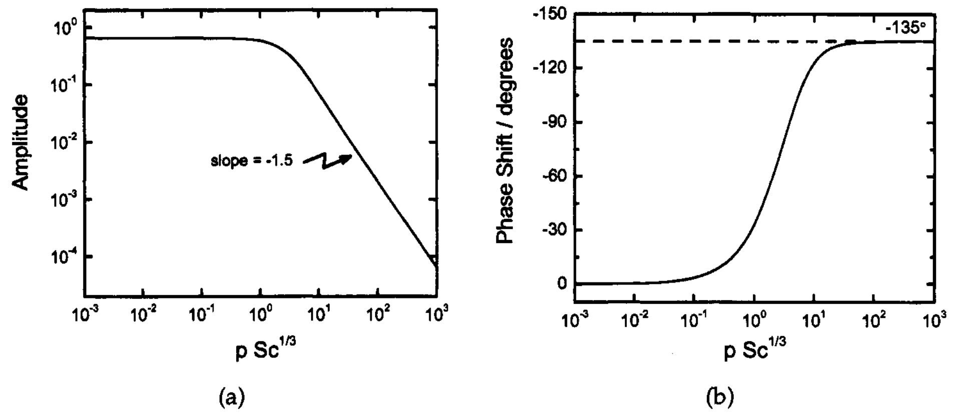

Figure 15.3: Dimensionless mass-transport transfer-function Z_c in Bode representation: a) modulus versus the dimensionless frequency $pSc^{1/3}$; and b) phase shift versus the dimensionless frequency $pSc^{1/3}$.

$$t_5 = -2\left(\frac{3}{a^4}\right)^{1/3} \int_0^\infty \xi^3 \mathrm{Re}\left\{\theta_{i,0}\right\} d\xi \tag{15.35}$$

and

$$t_6 = -2\left(\frac{3}{a^4}\right)^{1/3} \int_0^\infty \xi^3 \mathrm{Im}\left\{\theta_{i,0}\right\} d\xi \tag{15.36}$$

The concentration gradient at the wall is obtained from equation (15.28) where $K_2 = \widetilde{c}_i(0), \theta_i'(0) = 1$, and K_1 is given by equation (15.28). The general result of this section is therefore a relationship between the concentration and the concentration derivative, both evaluated at the electrode surface. In terms of the dimensional distance y, this can be expressed as

$$\left.\frac{d\widetilde{c}_i}{dy}\right|_{y=0} = \frac{\widetilde{c}_i(0)}{\delta_i}\theta_i'(0) + \frac{\Delta\Omega}{\overline{\Omega}}\left.\frac{d\overline{c}}{dy}\right|_{y=0} W_i \tag{15.37}$$

where $-1/\theta_i'(0)$ is the dimensionless convective diffusion impedance as given in equation (11.97).

15.2.1 Asymptotic Solution for Large Schmidt Numbers

When the Schmidt number is infinitely large, W_i is reduced to $\widetilde{f}'(p)(t_1 + jt_2)$ and appears as the product of a hydrodynamic transfer function $\widetilde{f}'(p)$ and a mass-transport transfer function $Z_c = t_1 + jt_2$. The mass-transport transfer function Z_c is presented in Figure 15.3. It is easily verified that W_i approaches 0.5 when the frequency tends toward zero, in agreement with the exponent of the rotation speed in the Levich equation. This value of 0.5 is also verified if the complete expression of W_i is used. The complex function $2W_i$ is presented in Figure 15.4 in

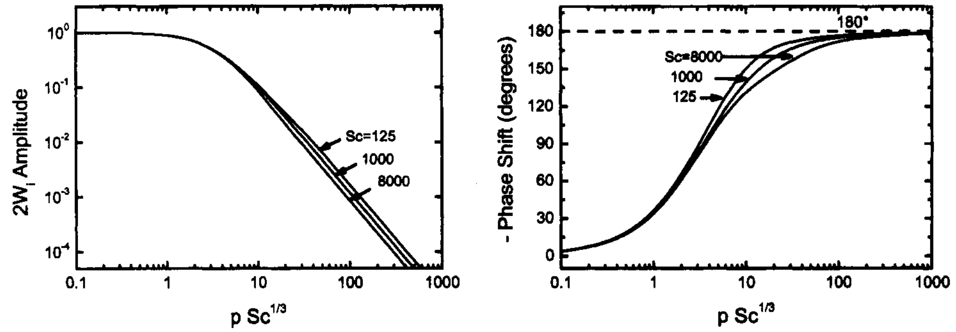

(a) (b)

Figure 15.4: Dimensionless EHD impedance W_i in Bode representation with Schmidt number as a parameter: a) modulus versus the dimensionless frequency $pSc^{1/3}$; and b) phase shift versus the dimensionless frequency $pSc^{1/3}$.

Bode format as a function of dimensionless frequency $p\mathrm{Sc}^{1/3}$ with Schmidt number Sc as a parameter.

15.2.2 Asymptotic Solution for High Frequencies

When the perturbation frequency is large, the distance over which a concentration wave proceeds is small. Thus, $\exp(-\xi^3)$ can be considered to be equal to one, and, the velocity modulation being rapidly damped close to the wall, the convective term can be disregarded in the homogeneous part of equation (15.25), which becomes

$$\frac{d^2\tilde{c}_i}{d\xi^2} - jK_i\theta_i = -\frac{\Delta\Omega}{\overline{\Omega}}\frac{3\tilde{f}'(p)\xi^2}{a}\left.\frac{d\tilde{c}_i}{d\xi}\right|_0 \tag{15.38}$$

The solution of the homogeneous equation is $\theta = \exp\left(-(jK_i)^{1/2}\xi\right)$ and the solution of equation (15.38) may be written as

$$\tilde{c}_i = \theta(\xi)\left[\int_0^{\xi}\theta^{-2}(\xi')\left(-\int_0^{\xi'}\frac{\Delta\Omega}{\overline{\Omega}}\frac{3\tilde{f}'(p)}{a}\xi''^2\theta(\xi'')\left.\frac{d\bar{c}}{d\xi}\right|_0 d\xi'' + K_1\right)d\xi' + \tilde{c}_i(0)\right] \tag{15.39}$$

where

$$K_1 = \frac{\Delta\Omega}{\overline{\Omega}}\frac{3\tilde{f}'(p)}{a}\left.\frac{d\tilde{c}_i}{d\xi}\right|_0\int_0^{\infty}\xi^2\theta(\xi)d\xi \tag{15.40}$$

and

$$\left.\frac{d\tilde{c}_i}{dy}\right|_0 = \frac{\Delta\Omega}{\overline{\Omega}}\frac{\tilde{f}'(p)}{a}\left.\frac{d\bar{c}}{dy}\right|_0\frac{6}{(jK_i)^{3/2}} \tag{15.41}$$

At high frequencies, the derivative $\left.\frac{d\widetilde{c}_i}{dy}\right|_0$ is proportional to the two complex quantities $\widetilde{f}'(p)$ and $(jK_i)^{-1.5}$, and the phase shift is the sum of the phase shift of each complex quantity. The phase shift of $\widetilde{f}'(p)$ tends toward $-45°$ when the dimensionless frequency p tends toward infinity (see equation (15.21)) and the phase shift of $(jK_i)^{-1.5}$ has a value of $-135°$. Thus, the phase shift of $\left.\frac{d\widetilde{c}_i}{dy}\right|_0$ tends toward $-180°$ when the dimensionless frequency tends toward infinity. In the same way, the modulus of $\widetilde{f}'(p)$ decreases with frequency with a slope of -0.5 in logarithmic coordinates (see Figure 15.2(a)), and the modulus of $(jK_i)^{-1.5}$ decreases with a slope of -1.5. Thus, the modulus of $\left.\frac{d\widetilde{c}_i}{dy}\right|_0$ decreases with a slope of -2 as shown in Figure 15.4(a).

15.3 Kinetic Transfer Function for Simple Electrochemical Reactions

Under the assumption that the interface is uniformly reactive, $c_i(0)$ is independent of the radial coordinate. A single electrode reaction can be written in symbolic form as

$$\sum_i s_i M_i^{z_i} \rightarrow ne^- \tag{15.42}$$

Following the treatment presented in Section 10.3, the Faradaic current can be written in the form

$$i_f = f(V, c_i(0)) \tag{15.43}$$

For minor species, in the presence of supporting electrolyte and with neglect of double-layer adsorption of these minor species, the concentration gradient is related to the Faradaic current density by

$$D_i \left.\frac{\partial c_i}{\partial y}\right|_0 = \frac{s_i}{nF} i_f \tag{15.44}$$

Following equation (10.3), a Taylor series expansion about the steady value can be written as

$$\widetilde{i}_f = \left(\frac{\partial f}{\partial V}\right)_{c_i(0)} \widetilde{V} + \sum_i \left(\frac{\partial f}{\partial c_i(0)}\right)_{V, c_j(0), j \neq i} \widetilde{c}_i(0) \tag{15.45}$$

Following the discussion presented in Chapter 10, the usual charge-transfer resistance R_t can be identified as the reciprocal of $(\partial f / \partial V)_{c_i(0)}$. Combination of equations (15.37), (15.44), and (15.45) yields

$$\widetilde{V} = R_t \widetilde{i}_f - \sum_i R_t \left(\frac{\partial f}{\partial c_i(0)}\right)_{V, c_j(0), j \neq i} \left[\frac{\delta_i}{\theta_i'(0)} \frac{s_i}{nFD_i} \widetilde{i}_f - \frac{\Delta\Omega}{\overline{\Omega}} \frac{W_i \delta_i}{\theta_i'(0)} \frac{s_i \overline{i}_f}{nFD_i}\right] \tag{15.46}$$

or

$$\widetilde{V} = R_t \widetilde{i}_f + Z_D \widetilde{i}_f + \frac{\Delta\Omega}{\overline{\Omega}} \frac{\overline{i}_f R_t}{nF} \sum_i \left(\frac{\partial f}{\partial c_i(0)}\right)_{V, c_j(0), i \neq j} \frac{W_i \delta_i}{\theta_i'(0)} \frac{s_i}{D_i} \tag{15.47}$$

where

$$Z_D = -R_t \sum_i \left(\frac{\partial f}{\partial c_i(0)} \right)_{V,c_j(0),j \neq i} \frac{\delta_i s_i}{nFD_i \theta_i'(0)} \tag{15.48}$$

The term Z_D represents the convective-diffusion impedance with its dimensionless form $-1/\theta_i'(0)$ (see Chapter 11). Considering now equations (14.27), (14.28) and (15.47), one obtains the relation between observable quantities corresponding to the general form of equation (14.22), i.e.,

$$\tilde{U} = Z\tilde{I} + \frac{\Delta\Omega}{\overline{\Omega}} \frac{1}{1 + j\omega C_D(R_t + Z_D)} \frac{\overline{I}R_t}{nF} \sum_i \left. \frac{\partial f}{\partial c_i(0)} \right|_{E,c_j(0),j \neq i} \frac{W_i \delta_i}{\theta_i'(0)} \frac{s_i}{D_i} \tag{15.49}$$

where

$$Z = R_e + \frac{R_t + Z_D}{1 + j\omega C_D(R_t + Z_D)} \tag{15.50}$$

The term Z represents the impedance of the usual Randles equivalent circuit (see Figure 10.5).

15.4 Interface with a 2-D or 3-D Insulating Phase

The main hypotheses for developing the EHD impedance theory are that the electrode interface is uniformly accessible and the electrode surface has uniform reactivity. However, in many cases, real interfaces deviate from this ideal picture due, for example, either to incomplete monolayer adsorption leading to the concept of partial blocking (2-D adsorption) or to the formation of layers of finite thickness (3-D phenomena). These effects do not involve the interfacial kinetics on bare portions of the metal, which, for simplification, will be assumed to be inherently fast. The changes will affect only the local mass transport toward the reaction sites. Before presenting an application of practical interest, the theoretical EHD impedance for partially blocked electrodes and for electrodes coated by a porous layer will be analyzed.

15.4.1 Partially Blocked Electrode

Integration of the nonstationary material balance equation requires that the steady-state concentration distribution be known. This is achieved by solving the steady-state part of

$$\frac{\partial c_i}{\partial t} + v_x \frac{\partial c_i}{\partial x} + v_y \frac{\partial c_i}{\partial y} = D_i \left(\frac{\partial^2 c_i}{\partial x^2} + \frac{\partial^2 c_i}{\partial y^2} \right) \tag{15.51}$$

Remember! 15.4 EHD *provides a means to reveal and quantify the influence of partially blocked electrodes and electrodes coated by porous layers.*

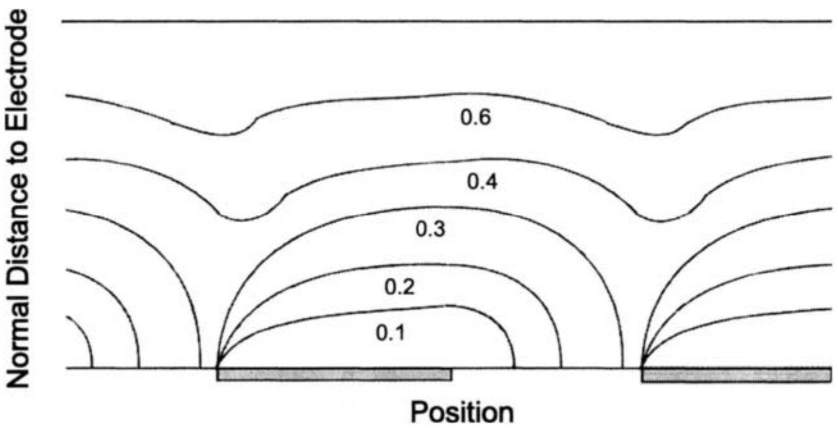

Figure 15.5: Concentration field over a partially blocked electrode. The active parts of the electrode are displayed in gray and the concentration is dimensionless $\theta = c/c(\infty)$. (Taken from Caprani et al.[232])

where $v_x = \sqrt{v_r^2 + v_\theta^2}$ is the longitudinal velocity and $v_y = \beta_y(t)y^2$ is the normal velocity. The steady-state iso-concentration lines, deduced from a numerical solution,[232] are plotted in Figure 15.5. The boundary conditions are that $c_i = 0$ for $y = 0$ on the active surfaces (shown in gray in Figure 15.5) and $\partial c_i/\partial y = 0$ on the insulating surfaces. The concentration profiles shown in Figure 15.5 correspond to the effect of two neighboring microelectrodes. Such an arrangement describes locally a periodical distribution of active and passive sites. It appears that the concentration profiles of the two leading edges coincide reasonably well and one may assume that the memory effect on the concentration distribution is lost over one or a few active sites. The iso-concentration lines are parallel to the electrode surface at large values of y (far from the electrode). This condition is the same as seen for a uniformly accessible disk electrode. The iso-concentration lines close to the electrode are similar to the iso-concentration lines of an isolated microelectrode (see Section 13.2).

For a partially blocked electrode, the diagrams show two characteristic frequencies and, whatever the mean rotation speed Ω, fall onto a single curve when plotted versus a dimensionless frequency $p = \omega/\Omega$, where $\omega/2\pi$ is the frequency modulation. The high-frequency domain is characteristic of the response of the sum of the active sites, as if they were not coupled by their diffusion layers.

This result is phenomenologically based on the theoretical analysis given by Deslouis et al.[233] for the frequency response of a small electrode to a flow modulation. The response of a partially blocked electrode surface was obtained from numerical calculations.[232] The main result of this approach is that, at variance with the case of a uniform active disk electrode, such a surface shared between active and passive sites displays two characteristic frequencies, one in the low-

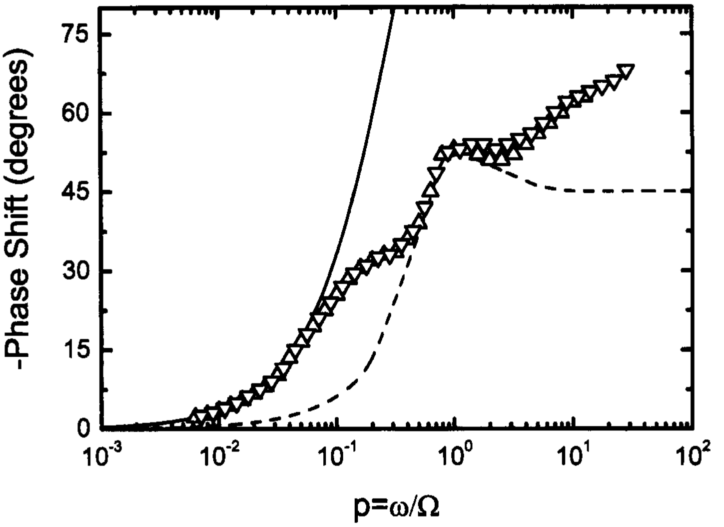

Figure 15.6: Phase shift of the EHD impedance corresponding to the ferricyanide reduction on a platinum electrode (area 0.38 cm^2) coated with a photoresist on which an array of circular sites of diameter d_{act} was patterned. $d_{act} = 649$ μm, $\Omega = 96$ rpm (▼) and 375 rpm (▲). Theoretical curve for a single microelectrode (dashed line), or for the active disk electrode (solid line). (Taken from Deslouis and Tribollet.[235])

frequency range corresponding to the uniform active disk response and one in the high-frequency range corresponding to the response of individual active sites, which are then assumed to behave without interactions.

The average active site dimension d_{act} was deduced from the two characteristic frequencies corresponding respectively to the high-frequency behavior and to the low-frequency behavior, p_{HF} and p_{LF} respectively, i.e.,

$$d_{act} = 2.1^{3/2} R \left(p_{HF}/p_{LF}\right)^{-3/2} \tag{15.52}$$

where R is the electrode radius, and p_{HF} and p_{LF} are obtained from the intercept on the EHD amplitude Bode diagrams of the low-frequency horizontal plateau and the two lines characterizing the high-frequency behaviors of the disk electrode and of the microelectrodes, respectively.

Experimental verification of the calculation was provided by Silva et al.[234] with arrays of microelectrodes prepared by photolithography. A very good agreement was found between the common microelectrode dimension measured by SEM microscopy and calculated from applications of equation (15.52). The phase-shift response of the microelectrode array in Figure 15.6 clearly shows that two time constants are resolved: one in the low-frequency range approaches the active disk response and the other at higher frequency fairly coincides with the microelectrode response. This approach was further extended to a fully active rough surface by phenomenological analogy where the dimensions of a single protrusion in the electrode plane played the same role as the characteristic dimension of a plane active

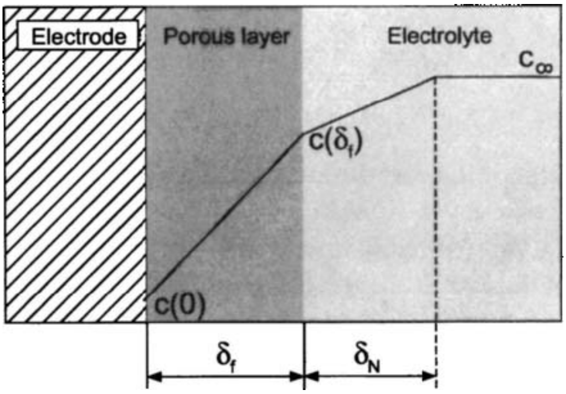

Figure 15.7: Schematic representation of an electrode covered by a porous layer: δ_f is the porous layer thickness, δ_N is the Nernst diffusion layer, c is the concentration of the electroactive species which reacts at the interface and diffuses through the porous layer and through the electrolyte.

site in the 2-D frame.[236]

15.4.2 Rotating Disk Electrode Coated by a Porous Film

Porous nonreacting layers covering reacting metallic interfaces may slow down the mass transfer of diffusing species. This decrease includes the effect of the diffusivity D_f, as well as that of the layer thickness δ_f. This problem was discussed in a more general way in Chapter 11.

A schematic representation of the system under investigation is presented in Figure 15.7. The concentration gradient is distributed between the fluid and the porous layer. In addition, the metal-layer interface is assumed to be uniformly reactive.

Two material balance equations can be written as follows:

1. In the porous layer, the concentration distribution $c^{(1)}$ is determined only by molecular diffusion following

$$\frac{\partial c^{(1)}}{\partial t} = D_f \frac{\partial^2 c^{(1)}}{\partial y^2} \tag{15.53}$$

2. In the fluid, the concentration distribution $c^{(2)}$ is governed by convective dif-

---

Remember! 15.5 *For a partially blocked electrode, all diagrams obtained at different rotation speeds merge on one diagram by using the normalized amplitude and the dimensionless frequency p. This is not observed for a coated electrode.*

fusion, i.e.,

$$\frac{\partial c^{(2)}}{\partial t} = D\frac{\partial^2 c^{(2)}}{\partial y_f^2} - v_y\frac{\partial c^{(2)}}{\partial y_f} \tag{15.54}$$

For simplicity, the origin of the coordinate y is taken to be at the metal–layer interface and that of y_f is at the layer–fluid interface ($y_f = y - \delta_f$).

Associated with equations (15.53) and (15.54) are boundary conditions that express the continuity of the concentration fields and of the fluxes for the steady state as well as for the time-dependent quantities. For $y = \delta_f$ or $y_f = 0$,

$$c^{(1)}(\delta_f) = c^{(2)}(0) \tag{15.55}$$

and

$$D_f\frac{\partial c^{(1)}}{\partial y} = D\frac{\partial c^{(2)}}{\partial y_f} \tag{15.56}$$

At $y_f = 0$,

$$v_y = 0 \tag{15.57}$$

At $y_f \to \infty$, $c^{(2)} \to c(\infty)$ (then $\bar{c}^{(2)} \to c(\infty)$ and $\tilde{c}^{(2)} \to 0$).

Steady-State Solutions

Equation (15.53) is reduced to the simple form

$$\frac{\partial^2 \bar{c}^{(1)}}{\partial y^2} = 0 \tag{15.58}$$

which leads to

$$J = D_f\frac{\bar{c}^{(1)}(\delta_f) - \bar{c}^{(1)}(0)}{\delta_f} \tag{15.59}$$

If a reaction of first order is assumed

$$J = k\bar{c}^{(1)}(0) \tag{15.60}$$

The flux in the electrolyte is given by

$$J = D\frac{c(\infty) - \bar{c}^{(2)}(0)}{\delta_N} \tag{15.61}$$

Remember! 15.6 *In contrast to Reminder 15.5, for an electrode coated by a porous film, all diagrams obtained at different rotation speeds do not collapse to one diagram by using the normalized amplitude and the dimensionless frequency p.*

By eliminating $\overline{c}^{(1)}(0)$ and $\overline{c}^{(2)}(0)$ between these last three equations, one obtains

$$J = \frac{c(\infty)}{\frac{1}{k} + \frac{\delta_N}{D} + \frac{\delta_f}{D_f}} \tag{15.62}$$

which can be written in the form

$$J^{-1} = J_k^{-1} + J_L^{-1} + J_{\Omega\to\infty}^{-1} \tag{15.63}$$

The physical meanings of the quantities appearing in this equation are: J_k is the kinetic flux equal to kc_∞, $J_L = Dc(\infty)/\delta_N$ is the limiting diffusion flux on a metallic surface, free from porous layer, and $J_{\Omega\to\infty} = D_f c(\infty)/\delta_f$ is the limiting flux when the entire concentration gradient is located within the porous layer, i.e., when $\Omega \to \infty$.

The interest of using reciprocal values is that the experimental plot of J^{-1} as a function of $\Omega^{-1/2}$ must be a straight line parallel to the line corresponding to Levich's result for the mass-transfer-limited case, which passes through the origin. The ordinate value of the intercept of this straight line at $\Omega^{-1/2} = 0$ is $J_k^{-1} + J_{\Omega\to\infty}^{-1}$. In the particular case of a very fast reaction, $J_k^{-1} \to 0$ and the value of the intercept is D_f/δ_f.

Impedances: AC and EHD

In the porous layer, the fluctuating part of equation (15.53) may be written as

$$\frac{\partial^2 \widetilde{c}^{(1)}}{\partial y^2} - \frac{j\omega}{D_f}\widetilde{c}^{(1)} = 0 \tag{15.64}$$

The solution is:

$$\widetilde{c}^{(1)} = M \exp\left[\frac{j\omega}{D_f} y^2\right]^{1/2} + N \exp - \left[\frac{j\omega}{D_f} y^2\right]^{1/2} \tag{15.65}$$

where M and N are integration constants obtained from the boundary conditions.

At the fluid–porous layer interface ($y_f = 0$), the relationship (15.37) can be applied since there is no additional process in the fluid, i.e.,

$$\left.\frac{\partial \widetilde{c}^{(2)}}{\partial y_f}\right|_{y_f=0} = \frac{\widetilde{c}^{(2)}(0)}{\delta_N}\theta'(0) + \frac{\Delta\Omega}{\overline{\Omega}} \left.\frac{d\overline{c}^{(2)}}{dy}\right|_{y_f=0} W \tag{15.66}$$

Then, from the boundary conditions at $y = \delta_f$, the constants M and N may be eliminated and the general expression is obtained:

$$\left.\frac{\partial \widetilde{c}^{(1)}(0)}{\partial y}\right|_0 = \frac{-\widetilde{c}^{(1)}}{\delta_f} \frac{(\frac{j\omega\delta_f^2}{D_f}) Z_D Z_{D,f} + \frac{D}{D_f}\frac{\delta_f}{\delta_N}}{Z_D + \frac{D}{D_f}\frac{\delta_f}{\delta_N} Z_{D,f}} + \Delta\Omega \frac{\frac{1}{\cosh(j\omega\delta_f^2/D_f)} \left.\frac{d\overline{c}^{(1)}}{dy}\right|_0 \frac{W}{\overline{\Omega}}}{1 + \frac{D}{D_f}\frac{\delta_f}{\delta_N}\frac{Z_{D,f}}{Z_D}} \tag{15.67}$$

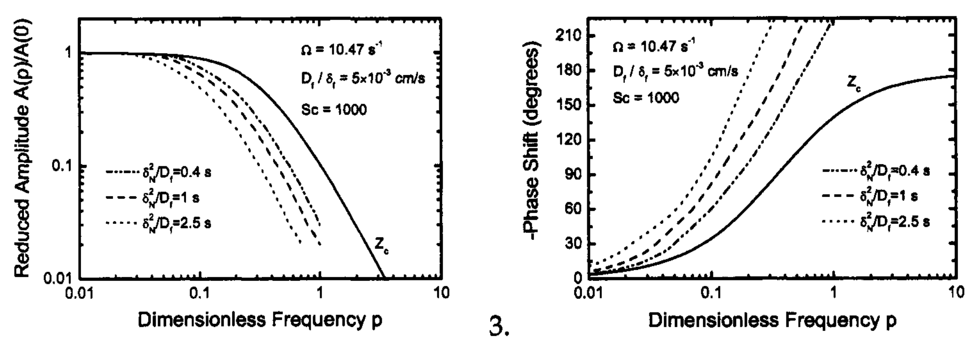

(a) (b)

Figure 15.8: Concentrostatic EHD impedance as a function of the dimensionless frequency p with rotation speed as a parameter. (Taken from Deslouis et al.[126]) The line marked Z_c represents the EHD impedance on a bare electrode: a) dimensionless modulus; and b) phase shift.

where $Z_{\mathrm{D}} = -1/\theta'(0)$ is the dimensionless convective diffusion in the solution (see equation (11.70)) and

$$Z_{\mathrm{D},f} = \frac{\tanh\sqrt{j\omega\delta_f^2/D_f}}{\sqrt{j\omega\delta_f^2/D_f}} \tag{15.68}$$

is the dimensionless diffusion impedance for a finite stagnant diffusion layer (see equation (11.70)). For $\Delta\Omega = 0$, equation (15.67) becomes similar to the result for a rotating disk presented as equation (11.72).

It may be easily verified that when the layer effect is gradually decreased (i.e., $\delta_f \rightarrow 0$ and $D_f \rightarrow D$) one finds again the relation (15.37). At the opposite extreme, when $\Omega \rightarrow \infty$, then $\delta \rightarrow 0$, the relation becomes

$$\left.\frac{\partial \tilde{c}^{(1)}}{\partial y}\right|_0 = -\frac{\tilde{c}^{(1)}(0)}{\delta_f}\frac{1}{Z_{\mathrm{D},f}} \tag{15.69}$$

In Figures 15.8(a) and (b), the amplitude and the phase shift corresponding to equation (15.67) for different angular velocities show that, in contrast with the simple behavior of a bare electrode, the data are no longer reducible by the dimensionless frequency p. In fact $\left.\frac{\partial \tilde{c}^{(1)}}{\partial y}\right|_0 / \Delta\Omega$ contains both W and $(-1/\theta'(0))$, which depend on p, for a given Schmidt number, and also a function of $j\omega\delta_f^2/D_f$. And so, an increase of Ω produces a shift of the Bode diagrams toward smaller p values, other parameters being kept constant. Frequency analysis provides both the diffusion time constant δ_f^2/D_f and the speed of diffusion D_f/δ_f. Thus, independent estimates can be obtained for δ_f and D_f.

Example 15.1 2-D and 3-D Blocking: *Apply the concepts of electrohydrodynamic impedance to scale deposit in seawater. This system shows behavior associated with both partially blocked surfaces and diffusion through porous layers.*

Solution: *Cathodic protection is widely used to protect immersed metallic structures from corrosion. When this technique is applied, in the range of* -0.8 *to* -1.2 *V (SCE), dissolved oxygen from seawater reduces onto metallic surface according to*

$$O_2 + 2H_2O + 2e^- \rightarrow H_2O_2 + 2OH^- \tag{15.70}$$

and

$$H_2O_2 + 2e^- \rightarrow 2OH^- \tag{15.71}$$

In addition, hydrogen evolution takes place following

$$H_2O + 2e^- \rightarrow H_2 + 2OH^- \tag{15.72}$$

The production of hydroxyl ions OH^- *by reactions (15.70), (15.71), and (15.72) allows precipitation of magnesium hydroxide*

$$Mg^{2+} + 2OH^- \leftrightarrows Mg(OH)_2 \downarrow \tag{15.73}$$

Moreover, these reactions lead to changes in inorganic carbonic equilibrium at the metallic interface

$$2OH^- + HCO_3^- \leftrightarrows H_2O + CO_3^{2-} \tag{15.74}$$

and allow precipitation of $CaCO_3$*, i.e.,*

$$Ca^{2+} + CO_3^{2-} \rightarrow CaCO_3 \downarrow \tag{15.75}$$

Calcareous deposition ($CaCO_3$ *and* $Mg(OH)_2$*) on the metallic surface creates a diffusional barrier toward oxygen and thus decreases the energy needed to maintain efficient protection. Knowledge of the formation time and characteristics of such layers are then essential to improve cathodic protection monitoring.*

Studies in seawater have been carried out with a gold rotating disk electrode. The EHD impedances were recorded during the calcareous deposition for different potentials and different values of mean velocity. As an example, diagrams corresponding to -1.2 *V(SCE) and 360 rpm are presented in Figure 15.9 as the logarithm of normalized modulus as a function of the logarithm of dimensionless frequency* p*. The corresponding dc current is indicated as a fraction of* I_0*, the dc current for a bare surface.*

The time constant with calcareous deposits was found to be the same as for a bare surface in the low-frequency range with a slight shift of diagrams to lower reduced frequencies when the deposition time increases. At high frequency (above $p = 1$*), a second time constant appeared. Both these features characterized the presence of a partially blocked surface with a moderate value of the active fraction of the electrode. The slight separation of the EHD diagrams observed in the low-frequency region, when the deposition time is*

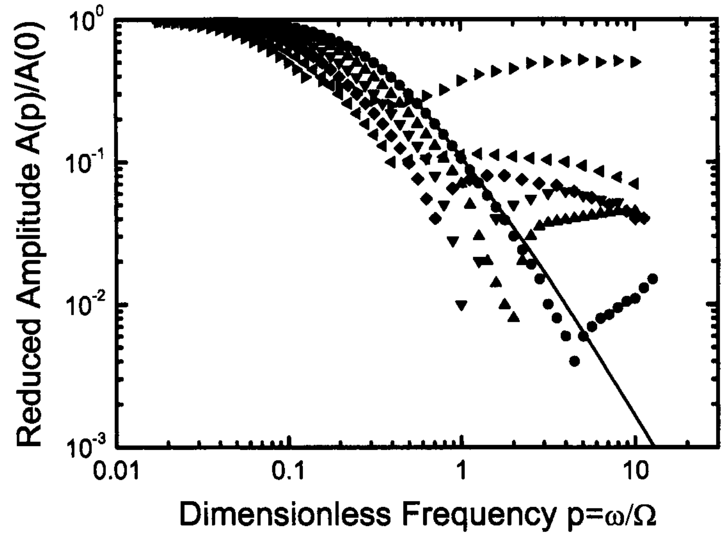

Figure 15.9: Modulus of the EHD impedance during the calcareous formation at −1.2 V(SCE) and 360 rpm. The solid line corresponds to $I = I_0$; $I/I_0 = 0.95$ (●), 0.87 (▲), 0.72 (▼), 0.55 (◆), 0.31 (◀), and 0.13 (▶). (Taken from Deslouis and Tribollet.[235])

increasing, accounted for the existence of diffusion through a porous layer. This correspond to the area covered by the $Mg(OH)_2$ *layer.*

The average crystal size d was calculated from EHD diagrams obtained for calcareous deposits formed at different applied potentials and at 360 rpm (Figure 15.10(a)) and for calcareous deposits formed at −1.2 V(SCE) and different electrode rotation speeds (Figure 15.10(b)). When analyzing these results, it seems that the applied potential does not affect the value of d. The crytal size is around 15 μm at the beginning of the scale formation and increases to around 30–40 μm for $I/I_0 \approx 0.5$. *The values obtained at the end of deposition increase to 200 μm. The influence of stirring is clearly defined (Figure 15.10(b)) and is consistent with previous work on* $CaCO_3$ *alone.*[237]

In a general way, the values of the crystal dimension d are in good agreement with the crystal size shown in SEM pictures (Figure 15.11). The crystal sizes are close to 15 μm at the beginning of deposition and stabilize at around 30 μm at the end of their formation. In the present case, the dimension d would therefore allow the determination of the size of crystals at the beginning of calcareous formation, when they are randomly distributed on the surface and do not coalesce. The growth of crystals can then be observed until approximately $I = 0.5I_0$.

For smaller I/I_0 *values, i.e., when rate of calcareous formation is larger, the d values increase very rapidly. Intuitively, one may suppose that this corresponds to overlapping of calcium carbonate crystals. The dimension d would then give the average distance between areas that remain active, and, therefore, the size of* $CaCO_3$ *aggregates. However, the corresponding theory is not yet available, and the above interpretation is speculative for the variations of d in the range* $0 < I/I_0 < 0.5$.

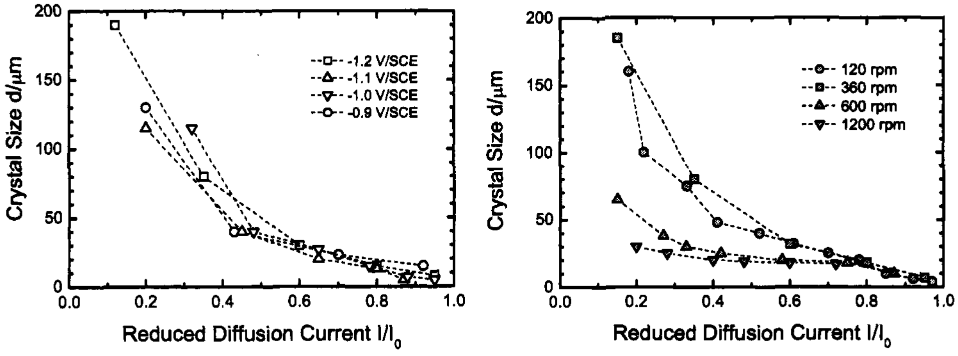

(a) (b)

Figure 15.10: Variation of average crystal size d during the calcareous formation: a) at 360 rpm and different potentials; and b) at −1.2 V(SCE) and different electrode rotation speeds. (Taken from Deslouis and Tribollet.[235])

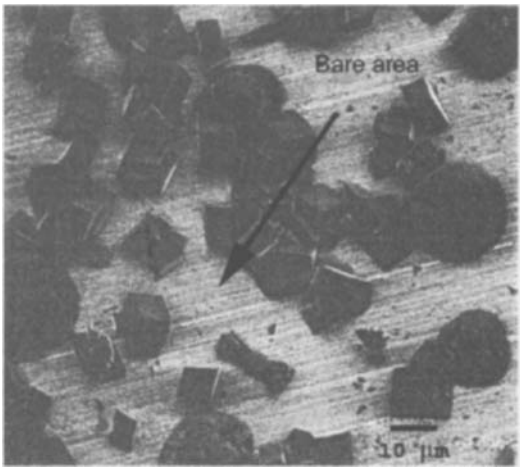

Figure 15.11: Calcareous deposit formed at −1.2 V(SCE) and 1200 rpm, $I/I_0 = 0.7$. (Taken from Deslouis and Tribollet[235] and reproduced with permission of Elsevier, Inc.)

Electrohydrodynamic impedance characterization of calcareous deposits showed mainly partially blocked electrode behavior and allowed the estimation of the average size of characteristic sites of the interface. These results have been confirmed by ex-situ *SEM images.*

Problems

15.1 From equation (15.37), deduce the expressions (14.21) and (14.22).

15.2 Derive the EHD impedance for the anodic dissolution of copper in a chloride medium where the reactions proceed according to

$$\mathrm{Cu} + \mathrm{Cl}^- \rightleftarrows \mathrm{CuCl}_{\mathrm{ads}} + \mathrm{e}^- \tag{15.76}$$

where $\mathrm{CuCl}_{\mathrm{ads}}$ is an adsorbed intermediate that reacts to form CuCl_2^- by

$$\mathrm{CuCl}_{\mathrm{ads}} + \mathrm{Cl}^- \rightleftarrows \mathrm{CuCl}_2^- \tag{15.77}$$

The mass-transfer limitation is due only to CuCl_2^-.

Electrochemical Impedance Spectroscopy
by Mark E. Orazem and Bernard Tribollet

Part IV

Interpretation Strategies

Electrochemical Impedance Spectroscopy
by Mark E. Orazem and Bernard Tribollet

Chapter 16

Methods for Representing Impedance

Impedance data are presented in different formats to emphasize specific classes of behavior. The impedance format emphasizes the values at low frequency, which typically are of greatest importance for electrochemical systems that are influenced by mass transfer and reaction kinetics. The admittance format, which emphasizes the capacitive behavior at high frequencies, is often employed for solid-state systems. The complex capacity format is used for dielectric systems in which the capacity is often the feature of greatest interest.

The method of representing impedance data has great impact on the use of graphical methods to visualize and interpret data. The material presented in this chapter supports the subsequent chapters on graphical methods. In Chapter 17, graphical methods are presented that require no specific model of the system under investigation. In Chapter 18, graphical methods are presented that have a basis in a deterministic model for a given process.

The methods for representing impedance data are illustrated here for the two simple *RC* electrical circuits shown in Table 16.1. A review of Chapters 1 and 4 may be useful. The summary of relationships among complex impedance, real and imaginary parts of the impedance, and the phase angle and magnitude found in Tables 1.1, 1.2, and 1.3 may also be useful.

Remember! 16.1 *The impedance representation emphasizes values at low frequency and is often used for electrochemical systems for which information is sought regarding mass transfer and reaction kinetics.*

Table 16.1: Summary of complex impedance, admittance, and capacitance characteristics for simple blocking and reactive circuits.

	(a)	(b)
Circuit	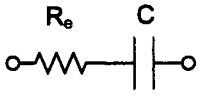 	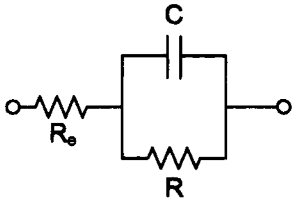
Classification	blocking	reactive
Complex impedance		
Z_r	R_e	$R_e + \frac{R}{1+(\omega RC)^2}$
Z_j	$-\frac{1}{\omega C}$	$-\frac{\omega CR^2}{1+(\omega RC)^2}$
Time constant	none	RC
Complex admittance		
Y_r	$\frac{R_e(\omega C)^2}{1+(\omega ReC)^2}$	$\frac{R_eR(\omega C)^2+1+\frac{R_e}{R}}{R\left[\left(1+\frac{R_e}{R}\right)^2+(\omega R_eC)^2\right]}$
Y_j	$\frac{\omega C}{1+(\omega ReC)^2}$	$\frac{\omega C}{\left(1+\frac{R_e}{R}\right)^2+(\omega R_eC)^2}$
Time constant	R_eC	$R_eC\left(1+2\frac{R_e}{R}+\left(\frac{R_e}{R}\right)^2\right)^{-1/2}$
Complex capacitance		
C_r	$\frac{C}{1+(\omega ReC)^2}$	$\frac{C}{\left(1+\frac{R_e}{R}\right)^2+(\omega R_eC)^2}$
C_j	$-\frac{R_e\omega(C)^2}{1+(\omega ReC)^2}$	$-\frac{R_eR(\omega C)^2+1+\frac{R_e}{R}}{R\omega\left[\left(1+\frac{R_e}{R}\right)^2+(\omega R_eC)^2\right]}$
Time constant	R_eC	$R_eC\left(1+2\frac{R_e}{R}+\left(\frac{R_e}{R}\right)^2\right)^{-1/2}$
Capacitance		
$C=-\frac{1}{\omega Z_j}$	C	$C+\frac{1}{\omega^2R^2C}$
Time constant	none	RC

16.1 Impedance Format

The impedance can be expressed as the complex ratio of potential and current contributions, i.e.,

$$Z = \frac{\widetilde{U}}{\widetilde{I}} \tag{16.1}$$

As discussed in Section 4.1.2, the impedance for a series arrangement of passive elements is additive. The impedance for the parallel arrangement of impedances Z_1 and Z_2 is given by equation (4.24).

For a resistor R_e and capacitor C in series, shown in Table 16.1(a), the impedance is given by

$$Z = R_e - j\frac{1}{\omega C} \tag{16.2}$$

The real part of the impedance is independent of frequency, and the imaginary part of the impedance tends to $-\infty$ as frequency tends toward zero according to $1/\omega$. In fact,

$$-\omega Z_j = \frac{1}{C} \tag{16.3}$$

for all frequencies ω.

The system comprising the resistor R_e and capacitor C in series provides an example of a class of systems for which, at the zero-frequency or dc limit, current cannot pass. Such systems are considered to have a blocking or ideally polarizable electrode. Depending on the specific conditions, batteries, liquid mercury electrodes, semiconductor devices, passive electrodes, and electroactive polymers provide examples of systems that exhibit such blocking behavior.

For a resistor R_e in series with the parallel combination of R and capacitor C, shown in Table 16.1(b), the impedance is given by

$$Z = R_e + \frac{R}{1 + j\omega RC} \tag{16.4}$$

or

$$Z = R_e + \frac{R}{1 + (\omega RC)^2} - j\frac{\omega CR^2}{1 + (\omega RC)^2} \tag{16.5}$$

The real part of the impedance tends toward $R_e + R$ as frequency tends toward zero. The imaginary part of the impedance tends toward zero as frequency tends toward zero such that

$$-\lim_{\omega \to 0} \frac{Z_j}{\omega} = CR^2 \tag{16.6}$$

A characteristic angular frequency $\omega_{RC} = 1/(RC)$ can be identified for which the imaginary part of the impedance has a maximum value

$$-Z_j(\omega_{RC}) = \frac{R}{2} \tag{16.7}$$

The real part of the impedance tends toward R_e as frequency tends toward ∞, and the imaginary part of the impedance tends toward zero such that

$$-\lim_{\omega\to\infty} \omega Z_j = \frac{1}{C} \tag{16.8}$$

The high-frequency limit for the imaginary part of the impedance given in equation (16.8) is identical to that given for the series arrangement as equation (16.3) for all frequencies.

The reactive system shown in Table 16.1(b) may be considered to be an example of a class of systems for which, at the zero-frequency or dc limit, the resistance to passage of current is finite, and current can pass. Many electrochemical and electronic systems exhibit such nonblocking or reactive behavior. Even though the impedance response of the systems represented in this chapter is extremely simple as compared to that of typical electrochemical and electronic systems, the blocking and nonblocking systems comprise a broad cross-section of electrochemical and electronic systems. The concepts described can therefore be easily adapted to experimental data.

The resistor R and capacitor C shown in Table 16.1 can take on different meanings for different electrochemical systems. The resistance may, for example, be associated with the charge-transfer resistance of an electrochemical reaction, with the resistance of an oxide or porous layer, or with the electronic resistance of a semiconductor. The capacitor C may be associated with the double layer for an electrode in electrolyte, with surface capacitance of a film, or with the space-charge region of a semiconductor. The resistor R_e may be associated with the Ohmic resistance of the electrolyte or with the frequency-independent resistance of a solid.

16.1.1 Complex-Impedance-Plane Representation

Impedance data are often represented in complex-impedance-plane or Nyquist format, as shown in Figure 16.1. The data are presented as a locus of points, where each data point corresponds to a different measurement frequency. One disadvantage of the complex-impedance-plane format is that the frequency dependence is obscured. This disadvantage can be mitigated somewhat by labeling some characteristic frequencies. In fact, characteristic frequencies should always be labeled to allow a better understanding of the time constants of the underlying phenomena.

The asymptotic limits of the real part of the impedance for the reactive circuit of Table 16.1(b) are R_e at high frequencies and $R_e + R$ at low frequencies. These limits are indicated in the complex-impedance-plane plot, and the characteristic

---

Remember! 16.2 *Complex-impedance-plane plots should have orthonormal axes, and characteristic frequencies should be labeled.*

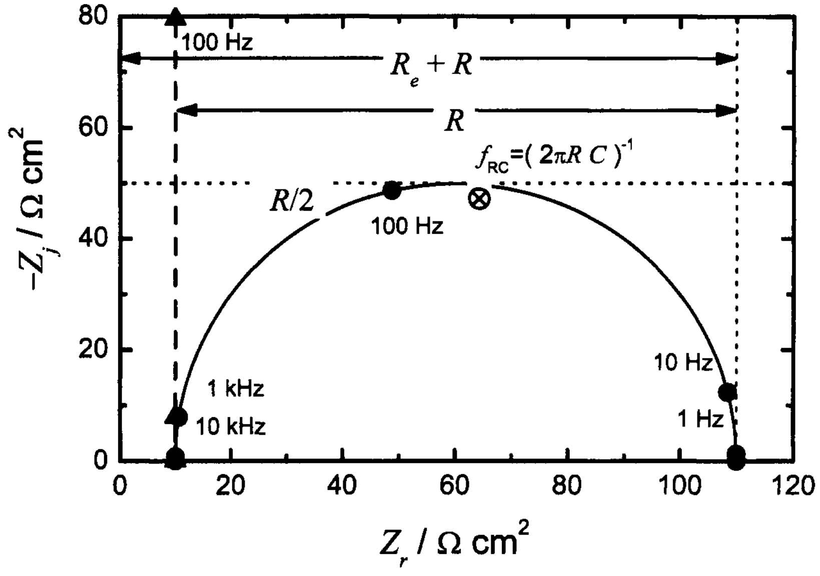

Figure 16.1: Impedance-plane or Nyquist representation of impedance data for $R_e = 10\ \Omega\text{cm}^2$, $R = 100\ \Omega\text{cm}^2$, and $C = 20\ \mu\text{F/cm}^2$. The blocking system of Table 16.1(a) is represented by △ and dashed lines, and the reactive system of Table 16.1(b) is represented by ○ and solid lines.

frequency for the system is shown at the peak where the negative imaginary impedance reaches a maximum value. For the system chosen here, $f_{RC} = 79.6$ Hz. The maximum value of the imaginary part of the impedance is equal to $R/2$ for a single RC circuit.

The real part of the impedance for the blocking circuit shown in Table 16.1(a) is equal to R_e for all frequencies. The tendency of the imaginary part to approach $-\infty$ as frequency tends toward zero appears as a vertical line in the complex-impedance-plane plot.

Complex-impedance-plane plots are very popular because the shape of the locus of points yields insight into possible mechanisms or governing phenomena. If the locus of points traces a perfect semicircle, for example, the impedance response corresponds to a single activation-energy-controlled process. A depressed semicircle indicates that a more detailed model is required, and multiple peaks provide clear indication that more than one time constant is required to describe the process. The significant disadvantages are that the frequency dependence is obscured, that low impedance values are obscured, and that apparent agreement between model and experimental data in impedance-plane format may obscure large differences in frequency and at low impedance values.

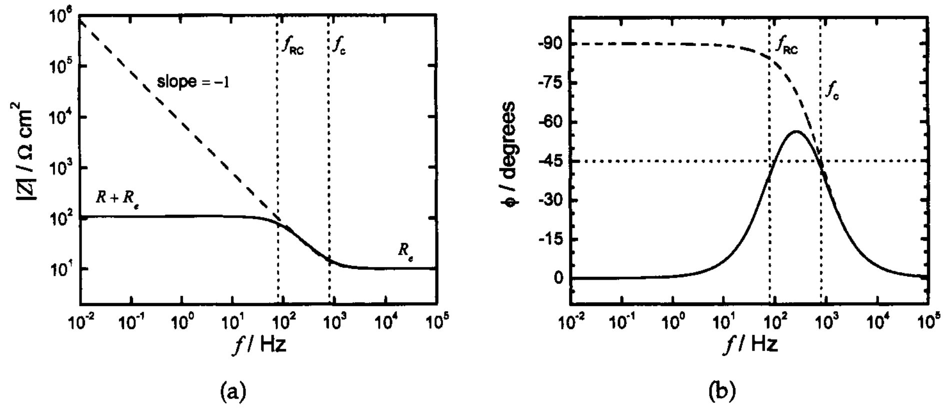

Figure 16.2: Bode representation of impedance data for $R_e = 10\ \Omega\text{cm}^2$, $R = 100\ \Omega\text{cm}^2$, and $C = 20\ \mu\text{F/cm}^2$. The blocking system of Table 16.1(a) is represented by dashed lines, and the reactive system of Table 16.1(b) is represented by solid lines. Characteristic frequencies are noted as $f_{RC} = (2\pi RC)^{-1}$ and $f_c = (2\pi R_e C)^{-1}$; a) magnitude and b) phase angle.

16.1.2 Bode Representation

The functionality with respect to frequency is seen more clearly in the Bode representation shown in Figures 16.2(a) and (b) for the magnitude and phase angle, respectively. Frequency is generally presented on a logarithmic scale to reveal the important behavior seen at lower frequencies. Note that, following customary practice, the frequency f given in Figure 16.2 has units of Hz (cycles/s); whereas the angular frequency ω used in the mathematical development has units of s^{-1} (radians/s). The conversion is given by $\omega = 2\pi f$.

The magnitude of the impedance of the blocking circuit of Table 16.1a can be expressed as

$$|Z| = \sqrt{R_e^2 + \left(\frac{1}{\omega C}\right)^2} \tag{16.9}$$

The magnitude tends toward R_e as frequency tends toward ∞ and toward ∞ as $1/\omega$ as frequency tends toward zero. The magnitude is usually presented on a logarithmic scale as a function of frequency on a logarithmic scale, as shown in Figure 16.2(a). The slope of the line at low frequencies, therefore, has a value of −1 for the blocking electrode considered here. A value with magnitude smaller than unity could provide an indication of a blocking electrode with a distribution of characteristic time constants. Such systems are described in Chapter 17.

The magnitude of the impedance of the reactive system of Table 16.1b can be expressed as

$$|Z| = \sqrt{\left[R_e + \frac{R}{1+(\omega RC)^2}\right]^2 + \left(\frac{\omega CR^2}{1+(\omega RC)^2}\right)^2} \tag{16.10}$$

The magnitude tends toward R_e as frequency tends toward ∞ and toward $R_e + R$ as frequency tends toward zero. The transition between low frequency and high frequency asymptotes has a slope of -1 on a log-log scale.

Following equation (4.32), the phase angle for the blocking configuration can be expressed as

$$\phi = \tan^{-1}\left(\frac{1}{\omega R_e C}\right) \tag{16.11}$$

The phase angle tends toward −90°s at low frequencies and toward zero at high frequencies. The phase angle at the characteristic angular frequency $\omega_c = (R_e C)^{-1}$ is equal to −45° (see equation (16.11)).

The phase angle for the reactive configuration can be expressed as

$$\phi = \tan^{-1}\left(\frac{\omega R^2 C}{R + R_e\left(1 + (\omega RC)^2\right)}\right) \tag{16.12}$$

The phase angle tends toward zero at low frequencies, indicating that the current and potential are in phase. The phase angle tends toward zero at high frequencies as well, due to the influence of the leading resistor R_e in equation (16.12). Note that, while the characteristic angular frequency for this circuit is $\omega_{RC} = (RC)^{-1}$, the phase angle at the characteristic angular frequency ω_{RC} is given by

$$\phi = \tan^{-1}\left(\frac{1}{1 + 2R_e/R}\right) \tag{16.13}$$

which is equal to 45° only if $R_e/R = 0$. The characteristic angular frequency for which the phase angle is equal to 45° can be expressed as

$$\omega_c = \frac{1}{2R_e C}\left(1 \pm \sqrt{1 - 4\frac{R_e}{R}\left(1 + \frac{R_e}{R}\right)}\right) \tag{16.14}$$

but this expression is valid only if

$$\frac{R_e}{R} \leq \frac{\sqrt{2} - 1}{2} \tag{16.15}$$

For the case presented here, the phase angle reaches 45° at frequencies of 100 and 696 Hz, values that have no direct correspondence to the characteristic frequency based on R of $f_{RC} = 79.6$ Hz or based on R_e of $f_c = 796$ Hz. The peak in the phase angle is seen at a characteristic frequency

$$f_c = \frac{1}{4\pi RC}\sqrt{1 + \frac{R}{R_e}} \tag{16.16}$$

which has a value of 264 Hz.

The popularity of the Bode representation stems from its utility in circuits analysis. The phase angle plots are sensitive to system parameters and, therefore, provide a good means of comparing model to experiment. The modulus is much less sensitive to system parameters, but the asymptotic values at low and high frequencies provide values for the dc and electrolyte resistance, respectively.

For electrochemical systems, however, the Bode representation has drawbacks. The influence of electrolyte resistance confounds the use of phase angle plots such as shown in Figure 16.2(b) to estimate characteristic frequencies. In addition, Figure 16.2(b) shows that the current and potential are in phase at high frequencies; whereas, at high frequencies, the current and surface potential are exactly out of phase. This result is seen because, at high frequencies, the impedance of the surface tends toward zero, and the Ohmic resistance dominates the impedance response. The electrolyte resistance, then, obscures the behavior of the electrode surface in the phase angle plots.

16.1.3 Electrolyte-Resistance-Corrected Bode Representation

If an accurate estimate for electrolyte resistance $R_{e,\text{est}}$ is available, a modified Bode representation is possible as

$$|Z|_{\text{adj}} = \sqrt{(R_e - R_{e,\text{est}})^2 + \left(\frac{1}{\omega C}\right)^2} \tag{16.17}$$

and

$$\phi_{\text{adj}} = \tan^{-1}\left(\frac{1}{(R_e - R_{e,\text{est}})\,\omega C}\right) \tag{16.18}$$

for the blocking configuration, and

$$|Z|_{\text{adj}} = \sqrt{\left[(R_e - R_{e,\text{est}}) + \frac{R}{1+(\omega RC)^2}\right]^2 + \left(\frac{\omega C R^2}{1+(\omega RC)^2}\right)^2} \tag{16.19}$$

and

$$\phi_{\text{adj}} = \tan^{-1}\left(\frac{\omega R^2 C}{R + (R_e - R_{e,\text{est}})\left(1+(\omega RC)^2\right)}\right) \tag{16.20}$$

for the reactive configuration. The results are presented in Figures 16.3(a) and (b) for magnitude and phase angle, respectively. The current and potential for the blocking electrode are shown correctly in Figure 16.3(b) to be out of phase at all frequencies. The current and potential for the reactive configuration is shown to be in phase at low frequencies and out of phase at high frequencies, and the phase angle has a value of −45° at the characteristic angular frequency ω_{RC}. This approach is applied for more complicated systems in Sections 17.1.2, 17.2.1, and Example 17.1.

Caution should be used when interpreting the electrolyte-resistance-corrected Bode plots. As seen in equation (16.20), nonzero values for $(R_e - R_{e,\text{est}})$ can give the appearance of an additional high-frequency relaxation process. When possible, an assessment of $R_{e,\text{est}}$ should be made independently of the regression.

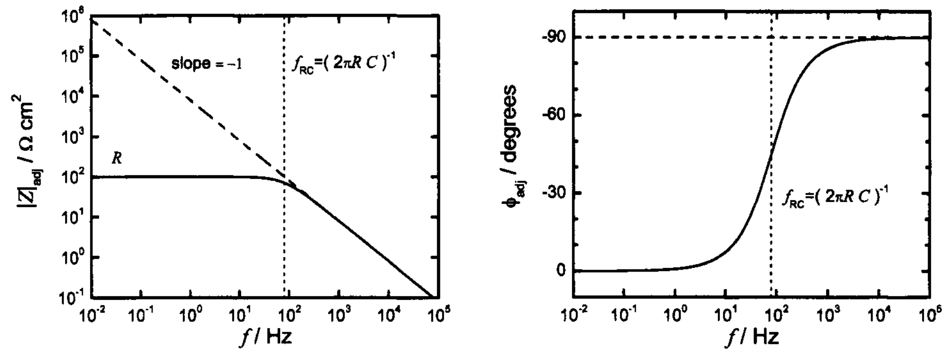

(a) (b)

Figure 16.3: Electrolyte-resistance-corrected Bode representation of impedance data for $R_e = 10\ \Omega\mathrm{cm}^2$, $R = 100\ \Omega\mathrm{cm}^2$, and $C = 20\ \mu\mathrm{F/cm}^2$. The blocking system of Table 16.1(a) is represented by dashed lines, and the reactive system of Table 16.1(b) is represented by solid lines. The characteristic frequency is given as $f_{RC} = (2\pi RC)^{-1}$;) a) magnitude and b) phase angle.

16.1.4 Impedance Representation

Plots of the real and imaginary components of the impedance as functions of frequency are presented in Figures 16.4(a) and (b), respectively. The impedance representation has the significant advantage that the characteristic frequencies can be readily identified. Following equation (16.5), the real part of the impedance of the reactive configuration has a value of $R_e + R/2$ at ω_{RC}. The magnitude of the imaginary part has a maximum value at ω_{RC}, and this value is equal to $R/2$. The imaginary part of the impedance for the blocking circuit shows no characteristic time constant in this representation, and the real part of the impedance is independent of frequency.

The behavior at lower impedance values is emphasized when the impedance components are plotted on a logarithmic scale, as shown in Figures 16.5(a) and (b) for real and imaginary parts of the impedance, respectively. Figure 16.5(b) in particular provides a rich source of insight into the experimental system. As in Figure 16.4(b), the maximum value is seen at the characteristic frequency. The slopes at low and high frequency are +1 and −1, respectively, for the simple reactive system presented in Table 16.1(b). Departure from ±1 provides an indication of distributed processes. Observation of multiple maxima shows that the data must be interpreted in terms of more than one process. Interpretation of Figures 16.4(b) and 16.5(b) in terms of characteristic frequencies is not confounded by the electrolyte resistance, as was seen for the Bode plots of phase angle.

As discussed in Chapter 21, the variances of stochastic errors are equal for real and imaginary parts of the impedance. Thus, another advantage of presenting real and imaginary parts of the impedance as a function of frequency is that comparison between data and levels of stochastic noise can be easily represented.

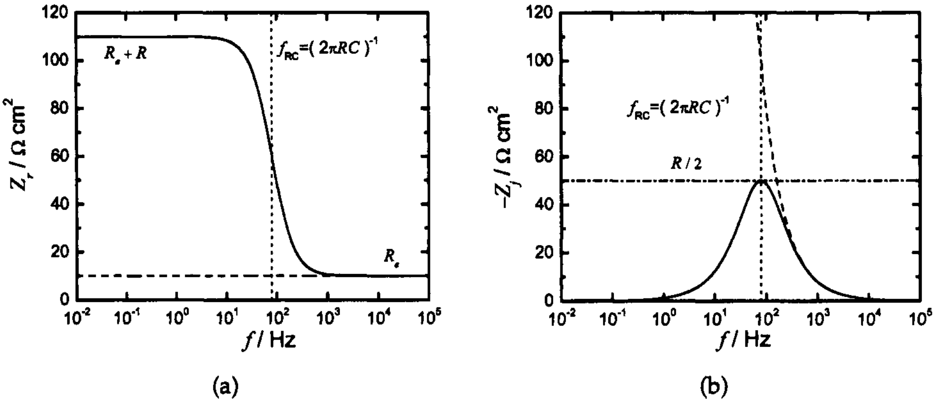

Figure 16.4: Real and imaginary parts of the impedance as a function of frequency for $R_e = 10\ \Omega\text{cm}^2$, $R = 100\ \Omega\text{cm}^2$, and $C = 20\ \mu\text{F/cm}^2$. The blocking system of Table 16.1(a) is represented by dashed lines, and the reactive system of Table 16.1(b) is represented by solid lines. The characteristic frequency is given as $f_{RC} = (2\pi RC)^{-1}$; a) real part of impedance and b) imaginary part of impedance.

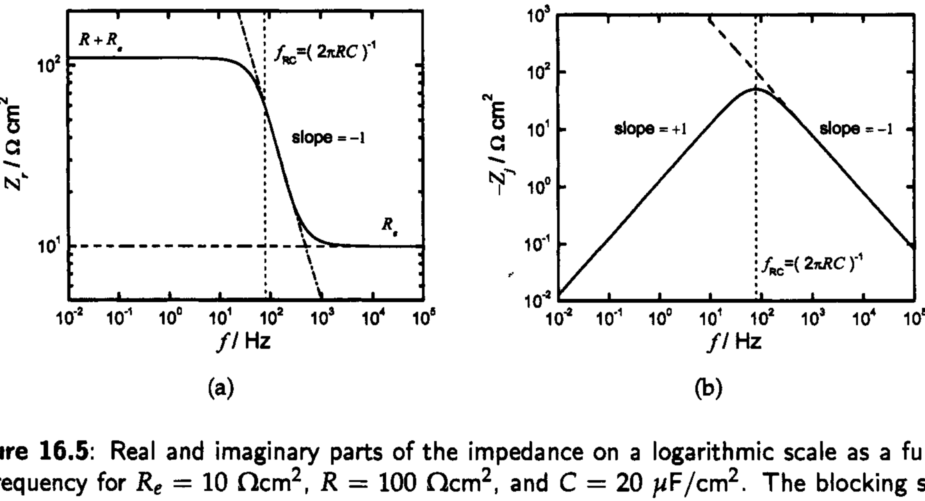

Figure 16.5: Real and imaginary parts of the impedance on a logarithmic scale as a function of frequency for $R_e = 10\ \Omega\text{cm}^2$, $R = 100\ \Omega\text{cm}^2$, and $C = 20\ \mu\text{F/cm}^2$. The blocking system of Table 16.1(a) is represented by dashed lines, and the reactive system of Table 16.1(b) is represented by solid lines. The characteristic frequency is given as $f_{RC} = (2\pi RC)^{-1}$; a) real part of impedance and b) imaginary part of impedance.

16.2 Admittance Format

The admittance can be expressed as the complex ratio of current and potential contributions, i.e.,

$$Y = \frac{1}{Z} = \frac{\tilde{I}}{\tilde{U}} \tag{16.21}$$

As discussed in Section 4.1.2, the admittance for a parallel arrangement of passive elements is additive.

Following equation (1.24), the admittance can be expressed in terms of real and imaginary components of the impedance as

$$Y = \frac{1}{Z} = \frac{Z_r}{Z_r^2 + Z_j^2} - j\frac{Z_j}{Z_r^2 + Z_j^2} \tag{16.22}$$

For the blocking system shown in Table 16.1(a), the impedance follows equation (4.26), and

$$Y = \frac{R_e\left(\omega C\right)^2}{1 + \left(\omega ReC\right)^2} + j\frac{\omega C}{1 + \left(\omega ReC\right)^2} \tag{16.23}$$

As angular frequency ω tends toward zero, the real admittance tends toward zero according to ω^2 such that

$$\lim_{\omega \to 0} \frac{Y_r}{\omega^2} = R_e C^2 \tag{16.24}$$

The imaginary admittance tends toward zero according to ω such that

$$\lim_{\omega \to 0} \frac{Y_j}{\omega} = C \tag{16.25}$$

As angular frequency ω tends toward ∞, the real admittance tends toward $1/R_e$, and the imaginary admittance tends toward zero according to $1/\omega$ such that

$$\lim_{\omega \to \infty} \omega Y_j = \frac{1}{R_e^2 C} \tag{16.26}$$

The maximum value for the imaginary part of the admittance is found at a characteristic angular frequency $\omega_c = (R_e C)^{-1}$ to be $Y_j(\omega_c) = (2R_e)^{-1}$.

Remember! 16.3 *The admittance representation emphasizes values at high frequency and is often used for solid-state systems for which information is sought regarding system capacitance. The admittance format has the advantage that it has a finite value for all frequencies, even for blocking electrodes.*

The corresponding development for the reactive system shown in Table 16.1(b) is somewhat more complicated. The admittance can be expressed as

$$Y = \frac{R_eR\,(\omega C)^2 + 1 + \frac{R_e}{R}}{R\left[\left(1+\frac{R_e}{R}\right)^2 + (\omega R_e C)^2\right]} + j\frac{\omega C}{\left(1+\frac{R_e}{R}\right)^2 + (\omega R_e C)^2} \tag{16.27}$$

As angular frequency ω tends toward zero, the real part of the admittance tends toward $1/(R_e + R)$, and the imaginary part of the admittance tends toward zero according to ω such that

$$\lim_{\omega\to 0}\frac{Y_j}{\omega} = \frac{R^2C}{(R_e + R)^2} \tag{16.28}$$

As angular frequency ω tends toward ∞, the real admittance tends toward $1/R_e$, and the imaginary admittance tends toward zero according to $1/\omega$ such that

$$\lim_{\omega\to\infty}\omega Y_j = \frac{1}{R_e^2C} \tag{16.29}$$

The high-frequency limit is the same as is found for the series combination of the resistance R_e and capacitance C shown as equation (16.26). The parallel resistance R does, however, influence the value obtained for the imaginary part of the admittance at the characteristic angular frequency $\omega_c = (R_eC)^{-1}$, i.e.,

$$Y_j(\omega_c) = \frac{1}{2R_e\left[1 + \frac{R_e}{R} + \frac{1}{2}\left(\frac{R_e}{R}\right)^2\right]} \tag{16.30}$$

In addition, the value of the characteristic angular frequency is shifted slightly to larger values, i.e.,

$$\omega_c = \frac{1}{R_eC}\sqrt{1 + 2\frac{R_e}{R} + \frac{R_e^2}{R^2}} \tag{16.31}$$

The maximum value for the imaginary admittance is given by

$$Y_j(\omega_c) = \frac{R}{2R_e(R + R_e)} \tag{16.32}$$

Thus, in the admittance plane, the locus of points for both the blocking and the single RC reactive system describes a semicircle.

16.2.1 Admittance-Plane Representation

Admittance-plane plots are presented in Figure 16.6 for the series and parallel circuit arrangements shown in Figure 4.3(a). The data are presented as a locus of points, where each data point corresponds to a different measurement frequency. As discussed for the impedance-plane representation (Figure 16.1), the admittance-plane format obscures the frequency dependence. This disadvantage can be mitigated somewhat by labeling some characteristic frequencies.

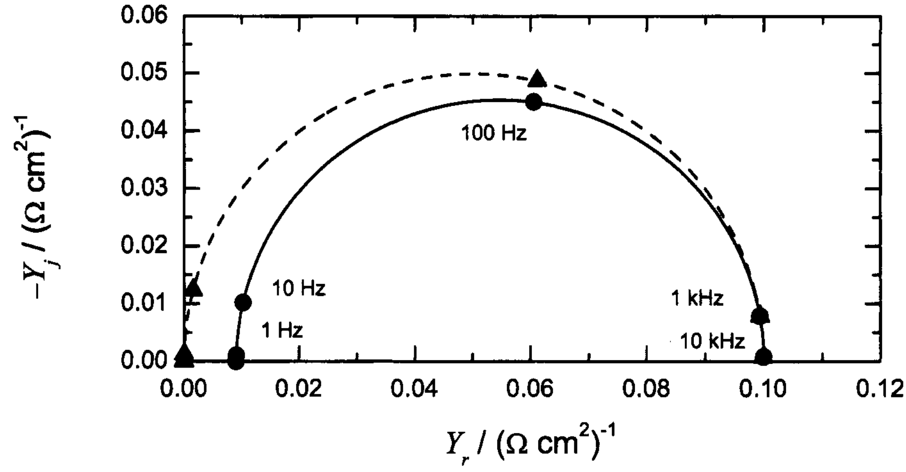

Figure 16.6: Admittance-plane representation for R_e = 10 Ωcm^2, R = 100 Ωcm^2, and C = 20 μF/cm^2. The blocking system of Table 16.1(a) is represented by △ and dashed lines, and the reactive system of Table 16.1(b) is represented by ○ and solid lines.

The high-frequency asymptote for the real part of the admittance is equal to $1/R_e$ for both blocking and reactive systems. The zero-frequency asymptote for the real part of the admittance is equal to zero for the blocking system and to $1/(R_e + R)$ for the reactive system. It is interesting to note that both the blocking and the reactive systems show a finite value at low frequencies. In contrast, the imaginary part of the impedance for the blocking circuit tends toward $-\infty$ as frequency tends toward zero in the impedance-plane plot shown in Figure 16.1. The presence of blocking behavior is revealed in Figure 16.6 by a high-frequency asymptote equal to zero for both real and imaginary parts of the impedance.

The maximum value for the imaginary part of the admittance is equal to $1/2R_e$ for the blocking system, and the characteristic angular frequency at the maximum is equal to $\omega_c = 1/R_eC$.

16.2.2 Admittance Representation

The real and imaginary parts of the admittance are presented as functions of frequency in Figures 16.7(a) and (b), respectively. The low- and high-frequency limits can be interpreted in terms of the relationship between impedance and admittance for the respective circuit. The corresponding plots in logarithmic format are presented as Figures 16.8(a) and (b), respectively. Presentation of admittance on linear or logarithmic scales as functions of frequency shows the dependence on frequency, and as compared to impedance, has the advantage that the imaginary part of the admittance for a blocking circuit has a finite value at low frequencies. On a logarithmic scale, deviations from the expected slopes of ±1 in Figure 16.8(b) or +2 for the blocking circuit in Figure 16.8(a) provide indications of processes

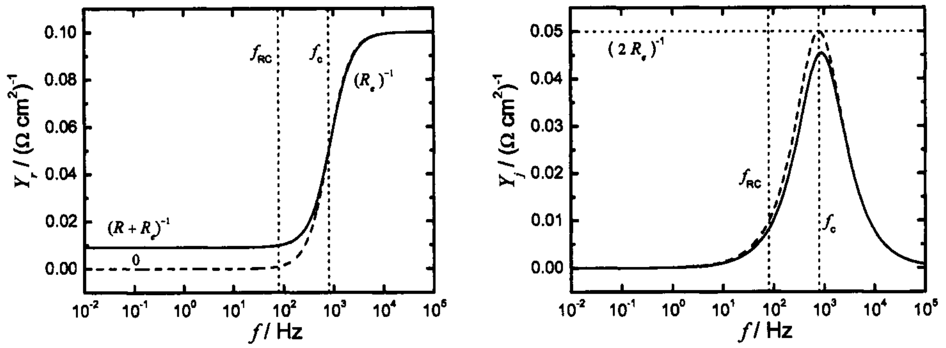

(a) (b)

Figure 16.7: Real and imaginary parts of the admittance as a function of frequency for $R_e = 10\ \Omega\text{cm}^2$, $R = 100\ \Omega\text{cm}^2$, and $C = 20\ \mu\text{F/cm}^2$. The blocking system of Table 16.1(a) is represented by dashed lines, and the reactive system of Table 16.1(b) is represented by solid lines. Characteristic frequencies are noted as $f_{RC} = (2\pi RC)^{-1}$ and $f_c = (2\pi R_e C)^{-1}$; a) real part of admittance and b) imaginary part of admittance.

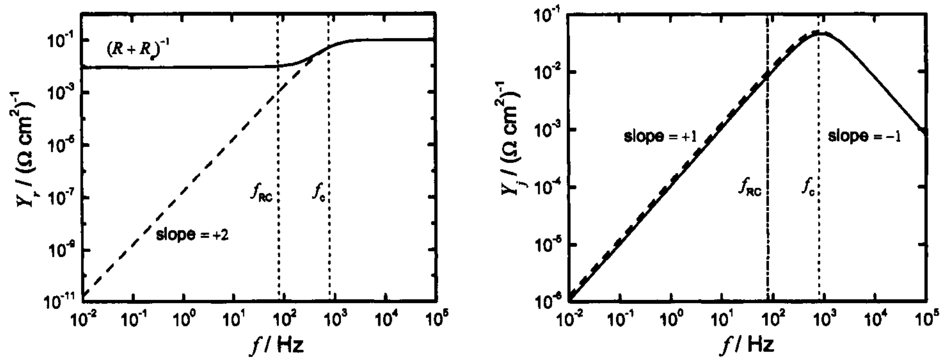

(a) (b)

Figure 16.8: Real and imaginary parts of the admittance on a logarithmic scale as a function of frequency for $R_e = 10\ \Omega\text{cm}^2$, $R = 100\ \Omega\text{cm}^2$, and $C = 20\ \mu\text{F/cm}^2$. The blocking system of Table 16.1(a) is represented by dashed lines, and the reactive system of Table 16.1(b) is represented by solid lines. Characteristic frequencies are noted as $f_{RC} = (2\pi RC)^{-1}$ and $f_c = (2\pi R_e C)^{-1}$; a) real part of admittance and b) imaginary part of admittance.

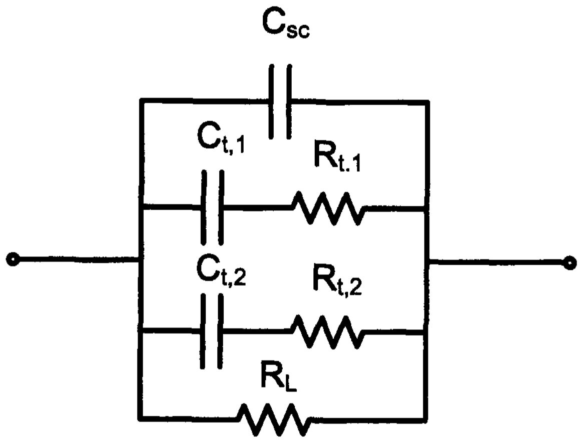

Figure 16.9: Electrical circuit analogue developed to account for the influence of two Shockley-Read-Hall electronic transitions through deep-level states. See the discussion of Figure 12.8.

characterized by distributed or multiple time constants.

The characteristic frequency evident as a peak for the imaginary part of the admittance in Figures 16.7(b) and 16.8(b) has a value corresponding exactly to $f_c = (2\pi R_e C)^{-1}$ for the blocking system. As shown by equation (16.31), the presence of a Faradaic process confounds use of graphical techniques to assess this characteristic frequency.

The admittance format is not particularly well suited for analysis of electrochemical and other systems for which identification of Faradaic processes parallel to the capacitance represents the aim of the impedance experiments. When plotted in impedance format, the characteristic time constant is that corresponding to the Faradaic reaction. When plotted in admittance format, the characteristic time constant is that corresponding to the electrolyte resistance, and that is obtained only approximately when Faradaic reactions are present.

As shown in Example 16.1, the admittance format is ideally suited for analysis of dielectric systems for which the leading resistance can be neglected entirely.

Example 16.1 Admittance of Dielectrics: *Find an expression for the admittance of the electrical circuit shown in Figure 16.9. Identify the characteristic frequencies.*

Solution: *The circuit corresponds to the dielectric response of a semiconductor device. The term C_{sc} represents the space-charge capacitance, and the terms $R_{t,1}$, $C_{t,1}$, $R_{t,2}$, and $C_{t,2}$ account for the potential-dependent occupancy of deep-level electronic states, which typically have a small concentration. The term R_L accounts for the leakage current, which would be equal to zero for an ideal dielectric.*

The admittance can be expressed as

$$\begin{aligned} Y(\omega) = \quad & \tfrac{1}{R_L} + \frac{\omega^2 R_{t,1} C_{t,1}^2}{1+(\omega R_{t,1} C_{t,1})^2} + \frac{\omega^2 R_{t,2} C_{t,2}^2}{1+(\omega R_{t,2} C_{t,2})^2} \\ & + j\omega \left[C_{sc} + \frac{\omega R_{t,1} C_{t,1}^2}{1+(\omega R_{t,1} C_{t,1})^2} + \frac{\omega R_{t,2} C_{t,2}^2}{1+(\omega R_{t,2} C_{t,2})^2} \right] \end{aligned} \tag{16.33}$$

As $\omega \to 0$, $Y_r \to 1/R_L$ and $Y_j \to \infty$. As $\omega \to \infty$, $Y_r \to 1/R_L + 1/R_{t,1} + 1/R_{t,2}$ and $Y_j \to 0$. The characteristic angular frequencies are $\omega_{t1} = (R_{t,1}C_{t,1})^{-1}$ and $\omega_{t2} = (R_{t,2}C_{t,2})^{-1}$. The characteristic angular frequencies could be easily identified from plots of real and imaginary parts of the admittance as functions of frequency.

The complex capacitance representation for this type of system is particularly interesting. See the discussion in Section 16.3 and Example 16.2.

16.2.3 Electrolyte-Resistance-Corrected Representation

If the electrolyte resistance R_e is removed from the expression for the admittance, the admittance is simplified to

$$Y = 0 + j\omega C \tag{16.34}$$

for the series configuration resulting in only C and

$$Y = \frac{1}{R} + j\omega C \tag{16.35}$$

for the parallel (reactive) configuration of R and C. The resulting real and imaginary parts of admittance are presented in Figures 16.10(a) and (b), respectively. The imaginary components of admittance for the series and parallel configurations, equations (16.34) and (16.35) respectively, are identical and can be used to recover the capacitance at any given frequency. The use of the admittance format to obtain the capacitance for dielectric systems motivates the development of analysis in terms of complex capacitance, as presented in the subsequent section.

16.3 Complex-Capacitance Format

The complex capacitance, defined to be

$$C(\omega) = C_r + jC_j = \frac{1}{j\omega Z} = \frac{Y}{j\omega} = -j\frac{Y}{\omega} \tag{16.36}$$

Remember! 16.4 *Like the admittance representation, the complex-capacitance representation emphasizes values at high frequency and is often used for solid-state and dielectric systems for which information is sought regarding system capacitance.*

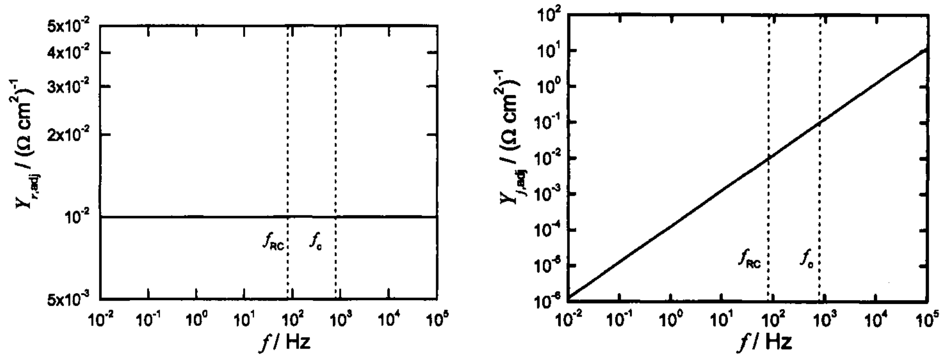

(a) (b)

Figure 16.10: Real and imaginary parts of the electrolyte-resistance-corrected admittance on a logarithmic scale as a function of frequency for $R_e = 10\ \Omega\text{cm}^2$, $R = 100\ \Omega\text{cm}^2$, and $C = 20\ \mu\text{F/cm}^2$. The blocking system of Table 16.1(a) is represented by dashed lines, and the reactive system of Table 16.1(b) is represented by solid lines. Characteristic frequencies are noted as $f_{RC} = (2\pi RC)^{-1}$ and $f_c = (2\pi R_e C)^{-1}$; a) real part of admittance and b) imaginary part of admittance.

has the advantage of being related to a physical property, the effective double-layer capacitance. For the blocking system of Table 16.1(a), the complex capacitance follows

$$C(\omega) = \frac{C}{1+(\omega ReC)^2} - j\frac{R_e\omega\,(C)^2}{1+(\omega ReC)^2} \tag{16.37}$$

The characteristic angular frequency for the blocking circuit is $\omega_c = 1/R_eC$, the same as is found for the admittance of the blocking circuit. At the characteristic angular frequency, the real part of the capacitance is equal to half the double-layer capacitance, and the imaginary part is equal to minus one-half of the double-layer capacitance. The complex-capacitance plot for the blocking circuit traces a semicircle.

The corresponding development for the reactive system of Table 16.1b yields

$$C(\omega) = \frac{C}{\left(1+\frac{R_e}{R}\right)^2 + (\omega R_e C)^2} - j\frac{R_eR\,(\omega C)^2 + 1 + \frac{R_e}{R}}{R\omega\left[\left(1+\frac{R_e}{R}\right)^2 + (\omega R_e C)^2\right]} \tag{16.38}$$

The characteristic angular frequency for which $C_r = C/2$ is given by equation (16.31), and the imaginary impedance at low frequencies tends toward $-\infty$.

16.3.1 Complex-Capacitance-Plane Representation

The complex-capacitance-plane plot is presented in Figure 16.11. The data are presented as a locus of points, where each data point corresponds to a different measurement frequency. As discussed for the impedance- and admittance-plane representations (Figures 16.1 and 16.6, respectively), the complex-capacitance-plane

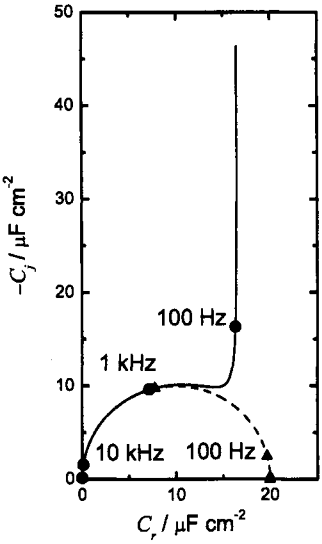

Figure 16.11: Complex-capacitance-plane plots for $R_e = 10\ \Omega\text{cm}^2$, $R = 100\ \Omega\text{cm}^2$, and $C = 20\ \mu\text{F/cm}^2$. The blocking system of Table 16.1(a) is represented by △ and dashed lines, and the reactive system of Table 16.1(b) is represented by ○ and solid lines.

format obscures the frequency dependence. This disadvantage can be mitigated by labeling some characteristic frequencies.

The double-layer capacitance of the blocking electrode can be obtained from the zero-frequency asymptote. The asymptotic value for the reactive system is scaled by the term $(1 + R_e/R)^{-2}$.

16.3.2 Complex-Capacitance Representation

The real and imaginary parts of the complex-capacitance are presented as functions of frequency in Figures 16.12(a) and (b), respectively. The low-frequency limit can be interpreted in terms of an effective double-layer capacitance. This relationship is exact for the blocking circuit of Table 16.1(a). The corresponding plots in logarithmic format are presented as Figures 16.13(a) and (b), respectively.

The characteristic frequency evident as a peak for the imaginary part of the complex-capacitance in Figures 16.12(b) and 16.13(b) has a value corresponding exactly to $f_c = (2\pi R_e C)^{-1}$ only for the blocking system. As found for data presentation in admittance format, the presence of a Faradaic process confounds use of graphical techniques to assess this characteristic frequency. Like the admittance format, the complex capacitance is not particularly well suited for analysis of electrochemical and other systems for which identification of Faradaic processes parallel to the capacitance represents the aim of the impedance experiments. It is particularly well suited for analysis of dielectric systems for which the electrolyte resistance can be neglected.

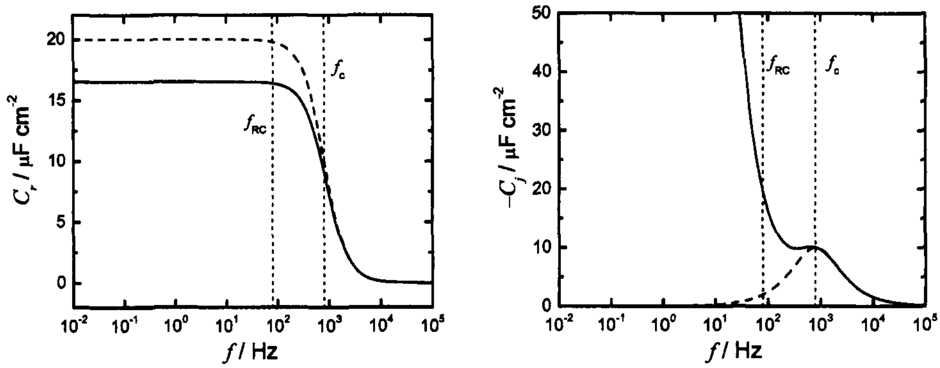

(a) (b)

Figure 16.12: Real and imaginary parts of the complex capacitance as a function of frequency for $R_e = 10\ \Omega\text{cm}^2$, $R = 100\ \Omega\text{cm}^2$, and $C = 20\ \mu\text{F/cm}^2$. The blocking system of Table 16.1(a) is represented by dashed lines, and the reactive system of Table 16.1(b) is represented by solid lines. Characteristic frequencies are noted as $f_{RC} = (2\pi RC)^{-1}$ and $f_c = (2\pi R_e C)^{-1}$; a) real part of complex capacitance and b) imaginary part of complex capacitance.

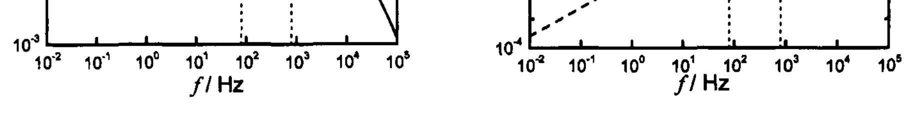

(a) (b)

Figure 16.13: Real and imaginary parts of the complex capacitance on a logarithmic scale as a function of frequency for $R_e = 10\ \Omega\text{cm}^2$, $R = 100\ \Omega\text{cm}^2$, and $C = 20\ \mu\text{F/cm}^2$. The blocking system of Table 16.1(a) is represented by dashed lines, and the reactive system of Table 16.1(b) is represented by solid lines. Characteristic frequencies are noted as $f_{RC} = (2\pi RC)^{-1}$ and $f_c = (2\pi R_e C)^{-1}$; a) real part of complex capacitance and b) imaginary part of complex capacitance.

Example 16.2 Complex Capacitance of Dielectrics: *Find an expression for the complex capacitance for the electrical circuit shown in Figure 16.9 and discussed in Example 16.1. Identify the limits and characteristic frequencies.*

Solution: *Insertion of equation (16.34) into the definition for complex capacitance*

$$C(\omega) = \frac{Y}{j\omega} \tag{16.39}$$

yields

$$\begin{aligned} C(\omega) &= C_{sc} + \frac{C_{t,1}}{1+(\omega R_{t,1}C_{t,1})^2} + \frac{C_{t,2}}{1+(\omega R_{t,2}C_{t,2})^2} \\ &\quad - j\omega\left[\frac{1}{\omega R_L} + \frac{\omega R_{t,1}C_{t,1}^2}{1+(\omega R_{t,1}C_{t,1})^2} + \frac{\omega R_{t,2}C_{t,2}^2}{1+(\omega R_{t,2}C_{t,2})^2}\right] \end{aligned} \tag{16.40}$$

As $\omega \rightarrow 0$, $C_r \rightarrow C_{sc} + C_{t_1} + C_{t,2}$. As $\omega \rightarrow \infty$, $C_r \rightarrow C_{sc}$. The characteristic angular frequencies are $\omega_{t1} = (R_{t,1}C_{t,1})^{-1}$ and $\omega_{t2} = (R_{t,2}C_{t,2})^{-1}$. The characteristic frequencies could be identified easily from plots of real and imaginary parts of the complex capacitance as functions of frequency.

16.4 Effective Capacitance

A more attractive representation of effective capacitance for electrochemical systems may be obtained directly from the imaginary part of the impedance as

$$C_{\text{eff}} = -\frac{1}{\omega Z_j} \tag{16.41}$$

In contrast to the complex capacitance described in Section 16.3, the effective capacitance described in equation (16.41) is defined to be a real number.

For the series circuit,

$$C_{\text{eff}} = C \tag{16.42}$$

and for the reactive circuit,

$$C_{\text{eff}} = C + \frac{1}{\omega^2 R^2 C} \tag{16.43}$$

Linear and logarithmic plots of effective capacitance are presented as functions of frequency in Figures 16.14(a) and (b), respectively. The high-frequency asymptote

---

Remember! 16.5 *The effective capacitance provides a means of quantitatively determining the interfacial capacitance of a system.*

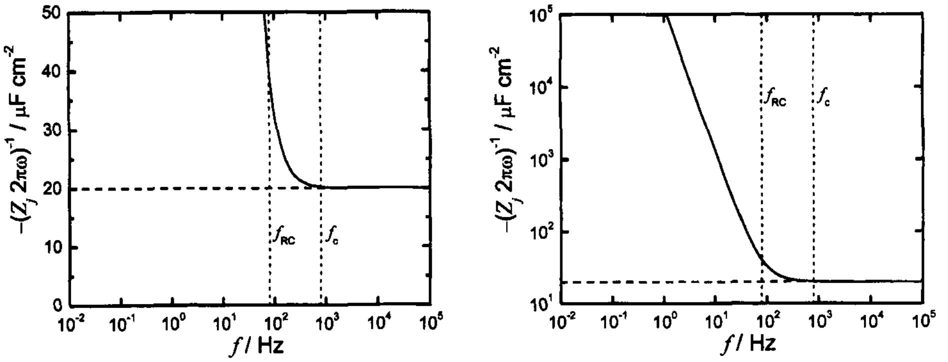

(a) (b)

Figure 16.14: Effective capacitance as a function of frequency for $R_e = 10\ \Omega\mathrm{cm}^2$, $R = 100\ \Omega\mathrm{cm}^2$, and $C = 20\ \mu\mathrm{F/cm}^2$. The blocking system of Table 16.1(a) is represented by dashed lines, and the reactive system of Table 16.1(b) is represented by solid lines. The characteristic frequencies noted are $f_{RC} = (2\pi RC)^{-1}$ and $f_c = (2\pi R_e C)^{-1}$; a) linear scale and b) logarithmic scale.

provides correct values for the double-layer capacitance for both blocking and reactive circuits. The characteristic angular frequency for the reactive system is seen in equation (16.43) to be $\omega_c = (R_e C)^{-1}$, and at this value, a factor of 2 (or 100 percent) error is seen for identification of double-layer capacitance. As seen in Figure 16.15, the error is diminished at frequencies larger than the characteristic frequency $f_{RC} = (2\pi RC)^{-1}$. At frequencies only one order of magnitude larger than f_{RC}, the error in assessment of double-layer capacitance is only 1 percent. Measurement at several different frequencies should be used to ensure that the capacitance is obtained at a frequency sufficiently larger than the largest characteristic relaxation frequency for the system.

Example 16.3 Evaluation of Double-Layer Capacitance: *Find the meaning of the effective capacitance obtained using equation (16.41) for the convective-diffusion impedance expressed as equation (11.20), i.e.,*

$$Z(\omega) = R_e + \frac{R_t + Z_{\mathrm{D}}(\omega)}{1 + j\omega C_{\mathrm{dl}}\left(R_t + Z_{\mathrm{D}}(\omega)\right)} \tag{16.44}$$

where $Z_{\mathrm{D}}(\omega)$ is a complex function of frequency that tends toward zero as frequency tends toward ∞.

Solution: *At high-frequencies, all models for convective diffusion to a rotating disk approach the Warburg impedance, given as equation (11.52). Thus, the convective diffusion impedance can be expressed as $Z_{\mathrm{D}}(\omega) = Z_{\mathrm{D}}(0)/\sqrt{j\omega\tau}$. Following Example 1.7, which*

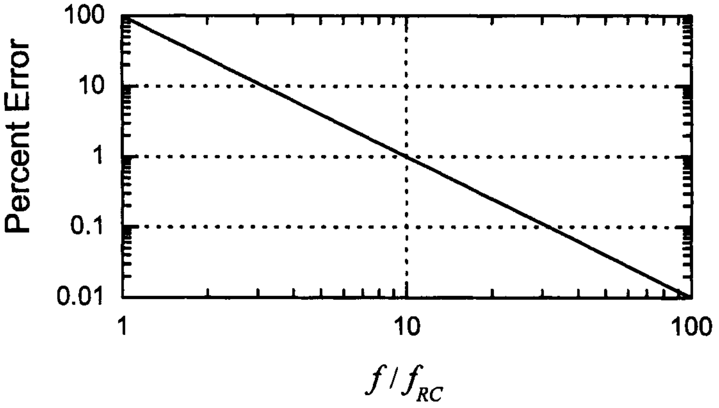

Figure 16.15: Error in assessment of the double-layer capacitance for the reactive system of Table 16.1(b) as a function of frequency scaled by the characteristic frequency $f_{RC} = (2\pi RC)^{-1}$.

provides a demonstration of methods used to determine the square root of complex numbers,

$$Z_D(\omega) = Z_D(0)\frac{0.7071}{\sqrt{\omega\tau_D}}(1-j) = A(\omega)(1-j) \tag{16.45}$$

The impedance can be expressed as

$$Z = R_e + \frac{R_t + A(\omega)(1-j)}{1 + j\omega C_{\text{dl}}\left(R_t + A(\omega)(1-j)\right)} \tag{16.46}$$

or

$$Z = R_e + \frac{R_t + A(\omega) - jA(\omega)}{1 + \omega C_{\text{dl}}A(\omega) + j\omega C_{\text{dl}}\left(R_t + A(\omega)\right)} \tag{16.47}$$

After multiplying by the complex conjugate, the real and imaginary contributions are obtained as

$$Z_r = R_e + \frac{R_t + A(\omega)}{\left(1 + \omega C_{\text{dl}}A(\omega)\right)^2 + \omega^2 C_{\text{dl}}^2\left(R_t + A(\omega)\right)^2} \tag{16.48}$$

and

$$Z_j = -\frac{A(\omega) + \omega C_{\text{dl}}\left(A^2(\omega) + \left(R_t + A(\omega)\right)^2\right)}{\left(1 + \omega C_{\text{dl}}A(\omega)\right)^2 + \omega^2 C_{\text{dl}}^2\left(R_t + A(\omega)\right)^2} \tag{16.49}$$

respectively. Following equation (16.41), the effective capacitance that can be obtained at the high-frequency limit is given as

$$C_{\text{eff}} = \lim_{\omega\to\infty} -\frac{1}{\omega Z_j} = C_{\text{dl}} \tag{16.50}$$

Thus, the high-frequency limit of the effective capacitance can be used to obtain the double-layer capacitance for even quite complicated systems. The reason this approach works is that, at high frequencies, the Faradaic current is blocked, and all current passes through the double-layer capacitor.

Problems

16.1 Consider the electrical circuit given as Figure 4.6(a). Use a spreadsheet program to plot the results for $R_0 = 10\Omega$, $R_1 = 50\Omega$, $C_1 = 20\mu\text{F}$, $R_2 = 500\Omega$, and $C_1 = 10\mu\text{F}$ in the following representations:

- **(a)** Impedance
- **(b)** Admittance
- **(c)** Complex capacitance

16.2 Use a spreadsheet program to plot the results of Problem 10.6 in the following representations:

- **(a)** Impedance
- **(b)** Admittance
- **(c)** Complex capacitance

16.3 Consider the equation used for a so-called constant phase element, e.g.,

$$Z(\omega) = R_e + \frac{R_t}{1 + (j\omega)^{\alpha} R_t Q} \qquad (16.51)$$

Plot the model results using the formats presented in this chapter, letting $R_e = 10\ \Omega\text{cm}^2$, $R_t = 100\ \Omega\text{cm}^2$, and $Q = 20\ \mu\text{Fs}^{\alpha-1}/\text{cm}^{-2}$. Allow α to be a parameter such that $1 > \alpha > 0.5$.

16.4 Verify equation (16.50) in Example 16.3.

Electrochemical Impedance Spectroscopy
by Mark E. Orazem and Bernard Tribollet

Chapter 17

Preliminary Graphical Methods

Graphical methods provide a first step toward interpretation and evaluation of impedance data. An outline of graphical methods is presented in Chapter 16 for simple reactive and blocking circuits. The same concepts are applied here for systems that are more typical of practical applications. The graphical techniques presented in this chapter do not depend on any specific model. The approaches, therefore, can provide a qualitative interpretation. Surprisingly, even in the absence of specific models, values of such physically meaningful parameters as the double-layer capacitance can be obtained from high- or low-frequency asymptotes.

The methods for graphical representation and interpretation of impedance data are presented here for impedance data characteristic of active and blocking electrodes. The material presented here is based on a paper by Orazem et al.[206] The classification of active systems is represented by a Randles circuit, as presented in Figure 17.1(a). The classification of blocking systems is represented by the circuit presented in Figure 17.1(b). The mathematical development was presented in previous chapters in terms of angular frequency ω. As experimental data are generally presented in terms of frequency $f = \omega/2\pi$, the graphical approaches developed in this chapter are presented in terms of frequency f.

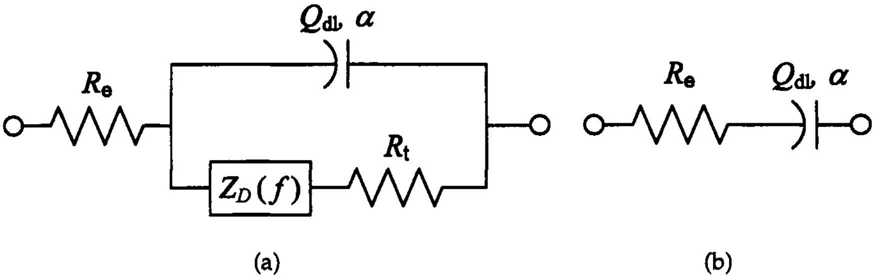

Figure 17.1: Equivalent circuits used to demonstrate the graphical representation of reactive impedance data: a) Randles circuit; and b) blocking circuit.

Table 17.1: Randles circuit parameters used for simulations.

$R_e/\Omega\mathrm{cm}^2$	$R_t/\Omega\mathrm{cm}^2$	$Q_{\mathrm{dl}}/\mathrm{M}\Omega^{-1}\mathrm{cm}^{-2}\mathrm{s}^{\alpha}$	α	$\tau_{\mathrm{D}}/\mathrm{s}$	$Z_{\mathrm{D}}(0)/\Omega\mathrm{cm}^2$
100	100	15.915	1.0	1	1,000
100	100	109.97	0.7	1	1,000
100	100	398.94	0.5	1	1,000

17.1 Application to a Randles Circuit

A Randles circuit is used here to demonstrate the graphical representation for reactive (nonblocking) systems. The impedance of the Randles circuit presented in Figure 17.1(a) is given by

$$Z(f) = R_e + \frac{(R_t + Z_D(f))}{1 + (j2\pi f)^{\alpha} Q_{\mathrm{dl}} (R_t + Z_D(f))} \tag{17.1}$$

where the convective-diffusion impedance $Z_D(f)$ was given by the expression for a finite stagnant diffusion layer of thickness δ_i as described in Section 11.4.2, i.e.,

$$Z_D(f) = Z_D(0)\frac{\tanh\left(\sqrt{j2\pi f \tau_D}\right)}{\sqrt{j2\pi f \tau_D}} \tag{17.2}$$

where τ_D is the time constant for diffusion given by $\tau_D = \delta_i^2/D_i$. The parameters α and Q_{dl} are associated with a constant-phase element (CPE) as discussed in Section 13.1.[3,71,104] When $\alpha = 1$, Q_{dl} has units of a capacitance, e.g., $\mu\mathrm{Fcm}^{-2}$, and represents the capacity of the double layer. When $\alpha \neq 1$, the system shows behavior that has been attributed to surface heterogeneity[181,182] or to continuously distributed time constants for charge-transfer reactions.[183–187] The phase angle associated with a CPE is independent of frequency.

The parameter values used for the simulations presented here are given in Table 17.1. The parameters were chosen such that the high-frequency CPE element would have a characteristic frequency f_{RC} of 100 Hz, corresponding to a time constant of 1.59 ms.

The Randles circuit provides an example of a class of systems for which, at the zero-frequency or dc limit, the resistance to passage of current is finite, and current can pass. Many electrochemical and electronic systems exhibit such nonblocking or reactive behavior. Even though the impedance response of the system presented in this section is relatively simple as compared to that of typical electrochemical and electronic systems, the nonblocking systems comprise a broad cross-section of electrochemical and electronic systems. The concepts described in this chapter therefore can be easily adapted to experimental data.

17.1.1 Traditional Representation of Data

As discussed in Section 16.1, impedance data are often represented in complex-impedance-plane or Nyquist formats accompanied with Bode representations in which the modulus and phase angle are presented as function of frequency. Such traditional representations of impedance data are given in Figure 17.2 for the circuit presented as Figure 17.1(a).

The complex-impedance-plane or Nyquist format is shown in Figure 17.2(a) for the Randles circuit. The data are presented as a locus of points, where each data point corresponds to a different measurement frequency. The asymptotic limits of the real part of the impedance for the reactive circuit shown in Figure 17.2(a) are R_e at high frequencies and $R_e + Z_D(0) + R_t$ at low frequency. Complex-impedance-plane plots are very popular because the shape of the locus of points yields insight into possible mechanisms or governing phenomena. If the locus of points traces a perfect semicircle, for example, the impedance response corresponds to a single activation-energy-controlled process. A depressed semicircle indicates that a more detailed model is required, and the multiple loops shown in Figure 17.2(a) provide clear indication that more than one time constant is required to describe the process. The significant disadvantages are that the frequency dependence is obscured, that low impedance values are obscured, and that apparent agreement between model and experimental data in complex-impedance-plane format may obscure large differences in frequency and at low impedance values.

The dependence on frequency is seen more clearly in the Bode representation shown in Figures 17.2(b) and (c) for the magnitude and phase angle of the Randles circuit. Frequency is generally presented on a logarithmic scale to reveal the important behavior seen at lower frequencies. For a process described by single RC element, the characteristic frequency is readily identified by inflections in the magnitude and phase angle plots. The magnitude of the impedance of the single RC reactive system tends toward R_e as frequency tends toward ∞ and toward $R_e + R_t$ as frequency tends toward zero. The phase angle has a value of $-45°$ at the characteristic frequency $f_{RC} = 1/(2\pi RC)$. The slope of the transition between low frequency and high frequency asymptotes can provide useful information concerning the nature of the impedance response if the characteristic time constants are well separated.

The phase angle, expressed as

$$\phi = \tan^{-1}\left(\frac{Z_j}{Z_r}\right) \tag{17.3}$$

tends toward zero at low frequencies, indicating that the current and potential are in phase. The phase angle tends toward zero at high frequencies as well, due to the influence of the leading resistor R_e in the value of Z_r used in equation (17.3). Dashed lines in Figures 17.2(b) and (c) indicate the characteristic frequencies associated with the time constants of the synthetic impedance data of Table 17.1. No clear correspondence is seen between the Bode plots and the time constants of the impedance data.

The popularity of the Bode representation stems from its utility in circuits analysis. The phase angle plots are sensitive to system parameters and, therefore, provide a good means of comparing model to experiment. The modulus is much less

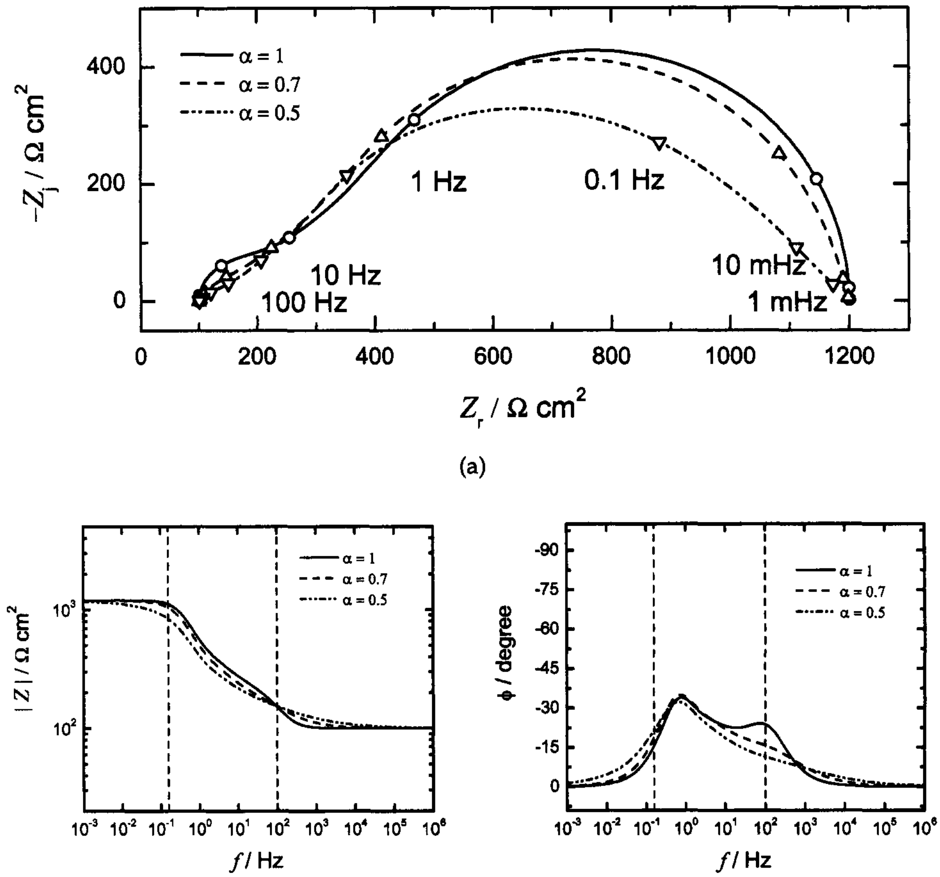

(a)

(b)

(c)

Figure 17.2: Traditional representation of impedance data for the Randles circuit presented as Figure 17.1(a) with α as a parameter. a) complex-impedance-plane or Nyquist representation (symbols are used to designate decades of frequency.); b) Bode representation of the magnitude of the impedance; and c) Bode representation of the phase angle. (Taken from Orazem et al.[206] and reproduced with permission of The Electrochemical Society.)

sensitive to system parameters, but the asymptotic values at low and high frequencies provide values for the dc and electrolyte resistance, respectively.

For electrochemical systems exhibiting an Ohmic or electrolyte resistance, however, the Bode representation has serious drawbacks. The influence of electrolyte resistance confounds the use of phase angle plots, such as shown in Figure 17.2(c), to estimate characteristic frequencies. In addition, Figure 17.2(c) shows that the current and electrode potential are in-phase at high frequencies; whereas, at high frequencies, for $\alpha = 1$, the current and interfacial potential are exactly out of phase. Even when $\alpha \neq 1$, the current and interfacial potential are not in-phase at high frequencies. The electrolyte resistance, then, obscures the behavior of the electrode surface in the phase angle plots.

17.1.2 Phase Angle and Modulus Corrected for Ohmic Resistance

If an accurate estimate for electrolyte resistance $R_{e,\text{est}}$ is available, a modified Bode representation is possible, following the development in Section 16.1.3, as

$$\phi_{\text{adj}} = \tan^{-1}\left(\frac{Z_j}{Z_r - R_{e,\text{est}}}\right) \tag{17.4}$$

and

$$|Z|_{\text{adj}} = \sqrt{(Z_r - R_{e,\text{est}})^2 + (Z_j)^2} \tag{17.5}$$

The results are presented in Figures 17.3(a) and (b) for magnitude and phase angle, respectively.

The slope of the corrected modulus yields valuable information concerning the existence of CPE behavior that is obscured in the traditional Bode presentation. At high frequencies, the corrected modulus is dominated by the contribution of the imaginary part of the impedance. The corrected modulus approaches zero according to $|Z|_{\text{adj}} \sim f^{-\alpha}$; thus, the slope on a log-log plot has a value of $-\alpha$ at high frequencies.

As seen in Figure 17.3(b), systems exhibiting purely capacitive behavior, i.e., where $\alpha = 1$, the current and potential are in-phase at low frequencies and out-of-phase at high frequencies. The phase angle has an inflection point at the characteristic frequency $f_{\text{RC}} = 100$ Hz and reaches a value of -90° at high frequency. Under conditions that CPE behavior is evident, i.e.,, when $\alpha \neq 1$, the phase angle reaches a high-frequency asymptote such that

$$\phi_{\text{adj}}(\infty) = -90\alpha \tag{17.6}$$

Remember! 17.1 *Interpretation of the phase angle in terms of interfacial properties is confounded by the contribution of the Ohmic resistance. The adjusted phase angle, given in equation (17.4), reveals the behavior of the interface.*

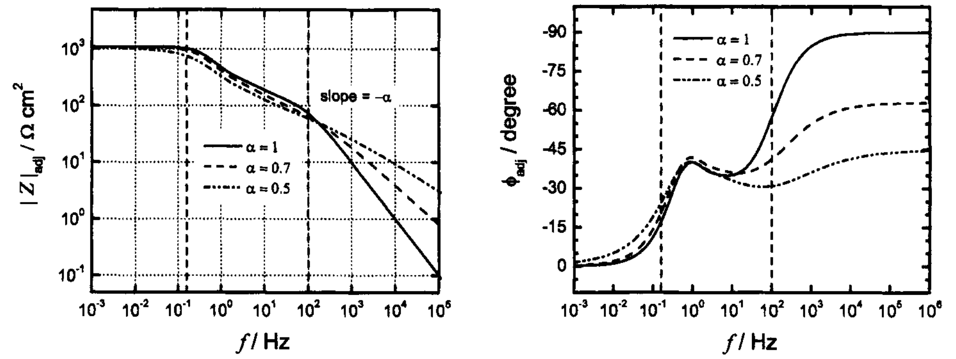

(a) (b)

Figure 17.3: Bode plots with α as a parameter for the Randles circuit presented as Figure 17.1(a) adjusted for the electrolyte resistance following equations (17.4) and (17.5): a) modulus; and b) phase angle. (Taken from Orazem et al.[206] and reproduced with permission of The Electrochemical Society.)

The corrected phase angle plots yield valuable information concerning the existence of CPE behavior that is obscured in the traditional Bode presentation.

As mentioned in Section 16.1.3, caution should be used when interpreting the electrolyte-resistance-corrected Bode plots. Incorrect estimates for $R_{e,\text{est}}$ can give the appearance of an additional high-frequency relaxation process. When possible, an assessment of $R_{e,\text{est}}$ should be made independently of the regression. In addition, noise in the experimental data can obscure the behavior of the corrected phase angle at high frequencies. At high frequencies, $Z_r \rightarrow R_{e,\text{est}}$. Thus, the argument to the inverse tangent in equation (17.4) will have a sign controlled by noise in the denominator, and the phase calculated from equation (17.4) will have values scattered about $\pm\phi_{\text{adj}}(\infty)$. This scatter will of course be evident as well in the Ohmic-resistance-corrected magnitude plots. Nevertheless, Bode plots corrected for Ohmic resistance are useful as a pedagogical tool and for determining whether CPE behavior is evident in the data.

17.1.3 Real and Imaginary Components

The difficulty with using the Ohmic-resistance-corrected Bode plots presented in the previous section is that an accurate estimate is needed for the electrolyte resistance and that, at high frequencies, the difference $Z_r - R_{e,\text{est}}$ is determined by stochastic noise. As discussed in Section 16.1.4, these difficulties can be obviated by plotting the real and imaginary components of the impedance.

The real part of the impedance, shown in Figure 17.4(a), provides the same information as is available from the modulus plots presented in Figure 17.2(b). The high frequency asymptote reveals the Ohmic electrolyte resistance, and the low frequency asymptote reveals the sum of the polarization impedance and the

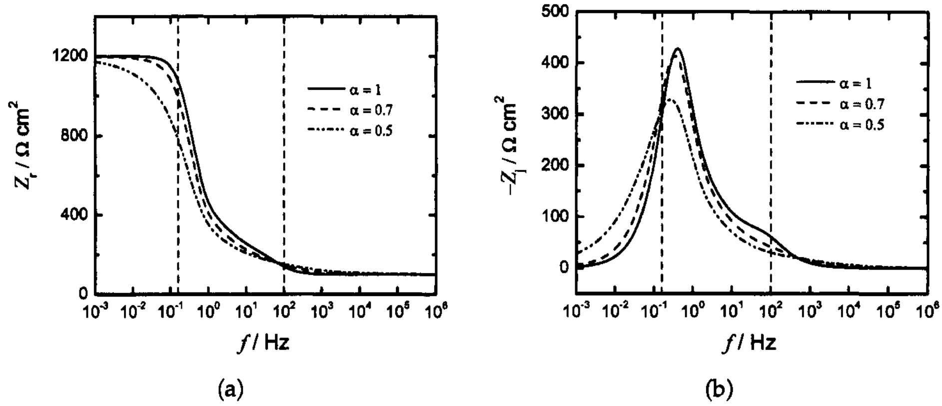

Figure 17.4: Real and imaginary parts of the impedance as a function of frequency with α as a parameter for the Randles circuit presented as Figure 17.1(a): a) real part; and b) imaginary part. (Taken from Orazem et al.[206] and reproduced with permission of The Electrochemical Society.)

electrolyte resistance. The imaginary part of the impedance, presented in Figure 17.4(b), has the significant advantage that the characteristic frequencies can be readily identified at the peak values. The imaginary part of the impedance is independent of electrolyte resistance, so correction for Ohmic resistance is not needed.

The behavior at lower impedance values is emphasized when the impedance components are plotted on a logarithmic scale, as shown in Figure 17.5. Figure 17.5 provides a rich source of insight into the experimental system. As in Figure 17.4(b), a characteristic frequency can be defined to exist at the maximum value. The slopes at low and high frequency are $+\alpha$ and $-\alpha$, respectively. Departure from ± 1 provides an indication of distributed processes. Observation of multiple maxima shows that the data must be interpreted in terms of more than one process. Interpretation of Figure 17.5 in terms of characteristic frequencies is not confounded by the electrolyte resistance, as was seen for the Bode plots of phase angle.

As discussed in Section 21.2, the variances of stochastic errors are equal for real and imaginary parts of the impedance. Thus, another advantage of presenting real and imaginary parts of the impedance as functions of frequency is that comparison between data and levels of stochastic noise can be easily represented.

Remember! 17.2 *As shown in Figure 17.5, the slope of the magnitude of the imaginary part of the impedance as a function of frequency in logarithmic coordinates yields the exponent of a CPE.*

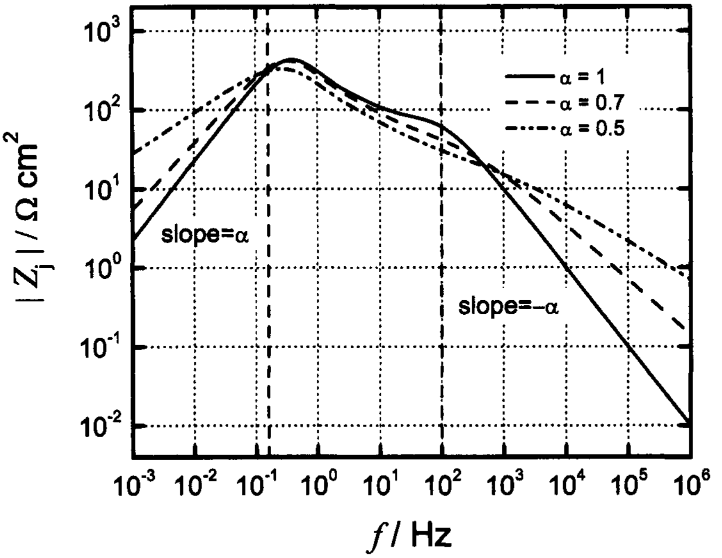

Figure 17.5: Imaginary part of the impedance as a function of frequency with α as a parameter for the Randles circuit presented as Figure 17.1(a). (Taken from Orazem et al.[206] and reproduced with permission of The Electrochemical Society.)

17.1.4 Effective High-Frequency Capacity or CPE Coefficient

An effective capacitance, or, when $\alpha \neq 1$, an effective CPE coefficient may be obtained directly from the imaginary part of the impedance as

$$Q_{\text{eff}} = \sin\left(\frac{\alpha\pi}{2}\right)\frac{-1}{Z_j(f)\,(2\pi f)^{\alpha}} \tag{17.7}$$

When $\alpha = 1$, the CPE coefficient Q becomes a capacitance, and equation (17.7) can be written

$$Q_{\text{eff}} = C_{\text{eff}} = \frac{-1}{Z_j(f)\,(2\pi f)} \tag{17.8}$$

In contrast to the complex capacitance described in Section 16.3, the effective capacitance described in equation (17.8) is defined to be a real number.

The ratio of effective CPE coefficient to the expected value is given in Figure 17.6. The high-frequency asymptote is seen to provide correct values for the double-layer CPE coefficient. The assessment should be made at frequencies significantly larger than the largest characteristic relaxation frequency for the system. At frequencies only one order of magnitude larger than f_{RC}, the error in assessment of double-layer CPE coefficient is only one percent. Measurement at several different frequencies should be used to ensure that the CPE coefficient is obtained at a frequency sufficiently larger than the largest characteristic relaxation frequency for the system.

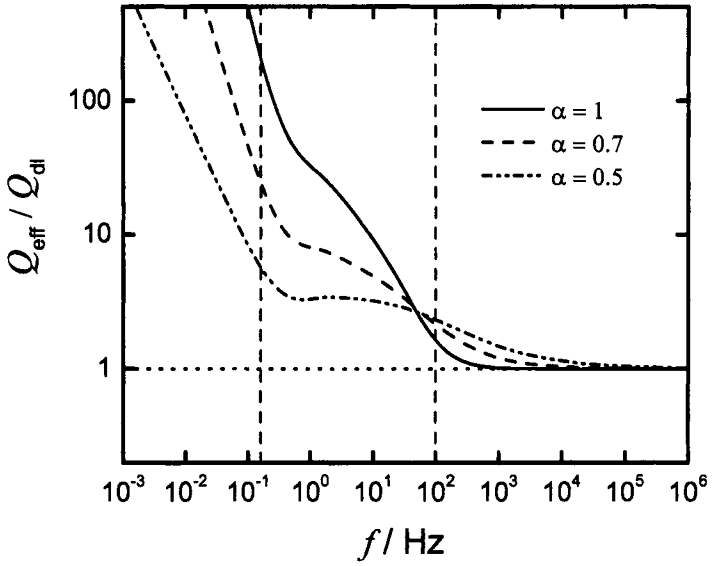

Figure 17.6: Effective CPE coefficient defined by equation (17.7), scaled by the input value of the double-layer CPE coefficient, as a function of frequency with α as a parameter for the Randles circuit presented as Figure 17.1(a). (Taken from Orazem et al.[206] and reproduced with permission of The Electrochemical Society.)

The high-frequency asymptote provides correct values for the double-layer capacitance for both blocking and reactive circuits. The percent error in the assessment of Q_{eff} is presented in Figure 17.7, which represents an extension of Figure 16.15. As seen in Figure 17.7, the error is diminished at frequencies larger than the characteristic frequency $f_{\text{RC}} = \left(2\pi R_f C_{\text{dl}}\right)^{-1}$. At frequencies only one order of magnitude larger than f_{RC}, the error in assessment of double-layer capacitance is one percent for $\alpha = 1$, but measurement at larger values of f/f_{RC} is required to achieve similar accuracy for values of α less than 1. Measurement at several different frequencies should be used to ensure that the capacitance is obtained at a frequency sufficiently larger than the largest characteristic relaxation frequency for the system.

Remember! 17.3 *Calculation of an effective capacitance or CPE coefficient according to equation (17.7) yields, in the high-frequency limit, properties associated with the electrode under study.*

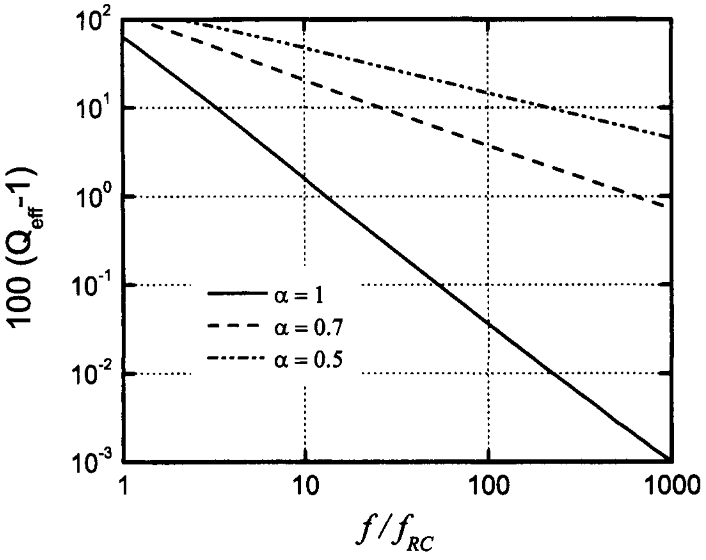

Figure 17.7: Error in assessment of the double-layer capacitance for the reactive system of Table 16.1b as a function of frequency scaled by the characteristic frequency $f_{RC} = \left(2\pi R_f C_{\mathrm{dl}}\right)^{-1}$ with α as a parameter.

17.2 Application to Blocking Electrodes

The impedance of the blocking circuit presented in Figure 17.1(b) is given by

$$Z(f) = R_e + \frac{1}{(j2\pi f)^\alpha Q} \tag{17.9}$$

The parameter values R_e, α, and Q used for the simulations presented here are the same as those given for the Randles circuit in Table 17.1.

17.2.1 Nyquist and Bode Representations

The complex impedance plane or Nyquist representation of the impedance for the blocking electrode of Figure 17.1(b) is presented in Figure 17.8(a). For $\alpha = 1$, the real part of the impedance for the blocking circuit is equal to R_e for all frequencies. The tendency of the imaginary part to approach $-\infty$ as frequency tends toward zero appears as a vertical line in the impedance plane plot given as Figure 17.8(a). For $\alpha \neq 1$, the real and imaginary parts tend toward $+\infty$ and $-\infty$, respectively, showing that, in contrast to the impedance of reactive systems, a finite dc limit is not seen. Under DC conditions, current cannot pass. The high-frequency limit, not visible on the scale presented, has a value of R_e for all values of α.

The Bode representation is presented in Figures 17.8(b) and (b) for modulus and phase angle, respectively. The traditional values of modulus and phase angle are

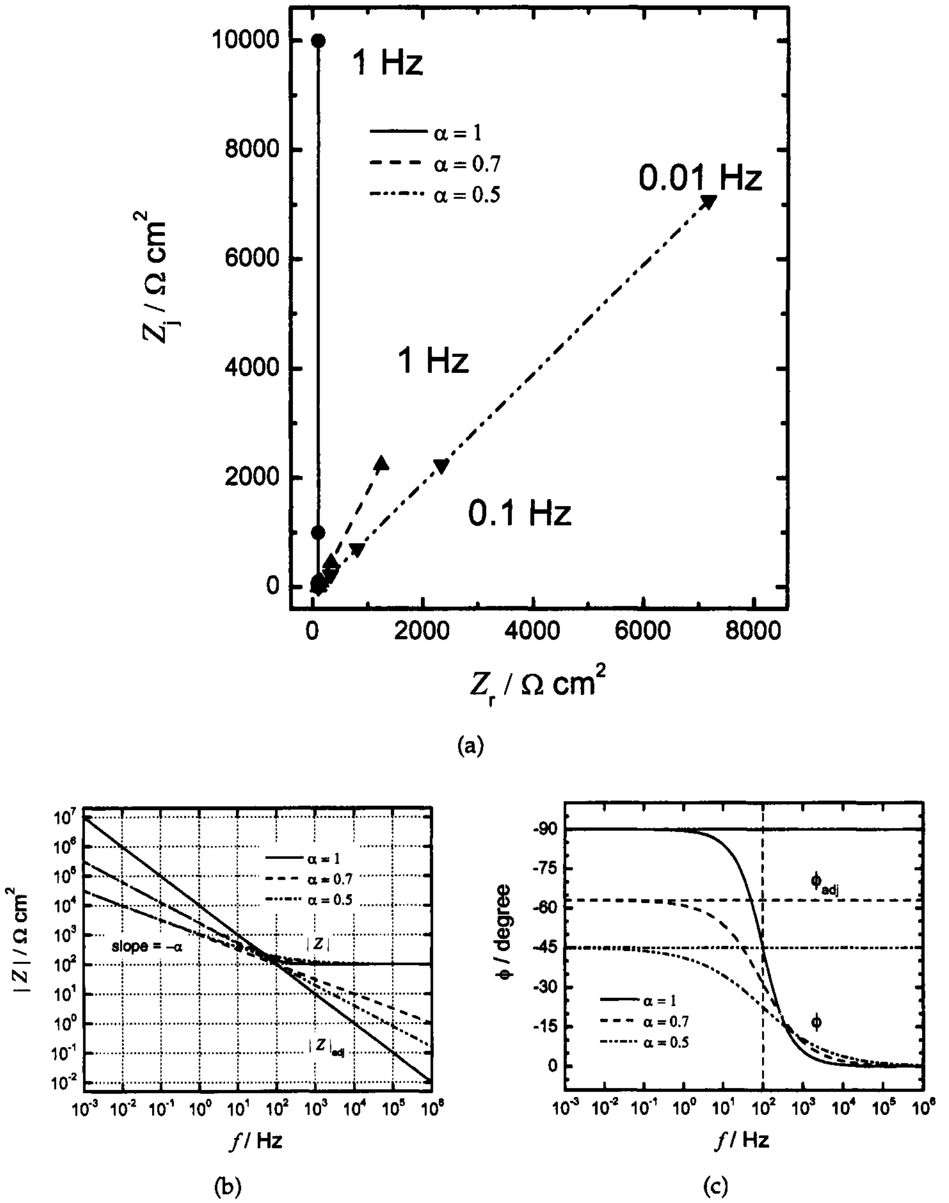

Figure 17.8: Nyquist and Bode representations of impedance data for the blocking circuit presented as Figure 17.1(b) with α as a parameter. a) complex-impedance-plane or Nyquist representation (symbols are used to designate decades of frequency): b) Bode representation of the magnitude of impedance; and c) Bode representation of the phase angle. (Taken from Orazem et al.[206] and reproduced with permission of The Electrochemical Society.)

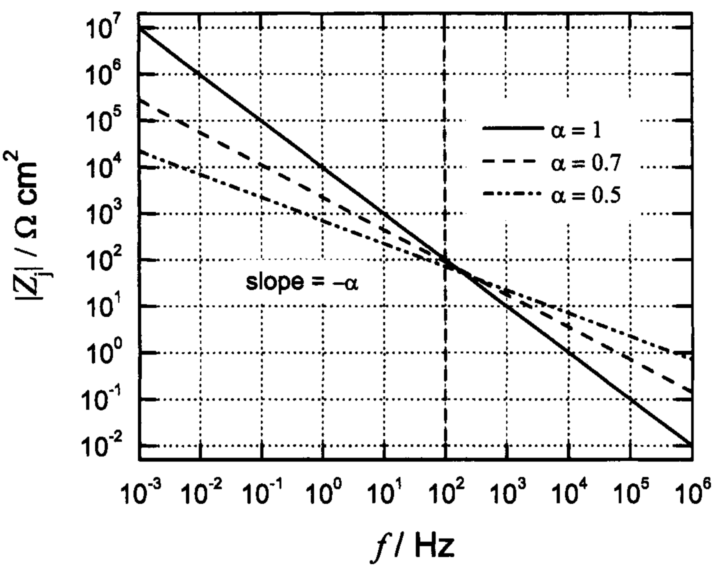

Figure 17.9: Imaginary part of the impedance as a function of frequency with α as a parameter for the blocking circuit presented as Figure 17.1(b). (Taken from Orazem et al.[206] and reproduced with permission of The Electrochemical Society.)

compared to the values adjusted for the electrolyte resistance following equations (17.4) and (17.5).

The magnitude, presented in Figure 17.8(b), tends toward R_e as frequency tends toward ∞ and toward ∞ as frequency tends toward zero. The slope of the line at low frequencies has a value of $-\alpha$ for the blocking electrode. Slopes with values smaller than unity could provide an indication of a blocking electrode with a distribution of characteristic time constants. The slope of the modulus corrected for Ohmic resistance is equal to $-\alpha$ for all frequencies.

The phase angle for the blocking configuration, shown in Figure 17.8(c), tends toward a constant value of $-90\alpha°$ at low frequencies and toward zero at high frequencies. As seen for the reactive system in Figure 17.2(c), the behavior at high frequencies is attributed to the confounding influence of the electrolyte resistance. The corrected phase angle is constant for all frequencies, with a value of $-90\alpha°$ as is shown in Figure 17.8(c). Again, accurate estimates for the Ohmic resistance are needed to generate the corrected plots.

17.2.2 Imaginary Component

The logarithm of the imaginary part of the impedance is presented in Figure 17.9. The imaginary part of the impedance presented in Figure 17.9 is identical to the Ohmic-resistance-corrected modulus presented in Figure 17.8(b), but has the advantage that it can be obtained directly without need for an estimate of the electrolyte resistance. The slope of the imaginary part of the impedance on a log-log

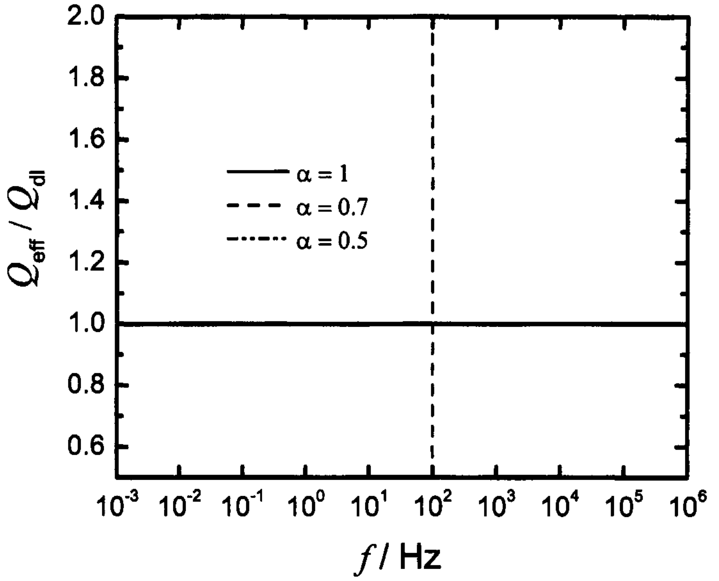

Figure 17.10: Effective CPE coefficient defined by equation (17.7), scaled by the input value of the double-layer CPE coefficient, as a function of frequency with α as a parameter for the blocking circuit presented as Figure 17.1(b). (Taken from Orazem et al.[206] and reproduced with permission of The Electrochemical Society.)

plot is independent of frequency and has a value of $-\alpha$.

17.2.3 Effective CPE Coefficient

The ratio of effective CPE coefficient, calculated using equation (17.7), to the expected value is given in Figure 17.10. The effective CPE coefficient is seen to be independent of frequency.

Example 17.1 Plots for Mg Alloys: *Consider the global impedance response for an as-cast magnesium alloy AZ91 presented in Figure 17.11 for the AZ91 alloy at the corrosion potential after different immersion times in 0.1 M NaCl.*[122,238] *What quantitative information can be obtained without considering a detailed process model such as discussed in Example 10.3?*

Solution: *The imaginary part of the impedance is plotted on a logarithmic scale in Figure 17.12. A line with slope* -0.856 ± 0.007 *is shown, which was fitted to the high-frequency data for* $t = 0.5$ *h of immersion. This slope has the value of* $-\alpha$*, and departure from* -1 *provides an indication of distributed processes. The low-frequency portion of the high-frequency capacitive loop has a slope of* 0.661 ± 0.008*. The lack of symmetry suggests that the high-frequency capacitance is in parallel with other reactive processes. Observation of*

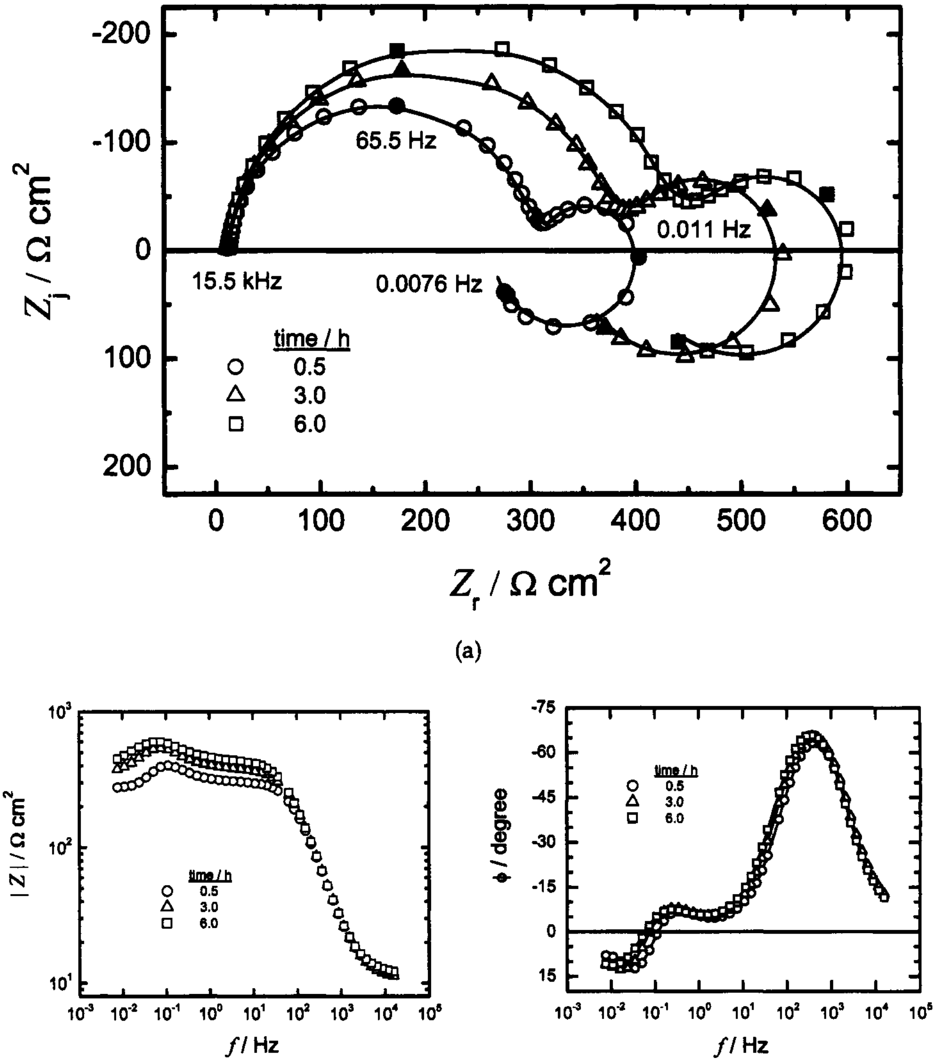

(a)

(b)

(c)

Figure 17.11: Traditional representation of impedance data obtained for the AZ91 alloy at the corrosion potential after different immersion times in 0.1 M NaCl: a) complex-impedance-plane or Nyquist representation (the lines represent the measurement model fit to the complex data sets); b) Bode representation of the magnitude of the impedance as a function of frequency; and c) Bode representation of the phase angle as a function of frequency. (Taken from Orazem et al.[206] and reproduced with permission of The Electrochemical Society.)

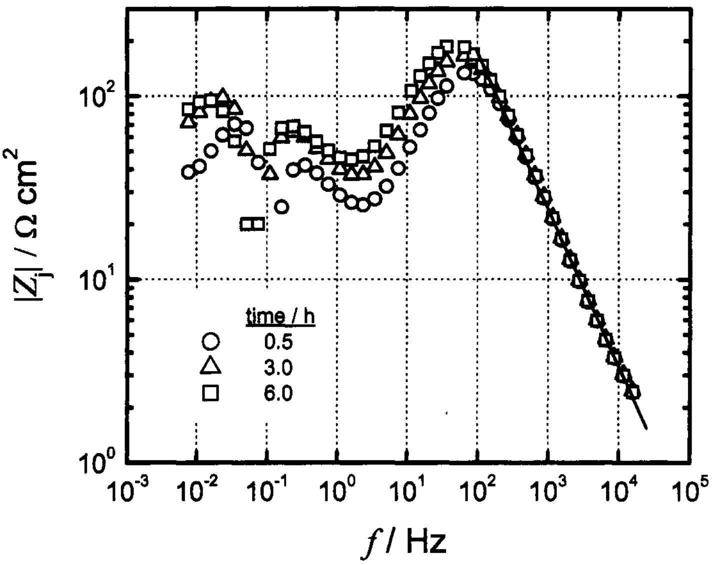

Figure 17.12: Imaginary part of the impedance as a function of frequency for the AZ91 alloy at the corrosion potential after different immersion times in 0.1 M NaCl. The line with slope -0.857 ± 0.007 was fitted to the high-frequency data for $t = 0.5$ h of immersion time. (Taken from Orazem et al.[206] and reproduced with permission of The Electrochemical Society.)

Table 17.2: Values for high-frequency component obtained from asymptotic values for the corrosion of an AZ91 Mg alloy.[206]

Immersion Time / h	0.5	3.0	6.0
α / dimensionless	0.856	0.872	0.877
$Q_{\mathrm{eff}}/\mathrm{M}\Omega^{-1}\mathrm{cm}^{-2}\mathrm{s}^{\alpha}$	22.7	19.1	18.5
$R_e/\Omega\mathrm{cm}^2$	10.65	10.45	11.4

multiple maxima also shows that the data must be interpreted in terms of more than one process.

The slopes at the high-frequency asymptotes appear to be in good agreement for the three data sets, but a more detailed analysis reveals some trending. Values for the CPE exponent are provided in Table 17.2. A small increase in the value of α is evident as the immersion time increases.

The value of α can be used in equation (17.7) to obtain an apparent CPE coefficient Q_{eff}. The resulting values of Q_{eff} are presented in Figure 17.13. The absence of a clearly identifiable asymptote may be attributed to high-frequency instrumental artifacts. The values for the CPE coefficient provided in Table 17.2 represent the average over the values for the 10 highest frequencies. A small reduction in the value of Q_{eff} is evident as the immersion time increases.

The value of α obtained from Figure 17.12 can also be used to find the solution resistance R_e used in equation (17.4) to yield the expected asymptotic value for adjusted phase

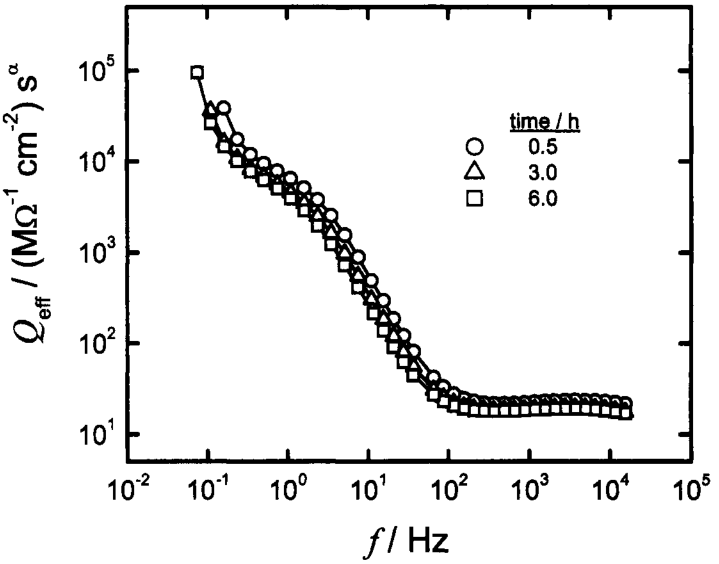

Figure 17.13: Effective CPE coefficient defined by equation (17.7) for the AZ91 alloy at the corrosion potential after different immersion times in 0.1 M NaCl. (Taken from Orazem et al.[206] and reproduced with permission of The Electrochemical Society.)

angle given by equation (17.4). The resulting Ohmic-resistance-corrected phase angle and magnitude are given in Figure 17.14. The slope of the high-frequency asymptote for magnitude corrected for electrolyte resistance has a value of $-\alpha$. Values for the electrolyte resistance are provided in Table 17.2.

17.3 Overview

The graphical representations presented here are intended to enhance analysis and to provide guidance for the development of appropriate physical models. While visual inspection of data alone cannot provide all the nuance and detail that can, in principle, be extracted from impedance data, the graphical methods described in this chapter can provide both qualitative and quantitative evaluation of impedance data.

The impedance plane or Nyquist plots presented as Figures 17.2(a), 17.8(a), and 17.11(a) provide a sense of the type of processes that govern the low-frequency behavior of the system. The shape of the low-frequency loop in Figure 17.2(a) is typ-

---

Remember! 17.4 *The graphical methods described in this chapter are general and can be applied to both reactive and blocking systems.*

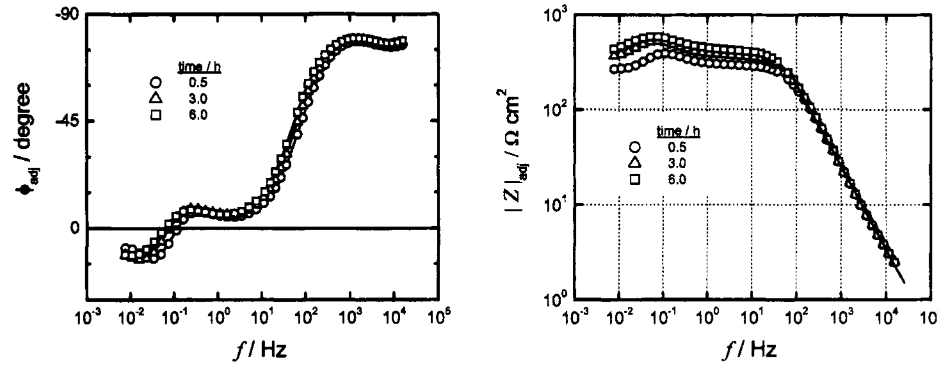

(a) (b)

Figure 17.14: Ohmic-resistance-corrected Bode plots for the AZ91 alloy at the corrosion potential after different immersion times in 0.1 M NaCl, with values adjusted for the electrolyte resistance following equation (17.4): a) phase angle; and b) modulus. (Taken from Orazem et al.[206] and reproduced with permission of The Electrochemical Society.)

ically associated with mass-transfer effects, although the shape is clearly distorted by the CPE behavior for $\alpha < 1$. A blocking behavior is suggested by the absence of a low-frequency dc limit in Figure 17.8(a). Three time constants are clearly evident in Figure 17.11(a).

Aside from values for asymptotic limits for the real part of the impedance, it is difficult to extract meaningful information from the traditional Bode plots when the Ohmic resistance is not negligible. In contrast, the Bode plots of magnitude and phase angle corrected for Ohmic resistance can be used to identify CPE behavior at high frequencies. Following equation (17.6), the high-frequency limit for the phase angle (Figures 17.3(b) and 17.14(a)) can be used to extract values for the CPE coefficient α. The Ohmic-resistance-corrected phase angle for the blocking system shown in Figure 17.8(c) is constant for all frequencies. The slope of the corrected modulus (Figures 17.3(a), 17.8(b), and 17.14(b)) can also be used to extract values for the CPE coefficient α.

The plots of the imaginary part of the impedance on a log-log scale shown in Figures 17.5 and 17.12 are particularly helpful. The slopes of the lines at low and high frequency in Figure 17.5 indicate clearly that two time constants can be discerned, that the high-frequency feature has CPE characteristics, and that the CPE characteristic extends to the low-frequency feature. This result indicates that the two time constants are coupled through a double-layer capacitive or constant-phase element. Log-log plots of imaginary impedance can be used to distinguish between a depressed impedance-plane semicircle caused by a continuous distribution of time constants associated with a CPE and that caused by contributions of discrete processes with closely overlapping but discrete time constants.

For the AZ91 data, the log of the imaginary part of the impedance shown in Figure 17.12 indicated a CPE behavior, meaning that the high-frequency feature had the characteristic of a distributed time constant rather than several discrete time constants. The absence of symmetry for the high-frequency feature suggested that the capacitive behavior was in parallel to other reactive processes. The decrease in α with immersion time suggests that the surface became more homogeneous with the growth of corrosion product layers.

For the blocking system, the plot of the imaginary part of the impedance on a log-log scale shown in Figure 17.9 yields the same information as the Ohmic-resistance-corrected modulus presented in Figure 17.8(b). The advantage of using Figure 17.9 is that no estimate is needed for the electrolyte resistance.

The effective CPE coefficient representation in Figures 17.6 and 17.13 yields, for $\alpha = 1$, information concerning the high-frequency capacitance of the system. In the case that $\alpha < 1$, Figures 17.6 and 17.13 yield an effective CPE coefficient Q_{eff} that can be related to the film capacitance through a model of the distributed time constants following Brug et al.[104]

The plots presented here have general application. They have been useful for evaluating the high-frequency behavior associated with local impedance measurements, where low-frequency measurements were not reliable and the frequency range was therefore not sufficient to allow regression analysis with a more detailed mathematical model.[194] The graphical analysis showed that, while high-frequency CPE behavior was evident in global impedance measurements for a Mg AZ91 alloy disk electrode, the local impedance measured near the center of the disk exhibited ideal RC behavior. The CPE behavior was thereby attributed to a 2-D radial distribution of the charge-transfer resistance. The capacitance extracted from high-frequency asymptotic behavior was used to estimate the area sampled by the local impedance technique.

As shown in Section 13.3, logarithmic plots of the imaginary part of the impedance can be used to show the high-frequency pseudo-CPE behavior caused by nonuniform current distribution. A graphical analysis similar to that demonstrated in Example 17.1 was employed by Huang et al.[205] to obtain values for parameters R_e, α, and Q associated with the impedance of a glassy carbon disk in KCl solutions and an oxide-covered stainless steel electrode in 0.05 M NaCl + 0.005 M Na_2SO_4 electrolyte.

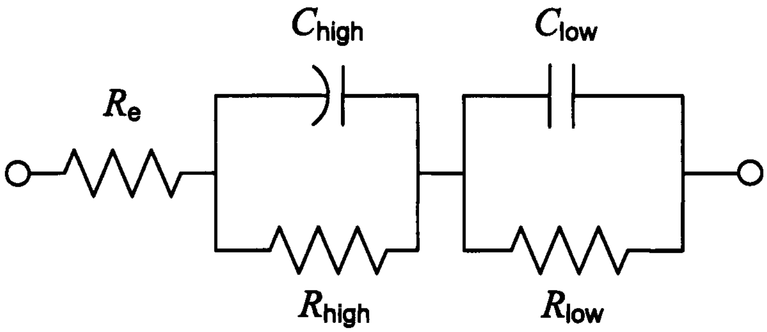

Figure 17.15: Equivalent circuit for Problem 17.1.

Problems

17.1 Consider the circuit presented in Figure 17.15. Upon choosing appropriate parameters that will yield time constants in a measurable frequency range, develop plots similar to Figures 17.2–17.6.

17.2 Develop plots similar to Figures 17.2–17.6 for the impedance data of the circuits given in Figure 17.1(a) with data presented in admittance rather than impedance format.

17.3 Consider the circuit presented in Figure 9.4 for an electrode covered by a film. Upon choosing appropriate parameters that will yield time constants in a measurable frequency range, develop plots similar to Figures 17.2–17.6.

Electrochemical Impedance Spectroscopy
by Mark E. Orazem and Bernard Tribollet

Chapter 18

Model-Based Graphical Methods

Under certain limiting conditions, graphical methods for analysis of impedance data can be based on the physics of the system under study. Use of such methods does not provide the detailed information that may be available from use of regression techniques, presented in Chapter 19. The graphical methods may, however, complement the development of detailed process models by identifying frequency ranges in which the process model must be improved.

The techniques presented here each involve analysis of data collected as a function of a system parameter such as temperature, potential, or disk rotation speed.

18.1 Mass Transfer

Graphical methods can be used to extract information concerning mass transfer if the data are collected under well-controlled hydrodynamic conditions. The systems described in Chapter 11 that are uniformly accessible with respect to convective diffusion would be appropriate. The analysis would apply to data collected on a rotating disk electrode as a function of disk rotation speed, or an impinging jet as a function of jet velocity.

18.1.1 Scaled Plots of Impedance

The experimental data presented in Figure 18.1(a) correspond to reduction of ferricyanide on a Pt rotating disk electrode.[85,239] The electrolyte consisted of 0.01 M $K_3Fe(CN)_6$ and 0.01 M $K_4Fe(CN)_6$ in 1 M KCl. The temperature was controlled at 25 ± 0.1°C. The electrode diameter was 5 mm, yielding a surface area of 0.1963 cm^2. A polishing technique was selected for the Pt disk electrode that provided the maximum steady mass-transfer-limited current. The electrode was polished with a 1,200-grit emery cloth, washed in deionized water, polished with alumina paste, and subjected to ultrasound cleaning in a 1:1 solution of water and ethyl alcohol. Experiments were conducted at 1/2 of the mass-transfer-limited current.

The part of the impedance influenced by mass transfer can be isolated by subtracting the electrolyte resistance. The data presented in Figure 18.1(a) were then

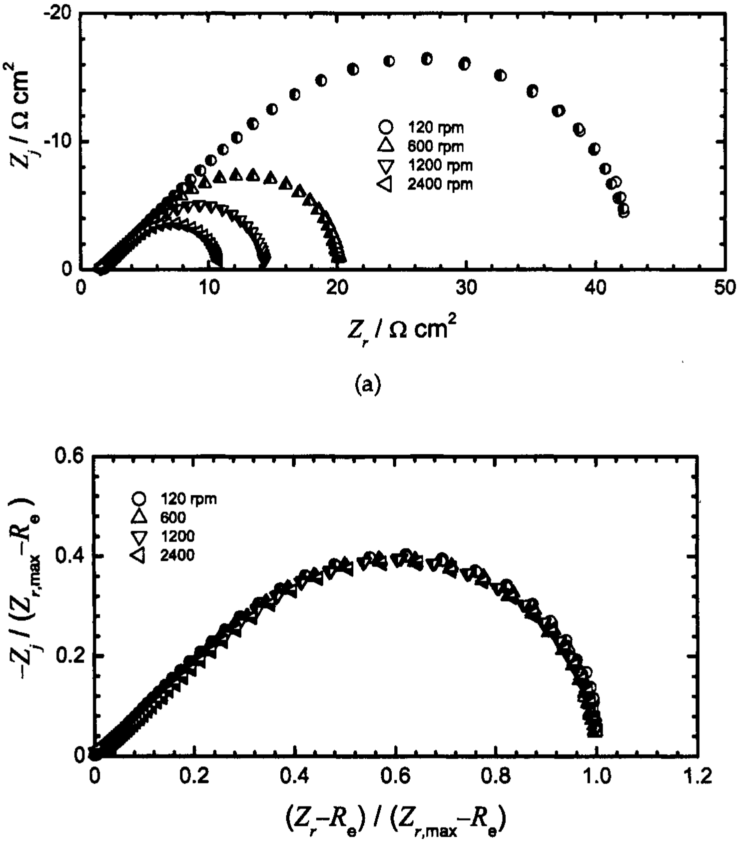

(a)

(b)

Figure 18.1: Impedance data as a function of frequency for reduction of ferricyanide on a rotating Pt disk electrode with rotation speed as a parameter; a) raw data and b) scaled data. (Taken from Durbha et al.[85,239])

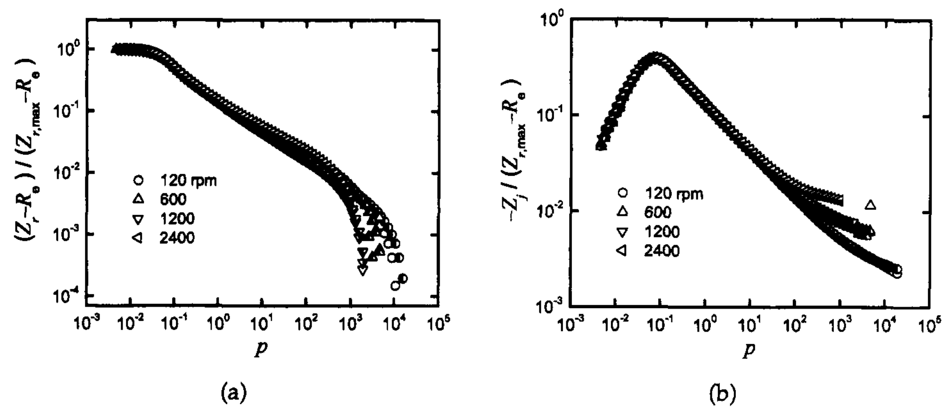

Figure 18.2: Impedance data from Figure 18.1 as a function of scaled frequency $p = \omega/\Omega$ for reduction of ferricyanide on a rotating Pt disk electrode; a) the real part of the impedance and b) the imaginary part of the impedance.

scaled by the zero frequency asymptotic value for the real part of the impedance, as seen in Figure 18.1(b). The superposition of impedance spectra is striking, but, in itself, does not constitute a proof that the impedance data were controlled by mass transfer. Scaled plots of impedance such as shown in Figure 18.1(b) provide, however, a useful means of identifying systems where the impedance has changed but the underlying physical phenomena are unchanged.

A more direct evaluation of the role of mass transfer is obtained by plotting the scaled impedance values as a function of dimensionless frequency $p = \omega/\Omega$, which is scaled by the rotation speed. The real and imaginary parts of the scaled impedance, shown in Figures 18.2(a) and (b), respectively, are superposed at low frequencies. Thus, the impedance values are, at low frequencies, controlled by convective mass transfer to the rotating disk. Differences are seen at higher frequencies that can be attributed to electrode kinetics.

18.1.2 Asymptotic Behavior at Low-Frequency

A graphical method was reported by Tribollet et al. that can be used to extract Schmidt numbers from experimental data in which the convective-diffusion impedance dominates.[135] The technique accounts for the finite value of the Schmidt

---

Remember! 18.1 *Scaled plots of impedance provide a useful means of identifying systems where the impedance has changed but the underlying physical phenomena are unchanged.*

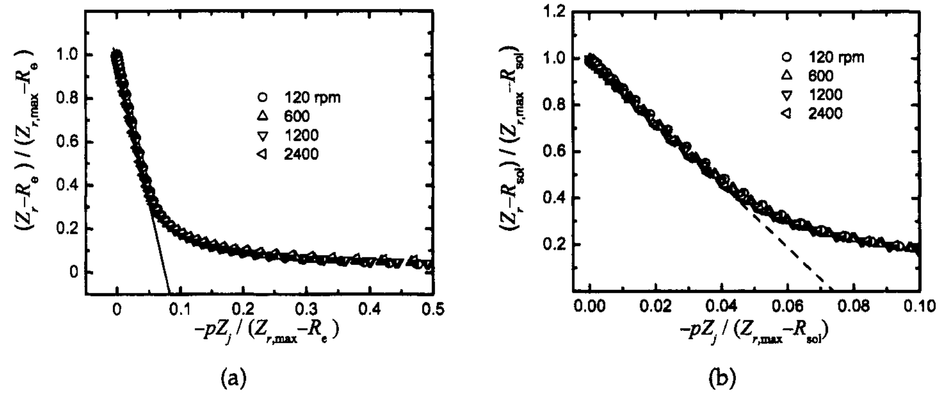

Figure 18.3: Illustration of the use of the method described by Tribollet et al.[135] to extract the Schmidt number from the low-frequency portion of the scaled measurement. Impedance data were taken from Figure 18.1: a) scale showing the approach to linearity as frequency tends toward zero; and b) regression of the linear portion of the plot shown in part a. The slope of the line was −13.52, resulting in a Schmidt number equal to 1,091.

number. The concept is based on the observation that

$$\lim_{p\to 0}\left(\frac{d\,\mathrm{Re}\{Z\}}{dp\,\mathrm{Im}\{Z\}}\right)=\lim_{p\to 0}\left(\frac{d\,\mathrm{Re}\left\{-\frac{1}{\theta_i'(0)}\right\}}{dp\,\mathrm{Im}\left\{-\frac{1}{\theta_i'(0)}\right\}}\right)=\lambda\,\mathrm{Sc}^{1/3}=s \qquad (18.1)$$

Thus, the quantity $\lambda\mathrm{Sc}^{1/3}$ may be obtained by plotting $\mathrm{Re}\{Z\}$ as a function of $p\,\mathrm{Im}\{Z\}$, and the straight line of slope $s=\lambda\mathrm{Sc}^{1/3}$ is fitted to the low frequency data. The constant λ was obtained taking into account the above development.

$$\lambda=\lim_{p\to 0}\left(\frac{d\,\mathrm{Re}\left\{-\frac{1}{\theta_i'(0)}\right\}}{dp\,\mathrm{Sc}^{1/3}\mathrm{Im}\left\{-\frac{1}{\theta_i'(0)}\right\}}\right)=1.2261+0.84\mathrm{Sc}^{-1/3}+0.63\mathrm{Sc}^{-2/3} \qquad (18.2)$$

The value of the Schmidt number is then obtained by solving the equation

$$1.2261\mathrm{Sc}^{2/3}+(0.84-s)\,\mathrm{Sc}^{1/3}+0.63=0 \qquad (18.3)$$

This approach is attractive because $d\,\mathrm{Re}\,\{Z\}/dp\,\mathrm{Im}\,\{Z\}$ is constant over a substantial frequency range.

An illustration of the asymptotic technique is presented in Figure 18.3 for the data presented in Figure 18.1(a). The scale presented in Figure 18.3(a) shows the approach to linearity as frequency tends toward zero. The data collected at different rotation speeds are superposed in Figure 18.3(a). Regression of the linear portion of the plot, shown in Figure 18.3(b), yields a slope of −13.52. Solution of equation (18.3) yields a Schmidt number equal to 1,091, in good agreement with the expected value of 1,100 for this system.

Regression of a process model for this system, reported by Orazem et al.,[85] yielded values for the Schmidt number that appeared to be a function of rotation speed. While the value obtained at 120 rpm of 1,114 was in good agreement with the value obtained by use of the low-frequency asymptotic relation, much larger values were obtained at higher rotation speeds. A regressed value of 1,222, for example, was reported for a rotation speed of 2,400 rpm. The superposition, at low frequencies, of data collected at all rotation speeds in Figure 18.3(a) suggests that the process model used by Orazem et al. did not account properly for a phenomenon evident at higher frequencies and that errors in fitting data at higher frequencies were propagated to lower frequencies in the form of an incorrect assessment of Schmidt number. The use of the asymptotic method can complement development of complete process models.

18.2 Reaction Kinetics: Arrhenius Relations

Systems that are governed by reaction kinetics show well-defined behaviors as a function of temperature and potential. If the system can be described as being controlled by a single activation-energy-controlled process, graphical methods can be used to cause the data to superpose.

The excitation of electrons in semiconducting systems, as described in Chapter 12, follows an Arrhenius temperature dependence, e.g.,

$$k = k_0 \exp\left(\frac{-\Delta E}{RT}\right) \tag{18.4}$$

where k_0 is a constant. As $R_t \propto 1/k_0$, for a system showing a single potential-dependent reaction, the charge-transfer resistance can be expected to follow

$$R_t = R_t^\circ \exp\left(\frac{\Delta E}{RT}\right) \tag{18.5}$$

Under the assumption that the capacitance is independent of temperature, the characteristic time constant for the system should follow the same Arrhenius temperature dependence, i.e.,

$$\tau_{RC} = \tau_{RC}^\circ \exp\left(\frac{\Delta E}{RT}\right) \tag{18.6}$$

Impedance data taken at different temperatures for systems governed by single-step activation-energy-controlled processes may be expected to superpose when properly normalized.

Graphical techniques based on application of an Arrhenius relationship are illustrated here for an *n*-GaAs single crystal diode with a Ti Schottky contact and a Au, Ge, Ni Schottky contact at the eutectic composition. This material has been well characterized in the literature and, in particular, has a well-known EL2 deep-level state that lies 0.83 to 0.85 eV below the conduction band edge.[156] Experimental details are provided by Jansen et al.[172,240]

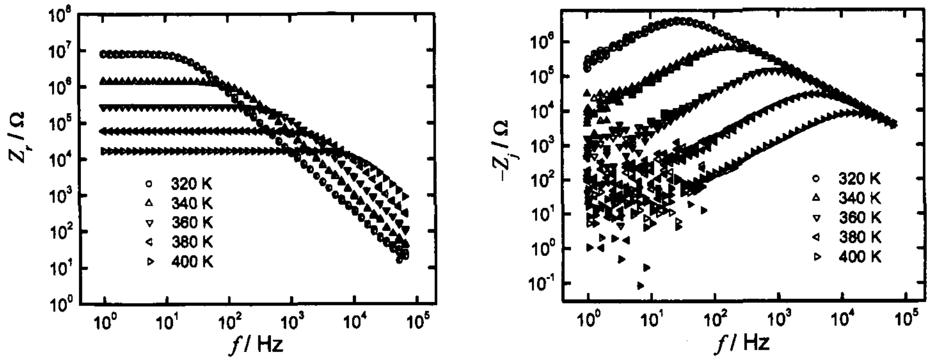

(a) (b)

Figure 18.4: Impedance data as a function of frequency for an *n*-GaAs/Ti Schottky diode with temperature as a parameter: a) the real part of impedance; and b) the imaginary part of impedance. (Taken from Jansen et al.[172])

The experimental data are presented in Figures 18.4(a) and (b) for the real and imaginary parts of the impedance, respectively, for data collected at temperatures ranging from 320 to 400 K. The logarithmic scale used emphasizes the scatter seen in the imaginary impedance at low frequencies. The impedance response is seen to be a strong function of temperature. The impedance plane plots shown in Figure 18.5, for data collected at 320 and 340 K, show the classic semicircle associated with a single relaxation process.

The reduced presentation of the data given in Figure 18.6 shows that the impedance response is dominated by a single relaxation process with an activation energy near 0.83 eV. The impedance data collected at different temperatures were normalized by the maximum mean value of the real part of the impedance and plotted against a normalized frequency defined by

$$f^* = \frac{f \exp\left(\frac{E}{kT}\right)}{f^\circ} \tag{18.7}$$

where E was given a value of 0.827 eV, and the characteristic frequency f° was given a value of 2.964×10^{14} Hz such that the imaginary part of the normalized impedance values reached a peak value near $f^* = 1$. The data collected at different temperatures are reduced to a single line. The extent to which the data are superposed is seen more clearly on the logarithmic scale shown in Figure 18.7.

Remember! 18.2 *Reduced presentation of impedance data in terms of scaled frequency (given, e.g., in Figures 18.2 and 18.6) provides verification of the origin of the impedance response.*

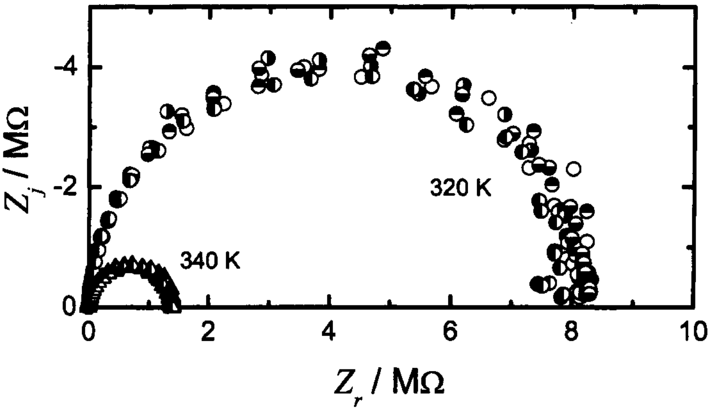

Figure 18.5: Impedance data in impedance-plane format for an n-GaAs/Ti Schottky diode with temperature as a parameter. (Taken from Jansen et al.[172])

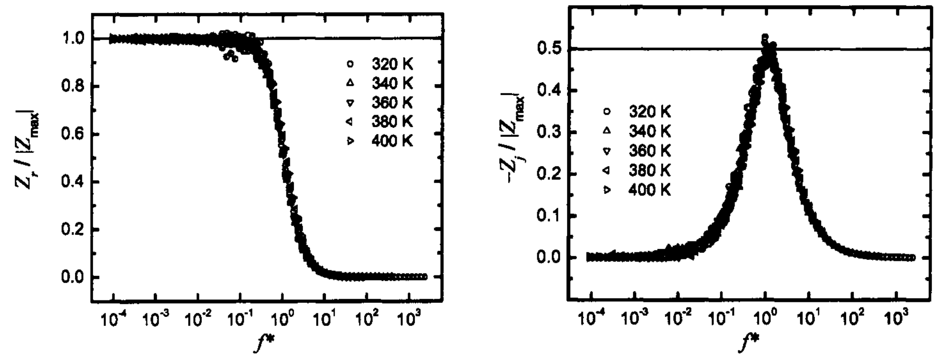

(a) (b)

Figure 18.6: Impedance data from Figure 18.4 collected for an n-GaAs/Ti Schottky diode as a function of frequency $f^* = \frac{f}{f_0}\exp(E/kT)$: a) real part of impedance; and b) imaginary part of impedance. (Taken from Orazem and Tribollet[241] and reproduced with permission of Elsevier, Inc.)

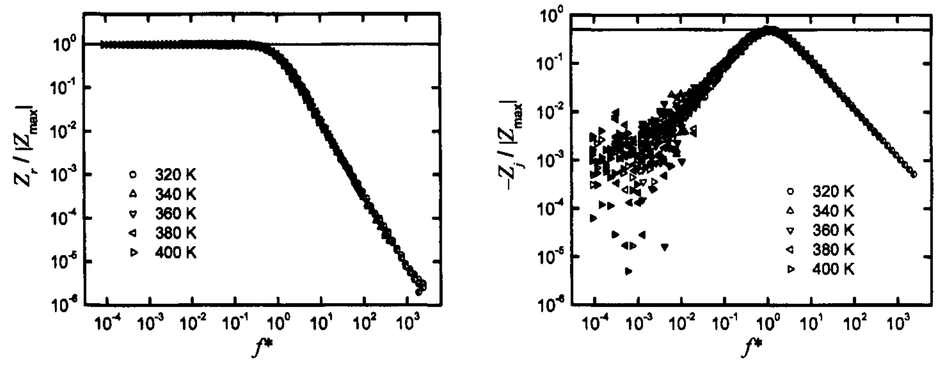

(a) (b)

Figure 18.7: Impedance data from Figure 18.4 collected for an n-GaAs/Ti Schottky diode as a function of frequency $f^* = \frac{f}{f_0}\exp\left(E/kT\right)$: a) real part of impedance; and b) imaginary part of impedance. (Taken from Orazem and Tribollet[241] and reproduced with permission of Elsevier, Inc.)

It is worth noting that, while the data do superpose nicely in Figures 18.6 and 18.7, the impedance data do in fact contain information on minor activation-energy-controlled electronic transitions.[172,240] The information concerning these transitions can be extracted by regression of an appropriate process model using a weighting strategy based on the error structure of the measurement.

18.3 Mott-Schottky Plots

Graphical techniques can be applied for single-frequency measurements when the frequency selected excludes the contributions of confounding phenomena. For example, impedance measurements on a semiconductor diode at a sufficiently high frequency exclude the influence of leakage currents and of electronic transitions between deep-level and band-edge states. Thus, the capacitance can be extracted from the imaginary part of the impedance as

$$C = \frac{1}{\omega Z_j} \tag{18.8}$$

The problem is reduced to one of identifying the relationship between semiconductor properties and the capacitance as a function of applied potential. The mathematical development is presented in Section 12.3.2.

Mott-Shottky plots of $1/C^2$ as a function of potential are particularly useful at larger doping levels. As seen in Figure 12.10(a), $1/C^2$ is linear over a broad range of potential. The slope of $1/C^2$ with respect to potential is negative for an n-type semiconductor and positive for a p-type semiconductor. The linear portion is given by equation (12.39) for an n-type semiconductor and by equation (12.40) for a p-type semiconductor.

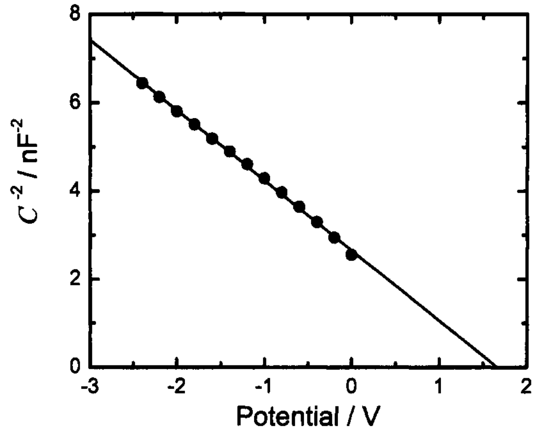

Figure 18.8: Mott-Schottky plot for an n-GaAs/Ti Schottky diode: $1/C^2$ as a function of applied potential.[242]

An example of the use of Mott-Schottky plots is presented in Figure 18.8. The capacitance was measured at a frequency of 1 MHz applied across the semiconductor sample described in Figure 18.4 as a function of reverse bias with a DLTS spectrometer.[242] Deep-level states are not expected to influence the signal at such a high frequency; thus, the slope can be interpreted in terms of the doping level.

Deviations from straight lines in Mott-Schottky plots are frequently attributed to the influence of potential dependent charging of surface or bulk states. While deviations can also be attributed to nonuniform dopant concentrations, this interpretation is supported by analytic and numerical calculations of the contribution of defects to the space charge as a function of applied potential (see, e.g., Dean and Stimming[180] or Bonham and Orazem[167]).

Remember! 18.3 *Deviations from ideal behavior can give important clues to the physical phenomena governing an experimental system.*

Table 18.1: Experimental diffusion impedance data obtained at a rotation speed of 600 rpm.

f/Hz	$Z_r/\Omega\text{cm}^2$	$Z_j/\Omega\text{cm}^2$	f/Hz	$Z_r/\Omega\text{cm}^2$	$Z_j/\Omega\text{cm}^2$
0.07942	997.9	−65.1	3.16	309	−273
0.1	992.2	−85.2	3.98	270.6	−253.7
0.1258	991	−97.8	5.02	239	−259.2
0.1584	973	−118	6.3	208.6	−197.9
0.1996	967	−149	7.94	188.8	−179.1
0.2512	940	−190	10	165.2	−159.1
0.316	920	−231	12.58	147.3	−141.6
0.398	882	−263	15.84	131.9	−126.4
0.502	831	−320	19.94	116.3	−112.8
0.63	764	−324.6	25.12	103.7	−100.4
0.794	692	−347	31.624	91.9	−89.04
1	613	−354	39.812	82.3	−79.43
1.258	544	−342	50.12	73.14	−70.85
1.584	470	−348	79.43	59.7	−57.6
1.994	409	−328	100	52.11	−50.11
2.52	356	−303			

Problems

18.1 The value of the Schmidt number may be used to determine which species participate in an electrochemical reaction. Estimate the value for the Schmidt number that could be expected to be determined by impedance measurements at 25 °C for the system 0.01 M $K_3Fe(CN)_6$, 0.01 M $K_4Fe(CN)_6$, 1 M KCl:

- **(a)** At the open circuit potential
- **(b)** At the cathodic mass-transfer-limited current
- **(c)** At the anodic mass-transfer-limited current

18.2 The experimental diffusion impedance data presented in Table 18.1 were obtained at a rotation speed of 600 rpm. Find the numerical value of the Schmidt number by using equation (18.3).

18.3 For simple reactions, the charge-transfer resistance may be given as a function of potential by equation (10.10). Develop a means of superposing impedance data taken at different potentials for such a system where the impedance response is given by equation (10.25).

18.4 Show how a linear dependence of capacitance on potential would influence the superposition developed in Problem 18.3.

Electrochemical Impedance Spectroscopy
by Mark E. Orazem and Bernard Tribollet

Chapter 19

Complex Nonlinear Regression

Complex nonlinear least-squares (CNLS) regression techniques, with application to impedance measurements, were developed in the late 1960s.[42–44] The CNLS approach provides a significant improvement over ordinary nonlinear least-squares (NLS) because a common set of parameters can be estimated by simultaneous regression of the model to both real and imaginary data.[243] Since the Kramers-Kronig relations constrain the real and imaginary parts of the complex quantity, the appropriate regression strategy should allow for the correlation of the real and imaginary parts of the complex model through the Kramers-Kronig relations. This chapter provides an overview of issues associated with regression. For a more detailed discussion of the mechanics of the regression techniques, the reader is referred to standard textbooks.[82,244–247] The discussion by Press et al.[248] is also helpful.

19.1 Concept

Macdonald provides a perspective on historical trends in the application of regression techniques to impedance spectroscopy.[3,4] The regression of models to impedance data generally employs a complex nonlinear application of the method of least squares.[249–251] Complex nonlinear least-squares regression techniques were developed in the late 1960s as an extension of nonlinear least squares (NLS) regression techniques.[42,43] The use of CNLS is consistent with the expectation that real and imaginary components of impedance data satisfy the constraints of the Kramers-Kronig relations.[53,54,252] The CNLS approach provides an improvement over NLS techniques because a combined model parameter set is estimated by simultaneous regression of the model to both real and imaginary parts of the measured spectrum. Weighted CNLS was first applied to impedance data by Macdonald et al.[44,45] The concept of weighting is critical for impedance spectroscopy because the impedance is a strong function of frequency.[253,240]

The regression of a complex function $\hat{Z}$ to complex data Z can be expressed in a least-squares sense as the minimization of the sum of squares

$$S = \left(Z - \hat{Z}(\omega|\mathbf{P})\right)^T \mathbf{V}^{-1} \left(Z - \hat{Z}(\omega|\mathbf{P})\right) \tag{19.1}$$

where $\mathbf{V}$ is a symmetric positive-definite variance-covariance matrix of the experimental stochastic errors, Z represents the complex impedance data measured at frequencies ω, and $\hat{Z}(\omega|\mathbf{P})$ represents the complex model calculated for frequency ω as a function of a parameter vector $\mathbf{P}$.[245,247] Under the assumption that the covariance terms in $\mathbf{V}$ can be neglected, i.e., that $\mathbf{V}$ is a diagonal matrix, and under the additional assumption that residual errors are uncorrelated, equation (19.1) can be replaced by

$$S = \sum_{k=1}^{N_{\mathrm{dat}}} \left[\frac{\left(Z_r(\omega_k) - \hat{Z}_r(\omega_k|\mathbf{P})\right)^2}{V_{r,k}} + \frac{\left(Z_j(\omega_k) - \hat{Z}_j(\omega_k|\mathbf{P})\right)^2}{V_{j,k}} \right] \tag{19.2}$$

where N_{dat} represents the number of measured values, $V_{r,k}$ and $V_{j,k}$ represent the real and imaginary components, respectively, of the variance of the stochastic errors, $Z_r(\omega_k)$ and $Z_j(\omega_k)$ represent the real and imaginary parts of the impedance data measured at frequency ω_k, and $\hat{Z}_r(\omega_k|\mathbf{P})$ and $\hat{Z}_j(\omega_k|\mathbf{P})$ represent the real and imaginary parts of the model value calculated for frequency ω_k as a function of a parameter vector $\mathbf{P}$.

The statement that the covariance terms in $\mathbf{V}$ can be neglected implies both that stochastic errors at one frequency are uncorrelated with errors at another frequency and that errors in real and imaginary parts of the impedance at a given frequency are not correlated. Use of equation (19.2) is therefore predicated on the assumption that errors in real and imaginary parts of the impedance are not correlated. If equation (19.2) is used under conditions where the error covariance terms cannot be neglected, the incorrect error structure will be reflected in the parameter estimates. Carson et al.[254] used numerical simulations to show that, when a Frequency Response Analyzer algorithm was used to obtain the impedance response from time-domain signals containing normally distributed errors, the real and imaginary parts of the impedance were uncorrelated. In contrast, use of a phase-sensitive-detection algorithm yielded correlation between real and imaginary components of the impedance.[255]

Remember! 19.1 *The weighting used for nonlinear regression employs an estimate for the variance of the data. As the variance of impedance data is strongly dependent on frequency, an independent assessment of the error structure is needed.*

19.2 Objective Functions

The regression procedure involves minimization of equation (19.2), which can be expressed as

$$S(\mathbf{P}) = \sum_{k=1}^{N_{\text{dat}}} \frac{\left(Z_r(f_k) - \hat{Z}_r(f_k|\mathbf{P})\right)^2}{\sigma_{r,k}^2} + \sum_{k=1}^{N_{\text{dat}}} \frac{\left(Z_j(f_k) - \hat{Z}_j(f_k|\mathbf{P})\right)^2}{\sigma_{j,k}^2} \tag{19.3}$$

where the minimized value of $S(\mathbf{P})$ can be regarded to be the χ^2 statistic. An objective function of this type has the attractive feature of emphasizing data for which the confidence is high and deemphasizing data for which the confidence is low. Methods to assess the variance of the measurement are discussed in Chapter 21.

The objective function, equation (19.3), is presented in Figure 19.1(a) for an RC circuit as a function of parallel resistor and RC-time-constant values. The circuit parameters were $R = 1\ \Omega\text{cm}^2$, and $\tau_{RC} = 1$ s (see, e.g., Figure 4.3(b) and the corresponding Example 4.2). The synthetic data were calculated for frequencies ranging from 1 to 10^5 Hz at a spacing of 10 points per decade, and the noise was determined by machine precision.

The objective of the regression procedure is to identify the parameter values that minimize equation (19.3). The objective function, given as a response surface in Figure 19.1(a), was found to be equal to zero at the set parameter values. Solid lines have been drawn on the bottom contour map to indicate the values for which the function is minimized.

Several features of the optimization problem are apparent in Figure 19.1(a). The model is nonlinear with respect to parameters; nevertheless, the objective function is well behaved near the solution where it can be approximated by a quadratic function. The contours projected onto the base of the plot have an elliptical shape. The major axis of the ellipse does not lie along either axis.

Each of the function-minimization procedures involves some assessment of the objective function contour in parameter space. This contour is easily visualized in three dimensions, as shown in Figure 19.1(a), but the large number of adjustable parameters used in typical regressions makes graphical visualization cumbersome if not impossible. Numerical methods, such as those described in this chapter, are therefore required.

Example 19.1 Nonlinear Models: *Show that the equation for the impedance of a Voigt element is nonlinear with respect to parameters.*

Solution: *The impedance of a Voigt element can be given as*

$$Z(\omega) = R_0 + \sum_{k}^{K} \frac{R_k}{1 + j\omega\tau_k} \tag{19.4}$$

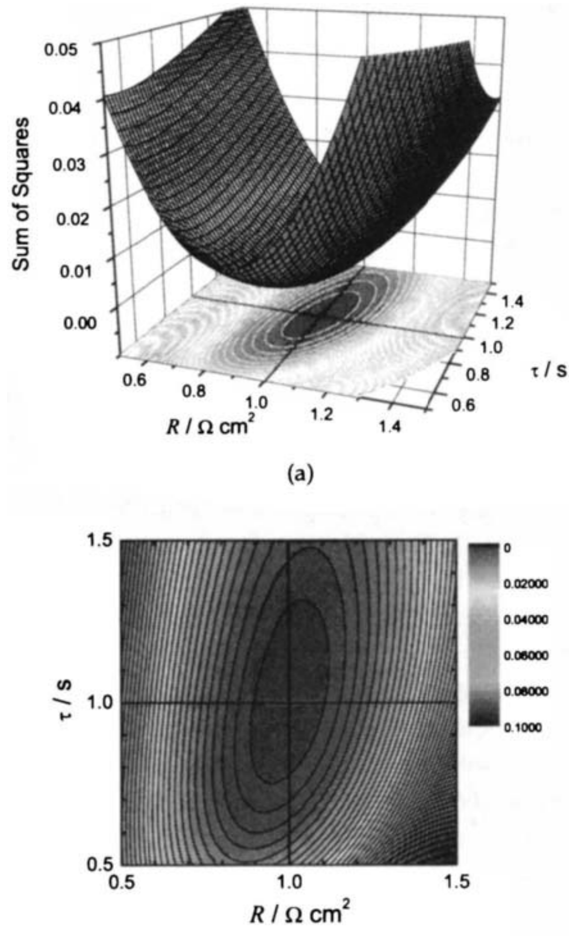

(a)

(b)

Figure 19.1: The objective function, equation (19.3), for an RC circuit as a function of parallel resistor and capacitor values. The circuit parameters were $R_1 = 1\ \Omega$, and $\tau_1 = 1$ s. The synthetic data were calculated for frequencies ranging from 1 to 10^5 Hz at a spacing of 10 points per decade, and the noise was determined by machine precision. The objective function at the set parameter values was found to be equal to zero: a) 3-D perspective drawing of the contour surface; b) 2-D representation of the contour surface.

Calculate first and second derivatives with respect to parameters.

$$\frac{\partial Z}{\partial R_0} = 1; \qquad \frac{\partial^2 Z}{\partial R_0^2} = 0 \tag{19.5}$$

$$\frac{\partial Z}{\partial R_k} = \frac{1}{1+j\omega\tau_k}; \qquad \frac{\partial^2 Z}{\partial R_k^2} = 0 \tag{19.6}$$

$$\frac{\partial Z}{\partial \tau_k} = -\frac{jR_k\omega}{(1+j\omega\tau_k)^2}; \qquad \frac{\partial^2 Z}{\partial \tau_k^2} = -\frac{2R_k\omega^2}{(1+j\omega\tau_k)^3} \tag{19.7}$$

The second derivatives of Z with respect to R_0 and R_k are equal to zero; thus, Z is linear with respect to the resistance parameters. The second derivatives of Z with respect to τ_k are not equal to zero; thus, Z is nonlinear with respect to the time constant τ_k.

19.3 Formalism of Regression Strategies

The nonlinear regression techniques discussed in Section 19.3.2 are extensions of the linear regression formalism described below. A more detailed description is provided by Press et al.[256]

19.3.1 Linear Regression

Consider a general model of the form

$$y(x) = \sum_{k=1}^{N_p} P_k X_k(x) \tag{19.8}$$

where $X_k(x)$ are arbitrary fixed functions of x called the *basis functions* and N_p represents the number of adjustable parameters P_k in the model. Equation (19.8) is linear with respect to parameters P_k even if $X_k(x)$ are nonlinear with respect to x.

A least-squares regression involves minimization of the objective function

$$\chi^2 = S(\mathbf{P}) = \sum_{i=1}^{N_{\text{dat}}} \frac{\left(y_i - \sum_{k=1}^{N_p} P_k X_k(x_i)\right)^2}{\sigma_i^2} \tag{19.9}$$

where y_i represents the measured values and σ_i represents the standard deviation of measurement i. At the minimum value, the derivative with respect to the parameters P_k vanishes. Thus,

$$\sum_{i=1}^{N_{\text{dat}}} \frac{\left(y_i - \sum_{j=1}^{N_p} P_j X_j(x_i)\right)}{\sigma_i^2} X_k(x_i) = 0 \tag{19.10}$$

Equation (19.10) represents a set of N_p equations of the form

$$\sum_{j}^{N_p} \alpha_{k,j} P_j = \beta_k \tag{19.11}$$

where

$$\beta_k = \sum_{i=1}^{N_{\text{dat}}} \frac{(y_i X_k(x_i))}{\sigma_i^2} \tag{19.12}$$

and

$$\alpha_{k,j} = \sum_{i=1}^{N_{\text{dat}}} \frac{(X_k(x_i) X_j(x_i))}{\sigma_i^2} \tag{19.13}$$

In vector form, equation (19.11) can be written

$$\boldsymbol{\alpha} \cdot \mathbf{P} = \boldsymbol{\beta} \tag{19.14}$$

or

$$\begin{aligned} \mathbf{P} &= \boldsymbol{\alpha}^{-1} \cdot \boldsymbol{\beta} \\ &= \mathbf{C} \cdot \boldsymbol{\beta} \end{aligned} \tag{19.15}$$

The inverse matrix $\mathbf{C} = \boldsymbol{\alpha}^{-1}$ provides an estimate for the confidence intervals for the estimated parameters. The diagonal elements of $[\mathbf{C}]$ are the variances of the fitted parameters, i.e.,

$$\sigma_{P_j}^2 = C_{j,j} \tag{19.16}$$

The off-diagonal elements of $\mathbf{C}$, $C_{j,k}$, are the covariances between parameters P_j and P_k, which show the extent of correlation among parameters. This correlation is undesirable for a regression. It can appear when too many parameters are being sought in the regression, but correlation among parameters may sometimes be unavoidable due to the structure of the model.

19.3.2 Nonlinear Regression

Consider a general function $f(\mathbf{P}) = 0$ that is nonlinear with respect to parameters P_k. Under the assumption that $f(\mathbf{P})$ is twice continuously differentiable, a Taylor-series expansion about a parameter set $\mathbf{P}_0$ yields

$$f(\mathbf{P}) = f(\mathbf{P}_0) + \sum_j^{N_p} \left.\frac{\partial f}{\partial P_j}\right|_{\mathbf{P}_0} \Delta P_j + \frac{1}{2} \sum_j^{N_p} \sum_k^{N_p} \left.\frac{\partial^2 f}{\partial P_j \partial P_k}\right|_{\mathbf{P}_0} \Delta P_j \Delta P_k + \ldots \tag{19.17}$$

Equation (19.17) is second order with respect to parameter increments ΔP_j and therefore describes a parabolic hypersurface. The assumption that, in the neighborhood of the minimum, the objective function can be described as a parabolic hypersurface, is supported by the results presented in Figure 19.1.

The optimal value for $\mathbf{P}$ is found when $f(\mathbf{P})$ has a minimum value. At the minimum, derivatives with respect to the parameter increments ΔP_i should be equal to zero; thus,

$$\frac{\partial f}{\partial \Delta P_j} = \left.\frac{\partial f}{\partial P_j}\right|_{\mathbf{P}_0} + \sum_k^{N_p} \left.\frac{\partial^2 f}{\partial P_j \partial P_k}\right|_{\mathbf{P}_0} \Delta P_k = 0 \tag{19.18}$$

Equation (19.18) represents a set of N_p equations of the form

$$\beta_j = \sum_k^{N_p} \alpha_{j,k} \Delta P_k \tag{19.19}$$

where

$$\beta_j = -\frac{1}{2} \left. \frac{\partial f}{\partial P_j} \right|_{\mathbf{P}_0} \tag{19.20}$$

and

$$\alpha_{j,k} = \frac{1}{2} \left. \frac{\partial^2 f}{\partial P_j \partial P_k} \right|_{\mathbf{P}_0} \tag{19.21}$$

where $\boldsymbol{\alpha}$ and $\boldsymbol{\beta}$ are generally functions of parameters $\mathbf{P}$. In vector form, equation (19.19) can be written

$$\boldsymbol{\beta} = \boldsymbol{\alpha} \cdot \Delta \boldsymbol{P} \tag{19.22}$$

or

$$\begin{aligned} \Delta \boldsymbol{P} &= \boldsymbol{\alpha}^{-1} \cdot \boldsymbol{\beta} \\ &= \mathbf{C} \cdot \boldsymbol{\beta} \end{aligned} \tag{19.23}$$

The general formulation described above can now be applied to the nonlinear least-squares problem.

A least-squares regression involves minimization of the objective function

$$\chi^2 = \sum_{i=1}^{N_{\text{dat}}} \frac{\left(Z_i - \hat{Z}(x_i|\mathbf{P})\right)^2}{\sigma_i^2} \tag{19.24}$$

where Z_i represents the measured values, $\hat{Z}(x_i|\mathbf{P})$ represents the model, which now may be nonlinear with respect to the parameter vector $\mathbf{P}$, and σ_i represents the standard deviation of measurement i. Under the understanding that the function f to be minimized is given by equation (19.24), the gradient of the objective function with respect to parameters $\mathbf{P}$ is given by

$$\frac{\partial \chi^2}{\partial P_k} = -2 \sum_i^{N_{dat}} \frac{\left(Z_i - \hat{Z}(x_i|\mathbf{P})\right)}{\sigma_i^2} \frac{\partial \hat{Z}(x_i|\mathbf{P})}{\partial P_k} \tag{19.25}$$

or

$$\beta_k = \sum_i^{N_{dat}} \frac{\left(Z_i - \hat{Z}(x_i|\mathbf{P})\right)}{\sigma_i^2} \frac{\partial \hat{Z}(x_i|\mathbf{P})}{\partial P_k} \tag{19.26}$$

The components of equation (19.25) can be written in vector form as $\nabla \chi^2(\mathbf{P}_0)$.

The second derivative of the objective function with respect to the parameters **P** is given by

$$\left.\frac{\partial^2\chi^2}{\partial P_j \partial P_k}\right|_{\mathbf{P}_0} = \tag{19.27}$$
$$2\sum_{i=1}^{N_{dat}} \frac{1}{\sigma_i^2}\left[\frac{\partial \hat{Z}(x_i|\mathbf{P})}{\partial P_j}\frac{\partial \hat{Z}(x_i|\mathbf{P})}{\partial P_k} - \left(Z_k - \hat{Z}(x_i|\mathbf{P})\right)\frac{\partial^2 \hat{Z}(x_i|\mathbf{P})}{\partial P_j \partial P_k}\right]$$

or $\nabla^2\chi^2(\mathbf{P}_0)$. Equation (19.27) is called the *Hessian* matrix, which involves both first and second derivatives of the model with respect to parameters. The matrix $\boldsymbol{\alpha}$ is equal to one-half of the Hessian matrix, i.e.,

$$\alpha_{j,k} = \sum_{i=1}^{N_{dat}} \frac{1}{\sigma_i^2}\left[\frac{\partial \hat{Z}(x_i|\mathbf{P})}{\partial P_j}\frac{\partial \hat{Z}(x_i|\mathbf{P})}{\partial P_k} - \left(Z_k - \hat{Z}(x_i|\mathbf{P})\right)\frac{\partial^2 \hat{Z}(x_i|\mathbf{P})}{\partial P_j \partial P_k}\right] \tag{19.28}$$

The second derivatives of the Hessian matrix are typically neglected in evaluation of equation (19.28), an action that is justified on two grounds. The first justification is that second derivatives are often small as compared to the first derivatives. For a linear problem, the second derivatives are identically equal to zero. The second justification is that the term is multiplied by $(y_k - y(x_i|\mathbf{P}))$, a term that, for a successful regression, should be uncorrelated with respect to x_i or to the model $y(x_i|\mathbf{P})$. Thus, the second derivative terms should tend to cancel when summed over all observations i. Accordingly,

$$\alpha_{j,k} \approx \sum_{i=1}^{N_{dat}} \frac{1}{\sigma_i^2}\left[\frac{\partial \hat{Z}(x_i|\mathbf{P})}{\partial P_j}\frac{\partial \hat{Z}(x_i|\mathbf{P})}{\partial P_k}\right] \tag{19.29}$$

is used in the nonlinear regression algorithms described in Section 19.4.

Equations (19.24) to (19.29) can be applied for complex nonlinear least-squares regression by concatenating the real and imaginary impedance data Z_i to form a data vector with length equal to twice the number of measured frequencies. A similar concatenation applies for the model values $\hat{Z}(x_i|\mathbf{P})$. Press et al.[256] provide a very approachable discussion of the least-squares methods and their implementation.

19.4 Regression Strategies for Nonlinear Problems

Some common regression strategies are summarized in this section. For a more detailed discussion, the reader is referred to standard textbooks.[82,244–247]

19.4.1 Gauss-Newton Method

The *Gauss-Newton Method* for solving the nonlinear set of equations (19.18) can be expressed as

$$\mathbf{P}_{j,\ell+1} = \mathbf{P}_{j,\ell} + \boldsymbol{\alpha}^{-1} \cdot \boldsymbol{\beta} \tag{19.30}$$

where ℓ is the interation counter, $\boldsymbol{\beta}$ is evaluated following equation (19.26), and $\boldsymbol{\alpha}$ is evaluated following equation (19.29). The Gauss-Newton Method is characterized by quadratic convergence near the solution, but convergence can be very slow far from the solution. Quadratic convergence has the characteristic that the number of significant digits in the solution doubles at every iteration. In some cases, the Gauss-Newton Method diverges and fails to yield a solution. Due to its extreme efficiency near the solution, the Gauss-Newton Method provides the basis for most methods of nonlinear optimization.

19.4.2 Method of Steepest Descent

The *Method of Steepest Descent* seeks a minimum value of the objective function by following the gradient of the objective function, i.e.,

$$\mathbf{P}_{j,\ell+1} = \mathbf{P}_{j,\ell} + \lambda\boldsymbol{\beta} \tag{19.31}$$

where $\boldsymbol{\beta}$ is evaluated following equation (19.26), and λ is a constant chosen to be sufficiently small as to avoid overrunning the minimum. A comparison of equations (19.30) and (19.31) shows that the matrix α in the Gauss-Newton Method modifies the Method of Steepest Descent by accounting for the curvature of the objective function surface. For this reason, α is called the *curvature matrix.*

The Method of Steepest Descent tends to be quite efficient far from the solution, but convergence can be painfully slow near the solution. Slow convergence is likely where the contours are attenuated and banana-shaped, i.e., where the method tends to change direction often with minimal changes in objective function value.

19.4.3 Levenberg-Marquardt Method

The *Levenberg-Marquardt Method* described in this section represents a compromise between the Gauss-Newton Method described in Section 19.4.1 and the Method of Steepest Descent described in Section 19.4.2. The Method of Steepest Descent is used far from the converged value, moving smoothly to the Gauss-Newton Method as the solution is approached.

The critical concepts encompassed by the Levenberg-Marquardt Method are the selection of the scaling factor for the Method of Steepest Descent and an approach for making a smooth transition from one method to the other. The curvature matrix α is replaced by α' such that

$$\begin{aligned} \alpha'_{jk} &= \alpha_{jk}(1+\lambda) && \text{for} \quad j = k \\ \alpha'_{jk} &= \alpha_{jk} && \text{for} \quad j \neq k \end{aligned} \tag{19.32}$$

The equation solved is

$$\mathbf{P}_{j,\ell+1} = \mathbf{P}_{j,\ell} + (\boldsymbol{\alpha}')^{-1} \cdot \boldsymbol{\beta} \tag{19.33}$$

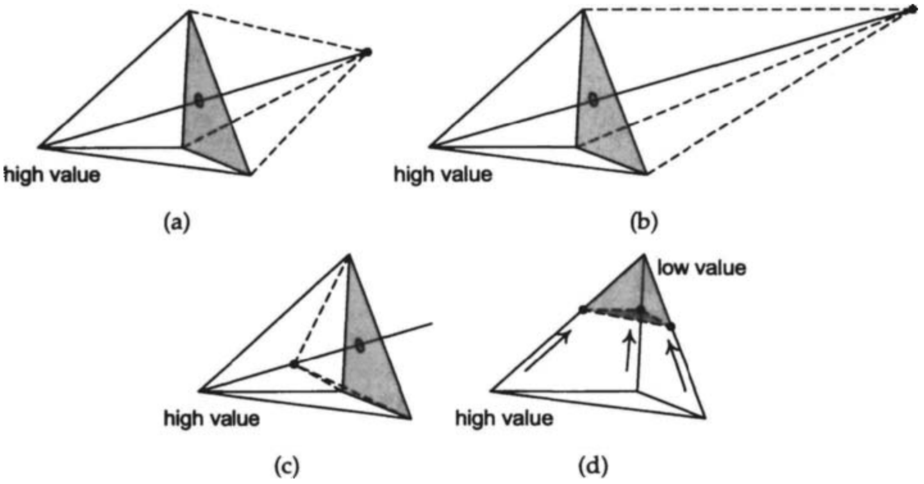

Figure 19.2: Schematic representation of the simplex algorithm. New points are denoted by closed circle •, and the vector mean of all except the highest value is denoted by an open circle ○: a) a reflection from the point with the highest value through the vector-mean of the remaining points; b) an expansion along the same line, taken if the resulting point yields a result that is lower than that seen at all other points; c) a contraction along the same line, taken if the reflection point yields a result that is worse than that seen at all other points; and d) a contraction among all dimensions toward the low point, taken if none of the actions taken yields a result that is better than than the highest value.

When λ is large, α' is diagonally dominant, and the method approaches that described in equation (19.31). When λ is small, the method approaches that described in equation (19.31).

19.4.4 Downhill Simplex Strategies

The *simplex* method requires evaluations only of the objective function to be minimized. It does not require evaluation of the derivatives and does not require inversion of a matrix that may have a zero determinant. The simplex method can therefore be more robust than the strategies described in Sections 19.4.1, 19.4.2, and 19.4.3.

A schematic representation of the downhill simplex algorithm is presented in Figure 19.2.

- The objective function is evaluated at $N + 1$ points in parameter space, where N is the number of adjustable parameters. The geometrical figure that is formed is called a *simplex*.

- The function is evaluated at the reflection of the point with highest value through the vector-average of opposing surface, as shown in Figure 19.2(a) for an optimization in three parameters. If the new point gives a result better than the highest value, but not better than the lowest value, the highest point is replaced with the new point. The reflections are designed such that the volume of the simplex is conserved.

- If the new point gives a result better than all other points, a further extrapolation is made along this line, as shown in Figure 19.2(b). Again, if the new point gives a result better than the highest value, but not better than the lowest value, the highest point is replaced with the new point.
- If the new point gives a result that is worse than the highest point, a contraction is performed along this line, as shown in Figure 19.2(c). If the new point gives a result better than the highest value, but not better than the lowest value, the highest point is replaced with the new point.
- If none of the actions taken yields a result that is better than the highest value, a contraction is performed among all dimensions toward the low point, as shown in Figure 19.2(d). The new simplex is shown as a shaded volume.

Convergence can be slow, especially if the minimum exists in a long narrow valley in parameter space. Press et al.[248] describe several more efficient multidimension optimization strategies.

19.5 Influence of Data Quality on Regression

Regression procedures can be sensitive to presence of singular or near-singular matrixes. In such cases, the normal set of equations does not have a unique solution, and *collinearity* is said to exist. A regression problem is called *ill-conditioned* if a small change in data causes large changes in estimates. Ill-conditioning is undesirable in regression analysis because it leads to unreliable parameter estimates with large variances and covariances.[247]

Regression problems in impedance spectroscopy may become ill-conditioned due to improper selection of measurement frequencies, excessive stochastic errors (noise) in the measured values, excessive bias errors in the measured values, and incomplete frequency ranges. The influences of stochastic errors and frequency range on regression are demonstrated by examples in this section. The issue of bias errors in impedance measurement is discussed in Chapter 22. The origin of stochastic errors in impedance measurements is presented in Chapter 21.

19.5.1 Presence of Stochastic Errors in Data

The regression procedure is strongly influenced by stochastic errors or noise in the measurement. One effect is illustrated in comparison of Figure 19.1 to Figure 19.3, in which stochastic noise with a standard deviation equal to 1 percent of the modulus was added to the synthetic data. Solid lines have been drawn on the bottom contour map to indicate the values for which the function is minimized. The presence of stochastic errors in the data does not introduce roughness in the parabolic

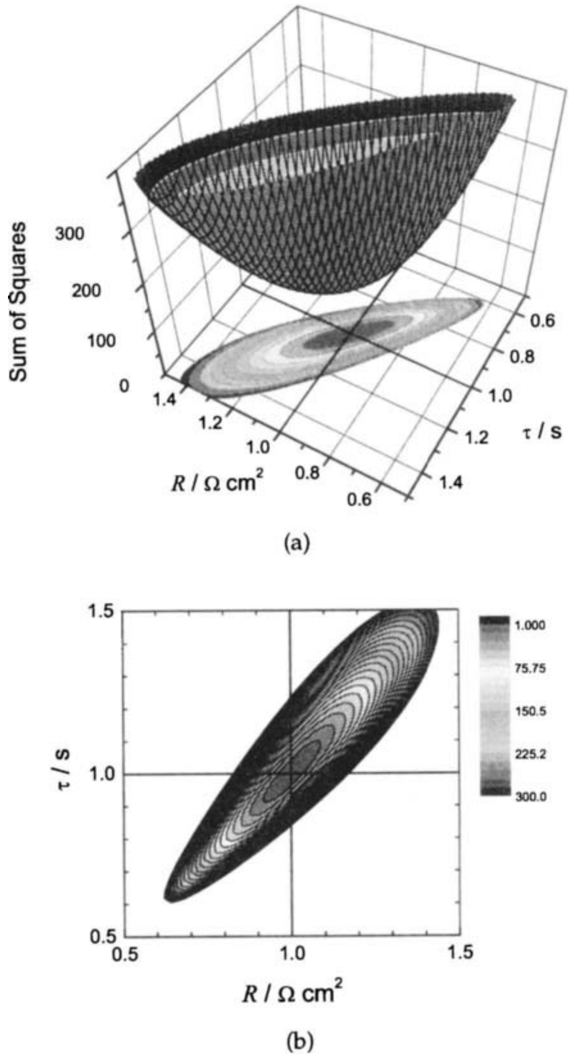

Figure 19.3: The objective function, equation (19.3), for an RC circuit as a function of parallel resistor and RC-time constant values. The circuit was the same as presented in Figure 19.1 with the exception that stochastic noise was added to the synthetic data with a standard deviation equal to 1 percent of the modulus. a) 3-D perspective drawing of the contour surface; b) 2-D representation of the contour surface.

hypersurface, which is a function of parameter. The noise has the effect of increasing the value of the minimum that can be found from zero to a number typically larger than the degree of freedom of the problem. The hypersurface presented in Figure 19.3 has been scaled by the number of data points, and has a minimum value between 1 and 2. The parabolic shape of the surface is more apparent and the approach to the minimum has a steeper slope, as is evident in change in scale from 0 to 0.1 in Figure 19.1(b) to 1 to 300 in Figure 19.3(b).

19.5.2 Ill-Conditioned Regression Caused by Stochastic Noise

The presence of stochastic errors can impede sensitivity to minor parameters. The response surface for a Voigt circuit with $R_0 = 1\ \Omega\text{cm}^2$, $R_1 = 100\ \Omega\text{cm}^2$, $\tau_1 = 0.001$ s, $R_2 = 200\ \Omega\text{cm}^2$, $\tau_2 = 0.01$ s, $R_3 = 5\ \Omega\text{cm}^2$, and $\tau_3 = 0.05$ s is presented in Figure 19.4(a) as a function of $\log_{10}(R_3)$ and $\log_{10}(\tau_3)$. The synthetic impedance data were calculated for frequencies from 1 to 10^5 Hz at a spacing of 10 measurements per decade. The response surface is presented as a function of logarithm of parameters to extend the range of parameters seen.

Even though the line-shape corresponding to R_3 and τ_3 is not discernible from the impedance data shown in Figure 19.5, a minimum in the objective function for noise-free data is seen clearly in Figure 19.4(a). Thus, values for R_3 and τ_3 could be obtained by regression to noise-free data.

Addition of stochastic noise with standard deviation equal to 1 percent of the modulus (see symbols in Figure 19.5) is sufficient to obscure the effect of R_3 and τ_3 in the impedance data. A broad minimum is seen in Figure 19.4(b). Figure 19.4(a) yields a finite confidence interval for parameters R_3 and τ_3; whereas, Figure 19.4(b) yields confidence intervals that extend over several orders of magnitude and, therefore, includes zero. Statistically significant values for R_3 and τ_3, therefore, could not be obtained by regression to the noisy data. Thus, even though the parameters R_3 and τ_3 were used to generate the synthetic data, these parameters could not be recovered by regression to the noisy data.

19.5.3 Ill-Conditioned Regression Caused by Insufficient Range

The frequency range of the measurement also has a direct impact on the number of parameters that can be identified by regression. Two impedance data sets are presented in Figure 19.6. The circles represent synthetic impedance data calculated for frequencies from 10^{-2} to 10^5 Hz at a spacing of 10 measurements per decade, and the triangles represent synthetic impedance data calculated for frequencies from 1

Remember! 19.2 *The presence of noise in data can have a direct impact on model identification and on the confidence interval for the regressed parameters. The correctness of the model alone does not determine the number of parameters that can be obtained.*

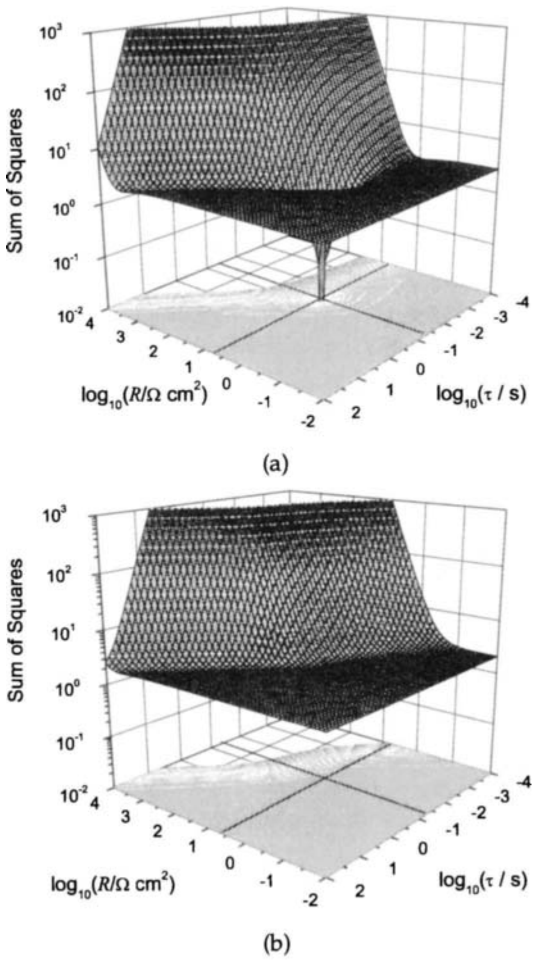

Figure 19.4: The objective function, equation (19.3), for a Voigt circuit with $R_0 = 1$ Ωcm², $R_1 = 100$ Ωcm², $\tau_1 = 0.001$ s, $R_2 = 200$ Ωcm², $\tau_1 = 0.01$ s, $R_3 = 5$ Ωcm², and $\tau_1 =$ 0.05 s, presented as a function of R_3 and τ_3. The synthetic impedance data were calculated for frequencies from 1 to 10^5 Hz at a spacing of 10 measurements per decade: a) noise level determined by machine precision; and b) stochastic noise added to the synthetic data with a standard deviation equal to 1 percent of the modulus.

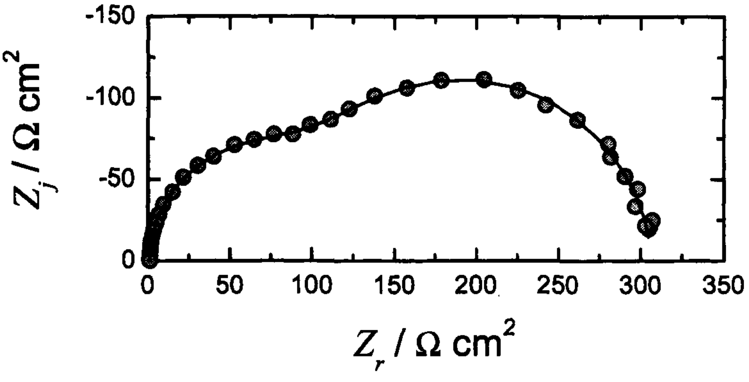

Figure 19.5: The impedance data used for Figure 19.4 in impedance-plane format. The solid line represents the noise-free data, and the symbols represent the data with added stochastic noise with a standard deviation equal to 1 percent of the modulus. Note that the third lineshape, with parameters $R_3 = 5\ \Omega\text{cm}^2$ and $\tau_1 = 0.05$ s, is not readily seen, even for the noise-free solid line.

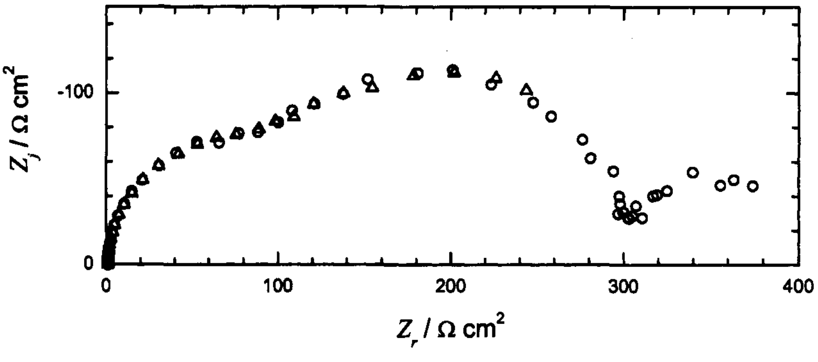

Figure 19.6: The impedance data for a Voigt circuit with $R_0 = 1\ \Omega\text{cm}^2$, $R_1 = 100\ \Omega\text{cm}^2$, $\tau_1 = 0.01$ s, $R_2 = 200\ \Omega\text{cm}^2$, $\tau_1 = 0.1$ s, $R_3 = 100\ \Omega\text{cm}^2$, and $\tau_1 = 10$ s. These data, with a standard deviation equal to 1 percent of the modulus, were used to generate Figure 19.7: ○) synthetic impedance data calculated for frequencies from 10^{-2} to 10^5 Hz at a spacing of 10 measurements per decade; and △) synthetic impedance data calculated for frequencies from 1 to 10^5 Hz at a spacing of 10 measurements per decade.

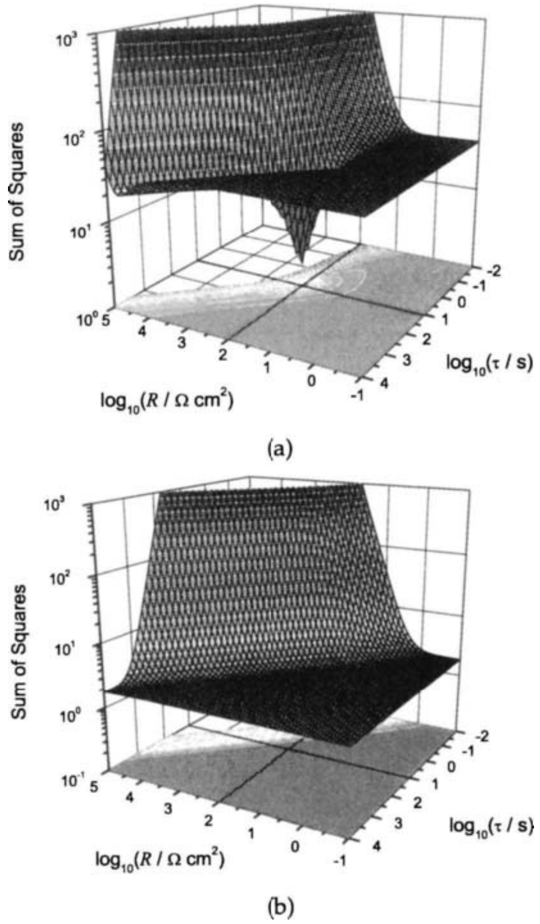

Figure 19.7: The objective function, equation (19.3), for the impedance data presented in Figure 19.6: a) synthetic impedance data collected from 10^{-2} to 10^5 Hz at a spacing of 10 measurements per decade; and b) synthetic impedance data collected from 1 to 10^5 Hz at a spacing of 10 measurements per decade.

to 10^5 Hz at the same spacing of 10 measurements per decade. The impedance data were calculated for a Voigt circuit with $R_0 = 1\ \Omega\text{cm}^2$, $R_1 = 100\ \Omega\text{cm}^2$, $\tau_1 = 0.01$ s, $R_2 = 200\ \Omega\text{cm}^2$, $\tau_2 = 0.1$ s, $R_3 = 100\ \Omega\text{cm}^2$, and $\tau_3 = 10$ s. Noise with a standard deviation equal to 1 percent of the modulus was added.

The corresponding response surfaces are presented as functions of parameters $\log_{10}(R_3)$ and $\log_{10}(\tau_3)$ in Figure 19.7(a) for the extended data set (10^{-2} to 10^5 Hz) and in Figure 19.7(b) for the truncated data set (1 to 10^5 Hz). The parameters R_3 and τ_3 can be readily identified from the response surface in Figure 19.7(a), but cannot be identified from Figure 19.7(b).

The response surfaces presented in this chapter have been given as a function of resistance and RC-time constant. Plots presented as functions of R and C have a similar appearance. The objective function, equation (19.3), is presented in Figure 19.8 for an RC circuit as a function of parallel resistor and capacitor values. The cir-

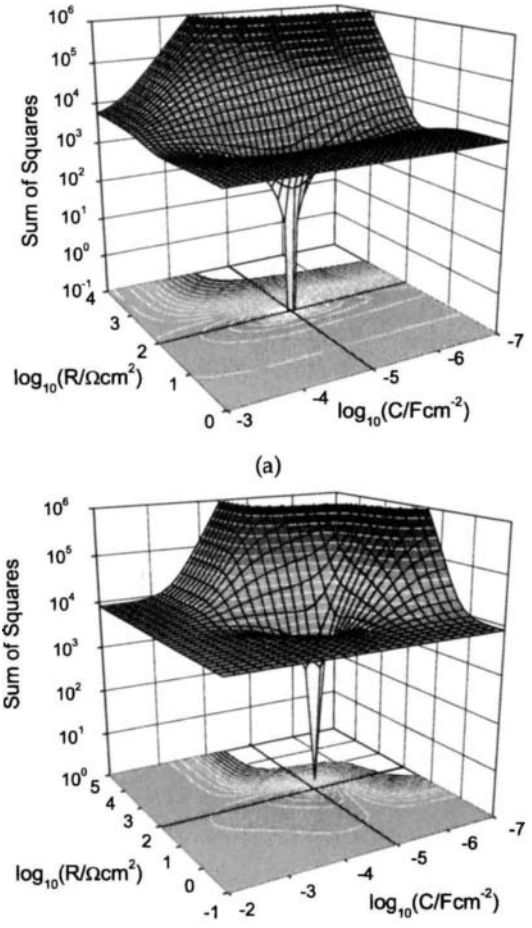

(a)

(b)

Figure 19.8: The objective function, equation (19.3), for an RC circuit as a function of parallel resistor and capacitor values. The circuit parameters were $R_0 = 1\ \Omega\text{cm}^2$, $R_1 = 100\ \Omega\text{cm}^2$, and $C_1 = 1 \times 10^{-5}$ F/cm^2. a) noise level determined by machine precision; and b) noise added with a standard deviation equal to 1 percent of the modulus.

cuit parameters were $R_0 = 1\,\Omega\mathrm{cm}^2$, $R_1 = 100\,\Omega\mathrm{cm}^2$, and $C_1 = 1 \times 10^{-5}\,\mathrm{F/cm}^2$ (see Figure 4.3(b) and the corresponding Example 4.2). The objective of the regression procedure is to identify the parameter values that minimize the objective function. Solid lines have been drawn on the bottom contour map to indicate the values for which the function is minimized.

19.6 Initial Estimates for Regression

The complex nonlinear least-squares regression requires initial estimates for the parameter values. As shown in the contour plots given, for example, in Figures 19.4(a), 19.7(a), and 19.8, the objective function is insensitive to the parameters when the parameter value is far from the correct converged value. Good starting values will facilitate convergence, and poor starting values may result in convergence to a local minimum that does not represent the physics of the system.

Selection of an appropriate initial value for the time constant τ_k is critical for regression of the Voigt model (see equation (20.5)) to impedance data. Inductive loops can be modeled by the Voigt model by allowing the resistance values R_k to be negative while forcing the time constant τ_k to be positive. It is important in this case that the time constant for the element with a negative resistance be consistent with the frequency range that shows inductive behavior. The time constant τ_k should be large, for example, to capture features at small frequencies.

Physical insight may provide good guidelines for selection of initial estimates for parameters used in process models such as diffusion coefficients and interfacial capacities. Another approach, described, for example, by Draper and Smith,[247] is to substitute into the postulated model a subset of the data equal to the number of parameters to be regressed and then solve the resulting equations for the parameters. The data points chosen should be spaced in frequency so as to capture the influence of each of the parameters. It can be helpful to explore the asymptotic limiting behavior where some of the parameters may have negligible influence on the impedance response. This approach ignores the scatter of the data, but the parameters so obtained can be used as initial guesses for the nonlinear regression.

19.7 Regression Statistics

The fitting procedure should provide three pieces of information:

- Parameter estimates
- Confidence intervals for the parameter estimates

Remember! 19.3 *The frequency range of the data can have a direct impact on model identification.*

- A statistical measure of the quality of the regression

The statistical measure of the quality of the regression is used to determine whether the model provides a meaningful representation of the data. The parameter estimates are reliable only if the model provides a statistically adequate representation of the data. The evaluation of the quality of the regression requires an independent assessment of the stochastic errors in the data, information that may not be available. In such cases, visual inspection of the fitting results may be useful. Issues associated with assessment of regression quality are discussed further in Section 19.7.2 and Chapter 20.

19.7.1 Confidence Intervals for Parameter Estimates

For linear regressions, the standard deviations for a parameter estimate P_j are given by

$$\sigma_j = \sqrt{C_{j,j}} \tag{19.34}$$

as described in Section 19.3.1. This result applies under the assumption that the fitting errors are normally distributed. As described in Chapter 21, the fitting errors comprise stochastic measurement errors, biased measurement errors, and errors associated with the inability of the model to describe the data.

Under the assumptions that the regression can be treated as being linear in the region of the χ^2 minimum and that fitting errors are normally distributed, equation (19.34) provides the standard deviation for parameter estimates in nonlinear regressions. Most commercial regression programs available for impedance spectroscopy provide both parameter estimates and the confidence interval based on the linear hypothesis. The size of the confidence interval relative to the parameter estimate can be used to determine the statistical significance of a parameter estimate. As described in Section 3.1.3, the probability is 67 percent that the parameter P_j lies within $P_j \pm \sigma_j$ and the probability is 95.4 percent that the parameter P_j lies within $P_j \pm 2\sigma_j$. Generally, the regression for a parameter is deemed not statistically meaningful if the confidence interval for that parameter includes zero.

A second and more generally applicable approach for determining the confidence interval for parameters is to create a surface of constant $\chi^2_{\text{min}} + \Delta\chi^2$. These surfaces resemble, for two parameters, the contours presented in Figure 19.1. The confidence level for a given $\Delta\chi^2$ can be obtained by Monte Carlo simulations, and the confidence interval for a specific parameter can be obtained by the projection of the $\Delta\chi^2$ onto the appropriate domain. Methods are described by Press et al.[256]

Remember! 19.4 *The model identification problem is intricately linked to the error identification problem. Analysis of data requires analysis of the error structure of the measurement.*

19.7.2 Statistical Measure of the Regression Quality

The minimum value of the χ^2 statistic is commonly used to provide a figure of merit for the quality of regression. As shown in equation (19.9), the χ^2 statistic accounts for the variance of the experimental data. In principle, for a model that well describes the data, the minimum value of the χ^2 statistic has a mean value of the degree of freedom ν with standard deviation $\sqrt{2\nu}$. Thus, for a good fit,

$$\frac{\chi^2_{\text{min}}}{\nu} = 1 \pm \sqrt{\frac{2}{\nu}} \tag{19.35}$$

The use of equation (19.35) to assess the quality of a regression is valid only for an accurate estimate of the variance of the stochastic errors in the impedance data.

An independent method to identify the stochastic errors of impedance data is described in Chapter 21. An alternative approach has been to use the method of maximum likelihood,[79] in which the regression procedure is used to obtain a joint estimate for the parameter vector **P** and the error structure of the data.[253,257] The maximum likelihood method is recommended under conditions where the error structure is unknown,[79] but the error structure obtained by simultaneous regression is severely constrained by the assumed form of the error-variance model. In addition, the assumption that the error variance model can be obtained by minimizing the objective function ignores the differences among the contributions to the residual errors shown in Chapter 21. Finally, the use of the regression procedure to estimate the standard deviation of the data precludes use of the χ^2 statistic as a quantitative assessment of the quality of the regression.

Problems

19.1 Create a synthetic data set for a system with a constant-phase element as given in equation (13.2) with parameters $R_e = 10\ \Omega\text{cm}^2$; $R_t = 10^3\ \Omega\text{cm}^2$; $Q = 100\ \text{s}^\alpha/\text{M}\Omega\text{cm}^2$; and $\alpha = 0.7$ with frequencies ranging from $10^{-2} - 10^4$ Hz spaced logarithmically with 10 measurements per decade. Use a commercial regression software or create your own to regress a Voigt model (see, e.g., equation (4.28)) to the data using modulus weighting. Find the maximum number of Voigt elements that can be added without including zero in the 2σ (95.4 percent) confidence interval.

19.2 Generate the synthetic data described in Problem 19.1, adding independent normally distributed random numbers $N(0,\sigma)$ to both real and imaginary parts of the impedance where $\sigma = a|Z|$ and the value of a is given below:

- **(a)** Generate the synthetic data set for $a = 0.01$. Perform the regression using modulus weighting for which $\sigma = 0.01|Z|$. Identify the value of the resulting χ^2 statistic and the number of parameters that can be obtained without including zero in the 2σ (95.4 percent) confidence interval.
- **(b)** Generate the synthetic data set for $a = 0.05$. Perform the regression using modulus weighting for which $\sigma = 0.01|Z|$. Identify the value of the

resulting χ^2 statistic and the number of parameters that can be obtained without including zero in the 2σ (95.4 percent) confidence interval.

19.3 Generate the synthetic data described in Problem 19.1, adding independent normally distributed random numbers $N(0,\sigma)$ to both real and imaginary parts of the impedance where $\sigma = 0.01|Z|$.

- **(a)** Truncate the synthetic data set by removing the data below a frequency of 1 Hz. Perform the regression using modulus weighting for which $\sigma = 0.01|Z|$. Identify the value of the resulting χ^2 statistic and the number of parameters that can be obtained without including zero in the 2σ (95.4 percent) confidence interval.
- **(b)** Truncate the synthetic data set by removing the data below a frequency of 10 Hz. Perform the regression using modulus weighting for which $\sigma = 0.01|Z|$. Identify the value of the resulting χ^2 statistic and the number of parameters that can be obtained without including zero in the 2σ (95.4 percent) confidence interval.

19.4 Perform the regression for the data presented in Problem 19.2(a), but use a weighting based on $\sigma = 0.05|Z|$. Compare the resulting value of the χ^2 statistic and the number of parameters that can be obtained without including zero in the 2σ (95.4 percent) confidence interval to that obtained for Problem 19.2(a).

Electrochemical Impedance Spectroscopy
by Mark E. Orazem and Bernard Tribollet

Chapter 20

Assessing Regression Quality

The chapters presented in Part III describe development of mathematical models that can be used for interpretation of impedance measurements. These models may be regressed to data using the approaches presented in Chapter 19. A systematic approach is presented in this chapter to determine whether the model provides a statistically adequate description of the data.

20.1 Methods to Assess Regression Quality

Both quantitative and qualitative approaches may be used to assess the quality of a regression.

20.1.1 Quantitative Methods

As discussed in Section 19.7.2, the weighted χ^2 statistic defined in equation (19.24) provides a useful single numerical value for assessing the quality of a regression. As the differences between the observed and modeled values diminish, the χ^2 statistic becomes smaller. For a successful regression, the χ^2 statistic approaches the degree of freedom for the regression ν, given by equation (3.42). This assessment, however, requires an independent assessment of the stochastic errors in the impedance measurement. The influence of an inaccurate error analysis is illustrated in Section 20.2.1. The utility of an accurate error structure is illustrated in Sections 20.2.2 and 20.2.3.

In some cases, the models used for impedance are strictly defined. Others, such as the Voigt model, allow use of an arbitrary number of parameters. The fit of a Voigt model can be improved by sequentially adding RC elements, and the best model is achieved when the χ^2 statistic reaches a minimum value.

One potential concern is that there may be an inadequate sensitivity of the χ^2/ν statistic for identifying overfitting of data. Other criteria, such as the Akaike information criteria,[258–260] provide additional penalties for adding parameters to a model. The Akaike performance index is given by

$$A_{\mathrm{PI}} = \sum \chi^2 \frac{1 + N_p/N_{\mathrm{dat}}}{1 - N_p/N_{\mathrm{dat}}} \tag{20.1}$$

The related Akaike information criterion is given by

$$A_{\mathrm{IC}} = \log\left(\sum \chi^2 \left(1 + 2N_p/N_{\mathrm{dat}}\right)\right) \tag{20.2}$$

As was discussed for the χ^2 statistic, the maximum number of parameters obtainable by regression is found where the Akaike information criteria reach minimum values.

Another quantitative assessment is obtained from the estimated confidence intervals for the regressed parameters, discussed in Section 19.7.1. The estimated confidence intervals, given by equation (19.34) under the assumptions that the regression can be treated as being linear in the region of the χ^2 minimum and that fitting errors are normally distributed, do not indicate the quality of the regression, but they do indicate whether the values obtained for a specific parameter are statistically significant. The probability is 95.4 percent that the parameter P_j lies within $P_j \pm 2\sigma_j$. Generally, the regression for a parameter is not statistically meaningful if the confidence interval for that parameter includes zero. Observation that the 95.4 percent confidence interval includes zero provides a third means of determining whether the model has too many parameters. Generally, all three approaches provide the same number of statistically significant parameters.

20.1.2 Qualitative Methods

The quality of a regression can also be assessed by visual inspection of plots. Of course, some plots are more sensitive than others to the level of agreement between model and experiment. As will be demonstrated in this chapter, the plot types can be categorized as given in Table 20.1. The comparison of plot types is presented in the subsequent sections for regression of models to a specific impedance data set.

20.2 Application of Regression Concepts

The data used for the present analysis were obtained by Durbha.[239] The electrolyte contained 0.01 M potassium ferricyanide, 0.01 M potassium ferrocyanide, and 1 M KCl in distilled water. A 5-mm-diameter Pt rotating disk was used as the working electrode, a Pt mesh was used as the counterelectrode, and a saturated calomel electrode was used as a reference electrode. The disk was rotated by a high-speed, low-inertia rotating disk apparatus developed at the CNRS.[261] The temperature of the electrolyte was controlled at 25.0±0.1°C. The surface-polishing treatment followed wet polishing with 1,200-grit emery cloth, polishing with alumina paste, and ultrasonic cleaning. This was the procedure that gave the largest value for the mass-transfer-limited current and was therefore assumed to result in the smallest amount of surface blocking.

Table 20.1: Characterization of impedance plot types in terms of sensitivity to discrepancies between model and experimental values.

Poor Sensitivity	
Modulus	The Bode magnitude representation is singularly incapable of distinguishing between impedance models unless they provide extremely poor fits to impedance data.
Real	The real impedance representation is similarly insensitive to fit quality.
Modest Sensitivity	
Complex-impedance-plane	These plots are sensitive only for large impedance values. Impedance data at high-frequency values are typically obscured.
Imaginary	The imaginary impedance representation is modestly sensitive to fit quality.
Log-imaginary	These plots emphasize small values, and values of the slope that differ from ±1 may suggest the need for new models.
Phase angle	The high-frequency behavior in these plots is counterintuitive due to the role of solution resistance.
Modified phase angle	Ohmic-resistance-corrected phase angle plots may confirm the existence of a CPE.
Excellent Sensitivity	
Residual error plots	Appearance of trending indicates a need to improve the model or to remove data that are inconsistent with the Kramers-Kronig relations.

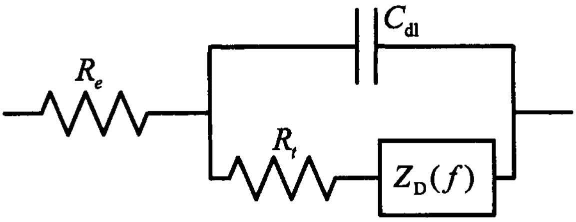

Figure 20.1: Electrical circuit corresponding to convective diffusion to a disk electrode.

The potentials and currents were measured and controlled by a Solatron 1286 potentiostat, and a Solatron 1250 frequency response analyzer was used to apply the sinusoidal perturbation and to calculate the transfer function. The impedance data analyzed in this section were taken after 12 hours of immersion and were found by the methods described in Chapter 22 to be consistent with the Kramers-Kronig relations.

For the purpose of demonstrating the means of assessing regression quality, three models were applied for the analysis of the impedance data:

1. A Nernst stagnant-diffusion-layer model was used to account for the diffusion impedance. This model is often used to account for mass transfer in convective systems, even though it is well known that this model cannot account accurately for the convective diffusion associated with a rotating disk electrode.[150]

2. Following Agarwal et al.,[56,86,262] a measurement model based on the Voigt series was used to assess the error structure.

3. A refined process model was used that correctly accounts for convective diffusion to a rotating disk electrode under the assumption that the surface is uniformly accessible. This model also employs a constant-phase element to address complexities seen at high frequency.[85]

20.2.1 Finite-Diffusion-Length Model

The equivalent circuit presented in Figure 20.1 was regressed to the impedance data. The mathematical formulation for the model is given as

$$Z(f) = R_e + \frac{R_t + Z_D(f)}{1 + (j2\pi f C)(R_t + Z_D(f))} \tag{20.3}$$

where, under assumption of a Nernst stagnant diffusion layer (as shown in equation (11.70)),

$$Z_D(f) = Z_D(0)\frac{\tanh\sqrt{j2\pi f\tau}}{\sqrt{j2\pi f\tau}} \tag{20.4}$$

The regression was weighted by the error structure for the measurement determined using the measurement model approach described in Chapter 21.

Table 20.2: Estimated χ^2/ν values for the regression of the model presented in Figure 20.1 to impedance data obtained for reduction of ferricyanide on a Pt rotating disk electrode.

Estimated Noise Level:	3 %	1 %	0.1 %	Measured
Model for σ	$0.03\|Z\|$	$0.01\|Z\|$	$0.001\|Z\|$	$9 \times 10^{-6}\|Z\|^2$
χ^2/ν	0.97	8.7	870	1,820

Quantitative Assessment

Due to the appearance of the variance in equation (19.24), the χ^2 statistic provides a useful measure of the quality of a fit only if the variance of the measurement is known. The techniques described in Chapter 21 may be used to assess the standard deviation of an impedance measurement as a function of frequency. In the absence of such an assessment, researchers have used assumed error structures, but, in this case, the numerical value of the χ^2 statistic cannot be used to assess the quality of a regression. This situation is illustrated in Table 20.2, where the value of χ^2/ν is presented as a function of the assumed error structure for the regression of the model presented in equations (20.3) and (20.4) to the experimental data. Under the assumption that the standard deviation of the measurement was 3 percent of the modulus, $\chi^2/\nu = 0.97$. This value would indicate that the fitting errors were of the order of the noise in the measurement, indicating that the model provides an excellent fit to the data. On the other hand, assumption that the standard deviation of the measurement was 0.1 percent of the modulus yields $\chi^2/\nu = 870$. This value would indicate that the fitting errors were much larger than the noise in the measurement, indicating that the model provides an inadequate representation of the data. Thus, depending on the assumed error structure, the χ^2 statistic can be used to support or reject the model. In fact, for this regression and using the experimentally determined stochastic error structure, $\chi^2/\nu = 1,820$. The fitting errors were indeed much larger than the noise in the measurement.

Visual Inspection

A qualitative assessment of the fit quality can be obtained in the comparison of the calculated to experimental values shown in complex-impedance-plane or Nyquist format in Figure 20.2. The results at high frequency are not visible in Nyquist plots, but a clear discrepancy is evident at lower frequencies where the impedance values are larger and therefore more visible.

The discrepancy is not evident, however, in the Bode magnitude plot presented in Figure 20.3(a). In fact, the Bode magnitude representation is singularly incapable

---

Remember! 20.1 *If the experimental error structure is not known, the numerical value of the χ^2 statistic cannot be used to assess the quality of a regression.*

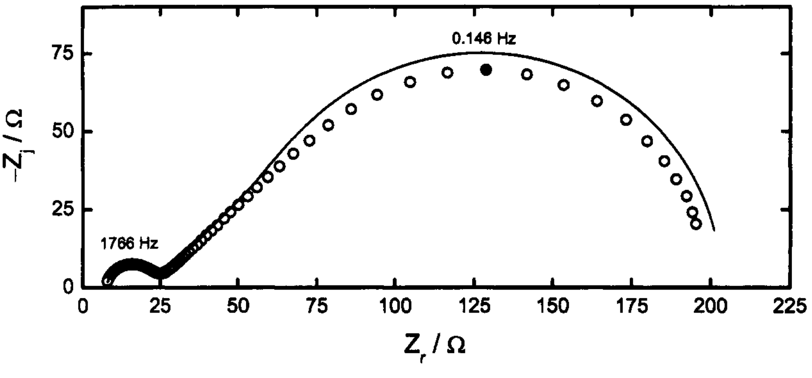

Figure 20.2: Comparison in complex-impedance-plane format of the model presented in Figure 20.1 to impedance data obtained for reduction of ferricyanide on a Pt rotating disk electrode.

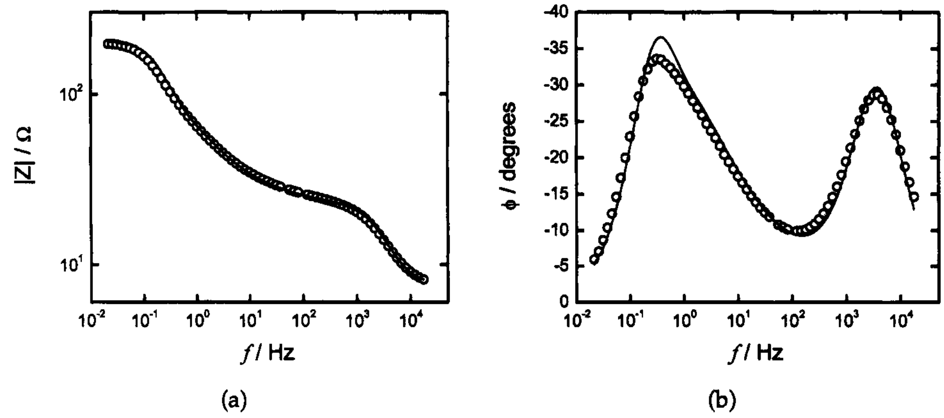

Figure 20.3: Comparison in Bode format of the model presented in Figure 20.1 to impedance data obtained for reduction of ferricyanide on a Pt rotating disk electrode: a) modulus; and b) phase angle.

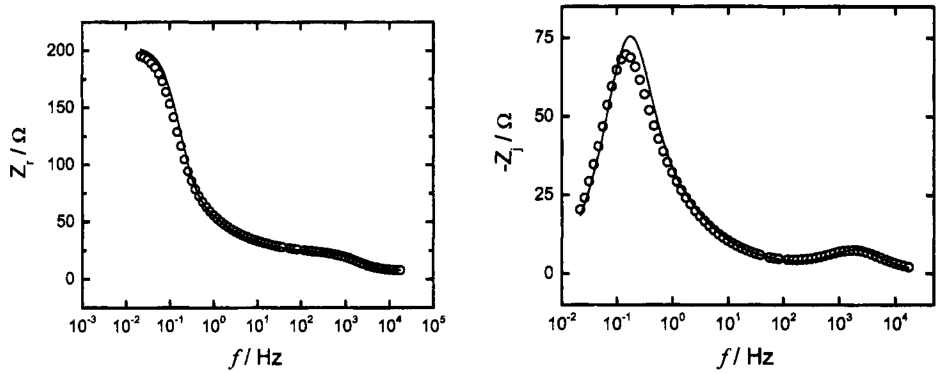

(a) (b)

Figure 20.4: Comparison in impedance format of the model presented in Figure 20.1 to impedance data obtained for reduction of ferricyanide on a Pt rotating disk electrode: a) real; and b) imaginary.

of distinguishing between impedance models unless they provide extremely poor fits to impedance data. The Bode phase-angle representation in Figure 20.3(b) is more sensitive and, for the present example, reveals discrepancies at both high and intermediate frequencies.

The sensitivity of the impedance representation, presented in Figures 20.4(a) and (b) for real and imaginary parts respectively, is somewhat comparable to that seen for the Bode representation. The real part of the impedance is as insensitive to model quality as is the Bode modulus, and the imaginary impedance plots show a discrepancy between model and experiment at intermediate frequencies.

The greatest sensitivity is observed for plots of residual errors. Residual errors normalized by the value of the impedance are presented in Figures 20.5(a) and (b), respectively, for the real and imaginary parts of the impedance. The experimentally measured standard deviation of the stochastic part of the measurement is presented as dashed lines in Figure 20.5. The interval between the dashed lines represents the 95.4 percent confidence interval for the data ($\pm 2\sigma$). Significant trending is observed as a function of frequency for residual errors of both real and imaginary parts of the impedance.

The plot of the absolute value of the imaginary part of the impedance with respect to frequency on a logarithmic scale, shown in Figure 20.6, shows discrepancies at small impedance values, in particular at high frequency. As described in Section 17.1.3, the imaginary part of the impedance at high frequency appears as

---

Remember! 20.2 *The Bode magnitude and real impedance plots are relatively insensitive to the quality of the fit of a model to impedance data.*

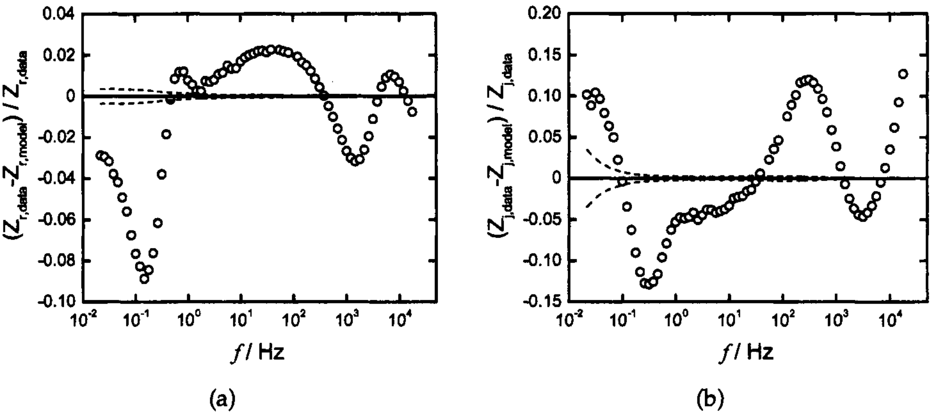

Figure 20.5: Normalized residual errors for the fit of the model presented in Figure 20.1 to impedance data obtained for reduction of ferricyanide on a Pt rotating disk electrode: a) real; and b) imaginary.

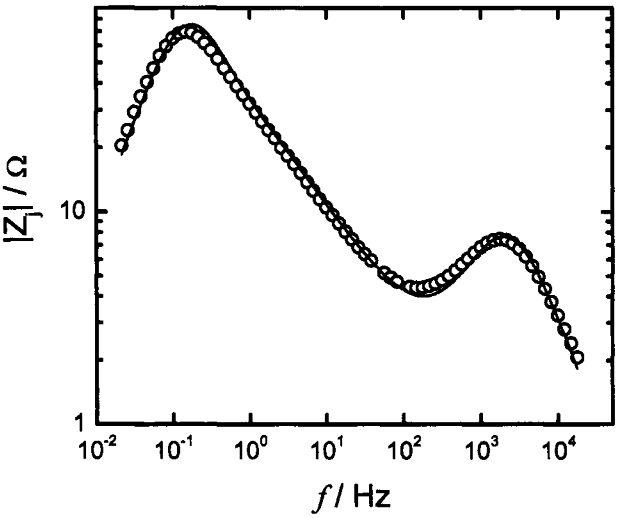

Figure 20.6: Comparison in log-imaginary-impedance format of the model presented in Figure 20.1 to impedance data obtained for reduction of ferricyanide on a Pt rotating disk electrode.

a straight line in Figure 20.6, but the slope of this line differs from the value of -1 constrained by the model. This result suggests that the high-frequency capacitive loop may be modeled as a CPE.

20.2.2 Measurement Model

The measurement model method for distinguishing between bias and stochastic errors is based on using a generalized model as a filter for nonreplicacy of impedance data. The measurement model is composed of a superposition of line-shapes that can be arbitrarily chosen subject to the constraint that the model satisfies the Kramers-Kronig relations. The model presented in Figure 21.8, composed of Voigt elements in series with a solution resistance, i.e.,

$$Z = R_0 + \sum_{k=1}^{K} \frac{R_k}{1 + j2\pi f \tau_k} \tag{20.5}$$

has been shown to be a useful measurement model. With a sufficient number of parameters, the Voigt model is able to provide a statistically significant fit to a broad variety of impedance spectra.[56] In the context of the present chapter, it provides a fit quality that can be the goal for model development.

Quantitative Assessment

The measurement comprised real and imaginary parts of the impedance for 70 frequencies; thus, the vector of data for complex regression included 140 data. The measurement model with 11 Voigt elements (23 parameters) yielded the smallest value of χ^2, the smallest value of the Akaike information criteria, and the largest number of parameters with 95.4 percent confidence intervals that did not include zero. The degree of freedom for this problem was $\nu = 140 - 23 = 117$. The regression was weighted according to the error structure obtained from repeated impedance measurements and using the measurement model (Section 21.5) to filter imperfect replication. The χ^2 statistic for this regression yielded a value of $\chi^2/\nu = 1.22$ with standard deviation $\sqrt{2/\nu} = 0.13$, which suggests that the residual errors are nearly of the same order as the stochastic errors.

Visual Inspection

The fit of the measurement model with 11 Voigt elements is presented in complex-impedance-plane format in Figure 20.7. The discrepancies evident in Figure 20.2 for the model presented in Section 20.2.1 are not apparent in Figure 20.7.

An excellent agreement is seen as well for the Bode format plots in Figures 20.8(a) and (b). As discussed in Section 20.2.1, however, a good agreement between model and experiment in modulus plots does not provide a reliable assessment of fit quality. The agreement between model and experiment in Figure 20.8(b) is better than that seen in Figure 20.3(b).

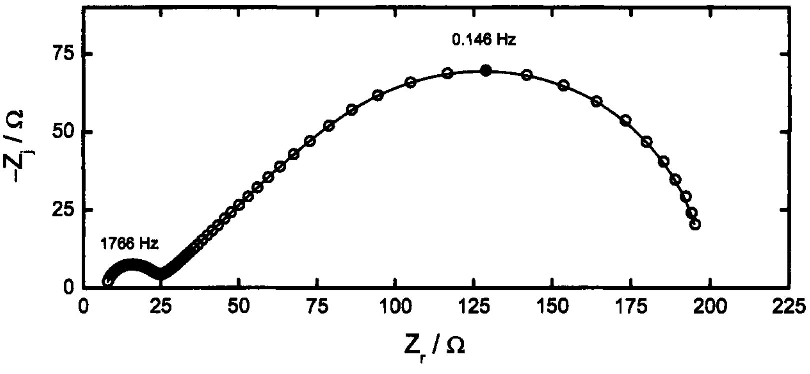

Figure 20.7: Comparison in complex-impedance-plane format of the measurement model to impedance data obtained for reduction of ferricyanide on a Pt rotating disk electrode.

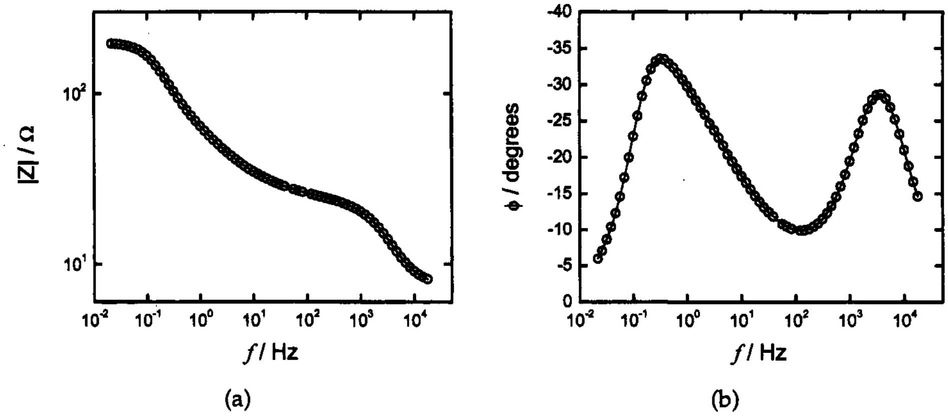

(a)

(b)

Figure 20.8: Comparison in Bode format of the measurement model to impedance data obtained for reduction of ferricyanide on a Pt rotating disk electrode: a) modulus; and b) phase angle.

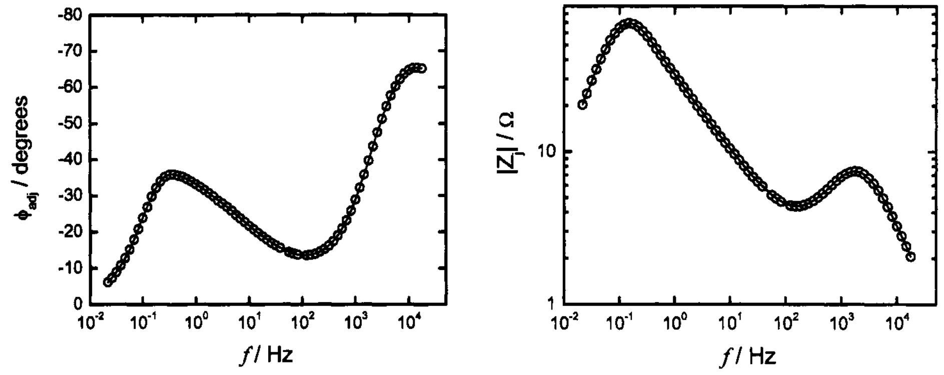

(a) (b)

Figure 20.9: Comparison of the measurement model to impedance data obtained for reduction of ferricyanide on a Pt rotating disk electrode: a) Ohmic-resistance-corrected phase angle; and b) log-imaginary impedance.

The Ohmic-resistance-corrected phase-angle plot, discussed in Section 17.1.2, provides confirmation of the conclusion, drawn from Figure 20.6, that CPE behavior is evident at high frequencies. The constant phase-angle shown in Figure 20.9(a) reaches a value of 67° at high frequency, corresponding to a CPE exponent value of $\alpha = 0.75$. The value of the slope in the high-frequency range of the data shown in Figure 20.6 is -0.75, also corresponding to $\alpha = 0.75$. The measurement model is seen to be fully capable of representing the CPE behavior evident in Figure 20.9(b).

The real and imaginary parts of the impedance are presented in Figures 20.10(a) and (b), respectively. An excellent agreement between model and experiment is observed, but, as discussed in Section 20.2.1, a good agreement between model and experiment in real impedance plots does not provide a reliable assessment of fit quality.

The residual errors are presented in Figures 20.11(a) and (b) for the real and imaginary parts of the impedance, respectively. The dashed lines represent the experimentally determined noise level of the measurement. The scales used to present the results in Figure 20.11 are in stark contrast to the scales used in Figure 20.5. The residual error plots show that the measurement model provides a substantially better fit to the data than does the finite-diffusion-length model.

20.2.3 Convective-Diffusion-Length Model

The quantitative and qualitative analysis presented in Section 20.2.1 demonstrates that the finite-diffusion-layer model provides an inadequate representation for the impedance response associated with a rotating disk electrode. The presentation in Section 20.2.2 demonstrates that a generic measurement model, while not providing a physical interpretation of the disk system, can provide an adequate representation of the data. Thus, an improved mathematical model can be developed.

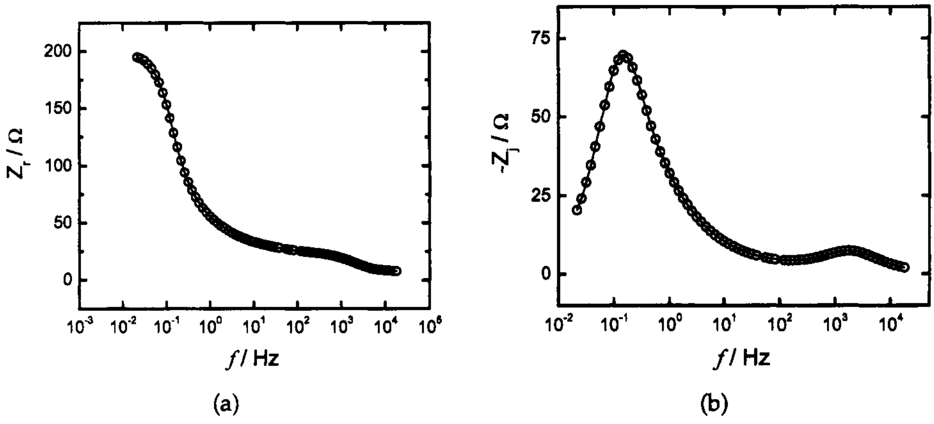

Figure 20.10: Comparison in impedance format of the measurement model to impedance data obtained for reduction of ferricyanide on a Pt rotating disk electrode: a) real; and b) imaginary.

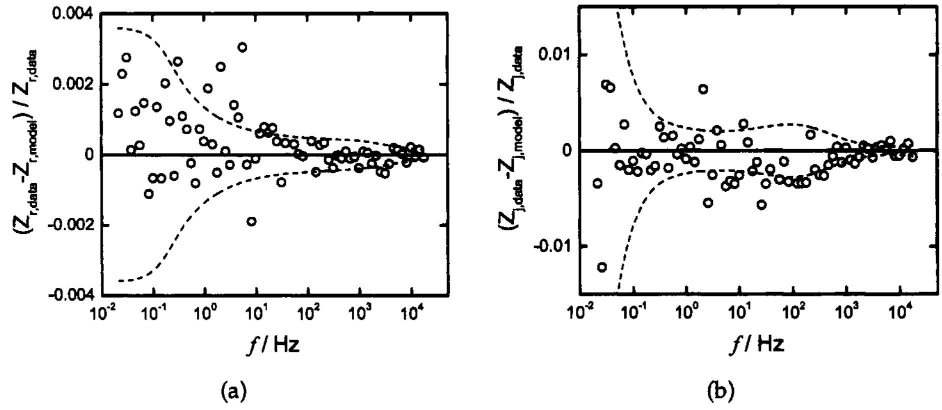

Figure 20.11: Normalized residual errors for the fit of the convective-diffusion models presented in Figure 20.12 to impedance data obtained for reduction of ferricyanide on a Pt rotating disk electrode: a) real; and b) imaginary.

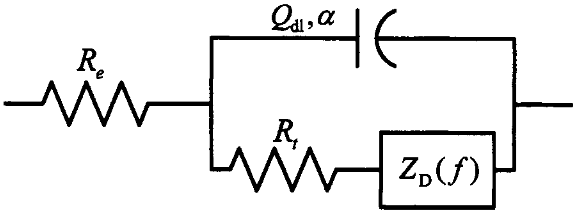

Figure 20.12: Electrical circuit corresponding to convective diffusion to a disk electrode with high-frequency CPE behavior.

Refined models for mass transfer to a disk electrode are presented in Section 11.6. The equivalent circuit presented in Figure 20.12 was regressed to the impedance data. The mathematical formulation for the model is given as equation (17.1). Four models were considered for the convective-diffusion term $Z_D(f)$:

1. The finite-diffusion model given as equation (20.4)
2. The one-term convective-diffusion model consisting of the first term in equation (11.97)
3. The two-term convective-diffusion model consisting of the first two terms in equation (11.97)
4. The three-term convective-diffusion model consisting of all terms given in equation (11.97)

The three-term convective-diffusion model provides the most accurate solution to the one-dimensional convective-diffusion equation for a rotating disk electrode. The one-dimensional convective-diffusion equation applies strictly, however, to the mass-transfer-limited plateau where the concentration of the mass-transfer-limiting species at the surface can be assumed to be both uniform and equal to zero. As described elsewhere,[199,263] the concentration of reacting species is not uniform along the disk surface for currents below the mass-transfer-limited current, and the resulting nonuniform convective transport to the disk influences the impedance response.[264,265]

Quantitative Assessment

The regression was weighted by the variance of the measurement, determined from experimental data using the measurement model analysis described in Section 21.5. Because the weighting was based on the experimental stochastic error structure, the χ^2/ν statistic presented in Table 20.3 provides a meaningful quantitative assessment of the quality of the regression. Ideally, as discussed in Section 19.7.2, χ^2/ν should have a value of unity for an excellent regression. The χ^2/ν statistic had a value of 1820 for the regression using the finite-diffusion model described in Section 20.2.1. Inclusion of a CPE to describe the high-frequency capacitive loop improved the value to $\chi^2/\nu = 107$. The large values of χ^2/ν are

Table 20.3: χ^2/ν values for the regression of the models presented in Figure 20.1 to impedance data obtained for reduction of ferricyanide on a Pt rotating disk electrode.

Model:	No CPE	With CPE				Voigt
	Finite	Finite	1-Term	2-Term	3-Term	Model
ν	135	134	134	134	134	117
χ^2/ν	1820	107	46.7	46.2	46.2	1.22

consistent with the understanding that these models are not accurate because they describe diffusion through a stagnant layer of fluid and do not account for the distribution of axial velocity within the diffusion layer.

The one-term numerical convective-diffusion model, which treats the Schmidt number as being infinitely large, shows significant improvement, yielding $\chi^2/\nu =$ 46.7. Addition of a second term yields a slightly smaller number, i.e., $\chi^2/\nu =$ 46.2, but addition of yet another term makes no improvement in the quality of the regression. Nevertheless, it was possible to obtain a χ^2/ν statistic with value close to unity. The regression of a Voigt measurement model, which has no particular physical interpretation, yielded $\chi^2/\nu = 1.22$. It is important to note that each of the four models employing a CPE has the same number of adjustable parameters. The difference between the models is due to the different accuracy of the solution to the one-dimensional convective-diffusion equation.

The result obtained with the Voigt measurement model shows that it is possible to obtain a regression using passive elements that describes the data to within the noise level of the measurement. The observation that the three-term model did not improve the regression shows that the regression cannot be improved by refining the solution to the one-dimensional convective-diffusion equation. Instead, the assumption of radial uniformity, implicit in the one-dimensional model, must be relaxed.

Visual Inspection

As described in Sections 20.2.1 and 20.2.2, the quality of the regressions can be assessed to varying degrees of success by inspection of plots. The Nyquist or complex-impedance-plane representation given in Figure 20.13 reveals the difference between the finite-diffusion-length model and the models based on numerical solution of the convective-diffusion equation, but cannot be used to distinguish the models based on one-term, two-term, and three-term expansions.

The logarithmic plot presented in Figure 20.14 cannot be used to distinguish the

Remember! 20.3 *Careful examination of the regression statistics and residual errors can guide model development.*

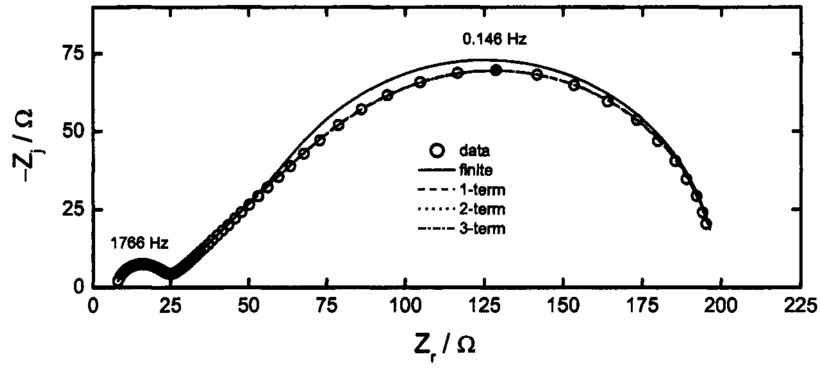

Figure 20.13: Comparison in complex-impedance-plane format of the convective-diffusion models presented in Figure 20.12 to impedance data obtained for reduction of ferricyanide on a Pt rotating disk electrode.

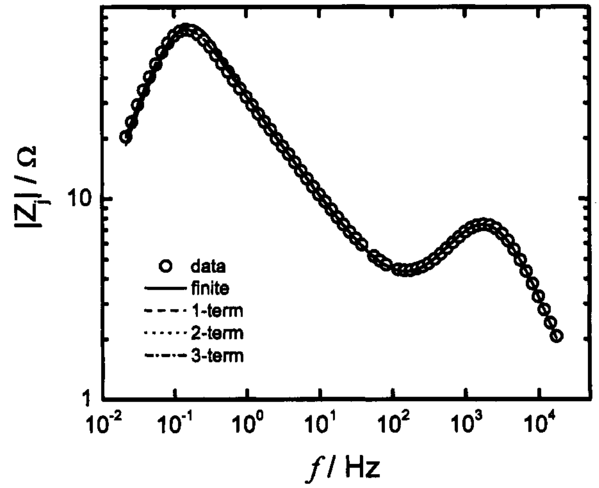

Figure 20.14: Comparison in log-imaginary-impedance format of the convective-diffusion models presented in Figure 20.12 to impedance data obtained for reduction of ferricyanide on a Pt rotating disk electrode.

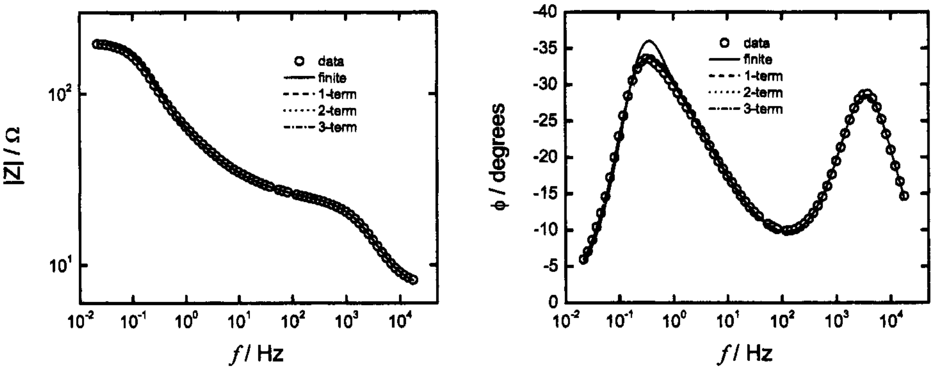

(a) (b)

Figure 20.15: Comparison in Bode format of the convective-diffusion models presented in Figure 20.12 to impedance data obtained for reduction of ferricyanide on a Pt rotating disk electrode: a) modulus; and b) phase angle.

model based on finite-stagnant-diffusion layer or the convective-diffusion models based on one-term, two-term, and three-term expansions. The logarithmic presentation in Figure 20.14 does show that each of the models considered used a CPE to account for high-frequency dispersion.

As shown in Figure 20.15(a), plots of the magnitude of the impedance cannot distinguish any of the models considered in this section, whereas the difference between the finite-diffusion-length model and the models based on numerical solution of the convective-diffusion equation are apparent in plots of the phase angle (Figure 20.15(b)). Figure 20.15(b) cannot be used, however, to distinguish the models based on one-term, two-term, and three-term expansions.

As shown in Figure 20.16(a), plots of the real part of the impedance cannot distinguish any of the models considered in this section, whereas the difference between the finite-diffusion-length model and the models based on numerical solution of the convective-diffusion equation are apparent in plots of the imaginary part of the impedance (Figure 20.16(b)). Figure 20.16(b) cannot be used, however, to distinguish the models based on one-term, two-term, and three-term expansions.

As described in Sections 20.2.1 and 20.2.2, plots of the residual errors provide the most sensitive assessment of fit quality. The normalized residual errors for the regressions treated in the section are presented in Figures 20.17(a) and (b) for the real and imaginary parts of the impedance, respectively. The distinction between the finite-diffusion-length model and the models based on numerical solution of the convective-diffusion equation are readily apparent. The differences between the models based on numerical solution of the convective-diffusion equation are not so apparent on the scale presented in Figures 20.17(a) and (b).

The distinction among the models based on numerical solution of the one-dimensional convective-diffusion equation are also not very evident in the plots

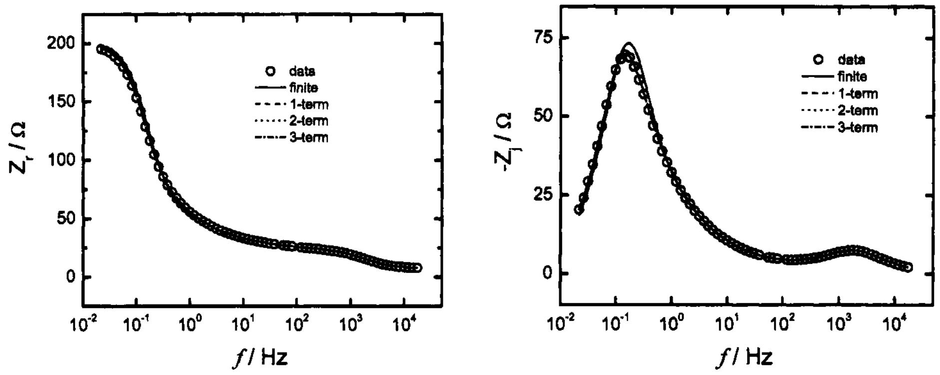

(a) (b)

Figure 20.16: Comparison in impedance format of the convective-diffusion models presented in Figure 20.12 to impedance data obtained for reduction of ferricyanide on a Pt rotating disk electrode: a) real; and b) imaginary.

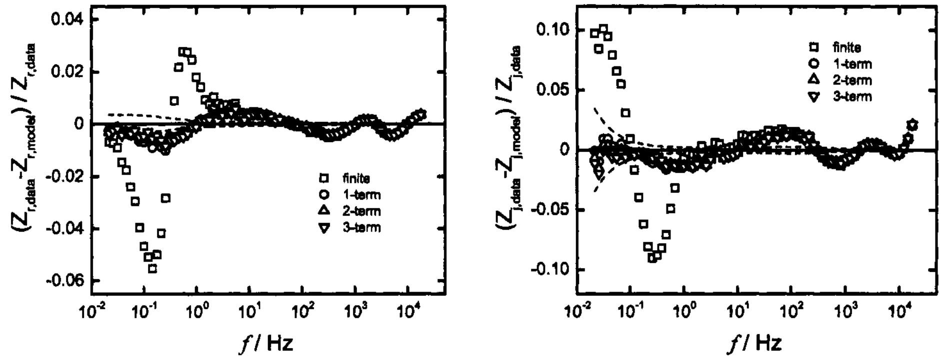

(a) (b)

Figure 20.17: Normalized residual errors for the fit of the convective-diffusion models presented in Figure 20.12 to impedance data obtained for reduction of ferricyanide on a Pt rotating disk electrode: a) real; and b) imaginary.

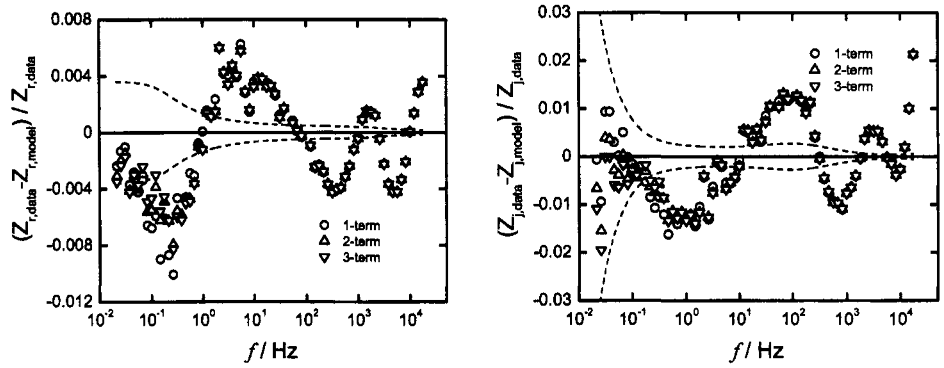

(a) (b)

Figure 20.18: Normalized residual errors for the fit of the convective-diffusion models presented in Figure 20.12 to impedance data obtained for reduction of ferricyanide on a Pt rotating disk electrode: a) real; and b) imaginary.

of the real and imaginary normalized residual errors for the models based on one-term, two-term, and three-term expansions presented in Figures 20.18(a) and (b), respectively. The distinction between an excellent fit and a poor fit can be seen by comparison between the residual errors presented in Figure 20.18, which are based on solution of the one-dimensional convective-diffusion equation, and those presented in Figure 20.11, which are based on regression by a Voigt measurement model. The normalized residual errors in Figure 20.18 show significant trending, whereas the normalized residual errors in Figure 20.11 do not. This assessment, which is based on visual inspection of the plots of normalized residual errors, is reflected as well in the quantitative assessment provided by the χ^2/ν statistic presented in Table 20.3.

Problems

20.1 Compare the plots described in Table 20.1 for the regression mentioned in Problem 19.2.

20.2 Plot χ^2/ν as a function of the number of Voigt elements for the regressions mentioned in Problem 19.2.

20.3 Statistics textbooks show different ways to visualize residual errors. A useful alternative representation involves scaling the residual errors by the standard deviation. Create such plots for the regression mentioned in Problem 19.2.

20.4 Monte Carlo simulation can be used to explore the influence of random noise on the parameter estimation. Consider the following protocol:

1. Use a measurement model to identify error structure.
2. Use a measurement model on Kramers-Kronig-consistent data set to get a model for data.
3. Add to the model values obtained in the previous step a normally distributed random error with an experimentally determined standard deviation.
4. Fit the resulting model to each synthetic data set, and obtain a distribution of parameter values.

Contrast this approach to that presented in Examples 3.2 and 3.3.

Electrochemical Impedance Spectroscopy
by Mark E. Orazem and Bernard Tribollet

Part V

Statistical Analysis

Electrochemical Impedance Spectroscopy
by Mark E. Orazem and Bernard Tribollet

Chapter 21

Error Structure of Impedance Measurements

The regression procedures described in Chapter 19 require, in addition to an adequate deterministic model, a quantitative assessment of measurement characteristics. The weighting strategy should generally account for the magnitude of stochastic errors. In addition, the regressed data set either should include only data that have not been corrupted by bias errors, or, as an alternative approach, could incorporate bias errors into the weighting strategy.

While the nature of the error structure of the measurements is often ignored or understated in electrochemical impedance spectroscopy, recent developments have made possible experimental identification of error structure. Quantitative assessment of stochastic and experimental bias errors has been used to filter data, to design experiments, and to assess the validity of regression assumptions.

21.1 Error Contributions

The error contributions to an impedance measurement can expressed in terms of the difference between the observed value $Z_{\mathrm{ob}}(\omega)$ and a model value $Z_{\mathrm{mod}}(\omega)$ as

$$Z_{\mathrm{ob}}(\omega) - Z_{\mathrm{mod}}(\omega) = \varepsilon_{\mathrm{fit}}(\omega) + \varepsilon_{\mathrm{stoch}}(\omega) + \varepsilon_{\mathrm{bias}}(\omega) \qquad (21.1)$$

where $\varepsilon_{\mathrm{res}}$ represents the residual error, $\varepsilon_{\mathrm{fit}}(\omega)$ is the systematic error that can be attributed to inadequacies of the model, $\varepsilon_{\mathrm{stoch}}(\omega)$ is the stochastic error with expectation $\mathrm{E}\left\{\varepsilon_{\mathrm{stoch}}(\omega)\right\} = 0$, and $\varepsilon_{\mathrm{bias}}(\omega)$ represents the systematic experimental bias error that cannot be attributed to model inadequacies. Typically, the impedance is a strong function of frequency and can vary over several orders of magnitude over the experimentally accessible frequency range. The stochastic errors of the impedance measurement are strongly heteroscedastic, which, in this case, means that the variance of the stochastic errors is a strong function of frequency. Selection of an appropriate weighting strategy is, therefore, critical for interpretation of data.

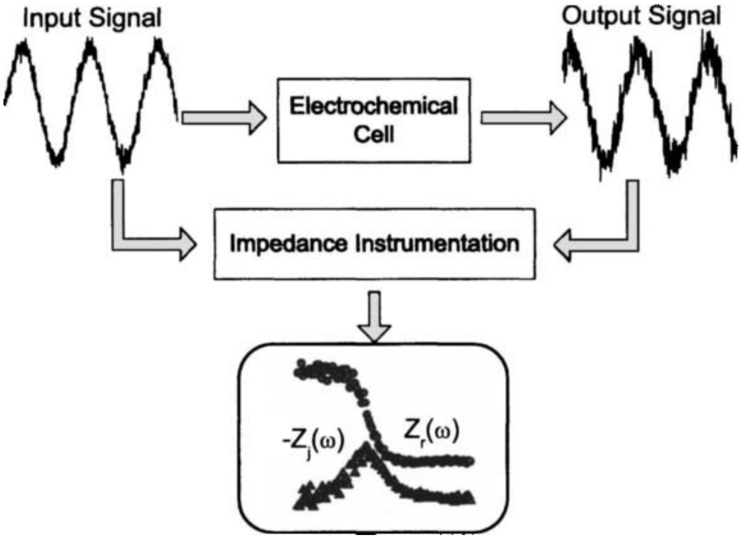

Figure 21.1: A schematic representation of the propagation of time-domain errors through an electrochemical cell and impedance instrumentation to the frequency domain.

A distinction is drawn in equation (21.1) between stochastic errors that are randomly distributed about a mean value of zero, errors caused by the lack of fit of a model, and experimental bias errors that are propagated through the model. The problem of interpretation of impedance data is therefore defined to consist of two parts: one of identification of experimental errors, which includes assessment of consistency with the Kramers-Kronig relations (see Chapter 22), and one of fitting (see Chapter 19), which entails model identification, selection of weighting strategies, and examination of residual errors. The error analysis provides information that can be incorporated into regression of process models. The experimental bias errors, as referred to here, may be caused by nonstationary processes or by instrumental artifacts.

21.2 Stochastic Errors in Impedance Measurements

While the error terms given in equation (21.1) are functions of frequency, it is important to note that the signals used to generate impedance are functions of time, not frequency. The schematic representation shown as Figure 21.1 illustrates the process. The error $\varepsilon_{\text{stoch}}(\omega)$ arises from an integration of time-domain signals that contain noise originating from instrumental sources, thermal fluctuations of resistivity, thermal fluctuations of the concentration of species and the rates of electrochemical reactions, and macroscopic events such as pitting and bubble nucleation.

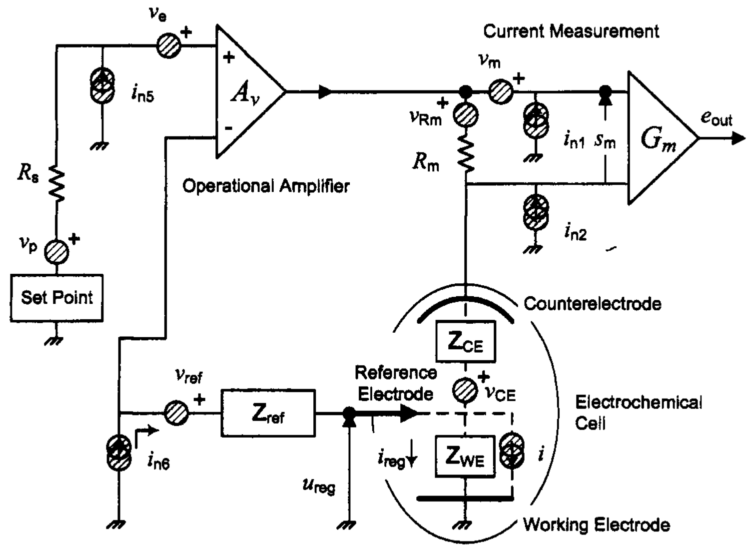

Figure 21.2: A schematic representation of an electrochemical cell under potentiostatic regulation, with sources of potential noise indicated as shaded circles and sources of current noise indicated as shaded double circles (see Gabrielli et al.[266]).

21.2.1 Stochastic Errors in Time-Domain Signals

Following Gabrielli et al.,[266] the potential imposed between the working electrode and the reference electrode

$$U_{\text{reg}} = \overline{U}_{\text{reg}} + u_{\text{reg}} \tag{21.2}$$

contains a stochastic noise u_{reg}. The noise in the regulation signal contains contributions from both potential and current sources that are identified in Figure 21.2. These noise contributions can be expressed conveniently in the frequency domain as

$$u_{\text{reg}} = \frac{Z_{\text{WE}}}{Z_{\text{WE}}A_v + Z_{\text{WE}} + R_{\text{m}} + Z_{\text{CE}}} \tag{21.3}$$
$$\left\{A_v\left[v_{\text{e}} + v_{\text{p}} + R_{\text{s}}i_{\text{n5}} + v_{\text{ref}}\right] - v_{\text{R}_{\text{m}}} - v_{\text{CE}} - \left(R_{\text{m}} + Z_{\text{CE}}\right)\left(i - i_{\text{n6}}\right) + R_{\text{m}}i_{\text{n2}}\right\}$$

where Z_{WE} is the impedance of the working electrode, Z_{CE} is the impedance of the counterelectrode, Z_{ref} is the impedance of the counterelectrode, A_v is the gain of the operational amplifier, R_{m} is the resistance of the current measurement circuit, R_{s} is the resistance of the potential control circuit, v_{e}, v_{p}, v_{ref}, $v_{\text{R}_{\text{m}}}$, and v_{CE} represent voltage noise contributions shown as shaded circles in Figure 21.2, and i,

---

Remember! 21.1 *The stochastic errors in impedance measurements arise from an integration of time-domain signals that contain noise originating from the electrochemical cell and the instrumentation.*

---

i_{n1}, i_{n2}, i_{n5}, and i_{n6} represent current noise contributions shown as shaded double circles in Figure 21.2. The electrochemical noise i arises from molecular-scale fluctuations.[267,268] The current noise contributions act through resistors R_{m} and R_{s} to generate voltage noise contributions.

Under the assumptions that the gain of the operational amplifier A_v is large and that the reference electrode impedance Z_{ref} is small, the dominant stochastic error in the regulation signal consists of additive contributions from the reference electrode and the operational amplifier as

$$u_{\mathrm{reg}} = v_{\mathrm{e}} + v_{\mathrm{p}} + R_{\mathrm{s}} i_{\mathrm{n5}} + v_{\mathrm{ref}} \tag{21.4}$$

As equation (21.4) is not a function of frequency, it applies to both time and frequency domains.

The regulation noise induces, through the electrochemical cell impedance, a parasitic current fluctuation $i_{\mathrm{reg}}(t)$ that can be calculated from

$$i_{\mathrm{reg}}(t) = \mathrm{IFFT}\left\{\mathrm{FFT}\{u_{\mathrm{reg}}(t)\}/Z(\omega)\right\} \tag{21.5}$$

where the notation IFFT$\{x\}$ represents the *inverse Fourier transform* of the function x, and FFT$\{x\}$ represents the *Fourier transform* of the function x. The potential difference across the inputs to the current follower is given as

$$S_{\mathrm{m}} = \overline{S}_{\mathrm{m}} + s_{\mathrm{m}} \tag{21.6}$$

where

$$s_{\mathrm{m}} = v_{\mathrm{m}} + v_{\mathrm{R_m}} + R_m \left(i + i_{\mathrm{reg}} - i_{\mathrm{n2}} - i_{\mathrm{n6}}\right) \tag{21.7}$$

The response of the current measurement channel is given by $E_{\mathrm{out}} = G_m S_{\mathrm{m}}$, and the noise in the current measurement channel is given by

$$e_{\mathrm{out}} = G_m \left[v_{\mathrm{m}} + v_{\mathrm{R_m}} + R_m \left(i + i_{\mathrm{reg}} - i_{\mathrm{n2}} - i_{\mathrm{n6}}\right)\right] \tag{21.8}$$

Thus, the noise in both current and potential measurement channels consists of sums of noise contributions. A similar development has been presented for zero-resistance ammeters.[269]

The investigation of noise sources suggests that instrumental and electrochemical noise can be represented by stochastic signals added to the time-averaged measured and controlled signals. The instrumental noise sources can be assumed to have a very high frequency; thus the evaluations of the instrumental noise at any two instances in time, t and $t+\tau$, are uncorrelated. The added signals should be statistically independent with the exception of the term $i_{reg}(t)$, which is correlated with both $e_{reg}(t)$ and $i_{reg}(t+\tau)$.

For most potentiostats, the assumption $A_v >> 1$ becomes invalid at frequencies above 1 to 10 kHz. In this case, the noise terms are still additive, but the interaction between the gain of the operational amplifier and the cell impedance results in additional correlation between the input and output channels.

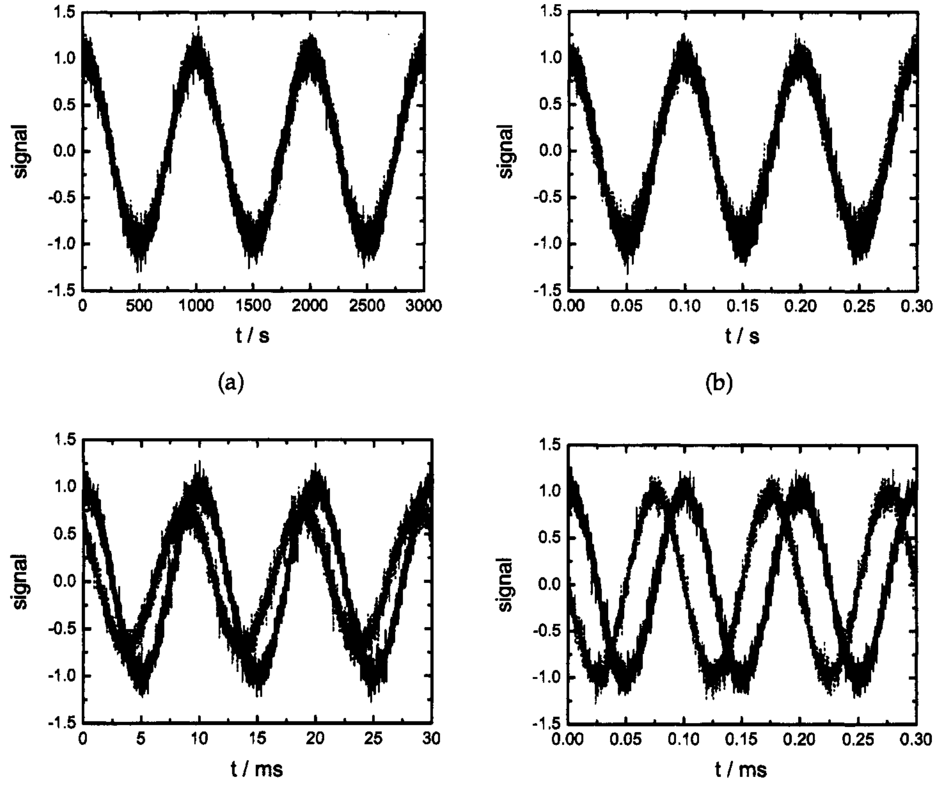

(a) (b)

(c) (d)

Figure 21.3: The current density response to a sinusoidal potential input for the system presented in Section 7.3 with parameters $C_{\mathrm{dl}} = 31$ μF/cm^2, $nFk_a = nFk_c = 0.14$ mA/cm^2, $b_a = 19.5$ V^{-1}, $b_c = 19.5$ V^{-1}, and $\overline{V} = 0.1$ V: a) 1 mHz; b) 10 Hz; c) 100 Hz; and d) 10 kHz. The signals include normally distributed additive errors with a magnitude of 10 percent of the magnitude of the respective signal. The solid line represents the potential input and the dashed line represents the resulting current density.

21.2.2 Transformation from Time Domain to Frequency Domain

The influence of noise on the impedance response can be illustrated by an extension of the analysis presented in Section 7.3. The current density response to a 10-mV-amplitude ($b_a\Delta V = 0.19$) sinusoidal potential input is presented in Figure 21.3 for the system presented in Section 7.3 with parameters $C_{\mathrm{dl}} = 31$ μF/cm^2, $Fk_a = nFk_c = 0.14$ mA/cm^2, $b_a = 19.5$ V^{-1}, $b_c = 19.5$ V^{-1}, and $\overline{V} = 0.1$ V. These parameters yield a value of charge-transfer resistance $R_t = 51.08$ Ωcm^2 and a characteristic frequency of 100 Hz. The potential and current signals were scaled by the maximum value of the signal. The results presented in Figure 21.3 can be compared to the results presented in Figure 7.4 for a linear response to a 1 mV potential perturbation and to Figure 8.2 for a nonlinear response to a 40 mV potential perturbation. The slight phase shift evident in Figure 8.2(b) for a 10 Hz input signal

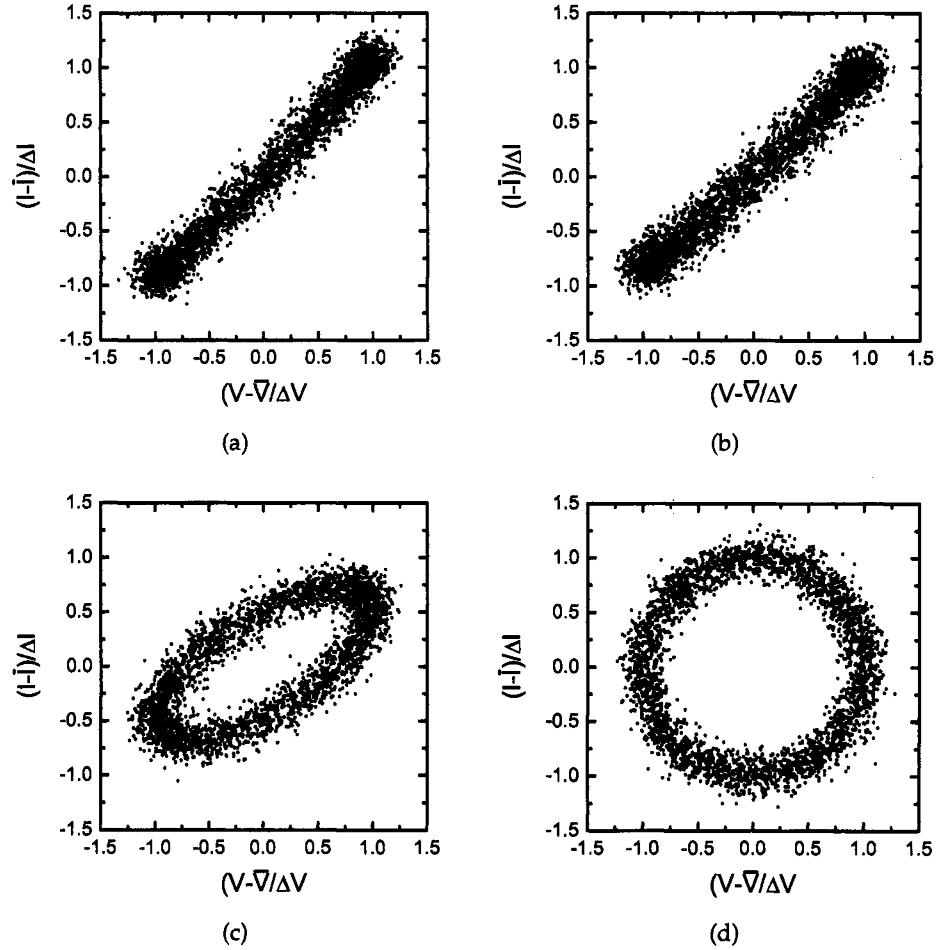

Figure 21.4: Lissajous plots for the system presented in Figure 21.3: a) 1 mHz; b) 10 Hz; c) 100 Hz; and d) 10 kHz.

is almost obscured by the noise in Figure 21.3(b). The larger phase shift associated with higher frequencies, e.g., Figures 8.2(c) and (d) for frequencies of 100 Hz and 10 kHz, respectively, can be discerned in Figures 21.3(c) and (d).

While the presence of additive errors obscures the phase differences in the signals presented in Figure 21.3, repeated sampling at a given frequency allows identification of the transfer-function response, as shown in the corresponding Lissajous plots presented in Figure 21.4. The linear response presented in Figure 21.4(a) for measurement at 1 mHz can be compared to the slightly broader Lissajous plot presented in Figure 21.4(b) for 10 Hz. An elliptical shape can be seen at the characteristic frequency of 100 Hz in Figure 21.4(c), and a perfectly circular response is evident for 10 kHz in Figure 21.4(d). The ideal Lissajous response for these frequencies is given by the 1 mV curves in Figure 8.3.

Figures 21.3 and 21.4 illustrate the transformation of time-domain stochastic errors to the frequency domain. The impedance can be calculated, for example, by the phase-sensitive-detection methods presented in Section 7.3.2 or the Fourier analysis presented in Section 7.3.3. The nature of the errors in the frequency domain will be influenced by the characteristics of the methods used to transform the time-domain signals to the frequency domain.

21.2.3 Stochastic Errors in Frequency Domain

The magnitude of the stochastic errors in impedance measurements depends on the selection of experimental parameters as detailed in Chapter 8. The simulation results described by Carson et al.[100,254,255] in particular provide insight into differences between commonly used impedance instrumentation, including methods based on Fourier analysis[254] and on phase-sensitive detection.[255]

Some general properties for stochastic errors have been established for impedance measurements through experimental observation and simulations. The results described here correspond to additive time-domain errors. The comparison between simulations and experimental results obtained via Fourier analysis supports the suggestion[266] that the nature of experimental time-domain errors is likely to be additive rather than proportional:[254]

- Impedance measurements are, in general, heteroscedastic, which means that the variance of the stochastic errors is a strong function of frequency. It is important, therefore, to use a weighting strategy that accounts for the frequency dependence of the stochastic errors.

- The measurement technique may introduce undesired correlation in the impedance results. Carson et al.[255] showed that a phase-sensitive detection technique employing only one reference signal yielded significant correlation between the real and imaginary parts of the stochastic error structure of the impedance. In a companion paper, Carson et al.[100] showed that the different statistical properties obtained with phase-sensitive-detection (lock-in amplifier) simulations could be attributed in part to bias errors introduced when the square-wave reference signal was in phase with the measured signal. Modern phase-sensitive-detection instruments employ more than one reference signal and may thereby avoid this undesired correlation.

- When time-domain errors are additive, Fourier analysis techniques provide statistical properties that are intrinsic to transfer-function measurements.

- In the absence of instrument-induced correlations, stochastic errors in the frequency-domain are normally distributed. The appearance of a normal distribution of frequency-domain stochastic errors can be regarded to be a consequence of the Central Limit Theorem applied to the methodology used to measure the complex impedance.[270] This result validates an essential assumption routinely used during regression analysis of impedance (and other frequency-domain) data.

Table 21.1: Statistical properties of impedance values obtained by Fourier analysis techniques.[254]

$$\sigma^2_{Z_r} = \sigma^2_{Z_j} \tag{21.9}$$

$$\sigma_{Z_r Z_j} = 0 \tag{21.10}$$

$$\sigma_{|Z|\phi} = 0 \tag{21.11}$$

$$\sigma^2_{|Z|} = |Z|^2 \sigma^2_{\phi} \tag{21.12}$$

- In the absence of bias errors, the errors in the real and imaginary impedance are uncorrelated and the variances of the real and imaginary parts of the complex impedance are equal. Some specific identities are given in Table 21.1.

In a general sense, the frequency-domain error structure is determined by the nature of errors in the time-domain signals and by the method used to process the time-domain data into the frequency domain. The cell impedance influences the frequency-dependence of the variance of the measurements, but the cell impedance does not influence whether the variances of real and imaginary components are equal or whether errors in the real and imaginary components are uncorrelated.

The statistical properties described above for frequency-domain stochastic errors are based on the equations for the instruments actually used for the measurement of complex quantities. While the statistical properties are developed here for electrochemical impedance spectroscopy, they are also valid for measurement of other complex quantities so long as the complex quantities are measured through similar physical principles.

21.3 Bias Errors

Bias errors are systematic errors that do not have a mean value of zero and that cannot be attributed to an inadequate descriptive model of the system. Bias errors can arise from instrument artifacts, parts of the measured system that are not part of the system under investigation, and nonstationary behavior of the system. Some types of bias errors lead the data to be inconsistent with the Kramers-Kronig relations. In those cases, bias errors can be identified by checking the impedance data for inconsistencies with the Kramers-Kronig relations. As some bias errors are themselves consistent with the Kramers-Kronig relations, the Kramers-Kronig relations cannot be viewed as providing a definitive tool for identification of bias errors.

21.3.1 Instrument Artifacts

Limitations of instruments such as potentiostats can influence the measured impedance response. Such influences can be expected at impedance extremes. For example, the impedance response of low-impedance systems such as fuel cells and batteries shows artifacts at high frequency. High-frequency artifacts have also been attributed to reference electrodes. In many cases, instrument artifacts lead to inconsistencies with the Kramers-Kronig relations; however, this is not always the case. As discussed in Section 8.3.2, the experimentalist is encouraged to confirm the high-frequency behavior of electrochemical systems by measuring the impedance of an electrical circuit exhibiting the measured response and by comparing the high-frequency response to limiting values obtained by other experimental methods.

21.3.2 Ancillary Parts of the System under Study

The impedance response of low-impedance systems may include the finite impedance behavior of wires and connectors. These may be considered, from the perspective of model identification, as yielding artifacts in the measured response. Such artifacts may be simply resistive, but may also exhibit a capacitive or even an inductive frequency dependence. Such artifacts will be generally consistent with the Kramers-Kronig relations.

21.3.3 Nonstationary Behavior

Most electrochemical systems show some nonstationary behavior due, for example, to growth of surface films, changes in concentrations of reactants or products in the electrolyte, or changes in surface reactivity. As discussed in Section 21.3.4, the issue is not whether a system is perfectly stationary, but, rather, whether the system has changed substantially during the course of the impedance measurement. The Kramers-Kronig relations are particularly useful for identification of artifacts introduced by nonstationary behavior. These artifacts are most visible at low frequencies, but can be seen at all frequencies if the system change is sufficiently rapid.

Remember! 21.2 *Bias errors in impedance measurements can arise from instrument artifacts, parts of the measured system that are not part of the system under investigation, and nonstationary behavior of the system.*

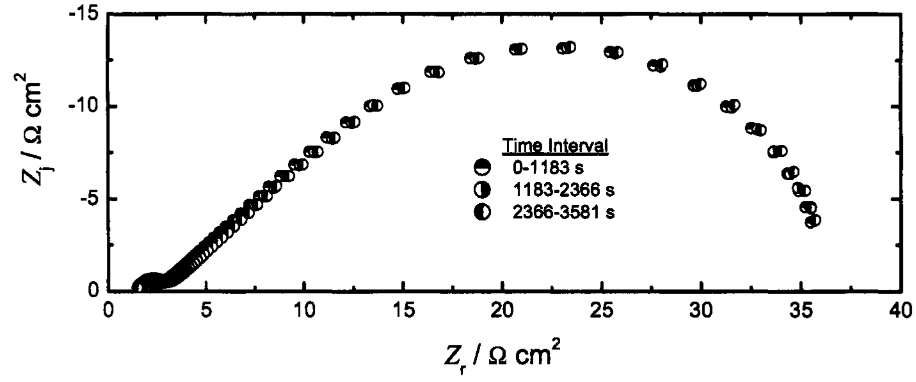

Figure 21.5: A series of three repeated impedance measurements. The data were collected for reduction of ferricyanide on a rotating Pt disk electrode.

21.3.4 Time Scales in Impedance Spectroscopy Measurements

When envisioning a family of impedance measurements, three measurement time scales become evident. The first time scale is that required for measuring a set of replicated measurements. Such a set of measurements is shown in Figure 21.5 for reduction of ferricyanide on a rotating Pt disk electrode. The time required for the set of three measurements was 3581 s (1 h).

The time required to measure a set of N replicated measurements can be given by

$$\tau_{\text{set}} = \sum_{k=1}^{N} \tau_{\text{meas},k} \tag{21.13}$$

where $\tau_{\text{meas},k}$ is the time required for each individual scan. The characteristic frequency for the series of impedance scans is given by

$$f_{\text{set}} = \frac{1}{\tau_{\text{set}}} \tag{21.14}$$

Systems containing stochastic errors with frequency much smaller than f_{set} may appear to be stationary on the time scale of the impedance measurements.

The time required for each frequency scan can be seen in Figure 21.6(a). The average time required for each scan was 1194 s (0.33 h). The time required for a measurement at each individual frequency is illustrated in Figure 21.6(b). At low frequencies, the time required generally corresponds to three or four cycles, but at high frequencies, a much larger number of cycles is needed to account for the smaller signal-to-noise level.

The time required to measure a complete spectrum is given by

$$\tau_{\text{meas}} = \sum_{k=1}^{N} \frac{N_k}{f_k} \tag{21.15}$$

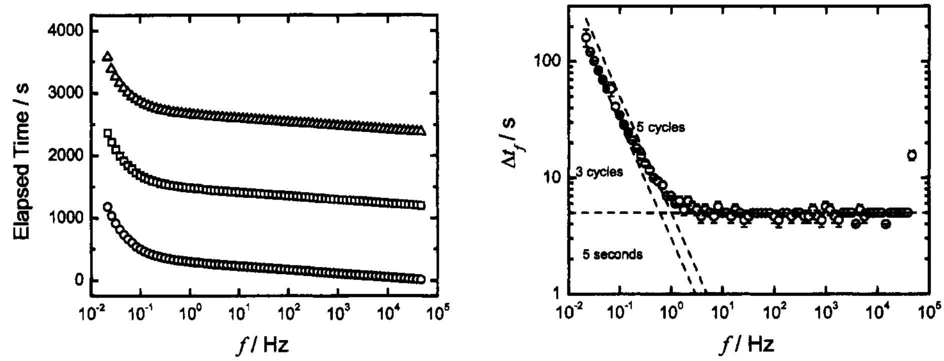

(a) (b)

Figure 21.6: Elapsed time for the measurements presented in Figure 21.5: a) elapsed time; and b) time required for measurement at each frequency. The standard deviation reflects variability among the three impedance measurements.

where N_k represents the number of cycles needed to make the measurement at frequency f_k. The characteristic frequency corresponding to an impedance scan is given by

$$f_{\text{meas}} = \frac{1}{\tau_{\text{meas}}} \tag{21.16}$$

Stochastic errors with frequency larger than f_{meas} and smaller than f_{N_f} will generate a bias error in the measurement. The resulting spectrum will show inconsistencies with the Kramers-Kronig relations (see Chapter 22). Stochastic errors with frequency much smaller than f_{meas} may also generate data that are inconsistent with the Kramers-Kronig relations.

The time required for measurement at each frequency depends on the type of measurement made and on the experimental parameters. For example, the time required for a measurement at each individual frequency is illustrated in Figure 21.7 for EHD measurements (see Chapter 15). The extreme noise level observed at high frequencies increases greatly the time required to achieve a given closure error in the measurements.

If N_f cycles are needed for the measurement at frequency f, the characteristic frequency for an impedance measurement at a given frequency is given by

$$f_{N_f} = \frac{f}{N_f} \tag{21.17}$$

Stochastic errors with frequency much larger than f_{N_f} will appear as a stochastic error in the measurement; whereas, stochastic errors with frequency much smaller than f_{N_f} will appear as a bias error in the measurement. The significance of the bias error will depend on the comparison between the error frequency and the characteristic frequency of the entire measurement of the spectrum.

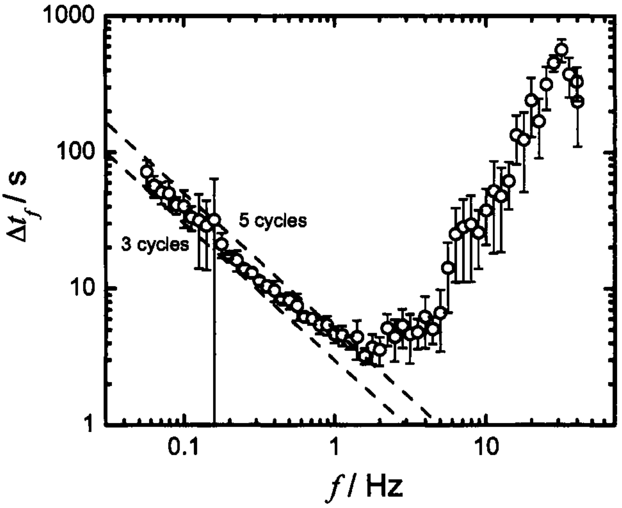

Figure 21.7: Time required for measurement at each frequency for EHD measurements. The standard deviation reflects variability between two measurements. The data were collected for reduction of ferricyanide on a rotating Pt disk electrode.

If the system is evolving very rapidly, changes can occur during the time in which one data point is collected. Impedance spectroscopy may not be a feasible experimental technique for such systems. For systems showing a slower rate of change, the impedance at each frequency may be measurable, but significant change can occur between the start and end of a complete frequency scan. These types of non-stationarities result in the data being inconsistent with the Kramers-Kronig relations. The issues arising out of these inconsistencies are discussed in Chapter 22. At a still slower rate of evolution, the change in the system during one complete scan may be small enough to be ignored, but nonnegligible differences can be seen between successive spectra. Such pseudo-stationary impedance scans are typically observed for even the most stationary electrochemical systems.

21.4 Incorporation of Error Structure

Three approaches have been documented in the literature for incorporating the error structure of impedance data into interpretation strategies. One approach has been to assume a standard form for the stochastic errors. Two models are commonly used. Zoltowski[271] and Boukamp[46,272] advocated use of modulus weighting. Use of a modulus weighting strategy invokes an assumption that the standard deviation is proportional to the frequency-dependent modulus $|Z(\omega)|$ of the impedance, i.e.,

$$\sigma_{Z_r}(\omega) = \sigma_{Z_j}(\omega) = \alpha_M |Z(\omega)| \tag{21.18}$$

where $\sigma_{Z_r}(\omega)$ and $\sigma_{Z_j}(\omega)$ represent the standard deviation of the real and imaginary parts of the impedance, respectively. The parameter α_M is assumed to be independent of frequency and is often arbitrarily assigned a value based on an assumed noise level of the measurement. Macdonald et al.[243,253,257] advocated use of a modified proportional weighting strategy, i.e.,

$$\sigma_{Z_r}^2(\omega) = \alpha^2 + \sigma^2 \left|F'(\omega,\theta)\right|^{2\zeta} \tag{21.19}$$

and

$$\sigma_{Z_j}^2(\omega) = \alpha^2 + \sigma^2 \left|F''(\omega,\theta)\right|^{2\zeta} \tag{21.20}$$

where α, σ, and ζ are error structure parameters, $F'(\omega,\theta)$ and $F''(\omega,\theta)$ are real and imaginary parts of the model immittance function, respectively, and θ is a vector of model parameters. The immittance is a general term that can represent either the admittance or impedance of an electrical circuit. There are fundamental differences between the two commonly used standard weighting strategies. Under equation (21.18), $\sigma_{Z_r} = \sigma_{Z_j}$, whereas equations (21.19) and (21.20) state that, in general, $\sigma_{Z_r} \neq \sigma_{Z_j}$ unless errors are assumed to be independent of frequency (i.e., $\sigma = 0$) or unless $F'(\omega,\theta) = F''(\omega,\theta)$.

A second approach has been to use the regression procedure to obtain an estimate for the error structure of the data.[253,257] A sequential regression is employed in which the parameters for an assumed error structure model, e.g., equations (21.19) and (21.20), are obtained directly from regression to the data.[253] In more recent work, the error variance model was replaced by

$$\sigma_{Z_r}^2(\omega) = \alpha^2 + \left|F'(\omega,\theta)\right|^{2\zeta} \tag{21.21}$$

and

$$\sigma_{Z_j}^2(\omega) = \alpha^2 + \left|F''(\omega,\theta)\right|^{2\zeta} \tag{21.22}$$

where parameters α and ζ are obtained by regression, and an extension of modulus weighting can be obtained by replacing the functions $F'(\omega,\theta)$ and $F''(\omega,\theta)$ with $|F(\omega,\theta)|$.[273] Independent of the assumed form of the error variance model, the assumption that the error variance model can be obtained by minimizing the objective function ignores the differences among the contributions to the residual errors shown in equation (21.1). The error structure obtained by simultaneous regression is also severely constrained by the assumed form of the error-variance model.

The third approach is to use experimental methods to assess the error structure. Independent identification of error structure is the preferred approach, but even minor nonstationarity between repeated measurements introduces a significant bias error in the estimation of the stochastic variance. Dygas and Breiter report on the use of intermediate results from a frequency-response analyzer to estimate the variance of real and imaginary components of the impedance.[274] Their approach allows assessment of the variance of the stochastic component without the need for replicate experiments. The drawback is that their approach cannot be used to assess bias errors and is specific to a particular commercial impedance instrumentation. Van Gheem et al.[275,276] have proposed a structured multi-sine

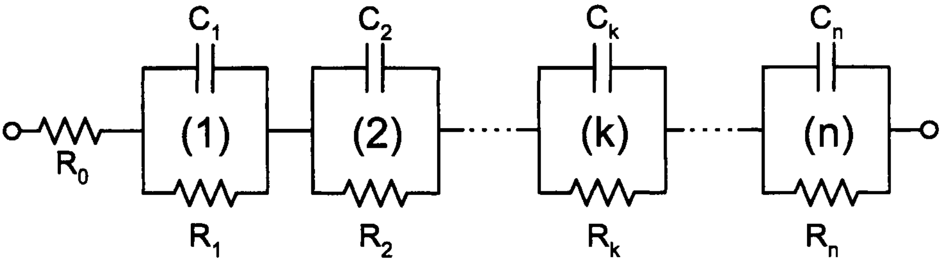

Figure 21.8: A schematic representation of a Voigt circuit used by Agarwal et al.[56,86,262] as a measurement model.

signal that can be used to assess stochastic and bias errors without use of replicated measurements.

Measurement models, developed for impedance spectroscopy by Agarwal et al.,[56,86,262] are generally applicable and can be used to estimate both stochastic and bias errors of a measurement from imperfectly replicated impedance measurements. Orazem et al.[277] used a measurement model approach to show that a general model for the error structure could take the form

$$\sigma_{Z_r} = \sigma_{Z_j} = \alpha|Z_j| + \beta|Z_r - R_e| + \gamma\frac{|Z|^2}{R_m} + \delta \tag{21.23}$$

where α, β, γ, and δ are constants to be determined for a specific potentiostat, set of measurement parameters, and electrochemical system. Standard deviations for practical systems have been reported that are on the order of 0.2 to 0.04 percent of the modulus.[85] The drawback of the measurement model approach is that replicated measurements are required. The measurement model approach is presented in Section 21.5.

21.5 Measurement Models for Error Identification

The measurement model method for distinguishing between bias and stochastic errors is based on using a generalized model as a filter for nonreplicacy of impedance data. The measurement model is composed of a superposition of line-shapes that can be arbitrarily chosen. The model shown in Figure 21.8, composed of Voigt elements in series with a solution resistance, has been shown to be a useful and general measurement model.

While the line-shapes parameters may not be unequivocally associated with a set of deterministic or theoretical parameters for a given system, the measurement model approach has been shown to adequately represent the impedance spectra obtained for a large variety of electrochemical systems.[56] The line-shape models represent the low-frequency stationary components of the impedance spectra (in a Fourier sense). Regardless of their interpretation, the measurement model representation can be used to filter and thus identify the nonstationary (drift) and high-frequency (noise) components contained in the same impedance spectrum.

At first glance, it may not be obvious that such an approach should work. It is well known, for example, that the impedance spectrum associated with an electrochemical reaction limited by the rate of diffusion through a stagnant layer (either the Warburg or the finite-layer diffusion impedance) can be approximated by an infinite number of *RC* circuits in series (the Voigt model). In theory, then, a measurement model based on the Voigt circuit should require an infinite number of parameters to adequately describe the impedance response of any electrochemical system influenced by mass transfer.

In practice, stochastic errors (or noise) in the measurement limit the number of Voigt parameters that can be obtained from experimental data. An infinite number of Voigt parameters cannot be obtained even from synthetic data because round-off errors limit the information content of the calculation.[56] The residual errors associated with fitting a Voigt model to experimental impedance data that are influenced by mass transfer can, with appropriate weighting, be made to be of the order of the stochastic noise in the measurement. A Voigt circuit, or any equivalent circuit, can therefore yield an appropriate measurement model for electrochemical impedance spectra. It is evident that the measurement model composed of Voigt elements may not be the most parsimonious or efficient model for a given spectrum. In effect, by using the measurement model, one takes advantage of the noise present in any measurement, which limits the number of parameters that can be resolved, and the large number of measured frequencies as compared to the number of resolvable parameters.

Thus the Voigt circuit can provide an adequate description of impedance data influenced by mass transfer or by distributed-time-constant phenomena such as is described in Chapter 13. In addition, inductive loops can be fitted by a Voigt circuit by using a negative resistance and capacitance in an element. Such an element will have a positive *RC* time constant. The Voigt circuit serves as a convenient generalized measurement model.

The use of measurement models to check for the consistency of the experimental data with the Kramers-Kronig relations was first proposed by Agarwal et al.[56,278] Boukamp and Macdonald described the use of distributed relaxation time models (DRT) as measurement models for assessing consistency of data with the Kramers-Kronig relations.[279] The approach taken was similar to that of Agarwal et al. with the exception that assumed rather than experimentally measured error structures were used to weight the regressions. A linearized application of measurement models was suggested by Boukamp that eliminated the need for sequential increase in the number of line-shape parameters at the expense of using one line-shape for every frequency measured.[280] The application of such a linearized model is also constrained by the need for an independent assessment of the level of noise in the measurement.

The use of measurement models to identify consistency with the Kramers-Kronig relations is equivalent to the use of Kramers-Kronig transformable circuit analogues. An important advantage of the measurement model approach is that it identifies a small set of model structures that are capable of representing a large variety of observed behaviors or responses. The problem of model discrimination is therefore significantly reduced. The inability to fit an impedance spectrum by a measurement model can be attributed to the failure of the data to conform to the assumptions of the Kramers-Kronig relations rather than the failure of the model. The measurement model approach, however, does not eliminate the problem of model multiplicity or model equivalence over a given frequency range. The reduced set of model structures identified for the measurement model makes it feasible to conduct studies aimed at identification of the error structure, the propagation of error through the model and through the Kramers-Kronig transformation, and issues concerning parameter sensitivity and correlation.

Another significant advantage of the measurement model approach is that the resulting models can be transformed analytically (in the Kramers-Kronig sense). This means that, in contrast to the other approaches for evaluation of consistency (e.g., fitting to polynomials), the real and imaginary parts of the impedance are related through a finite set of common parameters. The measurement models can therefore be used as statistical observers; that is, adequate identification and estimation of the model parameters over a given experimental region, e.g., a range of frequencies in the imaginary domain, will allow the description (or observation) of the behavior of the system over another region, i.e., the real domain. The selection of experimental region used for this evaluation will take advantage of the relative parameter sensitivity in the real and imaginary domains.

It should be noted that the error analysis methods using measurement models are sensitive to data outliers. Occasionally, outliers can be attributed to external influences. Most often, outliers appear near the line frequency and at the beginning of an impedance measurement. Data collected within ±5 Hz of the line frequency and its first harmonic (e.g., 50 and 100 Hz in Europe or 60 and 120 Hz in the United States) should be deleted. Startup transients cause some systems to exhibit a detectable artifact at the first frequency measured. This point, too, should be deleted.

21.5.1 Stochastic Errors

If a single model were to be regressed to all spectra showing nonstationary behavior, the resulting residual error would include contributions from the drift between scans as well as the lack of fit of the model, instrumental bias errors, and stochastic errors, i.e.,

$$\varepsilon_{\text{res}}(\omega) = \varepsilon_{\text{fit}}(\omega) + \varepsilon_{\text{inst}}(\omega) + \varepsilon_{\text{drift}}(\omega) + \varepsilon_{\text{stoch}}(\omega) \tag{21.24}$$

Direct calculation of the variance of the resulting residual errors would lead to a value that includes the contribution of the changing baseline.

Remember! 21.3 *The error analysis methods using measurement models are sensitive to data outliers.*

To eliminate the contribution of the changing baseline, a measurement model is regressed to each scan using the maximum number of parameters that can be resolved from the data. The parameters for the measurement model for each data set will be slightly different because the system changes from one experiment to the other. Hence, by regressing the measurement model to individual data sets separately, the effects of the change of the experimental conditions from one experiment to another are incorporated into the measurement model parameters. The variance of the real and imaginary residual errors can therefore be obtained as a function of frequency and provide a good estimate for the variance of the stochastic noise in the measurement. Thus,

$$\sigma_Z^2(\omega) = \frac{1}{N-1} \sum_{k=1}^{N} \left(\varepsilon_{\mathrm{res},k,k}(\omega) - \bar{\varepsilon}_{\mathrm{res},k}(\omega)\right)^2 \tag{21.25}$$

where $\varepsilon_{\mathrm{res},k,k}$ represents the residual error for scan k obtained from a model k. Shukla and Orazem have shown that the estimate for the variance of the stochastic noise obtained in this way is independent of the measurement model used.[281]

21.5.2 Bias Errors

There are several ways to assess consistency with the Kramers-Kronig relations. In principle, since the Voigt model is itself consistent with the Kramers-Kronig relations, the ability to fit this model to data within the noise level of the measurement should indicate that the data are consistent. An ambiguity exists when the data are not fully consistent, because the lack of fit of the model could be due to causes other than inconsistency with the Kramers-Kronig relations. Some other possible causes could be that the number of frequencies measured was insufficient to allow regression with a large enough number of Voigt parameters or that the initial guesses for the nonlinear regression could be poorly chosen.

While in principle a complex fit of the measurement model could be used to assess the consistency of impedance data, sequential regression to either the real or the imaginary provides greater sensitivity to lack of consistency. The optimal approach is to fit the model to the component that contains the greatest amount of information. The decision as to which component to fit is constrained by two conflicting considerations:

1. The standard deviations of the real and imaginary parts of the impedance are equal; therefore, the noise level represents a large percentage of the imaginary part of the impedance in the asymptotic limits where the imaginary impedance tends toward zero. In some cases, the value of the imaginary impedance can fall below the signal-to-noise threshold.

2. The imaginary part of the impedance is much more sensitive to contributions of minor line-shapes than is the real part of the impedance. Typically, more Voigt line-shapes can be resolved when fitting to the imaginary part of the impedance than can be resolved when fitting to the real part.

The solution resistance cannot be obtained by fitting the measurement model to the imaginary part of the impedance. The solution resistance is treated as an arbitrarily adjustable parameter when fitting to the imaginary part of the impedance.

Regression to one component with subsequent prediction of the other component provides a more sensitive method to assess consistency. A procedure for this analysis is described below:

1. Perform a fit to the imaginary part of the spectrum using error structure weighting. Increase the number of line-shapes used until the maximum number of statistically significant parameters is obtained. Ideally, the ratio of the sum of squares to the noise level should be within the F-test bounds given by the program.

2. Use a Monte Carlo simulation to identify the frequency-dependent confidence interval for the model prediction.

3. Examine the imaginary residual errors to determine whether they fall within the error structure. Should a few points lie outside the error structure at intermittent frequency values, do not be concerned. Assess prediction of the real part of the impedance by examining real residual plots with confidence intervals displayed. Real residual data points that are outside the confidence interval are considered to be inconsistent with the Kramers-Kronig relations and should be removed from the data set.

4. Typically, the number of line-shapes that can be determined in a complex fit will increase when data inconsistent with the Kramers-Kronig relations are removed. Deletion of data that are strongly influenced by bias errors increases the amount of information that can be extracted from the data. In other words, the bias in the complete data set induces correlation in the model parameters, which reduces the number of parameters that can be identified. Removal of the biased data results in a better-conditioned data set that enables reliable identification of a larger set of parameters.

Experimental data can, therefore, be checked for consistency with the Kramers-Kronig relations without actually integrating the equations over frequency, avoiding the concomitant quadrature errors. The use of measurement models does require an implicit extrapolation of the experimental data set, but the implications of the extrapolation procedure are quite different from extrapolations reported in the literature. The extrapolations done with measurement models are based on a common set of parameters for the real and imaginary parts and on a model structure that has been shown to adequately represent the observations. The confidence in the extrapolation using measurement models is, therefore, higher. For the application to a preliminary screening of the data, the use of measurement models is superior to the use of more specific electrical circuit analogues, because one can determine whether the residual errors are due to an inadequate model, to failure of data to conform to the Kramers-Kronig assumptions, or to experimental noise. The algorithm proposed by Agarwal et al.,[56,86,262] in conjunction with error structure weighting, provides a robust way to check for consistency of impedance data.

It should be emphasized that the approach presented in this section is part of an overall assessment of measurement errors. The measurement model is used as a filter for lack of replicacy to obtain a quantitative value for the standard deviation of the measurement as a function of frequency. The mean error identified in this way is equal to zero; thus, the standard deviation of the measurement does not incorporate the bias errors. In contrast, the standard deviation of repeated impedance measurements typically includes a significant contribution from bias errors because perfectly replicate measurements can rarely be made for electrochemical systems. Since the line-shapes of the measurement model satisfy the Kramers-Kronig relations, the Kramers-Kronig relations then can be used as a statistical observer to assess the bias error in the measurement.

Problems

21.1 Consider a system with a single electrochemical reaction with $R_e = 10\ \Omega$, $R_t = 100\ \Omega$, and $R_t C_{dl} = 1$ s. The noise level of the measurement is often assumed to follow equation (21.18) with $\sigma = 0.03\,|Z|$.

- **(a)** Plot the standard deviation of the real and imaginary parts of the impedance measurement as functions of frequency.
- **(b)** Plot the normalized standard deviation of the real and imaginary parts of the impedance measurement, scaled to the respective impedance component, as functions of frequency.
- **(c)** Plot the weighting factor $w = 1/\sigma^2$ for the real and imaginary parts of the impedance measurement as functions of frequency.

21.2 Use Figure 21.6 to estimate the time required for an impedance measurement from 100 kHz to 0.1 Hz with 8 measurements per decade. How does this value change if the measurement requires 10 measurements per decade?

21.3 Use Figure 21.6 to estimate the time required for an impedance measurement from 100 kHz to 0.1 mHz with 8 measurements per decade. How does this value change if the measurement requires 3 measurements per decade?

21.4 Use a spreadsheet program such as Microsoft Excel® or a computational programming environment such as Matlab® to reproduce the results presented in Figures 21.3 and 21.4.

21.5 Add normally distributed stochastic errors to the time-domain potential and current signals for the system described in Example 7.1. Then apply the Fourier analysis to calculate the impedance response at the characteristic frequency. Repeat this process, refreshing the random numbers used, so as to calculate the standard deviation of the resulting impedance. How does this result depend on the number of cycles used for the integration?

Electrochemical Impedance Spectroscopy
by Mark E. Orazem and Bernard Tribollet

Chapter 22

The Kramers-Kronig Relations

The Kramers-Kronig are integral equations that constrain the real and imaginary components of complex quantities for systems that satisfy conditions of linearity, causality, and stability. These relationships, derived independently by Kronig[53,252] and Kramers,[54,282] were initially developed from the constitutive relations associated with the Maxwell equations for description of an electromagnetic field at interior points in matter.[283]

The fundamental constraints are that the system be stable, in the sense that perturbations to the system do not grow, that the system responds linearly to a perturbation, and that the system be causal in the sense that a response to a perturbation cannot precede the perturbation. The Kramers-Kronig relationships were found to be entirely general with application to all frequency-domain measurements that could satisfy the above constraints. Bode extended the concept to electrical impedance and tabulated various extremely useful forms of the Kramers-Kronig relations.[87]

22.1 Mathematical Origin

The development presented here for the complex impedance, $Z = Z_r + jZ_j$, is general and can be applied, for example, to the complex refractive index, the complex viscosity, and the complex permittivity. The derivation for a general transfer function G follows that presented by Nussenzveig.[283] The development for the subsequent analysis in terms of impedance follows the approach presented by Bode.[87]

Remember! 22.1 *The Kramers-Kronig relations apply for systems that are linear, causal, and stable. The condition of stationarity is implicit in the requirement of causality.*

22.1.1 Background

The fundamental constraints for the system transfer functions associated with the assumptions of linearity, casuality, and stability are described in this section.

Theorem 22.1 (Linearity) The output is a linear function of the input. *A general output function $x(t)$ can be expressed as a linear function of the input $f(t)$ as*

$$x(t) = \int_{-\infty}^{+\infty} g\left(t, t'\right) f(t')dt' \tag{22.1}$$

where $g(t, t')$ provides the relationship between input and output functions.

Theorem 22.2 (Time-Translation Independence) The output depends only on the input. *This means that, if the input signal is advanced or delayed by a time increment, the output will be advanced or delayed by the same time increment. Thus, $x(t+\tau)$ corresponds to $f(t+\tau)$ such that $g(t, t')$ can depend only on the difference between t and t'. Equation (22.1) can be written*

$$x(t) = \int_{-\infty}^{+\infty} g\left(t - t'\right) f(t')dt' \tag{22.2}$$

where $g(t - t')$ provides the relationship between input and output functions. The assumption of time-translation independence can be considered to be a consequence of the assumption of primitive causality, discussed in Theorem 22.3.

The function $g(t - t')$ can be expressed in terms of frequency through use of the Fourier integral transform,[77] i.e.,

$$G(\omega) = \int_{-\infty}^{+\infty} g(\tau) \exp\left(-j\omega\tau\right) d\tau \tag{22.3}$$

Similarly, the input can be expressed as

$$F(\omega) = \int_{-\infty}^{+\infty} f(\tau) \exp\left(-j\omega\tau\right) d\tau \tag{22.4}$$

and the output can be expressed as

$$X(\omega) = \int_{-\infty}^{+\infty} x(\tau) \exp\left(-j\omega\tau\right) d\tau \tag{22.5}$$

The Fourier transform can be written with either negative or positive arguments in the exponential. The positive argument yields a positive imaginary impedance for the response of a capacitor to a potential perturbation, whereas the negative argument yields a negative imaginary impedance. The form used here yields results that are consistent with the electrical engineering conventions.

In frequency domain, the output can be expressed as a function of the input as

$$X(\omega) = G(\omega)F(\omega) \tag{22.6}$$

where $G(\omega)$ acts as a transfer function. Equation (22.3) can be expressed as

$$G(\omega) = \int_{-\infty}^{+\infty} g(\tau)\left(\cos(\omega\tau) - j\sin(\omega\tau)\right) d\tau \tag{22.7}$$

For a real-valued time-domain function $g(\tau)$, the function G has conjugate symmetry (see Section 1.3) such that

$$G(-\omega) = G_r + jG_j = \overline{G}(\omega) = G_r - jG_j \tag{22.8}$$

Thus, $G_r(-\omega) = G_r(\omega)$ and $G_j(-\omega) = -G_j(\omega)$. The real part of G, G_r, is an even function of frequency, and the imaginary part G_j is an odd function of frequency.

The above development, expressed for general input, output, and transfer functions, can be presented in terms of impedance $Z(\omega)$. The results stemming from equation (22.7) indicate that the impedance $Z(\omega)$ has conjugate symmetry and can be expanded in powers of frequency according to

$$Z(\omega) = Z_{r,0} + jZ_{j,0}\omega + Z_{r,1}\omega^2 + jZ_{j,1}\omega^3 + \ldots \tag{22.9}$$

and

$$Z = Z_{r,\infty} + \frac{jZ_{j,\infty}}{\omega} + \frac{Z^*_{r,1}}{\omega^2} + \frac{jZ^*_{j,1}}{\omega^3} + \ldots \tag{22.10}$$

where ω is the frequency and Z_{r0}, Z_{j0}, $Z_{r,\infty}$, and $Z_{j,\infty}, \ldots$ are coefficients in the corresponding power series expansion. Equations (22.9) and (22.10) apply to electrical circuits such as the Voigt circuit used by Agarwal et al. as a measurement model.[56]

Example 22.1 Verification of Equations (22.9) and (22.10): *Show that the assumption that the real part of the impedance is an even function of frequency and the imaginary is an odd function of frequency is consistent with the impedance response of a Voigt series.*

Solution: *The impedance response can be expressed in terms of resistance R_k and capacitance C_k by*

$$Z = R_0 + \sum_{k=1}^{n} \frac{R_k}{1 + j\omega C_k R_k} \tag{22.11}$$

The real and imaginary parts of the impedance can be written as

$$Z_r = R_0 + \sum_{k=1}^{n} \frac{R_k}{1 + \omega^2 C_k^2 R_k^2} \tag{22.12}$$

and

$$Z_j = -\omega \sum_{k=1}^{n} \frac{C_k R_k^2}{1 + \omega^2 C_k^2 R_k^2} \tag{22.13}$$

respectively. The real part of the impedance is an even function of ω, and the imaginary part is an odd function of ω. In the low-frequency limit ($\omega \rightarrow 0$),

$$Z_r = R_0 + \sum_{k=1}^{n} R_k - \omega^2 \sum_{k=1}^{n} R_k^3 C_k^2 \tag{22.14}$$

and

$$Z_j = -\omega \sum_{k=1}^{n} C_k R_k^2 + \omega^3 \sum_{k=1}^{n} C_k^3 R_k^4 \tag{22.15}$$

The sum of equations (22.14) and (22.15) yields the first four terms of equations (22.9).

In the high-frequency limit ($\omega \rightarrow \infty$),

$$Z_r = R_0 + \frac{1}{\omega^2} \sum_{k=1}^{n} \frac{1}{C_k^2 R_k} \tag{22.16}$$

and

$$Z_j = -\frac{1}{\omega} \sum_{k=1}^{n} \frac{1}{C_k} \tag{22.17}$$

The sum of equations (22.16) and (22.17) yields the first three terms of equation (22.10).

Example 22.2 Application of Equations (22.9) and (22.10): *Using a Voigt model, find values for the four terms of equation (22.9) and for the four terms of equation (22.10).*

Solution: *The sum of equations (22.14) and (22.15) yields the first four terms of equation (22.9):*

$$Z_{r,0} = R_0 + \sum_{k=1}^{n} R_k \tag{22.18}$$

$$Z_{j,0} = -\sum_{k=1}^{n} C_k R_k^2 \tag{22.19}$$

$$Z_{r,1} = -\sum_{k=1}^{n} R_k^3 C_k^2 \tag{22.20}$$

and

$$Z_{j,1} = \sum_{k=1}^{n} C_k^3 R_k^4 \tag{22.21}$$

The sum of equations (22.16) and (22.17) yields the first three terms of equation (22.10):

$$Z_{r,\infty} = R_0 \tag{22.22}$$

$$Z_{j,\infty} = -\sum_{k=1}^{n} \frac{1}{C_k} \tag{22.23}$$

and

$$Z_{r,1}^{*} = \sum_{k=1}^{n} \frac{1}{C_k^2 R_k} \tag{22.24}$$

The fourth term is not given by equations (22.16) and (22.17). It can be obtained from equation (22.13) for large value of ω, i.e.,

$$\begin{aligned} Z_j &= -\omega \sum_{k=1}^{n} \frac{C_k R_k^2}{1+\omega^2 C_k^2 R_k^2} \\ &= -\sum_{k=1}^{n} \frac{1}{\omega C_k} \frac{1}{1+\frac{1}{\omega^2 C_k^2 R_k^2}} \\ &= -\sum_{k=1}^{n} \frac{1}{\omega C_k} \left(1 - \frac{1}{\omega^2 C_k^2 R_k^2}\right) \end{aligned} \tag{22.25}$$

Thus,

$$Z_j = -\sum_{k=1}^{n} \frac{1}{\omega C_k} + \sum_{k=1}^{n} \frac{1}{\omega^3 C_k^3 R_k^2} \tag{22.26}$$

and

$$Z_{j,1}^{*} = \sum_{k=1}^{n} \frac{1}{C_k^3 R_k^2} \tag{22.27}$$

which is the fourth term in equation (22.10).

Theorem 22.3 (Primitive Causality) The output response to a perturbation cannot precede the input perturbation. *If $f(t) = 0$ for $t < 0$, then $x(t) = 0$ for $t < 0$. This implies that $g(\tau) < 0$ for $t < 0$. Thus, equation (22.3) can be written*

$$G(\omega) = \int_{0}^{+\infty} g(\tau) \exp(-j\omega\tau)\, d\tau \tag{22.28}$$

This important result means that G is analytic and continuous within the negative imaginary frequency plane.

The assumptions presented above, including equation (22.28), are not sufficient for derivation of dispersion relations. The value of the function $G(\omega)$ must be constrained as $\omega \rightarrow 0$. In order for G to represent a causal transform, G must satisfy[283]

$$\lim_{\omega \to \infty} G(\omega) \rightarrow 0 \tag{22.29}$$

A function G that satisfies equation (22.29) can be shown, by use of Cauchy's Integral Formula (Theorem A.3), to be a causal transform. The properties of G implicit in Theorems 22.1–22.3 and equation (22.29) allow derivation of dispersion relations such as the Kramers-Kronig relations. Equation (22.29), however, does not apply for impedance or related electrochemical transfer functions. A weaker restriction can be applied, as discussed in Theorem 22.4.

Theorem 22.4 (Stability) The output response to an input impulse cannot increase with time. *This statement can be expressed as requiring that the total output energy cannot exceed the total input energy.*[283] *A consequence of this statement is that* $G(\omega)$ *is bounded, i.e.,*

$$|G(\omega)|^2 \leq A \tag{22.30}$$

where A *is a constant.*

The function G that satisfies Theorem 22.4 is not a causal transform because the imaginary part of G does not contain all the information needed to obtain the real part. An additive constant cannot be determined by the transformation. By subtracting an additive constant, a modified function is obtained that is a causal transform.

22.1.2 Application of Cauchy's Theorem

As shown in equation (22.10), the real part of the impedance tends toward a finite value as frequency tends toward infinity. The transfer function $Z(x) - Z_{r,\infty}$ tends toward zero with increasing frequency. As $Z(x)$ is analytic, Cauchy's integral theorem, given in Appendix A as Theorem (A.2), can be written as

$$\oint \left(Z(x) - Z_{r,\infty}\right) dx = 0 \tag{22.31}$$

where x is an independent and continuous variable that represents the complex frequency.

The first step in the analysis is to combine Z with some other function in such a way that the result vanishes as rapidly as $1/\omega^2$ as ω tends to infinity. In this way, the contribution of the large semicircular path to the contour integral (see, e.g., Figure 22.1) can be neglected.

22.1.3 Transformation from Real to Imaginary

In order to evaluate the real or imaginary part of impedance at a particular frequency, a pole is created at ω, as shown in Figure 22.1. From considerations of symmetry, a complementary pole is created at $-\omega$. If $Z_r(\omega)$, the value assumed by Z_r at $x = \omega$, is subtracted from Z, the resulting contour integral can be written as:

$$\oint \left[\frac{Z(x) - Z_r(\omega)}{x - \omega} - \frac{Z(x) - Z_r(\omega)}{x + \omega}\right] dx = 0 \tag{22.32}$$

Note that the constant used in equation (22.31), $Z_{r,\infty}$, cancels in the integrand such that

$$\lim_{x \to \infty} \frac{\left(Z(x) - Z_r(\omega)\right)}{x} \to 0 \tag{22.33}$$

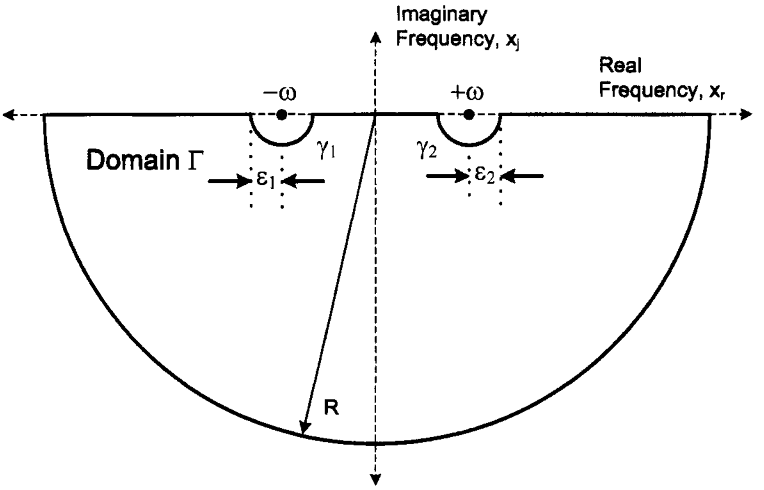

Figure 22.1: Domain of integration for application of Cauchy's integral formula. Poles are placed at frequencies $\pm\omega$ on the real frequency axis.

according to $1/x^3$ rather than $1/x$ (see Theorem (A.5)). Equation (22.32) is equal to zero because, following the condition of causality, the integrand is analytic in the domain considered and the path of integration (as shown in Figure 22.1) is a closed loop (see Theorem (A.2)). The contributions to equation (22.32) are given as

$$\begin{aligned}\oint\left[\frac{Z(x)-Z_r(\omega)}{x-\omega}-\frac{Z(x)-Z_r(\omega)}{x+\omega}\right]dx = \\ \int_{-\infty}^{+\infty}\left(\frac{Z(x)-Z_r(\omega)}{x-\omega}-\frac{Z(x)-Z_r(\omega)}{x+\omega}\right)dx \\ +\int_{\gamma_1}\left(\frac{Z(x)-Z_r(\omega)}{x-\omega}-\frac{Z(x)-Z_r(\omega)}{x+\omega}\right)dx \\ +\int_{\gamma_2}\left(\frac{Z(x)-Z_r(\omega)}{x-\omega}-\frac{Z(x)-Z_r(\omega)}{x+\omega}\right)dx \\ +\int_{\Gamma}\left(\frac{Z(x)-Z_r(\omega)}{x-\omega}-\frac{Z(x)-Z_r(\omega)}{x+\omega}\right)dx = 0\end{aligned} \tag{22.34}$$

where, as shown in Figure 22.1, integration at γ_1 and γ_2 refers to semicircular paths centered at $-\omega$ and $+\omega$, respectively, and integration at Γ refers to integration along the large semicircle of radius R.

The concepts developed in Section A.3.2 can be used to evaluate the contributions to equation (22.35). Under the assumption that $Z(x) - Z(\omega)$ approaches a finite value as $x \longrightarrow \infty$,

$$\lim_{R\rightarrow\infty}\int_{\Gamma}\left(\frac{Z(x)-Z_r(\omega)}{x-\omega}-\frac{Z(x)-Z_r(\omega)}{x+\omega}\right)dz = 0 \tag{22.35}$$

where R is the radius of the semicircular path shown in Figure 22.1. Therefore, the non-zero contributions to the integral in equation (22.32) result from the path of integration along the real frequency axis and at the two small semicircular indentations.

If the radii ε_1 and ε_2 of the semicircular paths γ_1 and γ_2 approach zero, the term $1/(x+\omega)$ dominates along path γ_1, and $1/(x-\omega)$ is the dominant term along path γ_2. From an application of Cauchy's Integral Formula, Theorem (A.3), to a half-circle,

$$-\int_{\gamma_1} \frac{Z(x) - Z_r(\omega)dx}{x+\omega} = -j\pi\left(Z(-\omega) - Z_r(\omega)\right) \tag{22.36}$$

and

$$\int_{\gamma_2} \frac{Z(x) - Z_r(\omega)dx}{x-\omega} = j\pi\left(Z(\omega) - Z_r(\omega)\right) \tag{22.37}$$

Since $Z_j(\omega)$ and $Z_r(\omega)$ are odd and even functions of frequency, respectively, the value of $Z(x)$ evaluated at ω is

$$\lim_{x\to\omega} Z(x) = Z_r(\omega) + jZ_j(\omega) \tag{22.38}$$

and the value at $-\omega$ is given by

$$\begin{aligned}\lim_{x\to-\omega} Z(x) &= Z_r(-\omega) + jZ_j(-\omega)\\ &= Z_r(\omega) - jZ_j(\omega)\end{aligned} \tag{22.39}$$

Thus, equation (22.35) takes the form

$$\begin{aligned}&\fint_{-\infty}^{+\infty}\left(\frac{(Z_r(x)+jZ_j(x)) - Z_r(\omega)}{x-\omega} - \frac{(Z_r(x)+jZ_j(x)) - Z_r(\omega)}{x+\omega}\right)dx \\ &\quad = -2\pi Z_j(\omega)\end{aligned} \tag{22.40}$$

where $\fint_{-\infty}^{+\infty} f(x)dx$ represents the Cauchy principal value of the integral, defined in equation (A.26).

Equation (22.35) can be expressed as

$$2\omega\fint_{-\infty}^{+\infty}\left(\frac{(Z_r(x)+jZ_j(x)) - Z_r(\omega)}{x^2-\omega^2}\right)dx = -2\pi Z_j(\omega) \tag{22.41}$$

The integral from $-\infty$ to $+\infty$ can be separated as

$$\begin{aligned}&\fint_{-\infty}^{0}\left(\frac{(Z_r(x)+jZ_j(x)) - Z_r(\omega)}{x^2-\omega^2}\right)dx + \fint_{0}^{+\infty}\left(\frac{(Z_r(x)+jZ_j(x)) - Z_r(\omega)}{x^2-\omega^2}\right)dx \\ &\quad = -\frac{\pi}{\omega}Z_j(\omega)\end{aligned} \tag{22.42}$$

The odd and even properties of the imaginary and real components of $Z(x)$ are again used to yield

$$Z_j(\omega) = -\frac{2\omega}{\pi}\int_0^\infty \frac{Z_r(x) - Z_r(\omega)}{x^2 - \omega^2}dx \tag{22.43}$$

Evaluation of the integral at $x \rightarrow \omega$ poses no particular problem because, by l'Hôpital's rule,

$$\lim_{x\rightarrow\omega} \frac{Z_r(x) - Z_r(\omega)}{x^2 - \omega^2} = \frac{1}{2x}\frac{dZ_r(x)}{dx} = \frac{1}{2}\frac{dZ_r(x)}{d\ln(x)} \tag{22.44}$$

A similar development can be used to obtain the real part of the impedance as a function of the imaginary part.

22.1.4 Transformation from Imaginary to Real

As shown in equation (22.10), the real part of the impedance tends toward a finite value as frequency tends toward infinity. To allow the integrand to tend toward zero with increasing frequency according to $1/\omega^2$, the integral is written in terms of

$$Z^*(x) = Z(x) - Z_{r,\infty} \tag{22.45}$$

Thus, an equation corresponding to equation (22.32) can be written as

$$\oint \left[\frac{xZ^*(x) - j\omega Z_j(\omega)}{x - \omega} - \frac{xZ^*(x) - j\omega Z_j(\omega)}{x + \omega}\right]dx = 0 \tag{22.46}$$

where poles are created at $\pm\omega$, as shown in Figure 22.1. The contribution around the contour of radius R vanishes as $R \rightarrow \infty$.

The integrals along the semicircular paths γ_1 and γ_2 yield

$$-\int_{\gamma_1} \frac{xZ^*(x) - j\omega Z_j(\omega)dx}{x + \omega} = -j\pi\left((-\omega)Z^*(-\omega) - j\omega Z_j(\omega)\right) \tag{22.47}$$

and

$$\int_{\gamma_2} \frac{xZ^*(x) - j\omega Z_j(\omega)dx}{x - \omega} = j\pi\left(\omega Z^*(\omega) - j\omega Z_j(\omega)\right) \tag{22.48}$$

respectively.

The odd and even character of the imaginary and real parts are used to obtain the value of $xZ^*(x)$ at $\pm\omega$, i.e.,

$$\lim_{x\rightarrow\omega} xZ^*(x) = \omega Z_r(\omega) - \omega Z_{r,\infty} + j\omega Z_j(\omega) \tag{22.49}$$

and the value at $-\omega$ is given by

$$\begin{aligned}\lim_{x\rightarrow-\omega} xZ^*(x) &= -\omega Z_r(-\omega) + \omega Z_{r,\infty} - j\omega Z_j(-\omega) \\ &= -\omega Z_r(\omega) + \omega Z_{r,\infty} + j\omega Z_j(\omega)\end{aligned} \tag{22.50}$$

Thus, equation (22.46) takes the form

$$\begin{aligned}&\fint_{-\infty}^{+\infty}\left(\frac{xZ^*(x)-j\omega Z_j(\omega)}{x-\omega}-\frac{xZ^*(x)-j\omega Z_j(\omega)}{x+\omega}\right)dx \\ &\quad= -2j\pi\omega\left(Z_r(\omega)-Z_{r,\infty}\right)\end{aligned} \tag{22.51}$$

Equation (22.51) can be expressed as

$$\begin{aligned}&2\omega\fint_{-\infty}^{+\infty}\left(\frac{x\left(Z_r(x)-Z_{r,\infty}+jZ_j(x)\right)-j\omega Z_j(\omega)}{x^2-\omega^2}\right)dx \\ &\quad= -2j\pi\left(Z_r(\omega)-Z_{r,\infty}\right)\end{aligned} \tag{22.52}$$

The integral from $-\infty$ to $+\infty$ can be expressed as the sum of integrals from $-\infty$ to 0 and 0 to $+\infty$. The odd and even properties of the imaginary and real components of $Z(x)$ are again used to yield

$$Z_r(\omega) = Z_{r,\infty} - \frac{2}{\pi}\fint_0^{\infty}\frac{xZ_j(x)-\omega Z_j(\omega)}{x^2-\omega^2}dx \tag{22.53}$$

Evaluation of the integral of equation (22.53) at $x \rightarrow \omega$ poses no particular problem because, by l'Hôpital's rule,

$$\lim_{x\rightarrow\omega}\frac{xZ_j(x)-\omega Z_j(\omega)}{x^2-\omega^2} = \frac{1}{2x}\frac{xdZ_j(x)}{dx} = \frac{1}{2}\frac{dxZ_j(x)}{d\ln(x)} \tag{22.54}$$

Through equation (22.53), the imaginary part of the impedance can be used to obtain the real part of the impedance if the asymptotic value at high frequency is known.

22.1.5 Application of the Kramers-Kronig Relations

Some different forms of the Kramers-Kronig relations are presented in Table 22.1. Equations (22.55) and (22.56), called the *Plemelj formulas*, are obtained directly from consideration of causality in a linear system. Equations (22.57) and (22.58) are mathematically equivalent to equations (22.59) and (22.60), respectively, because

$$\fint_0^{\infty}\frac{1}{x^2-\omega^2}dx = 0 \tag{22.67}$$

A series of equations have been developed to relate the phase angle to the modulus, represented by equations (22.61), (22.62), (22.63), and (22.64). Equations (22.65) and (22.66) were developed by Ehm et al.[284] in terms of the natural logarithm of the complex impedance. Some key relationships among the real and imaginary

Table 22.1: Compilation of various forms of the Kramers-Kronig relations.

$$Z_j(\omega) = -\frac{1}{\pi}\fint_{-\infty}^{+\infty}\frac{Z_r(x)}{x-\omega}dx \tag{22.55}$$

$$Z_r(\omega) = Z_{r,\infty} + \frac{1}{\pi}\fint_{-\infty}^{+\infty}\frac{Z_j(x)}{x-\omega}dx \tag{22.56}$$

$$Z_j(\omega) = -\frac{2\omega}{\pi}\fint_{0}^{\infty}\frac{Z_r(x)}{x^2-\omega^2}dx \tag{22.57}$$

$$Z_r(\omega) = Z_{r,\infty} - \frac{2}{\pi}\fint_{0}^{\infty}\frac{xZ_j(x)}{x^2-\omega^2}dx \tag{22.58}$$

$$Z_j(\omega) = -\frac{2\omega}{\pi}\fint_{0}^{\infty}\frac{Z_r(x)-Z_r(\omega)}{x^2-\omega^2}dx \tag{22.59}$$

$$Z_r(\omega) = Z_{r,\infty} - \frac{2}{\pi}\fint_{0}^{\infty}\frac{xZ_j(x)-\omega Z_j(\omega)}{x^2-\omega^2}dx \tag{22.60}$$

$$\phi(\omega) = -\frac{\omega}{\pi}\fint_{0}^{\infty}\frac{\ln\left(|Z(x)|\right)}{x^2-\omega^2}dx \tag{22.61}$$

$$\phi(\omega) = -\frac{\omega}{\pi}\fint_{0}^{\infty}\frac{\ln\left(|Z(x)|\right)-\ln\left(|Z(\omega)|\right)}{x^2-\omega^2}dx \tag{22.62}$$

$$\phi(\omega) = -\frac{1}{2\pi}\fint_{0}^{\infty}\ln\left|\frac{x-\omega}{x+\omega}\right|\frac{d\ln|Z(x)|}{dx}dx \tag{22.63}$$

$$\ln\left(|Z(\omega)|\right) = \frac{2}{\pi}\fint_{-\infty}^{+\infty}\frac{\phi(x)}{x-\omega}dx \tag{22.64}$$

$$\operatorname{Re}\left\{\ln\left(Z(\omega)\right)\right\} = \operatorname{Re}\left\{\ln\left(Z(0)\right)\right\} + \frac{2\omega^2}{\pi}\fint_{0}^{\infty}\frac{\operatorname{Im}\left\{\ln\left(Z(x)\right)\right\}}{x\left(x^2-\omega^2\right)}dx \tag{22.65}$$

$$\operatorname{Im}\left\{\ln\left(Z(\omega)\right)\right\} = -\frac{2\omega}{\pi}\fint_{0}^{\infty}\frac{\operatorname{Re}\left\{\ln\left(Z(x)\right)\right\}}{x^2-\omega^2}dx \tag{22.66}$$

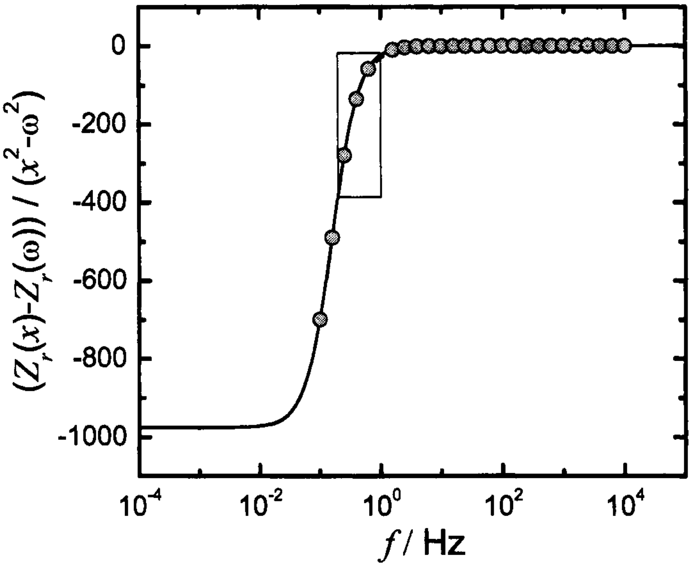

Figure 22.2: The integrand of equation (22.59) as a function of frequency for a single Voigt element ($R_0 = 10\ \Omega$, $R_1 = 1000\ \Omega$, $C_1 = 10^{-3}$ F). Symbols represent synthetic impedance data collected at 5 points per decade over a frequency range of 0.1–10,000 Hz. The equations are evaluated at a frequency of 1 Hz. The box identifies the region of the plot expanded as Figure 22.3.

components of the natural logarithm of the complex impedance and phase angle are given as equations (1.113) and (1.114) in Table 1.7.

The Kramers-Kronig relations are extremely general and have been applied to a wide variety of research areas. In the field of optics, for which the validity of the Kramers-Kronig is not in question, the relationship between real and imaginary components has been exploited to complete optical spectra. In other areas where data cannot be assumed to satisfy the requirements of the Kramers-Kronig relations, the equations presented in Table 22.1 have been used to check whether real and imaginary components of complex variables are internally consistent. Failure of the Kramers-Kronig relations is assumed to correspond to a failure within the experiment to satisfy one or more of the constraints of linearity, stability, or causality.

There are inherent difficulties in the direct application of the Kramers-Kronig relations to experimental data. Some of these difficulties are evident in Figure 22.2 where the integrand of equation (22.59) is given as a function of frequency for a single Voigt element. The major difficulty in applying this approach is that the measured frequency range may not be sufficient to allow integration over the frequency limits of zero to infinity. Therefore, discrepancies between experimental data and the impedance component predicted through application of the Kramers-Kronig relations could be attributed to use of a frequency domain that is too narrow as well as to failure to satisfy the constraints of the Kramers-Kronig equations.

A second issue is that the integral equations do not account explicitly for the stochastic character of experimental data. This requires solution of the Kramers-Kronig relations in an expectation sense, as discussed in the following section. The methods used to address the incomplete sampled frequency range will be described in a subsequent section.

22.2 The Kramers-Kronig in an Expectation Sense

The contribution of stochastic error $\varepsilon(\omega)$ to the observed value of the impedance at any given frequency ω can be expressed as

$$Z_{\mathrm{ob}}(\omega) = Z(\omega) + \varepsilon(\omega) = (Z_r(\omega) + \varepsilon_r(\omega)) + j(Z_j(\omega) + \varepsilon_j(\omega)) \tag{22.68}$$

where $Z(\omega)$, $Z_r(\omega)$, and $Z_j(\omega)$ represent the error-free values of the impedance that conform exactly to the Kramers-Kronig relations. The measurement error $\varepsilon(\omega)$ is a complex stochastic variable such that

$$\varepsilon(\omega) = \varepsilon_r(\omega) + j\varepsilon_j(\omega) \tag{22.69}$$

At any frequency ω the expectation of the observed impedance $\mathrm{E}\left(Z_{\mathrm{ob}}(\omega)\right)$, defined in equation (3.1), is equal to the value consistent with the Kramers-Kronig relations, i.e.,

$$\mathrm{E}\left\{Z_{\mathrm{ob}}(\omega)\right\} = Z(\omega) \tag{22.70}$$

if and only if both

$$\mathrm{E}\left\{\varepsilon_r(\omega)\right\} = 0 \tag{22.71}$$

and

$$\mathrm{E}\left\{\varepsilon_j(\omega)\right\} = 0 \tag{22.72}$$

Equations (22.71) and (22.72) are satisfied for errors that are stochastic and do not include the effects of bias.

22.2.1 Transformation from Real to Imaginary

Equation (22.43) can be applied to obtain the imaginary part from the real part of the impedance spectrum only in an expectation sense, i.e.,

$$\mathrm{E}\left\{Z_j(\omega)\right\} = \frac{2\omega}{\pi}\mathrm{E}\left\{\int_0^\infty \frac{Z_r(x) - Z_r(\omega) + \varepsilon_r(x) - \varepsilon_r(\omega)}{x^2 - \omega^2}\right\}dx \tag{22.73}$$

Remember! 22.2 *Impedance data that do not satisfy the Kramers-Kronig relations must violate at least one of the required conditions of stability, linearity, and causality. Satisfaction of the Kramers-Kronig relations is a necessary but not sufficient condition for meeting conditions of stability, linearity, and causality.*

For a given evaluation of equation (22.73),

$$\begin{aligned} Z_j^{kk}(\omega) + \varepsilon_j^{kk}(\omega) &= \frac{2\omega}{\pi}\left[\mathrm{E}\left\{\fint_0^\infty \frac{Z_r(x) - Z_r(\omega) + \varepsilon_r(x) - \varepsilon_r(\omega)}{x^2 - \omega^2}dx\right\}\right. \\ &\quad \left. + \int_0^\infty \frac{\varepsilon_r(x)}{x^2 - \omega^2}dx\right] \end{aligned} \tag{22.74}$$

where $Z_j^{kk}(\omega)$ represents the value of the imaginary part of the impedance obtained by evaluation of the Kramers-Kronig integral equation and $\varepsilon_j^{kk}(\omega)$ represents the error in the evaluation of the Kramers-Kronig relations caused by the second integral on the right-hand side.

It is evident from equation (22.74) that, for the expected value of the observed imaginary component to approach its true value in the Kramers-Kronig sense, it is necessary that $\mathrm{E}\left\{\varepsilon_j^{kk}(\omega)\right\} = 0$. Thus, the requirements are that equation (22.71) be satisfied and that

$$\mathrm{E}\left\{\frac{2\omega}{\pi}\fint_0^\infty \frac{\varepsilon_r(x)}{x^2 - \omega^2}\right\}dx = 0 \tag{22.75}$$

Requirements (22.71) and (22.75) place well-defined constraints on the evaluation of the Kramers-Kronig integral equations.

For the first condition to be met, it is necessary that the process be stationary in the sense of replication at every measurement frequency.

The second condition can be satisfied in two ways. In the hypothetical case where all frequencies can be sampled, the expectation can be carried to the inside of the integral, and equation (22.75) results directly from equation (22.71).

In the more practical case where the impedance is sampled at a finite number of frequencies, $\varepsilon_r(x)$ represents the error between an interpolated function and the "true" impedance value at frequency x. This error is seen in Figure 22.3, where a region of Figure 22.2 was expanded to demonstrate the discrepancy between a straight-line interpolation between data points and the model that conforms to the interpolation of the data. This error is composed of contributions from the quadrature and/or interpolation errors and from the stochastic noise at the measurement frequency ω. Effectively, equation (22.75) represents a constraint on the integration procedure. In the limit that quadrature and interpolation errors are negligible, the residual errors $\varepsilon_r(x)$ should be of the same magnitude as the stochastic noise $\varepsilon_r(\omega)$.

22.2.2 Transformation from Imaginary to Real

The Kramers-Kronig relations for obtaining the real part from the imaginary part of the spectrum can be expressed as equation (22.53), which, in terms of expectations,

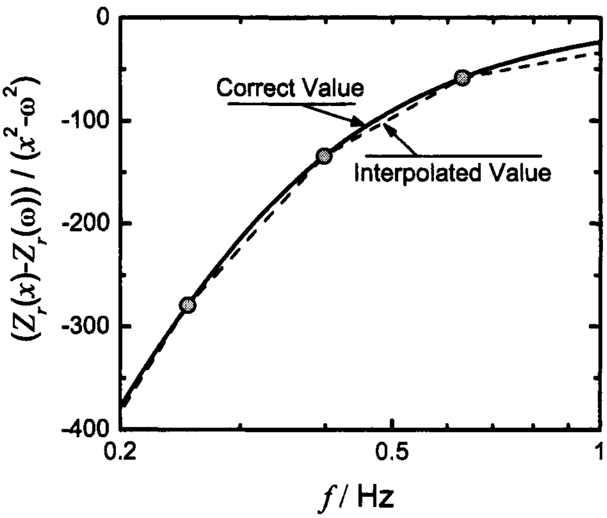

Figure 22.3: A region of Figure 22.2 is expanded to demonstrate the discrepancy between a straight-line interpolation between data points and the model that conforms to the interpolation of the data. System parameters are as given in Figure 22.2.

becomes

$$\mathrm{E}\left(Z_r(\omega)-Z_{r,\infty}\right)=-\frac{2}{\pi}\mathrm{E}\left\{\int_0^\infty\frac{xZ_j(x)-\omega Z_j(\omega)+x\varepsilon_j(x)-\omega\varepsilon_j(\omega)}{x^2-\omega^2}dx\right\}\tag{22.76}$$

For a given evaluation of equation (22.76),

$$\begin{aligned}Z_r^{kk}(\omega)-Z_{r,\infty}+\varepsilon_r^{kk}(\omega)&=\varepsilon_{Z_{r,\infty}}^{kk}\\&-\frac{2\omega}{\pi}\left[\mathrm{E}\left\{\int_0^\infty\frac{xZ_j(x)-\omega Z_j(\omega)+x\varepsilon_r(x)-\omega\varepsilon_r(\omega)}{x^2-\omega^2}dx\right\}\right.\\&\left.+\int_0^\infty\frac{x\varepsilon_j(x)}{x^2-\omega^2}dx\right]\end{aligned}\tag{22.77}$$

Following the discussion of equation (22.74), the necessary conditions for application of the Kramers-Kronig relations are that equation (22.72) be satisfied and that

$$\mathrm{E}\left\{\frac{2}{\pi}\int_0^\infty\frac{x\varepsilon_j(x)}{x^2-\omega^2}\right\}dx=0\tag{22.78}$$

Under the assumption that the impedance is sampled at a finite number of frequencies, $\varepsilon_j(x)$ represents the error between an interpolated function and the "true" impedance value at frequency x. This term is composed of contributions from the quadrature and/or interpolation errors and from the stochastic noise at the measurement frequency ω. As does equation (22.75), equation (22.78) provides a well-defined constraint on the integration procedure.

22.3 Methods for Application

In principle, the Kramers-Kronig relations can be used to determine whether the impedance spectrum of a given system has been influenced by bias errors caused, for example, by instrumental artifacts or time-dependent phenomena. Although this information is critical to the analysis of impedance data, the Kramers-Kronig relations have not found widespread use in the analysis and interpretation of electrochemical impedance spectroscopy data due to difficulties with their application. The integral relations require data for frequencies ranging from zero to infinity, but the experimental frequency range is necessarily constrained by instrumental limitations or by noise attributable to the instability of the electrode.

The Kramers-Kronig relations have been applied to electrochemical systems by direct integration of the equations, by experimental observation of stability and linearity, by regression of specific electrical circuit models, and by regression of generalized measurement models.

22.3.1 Direct Integration of the Kramers-Kronig Relations

Direct integration of the Kramers-Kronig relations involves calculating one component of the impedance from the other, e.g., the real component of impedance from the measured imaginary component. The result is compared to the experimental values obtained. The integral equations, for example, equation (22.60), require integration from 0 to ∞. One difficulty in applying this approach, as shown in Figure 22.2, is that the measured frequency range may not be sufficient to allow integration over the frequency limits of zero to infinity. Therefore, discrepancies between experimental data and the impedance component predicted through application of the Kramers-Kronig relations could be attributed to the use of a frequency domain that is too narrow, as well as to the failure to satisfy the constraints of the Kramers-Kronig equations. An interpolation function is required to allow extrapolation of the integrand into the experimentally inaccessible frequency regime.

A second issue is that the interpolation function must satisfy equations (22.75) or (22.78). It is clear that a suboptimal interpolation, such as the straight-line interpolation shown in Figure 22.3, will bias the estimate of the impedance through the Kramers-Kronig relations.

Two approaches for interpolation function have been used. In one, polynomials, e.g., in powers of ω^n, are fit to impedance data. Usually, a piecewise regression is required. While piece-wise polynomials are excellent for smoothing, the best example being splines, they are not very reliable for extrapolation and result in a relatively large number of parameters. A second approach is to use interpolation formulas based on the expected asymptotic behavior of a typical electrochemical system.

22.3.2 Experimental Assessment of Consistency

Experimental methods can be applied to check whether impedance data conform to the Kramers-Kronig assumptions. A check for linear response can be made by observing whether spectra obtained with different magnitudes of the forcing function are replicates or by measuring higher-order harmonics of the impedance response (see Section 8.2.2). Stationary behavior can be also be identified experimentally by replication of the impedance spectrum. Spectra are replicates if the spectra agree to within the expected frequency-dependent measurement error. If the experimental frequency range is sufficient, the extrapolation of the impedance spectrum to zero frequency can be compared to the corresponding values obtained from separate steady-state experiments. The experimental approach to evaluating consistency with the Kramers-Kronig relations shares constraints with direct integration of the Kramers-Kronig equations. Because extrapolation is required, the comparison of the dc limit of impedance spectra to steady-state measurement is possible only for systems for which a reasonably complete spectrum can be obtained. Experimental approaches for verifying consistency with the Kramers-Kronig relations by replication are further limited in that, without an *a priori* estimate for the confidence limits of the experimental data, the comparison is more qualitative than quantitative. A method is therefore needed to evaluate the error structure, or frequency-dependent confidence interval, for the data that would be obtained in the absence of nonstationary behavior. Such methods are described in Chapter 21.

22.3.3 Regression of Process Models

Electrical circuits consisting of passive and distributed elements can be shown to satisfy the Kramers-Kronig relations. Therefore, successful regression of an electrical circuit analogue to experimental data implies that the data must also satisfy the Kramers-Kronig relations. This approach has the advantage that integration over an infinite frequency domain is not required; therefore a portion of an incomplete spectrum can be identified as being consistent without use of extrapolation algorithms.

Perhaps the major problem with the use of electrical circuit models to determine consistency is that interpretation of a poor fit is ambiguous. A poor fit could

Remember! 22.3 *An insufficient experimental frequency range makes direct integration of the Kramers-Kronig relations problematic. Regression-based approaches, such as use of a measurement model, are preferred.*

be attributed to inconsistency of the data with the Kramers-Kronig relations or to use of an inadequate model or to regression to a local rather than global minimum (perhaps caused by a poor initial guess). A second unresolved issue deals with the regression itself, i.e., selection of the weighting to be used for the regression, and identification of a criterion for a good fit. A good fit could be defined by residual errors that are of the same size as the noise in the measurement, but, in the absence of a means of determining the error structure of the measurement, such a criterion is speculative at best.

22.3.4 Regression of Measurement Models

The concept of the measurement model as a tool for assessment of the error structure was applied to impedance spectroscopy initially by Agarwal et al.[56,86,262] The measurement model is described in greater detail in Chapter 21.

From the perspective of the approach proposed here, the use of measurement models to identify consistency with the Kramers-Kronig relations is equivalent to the use of Kramers-Kronig transformable circuit analogues, discussed in Section 22.3.3. An important advantage of the measurement model approach is that it identifies a small set of model structures that are capable of representing a large variety of observed behaviors or responses. The problem of model discrimination is therefore significantly reduced. The inability to fit an impedance spectrum by a measurement model can be attributed to the failure of the data to conform to the assumptions of the Kramers-Kronig relations rather than the failure of the model. The measurement model approach, however, does not eliminate the problem of model multiplicity or model equivalence over a given frequency range. The reduced set of model structures identified by the measurement model makes it feasible to conduct studies aimed at identification of the error structure, the propagation of error through the model and through the Kramers-Kronig transformation, and issues concerning parameter sensitivity and correlation.

The use of measurement models is superior to the use of polynomial fitting because fewer parameters are needed to model complex behavior and because the measurement model satisfies the Kramers-Kronig relations implicitly. Experimental data can, therefore, be checked for consistency with the Kramers-Kronig relations without actually integrating the equations over frequency, avoiding the concomitant quadrature errors. The use of measurement models does require an implicit extrapolation of the experimental data set, but the implications of the extrapolation procedure are quite different from extrapolations reported in Section 22.3.1. The extrapolation done with measurement models is based on a common set of parameters for the real and imaginary parts and on a model structure that has been shown to adequately represent the observations. The confidence in the extrapolation using measurement models is, therefore, higher.

The use of measurement models is superior to the use of more specific electrical circuit analogues because one can determine whether the residual errors are due to an inadequate model, to failure of data to conform to the Kramers-Kronig assumptions, or to experimental noise.

Problems

22.1 Use a circuit with $R_e = 10\ \Omega\text{cm}^2$, $R_t = 100\ \Omega\text{cm}^2$, and $C_{\text{dl}} = 20\ \mu\text{F/cm}^2$ to verify the equations given in Table 22.1. This problem requires use of a spreadsheet program such as Microsoft Excel® or a computational programming environment such as Matlab®.

- **(a)** Equation (22.55)
- **(b)** Equation (22.56)
- **(c)** Equation (22.57)
- **(d)** Equation (22.58)
- **(e)** Equation (22.59)
- **(f)** Equation (22.60)
- **(g)** Equation (22.61)
- **(h)** Equation (22.62)
- **(i)** Equation (22.63)
- **(j)** Equation (22.64)
- **(k)** Equation (22.65)
- **(l)** Equation (22.66)

22.2 Verify that the impedance response that includes a CPE, following equation (13.2), satisfies the Kramers-Kronig relations.

22.3 Using the results of Problem 8.6, explore whether the Kramers-Kronig relations can be used to detect a nonlinearity in the impedance response. Discuss the implication of your result on experimental design.

22.4 Why are the assumptions of linearity, causality, and stability necessary for the derivation of the Kramers-Kronig relations?

22.5 What is a causal transform? Why is the impedance Z not a causal transform?

22.6 It is sometimes said that a finite impedance is needed in order for application of the Kramers-Kronig relations to an electrochemical system. Yet, blocking electrodes do not have a finite impedance. Do the Kramers-Kronig relations apply for blocking electrodes? If so, how can they be applied?

Electrochemical Impedance Spectroscopy
by Mark E. Orazem and Bernard Tribollet

Part VI

Overview

Electrochemical Impedance Spectroscopy
by Mark E. Orazem and Bernard Tribollet

Chapter 23

An Integrated Approach to Impedance Spectroscopy

The foundation of this textbook is a philosophy that integrates experimental observation, model development, and error analysis. This approach is differentiated from the usual sequential model development for given impedance spectra[3,4] by its emphasis on obtaining additional supporting observations to guide model selection, use of error analysis to guide regression strategies and experimental design, and use of models to guide selection of new experiments.

23.1 Flowcharts for Regression Analysis

While impedance spectroscopy can be a sensitive tool for analysis of electrochemical and electronic systems, an unambiguous interpretation of spectra cannot be obtained by examination of raw data. Instead, interpretation of spectra requires development of a model that accounts for the impedance response in terms of the desired physical properties. Model development should take into account both the impedance measurement and the physical and chemical characteristics of the system under study.

It is useful to envision a flow diagram for the measurement and interpretation of experimental measurements such as impedance spectroscopy. Barsoukov and Macdonald proposed such a flow diagram for a general characterization procedure consisting of two blocks comprising the impedance measurement, three blocks comprising a physical (or process) model, one block for an equivalent electrical circuit, and blocks labeled curve fitting and system characterization.[3,4] They suggested that impedance data may be analyzed for a given system by using either an exact mathematical model based on a plausible physical theory or a comparatively empirical equivalent circuit. The parameters for either model can be estimated by complex nonlinear least-squares regression. The authors observed that ideal electrical circuit elements represent ideal lumped constant properties, whereas the physical properties of electrolytic cells are often distributed. The distribution of cell properties motivates use of distributed impedance elements such as constant-phase elements (CPE). An additional problem with equivalent circuit analysis, which the authors suggest is not shared by the direct comparison to the theoretical model, is that circuit models are ambiguous and different models may provide equivalent fits to a given spectrum. The authors suggest that identification of the appropriate equivalent circuit can be achieved only by employing physical intuition and by carrying out several sets of measurements with different conditions.

A similar flow diagram was presented by Huang et al.[285] for solid-oxide fuel cells (SOFCs). The diagram accounts for the actions of measuring impedance data, modeling, fitting the model, interpreting the results, and optimizing the fuel cell for power generation. The authors emphasize that the interpreting action depends more on the electrochemical expertise of the researchers than on a direct mapping from model parameters to SOFC properties.

While helpful, the flow diagrams proposed by Barsoukov and Macdonald[4] and Huang et al.[285] are incomplete because they do not account for the role of independent assessment of experimental error structure and because they do not emphasize the critical role of supporting experimental measurements. Orazem et al. proposed a flow diagram consisting of three elements: experiment, measurement model, and process model.[286] The measurement model was intended to assess the stochastic and bias error structure of the data; thus, their diagram accounts for the independent assessment of experimental error structure. Their diagram does not, however, account for supporting nonimpedance measurements, and the use of regression analysis, while implied, is not shown explicitly. The object of this chapter is to formulate a comprehensive approach that can be applied to measurement and interpretation of impedance spectra.

23.2 Integration of Measurements, Error Analysis, and Model

A refined philosophical approach toward the use of impedance spectroscopy is outlined in Figure 23.1, where the triangle evokes the concept of an operational amplifier for which the potential of input channels must be equal. Sequential steps are taken until the model provides a statistically adequate representation of the data to within the independently obtained stochastic error structure. The different aspects that comprise the philosophy are presented in this section.

Remember! 23.1 *The philosophical approach of this textbook integrates experimental observation, model development, and error analysis.*

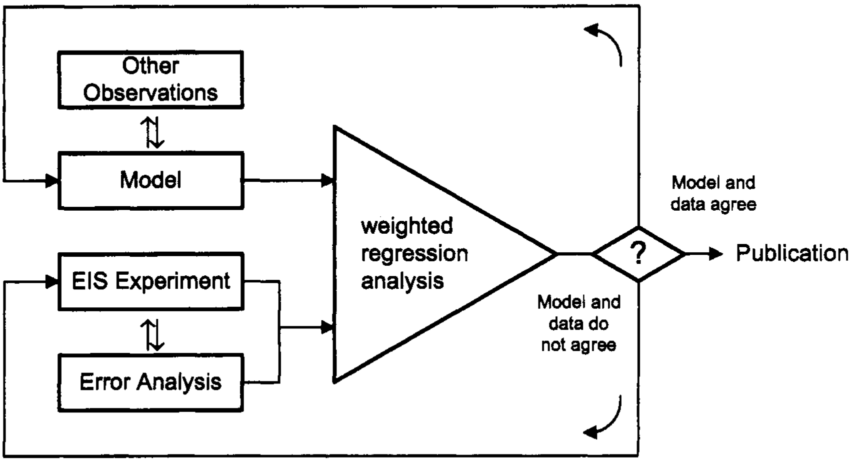

Figure 23.1: Schematic flowchart showing the relationship between impedance measurements, error analysis, supporting observations, model development, and weighted regression analysis. (Taken from Orazem and Tribollet[241] and reproduced with permission of Elsevier, Inc.)

23.2.1 Impedance Measurements Integrated with Error Analysis

All impedance measurements should begin with measurement of a steady-state polarization curve. The steady-state polarization curve is used to guide selection of an appropriate perturbation amplitude and can provide initial hypotheses for model development. The impedance measurements can then be made at selected points on the polarization curve to explore the potential dependence of reaction rate constants. Impedance measurements can also be performed at different values of state variables such as temperature, rotation speed, and reactant concentration. Impedance scans measured at different points of time can be used to explore temporal changes in system parameters. Some examples include growth of oxide or corrosion-product films, poisoning of catalytic surfaces, and changes in reactant or product concentration.

The impedance measurements should also be conducted in concert with error analysis with emphasis on both stochastic and systematic bias errors. The bias errors can be defined to be those that result in data that are inconsistent with the Kramers-Kronig relations. An empirical error analysis can be undertaken using the measurement model approach suggested by Agarwal et al.[56,86,262,287] It should be noted, however, that this approach is not definitive, because Kramers-Kronig-consistent artifacts can be caused by electrical leads and the electronics. Use of dummy cells can help identify artifacts that are consistent with the Kramers-Kronig relations. As an alternative approach for identification of the stochastic part of the error structure, Dygas and Breiter have shown that impedance instrumentation could, in principle, provide standard deviations for the impedance measurements at each frequency.[288]

The feedback loop shown in Figure 23.1 between *EIS experiment* and *error analysis* indicates that the error structure is obtained from the measured data and that knowledge of the error structure can guide improvements to the experimental design. The magnitude of perturbation, for example, should be selected to minimize stochastic errors while avoiding inducing a nonlinear response. The frequency range should be selected to sample the system time constants, while avoiding bias errors associated with nonstationary phenomena. In short, the experimental parameters should be selected so as to minimize the stochastic error structure while, at the same time, allowing for the maximum frequency range that is free of bias errors.

23.2.2 Process Models Developed Using Other Observations

The model identified in Figure 23.1 represents a process model intended to account for the hypothesized physical and chemical character of the system under study. From the perspective embodied in Figure 23.1, the objective of the model is not to provide a good fit with the smallest number of parameters. The objective is rather to use the model to gain a physical understanding of the system. The model should be able to account for, or at least be consistent with, all experimental observations. The supporting measurements therefore provide a means for model identification. The feedback loop shown in Figure 23.1 between *model* and *other observations* is intended to illustrate that the supporting measurements guide model development and the proposed model can suggest experiments needed to validate model hypotheses. The supporting experiments can include both electrochemical and nonelectrochemical measurements.

Numerous scanning electrochemical methods such as scanning reference electrodes, scanning tunneling microscopy, and scanning electrochemical microscopy can be used to explore surface heterogeneity. Scanning vibrating electrodes and probes can be used to measure local current distributions. Local electrochemical impedance spectroscopy provides a means of exploring the distribution of surface reactivity. Measurements can be performed across the electrode at a single frequency to create an image of the electrode or, alternatively, performed at a given location to create a complete spectrum. Other experiments may include *in-situ* and *ex-situ* surface analysis, chemical analysis of electrolytes, and both *in-situ* and *ex-situ* visualization and/or microscopy. Transfer-function methods such as electrohydrodynamic (EHD) impedance spectroscopy allow isolation of the phenomena that influence the electrochemical impedance response.[52]

Remember! 23.2 *Impedance spectroscopy is* not *a standalone technique. Other observations are required to validate a given interpretation of the impedance spectra.*

23.2.3 Regression Analysis in Context of Error Structure

The goal of the operation represented by the triangle in Figure 23.1 is to develop a model that provides a good representation of the impedance measurements to within the noise level of the measurement. The error structure for the measurement clearly plays a critical role in the regression analysis. The weighting strategy for the complex nonlinear least-squares regression should be based on the variance of the stochastic errors in the data, and the frequency range used for the regression should be that which has been determined to be free of bias errors. In addition, knowledge of the variance of the stochastic measurement errors is essential to quantify the quality of the regression.

Sequential steps are taken until the model provides a statistically adequate representation of the data to within the independently obtained stochastic error structure. The comparison between model and experiment can motivate modifications to the model or to the experimental parameters.

23.3 Application

Two systems are described in the following examples that illustrate the approach outlined in Figure 23.1.

Example 23.1 Model Identification: *Two models have been proposed for data collected for an n-GaAs Schottky diode at different temperatures. One model uses a CPE that accounts for implicit distributed relaxation processes.*[187] *This model fits the data very well with a minimal number of parameters. A second model accounts for discrete energy levels and provides a fit of equivalent regression quality at each temperature.*[172,240] *Which model provides the better fit for the measurements?*

Solution: *Orazem et al.*[240] *and Jansen et al.*[172] *described the impedance response for an n-type GaAs Schottky diode with temperature as a parameter. The system consisted of an n-GaAs single crystal with a Ti Schottky contact at one end and a Au, Ge, Ni Schottky contact at the eutectic composition at the other end. This material has been well characterized in the literature and, in particular, has a well-known EL2 deep-level state that lies 0.83 to 0.85 eV below the conduction band edge.*[156] *Experimental details are provided by Jansen et al.*[172]

The experimental data are presented in Figures 18.4(a) and (b) for the real and imaginary parts of the impedance, respectively, for temperatures ranging from 320 to 400 K.

Remember! 23.3 *The object of modeling is not to provide a good fit with the smallest number of parameters. The object is rather to use the model to learn about the physics and chemistry of the system under study.*

The logarithmic scale used in Figure 18.4 emphasizes the scatter seen in the imaginary impedance at low frequencies. The impedance response is seen to be a strong function of temperature. The impedance-plane plots shown in Figure 18.5, for data collected at 320 and 340 K, show the classic semicircle associated with a single relaxation process.

Jansen and Orazem showed that the impedance data could be superposed as given in Figure 18.6.[172] *The impedance data collected at different temperatures were normalized by the maximum mean value of the real part of the impedance and plotted against a normalized frequency defined by equation (18.7) where* $E = 0.827$ *eV, and the characteristic frequency* f° *was assigned a value of* 2.964×10^{14} *Hz such that the imaginary part of the normalized impedance values reached a peak value near* $f^* = 1$. *The data collected at different temperatures are reduced to a single line. The extent to which the data are superposed is seen more clearly on the logarithmic scale shown in Figure 18.7. The superpositions shown in Figures 18.6 and 18.7 suggest that the system is controlled by a single-activation-energy-controlled process.*

A closer examination of Figure 18.6(b) reveals that the maximum magnitude of the scaled imaginary impedance is slightly less than 0.5, whereas the corresponding value for a single-activation-energy-controlled process should be identically 0.5. Regression analysis using the traditional weighting strategies under which the standard deviation of the experimental values was assumed to be proportional to the modulus of the impedance, $\sigma_r = \sigma_j = \alpha|Z|$, *to the magnitude of the respective components of the impedance,* $\sigma_r = \alpha_r|Z_r|$ *and* $\sigma_j = \alpha_j|Z_j|$, *or independent of frequency,* $\sigma_r = \sigma_j = \alpha$, *yielded one dominant RC time constant with only a hint that other parameters could be extracted. Jansen et al.*[172,240] *used the measurement model approach described by Agarwal et al.*[56,86,262,287] *to identify the stochastic error structure for the impedance data. When the data were regressed using this error structure for a weighting strategy, additional parameters could be resolved, revealing additional activation energies. Thus, while the data do superpose nicely in Figures 18.6 and 18.7, the impedance data do in fact contain information on minor activation-energy-controlled electronic transitions.*[172,240] *The information concerning these transitions could be extracted by regression of an appropriate process model using a weighting strategy based on the error structure of the measurement.*

Two models have been proposed for the data presented above. Macdonald proposed a distributed-time-constant model that accounts for distributed relaxation processes.[187] *This model fits the data very well and has the advantage that it requires a minimal number of parameters. A second model, presented in Figure 23.2, accounts for discrete energy levels and provides a fit of equivalent regression quality at each temperature.*[172,240] *In Figure 23.2,* C_n *is the space-charge capacitance,* R_n *is a resistance that accounts for a small but finite leakage current, and the parameters* $R_1 \ldots R_k$ *and* $C_1 \ldots C_k$ *are attributed to the response of discrete deep-level energy states. Parameters corresponding to deep-level states were added sequentially to the model, subject to the constraint that the* 2σ *(95.4 percent) confidence interval for each of the regressed parameters may not include zero. Including the space-charge capacitance and leakage resistance, four resistor-capacitor pairs could be obtained from the impedance data collected at 300, 320, and 340 K; three resistor-capacitor pairs could be obtained from the data collected at 360, 380, and 400 K; and two resistor-capacitor pairs could be obtained from the data collected at 420 K.*[172] *This model has the*

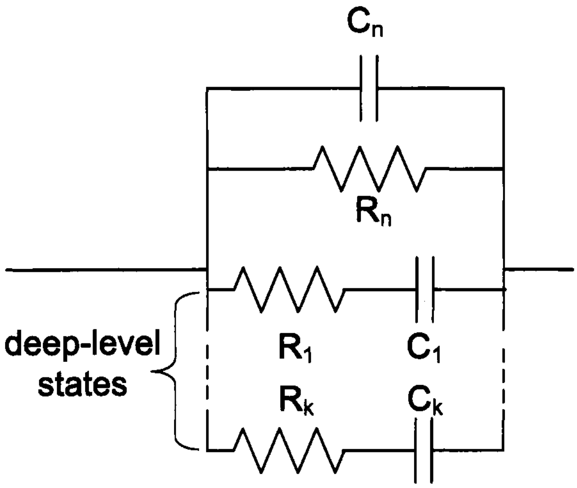

Figure 23.2: Electrical circuit corresponding to the model presented by Jansen et al.[172] in which C_n is the space-charge capacitance, R_n is a resistance that accounts for a small but finite leakage current, and the parameters $R_1 \ldots R_k$ and $C_1 \ldots C_k$ are attributed to the response of discrete deep-level energy states. (Taken from Orazem and Tribollet[241] and reproduced with permission of Elsevier, Inc.)

disadvantage that up to eight parameters are required, depending on the temperature, as compared to the three parameters required for the distributed-time-constant model. The question to be posed, then, is "which is the better model for the measurements?"

If the goal of the regression is to provide the most parsimonious model for the data, the model with the smallest number of parameters and a continuous distribution of activation energies is the best model. If the goal of the regression is to provide a quantitative physical description of the system for which the data were obtained, additional measurements are needed to determine whether the activation energies are discrete or continuously distributed. In this case, deep-level transient spectroscopy (DLTS) *measurements indicated that the n-GaAs diode contained discrete deep-level states. In addition, the energy levels and state concentrations obtained by regression of the second model were consistent with the results obtained by DLTS.[172] Thus, the second model with a larger number of parameters provides the more useful description of the GaAs diode. The choice between the two models could not be made without the added experimental evidence.*

Example 23.1 demonstrates the importance of coupling experimental observation, model development, and error analysis. The measurements conducted at different temperatures allowed identification of discrete activation energies for electronic transitions. Use of a weighting strategy based on the observed stochastic error structure increased the number of parameters that could be obtained from the regression analysis. Thus, four discrete activation-energy-controlled processes could be identified, but at the expense of a corresponding model that required eight parameters. A regression of almost the same quality could be obtained under the assumption of a continuous distribution of activation energies, and this model re-

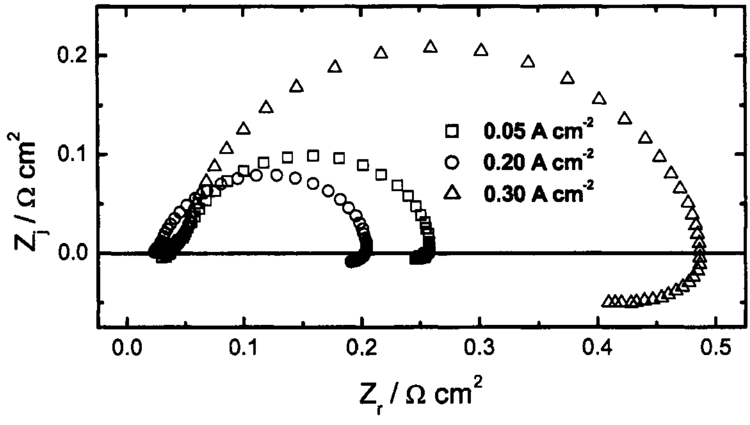

Figure 23.3: Electrochemical impedance results obtained for a single-cell PEM fuel cell with current density as a parameter. (Taken from Roy et al.[293] and reproduced with permission of The Electrochemical Society.)

quired only three parameters. Discrimination between the two models requires additional experimental observations, such as the DLTS identification of electronic transitions involving discrete deep-level states.

Example 23.2 Models to Propose Experiments: *Impedance data obtained for PEM fuel cells often reveal low-frequency inductive loops that have been attributed to parasitic reactions in which the* Pt *catalyst reacts to form* PtO *and subsequently forms* Pt^+ *ions.*[289] *Suggest experiments that could be used to support or reject this model.*

Solution: *Low-frequency inductive features*[290–292] *are commonly seen in impedance spectra for PEM fuel cells. Makharia et al.*[290] *suggested that side reactions and intermediates involved in the fuel cell operation can be possible causes of the inductive loop seen at low frequency. However, such low-frequency inductive loops could also be attributed to nonstationary behavior, or, due to the time required to make measurements at low frequencies, nonstationary behavior could influence the shapes of the low-frequency features.*

A typical result is presented in Figure 23.3 for the impedance response of a single 5 cm^2 PEMFC with hydrogen and air as reactants.[293] *The measurements were conducted in galavanostatic mode for a frequency range of 1 kHz to 1 mHz with a 10 mA peak-to-peak sinusoidal perturbation. Roy and Orazem*[289] *used the measurement model approach developed by Agarwal et al.*[56,86,262,287] *to demonstrate that, for the fuel cell under steady-state operation, the low-frequency inductive loops seen in Figure 23.3 were consistent with the Kramers-Kronig relations. Therefore, the low-frequency inductive loops could be attributed to process characteristics and not to nonstationary artifacts.*

Roy et al.[293] *proposed that the low-frequency inductive loops observed in PEM fuel cells could be caused by parasitic reactions in which the* Pt *catalyst reacts to form* PtO *and subsequently forms* Pt^+ *ions. They also showed that a reaction involving formation of*

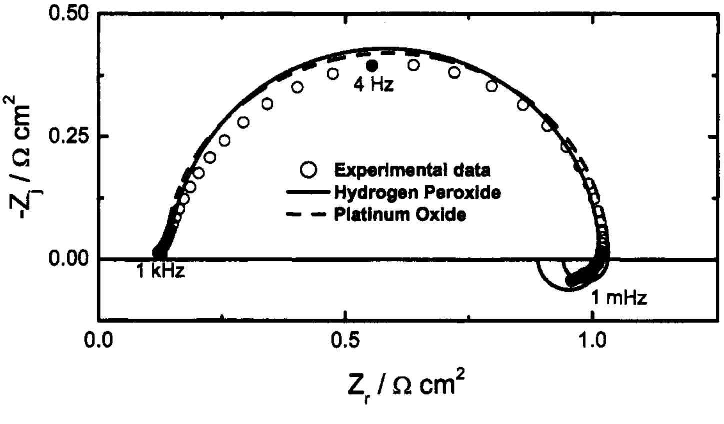

Figure 23.4: Comparison of the impedance response for a PEM fuel cell operated at 0.2 A/cm^2 to model predictions generated using a reaction sequence involving formation of hydrogen peroxide and a reaction sequence involving formation of PtO. (Taken from Roy et al.[293] and reproduced with permission of The Electrochemical Society.)

hydrogen peroxide could yield the same inductive features. A comparison between the two models and the experimental results is shown in Figure 23.4, and the corresponding values for the real and imaginary parts of the impedance are presented as a function of frequency in Figures 23.5(a) and (b), respectively. The model calculations were not obtained by regression but rather by simulation using approximate parameter values. Regression was not used because the model was based on the assumption of a uniform membrane-electrode assembly (MEA), whereas the use of a serpentine flow channel caused the reactivity of the MEA to be very nonuniform. The parameters were first selected to reproduce the current-potential curve and then the same parameters were used to calculate the impedance response for each value of current density. The potential (or current) dependence of model parameters was that associated with the Tafel behavior assumed for the electrochemical reactions.

While reaction parameters were not identified by regression to impedance data, the simulation presented by Roy et al.[293] *demonstrates that side reactions proposed in the literature can account for low-frequency inductive loops. Indeed, the results presented in Figures 23.4 and 23.5 show that both models can account for low-frequency inductive loops. Other models can also account for low-frequency inductive loops so long as they involve potential-dependent adsorbed intermediates.*[215] *It is generally understood that equivalent circuit models are not unique and have therefore an ambiguous relationship to physical properties of the electrochemical cell. As shown by Roy et al.,*[293] *even models based on physical and chemical processes are ambiguous. In the present case, the ambiguity arises from uncertainty as to which reactions are responsible for the low-frequency inductive features.*

Resolution of this ambiguity requires additional experiments. The processes and reactions hypothesized for a given model can suggest experiments to support or reject the underlying hypothesis. For example, the proposed formation of PtO *is consistent with a*

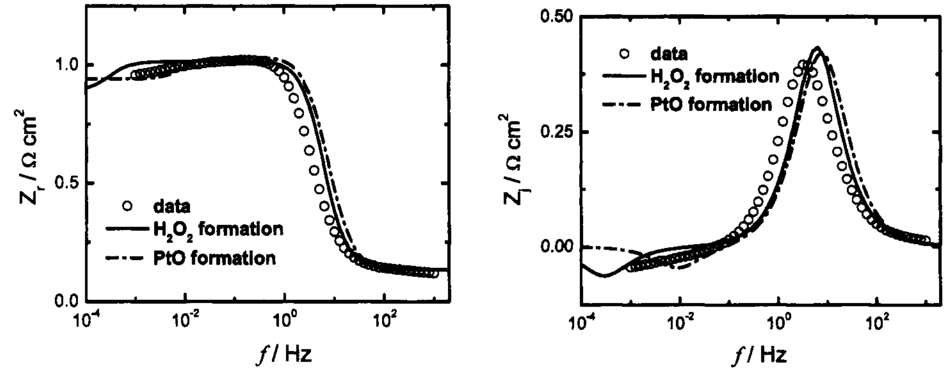

(a) (b)

Figure 23.5: Comparison of the impedance response for a PEM fuel cell operated at 0.2 A/cm^2 to model predictions generated using a reaction sequence involving formation of hydrogen peroxide and a reaction sequence involving formation of PtO: a) Real part of impedance; and b) imaginary part of impedance. (Taken from Roy et al.[293] and reproduced with permission of The Electrochemical Society.)

decrease in the active catalytic surface area and a loss of Pt *ions in the effluent. Cyclic voltammetry after different periods of fuel cell operation could be used to explore reduction in electrochemically active area.* Inductively coupled plasma mass spectroscopy (ICPMS) *could be used to detect residual* Pt *ions in the fuel cell effluent, and* ex-situ *techniques could detect formation of* PtO *in the catalyst layer. A different set of experiments could be performed to explore the hypothesis that peroxide formation is responsible for the inductive loops. Platinum dissolution has been observed in PEM fuel cells,*[294] *and peroxide formation has been implicated in the degradation of PEM membranes.*[295–297] *Thus, it is likely that both reactions are taking place and contributing to the observed low-frequency inductive loops.*

Example 23.2 demonstrates the utility of the error analysis for determining consistency with the Kramers-Kronig relations. In this case, the low-frequency inductive loops were found to be consistent with the Kramers-Kronig relations at frequencies as low as 0.001 Hz so long as the system had reached a steady-state operation. The mathematical models that were proposed to account for the low-frequency features were based on plausible physical and chemical hypotheses. Nevertheless, the models are ambiguous and require additional measurements and observations to identify the most appropriate for the system under study.

The philosophy described here and embodied in Figure 23.1 cannot always be followed to convergence. Often the hypothesized model is inadequate and cannot reproduce the experimental results. Even if the proposed reaction sequence is correct, surface heterogeneities may introduce complications that are difficult to model. The accessible frequency range may be limited at high frequency for systems with a very small impedance. The accessible frequency range may be limited at low frequency for systems subject to significant nonstationary behavior. The experimentalist may need to accept a large level of stochastic noise for a system with a large impedance. In cases where the models are unable to explain all features of the experiment, the graphical methods presented in Chapter 17 can nevertheless yield quantitative information.

Problems

23.1 Suggest supporting experiments that could be used to support or reject the model described in:
  - **(a)** Example 10.1
  - **(b)** Example 10.2
  - **(c)** Problem 10.3
  - **(d)** Problem 10.4
  - **(e)** Problem 10.5
  - **(f)** Example 23.1

23.2 Several prominent leaders in impedance research have proposed creating a catalog of impedance spectra with unique interpretations associated with different shapes of the impedance diagrams. Discuss the potential and limitations of such a catalog.

23.3 Explain the role of error analysis in:
  - **(a)** Experimental design
  - **(b)** Regression analysis
  - **(c)** Model identification

23.4 Why is impedance spectroscopy not a standalone technique? Can other electrochemical techniques such as cyclic voltammetry be considered standalone techniques? Explain your answers.

Electrochemical Impedance Spectroscopy
by Mark E. Orazem and Bernard Tribollet

Part VII

Reference Material

Electrochemical Impedance Spectroscopy
by Mark E. Orazem and Bernard Tribollet

Appendix A

Complex Integrals

Chapter 1 provides a framework for the analysis of complex variables. This section provides a summary of important definitions before describing complex integration in greater detail. This work provides support for the discussion of the Kramers-Kronig relations in Chapter 22. For more detailed analysis, the reader is directed to textbooks.[72–74,77]

A.1 Definition of Terms

Definition A.1 (Limit) *The* limit *of a function* $f(z)$ *at* $z \longrightarrow z_0$,

$$\lim_{z \longrightarrow z_0} f(z) = \ell \tag{A.1}$$

means that, given an $\varepsilon > 0$, *there exists a* δ *such that* $|f(z) - \ell| < \varepsilon$ *when* $0 < |z - z_0| < \delta$.

Note that z may approach z_0 from any direction in the complex plane, and the value of the limit ℓ is independent of the direction of approach.

Definition A.2 (Continuous Function) *A function* $f(z)$ *is* continuous *at* z_0 *if*

$$\lim_{z \longrightarrow z_0} f(z) = f(z_0) \tag{A.2}$$

A function $f(z)$ *is continuous if it is continuous at every point of its domain.*

Definition A.3 (Derivative of a Function) *The* derivative *of a function* $f(z)$ *at* z_0 *is*

$$f'(z_0) = \lim_{z \longrightarrow z_0} \frac{f(z) - f(z_0)}{z - z_0} \tag{A.3}$$

If $f(z)$ *has a derivative at* z_0, $f(z)$ *is* differentiable *at* z_0.

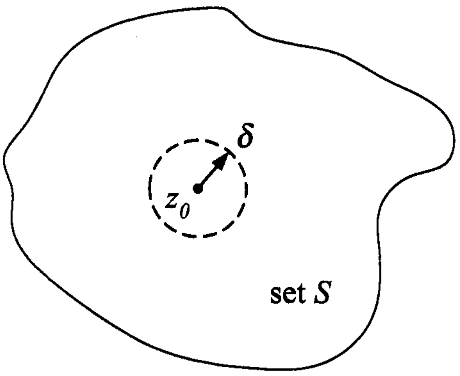

Figure A.1: Representation of the δ-neighborhood of the point z_0 within set S.

Definition A.4 (Neighborhood of a Point) *The set of all points z that satisfy the inequality*

$$|z - z_0| < \delta \tag{A.4}$$

is called the δ-neighborhood *of the point* z_0.

A δ-neighborhood of the point z_0 is illustrated in Figure A.1.

Definition A.5 (Set) *A point z_0 is an* interior *point of a set S if there exists some neighborhood of z_0 that contains only points of S. A point z_0 is an* exterior *point of the set S if there exists some neighborhood of z_0 that contains only points that are not in set S. If z_0 is neither an exterior nor an interior point of S, it must be a* boundary *point of S.*

Definition A.6 (Open and Closed Sets) *An* open *set contains only* interior *points. If a set contains its* boundary *points, it is a* closed *set.*

Definition A.7 (Curve) *A curve C is described by a function*

$$z = z_r(t) + jz_j(t) \tag{A.5}$$

where $z_r(t)$ and $z_j(t)$ are continuous functions of parameter t defined for $a \leq t \leq b$. If $z(a) = z(b)$, curve C is closed. *If curve C does not cross itself, curve C is* simple.

Definition A.8 (Connected Sets) *An* open *set is* connected *if every pair of points z and w can be joined by a polygonal line that exists entirely within S.*

Two open sets are shown in Figure A.2. Set A is *connected* because a continuous line can be drawn between any two points within the set. Set B is not *connected* because it consists of two separated sections across which a continuous line cannot be drawn. Similarly, the set of all points that do not lie on the closed curve $|z| = 1$ is an open set which is not connected.

Definition A.9 (Domain) *An* open *set that is* connected *is a* domain.

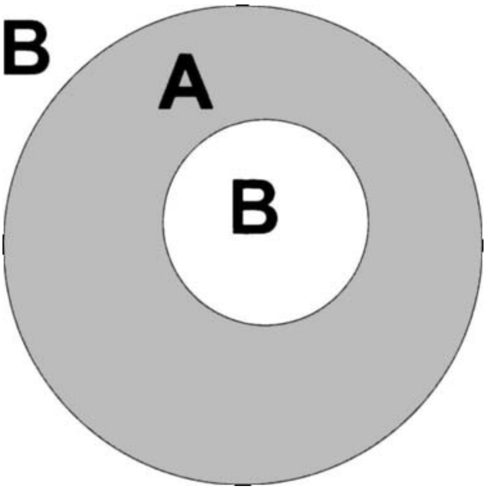

Figure A.2: Representation of two open sets. Set A is *connected* because a continuous line can be drawn between any two points within the set. Set B is *not connected* because it consists of two separated sections across which a continuous line cannot be drawn.

The set A is a domain, whereas B is not because set B is not connected.

Definition A.10 (Region) *A* domain, *together with or without its boundary points, is a* region. *If the region contains all the domain and its boundary points, it is a* closed region.

The set A, with or without its boundary points, is a region; whereas B is not because set B is not a domain.

Definition A.11 (Analytic Function) *If a function $f(z)$ is differentiable at every point within a neighborhood of z_0, $f(z)$ is* analytic *at z_0.*

Analytic functions are also called *regular* and *holomorphic*. If $f(z)$ is analytic for all finite values of z, it is an *entire function*. If $f(z)$ is not analytic at a point z_0, the point z_0 is a *singular* point.

A.2 Cauchy-Riemann Conditions

The Cauchy-Riemann conditions describe the criteria under which a complex function is analytic.

Theorem A.1 (Cauchy-Riemann Conditions) *The complex function*

$$f(z) = u(x,y) + jv(x,y) \tag{A.6}$$

is analytic in a region G if and only if du/dx, du/dy, dv/dx, and dv/dy are continuous and satisfy

$$\frac{\partial u}{\partial x} = \frac{\partial v}{\partial y} \quad \text{and} \quad \frac{\partial u}{\partial y} = -\frac{\partial v}{\partial x} \tag{A.7}$$

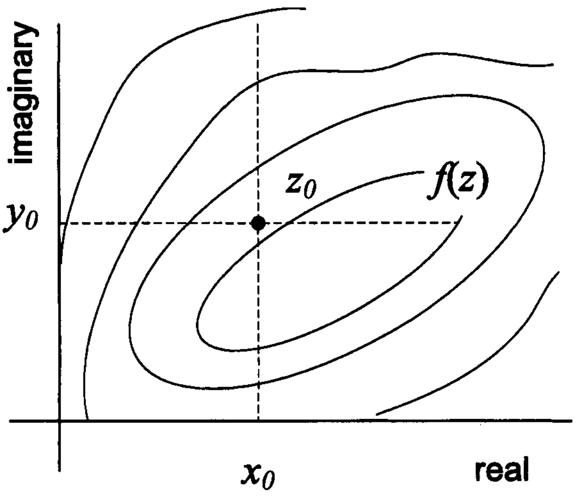

Figure A.3: Representation of two paths approaching z_0. The function $f(z)$ is presented in the form of a contour map as a function of real and imaginary parts of the complex independent variable z.

in the region G.

Following Definition A.11, the function $f(z)$ is analytic at z_0 if it is differentiable at every point in the neighborhood of z_0. Definitions A.1 and A.3 state that the value of the derivative should be independent of the path chosen. A general complex function $f(z)$ is presented in Figure A.3 in the form of a contour map as a function of real and imaginary parts of the complex independent variable z. The derivative along the real axis df/dx at constant y is given by

$$\begin{aligned} f'(z_0) &= \lim_{\Delta x \to 0} \frac{u(x_0+\Delta x, y_0) - u(x_0, y_0)}{\Delta x} \\ &+ j \lim_{\Delta x \to 0} \frac{v(x_0+\Delta x, y_0) - v(x_0, y_0)}{\Delta x} \end{aligned} \tag{A.8}$$

where $\Delta z = \Delta x$. Equation (A.8) can be written

$$f'(z_0) = \frac{\partial u}{\partial x} + j\frac{\partial v}{\partial x} \tag{A.9}$$

Remember! A.1 *The concept of an analytic function is critical to the derivation of the Kramers-Kronig relations as given in Section 22.1.*

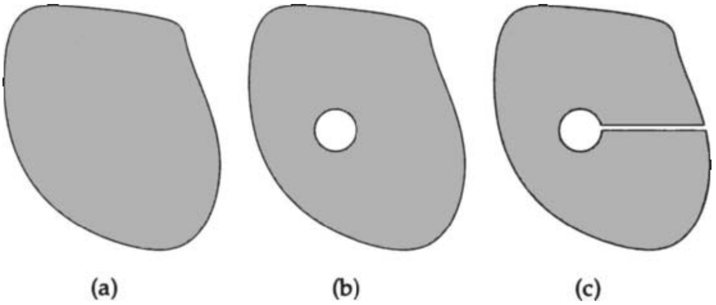

Figure A.4: The concept of connectedness: a) a simply connected domain; b) a doubly connected domain; and c) a doubly connected domain that has been converted into a simply connected domain by introducing a pair of cuts.

For the derivative along the imaginary axis at constant x, $\Delta z = j\Delta y$. Thus,

$$\begin{aligned} f'(z_0) &= \lim_{\Delta y \to 0} \frac{u(x_0, y_0 + \Delta y) - u(x_0, y_0)}{j\Delta y} \\ &+ j \lim_{\Delta y \to 0} \frac{v(x_0, y_0 + \Delta y) - v(x_0, y_0)}{j\Delta y} \end{aligned} \tag{A.10}$$

or

$$f'(z_0) = -j\frac{\partial u}{\partial y} + \frac{\partial v}{\partial y} \tag{A.11}$$

As the values obtained for $f'(z_0)$ should be independent of direction, equation (A.7) must be satisfied. The additional requirement is that partial derivatives be continuous.

A.3 Complex Integration

An understanding of the use of the Kramers-Kronig relations requires an understanding of integration in a complex plane. While the subject leads to the very powerful tool of conformal mapping, the discussion is limited here to that needed to understand the derivation of the Kramers-Kronig relations.

A.3.1 Cauchy's Theorem

Definition A.12 (Simply Connected Domain) *A domain is* simply connected *if every simple closed curve* C *in the domain encloses only points of the domain.*

The meaning of Definition A.12 is more readily understood with the aid of Figure A.4. A simply connected domain is shown in Figure A.4(a). The simply connected domain of Figure A.4(a) was converted into a doubly connected domain by introducing a hole in the domain (see Figure A.4(b)). The doubly connected domain of Figure A.4(b) can be converted into a simply connected domain by introducing a pair of cuts, as shown in Figure A.4(c).

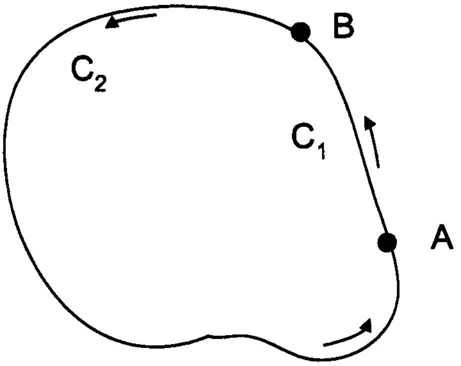

Figure A.5: Demonstration of the path independence for the value of the integral of an analytic function between two points in a simply connected domain.

Theorem A.2 (Cauchy's Theorem) *If $f(z)$ is analytic in a simply connected domain D, and if C is a simple closed contour that lies in D, then*

$$\int_C f(z)dz = 0 \tag{A.12}$$

The integral around the closed contour is also designated $\oint f(z)dz$. A major consequence of Cauchy's theorem is that the value of the integral from one point to another is independent of the path. Two paths C_1 and C_2 between points A and B are shown in Figure A.5. The contour directions are the same; thus,

$$\int_C f(z)dz = \int_{C_1} f(z)dz + \int_{C_2} f(z)dz \tag{A.13}$$

In order to have the direction of integration be from A to B for both contours, the direction of integration along contour C_2 is changed by integrating along $-C_2$. Thus, from equation (A.12),

$$\int_{C_1} f(z)dz = \int_{-C_2} f(z)dz = -\int_{C_2} f(z)dz \tag{A.14}$$

The value of the integral depends only on the end points of the integration.

As shown in Figure A.4, a multiply connected domain can be transformed into a singly connected domain by making suitable cuts. The integral around the closed contour of the new simply connected domain is expressed as the sum of contributions from the curves making up the boundary of the domain. An example is

---

Remember! A.2 *The derivation of the Kramers-Kronig relations in Section 22.1 makes use of Cauchy's Theorem, given as Theorem A.2.*

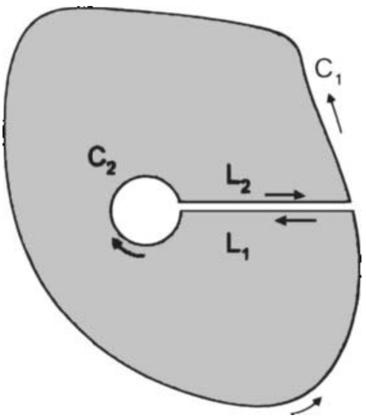

Figure A.6: Demonstration of the integration for a doubly connected domain that has been transformed into a simply connected domain.

shown in Figure A.6. The integration path encompasses contours C_1, L_1, L_2, and C_2. Thus,

$$\int_C f(z)dz = \int_{C_1} f(z)dz + \int_{L_1} f(z)dz + \int_{C_2} f(z)dz + \int_{L_2} f(z)dz \qquad \text{(A.15)}$$

As the directions of integration along contours L_1 and L_2 are opposite, their contributions will cancel. Thus,

$$\int_{C_1} f(z)dz = -\int_{C_2} f(z)dz = \int_{-C_2} f(z)dz \qquad \text{(A.16)}$$

Example A.1 Application of Cauchy's Theorem: *Find the numerical value for the integral* $\oint (z-a)^{-1}dz$ *for the case where* $z = a$ *is outside the domain.*

Solution: *If the point* $z = a$ *lies outside the domain, the function* $(z-a)^{-1}$ *is analytic everywhere. Thus, via Cauchy's Theorem (Theorem A.2),* $\oint (z-a)^{-1}dz = 0$.

Example A.2 Special Case of Cauchy's Integral Formula: *Find the numerical value for the integral* $\oint (z-a)^{-1}dz$ *for the case where* $z = a$ *is inside the domain.*

Solution: *If the point* $z = a$ *lies inside the domain, the function* $(z-a)^{-1}$ *has a singularity at* $z = a$*. It can be enclosed by a circle of radius* ε *centered at* $z = a$ *such that, on the boundary of the domain, the function is analytic (see Figure A.6). From equation (A.16),*

$$\int_{C_1} \frac{1}{z-a}dz = \int_{-C_2} \frac{1}{z-a}dz \qquad \text{(A.17)}$$

To evaluate the integral around the singularity, let

$$z = a + \varepsilon e^{j\theta}; \qquad 0 \le \theta \le 2\pi \tag{A.18}$$

The integral around C_2 *becomes*

$$\int\limits_{-C_2} \frac{1}{z-a}dz = \int_0^{2\pi} \frac{j\varepsilon e^{j\theta}}{\varepsilon e^{j\theta}}d\theta = j\int_0^{2\pi} d\theta = 2j\pi \tag{A.19}$$

Thus,

$$\int\limits_{C_1} \frac{1}{z-a}dz = 2j\pi \tag{A.20}$$

This result is a special case of Cauchy's Integral Formula.

Theorem A.3 (Cauchy's Integral Formula) *If* $f(z)$ *is analytic in a simply connected domain D, and if C is a simple positively oriented (counterclockwise) closed contour that lies in D, then, for any point* z_0 *that lies interior to C,*

$$\int\limits_{C} \frac{f(z)}{z-z_0}dz = 2\pi j f(z_0) \tag{A.21}$$

Definition A.13 (Residue) *If* z_0 *is an isolated singular point of* $f(z)$*, then there exists a* Laurent series

$$f(z) = \sum_{n=-\infty}^{\infty} b_n(z-z_0)^n \tag{A.22}$$

valid for $0 < |z - z_0| < R$*, for some positive value of* R*. The coefficient* b_{-1} *of* $(z-z_0)^{-1}$ *is the* residue *of* $f(z)$ *at* z_0*, designated as* Res $[f(z), z_0]$. *If C is a positively oriented simple closed curve in* $0 < |z - z_0| < R$ *that contains* z_0*, then*

$$b_{-1} = \frac{1}{2\pi j}\int\limits_{C} f(z)dz \tag{A.23}$$

Theorem A.4 (Cauchy's Residue Theorem) *If* $f(z)$ *is analytic in a simply connected domain D, except at a finite number of singular points* $z_1, \ldots, z_k$ *and if C is a simple positively oriented (counterclockwise) closed contour that lies in D, then*

$$\int\limits_{C} f(z)dz = 2\pi j \sum_{n=1}^{k} \text{Res}\,[f(z), z_n] \tag{A.24}$$

Remember! A.3 *The derivation of the Kramers-Kronig relations in Section 22.1 makes use of Cauchy's Integral Formula for evaluation of a function at a singularity, given as Example A.2.*

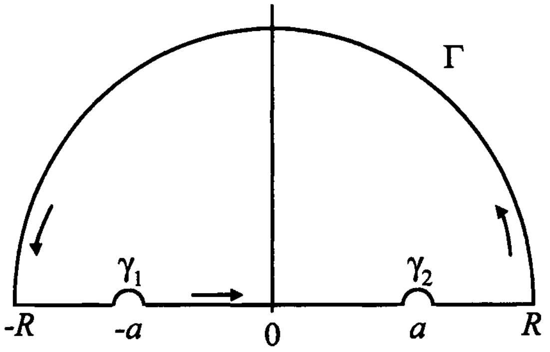

Figure A.7: Demonstration of integration for a domain with two poles on the real axis.

A.3.2 Improper Integrals of Rational Functions

Definition A.14 (Cauchy Principal Value of Integral) *For real x, if $f(x)$ is a continuous function on $-\infty < x < +\infty$, the improper integral of $f(x)$ over $[-\infty, +\infty]$ is*

$$\int_{-\infty}^{\infty} f(x)dx = \lim_{a\to-\infty} \int_{a}^{0} f(x)dx + \lim_{a\to\infty} \int_{0}^{a} f(x)dx \tag{A.25}$$

provided the limits exist. The Cauchy principal value *of the integral over the interval $[-\infty, +\infty]$ is given as*

$$\fint_{-\infty}^{+\infty} f(x)dx = \lim_{a\to\infty} \int_{-a}^{a} f(x)dx \tag{A.26}$$

Theorem A.5 (Evaluation of the Cauchy Principal Value of an Integral) *If a function $f(z)$ is analytic in a simply connected domain D, except at a finite number of singular points $z_1, \ldots, z_k$, if $f(x) = P(x)/Q(x)$ where $P(x)$ and $Q(x)$ are polynomials, $Q(x)$ has no zeros, and the degree of $P(x)$ is at least two less than the degree of $Q(x)$, and if C is a simple positively oriented (counterclockwise) closed contour that lies in D, then*

$$\fint_{-\infty}^{+\infty} f(x)dz = 2\pi j \sum_{n=1}^{k} \text{Res}\,[f(z), z_n] \tag{A.27}$$

where $z_1, \ldots, z_k$ are poles of $f(z)$ that lie in the upper half-plane.

Example A.3 Poles on a Real Axis: *Evaluate the integral $\int_{-\infty}^{\infty}(z^2 - a^2)^{-1}dx$ where a is a real number.*

Solution: *The function $\frac{1}{z^2-a^2}$ has two poles on the real axis located at $x = a$ and $x = -a$, respectively. The integration will be performed on the contour shown in Figure A.7. The contour is chosen to avoid the singular points a and −a, and integration in the imaginary* *plane is at a value of R sufficiently large that it encircles all poles in the domain. A semicircle of radius ε is placed at the poles. The integral over the entire contour can be expressed as*

$$\begin{aligned}\int_C \frac{1}{z^2-a^2}dz = {} & \int_{-R}^{-a-\varepsilon} \frac{1}{x^2-a^2}dx + \int_{\gamma_1} \frac{1}{z^2-a^2}dz + \int_{-a+\varepsilon}^{a-\varepsilon} \frac{1}{x^2-a^2}dx + \\ & \int_{\gamma_2} \frac{1}{z^2-a^2}dz + \int_{-a-\varepsilon}^{R} \frac{1}{x^2-a^2}dx + \int_{\Gamma} \frac{1}{z^2-a^2}dz \qquad \text{(A.28)} \\ = {} & 2\pi j \sum_{n=1}^{2} \text{Res}\left[\frac{1}{z^2-a^2}, z_n\right] \\ = {} & 0\end{aligned}$$

For sufficiently large R,

$$\int_{\Gamma} \frac{1}{z^2-a^2}dz \to 0 \qquad \text{(A.29)}$$

Thus, in the limit that R ⟶ ∞ and ε ⟶ 0, equation (A.28) becomes

$$\int_{-\infty}^{\infty} \frac{1}{x^2-a^2}dx = -\int_{\gamma_1} \frac{1}{z^2-a^2}dz + -\int_{\gamma_2} \frac{1}{z^2-a^2}dz \qquad \text{(A.30)}$$

Thus, the integral along the real axis can be evaluated by evaluating the integrals along the contours that skirt the poles.

To evaluate the integral at γ_1*, let*

$$z = -a + \varepsilon e^{j\theta} \qquad \text{(A.31)}$$

Then,

$$\int_{\gamma_1} \frac{1}{z^2-a^2}dz = \int_{\pi}^{0} \frac{1}{\varepsilon e^{j\theta}\left(\varepsilon e^{j\theta} - 2a\right)} j\varepsilon e^{j\theta} d\theta \qquad \text{(A.32)}$$

As $\varepsilon \to 0$,

$$j\int_{\pi}^{0} \frac{1}{\left(\varepsilon e^{j\theta} - 2a\right)} d\theta \to \frac{j\pi}{2a} \qquad \text{(A.33)}$$

To evaluate the integral at γ_2*, let*

$$z = a + \varepsilon e^{j\theta} \qquad \text{(A.34)}$$

Thus,

$$\int_{\gamma_2} \frac{1}{z^2-a^2}dz = j\int_{\pi}^{0} \frac{1}{\left(\varepsilon e^{j\theta} + 2a\right)} d\theta \to -\frac{j\pi}{2a} \qquad \text{(A.35)}$$

Equation (A.30) can be expressed as

$$\begin{aligned}\int_{-\infty}^{\infty} \frac{1}{x^2-a^2}dx &= -\frac{j\pi}{2a} + \frac{j\pi}{2a} \\ &= 0 \qquad \text{(A.36)}\end{aligned}$$

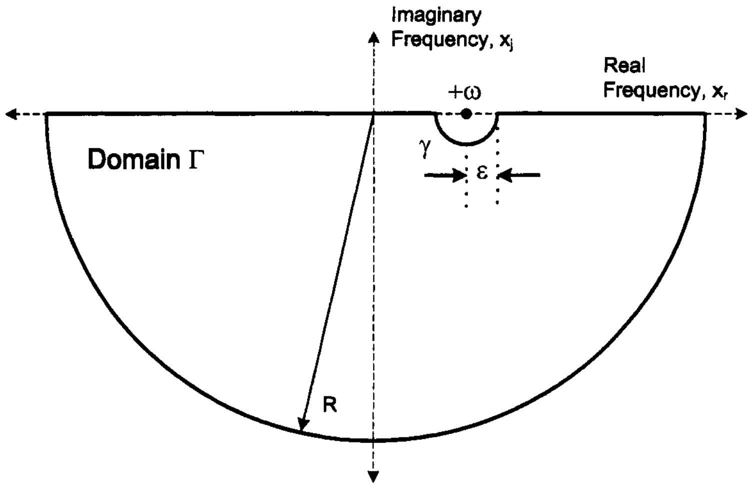

Figure A.8: Domain of integration for development application of Cauchy's integral formula. A pole is placed at frequency $+\omega$ on the real frequency axis.

Problems

A.1 Show that e^z is an analytic function in any domain.

A.2 Show that the exponential of the complex conjugate $e^{\bar{z}}$ is not an analytic function in any domain.

A.3 Beginning with

$$\oint_{\Gamma} \frac{G(x)}{x-\omega} dx = 0 \tag{A.37}$$

derive equations (22.55) and (22.56). The domain Γ is shown in terms of complex frequency x in Figure A.8.

Electrochemical Impedance Spectroscopy
by Mark E. Orazem and Bernard Tribollet

Appendix B

Tables of Reference Material

The following tables provide equations, constants, physical properties, and statistical values that may be useful for the student.

Complex Variables

Table 1.1 Identities for the complex number j. 5
Table 1.3 Relationships between polar and rectangular coordinates for the complex variable $z = z_r + jz_j$. 10
Table 1.3 Relationships between polar and rectangular coordinates for the complex variable $z = z_r + jz_j$. 10
Table 1.4 Properties for the complex conjugates of $z = z_r + jz_j$ and $w = w_r + jw_j$. 14
Table 1.5 Properties for the absolute value of $z = z_r + jz_j$ and $w = w_r + jw_j$. 14
Table 1.6 Trigonometric and hyperbolic relationships for the complex variable $z = z_r + jz_j$. 17
Table 1.7 Functional relationships of complex variables commonly encountered in impedance spectroscopy, where x and y are real numbers, and $z = x + jy$. 19

Statistics

Table 3.1 Properties of the *expectation* where c is a constant and x and y are random variates. 36
Table 3.2 Properties of the *variance* where c is a constant and x and y are random variates. 36
Table 3.3 Student's t-test values. 50
Table 3.4 F-test values for comparison of variance of samples with equal degrees of freedom, i.e., $\nu_1 = \nu_2 = \nu$. 52
Table 3.8 χ^2-test values for degree of freedom ν and confidence level p. 57

Physical Properties

Table 5.2 Typical values of diffusion coefficients for ions at infinite dilution in water at 25 °C. 86
Table 5.4 Typical ranges of values for capacitance. 95
Table 12.1 Physical properties for GaAs at 300 K. 215

Selected Electrochemical Notation

Table 5.1 Definitions and notation for potentials used in electrochemical systems. 81
Table 7.2 Definitions and notation for local impedance variables. 125

Relationships for Impedance

Table 10.1 Some useful relationships for the development of the impedance response associated with Faradaic reactions. 166
Table 16.1 Summary of complex impedance, admittance, and capacitance characteristics for simple blocking and reactive circuits. 310
Table 21.1 Statistical properties of impedance values obtained by Fourier analysis techniques. 414
Table 22.1 Compilation of various forms of the Kramers-Kronig relations. 437

Electrochemical Impedance Spectroscopy
by Mark E. Orazem and Bernard Tribollet

Appendix C

List of Examples

The following examples are presented throughout the text to illustrate concepts, calculations, and derivations.

Complex Variables

Example 1.1 Multiplication of Complex Numbers 6
Example 1.2 Division of Complex Numbers 7
Example 1.3 Rectangular Coordinates 9
Example 1.4 Polar Coordinates 10
Example 1.5 De Moivre's Theorem 11
Example 1.6 *n*th Roots of Complex Variables 12
Example 1.7 Square Roots of Complex Variables 12
Example 1.8 Exponential Form 18

Differential Equations

Example 2.1 Linear First-Order Differential Equation 24
Example 2.2 Convective Diffusion Equation 25
Example 2.3 Complex Roots for an ODE 27
Example 2.4 Diffusion in a Finite Domain 27
Example 2.5 Diffusion in an Infinite Domain 30
Example 2.6 Foundation for Warburg Impedance 32

Statistics

Example 3.1 Error Propagation 43
Example 3.2 Continuation of Example 3.1 44
Example 3.3 Continuation of Example 3.2 45
Example 3.4 Evaluation of Impedance Data 51
Example 3.5 Evaluation of Chi-Squared Statistics 56

Electrical Circuits

Example 4.1 Impedance in Series 65
Example 4.2 Impedance in Parallel 66
Example 4.3 Bode Representation of Elemental Circuits 68
Example 4.4 Impedance Expression for a Nested Circuit 68

Electrochemistry

Example 5.1 Rate Expression for Copper Dissolution 84

Electrochemical Instrumentation

Example 6.1 Negative Feedback 99
Example 6.2 Current Follower 100
Example 6.3 Voltage Adder 100

Experimental Methods

Example 7.1 Lissajous Analysis 115
Example 7.2 Fourier Analysis 121

Experimental Design

Example 8.1 Guideline for Linearity 134
Example 8.2 Influence of Ohmic Resistance on Linearity 139
Example 8.3 Influence of Capacitance on Linearity 144

Equivalent Circuit Analogs

Example 9.1 Time-Dependent Ohmic Resistance 161

Kinetic Impedance

Example 10.1 Iron in Anaerobic Solutions 167
Example 10.2 Iron in Aerobic Solutions 171
Example 10.3 Corrosion of Magnesium 176

Diffusion Impedance

Example 11.1 Diffusion with First-Order Reaction 187
Example 11.2 Diffusion of Two Species 188
Example 11.3 Diffusion through a Film with $\epsilon = 1.0$ 192

Example 11.4 Continuation of Example 11.3 194
Example 11.5 Diffusion Impedances in Series 198

Semiconductors

Example 12.1 Mott-Schottky Plots 229

Time-Constant Dispersion

Example 13.1 Flux on a Small Circular Electrode 239
Example 13.2 Characteristic Frequency 249
Example 13.3 Derivation of the de Levie Formula 254
Example 13.4 Corrosion of Cast Iron in Drinking Water 255

Electrohydrodynamic Impedance

Example 15.1 2-D and 3-D Blocking 303

Methods for Representing Impedance

Example 16.1 Admittance of Dielectrics 323
Example 16.2 Complex Capacitance of Dielectrics 328
Example 16.3 Evaluation of Double-Layer Capacitance 329

Preliminary Graphical Methods

Example 17.1 Plots for Mg Alloys 345

Complex Nonlinear Regression

Example 19.1 Nonlinear Models 365

Kramers-Kronig Relations

Example 22.1 Verification of Equations (22.9) and (22.10) 429
Example 22.2 Application of Equations (22.9) and (22.10) 430

Integrated Approach

Example 23.1 Model Identification 453
Example 23.2 Models to Propose Experiments 456

Complex Integration

Example A.1 Application of Cauchy's Theorem 469
Example A.2 Special Case of Cauchy's Integral Formula 469
Example A.3 Poles on a Real Axis 471

Electrochemical Impedance Spectroscopy
by Mark E. Orazem and Bernard Tribollet

List of Symbols

Roman

$\mathcal{A}$	temperature-dependent coefficient used in the development for thermo-electrochemical impedance, see Section 14.3.1
A	lumped parameter in expression for impedance response of a reaction dependent on potential and surface coverage, equation (10.79)
a	constant used for the velocity expansion for a rotating disk, $a = 0.51023$, see Section 11.6.1
A_i	activation energy for diffusion, see Section 14.3.1
A_{IC}	Akaike information criterion, see equation (20.2)
a_{IJ}	constant used for the velocity expansion for an impinging jet with value determined by experiment, see Section 11.7.1
A_{op}	open-loop gain for an operational amplifier, see Section 6.1
A_{PI}	Akaike performance index, see equation (20.1)
A_v	gain of the operational amplifier, see Figure 21.2 and equation (21.4)
B	lumped parameter in expression for impedance response of a reaction dependent on potential and surface coverage, equation (10.79)
B	magnetic field, T, see Section 14.1
b	constant used for the velocity expansion for a rotating disk, $b = -0.61592$, see Section 11.6.1
b	kinetic parameter defined in equation (5.15), V^{-1}
$\mathbf{C}$	covariance matrix for regression analysis, see equation (19.16)
$\mathcal{C}$	complex capacitance, see equation (16.36), F or $\mathrm{F/cm^2}$
C	capacitance, $\mathrm{F/cm^2}$ or F ($1\mathrm{F} = 1\mathrm{C/V}$)
C_0	interfacial capacitance, $\mathrm{F/cm^2}$

C_{dl}	double-layer capacitance, $\mathrm{F/cm^2}$ or F ($1\mathrm{F} = 1\mathrm{C/V}$)
CE	counterelectrode, see Figure 6.6
C_{eff}	effective capacitance, see equation (16.41), F or $\mathrm{F/cm^2}$
c_i	volumetric concentration of species i, $\mathrm{mol/cm^3}$
C_{Y}	oxide capacitance associated with the Young impedance, equation (13.86), $\mathrm{F/cm^2}$
d	distance between potential sensing electrodes in the sensor used for local impedance spectroscopy measurements, see equation (7.40), cm
d_{act}	average diameter of the active portion of a partially blocked electrode, see equation (15.52)
D_i	diffusion coefficient for species i, $\mathrm{cm^2/s}$
E	electronic energy, eV
E_c	conduction-band energy, eV
E_{F}	Fermi energy, eV
e_{out}	noise in the output from the current follower, V, see Figure 21.2 and equation (21.8)
E_{out}	potential output from the current follower, V
E_v	valence-band energy, eV
F	statistic used for testing equality of variances, see Section 3.3.3
$\tilde{f}$	complex oscillating variable used in expression for radial velocity for a rotating disk electrode, see equation (15.10)
F	Faraday's constant, $96,487$ C/equiv
F	dimensionless radial component of velocity for laminar flow to a disk electrode, see equation (11.74)
f	frequency, $f = \omega/2\pi$, Hz
$F(\omega)$	general frequency-dependent input function, see equation (22.4)
$f(t)$	general time-dependent input function, see equation (22.1)
$f(E)$	dimensionless probability of occupancy of a state of energy E
f_i	activity coefficient for species i, dimensionless

f_{meas}	characteristic frequency for measurement comprising a range of perturbation frequencies, see equation (21.16), Hz
f_{N_f}	characteristic frequency for measurement of impedance at a frequency f using N cycles, see equation (21.17), Hz
f_{set}	characteristic frequency for measurement of a series of spectra, see equation (21.14), Hz
f^*	normalized frequency, see equation (18.7)
$\widetilde{g}$	complex oscillating variable used in expression for angular velocity for a rotating disk electrode, see equation (15.11)
G	dimensionless angular component of velocity for laminar flow to a disk electrode, see equation (11.75)
g	gravitational acceleration, cm/s^2
$G(\omega)$	general transfer function, see equation (22.3)
$G(W)$	generic transfer function relating input and output quantities for an electrochemical system, see equation (14.1)
$\Delta G^{\ddagger}$	free energy of activation, see, e.g., equation (5.38)
$\Delta G^{\ddagger}_{\mathrm{chem}}$	chemical contribution to the free energy of activation, see, e.g., equation (5.38)
$\Delta G^{\ddagger}_{\mathrm{elec}}$	electrical contribution to the free energy of activation, see, e.g., equation (5.38)
G_i	rate of generation of species i, e.g., holes or electrons in a semiconductor, $(\mathrm{cm}^3\mathrm{s})^{-1}$
$G(\tau)$	distribution function for time constants used in developing the formula for a CPE, see equation (13.7)
$g(t,t')$	function showing a linear relationship between input and output functions, see equation (22.1)
H	hypothesis, see Section 3.3
$\widetilde{h}$	complex oscillating variable used in expression for axial velocity for a rotating disk electrode, see equation (15.12)
H	dimensionless axial component of velocity for laminar flow to a disk electrode, see equation (11.76)
h	Planck constant, $h = 6.626 \times 10^{-34}$ J s

H_i	generic transfer function relating the time derivative of state quantities for an electrochemical system to the state and input quantities, see equation (14.2)
F_k	generic transfer function relating the output quantities for an electrochemical system to the state and input quantities, see equation (14.3)
I	current, A
i	current density, mA/cm^2
i_0	exchange current density, see equation (5.14), mA/cm^2
i_0	output current for an operational amplifier, see Figure 6.1(a), A
i_a	anodic current density, mA/cm^2
i_C	charging current density, mA/cm^2
i_c	cathodic current density, mA/cm^2
ΔI	amplitude of sinusoidal current signal, see, e.g., equation (4.7), A
i_f	Faradaic current density, mA/cm^2
i_k	kinetically controlled current density, $i_k = -k_c nFc_i(\infty)\exp(-b_c\eta_s)$, see equation (5.26), mA/cm^2
i_lim	mass-transfer-limited current density, $i_\mathrm{lim} = -nFD_ic_i(\infty)/\delta_i$, see equation (5.26), mA/cm^2
i_n1	current noise contribution from differential amplifiers, A, see Figure 21.2 and equation (21.4)
i_n2	current noise contribution from differential amplifiers, A, see Figure 21.2 and equation (21.4)
i_n5	current noise contribution from differential amplifiers, A, see Figure 21.2 and equation (21.4)
i_n6	current noise contribution from differential amplifiers, A, see Figure 21.2 and equation (21.4)
i_probe	current density measured by a small local-impedance-spectroscopy sensor located near an electrode, see equation (7.40), mA/cm^2
iR_e	Ohmic potential drop between the solution adjacent to the working electrode and the location of a reference electrode, i.e., $iR_e = \Phi_0 - \Phi_\mathrm{ref}$, see Table 5.1, V

i_{reg}	parasitic current noise arising from noise in the voltage control, A, see Figure 21.2 and equation (21.5)
i_S	power current for an operational amplifier, see Figure 6.1(a), A
$\mathbf{J}$	identity matrix
J	dimensionless exchange current density, see e.g., equation (5.68)
j	imaginary number, $j = \sqrt{-1}$
J_i	local mass-transfer flux, see Example 13.2, mol/cm^{2}s
K	dimensionless frequency associated with the geometry of a disk electrode, see equation (13.47)
K	lumped-parameter rate constant for an electrochemical reaction which includes the equilibrium potential difference, see equation (10.7), mA/cm^2
k	Boltzmann constant $k = 8.617 \times 10^{-5}$ eV/K
K^*	lumped-parameter rate constant for an electrochemical reaction, see, e.g., equation (10.6), mA/cm^2
k^*	rate constant for electrochemical reaction that includes the exponential dependence on potential, see equation (5.36)
k	rate constant for electrochemical reaction that excludes the exponential dependence on potential, see, e.g., equation (5.42)
K_i	dimensionless frequency associated, for example, with convective diffusion of species i, see, e.g., equations (11.66) and (13.34)
k_M	mass-transfer coefficient, cm/s
$\mathrm{K}_{x,i}$	dimensionless position-dependent frequency associated with diffusion of species i, see equation (13.23)
ℓ	depth of a pore, cm
L	inductance, H ($1H = 1\text{Vs}^2/\text{C}$)
L	length of an electrode, cm
M	mass, g
M_i	symbol for the chemical formula of species i, see equation (5.41)
N	normal distribution function, see Section 3.1.3
N	collection efficiency for a ring-disk electrode, see equation (14.31)

n	electron concentration, cm^{-3}
n	number of electrons transferred in electrochemical reaction, see equation (5.14), dimensionless
N_c	effective density of conduction-band states, cm^{-3}
N_{dat}	number of measured values, see equation (19.2)
N_f	number of cycles for an impedance measurement, see equation (21.17)
N_i	flux of species i, $\text{mol/cm}^2\text{s}$
n_i	intrinsic concentration, see equation (12.9), cm^{-3}
N_p	number of parameters, see equation (19.8)
n_t	electron concentration in deep-level states, cm^{-3}
N_v	effective density of valence-band states, cm^{-3}
n_x	sample size used to calculate the standard error of sample distribution x, see equation (3.10)
$\mathbf{P}$	parameter vector used in regression analysis, see equation (19.1)
P	probability, see Section 3.1.4
p	probability of observing the given sample result under the assumption that the null hypothesis is true, see Section 3.3.1
p	dimensionless frequency, $p = \omega/\Omega$
p	hole concentration, cm^{-3}
p	pressure, atm
$\Delta\boldsymbol{P}$	parameter vector for nonlinear regression analysis, see equation (19.19)
$p_{i,k}$	reaction order for anodic reactants i in reaction k, see equation (5.42)
Q	significance level at which the hypothesis that the variances are not equal can be rejected, see equation (3.40)
Q	CPE coefficient, see equation (13.2), $\text{s}^{\alpha}/\Omega\text{cm}^2$
q	charge, C/cm^2
$q_{i,k}$	reaction order for cathodic reactants i in reaction k, see equation (5.42)
R	resistance, Ωcm^2 or Ω ($1\Omega = 1\text{Vs/C}$)
R	universal gas constant, 8.3143 J/mol K

r	radial coordinate, cm
r	rate of reaction, mol/cm^{2}s
r_0	radius of a disk electrode, cm
Re	Reynolds number, $\mathrm{Re} = \rho v 2R/\mu$, dimensionless
R_e	electrolyte or Ohmic resistance, Ω or Ωcm^2
REF	reference electrode, see Figure 6.6
R_m	resistance of the current measurement circuit, Ω, see Figure 21.2 and equation (21.4)
R_s	resistance of the potential control circuit, Ω, see Figure 21.2 and equation (21.4)
R_t	charge-transfer resistance, Ωcm^2
S	weighted sum of squares, see equation (19.1)
s	slope defined by equation (18.1)
Sc	Schmidt number, $\mathrm{Sc} = \nu/Di$, dimensionless
Sh	Sherwood number, $\mathrm{Sh} = k_M d/D$, dimensionless
$s_{i,k}$	stoichiometric coefficient for species i in reaction k, see equation (5.41)
S_m	potential difference across the inputs to the current follower, V, see equation (21.6)
s_m	gain of the current follower, see Figure 21.2
s_m	noise in the potential difference across the inputs to the current follower, V, see Figure 21.2 and equation (21.6)
s_x	standard error of sample distribution x, see equation (3.10)
t	statistic used for testing equality of means, see Section 3.3.2
T	temperature, K
T	time corresponding to an integer number of cycles, s
t	time, s
t_cycle	period of a cycle at frequency f, s
t_i	transfer function defined by equations (15.31) to (15.36)

U	electrode potential with respect to a reference electrode, $U = \Phi_{\mathrm{m}} - \Phi_{\mathrm{ref}}$, see Table 5.1, V
u_i	mobility of species i, related to diffusivity by equation (5.57)
$\mathbf{V}$	variance-covariance matrix used in regression analysis, see equation (19.1)
V	interfacial potential for the working electrode, see Table 5.1, V
V	potential, V
v	velocity, cm/s
V_+	potential at the positive input terminal for an operational amplifier, see Figure 6.1(a), V
V_-	potential at the negative input terminal for an operational amplifier, see Figure 6.1(a), V
V_0	output potential for an operational amplifier, see Figure 6.1(a), V
$V_{0,k}$	interfacial potential under equilibrium conditions for a given reaction k, $V_{0,k} = (\Phi_{\mathrm{m}} - \Phi_0)_{0,k}$, see Table 5.1, V
ν_{CE}	voltage noise contribution, V, see Figure 21.2 and equation (21.4)
ΔV	amplitude of sinusoidal potential signal, see, e.g., equation (4.6), V
ν_{e}	voltage noise contribution, V, see Figure 21.2 and equation (21.4)
ν_{p}	voltage noise contribution, V, see Figure 21.2 and equation (21.4)
ν_{ref}	voltage noise contribution, V, see Figure 21.2 and equation (21.4)
$\nu_{\mathrm{R_m}}$	voltage noise contribution, V, see Figure 21.2 and equation (21.4)
V_S	potential of the power leads for an operational amplifier, see Figure 6.1(a), V
W	width of an electrode, cm
WE	working electrode, see Figure 6.6
W_i	transfer function associated with the electrohydrodynamic impedance for species i, see equation (15.29)
W_k	generic input quantities for an electrochemical system, see Figure 14.1
$X(\omega)$	general frequency-dependent output function, see equation (22.5)
$x(t)$	general time-dependent output function, see equation (22.1)

X_k	generic state quantities for an electrochemical system, see Figure 14.1
Y	admittance, $Y = 1/Z$, $1/\Omega\text{cm}^2$
y	normal coordinate, cm
Y_k	generic output quantities for an electrochemical system, see Figure 14.1
Z	global impedance, see Table 7.2, Ωcm^2
z	local impedance, see Table 7.2, Ωcm^2
Z_0	global interfacial impedance, see Table 7.2, Ωcm^2
z_0	local interfacial impedance, see Table 7.2, Ωcm^2
Z_c	mass-transport transfer function defined in Section 15.2.1
Z_D	diffusion impedance, Ωcm^2
Z_e	global Ohmic impedance, see Table 7.2, Ωcm^2
z_e	local Ohmic impedance, Ωcm^2
Z_{eq}	interfacial impedance per unit pore area defined by equation (13.21)
Z_f	Faradaic impedance, Ωcm^2
z_i	charge associated with species i
Z_k	tabulated dimensionless values for diffusion impedance where $k = 1, 2, 3$, see equation (11.97) for a rotating disk electrode and equation (11.109) for a submerged impinging jet
Z_Y	Young impedance, equation (13.86), Ωcm^2

Greek

α	CPE exponent, see equations (13.1) and (13.2), dimensionless
α	probability of incorrectly rejecting the null hypothesis when it is actually true, see Section 3.3.1
α	symmetry factor used in electrode kinetics, see equation (5.14), dimensionless
$\boldsymbol{\alpha}$	tensor corresponding to the second derivative of the objective function with respect to parameter, see equation (19.21)
β	Tafel slope, see, e.g., equation (5.18), V/decade of current
$\boldsymbol{\beta}$	vector corresponding to the first derivative of the objective function with respect to parameter, see equation (19.20)

β_y	local wall velocity gradient, see equation (13.11)
Γ	maximum surface coverage, mol/cm^2
γ	fractional surface coverage
δ	thickness, cm
ϵ	porosity
ε	dielectric constant
$\varepsilon_{\text{bias}}$	bias error, see equation (21.1), Ω
$\varepsilon_{\text{drift}}$	bias error associated with nonstationary behavior, see equation (21.24), Ω
ε_0	permittivity of vacuum, 8.8542×10^{-14} F/cm, see Section 5.8
ε_{fit}	error associated with model inadequacy, see equation (21.1), Ω
$\varepsilon_{\text{inst}}$	bias error associated with instrumental artifacts, see equation (21.24), Ω
$\varepsilon_{\text{stoch}}$	stochastic error, see equation (21.1), Ω
ζ	dimensionless position, $\zeta = y\sqrt{\Omega/\nu}$
η_c	concentration overpotential defined by equation (5.75), see Table 5.1, V
η	dimensionless axial position, $\eta = y\sqrt{a/\nu}$
η_s	surface overpotential for a given reaction k, $\eta_s = V - V_{0,k}$, see Table 5.1, V
Θ_i	dimensionless concentration, see equation (11.43)
θ_i	dimensionless oscillating part of the concentration, $\theta_i(y) = \widetilde{c}_i/\widetilde{c}_i(0)$
κ	conductivity, see, e.g., equation (5.56), S/cm
λ	Debye length, see equation (5.77), cm
λ	constant used for analysis of impedance at low frequency, see equation (18.2)
λ	constant used for regression analysis in the method of steepest descent, equation (19.31), and the Levenberg-Marquardt methods, equation (19.32)
μ	fluid viscosity, g/cm s
μ_i	electrochemical potential of species i, J/mol
μ_x	mean value of sample distribution x defined by equation (3.1)
ν	degree of freedom

ν	kinematic viscosity, $\nu = \mu/\rho$, cm^2/s
ν	wave number, see Section 14.3.2
ξ	dimensionless position
π	$\pi = 3.141592654$
ρ	fluid density, g/cm^3
ρ_{sc}	charge density for a semiconductor, see equation (12.10), C/cm^3
σ_x	standard deviation of sample distribution x, see equation (3.9)
σ_{x_1,x_2}	cross-covariance of sample distributions x_1 and x_2, see equation (3.11)
σ_x^2	variance of sample distribution x, see equation (3.7)
τ	time constant, e.g., $\tau = RC$, s
τ_{RC}	characteristic RC time constant, s
τ_{rz}	shear stress, N/cm^2
τ_{meas}	time required to measure a complete spectrum, see equation (21.15), s
τ_{set}	time required to measure a series of spectra, see equation (21.13), s
Φ	potential, V
ϕ	dimensionless steam function for flow to a submerged impinging jet, see equations (11.98) and (11.99)
ϕ	phase angle for impedance, see equation (4.32)
Φ_0	potential of the electrolyte adjacent to the working electrode with respect to an unspecified but common reference potential, see Table 5.1, V
Φ_{m}	electrode potential with respect to an unspecified but common reference potential, see Table 5.1, V
Φ_{ref}	potential of a reference electrode with respect to an unspecified but common reference potential, see Table 5.1, V
φ	phase lag, see, e.g., equation (4.7)
χ^2	sum of squares used in regression analysis, see Sections 3.3.4 and 19.2
ψ	dimensionless parameter defined by equation (11.55)
Ω	rotation speed, s^{-1}
ω	angular frequency, $\omega = 2\pi f$, s^{-1}

ω_c	characteristic angular frequency, $\omega_c = 1/RC$, s^{-1}

General Notation

$\mathrm{Im}\{X\}$	imaginary part of X
$\mathrm{Re}\{X\}$	real part of X
$\overline{X}$	steady-state or time-averaged part of $X(t)$, see equation (11.7)
$\bar{z}$	complex conjugate of a complex number z, $\bar{z} = z_r - z_j$ of $X(t)$
$\langle X \rangle$	spatially averaged value of X
$\widetilde{X}$	oscillating part of $X(t)$, see equation (11.7)
$\mathrm{E}\{X\}$	expectation of $X(t)$, see equation (3.1) and Table 3.1
$\widehat{Z}$	model value for Z, see equation (19.1)
X'	first derivative of $X(t)$ with respect to position
θ	pertaining to the angular direction

Subscripts

0	located at the inner limit of the diffuse double layer
adj	pertaining to terms corrected for the Ohmic resistance
a	pertaining to anodic reactions
c	pertaining to cathodic reactions
CE	pertaining to the counterelectrode, see Figure 6.6
cell	pertaining to the electrochemical cell, see Section 8.1.1
d	associated with the diffuse region of charge, see Figure 5.13
dl	double layer
HF	high frequency
i	pertaining to chemical species i
ihp	located at the inner Helmholtz plane, see Figure 5.13
IJ	impinging jet, see Section 11.7
j	imaginary
ℓ	pertaining to a porous layer, see, e.g., Figure 9.4

LF	low frequency
m	located at the electrode surface, see Figure 5.13
mod	model value
ob	observed value
ohp	located at the outer Helmholtz plane, see Figure 5.13
r	pertaining to the radial direction
r	real
ref	pertaining to a reference electrode, see Figure 6.6
WE	pertaining to the working electrode, see Figure 6.6
y	pertaining to the axial direction
Z_j	pertaining to the imaginary part of the impedance
Z_r	pertaining to the real part of the impedance

Electrochemical Impedance Spectroscopy
by Mark E. Orazem and Bernard Tribollet

References

1. D. D. Macdonald, *Transient Techniques in Electrochemistry* (New York: Plenum Press, 1977).
2. C. Gabrielli, *Identification of Electrochemical Processes by Frequency Response Analysis,* Solartran instrumentation group monograph, The Solartran Electronic group Ltd., Farnborough, England (1980).
3. J. R. Macdonald, editor, *Impedance Spectroscopy: Emphasizing Solid Materials and Systems* (New York: John Wiley & Sons, 1987).
4. E. Barsoukov and J. R. Macdonald, editors, *Impedance Sprectroscopy Theory, Experiment, and Applications,* 2nd edition (New York: Wiley-Interscience, 2005).
5. J. G. Saxe, *The Poetical Works of John Godfrey Saxe* (Boston: Houghton, Mifflin, 1892).
6. O. Heaviside, *Electrical Papers,* volume 1 (New York: MacMillan, 1894).
7. O. Heaviside, *Electrical Papers,* volume 2 (New York: MacMillan, 1894).
8. W. Nernst, "Methode zur Bestimmung von Dielektrizitätskonstanten," *Zeitschrift für Elektrochemie,* **14** (1894) 622–663.
9. C. Wheatstone, "An Account of Several New Instruments and Processes for determining the Constants of a Voltaic Circuit," *Philosphical Transactions of the Royal Society,* **133** (1843) 303–327.
10. The Physical Society of London, *The Scientific Papers of Sir Charles Wheatstone* (London: Taylor and Francis, 1879).
11. J. Hopkinson and E. Wilson, "On the Capacity and Residual Charge of Dielectrics as Affected by Temperature and Time," *Philosophical Transactions of the Royal Society of London. Series A.,* **189** (1897) 109–135.
12. J. Dewar and J. A. Fleming, "A Note on Some Further Determinations of the Dielectric Constants of Organic Bodies and Electrolytes at Very Low Temperatures," *Proceedings of the Royal Society of London,* **62** (1898) 250–266.

13. C. H. Ayres, "Measurement of the Internal Resistance of Galvanic Cells," *Physical Review (Series I)*, **14** (1902) 17–37.

14. A. Finkelstein, "Über Passives Eisen," *Zeitschrift für Physikalische Chemie*, **39** (1902) 91–110.

15. E. Warburg, "Über das Verhalten sogenannter unpolarisirbarer Elektroden gegen Wechselstrom," *Annalen der Physik und Chemie*, **67** (1899) 493–499.

16. E. Warburg, "Über die Polarisationscapacität des Platins," *Annalen der Physik*, **6** (1901) 125–135.

17. A. Fick, "Über Diffusion," *Annalen der Physik*, **170** (1855) 59–86.

18. F. Krüger, "Über Polarisationskapazität," *Zeitschrift für Physikalische Chemie*, **39** (1902) 91–110.

19. R. E. Remington, "The High-Frequency Wheatstone Bridge as a Tool in Cytological Studies: With some Observations on the Resistance and Capacity of the Cells of the Beet Root," *Protoplasma*, **5** (1928) 338–399.

20. H. Fricke and S. Morse, "The Electric Resistance and Capacity of Blood for Frequencies between 800 and 4 1/2 Million Cycles," *Journal of General Physiology*, **9** (1925) 153–167.

21. H. Fricke, "The Electric Capacity of Suspensions with Special Reference to Blood," *Journal of General Physiology*, **9** (1925) 137–152.

22. J. F. McClendon, R. Rufe, J. Barton, and F. Fetter, "Colloidal Properties of the Surface of the Living Cell: 2. Electric Conductivity and Capacity of Blood to Alternating Currents of Long Duration and Varying in Frequency from 260 to 2,000,000 Cycles per Second," *Journal of Biological Chemistry*, **69** (1926) 733–754.

23. K. S. Cole, "Electric Phase Angle of Cell Membranes," *Journal of General Physiology*, **15** (1932) 641–649.

24. E. Bozler and K. S. Cole, "Electric Impedance and Phase Angle of Muscle in Rigor," *Journal of Cellular and Comparative Physiology*, **6** (1935) 229–241.

25. K. S. Cole, "Electric Impedance of Suspensions of Spheres," *Journal of General Physiology*, **12** (1928) 29–36.

26. H. Fricke, "The Theory of Electrolytic Polarization," *Philosophical Magazine*, **14** (1932) 310–318.

27. K. S. Cole and R. H. Cole, "Dispersion and Absorption in Dielectrics 1: Alternating Current Characteristics," *Journal of Chemical Physics*, **9** (1941) 341–351.

28. A. Frumkin, "The Study of the Double Layer at the Metal–Solution Interface by Electrokinetic and Electrochemical Methods," *Transactions of the Faraday Society*, **33** (1940) 117–127.

29. D. C. Grahame, "The Electrical Double Layer and the Theory of Electrocapillarity," *Chemical Reviews*, **41** (1947) 441–501.

30. D. C. Grahame, "Die Elektrische Doppelschicht," *Zeitschrift für Elektrochemie*, **59** (1955) 773–778.

31. P. I. Dolin and B. V. Ershler, "Kinetics of Processes on the Platinum Electrode: I. The Kinetics of the Ionization of Hydrogen Adsorbed on a Platinum Electrode," *Acta Physicochimica URSS*, **13** (1940) 747–778.

32. J. E. B. Randles, "Kinetics of Rapid Electrode Reactions," *Discussions of the Faraday Society*, **1** (1947) 11–19.

33. I. Epelboin, "Etude des Phénomènes Electrolytiques à l'aide de Courants Alternatifs Faibles et de Fréquence Variable," *Comptes Rendus Hebdomadaires des Séances de l'Académie des Sciences*, **234** (1952) 950–952.

34. H. Gerischer and W. Mehl, "Zum Mechanismus der Kathodischen Wasserstoffabscheidung an Quecksilber, Silber, und Kupfer," *Zeitschrift für Elektrochemie*, **59** (1955) 1049–1059.

35. A. Frumkin, "Adsorptionserscheinungen und Elektrochemishe Kinetik," *Zeitschrift für Elektrochemie*, **59** (1955) 807–822.

36. I. Epelboin and G. Loric, "Sur un Phénomène de Résonance observé en Basse Fréquence au Cours des Electrolyses Accompagnées d'une Forte Surtension Anodique," *Journal de Physique et le Radium*, **21** (1960) 74–76.

37. R. de Levie, "Electrochemical Responses of Porous and Rough Electrodes," in *Advances in Electrochemistry and Electrochemical Engineering*, P. Delahay, editor, volume 6 (New York: Interscience, 1967) 329–397.

38. J. S. Newman, "Frequency Dispersion in Capacity Measurements at a Disk Electrode," *Journal of The Electrochemical Society*, **117** (1970) 198–203.

39. E. Levart and D. Schuhmann, "Sur la Détermination Générale de L'impédance de Concentration (Diffusion Convective et Réaction Chimique) pour une Electrode à Disque Tournant," *Journal of Electroanalytical Chemistry*, **53** (1974) 77–94.

40. R. D. Armstrong, R. E. Firman, and H. R. Thirsk, "AC Impedance of Complex Electrochemical Reactions," *Faraday Discussions*, **56** (1973) 244–263.

41. I. Epelboin, M. Keddam, and J. C. Lestrade, "Faradaic Impedances and Intermediates in Electrochemical Reactions," *Faraday Discussions*, **56** (1975) 264–275.

42. R. J. Sheppard, B. P. Jordan, and E. H. Grant, "Least Squares Analysis of Complex Data with Applications to Permittivity Measurements," *Journal of Physics D—Applied Physics*, **3** (1970) 1759–1764.

43. R. J. Sheppard, "Least-Squares Analysis of Complex Weighted Data with Dielectric Applications," *Journal of Physics D—Applied Physics*, **6** (1973) 790–794.

44. J. R. Macdonald and J. A. Garber, "Analysis of Impedance and Admittance Data for Solids and Liquids," *Journal of The Electrochemical Society*, **124** (1977) 1022–1030.

45. J. R. Macdonald, J. Schoonman, and A. P. Lehnen, "The Applicability and Power of Complex Nonlinear Least Squares for the Analysis of Impedance and Immittance Data," *Journal of Electroanalytical Chemistry*, **131** (1982) 77–95.

46. B. Boukamp, "A Nonlinear Least Squares Fit Procedure for Analysis of Immittance Data of Electrochemical Systems," *Solid State Ionics, Diffusion & Reactions*, **20** (1986) 31–44.

47. A. A. Aksut, W. J. Lorenz, and F. Mansfeld, "The Determination of Corrosion Rates by Electrochemical DC and AC Methods: II. Systems with Discontinuous Steady State Polarization Behavior," *Corrosion Science*, **22** (1982) 611–619.

48. F. Mansfeld, M. W. Kendig, and S. Tsai, "Corrosion Kinetics in Low Conductivity Media: I. Iron in Natural Waters," *Corrosion Science*, **22** (1982) 455–471.

49. W. H. Smyrl and L. L. Stephenson, "Digital Impedance for Faradaic Analysis: 3. Copper Corrosion in Oxygenated 0.1N HCl," *Journal of The Electrochemical Society*, **132** (1985) 1563–1567.

50. C. Deslouis, I. Epelboin, C. Gabrielli, and B. Tribollet, "Impēdance Electromēcanique obtenue au Courant Limite de Diffusion à Partir d'une Modulation Sinusoidale de la Vitesse de Rotation d'une Electrode à Disque," *Journal of Electroanalytical Chemistry*, **82** (1977) 251–269.

51. C. Deslouis, I. Epelboin, C. Gabrielli, P. S.-R. Fanchine, and B. Tribollet, "Relationship between the Electrochemical Impedance and the Electrohydrodynamical Impedances Measured Using a Rotating Disc Electrode," *Journal of Electroanalytical Chemistry*, **107** (1980) 193–195.

52. C. Gabrielli and B. Tribollet, "A Transfer Function Approach for a Generalized Electrochemical Impedance Spectroscopy," *Journal of The Electrochemical Society*, **141** (1994) 1147–1157.

53. R. de L. Kronig, "On the Theory of Dispersion of X-Rays," *Journal of the Optical Society of America and Review of Scientific Instruments,* **12** (1926) 547–557.

54. H. A. Kramers, "Die Dispersion und Absorption von Röntgenstrahlen," *Physik Zeitschrift,* **30** (1929) 522–523.

55. D. D. Macdonald and M. Urquidi-Macdonald, "Application of Kramers-Kronig Transforms in the Analysis of Electrochemical Systems: 1. Polarization Resistance," *Journal of The Electrochemical Society,* **132** (1985) 2316–2319.

56. P. Agarwal, M. E. Orazem, and L. H. García-Rubio, "Measurement Models for Electrochemical Impedance Spectroscopy: I. Demonstration of Applicability," *Journal of The Electrochemical Society,* **139** (1992) 1917–1927.

57. F. Dion and A. Lasia, "The Use of Regularization Methods in the Deconvulation of Underlying Distributions in Electrochemical Processes," *Journal of Electroanalytical Chemistry,* **475** (1999) 28–37.

58. M. E. Orazem, P. Shukla, and M. A. Membrino, "Extension of the Measurement Model Approach for Deconvolution of Underlying Distributions for Impedance Measurements," *Electrochimica Acta,* **47** (2002) 2027–2034.

59. Z. Stoynov, "Differential Impedance Analysis - An Insight into the Experimental Data," *Polish Journal of Chemistry,* **71** (1997) 1204–1210.

60. D. Vladikova, Z. Stoynov, and L. Ilkov, "Differential Impedance Analysis on Single Crystal and Polycrystalline Yttrium Iron Garnets," *Polish Journal of Chemistry,* **71** (1997) 1196–1203.

61. Z. B. Stoynov and B. S. Savova-Stoynov, "Impedance Study of Non-Stationary Systems: Four-Dimensional Analysis," *Journal of Electroanalytical Chemistry and Interfacial Electrochemistry,* **183** (1985) 133–144.

62. C. Gabrielli, editor, *Proceedings of the First International Symposium on Electrochemical Impedance Spectroscopy,* volume 35:10 of *Electrochimica Acta* (1990).

63. D. D. MacDonald, editor, *Proceedings of the Second International Symposium on Electrochemical Impedance Spectroscopy,* volume 38:14 of *Electrochimica Acta* (1993).

64. J. Vereecken, editor, *Proceedings of the Third International Symposium on Electrochemical Impedance Spectroscopy,* volume 41:7-8 of *Electrochimica Acta* (1996).

65. O. R. Mattos, editor, *Proceedings of the Fourth International Symposium on Electrochemical Impedance Spectroscopy,* volume 44:24 of *Electrochimica Acta* (1999).

66. F. Deflorian and P. L. Bonora, editors, *Proceedings of the Fifth International Symposium on Electrochemical Impedance Spectroscopy,* volume 47:13-14 of *Electrochimica Acta* (2002).

67. M. E. Orazem, editor, *EIS-2004: Proceedings of the Sixth International Symposium on Electrochemical Impedance Spectroscopy*, volume 51:8-9 of *Electrochimica Acta* (2006).

68. R. S. Lillard, P. J. Moran, and H. S. Isaacs, "A Novel Method for Generating Quantitative Local Electrochemical Impedance Spectroscopy," *Journal of The Electrochemical Society*, **139** (1992) 1007–1012.

69. D. D. Macdonald, "Reflections on the History of Electrochemical Impedance Spectroscopy," *Electrochimica Acta*, **51** (2006) 1376–1388.

70. M. Sluyters-Rehbach and J. H. Sluyters, "Sine Wave Methods in the Study of Electrode Processes," in *Electroanalytical Chemistry*, A. J. Bard, editor, volume 4 (New York: Marcel Dekker, 1970) 1–128.

71. A. Lasia, "Electrochemical Impedance Spectroscopy and its Applications," in *Modern Aspects of Electrochemistry*, R. E. White, B. E. Conway, and J. O. Bockris, editors, volume 32 (New York: Plenum Press, 1999) 143–248.

72. R. Churchill and J. Brown, *Complex Variables and Applications*, 6th edition (New York: McGraw Hill, 1990).

73. G. Cain, *Complex Analysis* (Atlanta, GA: Georgia Institute of Technology, 1999).

74. C. F. C. M. Fong, D. D. Kee, and P. N. Kalomi, *Advanced Mathematics for Applied and Pure Sciences* (Amsterdam, The Netherlands: Gordon and Breach Science Publishers, 1997).

75. M. Sluyters-Rehbach, "Impedances of Electrochemical Systems: Terminology, Nomenclature, and Representation: I. Cells with Metal Electrodes and Liquid Solutions," *Pure and Applied Chemistry*, **66** (1994) 1831–1891.

76. R. Antaño-Lopez, M. Keddam, and H. Takenouti, "A New Experimental Approach to the Time-Constants of Electrochemical Impedance: Frequency Response of the Double Layer Capacitance," *Electrochimica Acta*, **46** (2001) 3611–3617.

77. C. R. Wylie, *Advanced Engineering Mathematics*, 3rd edition (New York: McGraw-Hill, 1966).

78. M. R. Spiegel, *Applied Differential Equations* (Englewood Cliffs, NJ: Prentice Hall, 1967).

79. G. W. Snedecor and W. G. Cochran, *Statistical Methods*, 6th edition (Ames, IA: the Iowa State University Press, 1961).

80. C. M. Grinstead and J. L. Snell, *Introduction to Probability* (Providence, RI: American Mathematical Society, 1999).

81. M. Abramowitz and I. A. Stegun, *Handbook of Mathematical Functions* (New York: Dover Publications, 1972).

82. G. E. P. Box and N. R. Draper, *Empirical Model-Building and Response Surfaces* (New York: John Wiley & Sons, 1987).

83. C. Deslouis, O. Gil, B. Tribollet, G. Vlachos, and B. Robertson, "Oxygen as a Tracer for Measurements of Steady and Turbulent Flows," *Journal of Applied Electrochemistry*, **22** (1992) 835–842.

84. Student, "The Probable Error of a Mean," *Biometrika*, **6** (1908) 1–25.

85. M. E. Orazem, M. Durbha, C. Deslouis, H. Takenouti, and B. Tribollet, "Influence of Surface Phenomena on the Impedance Response of a Rotating Disk Electrode," *Electrochimica Acta*, **44** (1999) 4403–4412.

86. P. Agarwal, O. D. Crisalle, M. E. Orazem, and L. H. García-Rubio, "Measurement Models for Electrochemical Impedance Spectroscopy: 2. Determination of the Stochastic Contribution to the Error Structure," *Journal of The Electrochemical Society*, **142** (1995) 4149–4158.

87. H. W. Bode, *Network Analysis and Feedback Amplifier Design* (New York: D. Van Nostrand, 1945).

88. J. S. Newman, *Electrochemical Systems*, 2nd edition (Englewood Cliffs, NJ: Prentice Hall, 1991).

89. J. Newman and K. E. Thomas-Alyea, *Electrochemical Systems* (New York: John Wiley & Sons, 2004).

90. G. Prentice, *Electrochemical Engineering Principles* (Englewood Cliffs, NJ: Prentice Hall, 1991).

91. A. J. Bard and L. R. Faulkner, *Electrochemical Methods: Fundamentals and Applications* (New York: John Wiley & Sons, 1980).

92. J. O. M. Bockris and A. K. N. Reddy, *Modern Electrochemistry: Ionics*, volume 1, 2nd edition (New York: Plenum Press, 1998).

93. J. O. M. Bockris and A. K. N. Reddy, *Modern Electrochemistry: Electrodics*, volume 2, 2nd edition (New York: Plenum Press, 2000).

94. E. Gileadi, *Electrode Kinetics for Chemists, Chemical Engineers, and Materials Scientists* (New York: VCH Publishers, 1993).

95. C. M. A. Brett and A. M. O. Brett, *Electrochemistry: Principles, Methods, and Applications* (Cary, NC: Oxford University Press, 1993).

96. C. Wagner, "Theoretical Analysis of the Current Density Distribution in Electrolytic Cells," *Journal of The Electrochemical Society*, **98** (1951) 116–128.

97. V. M.-W. Huang, V. Vivier, M. E. Orazem, N. Pébère, and B. Tribollet, "The Apparent CPE Behavior of a Disk Electrode with Faradaic Reactions," *Journal of The Electrochemical Society*, **154** (2007) C99–C107.

98. M. D. Groner, J. W. Elam, F. H. Fabreguette, and S. M. George, "Electrical Characterization of Thin Al_2O_3 Films Grown by Atomic Layer Deposition on Silicon and Various Metal Substrates," *Thin Solid Films*, **413** (2002) 186–197.

99. A. Carnot, I. Frateur, S. Zanna, B. Tribollet, I. Dubois-Brugger, and P. Marcus, "Corrosion Mechanisms of Steel Concrete Moulds in Contact with a Demoulding Agent Studied by EIS and XPS," *Corrosion Science*, **45** (2003) 2513–2524.

100. S. L. Carson, M. E. Orazem, O. D. Crisalle, and L. H. García-Rubio, "On the Error Structure of Impedance Measurements: Series Expansions," *Journal of The Electrochemical Society*, **150** (2003) E501–E511.

101. M. E. Van Valkenburg, *Network Analysis*, 3rd edition (Englewood Cliffs, NJ: Prentice-Hall, 1974).

102. V. M.-W. Huang, V. Vivier, M. E. Orazem, N. Pébère, and B. Tribollet, "The Apparent CPE Behavior of an Ideally Polarized Disk Electrode: A Global and Local Impedance Analysis," *Journal of The Electrochemical Society*, **154** (2007) C81–C88.

103. F. Zou, D. Thierry, and H. S. Isaacs, "High-Resolution Probe for Localized Electrochemical Impedance Spectroscopy Measurements," *Journal of The Electrochemical Society*, **144** (1997) 1957–1965.

104. G. J. Brug, A. L. G. van den Eeden, M. Sluyters-Rehbach, and J. H. Sluyters, "The Analysis of Electrode Impedances Complicated by the Presence of a Constant Phase Element," *Journal of Electroanalytic Chemistry*, **176** (1984) 275–295.

105. M. Eisenberg, C. W. Tobias, and C. R. Wilke, "Ionic Mass Transfer and Concentration Polarization at Rotating Electrodes," *Journal of The Electrochemical Society*, **101** (1954) 306–319.

106. D.-T. Chin, "Convective Diffusion on a Rotating Spherical Electrode," *Journal of The Electrochemical Society*, **118** (1971) 1434–1438.

107. K. Nisancioglu and J. Newman, "Current Distribution on a Rotating Sphere below the Limiting Current," *Journal of The Electrochemical Society*, **121** (1974) 241–246.

108. O. E. Barcia, J. S. Godinez, L. R. S. Lamego, O. R. Mattos, and B. Tribollet, "Rotating Hemispherical Electrode," *Journal of The Electrochemical Society*, **145** (1998) 4189–4195.

109. P. K. Shukla and M. E. Orazem, "Hydrodynamics and Mass-Transfer-Limited Current Distribution for a Submerged Stationary Hemispherical Electrode under Jet Impingement," *Electrochimica Acta*, **49** (2004) 2901–2908.

110. P. K. Shukla, M. E. Orazem, and G. Nelissen, "Impedance Analysis for Reduction of Ferricyanide on a Submerged Hemispherical Ni270 Electrode," *Electrochimica Acta*, **51** (2006) 1514–1523.

111. P. K. Shukla, *Stationary Hemispherical Electrode under Submerged Jet Impingement and Validation of the Measurement Model Concept for Impedance Spectroscopy*, Ph.D. dissertation, University of Florida, Gainesville, FL (2004).

112. J. Diard, B. LeGorrec, and C. Montella, "Deviation from the Polarization Resistance Due to Non-Linearity: 1. Theoretical Formulation," *Journal of Electroanalytical Chemistry*, **432** (1997) 27–39.

113. J. Diard, B. L. Gorrec, and C. Montella, "Deviation from the Polarization Resistance Due to Non-Linearity: 2. Application to Electrochemical Reactions," *Journal of Electroanalytical Chemistry*, **432** (1997) 41–52.

114. J. Diard, B. LeGorrec, and C. Montella, "Deviation from the Polarization Resistance Due to Non-Linearity: 3. Polarization Resistance Determination from Non-Linear Impedance Measurements," *Journal of Electroanalytical Chemistry*, **432** (1997) 53–62.

115. P. T. Wojcik, P. Agarwal, and M. E. Orazem, "A Method for Maintaining a Constant Potential Variation during Galvanostatic Regulation of Electrochemical Impedance Measurements," *Electrochimica Acta*, **41** (1996) 977–983.

116. P. T. Wojcik and M. E. Orazem, "Variable-Amplitude Galvanostatically Modulated Impedance Spectroscopy as a Tool for Assessing Reactivity at the Corrosion Potential without Distorting the Temporal Evolution of the System," *Corrosion*, **54** (1998) 289–298.

117. R. Pollard and T. Comte, "Determination of Transport Properties for Solid Electrolytes from the Impedance of Thin Layer Cells," *Journal of The Electrochemical Society*, **136** (1989) 3734–3748.

118. O. Devos, C. Gabrielli, and B. Tribollet, "Nucleation-Growth Process of Scale Electrodeposition: Influence of the Mass Transport," *Electrochimica Acta*, **52** (2006) 285–291.

119. L. Beaunier, I. Epelboin, J. C. Lestrade, and H. Takenouti, "Etude Electrochimique, et par Microscopie Electronique à Balayage, du Fer Recouvert de Peinture," *Surface Technology*, **4** (1976) 237–254.

120. L. Bousselmi, C. Fiaud, B. Tribollet, and E. Triki, "Impedance Spectroscopic Study of a Steel Electrode in Condition of Scaling and Corrosion: Interphase Model," *Electrochimica Acta*, **44** (1999) 4357–4363.

121. M. Stern and A. L. Geary, "Electrochemical Polarization: I. A Theoretical Analysis of the Shape of Polarization Curves," *Journal of The Electrochemical Society*, **104** (1957) 56–63.

122. G. Baril, G. Galicia, C. Deslouis, N. Pèbére, B. Tribollet, and V. Vivier, "An Impedance Investigation of the Mechanism of Pure Magnesium Corrosion in Sodium Sulfate Solutions," *Journal of The Electrochemical Society*, **154** (2007) C108–C113.

123. V. G. Levich, *Physicochemical Hydrodynamics* (Englewood Cliffs, NJ: Prentice Hall, 1962).

124. O. Devos, O. Aaboubi, J. P. Chopart, E. Merienne, A. Olivier, C. Gabrielli, and B. Tribollet, "EIS Investigation of Zinc Electrodeposition in Basic Media at Low Mass Transfer Rates Induced by a Magnetic Field," *Journal of Physical Chemistry B*, **103** (1999) 496–501.

125. R. B. Bird, W. E. Stewart, and E. N. Lightfoot, *Transport Phenomena* (New York: John Wiley & Sons, 1960).

126. C. Deslouis, B. Tribollet, M. Duprat, and F. Moran, "Transient Mass Transfer at a Coated Rotating Disk Electrode: Diffusion and Electrohydrodynamical Impedances," *Journal of The Electrochemical Society*, **134** (1987) 2496–2501.

127. A. C. West, "Comparison of Modeling Approaches for a Porous Salt Film," *Journal of The Electrochemical Society*, **140** (1993) 403–408.

128. E. L'Hostis, C. Compère, D. Festy, B. Tribollet, and C. Deslouis, "Characterization of Biofilms Formed on Gold in Natural Seawater by Oxygen Diffusion Analysis," *Corrosion*, **53** (1997) 4–10.

129. T. von Kármán, "Über Laminaire und Turbulente Reibung," *Zeitschrift für angewandte Mathematik und Mechanik*, **1** (1921) 233–252.

130. W. G. Cochran, "The Flow Due to a Rotating Disc," *Proceedings of the Cambridge Philosophical Society*, **30** (1934) 365–375.

131. B. Tribollet and J. Newman, "The Modulated Flow at a Rotating Disk Electrode," *Journal of The Electrochemical Society*, **130** (1983) 2016–2026.

132. J. S. Newman, "Schmidt Number Correction for the Rotating Disk," *Journal of Physical Chemistry*, **70** (1966) 1327.

133. C. Deslouis, C. Gabrielli, and B. Tribollet, "An Analytical Solution of the Nonsteady Convective Diffusion Equation for Rotating Electrodes," *Journal of The Electrochemical Society*, **130** (1983) 2044–2046.

134. B. Tribollet and J. Newman, "Analytic Expression for the Warburg Impedance for a Rotating Disk Electrode," *Journal of The Electrochemical Society*, **130** (1983) 822–824.

135. B. Tribollet, J. Newman, and W. H. Smyrl, "Determination of the Diffusion Coefficient from Impedance Data in the Low Frequency Range," *Journal of The Electrochemical Society*, **135** (1988) 134–138.

136. E. Levart and D. Schuhmann, "General Determination of Transition Behavior of a Rotating Disc Electrode Submitted to an Electrical Perturbation of Weak Amplitude," *Journal of Electroanalytical Chemistry*, **28** (1970) 45.

137. D.-T. Chin and C.-H. Tsang, "Mass Transfer to an Impinging Jet Electrode," *Journal of The Electrochemical Society*, **125** (1978) 1461–1470.

138. J. M. Esteban, G. Hickey, and M. E. Orazem, "The Impinging Jet Electrode: Measurement of the Hydrodynamic Constant and Its Use for Evaluating Film Persistency," *Corrosion*, **46** (1990) 896–901.

139. C. B. Diem and M. E. Orazem, "The Influence of Velocity on the Corrosion of Copper in Alkaline Chloride Solutions," *Corrosion*, **50** (1994) 290–300.

140. M. E. Orazem, J. C. Cardoso, Filho, and B. Tribollet, "Application of a Submerged Impinging Jet for Corrosion Studies: Development of Models for the Impedance Response," *Electrochimica Acta*, **46** (2001) 3685–3698.

141. H. Cachet, O. Devos, G. Folcher, C. Gabrielli, H. Perrot, and B. Tribollet, "In situ Investigation of Crystallization Processes by Coupling of Electrochemical and Optical Measurements: Application to $CaCO_3$ Deposit," *Electrochemical and Solid-State Letters*, **4** (2001) C23–C25.

142. O. Devos, C. Gabrielli, and B. Tribollet, "Nucleation-Growth Processes of Scale Crystallization under Electrochemical Reaction Investigated by In Situ Microscopy," *Electrochemical and Solid-State Letters*, **4** (2001) C73–C76.

143. M. T. Scholtz and O. Trass, "Mass Transfer in a Nonuniform Impinging Jet: I. Stagnation Flow-Velocity and Pressure Distribution," *AIChE Journal*, **16** (1970) 82–90.

144. M. T. Scholtz and O. Trass, "Mass Transfer in a Nonuniform Impinging Jet: II. Boundary Layer Flow-Mass Transfer," *AIChE Journal*, **16** (1970) 90–96.

145. C. Chia, F. Giralt, and O. Trass, "Mass Transfer in Axisymmetric Turbulent Impinging Jets," *Industrial Engineering and Chemistry*, **16** (1977) 28–35.

146. F. Giralt, C. Chia, and O. Trass, "Characterization of the Impingement Region in an Axisymmetric Turbulent Jet," *Industrial Engineering and Chemistry*, **16** (1977) 21–27.

147. D. Chin and C. Tsang, "Mass Transfer to an Impinging Jet Electrode," *Journal of The Electrochemical Society*, **125** (1978) 1461–1470.

148. F. Baleras, V. Bouet, C. Deslouis, G. Maurin, V. Sobolik, and B. Tribollet, "Flow Measurement in an Impinging Jet with Three-Segement Microelectrodes," *Experiments in Fluids*, **22** (1996) 87–93.

149. D. R. Gabe, G. D. Wilcox, J. Gonzalez-Garcia, and F. C. Walsh, "The Rotating Cylinder Electrode: Its Continued Development and Application," *Journal of Applied Electrochemistry*, **28** (1998) 759–780.

150. C. Deslouis, I. Epelboin, M. Keddam, and J. C. Lestrade, "Impédance de Diffusion d'un Disque Tournant en Régime Hydrodynamique Laminaire. Etude Expérimentale et Comparaison avec le Modèle de Nernst," *Journal of Electroanalytical Chemistry*, **28** (1970) 57–63.

151. A. S. Grove, *Physics and Technology of Semiconductor Devices* (New York: John Wiley & Sons, 1967).

152. M. A. Omar, *Elementary Solid-State Physics* (Reading, MA: Addison-Wesley, 1975).

153. N. B. Hannay, editor, *Semiconductors* (New York: Rheinhold, 1959).

154. M. E. Orazem, *Mathematical Modeling and Optimization of Liquid-Junction Photovoltaic Cells*, Ph.D. dissertation, University of California, Berkeley, California (1983).

155. J. S. Blakemore, "Semiconducting and Other Major Properties of Gallium Arsenide," *Journal of Applied Physics*, **53** (1982) R123–R181.

156. G. M. Martin and S. Makram-Ebeid, "The Mid–Gap Donor Level EL2 in GaAs," in *Deep Centers in Semiconductors*, S. T. Pantelides, editor (New York: Gordon and Breach Science Publishers, 1986) 455–473.

157. W. Shockley and J. W. T. Read, "Statistics of the Recombination of Holes and Electrons," *Physical Review*, **87** (1952) 835–842.

158. R. N. Hall, "Electron–Hole Recombination in Germanium," *Physical Review*, **87** (1952) 387.

159. C. Hwang and J. Brews, "Electron Activity coefficients in Heavily Doped Semiconductors with Small Effective Mass," *Journal of Physical Chemistry: Solids*, **32** (1971) 837–845.

160. D. B. Bonham and M. E. Orazem, "Activity Coefficients of Electrons and Holes in Semiconductors with a Parabolic Density of States," *Journal of The Electrochemical Society*, **133** (1986) 2081–2086.

161. M. E. Orazem and J. Newman, "Photoelectrochemical Devices for Energy Conversion," in *Modern Aspects of Electrochemistry*, R. E. White, J. O. Bockris, and B. E. Conway, editors, volume 18 (New York: Plenum Press, 1986) 61–112.

162. S. R. Morrison, *Electrochemistry at Semiconductor and Oxidized Metal Electrodes* (New York: Plenum Press, 1980).

163. R. Memming, "Processes at Semiconductor Electrodes," in *Comprehensive Treatise of Electrochemistry*, volume 7 (New York: Plenum Press, 1983) 529–592.

164. A. J. Bard, R. Memming, and B. Miller, "Terminology in Semiconductor Electrochemistry and Photoelectrochemical Energy Conversion (Recommendations 1991)," *Pure and Applied Chemistry*, **63** (1991) 569–596.

165. A. J. Nozik and R. Memming, "Physical Chemistry of Semiconductor–Liquid Interfaces," *Journal of Physical Chemistry*, **100** (1996) 13061–13078.

166. D. B. Bonham and M. E. Orazem, "A Mathematical Model for the Influence of Deep-Level Electronic States on Photoelectrochemical Impedance Spectroscopy: 1. Theoretical Development," *Journal of The Electrochemical Society*, **139** (1992) 118–126.

167. D. B. Bonham and M. E. Orazem, "A Mathematical Model for the Influence of Deep-Level Electronic States on Photoelectrochemical Impedance Spectroscopy: 2. Assessment of Characterization Methods Based on Mott-Schottky Theory," *Journal of The Electrochemical Society*, **139** (1992) 126–131.

168. C. T. Sah, "The Equivalent Circuit Model in Solid-State Electronics: I. The Single Energy Level Defect Centers," *Proceedings of the IEEE*, **55** (1967) 654–671.

169. C. T. Sah, "The Equivalent Circuit Model in Solid-State Electronics: II. The Multiple Energy Level Impurity Center," *Proceedings of the IEEE*, **55** (1967) 672–685.

170. C. T. Sah, "The Equivalent Circuit Model in Solid-State Electronics: III. Conduction and Displacement Currents," *Solid-State Electronics*, **13** (1970) 1547–1575.

171. C. T. Sah, *Fundamentals of Solid-State Electronics* (Singapore: World Scientific Publishing Co., 1991).

172. A. N. Jansen, P. T. Wojcik, P. Agarwal, and M. E. Orazem, "Thermally Stimulated Deep-Level Impedance Spectroscopy: Application to an n-GaAs Schottky Diode," *Journal of The Electrochemical Society*, **143** (1996) 4066–4074.

173. F. Hennig, *Emission and Capture of Electrons and Holes at Gold Centers in Silicon at Thermal Equilibrium*, Technical report, University of Illinois, Urbana-Champaign, Illinois (1974).

174. C. T. Sah, R. N. Noyce, and W. Shockley, "Carrier Generation and Recombination in P-N Junctions and P-N Junction Characteristics," *Proceedings of the Institute of Radio Engineers*, **45** (1957) 1228–1243.

175. T. Dickinson and R. Whitfield, "Some Experimental Factors Which Affect the Analysis of Impedance Measurements," *Electrochimica Acta*, **22** (1977) 385–389.

176. A. van der Ziel, *Fluctuation Phenomena in Semiconductors* (New York: Academic Press, 1959).

177. A. van der Ziel, *Noise in Solid State Devices and Circuits* (New York: John Wiley & Sons, 1986).

178. E. H. Nicollian and A. Goetzberger, "The Si–SiO_2 Interface: Electrical Properties as Determined by the Metal–Insulator–Silicon Conductance Technique," *Bell System Technical Journal*, **XLVI** (1967) 1055–1133.

179. M. P. Dare-Edwards, A. Hamnett, and P. R. Trevellick, "Alternating-Current Techniques in Semiconductor Electrochemistry," *Journal of the Chemical Society, Faraday Transactions*, **79** (1983) 2111–2124.

180. M. H. Dean and U. Stimming, "Capacity of Semiconductor Electrodes with Multiple Bulk Electronic States: I. Model and Calculations for Discrete States," *Journal of Electroanalytical Chemistry*, **228** (1987) 135–151.

181. Z. Lukacs, "The Numerical Evaluation of the Distortion of EIS Data Due to the Distribution of Parameters," *Journal of Electroanalytical Chemistry*, **432** (1997) 79–83.

182. Z. Lukacs, "Evaluation of Model and Dispersion Parameters and Their Effects on the Formation of Constant-Phase Elements in Equivalent Circuits," *Journal of Electroanalytical Chemistry*, **464** (1999) 68–75.

183. J. R. Macdonald, "Generalizations of Universal Dielectric Response and a General Distribution-of-Activation-Energies Model for Dielectric and Conducting Systems," *Journal of Applied Physics*, **58** (1985) 1971–1978.

184. J. R. Macdonald, "Frequency Response of Unified Dielectric and Conductive Systems Involving an Exponential Distribution of Activation Energies," *Journal of Applied Physics*, **58** (1985) 1955–1970.

185. R. L. Hurt and J. R. Macdonald, "Distributed Circuit Elements in Impedance Spectroscopy: A Unified Treatment of Conductive and Dielectric Systems," *Solid State Ionics*, **20** (1986) 111–124.

186. J. R. Macdonald, "Linear Relaxation: Distributions, Thermal Activation, Structure, and Ambiguity," *Journal of Applied Physics*, **62** (1987) R51–R62.

187. J. R. Macdonald, "Power-Law Exponents and Hidden Bulk Relaxation in the Impedance Spectroscopy of Solids," *Journal of Electroanalytical Chemistry*, **378** (1994) 17–29.

188. P. Zoltowski, "On the Electrical Capacitance of Interfaces Exhibiting Constant Phase Element Behavior," *Journal of Electroanalytical Chemistry*, **443** (1998) 149–154.

189. L. Young, "Anodic Oxide Films: 4. The Interpretation of Impedance Measurements on Oxide Coated Electrodes on Niobium," *Transactions of the Faraday Society*, **51** (1955) 1250–1260.

190. L. Young, *Anodic Oxide Films* (New York: Academic Press, 1961).

191. C. A. Schiller and W. Strunz, "The Evaluation of Experimental Dielectric Data of Barrier Coatings by Means of Different Models," *Electrochimica Acta*, **46** (2001) 3619–3625.

192. R. Jurczakowski, C. Hitz, and A. Lasia, "Impedance of Porous Au Based Electrodes," *Journal of Electroanalytical Chemistry*, **572** (2004) 355–366.

193. T. Pajkossy, "Impedance Spectroscopy at Interfaces of Metals and Aqueous Solutions - Surface Roughness, CPE and Related Issues," *Solid State Ionics*, **176** (2005) 1997–2003.

194. J.-B. Jorcin, M. E. Orazem, N. Pébère, and B. Tribollet, "CPE Analysis by Local Electrochemical Impedance Spectroscopy," *Electrochimica Acta*, **51** (2006) 1473–1479.

195. C. H. Hsu and F. Mansfeld, "Technical Note: Concerning the Conversion of the Constant Phase Element Parameter Y_0 into a Capacitance," *Corrosion*, **57** (2001) 747–748.

196. M. A. Lévêque, "Les Lois de la Transmission de Chaleur par Convection," *Annales des Mines*, **13** (1928) 201–299.

197. C. Deslouis, B. Tribollet, and M. A. Vorotyntsev, "Diffusion-Convection Impedance at Small Electrodes," *Journal of The Electrochemical Society*, **138** (1991) 2651–2657.

198. J. S. Newman, "Resistance for Flow of Current to a Rotating Disk," *Journal of The Electrochemical Society*, **113** (1966) 501–502.

199. J. S. Newman, "Current Distribution on a Rotating Disk Below the Limiting Current," *Journal of The Electrochemical Society*, **113** (1966) 1235–1241.

200. K. Nisancioglu and J. Newman, "The Transient Response of a Disk Electrode," *Journal of The Electrochemical Society*, **120** (1973) 1339–1346.

201. K. Nisancioglu and J. Newman, "The Short-Time Response of a Disk Electrode," *Journal of The Electrochemical Society*, **121** (1974) 523–527.

202. P. Antohi and D. A. Scherson, "Current Distribution at a Disk Electrode during a Current Pulse," *Journal of The Electrochemical Society*, **153** (2006) E17–E24.

203. K. Nisancioglu, "The Error in Polarization Resistance and Capacitance Measurements Resulting from Nonuniform Ohmic Potential Drop to Flush-Mounted Probes," *Corrosion*, **43** (1987) 258–265.

204. K. Nisancioglu, "Theoretical Problems Related to Ohmic Resistance Compensation," in *The Measurement and Correction of Electrolyte Resistance in Electrochemical Tests*, L. L. Scribner and S. R. Taylor, editors, STP 1056 (Philadelphia, PA: American Society for Testing and Materials, 1990) 61–77.

205. V. M.-W. Huang, V. Vivier, I. Frateur, M. E. Orazem, and B. Tribollet, "The Global and Local Impedance Response of a Blocking Disk Electrode with Local CPE Behavior," *Journal of The Electrochemical Society*, **154** (2007) C89–C98.

206. M. E. Orazem, N. Pébère, and B. Tribollet, "A New Look at Graphical Representation of Impedance Data," *Journal of The Electrochemical Society*, **153** (2006) B129–B136.

207. I. Frateur, C. Deslouis, M. E. Orazem, and B. Tribollet, "Modeling of the Cast Iron/Drinking Water System by Electrochemical Impedance Spectroscopy," *Electrochimica Acta*, **44** (1999) 4345–4356.

208. M. Keddam, C. Rakotomavo, and H. Takenouti, "Impedance of a Porous Electrode with an Axial Gradient of Concentration," *Journal of Applied Electrochemistry*, **14** (1984) 437–448.

209. A. Lasia, "Porous Eelectrodes in the Presence of a Concentration Gradient," *Journal of Electroanalytical Chemistry*, **428** (1997) 155–164.

210. C. Hitz and A. Lasia, "Experimental Study and Modeling of Impedance of the HER on Porous Ni Electrodes," *Journal of Electroanalytic Chemistry*, **500** (2001) 213–222.

211. C. Deslouis and B. Tribollet, "Flow Modulation Technique and EHD Impedance: A Tool for Electrode Processes and Hydrodynamic Studies," *Electrochimica Acta*, **35** (1990) 1637–1648.

212. O. Aaboubi, I. Citti, J.-P. Chopart, C. Gabrielli, A. Olivier, and B. Tribollet, "Thermoelectrochemical Transfer Function under Thermal Laminar Free Convection at a Vertical Electrode," *Journal of The Electrochemical Society*, **147** (2000) 3808–3815.

213. W. J. Albery and M. L. Hitchman, *Ring-Disc Electrodes* (Oxford, UK: Clarendon Press, 1971).

214. N. Benzekri, M. Keddam, and H. Takenouti, "AC Response of a Rotating Ring-Disk Electrode: Application to 2-D and 3-D Film Formation in Anodic Processes," *Electrochimica Acta*, **34** (1989) 1159–1166.

215. I. Epelboin, C. Gabrielli, M. Keddam, and H. Takenouti, "A Model of the Anodic Behavior of Iron in Sulphuric Acid Medium," *Electrochimica Acta*, **20** (1975) 913–916.

216. R. Antaño-Lopez, M. Keddam, and H. Takenouti, "A New Experimental Approach to the Time-Constants of Electrochemical Impedance: Frequency Response of the Double Layer Capacitance," *Electrochimica Acta*, **46** (2001) 3611–3617.

217. I. Citti, O. Aaboubi, J. P. Chopart, C. Gabrielli, A. Olivier, and B. Tribollet, "Impedance for Laminar Free Convection and Thermal Convection to a Vertical Electrode," *Journal of The Electrochemical Society*, **144** (1997) 2263–2271.

218. Z. A. Rotenberg, "Thermoelectrochemical Impedance," *Electrochimica Acta*, **42** (1997) 793–799.

219. S. L. Marchiano and A. J. Arvia, "Diffusional Flow under Non-Isothermal Laminar Free Convection at a Thermal Convective Electrode," *Electrochimica Acta*, **13** (1968) 1657–1669.

220. L. M. Peter, J. Li, R. Peat, H. J. Lewerenz, and J. Stumper, "Frequency Response Analysis of Intensity Modulated Photocurrents at Semiconductor Electrodes," *Electrochimica Acta*, **35** (1990) 1657–1664.

221. I. E. Vermeir, W. P. Gomes, B. H. Erné, and D. Vanmaekelbergh, "The Anodic Dissolution of InP Studied by the Optoelectrical Impedance Method: 2. Interaction between Anodic and Chemical Etching of InP in Iodic Acid Solutions," *Electrochimica Acta*, **38** (1993) 2569–2575.

222. S. Bruckenstein, M. I. Bellavan, and B. Miller, "Electrochemical Response of a Disk Electrode to Angular Velocity Steps," *Journal of The Electrochemical Society*, **120** (1973) 1351–1356.

223. K. Tokuda, S. Bruckenstein, and B. Miller, "The Frequency Response of Limiting Currents to Sinusoidal Speed Modulation at a Rotating Disk Electrode," *Journal of The Electrochemical Society*, **122** (1975) 1316–1322.

224. C. Deslouis, C. Gabrielli, P. S.-R. Fanchine, and B. Tribollet, "Electrohydrodynamical Impedance on a Rotating Disk Electrode," *Journal of The Electrochemical Society*, **129** (1982) 107–118.

225. D. T. Schwartz, "Multilayered Alloys Induced by Fluctuating Flow," *Journal of The Electrochemical Society*, **136** (1989) 53C–56C.

226. D. T. Schwartz, T. J. Rehg, P. Stroeve, and B. G. Higgins, "Fluctuating Flow with Mass-Transfer Induced by a Rotating-Disk Electrode with a Superimposed Time-Periodic Modulation," *Physics of Fluids A–Fluid Dynamics*, **2** (1990) 167–177.

227. B. Tribollet and J. S. Newman, "The Modulated Flow at a Rotating Disk Electrode," *Journal of The Electrochemical Society*, **130** (1983) 2016–2026.

228. J. S. Newman, "Numerical Solution of Coupled, Ordinary Differential Equations," *Industrial and Engineering Chemistry Fundamentals*, **7** (1968) 514–517.

229. C. Deslouis and B. Tribollet, "Flow Modulation Techniques in Electrochemistry," in *Advances in Electrochemical Science and Engineering*, H. Gerischer and C. W. Tobias, editors (New York: VCH Publishers, 1991) 205–264.

230. E. M. Sparrow and J. L. Gregg, "Flow about an Unsteadily Rotating Disc," *Journal of the Aerospace Sciences*, **27** (1960) 252–256.

231. V. Sharma, "Flow and Heat-Transfer Due to Small Torsional Oscillations of a Disk about a Constant Mean," *Acta Mechanica*, **32** (1979) 19–34.

232. A. Caprani, C. Deslouis, S. Robin, and B. Tribollet, "Transient Mass Transfer at Partially Blocked Electrodes: A Way to Characterize Topography," *Journal of Electroanalytical Chemistry*, **238** (1987) 67–91.

233. C. Deslouis, O. Gil, and B. Tribollet, "Frequency Response of Electrochemical Sensors to Hydrodynamic Fluctuations," *Journal of Fluid Mechanics*, **215** (1990) 85–100.

234. C. R. S. Silva, O. E. Barcia, O. R. Mattos, and C. Deslouis, "Partially Blocked Surface Studied by the Electrohydrodynamic Impedance," *Journal of Electroanalytical Chemistry*, **365** (1994) 133–138.

235. C. Deslouis and B. Tribollet, "Recent Developments in the Electro-Hydrodynamic (EHD) Impedance Technique," *Journal of Electroanalytical Chemistry*, **572** (2004) 389–398.

236. C. Deslouis, N. Tabti, and B. Tribollet, "Characterization of Surface Roughness by EHD Impedance," *Journal of Applied Electrochemistry*, **27** (1997) 109–111.

237. C. Deslouis, D. Festy, O. Gil, G. Rius, S. Touzain, and B. Tribollet, "Characterization of Calcareous Deposits in Artificial Sea Water by Impedance Techniques: I. Deposit of $CaCO_3$ without $Mg(OH)_2$," *Electrochimica Acta*, **43** (1998) 1891–1901.

238. G. Baril, C. Blanc, and N. Pébère, "AC Impedance Spectroscopy in Characterizing Time-Dependent Corrosion of AZ91 and AM50 Magnesium Alloys Characterization with Respect to Their Microstructures," *Journal of The Electrochemical Society*, **148** (2001) B489–B496.

239. M. Durbha, *Influence of Current Distributions on the Interpretation of the Impedance Spectra Collected for Rotating Disk Electrode*, Ph.D. dissertation, University of Florida, Gainesville, Florida (1998).

240. M. E. Orazem, P. Agarwal, A. N. Jansen, P. T. Wojcik, and L. H. García-Rubio, "Development of Physico-Chemical Models for Electrochemical Impedance Spectroscopy," *Electrochimica Acta*, **38** (1993) 1903–1911.

241. M. E. Orazem and B. Tribollet, "An Integrated Approach to Electrochemical Impedance Spectroscopy," *Electrochimica Acta*, (2008) in press.

242. A. N. Jansen, *Deep-Level Impedance Spectroscopy of Electronic Materials*, Ph.D. dissertation, University of Florida, Gainesville, Florida (1992).

243. J. R. Macdonald and J. L. D. Potter, "A Flexible Procedure for Analyzing Impedance Spectroscopy Results: Description and Illustrations," *Solid State Ionics*, **23** (1987) 61–79.

244. P. R. Beington, *Data Reduction and Error Analysis for the Physical Sciences* (New York: McGraw-Hill, 1969).

245. G. A. F. Seber, *Linear Regression Analysis* (New York: John Wiley & Sons, 1977).

246. H. W. Sorenson, *Parameter Estimation: Principles and Problems* (New York: Marcel Dekker, 1980).

247. N. R. Draper and H. Smith, *Applied Regression Analysis*, 3rd edition (New York: Wiley Interscience, 1998).

248. W. Press, S. A. Teukolsky, W. T. Vetterling, and B. P. Flannery, *Numerical Recipes in C: the Art of Scientific Computing*, 2nd edition (New York: Cambridge University Press, 1992).

249. A. M. Legendre, *Nouvelles Méthodes pour la Détermination des Orbites des Comètes: Appendice sur la Méthode des Moindres Carrés* (Paris: Courcier, 1806).

250. C. F. Gauss, "Theoria Combinationis Observationum Erroribus Minimis Obnoxiae," *Werke*, **Bd. 4** (1821) 3–26.

251. C. F. Gauss, "Supplementum Theoriae Combinationis Observationum Erroribus Minimis Obnoxiae," *Werke*, **Bd. 4** (1826) 104–108.

252. R. de L. Kronig, "Dispersionstheorie im Röntgengebeit," *Physik Zeitschrift*, **30** (1929) 521–522.

253. J. R. Macdonald, "Impedance Spectroscopy: Old Problems and New Developments," *Electrochimica Acta*, **35** (1990) 1483–1492.

254. S. L. Carson, M. E. Orazem, O. D. Crisalle, and L. H. García-Rubio, "On the Error Structure of Impedance Measurements: Simulation of Frequency Response Analysis (FRA) Instrumentation," *Journal of The Electrochemical Society*, **150** (2003) E477–E490.

255. S. L. Carson, M. E. Orazem, O. D. Crisalle, and L. H. García-Rubio, "On the Error Structure of Impedance Measurements: Simulation of Phase Sensitive Detection (PSD) Instrumentation," *Journal of The Electrochemical Society*, **150** (2003) E491–E500.

256. W. Press, S. Teukolsky, W. Vetterling, and B. Flannery, *Numerical Recipes in C*, 2nd edition (Cambridge: Cambridge University Press, 1992).

257. J. R. Macdonald and W. J. Thompson, "Strongly Heteroscedastic Nonlinear Regression," *Communications in Statistics: Simulation and Computation*, **20** (1991) 843–885.

258. A. M. Awad, "Properties of the Akaike Information Criterion," *Microelectronics and Reliability*, **36** (1996) 457–464.

259. T.-J. Wu and A. Sepulveda, "The Weighted Average Information Criterion for Order Selection in Time Series and Regression Models," *Statistics & Probability Letters*, **39** (1998) 1–10.

260. Y. Sakamoto, M. Ishiguso, and G. Kitigawa, *Akaike Information Criterion Statistics* (Boston, MA: D. Reidel, 1986).

261. B. Robertson, B. Tribollet, and C. Deslouis, "Measurement of Diffusion Coefficients by DC and EHD Electrochemical Methods," *Journal of The Electrochemical Society*, **135** (1988) 2279–2283.

262. P. Agarwal, M. E. Orazem, and L. H. García-Rubio, "Measurement Models for Electrochemical Impedance Spectroscopy: 3. Evaluation of Consistency with the Kramers-Kronig Relations," *Journal of The Electrochemical Society*, **142** (1995) 4159–4168.

263. M. Durbha and M. E. Orazem, "Current Distribution on a Rotating Disk Electrode Below the Mass-Transfer Limited Current: Correction for Finite Schmidt Number and Determination of Surface Charge Distribution," *Journal of The Electrochemical Society*, **145** (1998) 1940–1949.

264. P. W. Appel, *Electrochemical Systems: Impedance of a Rotating Disk and Mass Transfer in Packed Beds*, Ph.D. dissertation, University of California, Berkeley, Berkeley, California (1976).

265. M. Durbha, M. E. Orazem, and B. Tribollet, "A Mathematical Model for the Radially Dependent Impedance of a Rotating Disk Electrode," *Journal of The Electrochemical Society*, **146** (1999) 2199–2208.

266. C. Gabrielli, F. Huet, and M. Keddam, "Investigation of Electrochemical Processes by an Electrochemical Noise-Analysis: Theoretical and Experimental Aspects in Potentiostatic Regime," *Electrochimica Acta*, **31** (1986) 1025–1039.

267. C. Gabrielli, F. Huet, and M. Keddam, "Fluctuations in Electrochemical Systems: 1. General-Theory on Diffusion-Limited Electrochemical Reactions," *Journal of Chemical Physics*, **99** (1993) 7232–7239.

268. C. Gabrielli, F. Huet, and M. Keddam, "Fluctuations in Electrochemical Systems: 2. Application to a Diffusion-Limited Redox Process," *Journal of Chemical Physics*, **99** (1993) 7240–7252.

269. U. Bertocci and F. Huet, "Noise Resistance Applied to Corrosion Measurements: III. Influence of Instrumental Noise on the Measurements," *Journal of The Electrochemical Society*, **144** (1997) 2786–2793.

270. G. E. P. Box, J. S. Hunter, and W. G. Hunter, *Statistics for Experimenters: An Introduction to Design, Data Analysis and Model Building* (New York: John Wiley & Sons, 1978).

271. P. Zoltowski, "The Error Function for Fitting of Models to Immitance Data," *Journal of Electroanalytical Chemistry*, **178** (1984) 11–19.

272. B. Boukamp, "A Package for Impedance/Admittance Data Analysis," *Solid State Ionics, Diffusion & Reactions*, **18-19** (1986) 136–140.

273. J. R. Macdonald, *CNLS (Complex Nonlinear Least Squares) Immittance Fitting Program LEVM Manual: Version 7.11*, Houston, Texas (1999).

274. J. R. Dygas and M. W. Breiter, "Variance of Errors and Elimination of Outliers in the Least Squares Analysis of Impedance Spectra," *Electrochimica Acta*, **44** (1999) 4163–4174.

275. E. V. Gheem, R. Pintelon, J. Vereecken, J. Schoukens, A. Hubin, P. Verboven, and O. Blajiev, "Electrochemical Impedance Spectroscopy in the Presence of Non-Linear Distortions and Non-Stationary Behavior: I. Theory and Validation," *Electrochimica Acta*, **49** (2006) 4753–4762.

276. E. V. Gheem, R. Pintelon, A. Hubin, J. Schoukens, P. Verboven, O. Blajiev, and J. Vereecken, "Electrochemical Impedance Spectroscopy in the Presence of Non-Linear Distortions and Non-Stationary Behavior: II. Application to Crystallographic Pitting Corrosion of Aluminum," *Electrochimica Acta*, **51** (2006) 1443–1452.

277. M. E. Orazem, T. E. Moustafid, C. Deslouis, and B. Tribollet, "The Error Structure of Impedance Spectroscopy Measurements for Systems with a Large Ohmic Resistance with Respect to the Polarization Impedance," *Journal of The Electrochemical Society*, **143** (1996) 3880–3890.

278. P. Agarwal, O. C. Moghissi, M. E. Orazem, and L. H. García-Rubio, "Application of Measurement Models for Analysis of Impedance Spectra," *Corrosion*, **49** (1993) 278–289.

279. B. A. Boukamp and J. R. Macdonald, "Alternatives to Kronig-Kramers Transformation and Testing, and Estimation of Distribtuions," *Solid State Ionics*, **74** (1994) 85–101.

280. B. A. Boukamp, "A Linear Kronig-Kramers Transform Test for Immittance Data Validation," *Journal of The Electrochemical Society*, **142** (1995) 1885–1894.

281. P. K. Shukla, M. E. Orazem, and O. D. Crisalle, "Validation of the Measurement Model Concept for Error Structure Identification," *Electrochimica Acta*, **49** (2004) 2881–2889.

282. M. H. A. Kramers, "La Diffusion de la Lumière pas les Atomes," in *Atti Congresso Internazionale Fisici, Como*, volume 2 (1927) 545–557.

283. H. M. Nussenzveig, *Causality and Dispersion Relations* (New York: Academic Press, 1972).

284. W. Ehm, H. Gohr, R. Kaus, B. Roseler, and C. A. Schiller, "The Evaluation of Electrochemical Impedance Spectra Using a Modified Logarithmic Hilbert Transform," *ACH-Models In Chemistry*, **137** (2000) 145–157.

285. Q.-A. Huang, R. Hui, B. Wang, and J. Zhang, "A Review of AC Impedance Modeling and Validation in SOFC Diagnosis," *Electrochimica Acta*, **52** (2007) 8144–8164.

286. M. E. Orazem, P. Agarwal, and L. H. García-Rubio, "Critical Issues Associated with Interpretation of Impedance Spectra," *Journal of Electroanalytical Chemistry and Interfacial Electrochemistry*, **378** (1994) 51–62.

287. M. E. Orazem, "A Systematic Approach toward Error Structure Identification for Impedance Spectroscopy," *Journal of Electroanalytical Chemistry*, **572** (2004) 317–327.

288. J. R. Dygas and M. W. Breiter, "Measurements of Large Impedances in a Wide Temperature and Frequency Range," *Electrochimica Acta*, **41** (1996) 993–1001.

289. S. K. Roy and M. E. Orazem, "Error Analysis for the Impedance Response of PEM Fuel Cells," *Journal of The Electrochemical Society*, **154** (2007) B883–B891.

290. R. Makharia, M. F. Mathias, and D. R. Baker, "Measurement of Catalyst Layer Electrolyte Resistance in PEFCs using Electrochemical Impedance Spectroscopy," *Journal of the Electrochemical Society*, **152** (2005) A970–A977.

291. O. Antoine, Y. Bultel, and R. Durand, "Oxygen Reduction Reaction Kinetics and Mechanism on Platinum Nanoparticles Inside Nafion," *Journal of Electroanalytical Chemistry*, **499** (2001) 85–94.

292. Y. Bultel, L. Genies, O. Antoine, P. Ozil, and R. Durand, "Modeling Impedance Diagrams of Active Layers in Gas Diffusion Electrodes: Diffusion, Ohmic Drop Effects and Multistep Reactions," *Journal of Electroanalytical Chemistry*, **527** (2002) 143–155.

293. S. K. Roy, M. E. Orazem, and B. Tribollet, "Interpretation of Low-Frequency Inductive Loops in PEM Fuel Cells," *Journal of The Electrochemical Society*, **154** (2007) B1378–B1388.

294. R. M. Darling and J. P. Meyers, "Kinetic Model of Platinum Dissolution in PEMFCs," *Journal of the Electrochemical Society*, **150** (2003) A1523–A1527.

295. C. F. Zinola, J. Rodriguez, and G. Obal, "Kinetic of Molecular Oxygen Electroreduction on Platinum Modified by Tin Underpotential Deposition," *Journal of Applied Electrochemistry*, **31** (2001) 1293–1300.

296. A. Damjanovic and V. Brusic, "Electrode Kinetic of Oxygen Reduction on Oxide Free Pt Electrode," *Electochimica Acta*, **12** (1967) 615–628.

297. V. O. Mittal, H. R. Kunz, and J. M. Fenton, "Is H_2O_2 Involved in the Membrane Degradation Mechanism in PEMFC?" *Electrochemical and Solid-State Letters*, **9** (2006) A229–A302.

Electrochemical Impedance Spectroscopy
by Mark E. Orazem and Bernard Tribollet

Index

Numbers written in bold font refer to the page where the corresponding entry is defined. Numbers followed by an "e" refer to the page where the corresponding entry can be found in an example, and numbers followed by a "p" refer to the page where the corresponding entry can be found in a problem.

activation energy
    controlled process, 313, 453e
    diffusion, 278
    electrochemical, **82**, 267
    graphical method, 357–360
admittance, **319**
    dielectrics, 323e
adsoption
    reaction intermediates
        history, xxvi
        kinetics, 165, 176e, 173–179, 180, 181p, 265, 266, 274–277, 306p, 456e
    specific
        absence of, 227, 295
        history, xxvi
        partial blocking, 296
Argand diagram, **5**, 12, 13
axisymmetric electrode, 184, 205

bias error, 133, 147, 149–151, **407**, 414–418, 450
blind men, *see* elephant, parable of
Boltzmann
    constant, **212**
    distribution, **213**, 225–230
Butler-Volmer kinetics, **78**, 111

capacitance transfer function, 275–277
Cauchy's integral formula, 469e
Cauchy's theorem, 469e
Central Limit Theorem, 37, **39**, 39–42
charge
    dielectric, 95
    double layer, 80, 91–95
    electric, 62, 74
charge-transfer
    reaction, 21p, 74, 163–179, 234
    resistance, 20p, 96p, 112p, 136p, 155, 165, 188e, 245–246
chemical potential, 75
chi-squared test, 56
circuit calculations
    Bode representation, 68e
    nested elements, 68e
    parallel, 66e
    series, 65e
coating
    capacitance, 95, 128p
    EHD response, 299–302, 303e
    impedance, 158–159, 161e, 162p, 191, 192e, 194e, 194–197, 256e, 283
complex capacitance, **325**
    dielectrics, 328e
complex integration
    Cauchy's integral formula, 469e
    Cauchy's theorem, 469e
    poles, 471e
complex number, **5**
    de Moivre's theorem, 11e
    division, 7e
    exponential, 18e

    - multiplication, 6e
    - polar coordinates, 10e
    - rectangular coordinates, 9e
    - roots, 12e
    - square roots, 12e
- complex variables, 4–20
- constant-phase-element (CPE)
    - application, 233–237, 334–350, 382p, 450
    - concept, 68
    - formula, 21p, 234
    - history, xxvi, xxix
    - regression, 395–402
- convective diffusion impedance
    - impinging jet, 207
    - rotating cylinder, 209
    - rotating disk, 201–204
- convective-diffusion impedance
    - nonuniformly accessible electrode, 237–243
    - rotating cylinder, 209
- corrosion
    - cast iron, 255e
    - copper, 77, 84e, 181p, 306p
    - iron, 77
        - aerobic, 171e
        - anaerobic, 167e
    - magnesium, 176e, 181p, 345e
    - silver, 180p
    - with salt films, 159, 161e, 162p
- cross-covariance, **36**
- current distribution
    - mass-transfer-controlled, 90
    - nonuniform, 131, 209, 243
    - primary, 87–88
    - secondary, 89
    - tertiary, 90
- current follower, 100e

- deposition
    - zinc, 188e
- dielectric, 95
- dielectrics
    - admittance, 323e
    - complex capacitance, 328e
- differential equation
    - complex roots, 27e
    - diffusion, 25e, 27e, 30e
    - diffusion impedance, 32e
    - homogeneous, 23, 24, 25e, 26–28
    - linear ODE, 24e
    - nonhomogeneous, 23, 24e, 28–29
- diffusion impedance
    - convective
        - finite Schmidt number, 203–204, 207
        - impinging jet, 207
        - infinite Schmidt number, 203
        - Nernst hypothesis, 203
        - nonuniformly accessible electrode, 237–243
        - rotating cylinder, 209
        - rotating disk, 201–204
    - finite-length, 179e, 191–197, 421
    - nonuniformly accessible electrode, 237–243
    - rotating cylinder, 209
    - Warburg, xxv, 12e, 30e, 34p, 189–190, 241, 258, 329, 421
- distributed time constant
    - geometry-induced, 249e
    - mass transfer, 239e
    - porous electrode, 254, 255e
- distribution
    - Central Limit Theorem, 37, **39**, 39–42
    - current, *see* current distribution
    - normal, **37**
    - standard normal, **37**
- double layer, 80, 91–95

- effective capacitance, 329e
- electrical double layer, 80, 91–95
- electrochemical
    - reaction, 74, 163–179, 188e, 234, 245–246
- electrochemical interface, 101–103
- electrochemical kinetics, 84e

electrochemical potential, 75
  electrons, 212, 219–220
  equilibrium, 75, 95, 212
  expression, **219**
  gradient, 219–220
  relation to Fermi energy, 212
electrode
  axisymmetric, 184, 205
  impinging jet
    diffusion impedance, 207
    fluid mechanics, 206
    mass transfer, 206–207
    properties, 131
  nonuniformly accessible, 237–243
  ring-disk, 273–275
  rotating cylinder
    diffusion impedance, 209
    fluid mechanics, 207–209
    mass transfer, 209
    properties, 131
  rotating disk
    diffusion impedance, 201–204
    fluid mechanics, 199–200
    mass transfer, 200–201
    properties, 131
    state variables, 123
  rotating hemisphere
    properties, 131
electrogravimetry transfer function, 283–284
electrohydrodynamic impedance
  blocking, 303e
electrohydrodynamic transfer function, **293**
electroneutrality, **87**, 90, 91, 227
elephant, parable of, xxi–xxii
error propagation, 43–47, 58p
  linear, 43, 44e
  nonlinear, 45e
errors
  bias, 133, 147, 149–151, **407**, 414–418, 450
  fitting, **407**
  propagation, 43–47, 58p
  residual, **407**
  stochastic, 116, 133, 147–149, 204, 317, 338, 339, 364, 373–375, **407**, 408–414, 439–442, 450, 453
exchange current density, **78**, 79, 84, 85e, 89, 109, 152p
expectation, 35, **35**, 43, 407, 439–442
experimental systems
  calcareous deposits, 303e
  cathodic protection, 303e
  corrosion
    cast iron, 255e
    copper, 77, 84e, 181p, 306p
    iron, 77, 167e, 171e
    magnesium, 176e, 181p, 345e
    silver, 180p
    with salt films, 159, 161e, 162p
  deposition
    zinc, 188e
  dielectrics, 323e
  ferricyanide reduction
    diffusion with first-order reaction, 187e
    electrohydrodynamic impedance, 298, 417
    error structure, 51e
    kinetics, 81e
    rotating disk, 353–357, 362p, 386–402, 416
  ferrocyanide oxidation
    kinetics, 81e
    rotating disk, 362p
  GaAs, 214, 230p
    deep-level states, 223–225, 453e
    photoelectrochemical cells, 221–223
    Schottky diode, 357–361, 453e
  hydrogen evolution, 74
  oxygen evolution, 74, 77
  PEM fuel cell, 456e
  porous layers
    circuit model, 158–159
  transdermal drug delivery, 152p

F-test, 50–56, 58, 59p
Faraday
  cage, 149, **150**
  constant, **86**, 164, 274
Fermi energy, *see* electrochemical potential, **212**, 213
Fermi-Dirac distribution, **212**, 231p
ferricyanide reduction
  diffusion with first-order reaction, 187e
  electrohydrodynamic impedance, 298
  error structure, 51e
  kinetics, 81e
  rotating disk, 353–357, 362p, 386–402
    electrohydrodynamic impedance, 417
    impedance, 416
ferrocyanide oxidation
  kinetics, 81e
  rotating disk, 362p
finite-length diffusion impedance, 179e, 191–197, 421
fitting error, **407**
fluid mechanics
  impinging jet, 206
  rotating cylinder, 207–209
  rotating disk, 199–200

GaAs, 230p
galvanostat, 102
generalized transfer function, 265–269
graphical analysis
  admittance, 323e
  complex capacitance, 328e
  corrosion of Mg, 345e
  effective capacitance, 329e

Helmholtz double-layer, 93
Helmholtz plane, 80, 94
homogeneous
  differential equation, 4, 23, 24, 25e, 26–28
homogeneous reaction, 76, 256, 265
hydrogen evolution, 74
hypothesis tests, 47–56
  chi-squared, 56e, 56
  F-test, 50–56, 58, 59p
  Student's t-test, 49–50, 58, 59p
  t-test, 51e

imaginary number, **4**
immittance, **419**
impedance, **311**
impedance interpretation
  circuits, 161e
  kinetics, 167e, 171e, 176e
  mass transfer, 187, 188e, 192e, 194e, 198e
  Mott-Schottky plots, 229e
impedance measurement
  Fourier analysis, 121e
  linearity, 134e, 139e, 144e
  Lissajous analysis, 115e
impedance models
  convective diffusion
    finite Schmidt number, 203–204, 207
    impinging jet, 207
    infinite Schmidt number, 203
    Nernst hypothesis, 203
    nonuniformly accessible electrode, 237–243
    rotating cylinder, 209
    rotating disk, 201–204
  finite-length diffusion, 179e, 191–197, 421
  Warburg, xxv, 12e, 30e, 34p, 189–190, 241, 258, 329, 421
impinging jet electrode
  diffusion impedance, 207
  fluid mechanics, 206
  mass transfer, 206–207
  properties, 131
intermediates
  kinetics, 165, 176e, 173–179, 180, 181p, 265, 266, 274–277, 306p,

456e
intermediates, reaction
  history, xxvi
irrational number, **3**
IUPAC convention, 5

kinetics
  Butler-Volmer, **78**, 111
  reaction intermediates, 165, 176e, 173–179, 180, 181p, 265, 266, 274–277, 306p, 456e
  Tafel, 164–165, 167, 169, 171, 173, 178e, 188e, 457
  Tafel kinetics, **79**, 134e, 244–252
  Tafel slope, **78**, 109, 152p, 187e
Kramers-Kronig relations, 427–445
  application, 123, 150, 363, 387, 388, 408, 414–415
  history, xxvii, xxix
  measurement model, 393, 403, 423–425, 451–452, 456

mass transfer
  impinging jet, 206–207
  rotating cylinder, 209
  rotating disk, 200–201
mass-transfer-controlled current distribution, 90
mean, **35**
model identification, 453e
Mott-Schottky plots, 229e

negative feedback, 99e
Nernst hypothesis, 203
Nernst-Einstein equation, **220**
nonhomogeneous
  differential equation, 23, 24e, 28–29
nonuniform current distribution, 131, 209, 243
nonuniformly accessible electrode
  diffusion impedance, 237–243
normal distribution, **37**
number
  complex, **5**
  imaginary, **4**
  irrational, **3**
  rational, **3**
  real, **5**

operational amplifier
  current follower, 100e
  electrochemical interface, 101–103
  galvanostat, 102
  negative feedback, 99e
  potentiostat, 101–103
  voltage adder, 100e
oxygen evolution, 74, 77

partial differential equation
  similarity transformations, 29–32
PEM fuel cell, 456e
photoelectrochemical cells, 221–223
  deep-level states, 223–225
photoelectrochemical transfer function, 282–283
poles on a real axis, 471e
porous electrode
  corrosion, 255e
  de Levie Formula, 254e
porous layers
  circuit model, 158–159
potentiostat, 101–103
primary current distribution, 87–88
proposed experiments, 456e

rational number, **3**
reaction
  homogeneous, 76, 256, 265
reaction intermediates
  history, xxvi
  kinetics, 165, 176e, 173–179, 180, 181p, 265, 266, 274–277, 306p, 456e
real number, **5**
residual error, **407**
ring-disk transfer function, 273–275
rotating cylinder
  diffusion impedance, 209
  fluid mechanics, 207–209

- mass transfer, 209
- properties, 131

rotating disk electrode
- diffusion impedance, 201–204
- fluid mechanics, 199–200
- mass transfer, 200–201
- properties, 131
- state variables, 123

rotating hemisphere
- properties, 131

Schottky diode
- GaAs, 453e
  - Arrhenius-based plots, 357–360
  - Mott-Schottky Plots, 360–361

secondary current distribution, 89
similarity transformations, 29–32
standard deviation, **36**
standard error, **36**
standard normal distribution, **37**
stochastic error, 116, 133, 147–149, 204, 317, 338, 339, 364, 373–375, **407**, 408–414, 439–442, 450, 453
Student's t-test, 49–50, 58, 59p

Tafel kinetics, **79**, 134e, 164–165, 167, 169, 171, 173, 178e, 188e, 244–252, 457
Tafel slope, **78**, 109, 152p, 187e
tertiary current distribution, 90
thermoelectrochemical transfer function, 278–281
transdermal drug delivery, 152p
transfer function
- admittance, **319**
- capacitance, 275–277
- complex capacitance, **325**
- electrogravimetry, 283–284
- electrohydrodynamic, **293**
- general approach, 265–269
- impedance, **311**
- photoelectrochemical, 282–283
- ring-disk, 273–275
- thermoelectrochemical, 278–281

variance, **35**
variate, **35**
Voigt model
- even and odd properties, 429, 430e
- impedance, 65e, 375
- inductive loops, 380
- Kramers-Kronig analysis, 444–445
- nonlinearity, 365e
- regression, 380, 382p, 393–395, 420–425, 444–445
- statistical analysis, 56e, 393–395, 420–425

voltage adder, 100e

Warburg impedance, xxv, 12e, 30e, 34p, 189–190, 241, 258, 329, 421

zinc deposition, 188e